NEW PERSPECTIVES ON SOLAR PROMINENCES
IAU Colloquium 167

Edited by
David Webb, David Rust, and Brigitte Schmieder

REPORT DOCUMENTATION PAGE

Form Approved OMB No. 0704-0188

Public reporting burden for this collection of information is estimated to average 1 hour per response, including the time for reviewing instructions, searching existing data sources, gathering and maintaining the data needed, and completing and reviewing the collection of information. Send comments regarding this burden estimate or any other aspect of this collection of information, including suggestions for reducing this burden to Washington Headquarters Services, Directorate for Information Operations and Reports, 1215 Jefferson Davis Highway, Suite 1204, Arlington, VA 22202-4302, and to the Office of Management and Budget, Paperwork Reduction Project (0704-0188), Washington, DC 20503.

1. AGENCY USE ONLY (Leave blank)	2. REPORT DATE 13 October 1998	3. REPORT TYPE AND DATES COVERED Conference Proceedings

4. TITLE AND SUBTITLE

IAU Colloquium 167: New Perspectives on Solar Prominences

5. FUNDING NUMBERS

F6170897W037

6. AUTHOR(S)

Conference Committee

7. PERFORMING ORGANIZATION NAME(S) AND ADDRESS(ES)

Observatoire de Paris-Meudon
5 Place Janssen
Meudon Cedex Principal 92195
France

8. PERFORMING ORGANIZATION REPORT NUMBER

N/A

9. SPONSORING/MONITORING AGENCY NAME(S) AND ADDRESS(ES)

EOARD
PSC 802 BOX 14
FPO 09499-0200

10. SPONSORING/MONITORING AGENCY REPORT NUMBER

CSP 97-1007

11. SUPPLEMENTARY NOTES

12a. DISTRIBUTION/AVAILABILITY STATEMENT

Approved for public release; distribution is unlimited.

12b. DISTRIBUTION CODE

A

13. ABSTRACT (Maximum 200 words)

The Final Proceedings for IAU Colloquium 167: New Perspectives on Solar Prominences, 28 April 1997 - 4 May 1997

IAU Colloquium 167 on "New Perspectives on Solar Prominences" was held in Aussois, France from April 28 to May 3, 1997. The purpose of the meeting was to review, discuss and try to understand the new observations of prominences and their environment. One hundred and seven scientists from twenty-one countries participated.

14. SUBJECT TERMS

EOARD Geophysics, Metrology & Calibration, Solar Physics

15. NUMBER OF PAGES

515

16. PRICE CODE

N/A

17. SECURITY CLASSIFICATION OF REPORT	18. SECURITY CLASSIFICATION OF THIS PAGE	19. SECURITY CLASSIFICATION OF ABSTRACT	20. LIMITATION OF ABSTRACT
UNCLASSIFIED	UNCLASSIFIED	UNCLASSIFIED	UL

NSN 7540-01-280-5500

Standard Form 298 (Rev. 2-89)
Prescribed by ANSI Std. 239-18
298-102

NEW PERSPECTIVES ON SOLAR PROMINENCES
IAU Colloquium 167

A SERIES OF BOOKS ON RECENT DEVELOPMENTS IN ASTRONOMY AND ASTROPHYSICS

A SERIES OF BOOKS ON RECENT DEVELOPMENTS IN ASTRONOMY AND ASTROPHYSICS

Vol. 87-New Observing Modes for the Next Century
ed. Todd Boroson, John Davies, and Ian Robson   ISBN 1-886733-08-2

Vol. 88-Clusters, Lensing, and the Future of the Universe
ed. Virginia Trimble and Andreas Reisenegger   ISBN 1-886733-09-0

Vol. 89-Astronomy Education: Current Developments, Future Coordination
ed. John R. Percy   ISBN 1-886733-10-4

Vol. 90-The Origins, Evolution, and Destinies of Binary Stars in Clusters
ed. E. F. Milone and J. -C. Mermilliod   ISBN 1-886733-11-2

Vol. 91-Barred Galaxies, IAU Colloquium 157
ed. R. Buta, D. A. Crocker, and B. G. Elmegreen   ISBN 1-886733-12-0

Vol. 92-Formation of the Galactic Halo--Inside and Out
ed. H. L. Morrison and A. Sarajedini   ISBN 1-886733-13-9

Vol. 93-Radio Emission from the Stars and the Sun
ed. A. R. Taylor and J. M. Paredes   ISBN 1-886733-14-7

Vol. 94-Mapping, Measuring, and Modelling the Universe
ed. Peter Coles, Vicent Martinez, and Maria-Jesus Pons-Borderia   ISBN 1-886733-15-5

Vol. 95-Solar Drivers of Interplanetary and Terrestrial Disturbances: Proceedings of 16th
International Workshop, National Solar Observatory/Sacramento Peak
ed. K.S. Balasubramaniam, S. L. Keil, and R. N. Smartt   ISBN 1-886733-16-3

Vol. 96-Hydrogen-Deficient Stars
ed. C. S. Jeffery and U. Heber   ISBN 1-886733-17-1

Vol. 97-Polarimetry of the Interstellar Medium
ed. W. G. Roberge and D. C. B. Whittet   ISBN 1-886733-18-X

Vol. 98-From Stars to Galaxies: The Impact of Stellar Physics on Galaxy Evolution
ed. Claus Leitherer, Uta Fritze-von Alvensleben, and John Huchra   ISBN 1-886733-19-8

Vol. 99-Cosmic Abundances: Proceedings of the 6th Annual October Astrophysics Conference
ed. Stephen S. Holt and George Sonneborn   ISBN 1-886733-20-1

Vol. 100-Energy Transport in Radio Galaxies and Quasars
ed. P. E. Hardee, A. H. Bridle, and J. A. Zensus   ISBN 1-886733-21-X

Vol. 101-Astronomical Data Analysis Software and Systems V
ed. George H. Jacoby and Jeannette Barnes   ISSN   1080-7926

Vol. 102-The Galactic Center, 4th ESO/CTIO Workshop
ed. Roland Gredel   ISBN 1-886733-22-8

Vol. 103-The Physics of Liners in View of Recent Observations
ed. M. Eracleous, A. Koratkar, C. Leitherer, and L. Ho   ISBN 1-886733-23-6

Vol. 104-Physics, Chemistry, and Dynamics of Interplanetary Dust, IAU Colloquium 150
ed. Bo A. S. Gustafson and Martha S. Hanner   ISBN 1-886733-24-4

Vol. 105-Pulsars: Problems and Progress, IAU Colloquium 160
ed. M. Bailes, S. Johnston, and M.A. Walker   ISBN 1-886733-25-2

Vol. 106-Minnesota Lectures on Extragalactic Neutral Hydrogen
ed. Evan D. Skillman   ISBN 1-886733-26-0

Vol. 107-Completing the Inventory of the Solar System: A Symposium held in conjunction with
the 106th Annual Meeting of the ASP
ed. Terrence W. Rettig and Joseph M. Hahn   ISBN 1-886733-27-9

Volume 150

NEW PERSPECTIVES ON SOLAR PROMINENCES
IAU Colloquium 167

Proceedings of a meeting held in Aussois, France
28 April - 4 May 1997

**Edited by
David Webb, David Rust, and Brigitte Schmieder**

Table of Contents

Stellar Filaments

Instrumentation

Preface

IAU Colloquium 167 on "New Perspectives on Solar Prominences" was held in Aussois, France from April 28 to May 3, 1997. The purpose of the meeting was to review, discuss and try to understand the new observations of prominences and their environment. One hundred and seven scientists from twenty-one countries participated. The sponsors were the International Astronomical Union (IAU), the Scientific Committee for Solar-Terrestrial Physics (SCOSTEP), the European Office for Aerospace Research and Development (EOARD), l'Observatoire de Paris, le Centre National de la Recherche Scientifique (CNRS), le Commissariat à l'Énergie Atomique (CEA), and le Centre National d'Etudes Spatiales (CNES).

The meeting site was the Centre Paul Langevin, a conference center run by CNRS in Aussois in the French Alps. Scientific sessions were held each morning and early evening. In the afternoons, participants were free to hike in the Alps or linger over poster papers. The afternoon breaks in the alpine air kept the participation level in the scheduled sessions high and the discussions unusually lively. Late evenings were filled with videos of erupting prominences, both simulated and real, a banquet, and a well-received concert of baroque and classical music played for us by several of the participants – Veronique Bommier, Bernard Foing, Petr Heinzel, Pierre Mein, and Jean Francois Mein.

Prominences have been known from eclipse observations for several centuries. Twentieth-century research on them began with the invention of the spectroheliograph, which led to the subsequent pioneering studies by Lucien d'Azambuja and his colleagues at the Observatory of Paris at Meudon. The spectroheliograph enabled d'Azambuja to see prominences without an eclipse, and to describe their characteristics and global distribution in detail. The Colloquium and the Proceedings are dedicated to d'Azambuja and his work, which is discussed in the introductory article of this book.

Measurements of magnetic fields in prominences, begun in the 1960s, enabled realistic testing of prominence models proposed in the 1950s. The magnetic field observations became the starting point for all modern discussions of the physical processes involved in the birth and stability of prominences and of their dissolution and ejection from the Sun. Prominence material is either hoisted from the chromosphere by emerging magnetic fields or siphoned up along magnetic flux tubes. Or it may condense from the corona during magnetic field reconnection or contraction. Advocates of all these possibilities attended the colloquium, leading to spirited debates about prominence origins. On the other hand, prominence stability was hardly touched on, possibly because the most popular magnetic models, such as those originally proposed by Kippenhahn and Schlüter and Kuperus and Raadu, have been shown to provide prominences with stable support against gravity and a shield against thermal conduction from the corona.

Since early 1996, space observations of prominences have been available on a daily basis from the Solar and Heliospheric Observatory. Conference participants were dazzled by the images and other data from the SOHO EIT (Extreme-

Ultraviolet Imaging Telescope), LASCO (Large Angle Spectrometric Corona-graph), SUMER (Solar Untraviolet Measurements of Emitted Radiation), and UVCS (Ultraviolet Coronagraph Spectrometer for SOHO) instruments. An EIT image of a quiescent prominence obtained on June 23, 1997 graces the cover of this book. Results of analyses of the SOHO data are presented throughout this book and are yielding a much clearer picture than before of how prominences interact with the corona.

A highlight of the colloquium was discussion of the new evidence for a global pattern of helical magnetic fields in the solar atmosphere, as revealed by the distribution of filaments, north and south of the equator, according to their chirality. It is now clear that the helical fields in prominences can help us to understand the solar dynamo, which drives the 22-year solar magnetic cycle.

A special highlight of the Colloquium was the session on stellar promi-nences. Evidence of prominence-like clouds of material was reported to have been detected in a few active field dwarf stars. These are rapid rotators, and the prominences are often in Keplerian orbits. Patrick Brendan Byrne led the discussions. Tragically, while this volume was being edited, Dr. Byrne died while observing with the Herschel Telescope at the Observatorio de Roque de Los Muchachos in La Palma (Canary Islands). He passed away just days before celebrating his 50th birthday, at the peak of an intense and scientifically fruitful life. The community of his colleagues and friends mourns the loss of one of our science's most active and competent members. He entered this research field when he organized with Marcello Rodono IAU Colloquium 71 on "Activity in Red Dwarf Stars". He co-edited the conference proceedings, a hefty 668-page book that is still quoted often. As Editors of the Colloquium 167 Proceedings, we have the privilege of printing Dr. Byrne's last paper, a review of the evidence for prominences on cool late-type stars.

Acknowledgments. Edward Cliver of the Air Force Research Laboratory originally suggested that a colloquium on prominences would be timely, and we are grateful for his help in making it happen. It takes months of work by many people to make a successful conference and we are especially grateful to the following: The members of the Local Organizing Committee – led by B. Schmieder and including T. Amari, K. Bocchialini, V. Bommier, P. Demoulin, J. M. Malherbe, Z. Mouradian and D. Webb – for making our meeting so pleasant and fruitful; E. Cliver (USA), O. Engvold (Norway), V. Gaizauskas (Canada), I. Kim (Russia), Z. Mouradian (France), G. Peres (Italy), T. Sakurai (Japan), R. Schwenn (Germany), and J-X. Wang (China) who served with us on the Scientific Organizing Committee and ensured a productive scientific meeting; M. Rodono for the Byrne tribute; and, finally, K. S. Balasubramaniam and John Mariska who provided invaluable advice on preparation of the manuscript.

Bedford, MA, USA   David Webb, David Rust and Brigitte Schmieder

April 1998

Workshop Participants

URSULA ALLEN, University of Colorado, Dept. of Physics, CB390,
   Boulder, CO 80309-0390, USA. E-mail: allenu@dosxx.colorado.edu

SPIRO K. ANTIOCHOS, Naval Research Lab, Code 7675, Washington,
   DC 20375-5352, USA. E-mail: antiochos@nrl.navy.mil

ULRICH ANZER, Max-Planck-Institut für Astrophysik, Karl-
   Schwarzschild-Str. 1, D-85740 Garching, Germany.
   E-mail: ula@mpa-garching.mpg.de

GUILLAUME AULANIER, Observatoire de Paris, LPSH-DASOP,
   F-92125 Meudon Cedex, France. E-mail: aulanier@mesopb.obspm.fr

JOSE LUIS BALLESTER, Universitat de les Illes Balears, Departament
   de Fisica, E-07071 Palma De Mallorca, Spain. E-mail: dfsjlb0.ps.uib.es

VLADIMIR BASHKIRTSEV, Inst. of Solar-Terrestrial Physics, P.O. Box
   4026, Irkutsk 33, 664033 Irkutsk, Russia. E-mail: root@sitmis.su

MITCHELL BERGER, University College London, Gower St., London
   WCIE GBT, UK. E-mail: mberger@math.ucl.ac.uk

KARINE BOCCHIALINI, Institut d'Astrophysique Spatiale, Bat. 121
   Université Paris XI, F-91405 Orsay Cedex, France.
   E-mail: bocchialini@ias.fr

VERONIQUE BOMMIER, Observatoire de Paris, Section de Meudon,
   DAMAP, 5 Place Jules Janssen, F-92195 Meudon Cedex, France.
   E-mail: veronique.bommier@obspm.fr

P. BRENDAN BYRNE, Armagh Observatory, College Hill, Armagh
   BT61 9DG, N. Ireland. E-mail: pbb@star.arm.ac.uk

DIRK CALLEBAUT, Physics Dept. UIA, University of Antwerp,
   Belgium. E-mail: calldirk@hhipe.uia.ac.be

NICHOLAS CARTLEDGE, Dept. of Mathematics, Univ. of St. Andrews,
   Fife, KY16 9SS, St. Andrews, UK. E-mail: nick@dcs.st-and.ac.uk

JAMES CHEN, Naval Research Lab, Code 6790, Washington, DC 20375,
   USA. E-mail: chen@ppdu.nrl.navy.mil

C. Z. CHENG, Princeton Plasma Physics Laboratory, P.O. Box 451,
   Princeton, NJ 08543-0451, USA. E-mail: fcheng@pppl.gov

FRANCA CHIUDERI-DRAGO, Univ. of Florence, Observatoire de Paris,
   L.P.S.H., 5 Place J. Janssen, F-92195, Meudon Cedex, France.
   E-mail: drago@mesioa.obspm.fr

GWANG-SON CHOE, Princeton Plasma Physics Laboratory, P.O. Box
   451, Princeton, NJ 08543, USA. E-mail: gchoe@pppl.gov

ANGELA CIARAVELLA, Harvard-Smithsonian Astrophysical Observatory,
   60 Garden St., Cambridge, MA, 02138, USA.
   E-mail: aciaravella@cfa.harvard.edu

HELEN COFFEY, World Data Center A for Solar-Terrestrial, Physics,
    NOAA, NGDC E/GC2, 325 Broadway, Boulder, CO 80303, USA.
    E-mail: hcoffey@ngdc.noaa.gov

CLAUS DE BOER, Max-Planck-Institut für Aeronomie, D-37191
    Katlenburg-Lindau, Germany. E-mail: cboer@osf1.mpae.gwdg.de

CECILE DELANNÉE, Institut d'Astrophysique de Paris (CNRS), 98 bis
    bd, Arago, F-75014 Paris, France. E-mail: delannee@iap.fr

PASCAL DÉMOULIN, Observatoire de Paris, Section de Meudon, L.P.S.H.
    -DASOP, 5 Place Jules Janssen, F-92195, Meudon Cedex,
    France. E-mail: demoulin@mesiob.obspm.fr

VLADIMIR N. DERMENDJIEV, Institute of Astronomy, Bulgarian
    Academy of Sciences, 72 Tzarigradsko chausee 1784, Sofia, Bulgaria.
    E-mail: vlderm@phys.acad.bg

DANA DOKOUPILOVÁ, Astronomical Observatory, Vsetínská 78, Valašské
    Meziříčí 757 01, Czech Republic

IVAN DOROTOVIČ, Slovak Central Observatory, P.O. Box 42, 947 01,
    Hurbanovo, Slovak Republic. E-mail: dorotovic@kemar.sk

CRISTIANA DUMITRACHE, Astronomical Institute of Romanian
    Academy, Str. Cutitul de Argint 5, 75212 Bucharest, Romania.
    E-mail: crisd@roimar.imar.ro

ODDBJORN ENGVOLD, University of Oslo, Inst. of Theoretical
    Astrophysics, P.O. Box 1029, Blindern, N-0315, Oslo, Norway.
    E-mail: oddbjorn.engvold@astro.uio.no

MIGUEL FERREIRA, University of St. Andrews, North Haugh, Fife
    KY16 9SS, St. Andrews, UK. E-mail: jmtdsf@st-andrews.ac.uk

BORIS FILIPPOV, Russian Academy of Sciences, IZMIRAN, 142092 Troitsk,
    Moscow Region, Russia. E-mail: bfilip@izmiran.troitsk.ru

BERNARD H. FOING, ESA Space Science, ESTEC/SO, Postbus 299,
    2200 AG Noordwijk, The Netherlands. E-mail: bfoing@estec.esa.nl

TERRY FORBES, EOS Inst., Morse Hall, Univ. of New Hampshire,
    Durham, NH 03824, USA. E-mail: terry.forbes@unh.edu

PETER FOUKAL, CRI, Inc., 21 Erie Street, Cambridge, MA 02139, USA.
    E-mail: pfoukal@world.std.com

VICTOR GAIZAUSKAS, Herzberg Inst. of Astroph., Nat. Res. Council of
    Canada, 100 Sussex Drive, Ottawa, Ontario, K1A 0R6 Canada.
    E-mail: vgaizauskas@solar.stanford.edu

KLAUS GALSGAARD, Dept. Math. and Computer Science, Univ. of St.
    Andrews, North Haugh, KY16 9SS, St. Andrews, UK.
    E-mail: klaus@dcs.st-and.ac.uk

NAT GOPALSWAMY, Dept. of Astronomy, University of Maryland,
    College Park, MD 20742, USA. E-mail: gopals@fugee.gsfc.nasa.gov

ALEXEY GORSHKOV, Sternberg Astronomical Institute, Universitetsky
    pr., 13 Moscow 119899, Russia. E-mail: gorshkov@sai.msu.su

S. S. GUPTA, Indian Institute of Astrophysics, Observatory, Kodaikanal
      624103, India. E-mail: ssg@iiap.ernet.in

KAREN HARVEY, Solar Physics Research Corp., 4720 Calle Desecada,
      Tucson, AZ 85718, USA. E-mail: kharvey@solar.stanford.edu

PETR HEINZEL, Astronomical Institute, Ondřejov, 25165 Ondřejov, Czech
      Republic. E-mail: pheinzel@asu.cas.cz

JEAN-CLAUDE HENOUX, Observatoire de Paris - Section de Meudon,
      L.P.S.H.-DASOP, 5 Place Jules Janssen, F-92195 Meudon Cedex,
      France. E-mail: henoux@mesiob.obspm.fr

EIJIRO HIEI, Meisei University, 2-1-1, Hodokubo, Hino, Tokyo 191, Japan.
      E-mail: hiei@corona.mtk.nao.ac.jp

ALAN HOOD, University of St. Andrews, Dept. of Mathematics and
      Computational Sciences, North Haugh, St. Andrews KY16 9SS, UK.
      E-mail: alan@dcs.st-and.ac.uk

BORIS IOSHPA, Izmiran, Troitsk, 142092 Moscow, Russia. E-mail:
      ioshpa@izmrian.troitsk.ru

MOIRA JARDINE, Univ. of St. Andrews, School of Physics & Astronomy,
      North Haugh, Fife, St. Andrews KY16 9SS UK.
      E-mail: mmj@st-and.ac.uk

JANA KASPAROVÁ, Astronomical Observatory, Valašské, Meziřičí, 75611,
      Valašská Polanka 75, Czech Republic.
      E-mail: kasparov@menza.mff.cuni.cz

JOSEF KHAN, ISAS, 3-1-1 Yoshinodai, Sagamihara-shi, Kanagawa-ken 229,
      Japan. E-mail: khan@isasxa.solar.isas.ac.jp

IRAIDA KIM, Sternberg State Astr. Inst., Moscow State Univ., Universitet-
      sky pr. 13, Moscow 119899, Russia. E-mail: kim@sai.msu.su

EDWARD KONONOVICH, Sternberg Astronomical Inst., Moscow State
      Univ., Universitetsky pr., 13, Moscow 119899 Russia.
      E-mail: konon@sai.msu.su

PAVEL KOTRČ, Astronomical Inst., Czech Academy of Sciences, CZ 251 65,
      Ondřejov, Czech Republic. E-mail: pkotrc@asu.cas.cz

SERGE KOUTCHMY, Institut d'Astrophysique de Paris, 98 Bis Boulevard
      Arago, F-75014 Paris, France. E-mail: koutchmy@iap.fr

KIRILL KUZANYAN, Dept. of Mathematics, University of Exeter, Laver
      Bldg., North Park Road, Exeter EX4 4QE UK.
      E-mail: kuzanyan@maths.ex.ac.uk

ANDREY LEBEDEV, Sternberg Astronomical Institute, B-1640, Moscow
      State University, 1117 234 Moscow, Russia. E-mail: andrey@sai.msu.su

LIBOR LENŽA, Valašské Meziřičí Astronomical Observatory,
      Vsetínská 78 Str., Valašské Meziřičí 75701, Czech Republic.

JEAN-LOUIS LEROY, UPS THÉMIS, Instituto de Astrofisica de Canarias,
      Via Lactea s/n, 38200 La Laguna, Tenerife, Canary Islands.
      E-mail: leroy@obs-mip.fr; leroy@ll.iac.es

HAOSHENG LIN, National Solar Obs., Sacramento Peak, P.O. Box 62,
   Sunspot, NM 88349, USA. E-mail: lin@sunspot.noao.edu

AARON LONGBOTTOM, Dept. Mathematical & Computational Sciences,
   Univ. of St. Andrews, Fife, KY16 9SS, St. Andrews, UK.
   E-mail: aaron@dcs.st-and.ac.uk

BOHUSLAV LUKÁČ, Slovak Central Observatory, P.O. Box 42, 94701
   Hurbanovo, Slovak Republic. E-mail: lukacb@kemar.sk

DUNCAN H. MACKAY, Dept. of Mathematical Sciences, Univ. of
   St. Andrews, North Haugh, Fife, KY16 9SS, St. Andrews, UK.
   E-mail: duncan@dcs.st-and.ac.uk

JEAN-MARIE MALHERBE, Observatoire de Paris, Section de Meudon,
   L.P.S.H.-DASOP, 5 Place Jules Janssen, F-92195, Meudon Cedex,
   France. E-mail: malherbe@obspm.fr

PIETRUS MARTENS, ESA Space Science Dept/GSFC, Code 682.3,
   SOHO-EAF, NASA/GSFC, Greenbelt, MD 20815, USA.
   E-mail: pmartens@esa.nascom.nasa.gov

SARA MARTIN, Helio Research, Inc., 5212 Maryland Ave., La Crescenta,
   CA 91214 USA. E-mail: sara@primenet.com

GALINA MASHNICH, Inst. of Solar-Terrestrial Physics, P.O. Box 4026,
   Irkutsk 33, 664033 Irkutsk, Russia. E-mail: root@sitmus.su

ALAN MCALLISTER, Helio Research, Inc., NCAR/HAO, Boulder, CO
   80301, USA. E-mail: ahm@hao.ucar.edu

PIERRE MEIN, Observatoire de Paris - Section de Meudon, L.P.S.H.-
   DASOP, 5 Place Jules Janssen, F-92195 Meudon Cedex France.
   E-mail: meinp@obspm.fr

MILAN MINAROVJECH, Astronomical Inst., 05960 Tatranská Lomnica,
   Slovak Republic. E-mail: milanmin@ta3.sk

ROBERTO MOLOWNY-HORAS, Observatoire de Paris - Section de
   Meudon, Inst. de Astrofisica de Canarias Via Lactea s/n, 38200 La
   Laguna (Tenerife), Canary Islands. E-mail: rmolowny@iac.es

DANIEL MOSES, Naval Research Laboratory, Code 7660.1, Washington,
   DC 20375, USA. E-mail: moses@louis14.nrl.navy.mil

ZADIG MOURADIAN, Observatoire de Paris - Section de Meudon,
   L.P.S.H.-DASOP, 5 Place Jules Janssen, F-92195, Meudon Cedex,
   France. E-mail: mouradian@obspm.fr

LEON OFMAN, Hughes STX/NASA GSFC, Code 682.1, Greenbelt, MD
   20771, USA. E-mail: ofman@waves.gsfc.nasa.gov

RAMON OLIVER, Universitat de les Illes Balears, Departament de Física,
   E-07071 Palma de Mallorca, Spain. E-mail: dfsroh4@ps.uib.es

JOANA OLIVEIRA, ESA Space Science - University of Porto, ESTEC/SO
   Postbus 299, 2200 Ag, Noordwijk, The Netherlands.
   E-mail: joana@so.estec.esa.nl

FREDERIC PALETOU, Observatoire de la Côte d'Azur, Laboratoire G.D.
   Cassini, B.P. 4229, F-06304, Nice Cedex 4, France.
   E-mail: paletou@obs-nice.fr

YOUNG-DEUK PARK, Korea Astronomy Observatory, Bohyunsan Optical
    Astronomical Obs., Jacheon P.O. Box 1, Youngcheon-si, Kyungpook
    700-820, Korea. E-mail: ydpark@flare.boao.re.kr

GIOVANNI PERES, Astr. Inst. & Observatory of Palermo, IOAP, Piazza
    del Parlamento 1, 90134 Palermo, Italy.
    E-mail: peres@oapa.astropa.unipa.it

TEODOR PINTÉR, Slovak Central Observatory, P.O. Box 42, 94701
    Hurbanovo, Slovak Republic. E-mail: pintert@kemar.sk

SIMON PLUNKETT, USRA/NRL, NASA GSFC, Code 682.3, Greenbelt,
    MD 20771, USA. E-mail: plunkett@kreutz.nascom.nasa.gov

SORIN-ADRIAN POJOGA, Astronomical Inst. of Romania, Observatoire
    de Paris - Section de Meudon, L.P.S.H.-DASOP, 5 Place Jules Janssen,
    F-92195 Meudon Cedex, France. E-mail: pojoga@obspm.fr

DMITRI PONYAVIN, University of St. Petersburg, Institute of Physics,
    198900 St. Petersburg, Russia. E-mail: ponyavin@snoopy.niif.spb.su

FABRICE PORTIER-FOZZANI, LAS-CNRS, BP 8, F-13376, Marseille
    Cedex 12, France. E-mail: fpf@astrsp-mrs.fr

ERIC PRIEST, St. Andrews University, Mathematics Dept., North Haugh,
    St. Andrews, Fife KY16 8QR, UK. E-mail: eric@dcs.st-and.ac.uk

BOGDAN ROMPOLT, Astronomical Inst., Wroclaw University, ul.,
    Kopernika 11, PL 51-622 Wroclaw, Poland.
    E-mail: rompolt@astro.uni.wroc.pl

PAWEL RUDAWY, Astronomical Inst., Wroclaw University, ul. Kopernika
    11, PL 51-622 Wroclaw, Poland. E-mail: rudawy@astro.uni.wroc.pl

DAVID M. RUST, Johns Hopkins University, Applied Physics Laboratory,
    Johns Hopkins Road, Laurel, MD 20723, USA.
    E-mail: david.rust@jhuapl.edu

SERGE SAVY, ISAS, c/o Y. Ogawara, 3-1-1 Yoshinodai, Sagamihara,
    Kanagawa 229, Japan. E-mail: savy@isass0.solar.isas.ac.jp

BRIGITTE SCHMIEDER, Observatoire de Paris - Section Meudon, L.P.S.H.
    -DASOP, 5 Place Jules Janssen, F-92125 Meudon Cedex, France.
    E-mail: schmieder@mesioa.obspm.fr

NICK SCHUTGENS, Utrecht University - Faculty of Physics and
    Astronomy, Postbus 80,000, 3508 TA Utrecht, The Netherlands.
    E-mail: n.a.j.schutgens@fys.ruu.nl

NORBERT SEEHAFER, Inst. for Theoretical Physics & Astrophysics,
    Universität Potsdam, PF, 601553, D-14415 Potsdam, Germany.
    E-mail: seehafer@agnld.uni-potsdam.de

KYUNG SIM, Korea Astronomy Obs. San 36-1, Whaam-dong, Yusung-ku,
    Taejon, 305-348, Korea. E-mail: kjsim@hanul.issa.re.kr

RAYMOND N. SMARTT, NSO/SP, P.O. Box 62, Sunspot, NM 88349, USA.
    E-mail: rsmartt@sunspot.noao.edu

FRANK SOLBERG, Inst. of Theoretical Astrophysics, P.O. Box 1029,
    N-0315, Oslo, Norway. E-mail: fsolberg@astro.uio.no

DANIEL SPICER, NCCS, Code 930, NASA/GSFC, Greenbelt, MD 20771,
     USA. E-mail: spicer@gauss.gsfc.nasa.gov

GOTZ STELLMACHER, Institut d' Astrophysique, 98 bis Boulevard Arago,
     F-75014 Paris, France. E-mail: stell@iap.fr

EINAR TANDBERG-HANSSEN, NASA/MSFC, ES01, Huntsville, AL
     35812, USA. E-mail: tandberg@msfc.nasa.gov

YUTAKA UCHIDA, Science University of Tokyo, Physics Dept., 1-3
     Kagurazaka, Shinjuku-ku, Tokyo 162, Japan.
     E-mail: uchida@astrol.yy.kagu.sut.ac.jp

AAD VAN BALLEGOOIJEN, Center for Astrophysics, MS-15, 60 Garden
     St., Cambridge, MA 02138, USA. E-mail: vanballe@cfa.harvard.edu

GIJSBERTUS VAN DEN OORD, Astronomical Inst. Utrecht, Sterrekundig
     Inst., P.O. Box 80,000, 3508 TA Utrecht, The Netherlands.
     E-mail: oord@fys.ruu.nl

LIDIA VAN DRIEL-GESZTELYI, Observatoire de Paris - Section de
     Meudon, L.P.S.H.-DASOP, 5 Place Jules Janssen, F-92195 Meudon
     Cedex, France. E-mail: lvandrie@mesioq.obspm.fr

V. K. VERMA, Uttar Pradesh State Observatory, Manorapeak, Nainital
     -263 129, India. E-mail: verma@upso.ernet.in

IGOR VESELOVSKY, Inst. of Nuclear Physics, Moscow State Univ.,
     119899 Moscow, Russia. E-mail: veselov@dec1.npi.msu.su

JEAN-CLAUDE VIAL, Inst. d'Astrophysique Spatiale/CNRS, Université
     Paris XI - CNRS, Bâtiment 121, F-91405 Orsay Cedex,
     France. E-mail: vial@iaslab.ias.fr

BOJAN VRŠNAK, Faculty of Geodesy, Hvar Observatory, Kačićva 26,
     HR-10000 Zagreb, Croatia. E-mail: bojan.vrsnak@x400.srce.hr

JINGXIU WANG, Beijing Astronomical Observatory, Chinese Academy of
     Sciences, Beijing 100080, China. E-mail: wjx@ourstar.bao.ac.cn

TAKASHI WATANABE, Ibaraki University, Dept. of Environmental
     Sciences, Mito 310, Japan. E-mail: watanabe@env.sci.ibaraki.ac.jp

DAVID F. WEBB, Boston College, AFRL/VSBS, 29 Randolph Road,
     Hanscom AFB, MA 01731-3010, USA. E-mail: webb@plh.af.mil

EBERHARD WIEHR, Universitäts-Sternwarte, Geismarlandstr 11,
     D-37083 Göttingen, Germany. E-mail: ewiehr@tarzan.uni-sw.gwdg.de

YUZEF ZHUGZHDA, Kiepenheuer-Inst. für Sonnenphysik, Schöneckstr. 6,
     D-79104 Freiburg, Germany. E-mail: yuzef@kis.uni-freiburg.de

JACK ZIRKER, National Solar Observatory, P.O. Box 62, Sunspot, NM
     88349, USA. E-mail: jzirker@noao.edu

1 Takashi Watanabe
2 Petr Heinzel
3 Fabrice Portier-Fozzani
4 Guillaume Aulanier
5 S. S. Gupta
6 Einar Tandberg-Hanssen
7 Helen Coffey
8 Jingxiu Wang
9 David Webb
10 David Rust
11 Mitchell Berger
12 Dana Dokoupilova
13 Libor Lenza
14 Jana Kasparova
15 Alexey Gorshkov
16 Alan McAllister
17 Ulrich Anzer
18 Milan Minarovjech
19 Pawel Rudawy
20 Aad van Ballegooijen

21 Giovanni Peres
22 Igor Veselovsky
23 Karine Bocchialini
24 Bojan Vrsnak
25 Dmitri Ponyavin
26 Veronique Bommier
27 Oddbjorn Engvold
28 Karen Harvey
29 Franca Chiuderi-Drago
30 Roberto Molowny-Horas
31 Galina Mashnich
32 Jean-Marie Malherbe
33 Yutaka Uchida
34 Angela Ciaravella
35 Bohuslav Lukak
36 Alan Hood
37 Gotz Stellmacher
38 Brendan Byrne
39 Brigitte Schmieder
40 Terry Forbes

41 C. Z. Cheng
42 V. Verma
43 Klaus Galsgaard
44 Leon Ofman
45 Boris Ioshpa
46 James Chen
47 Lidia Van Driel-Gesztelyi
48 Sara Martin
49 Vladimir Bashkirtsev
50 Andrey Lebedev
51 Eijiro Hiei
52 Raymond Smartt
53 Peter Foukal
54 Cecile Delannee
55 Iraida Kim
56 Claus de Boer
57 Edward Kononovich
58 Kirill Kuzanyan
59 Bernard Foing
60 Nat Gopalswamy

61 Simon Plunkett
62 Jean-Claude Vial
63 Eberhard Wiehr
64 Duncan MacKay
65 Moira Jardine
66 Jean-Louis Leroy
67 Boris Filippov
68 Jose Ballester
69 Haosheng Lin
70 Serge Koutchmy
71 Christiana Dumitrache
72 Jack Zirker
73 Pascal Demoulin
74 Sorin-Adrian Pojoga
75 Ramon Oliver
76 Nick Schutgens
77 Frederic Paletou
78 Frank Solberg
79 Young-Deuk Park
80 Gijsbertus van denOord

81 Pietrus Martens
82 Serge Savy
83 Spiro Antiochos
84 Yozef Zhugzhda
85 Josef Khan
86 Victor Gaizauskas
87 Bogdan Rompolt
88 Pierre Mein
89 Daniel Spicer
90 Norbert Seehafer
91 Gwangson Choe
92 Kyung Sim
93 Pavel Kotrc
94 Zadig Mouradian
95 Ursula Allen

Introduction

Lucien d'Azambuja

M. J. Martres
Observatoire de Paris, 92195 Meudon Cedex, France

1. Lucien d'Azambuja ou l'histoire des protubérances solaires à Meudon (*French*)

En 1868, Lockyer et Janssen ont montré qu'il etait possible de faire un relevé journalier de la chromosphère et des protubérances au bord du Soleil en dehors des éclipses totales en utilisant un spectroscope. De 1892 à 1894, H. Deslandres, installé à l'Observatoire de Paris, montra "que la chromosphère entière est décelable dans la demi- sphère tournée vers la Terre" à l'aide d'un petit spectrohéliographe et d'un spectro-enregistreur de vitesses. Avec ces instruments de première génération il obtient des images de la chromosphère de calcium. "L'analyse spectrale et l'application du spectrohéliographe aux raies du spectre solaire ouvre un champ nouveau d'investigation extrêmement vaste" écrit-il. Mal à l'aise à Paris pour développer ses recherches, il s'installe à Meudon. Là, tout est à faire et il trouve peu de ressources. Il crée un sidérostat et un petit bâtiment pour recevoir les deux petits instruments de Paris, qu'il utilisera jusqu'en 1906. Mais en 1899 il a fait entrer à l'Observatoire de Meudon Lucien d'Azambuja, un jeune homme de 15 ans, soigneux et habile de ses mains pour l'aider dans ses installations et participer aux observations et aux recherches en cours.

Il entraine le jeune Lucien dans les missions d'éclipses totales du 28 Mai 1900 et du 30 Août 1905 - visibles en Espagne. Il faut noter que les observations accumulées de 1893 à 1906 forment déjà la collection la plus complète existant au monde, d'images photographiques de la raie K_2 (appelée K_{2-3} à Meudon) de diamètre solaire de 90 mm et, ajoute H. Deslandres "comparables aux meilleures faites en Amérique avec des appareils plus volumineux et plus puissants." En effet la concurrence est â pre entre Hale et Deslandres. Chacun d'eux a entrepris l'analyse de ses nouvelles images du Soleil et donne des noms aux structures ignorées jusque là. C'est ainsi qu'après avoir baptisé "filaments" les lignes noires qui apparaissent sur le disque, H. Deslandres conteste l'appellation "flocculus," (flocculi au pluriel) donné par Hale aux petits maxima de lumière du réseau chromosphérique aussi bien qu'aux structures plus importantes. H. Deslandres baptise ces dernières les "plages faculaires" par opposition avec les "flocculi" parce que les unes dépendent de la phase de l'activité solaire, les autres non.

En 1908, Hale aidé par Adams obtient avec son "Snow spectrohéliograph" les premières images monochromatiques de la raie rouge de l'hydrogène $H\alpha$. Mais H. Deslandres a, en 1907 chargé L. d'Azambuja de *l'installation du grand spectrohéliographe quadruple* (3 chambres de 3 m et 1 de 7 m) éclairé par un coelostat à 2 miroirs permettant diverses combinaisons. A ce propos, H. Deslandres déclare "C'est un appareil délicat et difficile à règler. Dans la recherche j'ai été aidé constamment par d'Azambuja, jeune astronome de talent dont le nom

est associé au mien dans la découverte." Au cours du deuxième semestre de 1908 apparaissent les premières images K_3 prises au grand spectrohéliographe dans sa combinaison de 14 m, et en janvier 1909 celles prises dans la région centrale de la raie $H\alpha$. Dans le même temps, l'enregistrement des vitesses radiales est poursuivi sans relâche avec l'appareil spécial que Meudon est jusque là le seul à posséder. L'installation nouvelle ainsi conçue doit permettre l'étude simultanée des formes et des mouvements: but fixé au spectrohéliographe par l'inventeur.

Les séries d'observations quotidiennes de cette periode ont apporté les résultats suivants:

* Les "couches supérieures" de la chromosphère solaire montrent des structures non décelables dans les enregistrements de la surface, K_1 et même K_2.

* Les images prises au centre des raies $H\alpha$ et K_3 montrent les mêmes structures caractéristiques, les "filament noirs" communs aux deux images appartiennent à la couche supérieure comme les "circum facules, les protubérances et les plages faculaires."

* "Le filament correspond aux vitesses d'ascension les plus intenses." Par contre, alors que Hale et Ellerman, et aussi L. d'Azambuja, ont quant à eux présenté les filaments comme la marque des protubérances sur le disque, Deslandres affirme que "la protubérance en général n'est pas sur le filament lui-même; vue au bord elle est plutôt sur le côté ou même sur un seul côté et si un prolongement lumineux correspond au filament lui-même, ce prolongement est habituellement plus faible que la protubérance elle-même."*

A la mort de Janssen, H. Deslandres, "le Maître," est devenu directeur de l'Observatoire de Meudon (1908) et il prépare le mémoire de synthèse de ses travaux et de leurs résultats pour accéder au grade de docteur es sciences (1910). Il incombe alors à L. d'Azambuja de poursuivre l'exploitation du nouvel instrument et l'étude des propriétés des différentes "couches" de la chromosphère solaire. Dès 1913, H. Deslandres et d'Azambuja, persuadés que les filaments constituent un des éléments les plus caractéristiques de la "couche supérieure" de cette atmosphère, ont proposé dans une note aux C. R. de l'Académie (t. 157, p. 413) une représentation graphique permettant à la fois de dégager leur individualité et de les suivre dans leur évolution: c'est la première ébauche d'une carte synoptique.

1914, la mobilisation de H. Deslandres et de L. d'Azambuja met le service solaire et l'observatoire en sommeil. Ce n'est qu'en 1919 que reprennent les enregistrements monochromatiques quotidiens dans les trois longueurs d'onde des raies $H\alpha$, K_3 et K_1 avec 2 des combinaisons du spectrohéliographe quadruple horizontal installé au bâtiment du grand sidérostat sur le 2-ème terrasse de l'Observatoire de Meudon (2 chambres de 3 m, réseau et prismes). d'Azambuja termine ses études universitaires, assure les observations de routine avec un personnel réduit souvent à lui seul. En 1923, Alfred Pérot, professeur à l'École Polytechnique et astronome à Meudon, introduit à l'observatoire l'un de ses assistants, Marguerite Roumens, qui mesure pour lui les spectres enregistrés à Meudon. Il meurt en 1925 et c'est au service solaire qu'elle se retrouve engagée comme assistante-auxiliaire. En 1925 Monsieur Deslandres est nommé directeur de l'Observatoire de Paris-Meudon, car ces 2 observatoires ont été alors regroupés sous une direction unique. Moins absorbé par les observations systématiques, d'Azambuja envisage de bénéficier des qualités exceptionnelles du nouveau spec-

trohéliographe pour reprendre et étendre les recherches antérieures sur le spectre solaire à des raies encore peu étudiées, celles de la partie "basse" de la chromosphère en particulier. - En effet l'interprétation des spectrohéliogrammes dépend de la connaissance précise de "l'aspect, en chaque point du disque, de la raie employée pour former l'image."

A partir de fin août 1925 jusqu'à la fin de l'été 1927, 145 spectres ont été photographiés avec le spectrographe double à 3 fentes au grand sidérostat de Meudon et l'assistance de Marguerite Roumens - De cet échantillon, 11 raies solaires ont été analysées, mesurées, interprètées - des raies d'un même élément mais d'importances différentes, de différents éléments on des raies d'éléments ionisés. - Les résultats obtenus ont fait l'object de la thèse de doctorat d'état de d'Azambuja – "Recherches sur la Structure de la Chromosphère Solaire." (Annales de Meudon, t. 8, fasc 2, 1930). Parallèlement, les règles de représentation des structures solaires sur des Cartes Synoptiques s'affinaient, en particulier celle des filaments qui étaient à l'époque la raison première de cette publication (voir note de L. d'Azambuja aux Comptes Rendus de l'Académie des Sciences, t. 173, p. 1450, 1921). Dès 1928, d'Azambuja publiait aux Annales de l'Observatoire de Paris, section de Meudon (t V1, fasc 1) les Cartes Synoptiques de la chromosphère solaire et catalogue des filaments de la couche supérieure des 11 rotations solaires de la période mars 1919 - janvier 1920. Déjà une collaboration est assurée par les observatoires de Kodaikanal (Indes du Sud) et de Mt. Wilson qui fournissent des clichés de complément pour les jours sans observation à Meudon.

Pour cette première publication 575 filaments ont pu être identifiés, soigneusement mesurés pour chaque jour d'observation et cartographiés - Au cours de la préparation, d'Azambuja a présenté à l'Académie des "mesures nouvelles de la vitesse de rotation des filaments – Evaluation de la hauteur de ces objets au-dessus de la chromosphère solaire" (C.R.A.S., 1923, t. 176, p. 950) - on verra par la suite que l'amélioration de cette évaluation est restée l'objet de tous les soins de d'Azambuja. Par la suite lorsque la relation filaments – taches a semblé intéressante une représentation des taches, des plages faculaires, a été soigneusement élaborée, le tout sous le contrôle pointilleux et sévère de d'Azambuja en personne; - ceci jusqu'à son départ de l'Observatoire en 1959 et pour la petite histoire.

Ainsi se poursuivaient la publication des Cartes Synoptiques de la chromosphère et dans le même temps l'exploitation des spectres et des images solaires du spectrohéliographe de Meudon. La collaboration scientifique commencée en 1926 pour la thèse du doctorat entre L. d'Azambuja et M. Roumens s'est poursuivie aussi jusqu'à la fin de leur carrière et bien au-delà car M. Roumens est devenue Mme L. d'Azambuja en 1935. Leur expérience et leurs connaissances partagées les ont conduits à vouloir exprimer le résultat de leurs travaux en un volumineux mémoire publié en co-signature en 1948 aux Annales de l'Observatoire de Meudon (t. 6, fasc 7) intitulé: "Étude d'ensemble des protubérances solaires et leur évolution effectuee à l'aide des spectrohéliogramms obtenus à l'Observatoire de Meudon et des Cartes Synoptiques de la chromosphère publiées par l'établissement."

Si ce mémoire fait superbement le point des connaissances sur ce sujet en 1948, la suite des recherches faites à Meudon en particulier, et partout dans le monde, sont en fait accrochées aux bases énoncées là.

Les cartes n'ont pas épuisé tout ce qu'elles pouvaient donner: on en a extrait les "rouleaux," les "points pivots," les relations avec les phénomènes éruptifs, les plages et les taches, les champs magnétiques dans les protubérances et le régions calmes ou actives du Soleil et en général tout ce qui concerne l'observation chromosphérique à moyen terme - Tous les développements expérimentaux si rapides des dernières décennies et les résultats obtenus ont pour support les caractères généraux reconnus et énoncés par des chercheurs comme L. et M. d'Azambuja.

Tous les astronomes solaires sont un peu les héritiers de ces pionniers de la recherche. Il ne faut pas oublier non plus qu'ils ont aussi dans le même temps participé, puis pour L. d'Azambuja, présidé à l'organisation de la discipline tant en France qu'à l'étranger mais cela est une autre histoire.

* Annales de Meudon: Mémoire de thèse, H. Deslandres 1910 (le fait que le filament et la protubérance ne sont que deux projections différentes d'un même objet a été officiellement reconnu en 1928). En 1911, H. Deslandres et L. d'Azambuja publient déjà des mesures de la vitesse de rotation de quelques filaments bien observés en 1906, 1908, 1909, 1910. (Note aux C.R.A.S., *153*, 442).

2. Lucien d'Azambuja or the history of solar prominences at Meudon (*English*)

In 1868 Lockyer and Janssen had shown that it was possible to make a daily record of the chromosphere and of prominences on the limb without total eclipses by utilizing a spectroscope. From 1892 to 1894, H. Deslandres, working at the Observatory in Paris, showed "that the entire chromosphere is observable on the half-sphere turned to the Earth" with the help of a small spectroheliograph and a "velocity meter." With these first-generation instruments he made images of the calcium chromosphere, and he wrote: "Spectral analysis and the application of the spectroheliograph on the dark lines of the solar spectrum open a vast new field of investigation." Because of difficulties in Paris in developing his research, he moved to Meudon. There he has to start from scratch, and he finds few resources. He makes a siderostat and erects a small building to house the two small instruments from Paris, which he will use until 1906. However, in 1899 he had hired at Meudon Observatory, Lucien d'Azambuja, a young man, 16 years old, careful and handy, to help with the work, particularly the ongoing observations and research.

He brings the young Lucien along on the eclipse expeditions to Spain in 28 May 1900 and 30 August 1905. One should note that the many observations from 1893 to 1906 constituted at the time the most complete collection in existence, of photographic images in the K_2 line (called K_{2-3} in Meudon) with solar diameter of 90 mm and, writes H. Deslandres: "comparable to the best made in America with bigger and more powerful instruments." The competition between Hale and Deslandres was really quite bitter. Each of them had analyzed their new images of the Sun and given names to structures never seen before. For example, after having coined the word "filament" for the dark lines visible on the disk, H. Deslandres contests the use of "flocculus" (flocculi in plural) given by Hale

Figure 1.   Lucien D'Azambuja: 1884 – 1970.

to small, bright areas of the chromosphere, as well as to larger structures. H. Deslandres calls these latter "plages faculaires," as opposed to "flocculi," since the former depend on the phase of solar activity, while the latter do not.

In 1908 Hale, aided by Adams, obtains the first monochromatic images in the red line of hydrogen $H\alpha$ with his Snow spectroheliograph. But in 1907 H. Deslandres charged L. d'Azambuja with the installation of the big quadruple spectroheliograph, fed by a versatile 2-mirror coelostat. In that connection H. Deslandres says: "This is a delicate instrument and difficult to operate. In the research I have been constantly aided by d'Azambuja, a young, talented astronomer whose name is associated with mine in the discovery." In the second half of 1908 came the first K_3 images from the big spectroheliograph, and in January 1909 those taken in the center of the $H\alpha$ line. At the same time radial velocity measurements were constantly made with the special instrument that only Meudon still possesses. This new instrumentation permits the simultaneous study of forms and velocities: the inventor's goal for the spectroheliograph.

The daily series of observations from this period led to the following results:

* The "higher layers" of the solar chromosphere show structures not seen in observations of the surface; K_1 and even K_2.

* Images taken in the center of the $H\alpha$ and the K_3 lines show the same characteristic structures: "dark filaments," the same in both images, part of the upper layer, as well as "circumfaculae, prominences and the plage faculaires."

* The filament corresponds to the strongest velocities of ascension. On the other hand, while Hale and Ellerman – and also L. d'Azambuja – have considered filaments as prominences seen on he disk, Deslandres was of the opinion that "the prominence is in general not on the filament itself; seen on the limb it is rather to one side, and if there is a bright structure which corresponds to the filament, this structure is in general less bright than the prominence itself."*

When Janssen dies in 1908, H. Deslandres becomes director of the Observatory at Meudon, and he writes his thesis, a synthesis of his work and the results, for the Doctor of Science degree (1910). Hence, it falls to L. d'Azambuja to continue using the new instrument and to study the properties of the different "layers" of the solar chromosphere. After 1913, when Deslandres and d'Azambuja were convinced that the filaments are one of the most characteristic elements of the "upper layer" of the chromosphere, they proposed, in a note to C. R. de l'Academie (Vol. 157, p. 413), a graphic representation that would allow both to study the filaments individually and to follow their evolution: this was the first draft of a synoptic map.

After 1914, with the drafting of H. Deslandres and L. d'Azambuja, the solar service at the observatory fell silent. It was only in 1919 that daily monochromatic observations in the three wavelengths of the lines $H\alpha$, K_3, and K_1 were restarted with the horizontal, quadruple spectroheliograph in the building of the big siderostat on the second terrace of the Meudon Observatory. L. d'Azambuja completes his university studies and takes care of the routine observations, often alone. In 1923, Alfred Pérot, professor at Ecole Polytechnique and astronomer at Meudon, brings to the observatory one of his assistants, Marguerite Roumens, who analyzes the spectra obtained at Meudon. Pérot dies in 1925 and she finds herself as assistant in the solar service. That year H. Deslandres is named director of the Observatoire Paris-Meudon, as the two observatories are placed under

one and same director. Less occupied with routine observations, d'Azambuja plans to take advantage of the exceptional quality of the new spectroheliograph to extend previous research on the solar spectrum, particularly the little studied "lower" part of the chromosphere. Remember that the interpretation of spectroheliograms relies on precise knowledge of the "appearance, at every point on the disk, of the spectral line used to obtain the image."

From the end of August 1925 to the end of the summer of 1927, 145 spectra were photographed with the double spectrograph with three slits fed by the big siderostat, with the assistance of Marguerite Roumens. From these data 11 solar lines were analyzed, measured and interpreted: lines from the same element but of different strength; lines from different elements; or lines from ionized elements. The obtained results constituted L. d'Azambuja's doctoral thesis: "Research on the Structure of the Solar Chromosphere" (Ann. de Meudon, Vol. 8, part 2, 1930). At the same time the rules for representing solar structures on the synoptic maps were developed, in particular rules for filaments which, at the time, was the main reason for this publication (see L. d'Azambuja's note to Comptes Rendus de l'Academie des Sciences, Vol. 173, p. 1450, 1921). Starting in 1928 d'Azambuja published in the Ann. de l'Observatoire de Paris, section de Meudon (Vol. VI, part 1) "The Synoptic Maps of the Solar Chromosphere and Catalogue of Filaments in the Upper Layer" for the 11 solar rotations in the period March 1919 – January 1920. Collaboration had been assured from the observatories of Kodaikanal (Southern India) and of Mt. Wilson, which would provide observations for the days when Meudon could not observe.

In this first publication 575 filaments were identified, carefully measured for each day of observation, and put on the maps. During the preparation, d'Azambuja made to the Academie the presentation "New measurements of the velocity of rotation of filaments – Evaluation of the height of these objects above the solar chromosphere" (C.R.A.S., 1923, Vol. 176, p. 950). Later, improvements on this evaluation remained d'Azambuja's major concern. Then, when the relationship filament – sunspot caught the interest, a scheme was carefully developed to display spots and plages faculaires, all under L. d'Azambuja's personal supervision, until he left the observatory in 1959.

In this way the production of the Synoptic Maps of the chromosphere continued, as did the study of the spectra and the solar images from the spectroheliograph at Meudon. The scientific collaboration between L. d'Azambuja and M. Roumens, that had begun in 1926 with the doctoral thesis, likewise continued until the end of their careers, and even longer because M. Roumens became Mrs. L. d'Azambuja in 1935. Their experience and their shared knowledge led them to publish the results of their works in 1948 in a voluminous joint memoir entitled, "A comprehensive study of solar prominences and their evolution from spectroheliograms obtained at the observatory and from Synoptic Maps of the chromosphere published at the institution" (Ann. de l'Observatoire de Meudon, Vol. 6, part 7).

This memoir superbly summarizes the knowledge of the subject matter as of 1948, and the continued research, in particular at Meudon, but in general all over the world, also built on the results presented there. The usefulness of the maps has not been exhausted. By using these maps new ideas have emerged regarding "pivot points", relationships with eruptive phenomena, prominence

magnetic fields, active and quite regions on the Sun, and in general, all that has to do with observations of the chromosphere. All the rapid experimental developments of the last decades and the obtained results have been supported by the knowledge of solar phenomena recognized and characterized by scientists like L. and M. d'Azambuja.

All solar astronomers are in a way inheritors of these research pioneers. Furthermore, we should not forget that L. d'Azambuja was active in the organizational aspects of his discipline, both in France, as well as on the international scene – but that is another story.

* Annales de Meudon: H. Deslandres, Thesis, 1910 (the fact that filaments and prominences are simply two different projections of the same object was officially recognized in 1928). In 1911, H. Deslandres and L. d'Azambuja published measurements of the rotation rate of several filaments that had been well recorded in 1906, 1908, 1909, and 1910 (Compte Rendu Acad. Sci., *153*, 442).

Translated from the French by E. Tandberg-Hanssen

The History of Solar Prominence Research:
Historical Introduction to IAU Colloquium No. 167
"New Perspectives on Solar Prominences"

Einar Tandberg-Hanssen

NASA Marshall Space Flight Center, Huntsville, AL 35812, USA

Abstract. We trace the history of observational solar prominence research from the early period when total solar eclipses provided the only means of observation, via the introduction of photography and spectroscopy in the 1860's, to the present epoch when application of the Zeeman and the Hanle effects makes possible determination of the all-important magnetic fields in prominences.

Dividing prominence models into two classes, those that treat the support of the prominence against gravity and those concerned with the physical conditions in the prominence plasma itself, we describe the progress made in both classes of models since the 1950's, when the first models were proposed. Finally, we comment on the necessity of combining aspects of the two classes of prominence models into a comprehensive picture that can account for the global nature of prominence support and stability, and where the adjacent coronal structures play an important role.

1. Introduction

About 150 years ago astronomers, for the first time, provided the correct – albeit incomplete – interpretation of the prominence phenomenon as "clouds in the solar corona." However, prominences had been observed since the Middle Ages, and explanations had at times been exotic.

At this colloquium, we are concentrating on those objects that fall into the category of quiescent prominences, i.e., the large, rather stable structures that, when observed on the solar disk in absorption (e.g., Hα), are often referred to as filaments.

Figure 1 may be taken as a defining picture of a quiescent prominence. Taken near solar activity minimum, it shows the prominence as part of the polar crown. Closer to activity maximum one also sees many smaller active-region filaments as shown in Figure 2, which also displays a quiescent prominence seen abovethe southeastern limb. These are the objects we shall keep in mind during the discussions at this colloquium.

For convenience, I shall first discuss the history of prominence research from an observational point of view by dividing the progress, somewhat arbitrarily, into three time periods, namely:
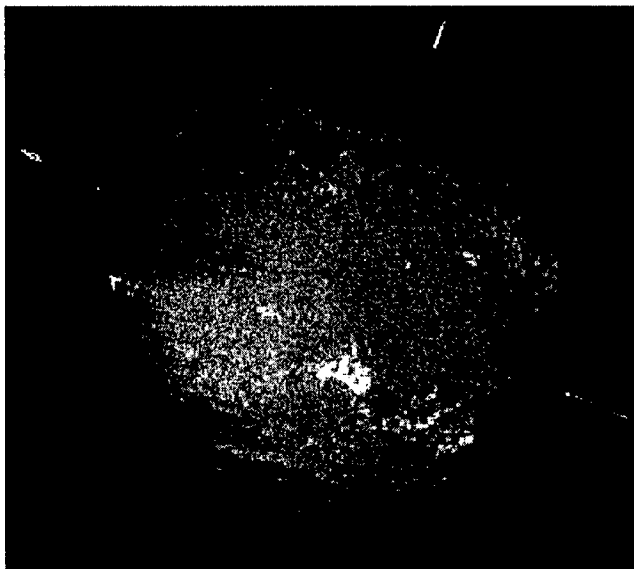
Figure 1.   Large quiescent prominence, part of the (south) polar crown, near solar minimum (courtesy Observatoire de Paris-Meudon and P. Mein).

(1) The speculative period, roughly before 1860;
(2) The spectrographic period, roughly between 1860 and 1960; and
(3) The polarimetric period, roughly after 1960.

Table 1.   Historic Eclipse Observations

Year (site)	Observer	Interpretation
1239	Muratori	"burning hole in the corona"
1733 (Sweden)	Vassenius	"clouds in lunar atmosphere"
1788	Ulloa	"hole in the Moon"
1842 (France, Italy)	Arago, Struve, etc.	"prominences a solar phenomenon"
1851 (Norway, Sweden)	Airy, Carrington	"solar cloud formation"
1860 (Spain)	Photography introduced	
1868 (India, Malacca)	Spectroscopy introduced	

2.   The Speculative Period

The only way prominences could be observed during this period was during total solar eclipses. In 1239 Muratori (see Secchi 1875) observed the corona during an eclipse and reported a burning hole. This "burning hole" in all probability was a prominence, or a cavity with a prominence inside it.

Medieval Russian chronicles (see Vyssotsky 1949) also mention prominen-
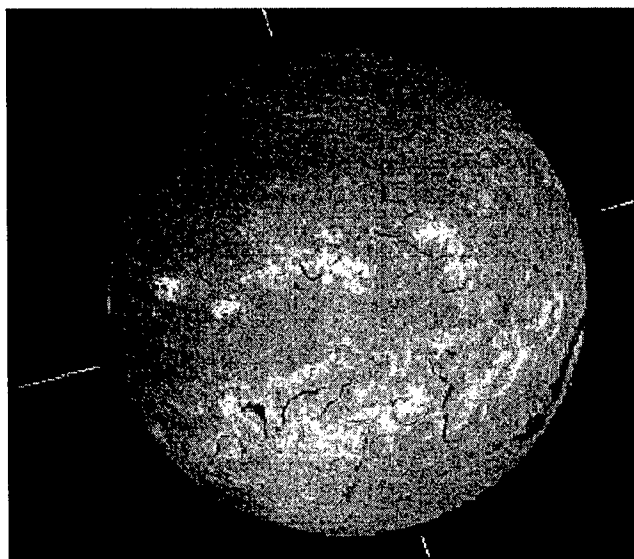
Figure 2.   Active and quiescent prominences, near solar maximum
(courtesy Observatoire de Paris-Meudon and P. Mein).

ces, but the first semi-scientific description came after the eclipse of May 2,
1733 in Sweden. During this event, Vassenius (1733) observed three or four
prominences and described them as reddish clouds in the lunar atmosphere.
Ulloa (1779) observed what probably was an active prominence during the eclipse
of 1778 and attributed it to a hole in the Moon.

These early observations of prominences were subsequently all but forgot-
ten, and all the experienced astronomers were taken by surprise when they
rediscovered the phenomenon during the eclipse of July 8, 1842 in France and
Italy. Even though they realized that this must be a solar phenomenon, their
descriptions of the shape of prominences were so vague that they could not pre-
vent others from believing that prominences were mountains on the Sun (see
Grant 1852).

Not until the eclipse in 1851, observed in Norway and Sweden, did a correct,
if incomplete, interpretation emerge: prominences are solar cloud formations.
Thus, in 4 years (2001) we can celebrate the sesquicentennial anniversary of a
correct interpretation, even though the detailed physical nature of these clouds
is still being debated, which is the reason we are all here in Aussois today.

3.   The Spectrographic Period

Spectroscopy was first used in eclipse observation in 1868, but I have let this pe-
riod start in 1860 when photography was introduced during the eclipse in Spain,
since the former technique depended on the latter. In both cases the recogni-

tion goes to Secchi (1868) and de la Rue (1868), who employed spectrographic methods on August 18, 1868 at the eclipse in India and Malacca to study the "chemistry of prominences." It was found that the spectrum of prominences consisted of bright lines, and from then on prominences were considered to be glowing masses of gas.

An interesting development followed immediately after the eclipse. Janssen (1868) realized that many of the emission lines were so brilliant that they should be visible without an eclipse. The next day he placed the slit of the spectrograph outside the limb of the Sun's image and observed prominence emission lines in full daylight. Independently and simultaneously, the same kind of observation was reported by Lockyer (1868a, b), who with Huggins, had tried to accomplish this for some time.

The 1868 eclipse also brought the discovery of the "open-slit" method, giving a series of monochromatic images of a prominence, corresponding to the emission lines observed with a normal slit. As a result of all these developments, the 1870's saw a great increase in knowledge of prominences, as also witnessed by Secchi's seminal book, *Le Soleil* (Secchi 1875–77).

Then in 1892, Hale invented the spectroheliograph (Hale and Ellerman 1903) and the following year Deslandres had his first instrument ready in France (Deslandres 1910). The importance of this kind of instrument is beautifully demonstrated in Figures 1 and 2 in this article.

In 1899 Deslandres hired 16-year-old Lucien d'Azambuja who soon became very adept, both as a mechanic and later as a bona fide scientist, and followed in Deslandres' footsteps.

The next great developments were due to Bernard Lyot who, with the invention of the birefringent filter and the coronagraph (Lyot 1936), made possible modern-day observations of prominences at any time without an eclipse. Figure 3 reproduces some of his early observations (June 1937) that also made possible the study of prominence development. The vast amount of data on prominences was brilliantly treated in the 1948 paper by the d'Azambujas: *Etude d'Ensemble des Protubérances Solaires et de leur Evolution*, which remains a standard reference (d'Azambuja and d'Azambuja 1948). It includes the disparition brusque phenomenon, which probably was first photographed by Deslandres in 1897 (Deslandres 1897) and studied by him with a spectroheliograph in 1899, and which will be lively debated at this colloquium.

4. Prominence Drawings

Before we embark on a discussion of the polarimetric period, a word on prominence drawings may be in order. Early drawings were often quite fanciful. Figure 4 shows a 17th century masterpiece from Kircher's "Mundus Subterraneus" of 1665.

With the introduction of photography in 1860, one might suppose that drawings of prominences seen during a total eclipse would lose their raison d'tre. However, for many years that was not the case. The introduction of photography was certainly a great step forward, but early photographs often could not compete with visual inspection of prominence fine-structure. Secchi himself was a master, and Figure 5 reproduces one of his well-known drawings.
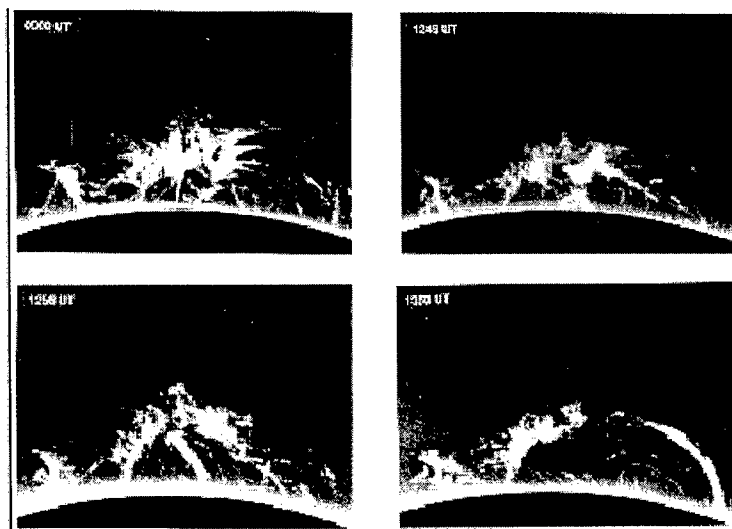
Figure 3.   Prominence photographs obtained by Lyot in 1937 with his coronagraph (courtesy Observatoire de Paris).
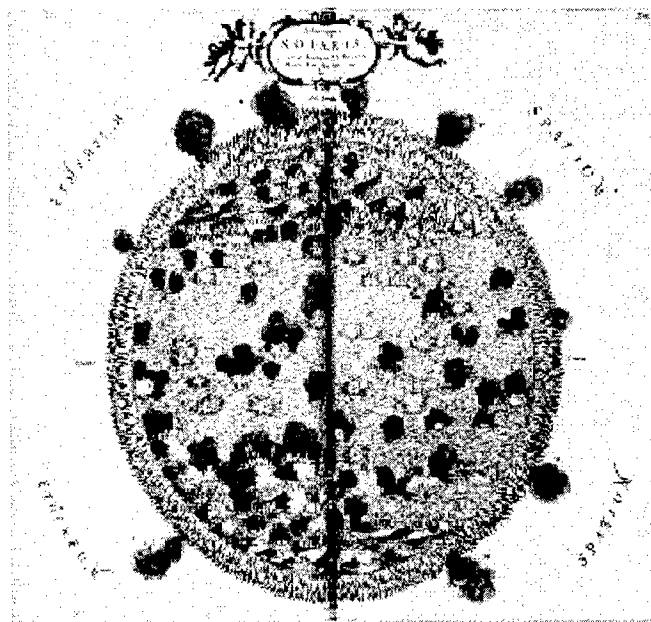
Figure 4.   17th century drawing from Kircher's Mundus Subterraneus, 1665 (courtesy Observatoire de Paris).
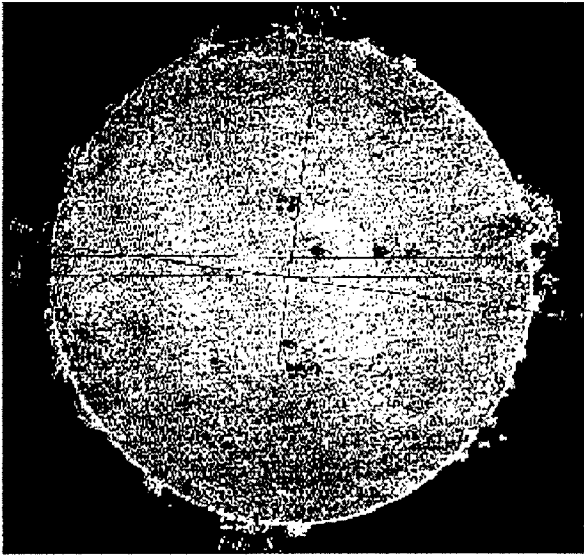
Figure 5.   Drawing of prominences observed at total solar eclipse
(Secchi in *Le Soleil*, 1877).

Figure 6 reproduces some other early drawings made by Fearnley in Norway in 1872–73, showing a disparition brusque, a quarter of a century before Deslandres' photographic observations.

5.   The Polarimetric Period

This period started in 1961 when Zirin and Severny made the first measurements of magnetic fields in prominences, using the Zeeman effect. Already in 1908, Hale had recorded the magnetic field in sunspots from Zeeman line displacements; later polarization characteristics of the Zeeman effect made it possible to observe the much weaker prominence fields, which is the basis for one of the two methods still being used.

In the 1970's, extensive Zeeman-effect measurements of prominences were performed at the High Altitude Observatory's Climax station, while great improvements were made by the French groups at Meudon and Pic-du-Midi, using the Hanle effect, the other method in current use. The magnetic fields in prominences were found to range from a few gauss to more than 100 gauss. Furthermore, it became clear that the field in quiescent prominences has an important component along the long axis of the prominence. We are still reaping the rich harvest of these efforts as the polarimetric period continues.
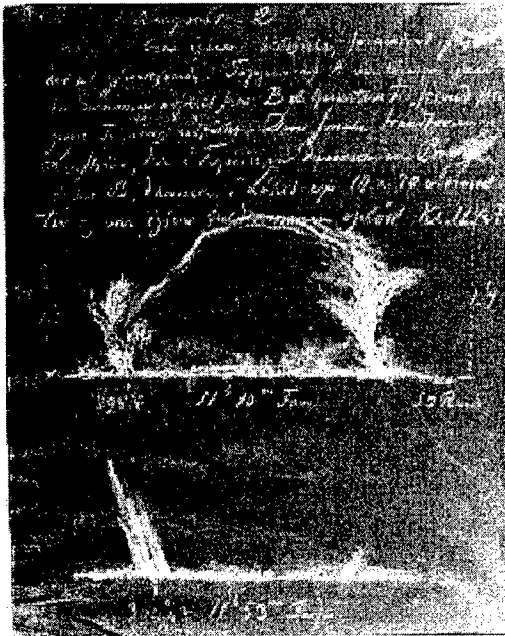
Figure 6.   Prominence drawing made by Fearnley in Norway, 1872–73
(courtesy Inst. for Theoretical Astrophysics, Oslo and O. Engvold).

6.   Development of Prominence Models, Interpretations, and Theory

During the later part of the spectroscopic period, serious discussions took place
as to the nature of prominences, and models were constructed to explain their
characteristics. Prominence models may be divided into two classes: those that
are concerned with the support of the prominence in the solar atmosphere, and
those that describe the internal, thermodynamic structure of the prominence
plasma.

6.1.   Prominence Support by Magnetic Fields

In 1951 – 100 years after the first, roughly correct, interpretation of the promi-
nence phenomenon – Menzel presented his model, showing that the prominence
could be supported in an assumed magnetic field; i.e., due to an equilibrium
between the Lorentz force and gravity (Bhatnagar et al. 1951). Refinements fol-
lowed quickly: Dungey's model, 1953 (Dungey 1953) and then the now-famous
Kippenhahn-Schlüter model in 1957 (Kippenhahn and Schlüter 1957). In 1972,
Anzer (1972) opened a new phase in the modeling research by using observed
magnetic fields and developing a method to calculate the electric current in qui-
escent prominences. Finally, as far as this overview is concerned, in 1974 came
the Kuperus and Raadu model for the so-called inverse-polarity prominences
(Kuperus and Raadu 1974). Notice that all these models are two-dimensional.

6.2. Internal Structure

More or less hand-in-hand with these developments in support mechanisms went research into the nature of the prominence plasma that was being supported. The early models of the plasma ignored the magnetic field but analyzed the temperature, density, and velocity structures; namely, the models due to de Jager (1959), Ivanov-Kholodny (1959), Jefferies and Orrall (1963), and Hirayama (1963). By the mid 1960's we could fairly well describe the thermodynamic nature of prominence plasmas.

6.3. Towards a Comprehensive Prominence Model

The last 20 years have seen increasingly sophisticated attempts at combining studies of the internal structures with analyses of magnetic-field supporting mechanisms. It is not the place in this historical introduction to go into details concerning these comprehensive model attempts. We shall hear about them in the days ahead, since the authors of several of these beautiful investigations are present here in Aussois. Of prime importance in these studies is the existence of a longitudinal component, and three-dimensional aspects, of the magnetic field in the prominence; a situation that entails the creation of helical fields, and points to magnetic reconnection as a basic mechanism in prominence behavior, intimately linked to the large-scale magnetic structure in the corona above and around the prominence (i.e., the helmet streamer with its coronal cavity). We shall surely hear more about these aspects as this colloquium proceeds.

References

Anzer, U. 1972, Solar Phys., 24, 324

d'Azambuja, L. and d'Azambuja, M. 1948, Ann. Obs. Paris-Meudon, 6, 7

Bhatnagar, P. L., Krook, M., and Menzel, D. H. 1951, Dynamics of Ionized Media, Rep. Conf. Univ. College, London

de Jager, C. 1959, Handbuch der Physik, 52, 80

de la Rue, W. 1868, MNRAS, 29, 73

Deslandres, H. 1897, Compt. Rend. Acad. Sci., 124, 171

Deslandres, H. 1910, Ann. Obs. Paris-Meudon, 4, I, 1

Dungey, J. W. 1953, MNRAS, 113, 180

Grant, R. 1852, History of Physical Astronomy, Robert Baldwin: London

Hale, G. E., and Ellerman, F. 1903, Publ. Yerkes Obs., 3, Part 1, 3

Hirayama, T. 1963, PASJ, 15, 122

Ivanov-Kholodny, G. S. 1959, AZh, 36, 589

Janssen, P. J. 1868, Compt. Rend. Acad. Sci., 67, 838

Jefferies, J. T. and Orrall, F. Q. 1963, ApJ, 137, 1232

Kippenhahn, R. and Schlüter, A. 1957, ZAp, 43, 36

Kuperus, M. and Raadu, M. A. 1974, A&A, 31, 189

Lockyer, J. N. 1868a, Compt. Rend. Acad. Sci., 67, 836

Lockyer, J. N. 1868b, Compt. Rend. Acad. Sci., 67, 949

Lyot, B. 1936, Compt. Rend. Acad. Sci., 202, 392.

Secchi, A. 1868, Compt. Rend. Acad. Sci. 66, 396.

Secchi, A. 1875-77, Le Soleil, Gauthier-Villars, Paris, Vols. 1 and 2

Ulloa, A. 1779, Phil. Trans. Roy. Soc. London, 69, 105

Vassenius, B. 1733, Phil. Trans. Roy. Soc. London, 38, 134

Vyssotsky, A. N. 1949, Meddelanden Lund. Obs., 2(126), 9

Filaments and Their Environment

Observations of Filament Structure and Dynamics

Oddbjørn Engvold

Institute of Theoretical Astrophysics, University of Oslo,
P.O. Box 1029, Blindern, N-0315 Oslo, Norway

Abstract. Past and recent observations of spatial and temporal variations in fine structure of solar prominences/filaments are reviewed. Magnetic fields permeate the prominence plasma and play a decisive role in shaping the fine structure and its dynamics. Consequently, the shape, orientation, and possibly the strength, of the magnetic field may be inferred from the observed sub-structures. The review discusses possible physical implications of small-scale structures in the low-β prominence plasma.

1. Introduction

The fine structure of prominences holds the answers to fundamental questions in prominence research, such as how and why prominences form and how they are supported. The reasons for their fibril nature and varied complex forms are essentially unanswered at present. Magnetic fields permeate the prominence plasma and thereby serve to support the dense plasma against gravity and provide thermal insulation against the hot, surrounding corona.

The basic properties of solar prominences (filaments) are described and discussed in great details in proceedings and text books (cf., Jensen et al. 1979, Poland 1986, Ballester and Priest 1988, Priest 1989, Ruzdjak and Tandberg-Hanssen 1990, and Tandberg-Hanssen 1995). It is the aim of the present review to discuss the physical significance of prominence structure, their dynamics, and relation to the environment.

One distinguishes between three basic types of filaments:

- *Active Region Filaments*, which form between and close to active region complexes.

- *Quiescent Filaments* that appear in or between weak remnants of active regions.

- *Intermediate Filaments* form between weak unipolar background field regions and active region complexes, and constitute a class in between to other two.

2.   Spatial Structures

Prominences, which are referred to as *filaments* when observed on the disk, always lie above the *Polarity Inversion*, i.e,. where the radial component of the network magnetic field changes sign. Quiescent filaments range in length from about 50,000 to 200,000 km. They appear sometimes as continuous, elongated structures, but frequently also broken up into trains of separate segments. Prominences may appear as vertical, thin sheets, ranging in height from 10,000 km to 80,000 km above the photosphere.

Quiescent prominences consist of numerous thin threads, 5,000 km to 15,000 km long, and from 200 km to 1,500 km in width (Dunn 1960, Engvold 1976). In some prominences one also sees small, bright knots of similar dimensions. The thickness of the threads appears to increase with height above the solar limb (Engvold 1976). In filaments on the disk many threads are inclined to the direction of the long axes of the filament by about 30°.

At semi-regular intervals along a filament, the threads form pointed structures extending out from the filament body, which are referred to as *barbs* (cf., Kiepenheuer 1953). The ends of large filaments, which invariably bridge opposite magnetic polarities in the photosphere below, often fan out in the shape of a thin "shroud".

When seen at some distance from disk center, quiescent filaments display a well defined, sharp upper edge, which is labeled the filament *spine*. A spine often consists of several thin, long absorbing threads. At the limb spines are less conspicuous and generally more diffuse in Hα. Images of prominences in HeII 304Å observed with EIT/SOHO invariably show much sharper upper edges, which suggests an increase of temperature with height.

3.   Filament Barbs and Inverse Polarity

Rust and Kumar (1994) subscribe to the idea that filaments represent large, twisted flux ropes, where screw threads of the helix provide locations of magnetic support. If all filaments on the northern hemisphere were left-handed helical fields, and the magnetic fields were filled with Hα emitting gas, the observed field direction would be *inverse*. This model appears to disagree with the fact that barbs are not recognized as upward curved screw threads of a helix, and that barbs are never seen to cross the polarity inversion (Martin et al. 1994).

When filaments are situated close to the solar limb, barbs are usually seen only on the center-near side, which suggests that they are directed downwards. In Hα filter-grams from the solar limb, prominence barbs have the appearance of slightly curved pillars rooted in the chromosphere.

It has been noticed by Martin and co-workers that filament barbs seem to connect to the minority polarity flux on either side of the polarity inversion line (Martin 1994), whereas coronal arches appear to be rooted in the network flux (majority polarity). The preference for barbs to connect to the minority polarity of magnetic fields is evidently essential for the formation process and very existence of quiescent prominences. Engvold and Yi (1997) found that barbs of quiescent filaments connect to the weak field intra-cell region of the photospheric supergranulation cells, rather than to the much stronger (∼ 1kG)

network field. Newly born barbs point into up-flow regions of the dynamic supergranulation cells, were possibly new weak magnetic flux emerges.

Martin et al. (1992) and Martin and Echols (1994) showed that barbs always bear to the right, when viewed from either side, in dextral filament channels, and to the left in sinistral channels. This latter relation is unambiguous, and one may therefore distinguish between dextral and sinistral filament channels simply from the "bearing" of the filament barbs.

4. Flows and Oscillations

The term *quiescent* is somewhat misleading in describing stable, large filaments, since they in reality are rather dynamic structures. One sees small-scale line-of-sight velocities of a few km s^{-1}, both in horizontal and vertical directions (Engvold 1972, Dunn 1960, Stellmacher and Wiehr 1994). Doppler measurements in disk filaments show both upwards and downwards mass motion (see Schmieder 1989, and papers cited therein). It was later noted by Yi et al. (1991) that the dominant vertical motion in the main body of filaments was oscillatory. Periodic velocities and intensity oscillations have a large range of periodicities, from less than 1 min to hours (Yi et al. 1991, Thompson and Schmieder 1991, Balthasar and Wiehr 1994). An excellent review of oscillations in prominence fine-structure is given by Joardar et al. (1997), who also discuss and classify hydromagnetic modes of oscillations in thin magnetic strings, which appear to be in good agreement with observations.

Unpublished observations in Hα by Jack Zirker and collaborators seem to show flow-type motions in barbs. The true sign of these flows is partly disturbed and confused by small-scale structures and motions in the chromosphere below.

5. The Nature of Fine-Structure Threads

It is generally assumed that the fine-structure threads outline their magnetic flux tubes. This view is substantiated by the fact that the threads of large, quiescent filaments are inclined relative to the filament long axis, similar to the magnetic field (Leroy 1989, Bommier et al. 1994, Bommier and Leroy 1998, these proceedings). On the other hand, one would not expect to find strongly inhomogeneous magnetic fields in low-β filament plasmas. Therefore, one is led to to speculate whether the fine threads seen in Hα could represent "veins" of dense plasma in a relatively uniform magnetic field, rather than individual flux ropes? Such a model is, however, at variance with a notable fluctuation in the line-of-sight velocity of neighboring threads (Engvold 1972, Zirker and Koutchmy 1990, 1991, Stellmacher and Wiehr 1994), which seems to imply that the threads represent separate flux tubes. A possible weak interaction between neighboring threads is indicated by the findings of Mein and Mein (1991) that the *velocity* threads seem to be slightly thicker than the *density* threads.

In hedgerow prominences the lifetime of vertical threads is ≤10 min (Engvold 1976). High resolution Hα filtergrams obtained with the SVST, La Palma, show individual, thin filament threads appearing and disappearing in the course of one minute. This suggests that prominence plasma may be undergoing rapid

variations in temperature and/or density. Such short lifetimes could imply that the prominence plasma is not in a stationary radiative state (Engvold 1980).

6.   Temperature Structure

The core temperatures and electron densities of prominence plasma are, respectively, $T_e = 6000\text{--}8000\text{K}$ and $N_e = 10^{10} - 10^{11}$ cm^{-3} (Hirayama 1990). There is evidence of more low temperature gas in the prominence and cavity regions than one detects with "normal" Hα exposure times. Leroy (1972) found signs of very faint Hα emission in the corona close to prominences. The same data was re-examined by Dermendjiev et al. (1994) who saw faint coronal Hα emission also in the form of long systems of drops and fibrils outlining large, smooth curves that one normally associates with magnetic loops. It was concluded from these studies that coronal cavities also contain a noticeable amount of low temperature gas. Furthermore, this view is supported by the observations of radio-filaments ($\lambda \geq 3$ cm) showing more cold filament material than Hα (Gopalswamy et al. 1991). The lower gas pressure in such regions must evidently be balanced by a higher magnetic pressure.

The fact that solar prominences contain gas at all temperatures between 10^4 K and 10^6 K is demonstrated by their strong EUV line emissions (Kjeldseth-Moe et al. 1979, de Boer et al. 1998, these proceedings). Pojoga (1994) studied the variation with height of the Emission Measure (EM) from EUV lines and concluded that the emitting structures have sub-resolution geometries. The nature of these geometries is still unknown. The following are two alternative scenarios:

1. The threads, situated in a hot coronal cavity with cold cores, are "wrapped" in a thin transition region perpendicular to the magnetic field (Chiuderi-Drago et al. 1992).

2. The individual threads are essentially isothermal, but a given thread may attain temperatures between 10^4 K and 10^6 K (Pojoga 1993).

Since magnetic flux ropes constituting filament threads must be anchored somewhere on either side of the filament, the ropes are evidently a lot longer than their observable lengths in Hα. The observational results from wave motions in filament threads (Yi et al. 1991, Yi and Engvold 1991) seem to support this view. These results suggest that temperature and/or density vary along a given flux rope.

7.   The Paradox of Vertical Magnetic Threads

Zirker et al. (1994) confirmed the results from earlier studies showing no evidence for "free fall" velocities in large, quiescent prominences where a vertical thread structure is well developed. The nagging question then becomes, if the threads are nearly vertical magnetic flux tubes, what prevents the gas from falling freely in the field of gravity?

Fontenla et al. (1996) studied stationary prominence thread models including ambipolar diffusion and horizontal magnetic fields. However, such models fail to explain the structural character and dynamic aspects of threads.

Jensen (1990) suggested that non-linear Alfvén waves might provide support of prominence plasma. A similar idea was put forward by de Pontieu and Haerendel (1994) who claimed that weakly-damped Alfvén waves could explain the acceleration of spicules. However, wave support does not work for prominences, for the following reason: If wave motion shall influence the pressure beyond the normal thermal gas pressure, the wave amplitude v must be:

$$v > (\frac{2kT}{\mu m_H})^{\frac{1}{2}} \qquad (0.1)$$

In the case of prominence plasma with T$\approx$ 8000K, the "equivalent" wave amplitude corresponds to 9.1 km s^{-1}. Therefore, in order to increase the pressure scale height by a factor 100, e.g. from 170 km to 17,000 km, the wave amplitude must be $v \geq$90 km s^{-1}. Such supersonic velocities are hardly ever observed in quiescent prominences.

Table 1. Estimates of radiative pressure exerted by absorption of some strong chromospheric lines. The values of $d\ell_s$ given in the 5th column are the maximum column heights that can be supported by the radiative pressure for a given line when $\rho = 7 \times 10^{-14}$ [g cm^{-3}]. $d\ell_{\tau \approx 1}$ is the distance in the gas element corresponding to an optical depth τ=1.

Transition	F_λ (*)	$\Delta\lambda$ [Å]	$\rho\, d\ell$ [g cm^{-2}]	$d\ell_s$ [km]	$d\ell_{\tau=1}$ [km]
Lyα	2.0×10^4	1.5	1.2×10^{-10}	0.017	0.005
Ly-C (912)	2.0×10^4	$\sim$120	$< 9.3 \times 10^{-9}$	<1.30	53
Hα	1.5×10^5	0.60	1.2×10^{-9}	0.170	610
Ba-C (3647)	3.2×10^6	$\sim$500	$< 6.1 \times 10^{-6}$	< 870	4×10^7
He I D$_3$	3.0×10^6	0.35	4.0×10^{-9}	0.570	900
He I 10830	1.0×10^6	0.75	2.9×10^{-9}	0.410	600
Ca II H	2.4×10^5	0.12	1.1×10^{-10}	0.160	150
Ca II K	2.4×10^5	0.14	1.3×10^{-10}	0.180	76

(*) Units: [erg cm^2 s^{-1} sr^{-1} Å^{-1}]

The pressure exerted by incident photospheric and chromospheric radiation will balance a prominence element of column mass $\rho d\ell$ when:

$$\rho\, d\ell = \frac{\pi F_\lambda \Delta\lambda}{g_\odot\, c} \qquad (0.2)$$

where F_λ is the mean monochromatic flux over the spectral width $\Delta\lambda$, $g_\odot$ is the acceleration of gravity, c is the speed of light, and ρ is gas density. For the sake of argument we may here assume a structure thickness $d\ell \simeq$100 km, which is the order of magnitude of the finest observed structures. A plasma density $\rho \simeq 7 \times 10^{-14}$ [g cm^{-3}] (Hirayama 1990) then yields a column mass

$\rho d\ell \simeq 7 \times 10^{-7}$ [g cm^{-2}]. It is important to note that radiative pressure provides support in the field of gravity for only an outer layer of thickness $\tau \simeq 1$. When an element is optically thin, only a correspondingly smaller fraction of the radiation will be absorbed and contribute to a radiative lift. Adopting incident radiative fluxes from Pierce and Allen (1977) and Vidal-Madjar (1977), and line absorption coefficients from Allen (1973), one finds (Table 1) that absorption in prominent lines of H, He and Ca can support less than 1% of this column mass. Prominence plasma is transparent to the vastly greater energy in the incident continuum radiation, which provides even less radiative push. Considering that this example was calculated for a very small column mass, we may safely conclude that radiation pressure cannot support prominences.

A possible solution to the paradox of vertical magnetic threads could be that a thread of thickness, for instance, 300 km is actually a "rope" of a many much thinner fibers, which each undergoes rapid changes in temperature. In a given fiber, newly condensed Hα emitting gas is rapidly heated again to high temperature, before it attains a free falling velocity much larger than a few km s^{-1}. The observable velocities along a resolved thread will be the collective result from many unresolved fibers in a thread. A more detailed study of such models is under way.

8. Associated Structures

8.1. Bright rims

Bright rims are often noticed in Hα filtergrams at the center-near side of filaments (Royds 1920, d'Azambuja and d'Azambuja 1948). Kostik and Orlova (1975) proposed that the brightening was the result of back scattering from the bottom parts of a filament to the chromosphere below. Some observers claim that the brightening is located in the lower edge of the filament. Heinzel et al. (1995) found that bright rims could result from diffusion of incident Hα radiation in the lower part of the filament. Paletou (1997) repeated these calculations in a 2-D geometry and concluded that radiative diffusion would be rather evenly distributed over the filament, and that the mechanism could not explain bright rims. Hence, the origin of filament bright rims is still not well understood.

8.2. Cavities

Eclipse observations have shown that quiescent prominences are embedded in a complex coronal structure of a darker cavity within arches at the base of thin coronal streamers (Saito and Tandberg-Hanssen 1973). The outer helmet streamer structure is often seen in white-light eclipse observations.

A unique set of high resolution, white-light images of the solar corona were obtained with the 3.6 m Canada-France-Hawaii Telescope on Mauna Kea during the eclipse of July 11, 1991 (Koutchmy et al. 1994, November and Koutchmy 1996). The images show arcades of concentric, fine-scale, dark and bright loop-like structures extending above a small prominence at the limb. A small coronal cavity close to the prominence contains numerous fine, dark threads which demonstrate better than any data before that a cavity region is highly structured and inhomogeneous.

8.3. Bright X-ray axial structures

Martin and McAllister (1995) studied the orientation of X-ray arcades over filament channels from Yohkoh data, and noticed a change in magnetic shear with altitude. The inferred change in direction of the magnetic field, from the low temperature up into the coronal arches above, is difficult to verify observationally. In Yohkoh images one occasionally sees transient, thin filamentary structures that run close to Hα filaments (Solberg and McAllister 1998, these proceedings). These X-ray filaments are, conceivably, associated with a layer of sheared magnetic fields, at some height in the cavity, where the magnetic spine of the filament touches the lower boundary of the helmet structure.

References

Allen C W. 1973, Astrophysical Quantities, Univ. of London, The Athlon Press

Ballester J L and Priest E R (eds.) 1988, Workshop on Dynamics and Structure of Solar Prominences, Universite de les Illes Baleares

Balthasar H and Wiehr E. 1994, A&A, 286, 639

Bommier V, Landi Degl'Innocenti E, Leroy J-L, and Sahal-Bréchot S. 1994, Solar Phys., 154, 231

Chiuderi Drago F, Engvold O, and Jensen E. 1992, Solar Phys., 139, 47

d'Azambuja L and d'Azambuja M. 1948, Ann. Obs. Paris-Meudon, VI, 7

Dermendjiev V N, Mouradian Z, Duchlev P, and Leroy J-L. 1994, Solar Phys., 149, 267

de Pontieu and Haerendel G. 1994, in Solar Coronal Structures, V. Rusin et al. (eds.), VEDA, Slovak Rep., p. 323

Dunn R B. 1960, PhD Thesis, Harvard University

Engvold O 1972, Solar Phys., 23, 346

Engvold O 1976, Solar Phys., 49, 283

Engvold O 1980, Solar Phys., 67, 351

Engvold O and Yi Z. 1997, in preparation

Fontenela J M, Rovira M, Vial J-P, and Gouttebroze P. 1996, ApJ, 466, 496

Gopalswamy N, White S M, and Kundu M R. 1991, ApJ, 379, 366

Heinzel P, Kotrc P, Mouradian, Z, and Buykliev G T. 1995, Solar Phys., 160, 19

Hirayama T. 1990, in Dynamics of Quiescent Prominences, (eds.) V. Ruzdjak and E. Tandberg-Hanssen, Lecture Notes in Physics 363, Springer-Verlag, New York, p. 187

Jensen E, Maltby P, and Orrall, F Q (eds.) 1979, Physics of Solar Prominences, IAU Coll. 44, Oslo

Jensen E. 1990, in Dynamics of Quiescent Prominences, (eds.) V. Ruzdjak and E. Tandberg-Hanssen, Lecture Notes in Physics, 363, Springer-Verlag, New York, p. 129

Joardar P S, Nakariakov V M, and Roberts B. 1997, Solar Phys., 173, 81

Kiepenheuer, K O 1953, in The Sun, G. P. Kuiper (ed.), Univ. of Chicago Press, Chicago, p. 395

Kjeldseth-Moe O, Cook J W, and Mango S A. 1979, Solar Phys., 61, 319

Kostik R I and Orlova T V. 1975, Solar Phys., 45, 119

Koutchmy S et al. 1994, A&A, 281, 249

Leroy J-L. 1972, Solar Phys., 25, 413

Leroy J-L. 1989, in Dynamics and Structure of Quiescent Solar Prominences, E.R. Priest (ed.), Kluwer Acad. Publ., Dordrecht, Holland, p. 77

Martin S F. 1994, BAAS, **26**, 1522

Martin S F, Marquette, W H, and Bilimoria R 1992, in The Solar Cycle, K. L. Harvey (ed.), ASP Conf. Ser., Vol. 27, San Francisco, p. 53

Martin S F, Bilimoria R and Tracadas P W. 1994, in Solar Surface Magnetism, (eds.) R J Rutten and C J Schrijver, Kluwer Acad. Publ., Dordrecht, Holland, p. 303

Martin S F and Echols C R. 1994, in Solar Surface Magnetism, (eds.) R J Rutten and C J Schrijver, Kluwer Acad. Publ., Dordrecht, Holland, p. 339

Martin S F and McAllister A H. 1995, BAAS, 27, 961

Mein P and Mein N. 1991, Solar Phys., 136, 317

November L J and Koutchmy S. 1996, ApJ, 466, 512

Paletou F. 1997, A&A, 317, 244

Pierce A K and Allen R G. 1977, The Solar Output and Its Variations, Colorado Associated University Press, Boulder, O.R. White (ed.), p. 169

Pojoga S. 1994, in Solar Coronal Structures, (eds.) V Rusin, P Heinzel and J-C Vial, VEDA Publ. Company, Slovak Rep., p. 357

Poland A I (ed.), 1986, Coronal and Prominence Plasmas, NASA Conference Publication 2442, Washington, DC

Priest E R (ed.), 1989, Dynamics and Structure of Quiescent Solar Prominences, Kluwer Acad. Publ., Dordrecht, Holland

Royds T. 1920, Kodaikanal Obs. Bull., 63, 289

Rust D M and Kumar A. 1994, Solar Phys., 155, 69

Ruzdjak V and Tandberg-Hanssen E (eds.) 1990, Lecture Notes in Physics 363, Springer-Verlag, New York

Saito K and Tandberg-Hanssen E. 1973, Solar Phys., 31, 105

Schmieder B. 1989, in Dynamics and Structure of Quiescent Solar Prominences, E R Priest (ed.), Kluwer Acad. Publ., Dordrecht, Holland, p. 15

Stellmacher G and Wiehr E. 1994, A&A, 290, 655

Tandberg-Hanssen E. 1995, The Nature of Solar Promiences, Kluwer Acad. Publ., Dordrecht, Holland

Thompson W T and Schmieder B. 1991, A&A, 243, 501

Vidal-Madjar A. 1977, The Solar Output and Its Variations, Colorado Associated University Press, Boulder, O.R.White (ed.), p. 213

Yi Z, Engvold O, and Keil S L. 1991, Solar Phys., 132, 63

Yi Z, Engvold O. 1991, Solar Phys., 134, 275

Zirker J B and Koutchmy S. 1990, Solar Phys., 127, 109

Zirker J B and Koutchmy S. 1991, Solar Phys., 131, 107

Zirker J B, Engvold O, and Yi Z. 1994, Solar Phys., 150, 81

Dynamics and Fine Structures in Quiescent Prominences (MSDP/Pic du Midi, SOHO/SUMER and CDS)

Kejun Li[2], J.-M. Malherbe[1], J.E. Wiik[4,5], B. Schmieder[1,4], Th. Roudier[3], T. Kucera[6], and A. Poland[6]

Abstract. During the June 1996 campaign using the MSDP spectrograph at Pic du Midi and SUMER/CDS (JOP 12) on board SOHO, quiescent prominences were observed. We present observations and physical quantities of the June 5 prominence. Doppler shifts, temperatures and electron densities of fine structures were deduced from Hα data.

1. Observations

Observations of the prominence were performed on June 5, 1996 between 09:30 to 11:00 UT in Hα with the MSDP spectrograph at Pic du Midi (11 simultaneous 2D channels of 4' x 30") together with the spectrographs on SUMER and CDS. Data were also recorded with the Meudon Spectroheliograph (Hα and CaII K) and with the Hα coronograph of Wroclaw Observatory (Rompolt and Rudawy 1997, private comm., Wiik et al. 1997). Figure 1 shows a set of data obtained at Meudon (spatial resolution of 1.8") and Pic du Midi (0.5") for chromospheric temperatures, and by SUMER (1.5") for transition zone temperatures. We also have data from CDS in various lines from 8×10^4 K to more than 10^6 K (Figure 2).

We have to date worked essentially on Hα line profiles in order to derive physical parameters from spectroscopic diagnostics. The profiles in Figure 3 show symmetrical line profiles, which have been fitted by a least square method to a cloud model; asymmetrical line profiles have been fitted using a two-cloud model (Li et al. 1994). We made the assumption that the source function can be considered as a constant if the optical thickness at the line center is less than unity. We derive with this method the line of sight velocity (Doppler shift), the column density of hydrogen at the second level, N_2 (from the Doppler width of the line and the optical thickness at line centre), the excitation temperature (from the source function and departure coefficients, see Gouttebroze et

---

[1] Observatoire de Paris, DASOP, 92195 Meudon, France

[2] Yunnan Observatory, Kunming, China

[3] Observatoire Midi Pyrénées, 65200 Bagnères de Bigorre, France

[4] University of Oslo, PO Box 1029, Blindern, 0315 Oslo, Norway

[5] Observatoire de Nice, BP 229, 06304 Nice Cedex 4, France

[6] NASA, GSFC, MD 20771, USA
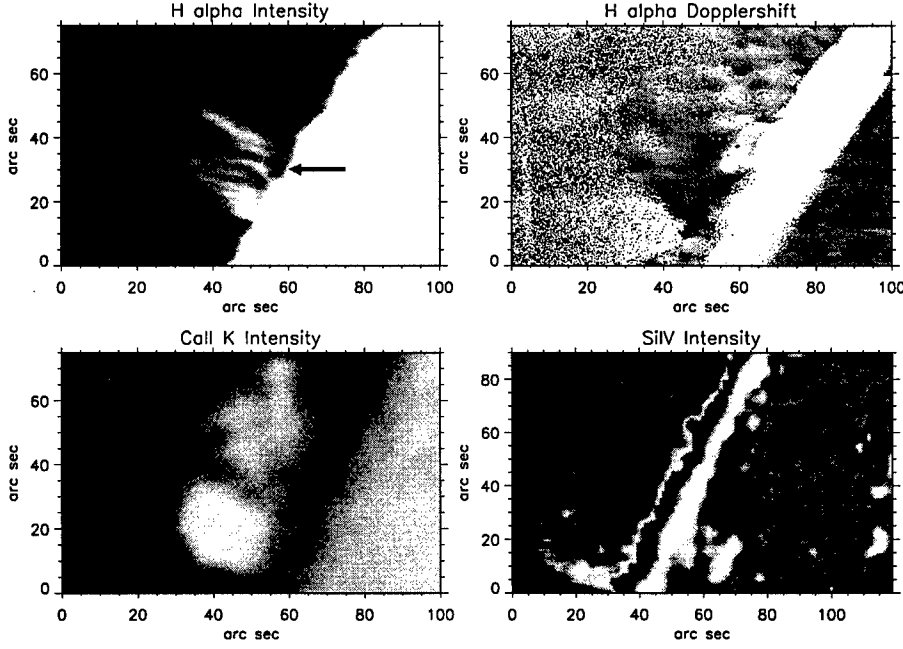
Figure 1.   Observations.   Top: MSDP/Pic du Midi; bottom left:
Meudon; bottom right: SUMER/SOHO

al. 1993), and a microturbulent velocity, V_t (assuming that the Doppler width
is the combination of a thermal and non-thermal component). We also com-
puted the electron density derived from the relationship between the emission
measure, E, and the integrated observed $H\alpha$ intensity given by Heinzel et al.
(1994). Values of n_e were, hence, obtained by this method according to the
equation, $n_e^2 D = 10^{28.9}$ (from observations), where D is the thickness of the
structure. Results are presented in the tables for some pixel locations covering
the prominence (in both tables, N_2 is expressed in terms of 10^{12} cm^{-2}).

Table 1. Physical quantities of some symmetrical $H\alpha$ line profiles

Prof.	$V_{//}(kms^{-1})$	$V_t(kms^{-1})$	$T_{ex}(K)$	N_2	$E\ (ergs^{-1}cm^{-2}sr^{-1})$
A	3.93	15.9	7181	1.85	0.67×10^5
B	2.49	14.2	6742	2.35	0.63×10^5
C	3.65	14.6	9633	0.88	0.77×10^5
D	2.97	13.4	10405	0.62	0.66×10^5

2.   Discussion and Conclusion

Tables 1 and 2 show that reasonable values are obtained from the cloud model
applied to symmetrical profiles. Table 3 shows the result of the two-cloud method

applied to asymmetrical profiles and reveals the existence of two structures with opposite velocities.
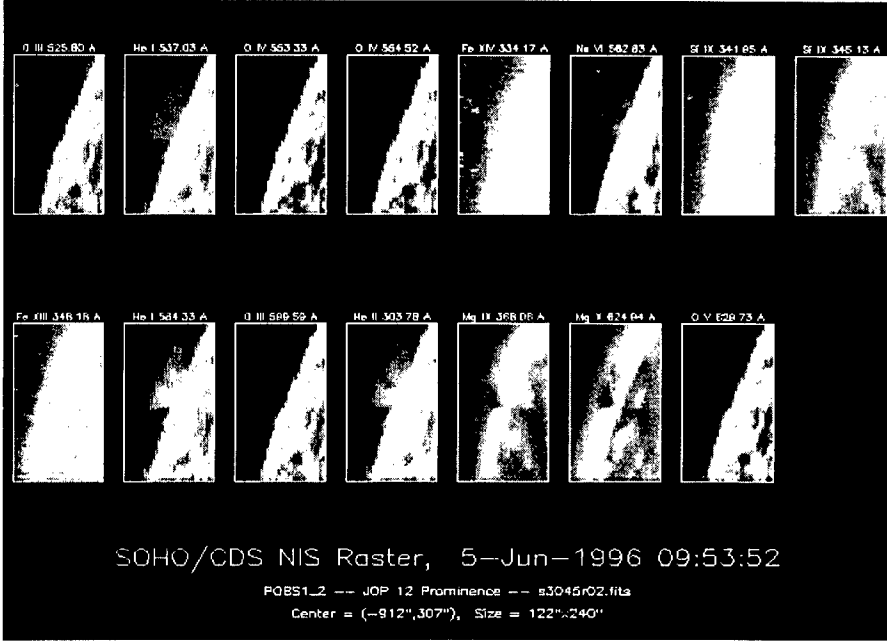
Figure 2.   Observations in different lines with CDS/SOHO

Table 2. Electron density, n_e, variation with thread thickness, D, derived from NTLE relationship between emission measure, E, and Hα intensity.

$D(km)$	1000	1500	2000	2500	3000	3500	4000
$log_{10}n_2$	4.15	3.98	3.85	3.75	3.68	3.61	3.55
$n_e(\times 10^{10}cm^{-3})$	2.82	2.30	1.99	1.78	1.63	1.51	1.41

Table 3. Physical quantities of some asymmetrical lines

Prof.	The first cloud				The second cloud			
	$V_{//}$ (km/s)	V_t (km/s)	T_{ex} (K)	N_2	$V_{//}$ (km/s)	V_t (km/s)	T_{exc} (K)	N_2
1	-19.48	9.2	6970	0.33	2.38	13.7	7978	1.23
2	-9.75	8.0	17542	0.19	6.20	24.6	8272	6.74
3	-15.57	9.3	7080	0.20	2.49	14.5	7379	1.19
4	-11.39	10.6	16854	0.58	10.1	15.9	21563	0.90
5	-3.42	22.8	21853	1.15	15.8	9.7	9588	1.18
6	9.29	21.2	15737	1.27	-15.8	16.1	12871	1.45

The different line profiles studied in Tables 1 and 3 are taken along a cross section of the prominence as indicated by an arrow in Figure 1. In particular, the asymmetrical profiles of Table 3 are observed in the "Hα black hole or cav-
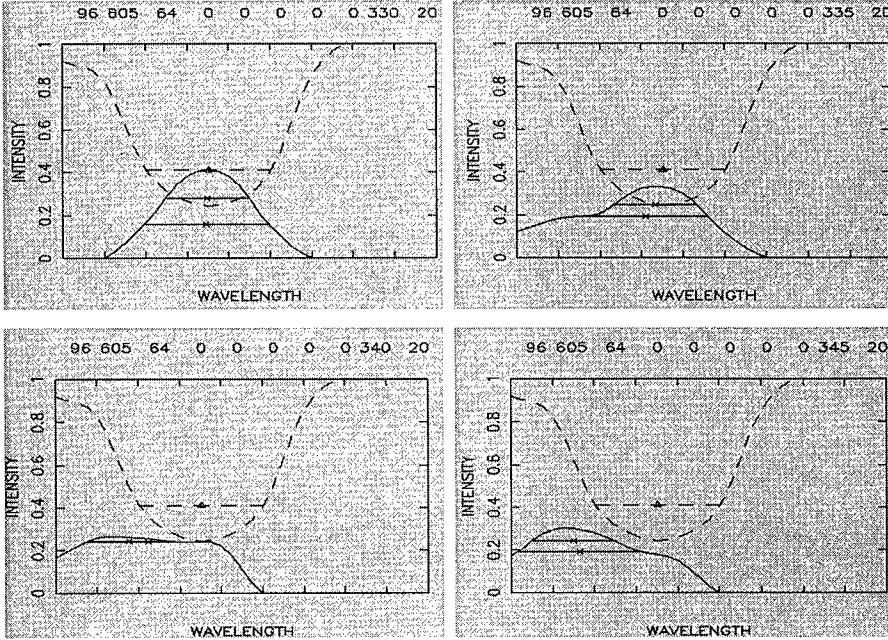
Figure 3. $H\alpha$ observed line profiles (MSDP/Pic du Midi; dashed line for mean chromospheric profile, continuous line for prominence profile). Both symmetric and asymmetric profiles are observed. The wavelength step between two consecutive channels is 0.26 $\mathring{A}$.

ity" at the bottom of the prominence. This "cavity" was well observed between 09:50 and 10:05 UT. Opposite radial velocities (magnitudes of the order of 10 km/s) are found inside this structure using the two-cloud inversion, which seems to reveal the presence of two dynamically different threads. The temperatures derived from our calculations are typical for prominences (10^4 K) and the electron densities are of the order of 2×10^{10} cm^{-3}, in agreement with previous results (Leroy and Bommier 1997, private communication).

References

Gouttebroze P., Heinzel P. and Vial J.-C. 1993, A&AS, 99, 513

Heinzel P., Gouttebroze˙P. and Vial J.-C. 1994, A&A, 292, 656

Li K. et al. 1994 Solar Phys., 150, 87

Wiik J.E. et al. 1997, JOSO Annual Report, 93

Observations of the Association of Prominences and the Surrounding Corona

Raymond N. Smartt

National Solar Observatory/Sacramento Peak, National Optical Astronomical Observatories, P.O. Box 62, Sunspot, NM 88349, USA

Zhenda Zhang

Department of Astronomy, Nanjing University, Nanjing, China

Vladimir S. Airapetian

Code 681/CSC, NASA/GSFC, Greenbelt, MD 20771, USA

Ira S. Kim

Sternberg State Astronomical Institute, Moscow State University, Universitetsky pr. 13, 119899 Moscow, Russia

Abstract. Emission-line coronal images in Fe XIV (530.3 nm) and FeX (637.5 nm) show faint enhancements at the location of quiescent prominences. Such enhancements can appear in the outer portions of a prominence, similar to the high-temperature sheath surrounding prominences as inferred from UV and EUV observations. The observational evidence supports the interpretation that this enhanced coronal emission is due to energy carried by the prominence threads and dissipated in the adjacent coronal region. Also, observed coronal loop interactions involving partial magnetic reconnection have associated Hα structures. These structures can have the appearance of an active prominence, similar to those typically observed in post flare loop systems. It appears that the association of such active prominences with the adjacent corona is fundamentally different from that of quiescent prominences. The observations indicate that these types of active prominences arise simply as a consequence of reconnection processes in the corona itself.

1. Introduction

Observations of quiescent prominences in UV and EUV lines reveal critical information about the prominence-corona transition region (PCTR). It is inferred that the outer layers of a prominence form a transition zone in a shell-like structure, or sheath, between the cool prominence itself and the hot corona. It is assumed that individual threads within a quiescent prominence also have a PCTR (e.g., Orrall and Schmahl 1976, Chiuderi Drago et al. 1992). But regardless of the exact distribution of sources of the PCTR within, or around, a typical quiescent prominence, the data lead to estimates of very small scale thicknesses (<100

km) for the separate layers, each corresponding to one temperature regime as characterized by a given line emission (Schmahl et al. 1974).

Observations with a 20-cm aperture emission-line coronagraph reveal occasional anomalous emission associated with quiescent prominences. The coronagraph records images in FeXIV (530.3 nm; $T\sim2\cdot10^6$), FeX (637.5 nm; $T\sim10^6$), and Hα. A particular case from these data that showed relatively strong prominence–associated coronal emission has been described (Smartt and Zhang 1984). As seen in the red-line image, the initially faint emission gradually changed in form over several hours to become concentrated around the periphery of this compact prominence, appearing as an enhanced band of coronal emission outlining the prominence. While much weaker, the green-line image also evolved to a similar form. The half-widths of the legs of these coronal enhancements were $\sim4\cdot10^3$ km for the red-line image, and $\sim3\cdot10^3$ km for the green-line image.

Since the PCTR, as observed in UV and EUV lines, spans the temperature transition between the cool prominence material and the ambient corona, it appears that the above visible-line coronal observations are not strictly part of the PCTR, except perhaps for some contribution from the low-temperature tail of the ionization equilibrium curve for FeX. Therefore it was concluded that these enhancements were evident primarily because of an enhanced density and/or temperature in this region. Density estimates for the PCTR for quiescent prominences have been found to be only marginally greater than those of the ambient corona (Wiik et al. 1994). For example, using line-sensitive line ratios of CIII, an average value of 1.3 10^9 cm^{-3} was found for the density within the interface where CIII is formed ($T = 9\cdot10^4$K) (Orrall and Schmahl 1976). Hence, it was further concluded that the observed visible coronal emission is due principally to a significant increase in the temperature in this region resulting from energy dissipation from the prominence to the adjacent coronal volume.

The observed relationship between visible coronal emission and quiescent prominences is extended to post-flare loop systems and the associated active prominences.

2. General Characteristics of Visible Corona/Quiescent Prominence Observations

a) In about 80% of the cases studied, red-line emission is evident, but mostly extremely weak, and typically showing only as fine features at the location of one or more of the central pillar-like structures in the prominence. These features can evolve in form and brightness, but such changes are usually evident only on time scales of hours.
b) If a red-line image is brighter, a corresponding green-line image is then evident, but is invariably weaker than the red-line image.
c) In most, but not all cases, the structure is similar in the two images.
d) Occasionally a red-line image appears to be surrounded by a coronal cavity, possibly a circumstance where the line-of-sight is along the long axis of the prominence. Such a cavity is usually only marginally apparent in the green-line image, the difference due possibly to the greater number of loops that appear in the green-line corona in general, as compared with the red-line corona, and hence the greater likelihood that foreground and background loops will obscure

such a cavity.

2.1. Interpretation

Coronal emission observed in association with quiescent prominences is due to energy released through processes intrinsic to the prominence structure and hence complex field configurations, but at a level that barely excites red-line emission and rarely green-line emission. The possible contribution to coronal heating by the propagation and damping of slow-mode, fast-mode, and Alfven MHD waves in a prominence has been investigated (Smartt and Zhang 1984). We have also considered the possibility that resonant absorption of surface Alfven waves produces the observed prominence-related coronal enhancements. In brief, surface Alfven waves generated at the photosphere propagate upwards along a magnetic loop. Energy flux conservation implies that the amplitude of a surface Alfven wave, δV, is proportional to $B^{-1/2}$ (Hollweg 1990) and, therefore, rapidly increases as the waves travel from the photosphere, through the chromosphere and into the transition region and beyond. For such a wave, δV reaches a maximum at the surface of the loop (prominence) and decreases rapidly towards the center, forming a velocity shear. Eventually, if the velocity shear associated with the Alfven waves becomes sufficiently large, a Kelvin-Helmholtz instability will be initiated in the outer parts of a loop, as shown numerically by Ofman and Davila (1994). This process converts the wave energy into MHD turbulence, the fluid motions directed primarily perpendicular to the magnetic field. The consequent large-scale turbulence is then expected to cascade to smaller sizes that are efficiently damped through viscous and ohmic dissipation processes. Our estimates of the heating rate show that large-scale motions initiated by a non-linear Alfven wave would introduce non-thermal broadening in high-temperature lines, ~15 km/s for typical parameters in the thin outer layers of a prominence, which could be checked observationally.

3.   Characteristics of Visible Corona/Active Prominence Systems

a) Coronal structures can differ between the two coronal line images, and these are often substantially different from the prominence Hα structure itself.
b) The green-line image is invariably brighter than the red-line image.
c) In one case where there was a small, detached portion of a prominence at a height ~140·10^3 km (highest part), there was a corresponding red-line feature at a height ~180·10^3 km, and a similar, but fainter green-line feature at a height ~230·10^3 km.
In the case of post-flare loop prominence systems:
d) Hα and coronal loops are typically present, but the loops are not coincident.
e) Faint, extensive diffuse emission can also appear in association with these systems in both coronal images.
f) Localized transient brightenings in the form of coronal loop interactions (CLI) are observed in visible coronal loop systems, especially evident in association with post-flare loops. Following a loop interaction, Hα can appear at the site of the interaction, typically increasing slowly in size and eventually linking with the surface.

3.1. Interpretation

The appearance of faint coronal emission at sites above a small detached portion of a prominence (as seen in Hα) suggests reconnection occurring higher in the corona (Schmeider et al. 1995). A CLI is interpreted as partial magnetic reconnection involving the coalescence instability (Smartt et al. 1993, Airapetian and Smartt 1995). At the onset of a CLI, it is found that the local plasma volume at the interaction site increases abruptly in density and temperature, followed by gradual cooling, with a maximum in the green-line image followed a few minutes later by a maximum in the red-line image and the eventual appearance of Hα, an obvious consequence of the interaction. It is noted that loop prominences associated with post-flare loops systems are usually interpreted as a result of reconnection via the Kopp-Pneuman (1976) model. In general then, for this class of active prominences, where the green-line signature is invariably brighter than the corresponding red-line component, we suggest that the Hα material is a direct outcome of reconnection in the corona.

4. Conclusion

Enhanced visible coronal emission observed in association with quiescent prominences is due to the dissipation of energy, associated with the prominence threads, into the immediate coronal environment. The level of this dissipation energy is biased towards the lower-temperature 637.5 nm (FeX) coronal line, rather than the higher-temperature 530.3 nm (FeXIV) line. In the case of post-flare loop systems, active prominences arise principally as a bi-product of reconnection in the corona itself. These can involve reconnection associated with the whole loop system, or simply local reconnection within the loop system at the site of a coronal loop interaction.

References

Airapetian, V.S. and Smartt, R.N. 1995, Ap.J., 445, 489

Chiuderi Drago, F., Engvold, O. and Jensen, E. 1992, Solar Phys., 139, 47

Hollweg, J.V. 1990, in Mechanisms of Chromospheric and Coronal Heating, (eds.) P. Ulmschneider et al., (Springer:Heidelberg), p. 423

Kopp, R.A. and Pneuman, G.W. 1976, Solar Phys., 50, 85

Ofman, L. and Davila, J.M. 1994, Geoph. Res. Let., 21, 2259

Orrall, F.Q. and Schmahl, E.J. 1976, Solar Phys., 50, 365

Schmahl, E., Foukal, P., Huber, M., Noyes, R., Reeves, E., Timothy, J., Vernazza, J. and Withbroe, G. 1974, Solar Phys., 39, 337

Schmeider, B., Heinzel, P., Wiik, J.E., Lemen, J., Anwar, B., Kotrc, P. and Hiei, E. 1995, Solar Phys., 156, 337

Smartt, R.N. and Zhang, Z. 1984, Solar Phys., 90, 315

Smartt, R.N., Zhang, Z and Smutko, M.F. 1993, Solar Phys., 148, 139

Wiik, J.E., Schmieder, B. and Noens, J.S. 1994, Solar Phys., 149, 51

First Year of Observations with SOHO/EIT of the "Quiet" Sun Corona

F. Portier-Fozzani, A. J. Maucherat and the EIT Team

Laboratoire d'Astronomie Spatiale, CNRS, BP8, 13376 Marseille Cedex 12, France

Abstract.   Since January 1996 (EIT first light) the Extreme Ultraviolet Telescope aboard SOHO has produced about 20,000 wide-field images of the corona and transition regions. Four different emission lines (He II, Fe IX/X, Fe XII, Fe XV) were selected to detail morphologies of magnetic structures in the corona. They show the different structures present in the corona with information about their topologies (Neupert et al. 1998). They provide the global temperature distribution in the quiet corona in the range 0.5 to 3×10^6 K.

The evolution of the corona during the first year of the SOHO mission revealed its nonuniform aspect and the nonregularity of the appearance of new active regions. Changes observed in active regions and coronal holes (e.g., August–September 1996) showed the complex role of magnetic fields including magnetic interactions and possible reconnections needed to explain some loop morphology evolution.

1. Introduction

A full description of the EIT Telescope aboard SOHO can be found in Delaboudiniere et al. (1995). Since February 1996 at least one image per day in all 4 wavelengths of the whole Sun have been taken (except during CCD bakeout done to increase efficiency). Movies were made on smaller areas to give shorter time evolution. The satellite observes the Sun 24 hours per day but, due to telemetry sharing, precise targets have to be chosen.

The Sun was at the minimum level of the 11 year cycle during 1996, but even at that time, some activity was present. Comparison between the amount of activity (determined by active region counts) with time and the sunspot number shows the well known links via magnetic fields. We followed the evolution with studies of 3D coronal structures (Portier-Fozzani et al. 1996).

2. 1996: A Full Year of Observations of the Quiet Sun's Corona

During January 1996 three Active Regions (ARs) were present. There was also another active fuzzy area, in which two new ARs appeared the next month. A decrease of activity was noted in March with only two large and two small ARs.

The lowest activity occurred in April with 4 small ARs: the "Quiet" Sun's

F. PORTIER-FOZZANI ET AL.
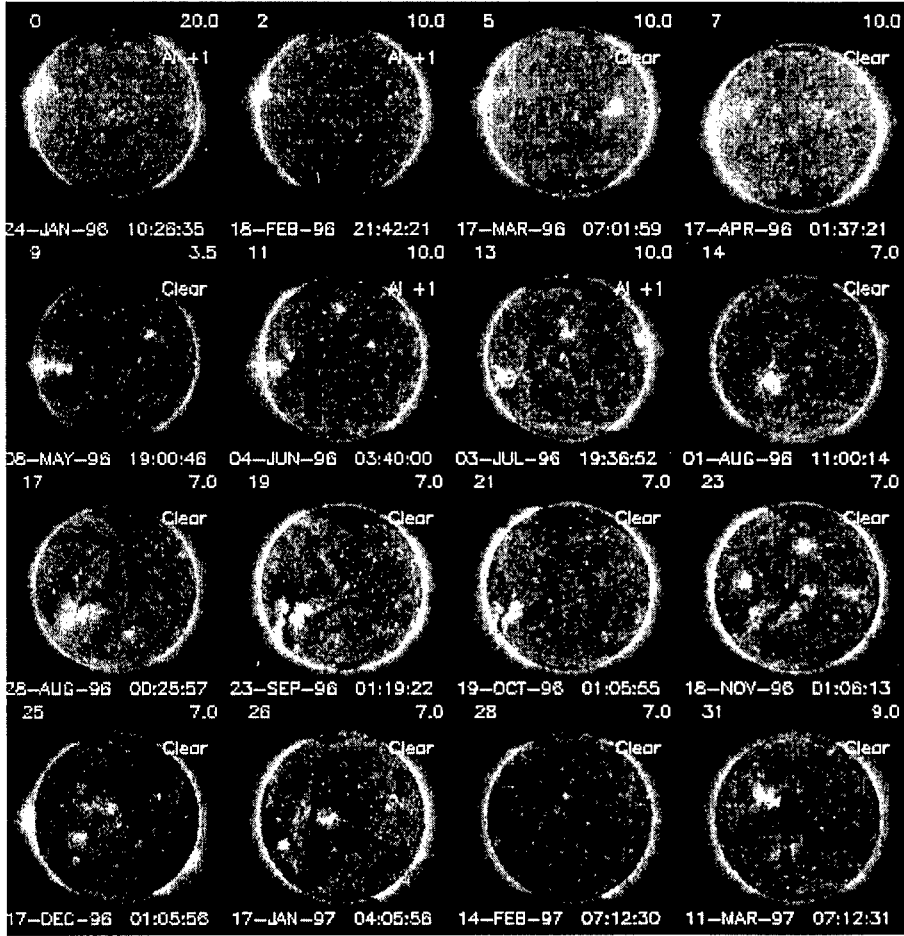
Figure 1.   Activity of the corona observed with SOHO EIT in FeXII at 195Å during the January 1996–March 1997 period.

corona remained in fact still active. During May, two large ARs were present, both shared and spread in four parts in June. July showed an increase of activity. ARs and Coronal Holes (CHs) became more frequent, introducing strong nonuniformity in the corona. An interaction between CHs and ARs began in August. A strong Equatorial Coronal Hole (ECH) developed from the North polar CH toward an AR loop present in the southern hemisphere (Figure 1). Then, in September, the morphology of the AR changed completely, with fewer loops inside. By October, the ECH had decreased. In November, 5 ARs were present and 7 in December, showing the increase of activity of the cycle.

K. Harvey (1997, private communication) found that the minimum of the sunspot number was in May 1996, but the appearance of the new cycle activity was unusual. From EIT results, the AR number was minimum around April 1996 (Portier-Fozzani 1997). On the other hand, the main presence of a large CH suggests that the minimum of coronal activity occurred during June–October.

3. Global Evolution of the Coronal Activity
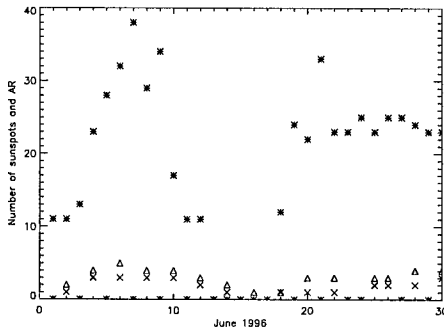
Figure 2.   Coronal and photospheric activity during June 1996: ($*$ represents the sunspot number, $\triangle$ the AR number and X the number of big ARs)

During that minimum period the corona appeared very nonuniform. An example is given by mid-February when the Sun had an active region on one side while the other side had nothing. Apparitions of AR were nonlinear with time; sometimes 1, 2 or 3 could appear during a short time like in October–December.

Phillips (1995) mentioned that ARs do not always correspond to sunspots despite the expected link via the magnetic field. This is mainly the case in 1996, except for the weak activity in June 1996 (Figure 2), where coronal numbers were proportional to sunspot numbers. The reason is probably that only a part of the sunspots influence strongly coronal activity and are able to build via the magnetic field some loops with high enough temperature to be seen at all wavelengths.

The number of large active regions seen on the disk are proportional to the absolute value of the magnetic field. This was expected because the plasma is frozen to the strong magnetic field and then creates large ARs (Klimchuk et al. 1998). Finally, by studying C,M,X flare eruptions, no observed links are noted between the numbers of ARs and flares. As there was no relation with

the time of the flares, this activity could be linked to AR's stability and not to their statistical numbers (Portier-Fozzani and Noens 1997).

4. Conclusions
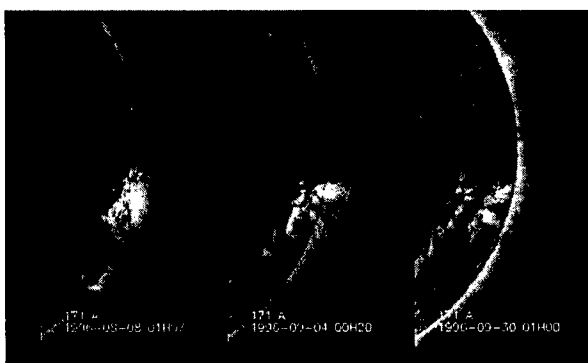
Figure 3.   Loop evolution in Fe IX/X

Magnetic fields drive coronal evolution. Synoptic EIT observations give us the possibility to study the global change of the corona with time. Comparison with other observations help us to understand the relationship between different physical processes present in the Sun at the minimum of the cycle. The evolution of the corona, such as changes in AR loop morphology (e.g., Figure 3), recall the role of different magnetic fields and possible reconnections (Portier-Fozzani et al. 1998). Thanks to a high telemetry rate, the birth of a CME was recorded on December 24, 1996 (Moses et al. 1998). In conclusion, observations will certainly yield more and more surprises as the activity cycle grows toward maximum, but even at the minimum lots of events occurred in the corona.

References

Delaboudiniere, J.-P. et al. Solar Phys., 162, 291

Klimchuk, J., D. Moses and F. Portier-Fozzani 1998, ApJ, submitted

Portier-Fozzani, F. et al. 1996, in Magnetic Reconnection in the Solar Atmo-
       sphere, (eds.) R. Bentley and J. Mariska, San Francisco, p. 402

Portier-Fozzani, F. and J.C. Noens 1997, in Science with Themis, Publication
       of Paris-Meudon Observatory, p. 281

Portier-Fozzani, F. June 1997, LAS Internal Report

Portier-Fozzani, F. 1998, A&A, submitted

Phillips, K. 1995, Guide to the Sun, Cambridge University Press

Neupert, W.M. et al. 1998, JGR, in press

Moses, D. et al. 1998, Solar Phys., submitted

The Plasma Environment of Prominences – SOHO Observations

D. Moses, C.M. Korendyke, N. Moulton[1]

Naval Research Laboratory, Code 7660.1, Washington, DC 20375, USA

J. Newmark

NASA/Goddard Space Flight Center, Greenbelt, MD 20771, USA

Abstract. We describe the observational capabilities of the SOHO EIT and LASCO instruments for prominence research. A detailed comparison of EIT He II λ304 and BBSO Hα images of a quiescent prominence reveals differences in fine scale structure which are attributed to differences in radiation emission and transport mechanisms. Absorption features present in coronal EIT images are attributed to dense prominence features located between the source of the coronal emission and the observer. These features provide the locations of prominence material in coronal image sequences. Observations of a prominence eruption in both EIT He II and LASCO C1 Fe XIV images show the heating of chromospheric material to coronal temperatures during the prominence eruption. In the last phase of the prominence eruption, a coronal mass ejection (CME) is initiated as a dark cavity forms over the prominence material and a bright loop-like structure forms over the dark cavity.

1. Introduction: The EIT and LASCO Instruments

Since the commissioning of the Solar and Heliospheric Observatory (SOHO) spacecraft in early 1996, the EUV Imaging Telescope (EIT) and the Large Angle Spectrometric Coronagraph (LASCO) have obtained new observations of prominences and prominence-associated phenomena. EIT images the Sun over a 45×45 arcmin field of view in four EUV passbands: Fe IX,X at 171 Å, Fe XII at 195 Å, Fe XV at 284 Å, and He II at 304 Å. Emission in the Fe lines is from coronal plasma at characteristic temperatures of 1.3 MK, 1.6 MK, and 2.0 MK, respectively. Emission in the He II passband is from transition region plasma with a characteristic temperature of 5.0×10^4 K. LASCO images provide coverage of the corona over a spatial range of 1.1 to 30 $R_\odot$ with three overlapping coronagraphs: C1 (1.1–3 $R_\odot$); C2 (2–6 $R_\odot$); C3 (4–30 $R_\odot$). The detector area is 1024×1024 pixels for both the EIT and LASCO instruments.

---

[1] Allied Signal Technical Services Corp., Camp Springs, MD, USA

2. EIT He II 304 Å Observations

The EIT He II imaging with a CCD detector improves the dynamic range of images by two orders of magnitude over previous He II film imagery of the NRL slitless spectrograph on Skylab (Tousey et al. 1977). Sounding rocket observations by the NASA/GSFC SERTS instrument (e.g., Jordan et al. 1993) have added significantly to the study of He II λ304. However, suborbital observations of the Sun in He II provide only a short sampling of highly varied and dynamic phenomena. The Lagrangian (L1) orbit of SOHO allows continuous imaging of the Sun, and the image cadence is limited primarily by the telemetry allocation. The highest sustained cadence of full disk, full resolution (1024×1024) He II images was obtained for 23 hours beginning 22:00 UT on March 18, 1997 at the rate of 9 per hour. A movie of this sequence can be viewed at http://lasco-www.nrl.navy.mil/iau/movie.html.

The EIT He II 304 Å bandpass width is 21 Å FWHM (Delaboudinière et al. 1995) and the only other line contributing significant power is the coronal Si XI 303.3 Å line. In the quiet Sun, the He II line intensity dominates on the disk, while the Si XI line intensity becomes greater than the He II intensity at heights > 20 arcsec above the limb (Thomas 1994).

The emission mechanism for He II is difficult to determine. Within the range of plasma conditions observed, collisional excitation, photoionization-recombination, radiative excitation, and resonant scattering can all be significant processes. A calculation including only collisional excitation using the CHIANTI procedures (Dere et al. 1997a) gives an emission measure of $2.2 \times 10^{27}\,\mathrm{cm}^{-5}$ for the average quiet Sun EIT count rate, while the value obtained from a number of other transition region lines is of the order of $2.8 \times 10^{26}\,\mathrm{cm}^{-5}$ (e.g., Dere and Mason 1993). This underestimate of the intensity of the He II solar emission has been long appreciated and has led to the exploration of alternative emission mechanisms (e.g., Jordan 1975, Zirin 1975, Laming and Feldman 1992). The difference between emission mechanisms on the disk and in prominences is an additional complication. Further diagnostics such as spectroscopy of the He II Balmer series (Laming and Feldman 1992), or filtergrams of another line of the He II Lyman series may help to specify the processes involved in solar He II emission.

A comparison of EIT He II and BBSO Hα images of a quiescent prominence on March 9, 1997 is illustrated in Figure 1. The Hα image was obtained at the Big Bear Solar Observatory by H. Zirin using the high resolution OSL CCD camera. It is immediately apparent that the contrast between disk and prominence is less for He II, allowing a wider dynamic range in the prominence. The outline of the prominence is well matched in the He II and Hα images, while the detailed structure visible in the two images is not. These differences are consistent with the description of quiescent prominence He II line emission by Laming and Feldman (1993), where photoionization and photoexcitation by coronal radiation are important processes. While the Hα structures appear to be excited by the chromospheric radiation below the prominence, the He II structures appear to be excited by coronal radiation surrounding the prominence. The fine scale He II features seen in Figure 1 can be interpreted as the optically thick surface of this prominence which surrounds the more dense features seen in Hα.
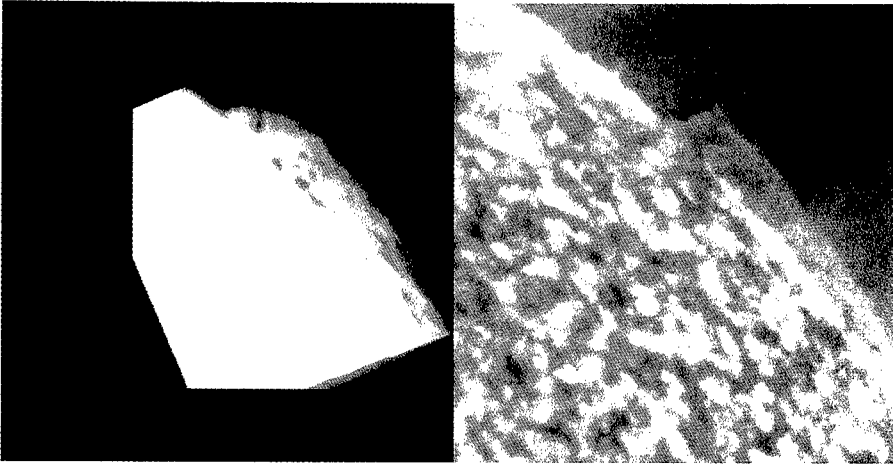
Figure 1.   BBSO Hα (left) and EIT He II λ304 (right) images of a quiescent prominence on March 9, 1997 show differences in fine scale structure which can be attributed to differences in emission mechanisms. (BBSO image courtesy of H. Zirin.)

3.   EUV Absorption Features

The observation of prominence absorption features in all the EIT passbands has been reported by Moses et al. (1997). Figure 2, the east limb on February 28, 1997, illustrates most of the characteristics of quiescent features. The figure is oriented so that solar north is to the right. To the north a prominence is seen in He II, associated with a helmet streamer structure that produces no significant absorption in the coronal lines. At the equator, a prominence aligned perpendicular to the line of sight contains absorption structures that are seen in all the coronal passbands (as well as in the He II passband). Most of the absorption structures in this prominence have the morphology of prominence feet (e.g., Tandberg-Hanssen 1995). The density, temperature, and elemental abundances in prominence feet can be expected to be quite different from those in the prominence itself. To the south is a prominence that extends onto the disk as a polar crown filament channel. In addition to the compact absorption feature seen in the coronal passbands, there is a coronal void surrounding the prominence. (This feature is a useful illustration of the amount of Si XI in the off-limb 304 Å image.)

The properties of absorption features in quiescent prominences can be summarized as follows: Absorption features in the coronal passbands are visible in only part of the prominence. Prominence absorption features in the coronal passbands are less visible on the disk than the limb because, in the case of a prominence on the disk, most of the coronal material along the line of sight is between the observer and the absorbing material (particularly for the prominence feet, which extend down to the photosphere). He II prominences can exist without any detectable coronal absorption features. The absorption features in

D. Moses et al.
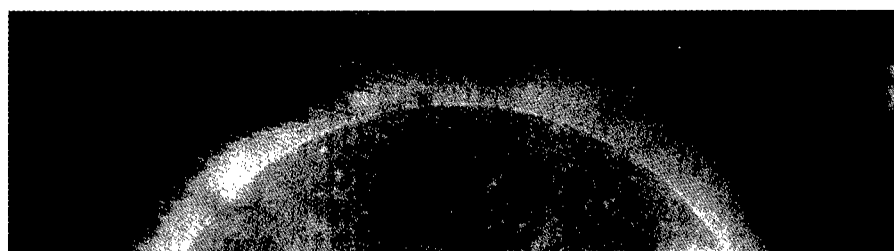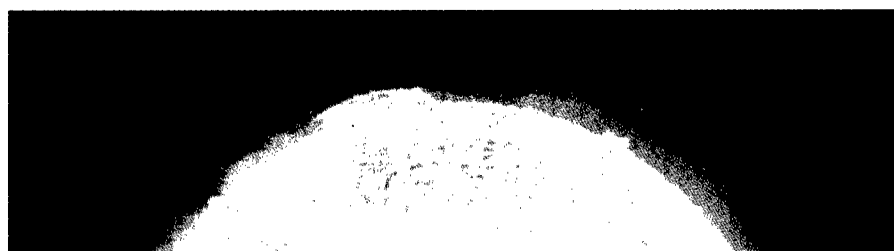
Figure 2.   February 28, 1997 image of three prominences on the east
limb (solar north is to the right). The prominences at the equator and
in the south can be seen as absorption features in the coronal channels.

He II are less visible than the coronal absorption features and do not necessarily match morphologically. This difference is readily appreciated as the difference between source and absorption regions in the He II and coronal images. The absorption features identified in the coronal lines are frequently below the observed surface of the He II structures in quiescent prominences (as are the Hα emission structures described in the previous section).

An absorption feature associated with an eruptive prominence on May 31, 1997 is illustrated in Figure 3. The geometry of this configuration is particularly clear for the Fe XII absorption feature, since the absorbing material is almost entirely between the observer and the coronal emission. Collisional excitation is a much greater component of the He II emission in an eruptive prominence, so the distribution of the He II source region is different than that of quiescent prominences. Thus, the filamentary absorption region in the He II image more closely matches that in the Fe XII image. However, differences in the fine structure of the absorption feature remain, which are understood to be generated by the mixing of absorbing material and source material. (Note the shading of the He II emission at the top of the prominence, which suggests that, in this region, a significant fraction of the He II is from resonant scattering of the on-disk He II.)

A combination of H I, He I and He II continuum absorption (Cheng, Smith, and Tandberg-Hanssen 1980, Foukal 1978, and Schmahl and Orrall 1979) constitutes a significant absorption mechanism for the EUV spectral range. Kucera, Andretta and Poland (1998) have investigated prominence absorption features in four coronal lines in the Lyman continuum (>504 Å) observed with the SOHO Coronal Diagnostic Spectrometer. They found H I continuum absorption clearly sufficient to describe the total absorption in observations where the geometry of both the prominence absorption and the coronal emission is well understood. A survey by Engvold et al. (1998) of coronal absorption features in EIT images has shown that, in the absorption features readily identified in coronal images, either the continuum absorption is optically thick or other mechanisms (e.g., resonant scattering by the Fe ions) are important.

4.   The EIT and LASCO "CME Watch"

The great observational advance of EIT is the ability to take an extended sequence of moderate cadence (3–4 images per hour), full disk images at full resolution. Moderate cadence, full field, full resolution Fe XII image sequences, under the observational program title "CME watch", have been the mainstay of the EIT observing program since April 1997. In the full resolution Fe XII images, the prominence absorption features trace the evolution of active prominences while the 1.5MK corona is being monitored. The transverse spatial scale of the prominence absorption features in the Fe XII images is such that a significant loss in prominence identification occurs in 2×2 binned images (5.2×5.2 arcsec^2 pixels). The full resolution CME watch is producing an extensive range of examples of prominence evolution and of the interaction of prominences with the lower corona.

Of particular interest is the relationship of the absorption features to coronal brightenings observed during moderate cadence coronal sequences. Coronal brightenings observed on-disk along neutral lines frequently show absorption

Large Scale Features
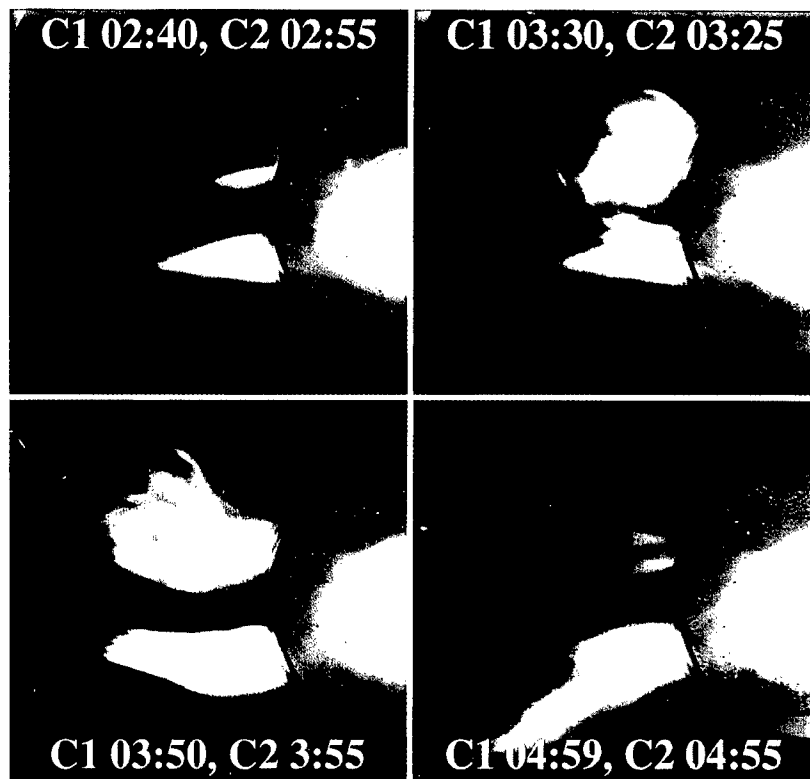
Feb. 23, Coronal Mass Ejection

Figure 3.   Eruptive prominence of May 31, 1997 visible as an absorption feature in Fe XII (top) and a mixture of absorption and emission in He II (bottom).

features imbedded in the coronal emission. The geometry required for such an observation implies closed field lines (for the impulsive coronal brightening) below a cooler, more dense structure (for the absorption). However, with the accumulation of many observations, examples have been observed at the limb that reveal more of the 3-dimensional configuration of coronal brightenings and require a more complicated model. The Fe XII sequence of October 9, 1997 is an example that can be viewed at http://lasco-www.nrl.navy.mil/iau/movie.html. During the sequence, the inner wall of the coronal cavity brightens, and then coronal emission extends across the coronal cavity. This emission crosses above *and* below the prominence structure seen in absorption. Viewed from above, the coronal material crossing above the filament would be more difficult to detect than the overall brightening that would be seen around the absorption feature. Thus, from a different perspective, one might interpret the observations to imply that the coronal emission was due strictly to the closing of field lines beneath

the prominence when, in reality, the situation is much more complicated. The classification and analysis of these events is an ongoing project.

The combination of LASCO and EIT observations extends the range over which the interaction between prominences and the corona can studied from the chromosphere to the heliosphere. Skylab-era observations provided the initial breakthrough observations of prominence eruptions and CMEs (e.g., Schmahl and Hildner 1977, Poland and Munro 1976) but were restricted by the limitations of photographic film. SOLWIND and SMM coronagraph observations greatly extended the coverage of CMEs, but observations of the initiation of prominence eruptions were restricted to ground based instruments for these missions (Webb 1988).

Extended intervals of moderate cadence, full field, full resolution observations (the CME watch) have proven to be the most productive LASCO/EIT observing programs for the study of prominence eruptions and CMEs. A typical cadence for the baseline $5.2\,\mathrm{Kb\,s^{-1}}$ telemetry rate is, per hour, 3–4 EIT images (either in the Fe XII or He II passbands), 1–2 C1 Fe XIV image sets, 1 C2 image and 1 C3 image. The C1 Fe XIV image is obtained with a tunable Fabry-Pèrot filter and requires, at the minimum, a line-center image at 5303 Å and an off-band image at 5309 Å.

The first CME that was well observed jointly by LASCO and EIT occurred on December 23, 1996 during the first period of high telemetry rate ($25\,\mathrm{Kb\,s^{-1}}$) observations (Dere et al. 1997b). The EIT observations in this sequence were made in the Fe XII passband. All three components of the CME – the prominence eruption, the coronal cavity and the bright loops typical of CMEs – were present at the earliest stages observed by EIT. Observed as an Fe XII absorption feature, the prominence eruption consisted of a symmetric elongation of the prominence into an upwardly expanding loop structure. The formation and acceleration of the bright loops that we interpret as the leading edge of the CME was coincident with the initiation of the prominence eruption to within the time resolution of the image cadence (12 minutes). Upon entering the C2 field of view, the CME has attained its terminal velocity of $400\,\mathrm{km\,s^{-1}}$.

The best example of a CME sequence obtained with He II EIT observations occurred on February 23, 1997 (Korendyke et al. 1998). The EIT He II and C1 Fe XIV observations are presented in Figure 4. As seen in Fe XIV (and in the EIT coronal passbands), a large dome of coronal emission built up over the active region containing a prominence before the prominence eruption began. Over the first hour of the eruption the coronal emission slowly expanded into a shell. From the last panel of Figure 4, it can be seen that the erupting prominence material begins to fill the coronal cavity behind the expanding shell. Since the C1 coronal image is Fe XIV emission, the cospatial prominence material visible in the overlapping region of Fe XIV and He II emission must be a multi-temperature plasma with a component that is heated during the eruption to coronal temperatures ($2 \times 10^6\,\mathrm{K}$). In the last panel of Figure 4, the outer shell of the CME is just beginning to open. Following this opening of the coronal structure, acceleration occurs so rapidly that in the next image set (Figure 5), the CME has obtained its terminal velocity of $870\,\mathrm{km\,s^{-1}}$.

The impulsive acceleration of a fast CME in the February 23, 1997 event is in marked contrast to the acceleration initiated at the beginning of the prominence

C1 and EIT Combined Images

Feb. 22, 12:42   **Feb. 23, 00:42**

Feb. 23, 02:08   **Feb. 23, 02:42**
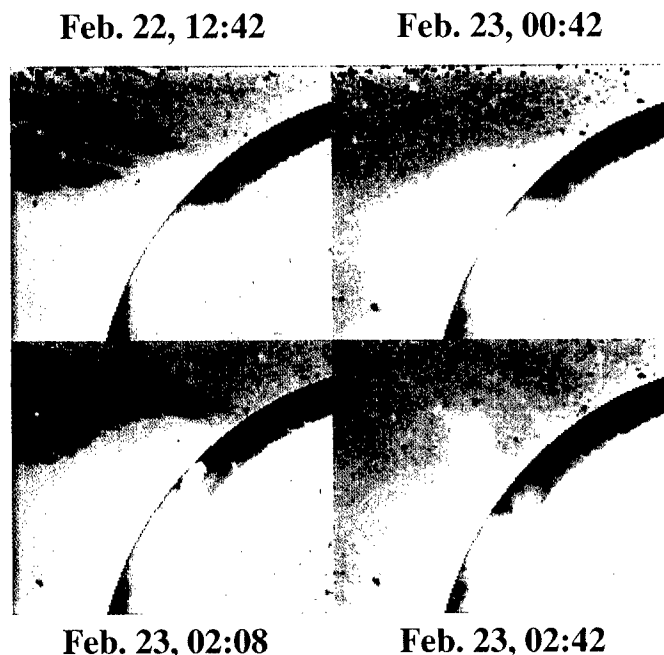
Figure 4.   February 23, 1997 prominence eruption (He II) and CME (Fe XIV) nested images illustrate the rapid heating of the chromospheric material to coronal temperatures and the sudden acceleration of the CME front.

eruption in the December 23, 1996 slow CME event. In both events, the CME had reached its terminal velocity upon entering the C2 field of view. Although the prominence velocity was approximately the same for both events, the twist and general complexity was much greater in the eruptive prominence associated with the fast CME. The large-scale evolution of the fast CME on February 23 is seen in Figure 5. The evolution observed in the C1 and EIT images is not apparent in the larger scale C2 images. In the later phase of the CME, as seen in the C2 images, the prominence eruption appears to be located in one leg of the overall CME, suggesting that the pre-existing coronal field configuration was complex (e.g., Webb 1998, these proceedings).

From the fast CME sequence of February 23, 1997, it is clear that the prominence eruption does not drive the CME. Although the prominence eruption and CME are associated, the acceleration of the CME is poorly matched to the evolution of the prominence. The event appears very different in each of the three instruments, demonstrating the observational advances achieved through the combination of the capabilities of EIT and LASCO. This new capability of imaging the corona below 1.5 $R_\odot$ with good temporal resolution provided by the LASCO C1 and EIT combination greatly extends our understanding of the initiation of CMEs.
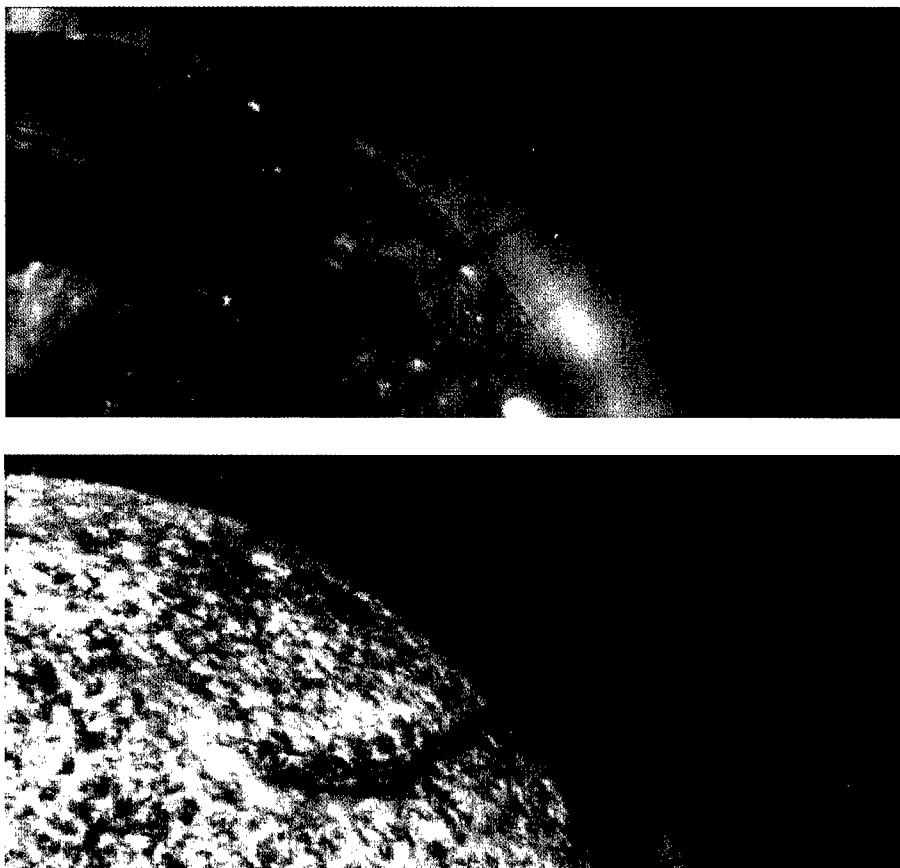
Figure 5. February 23, 1997 CME composite of FeXIV (C1) and continuum (C2) images illustrates the evolution of the event.

References

Cheng, C.C., Smith, J.B., and Tandberg-Hanssen, E. 1980, Solar Phys., 45, 393

Delaboudinière, J.-P. et al. 1995, Solar Phys., 162, 291

Dere, K.P., Landi, E., Mason, H.E., Monsignori Fossi, B.C., and Young, P.R. 1997a, A&A, 125, 149

Dere, K.P. et al. 1997b, Solar Phys., 175, 601

Dere, K.P. and Mason, H.E. 1993, Solar Phys., 144, 217

Engvold, O., Jakobsson, H., Tandberg-Hanssen, E., Harvey, K.L., Moses, D., and Gurman, J.B. 1998, in preparation

Foukal, P. 1978, ApJ, 223, 1046

Jordan, C. 1975, MNRAS, 170, 429

Jordan, S.D., Thompson, W.T., Thomas, R.J., Neupert, W.M. 1993, ApJ, 406, 346

Korendyke, C.M. et al. 1998, in preparation

Kucera, T.A., Andretta, V., and Poland, A.I. 1998, in preparation

Laming, J.M. and Feldman, U. 1992, ApJ, 386, 364

Laming, J.M. and Feldman, U. 1993, ApJ, 403, 434

Moses, D. et al. 1997, Solar Phys., 175, 571

Poland, A.I. and Munro, R.H. 1976, ApJ, 209, 927

Schmahl, E.J. and Hildner, E. 1977, Solar Phys., 55, 473

Schmahl, E.J. and Orrall, F.Q. 1979, ApJ, 231, L41

Tandberg-Hanssen 1995, The Nature of Solar Prominences, Kluwer Acad. Publ., Dordrecht, Holland

Thomas, R. 1994, EOS, 16, 269

Tousey, R., Bartoe, J.D.F., Brueckner, G.E., Purcell, J.D. 1977, Appl. Optics, 16, 870

Webb, D.W. 1988, J. Geophys. Res., 93, 1749

Zirin, H. 1975, ApJ, 199, L63

EUV and Microwave Observation of a Filament

F. Chiuderi-Drago[1]

DASOP-Observatoire de Paris-Meudon, 92195 Meudon Cedex, France

K. Bocchialini, S. Lamartinie, J.-C. Vial

*Institut d'Astrophysique Spatiale, Bât.121, Université Paris XI-CNRS,
91405 Orsay Cedex, France*

T. Bastian

National Radio Astronomy Observatory, Soccoro, NM 87801, USA

C.E. Alissandrakis

*Section of Astro-Geophysics, Department of Physics, Universiy of
Ioannina, 45110 Ioannina, Greece*

R. Harrison

*Space Science Department, Rutherford Appleton Laboratory, Chilton,
Didcot Oxfordshire OX11, 0XX, UK.*

J.-P. Delaboudinière, P. Lemaire

*Institut d'Astrophysique Spatiale, Bât.121, Université Paris XI-CNRS,
91405 Orsay Cedex, France*

Abstract. Simultaneous XUV and microwave ($\mu - w$) observations of
a solar filament, performed by several instruments onboard SOHO and
by the Very Large Array (VLA), are analyzed. The filament appears as
a dark structure, very similar in shape to the optical H_α filament, in all
images taken in the transition region (TR) lines observed by CDS, in the
Ne VIII lines observed by SUMER at $\lambda = 770$Å and 780Å and at all
radio wavelengths with 1.7 $cm \leq \lambda \leq 6$ cm. Contrary to that, in six TR
lines observed by SUMER at $\lambda > 1300$Å no trace of the filament, either
in absorption or in emission, is visible. Finally, at $\lambda = 21$ cm, as well as
in all images taken in coronal lines by CDS and EIT, a dark feature is
present at the filament position, although with less defined contours than
in the first-mentioned TR images. The constraints imposed by all these
observations are discussed and interpreted.

---

[1]Current address: Dipartimento di Astronomia, University of Florence, Largo E.Fermi 5, 50125
Firenze, Italy.

1. Introduction

A joint campaign to observe a filament on the Solar disk in the EUV and $\mu - w$ range of wavelengths has been proposed having in mind the following scientific motivation:

Previous observations of prominences in EUV lines (Schmahl and Orrall, 1986; Engvold, 1989), have supplied the Differential Emission Measure ($DEM = N^2 \, dh/dT$) as a function of temperature in the Prominence-Corona Transition Region (PCTR). If this quantity is used to compute the radio optical depth ($\tau \propto DEM$) and the corresponding brightness temperature, T_b, at $\mu - w$, the results strongly disagree with the observations with $T_b(obs) \ll T_b(calc)$. It must be pointed out that the above EUV observations were all performed on prominences observed at the limb, while all radio observations refer to filaments on the disk (Chiuderi Drago 1990).

This strong discrepancy was interpreted as due to a real difference between the physical parameters of the PCTR at the prominence top (disk observations) and at its side (limb observations) because of the different orientation of the magnetic field with respect to the temperature gradient. If the angle θ between these two directions is taken into account in the heat conduction, a first integral of the energy equation shows that the DEM scales as $\cos\theta$ (Chiuderi and Chiuderi Drago 1990). Since, according to Leroy (1989), $\theta \simeq \pi/2$ at the prominence top, while it is $30° \leq \theta \leq 90°$ on the side, the DEM is much lower at the prominence top, producing much lower optical depth and T_b at $\mu - w$. Therefore, a much lower intensity of EUV lines is expected.

A check of this assumption could come only by performing $\mu - w$ and EUV observations of the *same* filament on the disk, which was the objective of this joint program of observations performed on July 28, 1996.

2. Observations

The filament site, located at $\simeq 45°N$ and $\simeq 30°-45°W$, was observed by the SUMER, CDS and EIT instruments onboard SOHO and by the VLA at 2, 3.5, 6 and 21 cm. Full disk observations at 1.7cm (Nobeyama) were also available.

Due to space limitations, only one figure concerning some of the SUMER observations is presented here. More figures concerning observations withother instruments are shown by Alissandrakis et al. (1997). Below we will give a detailed description of the results obtained by all instruments involved in this campaign.

a) The filament appears as a dark feature with a shape very similar to the H_α filament at short radio wavelengths ($\lambda < 21cm$), in all images taken by CDS in the TR lines and by SUMER in the Ne VIII lines at $\lambda = 770$ and 780Å.

b) The filament does not appear at all in the images taken by SUMER in other TR lines at longer wavelengths such as those of Si IV at 1393 and 1402Å of O IV at 1401 and 1404Å and of C IV at 1548 and 1550Å.

c) The filament appears as a dark feature, although with less defined contours than in the previously mentioned cases, at $\lambda = 21 \ cm$ and in the coronal images observed by CDS and EIT.

In this paper we will not comment on these latter results, limiting our
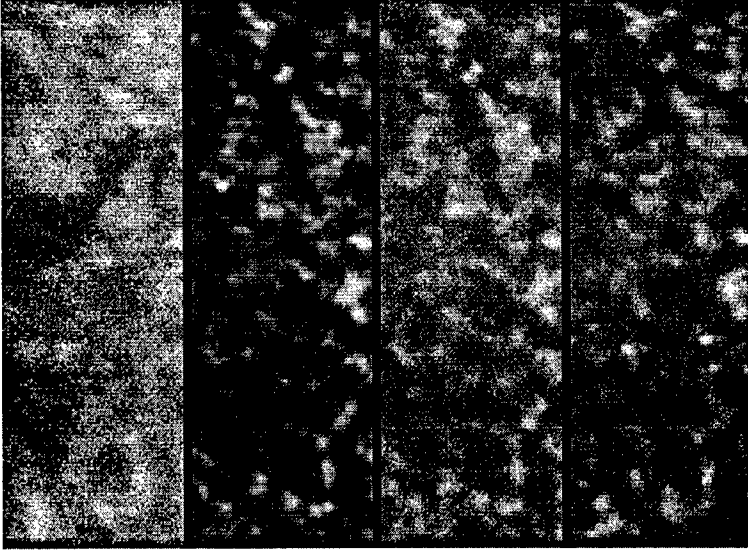
Figure 1.   Monochromatic images of the filament region taken by
SUMER. From left to right: Ne VIII at 770, Si IV at 1393.8, O IV
1401.2 and CIV at 1548Å. Each field of view is 100 x 296 arc-sec^2.

interpretation to the observations of Transition Region lines.

3.   Interpretation and Conclusions

From the above observations it appears that the visibility of the filament in a
given line formed in the Transition Region depends only on its wavelength, as
shown by the O IV images: that at $\lambda = 554$Å (CDS), clearly shows the filament
in absorption, while those at $\lambda = 1401$ and 1404Å (SUMER) do not.

Although there are no observations in the range 780Å$< \lambda <$1393Å, it ap-
pears reasonable to ascribe the observed absorption to the Lyman continuum
and to assume that the wavelength separating the ranges where the filament is
visible or not is $\lambda = 912$Å.

The dark feature seen in all lines at $\lambda < 912$Å is therefore due to the Ly-
continuum absorption of the radiation coming from the underlying Chromosphe-
re-Corona Transition Region (CCTR), within the cool body of the optical promi-
nence. (At shorter wavelengths the He I and He II continuum absorption could
also contribute.) This absorption is clearly not balanced by the proper emission
of PCTR above the filament. We may therefore conclude that the DEM in this
latter case is much smaller than in the former. This is also confirmed by the
much lower emission above the filament with respect to the surrounding back-
ground, seen at radio wavelengths, where the filament is totally thick and the
observed flux comes only from the PCTR above the filament.

On the other hand, at all lines with $\lambda > 912$Å, there is no absorption within
the prominence, and the total intensity observed above the filament should be

the sum of the CCTR emission and of the PCTR emission at its top. According to Schmahl and Orrall (1986) and Engvold et al. (1987), the EUV line intensities of the PCTR at the limb are ~ 0.5 and ~ 0.3 that of the quiet Sun. Assuming the same values above the filament, we would get an intensity ranging from 1.3 to 1.5 that of quiet Sun and the filament would clearly appear in emission. Since this is not the case, we must conclude that the EUV emission at the prominence top is smaller than that observed at its side.

Recent EUV observations made by Kucera et al. (1998, these proceedings) give a ratio of the PCTR to the CCTR line intensities at the limb equal to 0.1, putting some doubt on the possibility of distinguishing the filament in emission on the disk. It must be pointed out that the Kucera et al. observation refers to an eruptive, not to a quiescent prominence which the present paper refers to.

Due to the large fluctuations among the few EUV line observations of prominences, we cannot affirm that this emission indicates a difference in the PCTR parameters at the different faces of the prominence, as it appears from the comparison with $\mu - w$ observations. It is clear that the only way to check it is by observing the *same* filament on the disk and at the limb at both wavelengths.

References

Alissandrakis, C.E., Drago, F., Bastian, T., Bocchialini, K., Delaboudinière, J.-P., Lemaire, P., Vial, J.-C., Harrison, R.A, and Thompson, B. 1997, in Advances in the Physics of Sunspots, B. Schmieder, J.C. Toro del Iniesta and M. Vazquez (eds.), ASP Conf. Series, Vol. 118

Chiuderi, C. and Chiuderi Drago, F. 1990, Solar Phys., 132, 81

Chiuderi Drago, F. 1990, in Dynamics of Quiescent Prominences, V. Ruzdjak and E. Tandberg-Hanssen (eds.), Springer-Verlag, New York, p. 70

Engvold, O. 1989, in Dynamics and Structure of Quiescent Solar Prominences, E.R. Priest (ed.), Kluwer Acad. Publ., Dordecht, Holland, p. 47

Engvold, O., Kjeldseth-Moe, O. Bartoe, J-D.F. and Brueckner, G.E. 1987, 21st ESLAB Symp. ESA SP-275, p. 21

Leroy, J.L. 1989, in Dynamics and Structure of Quiescent Solar Prominences, E.R. Priest (ed.), Kluwer Acad. Publ., Dordrecht, Holland, p. 77

Schmahl, E.J. and Orrall, F.Q. 1986, in Coronal and Prominence Plasma, A. Poland (ed.), NASA Conf. Pub. 2442, p. 127

A Statistical Investigation of Prominence Fine Structure in the EUV

S. Pojoga[1], A. G. Nikoghossian[2] and Z. Mouradian

Observatoire de Paris-Meudon, 92195 Meudon Cedex, France

Abstract. A statistical approach is proposed for the study of the prominence fine structure. Intensity variations in several EUV lines are measured in different regions of prominences. The expected number of fine structural elements is derived.

1. Introduction

An important problem of solar prominences is to determine the geometrical and physical characteristics of fine structure elements which are difficult to detect directly from observations. Several methods have been used to derive the number of the sub-resolution fine structures (Orrall and Schmahl 1980, Engvold et al. 1989, Zirker and Koutchmy 1990). The present note suggests a new approach based on spatial fluctuations of the brightness of prominences.

2. Statement of the Problem

We propose to study the prominence spectrum by considering the transfer of radiation through randomly distributed fine structures. We compare the theoretical and observational intensity distributions and their characteristics, thus providing further information to estimate the geometrical and physical parameters of prominences. The statistical parameters measured and computed are the mean intensity, $\langle I \rangle$ and the relative mean square deviation (RelMSD), $\delta = \langle I^2 \rangle / \langle I \rangle^2 - 1$. The EUV multispectral observations allow us to consider several layers of the prominence-corona atmosphere, from the cool prominence to the hot coronal plasma.

The main hypothesis is that the observed intensities and their fluctuations are due only to the random number of structures on the line of sight, which is distributed according to the Poisson law. An idealized model problem accounting for the random character of the initial release of radiation energy was treated by Nikoghossian et al. (1997). We also suppose that the structural elements are identical and have a slab-like geometry such that each structure contains a central cool slab separated from the hot corona by two transition

[1] Astronomical Institute of Romanian Academy, 75212 Bucarest, Romania

[2] Byurakan Astrophysical Observatory, 378433 Byurakan, Armenia
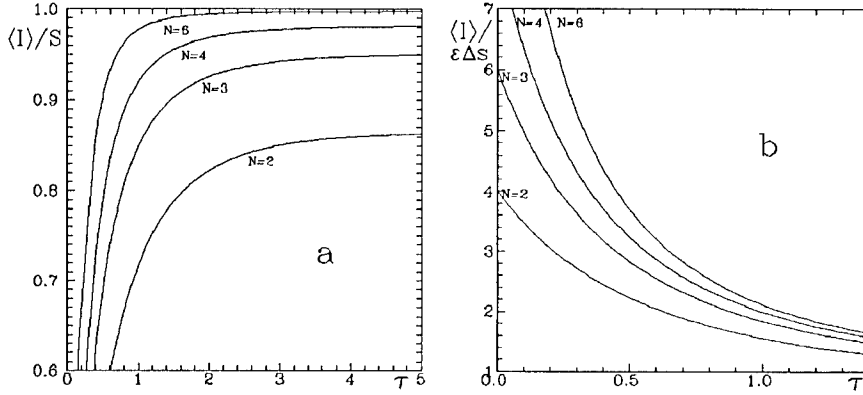
Figure 1.   Theoretical mean intensity $\langle I\left(N,\tau\right)\rangle$: a) Core emission, b) Interface emission.

regions. A detailed treatment of the problem, including a thread-like cylindrical model, is studied by Pojoga et al. (1998). Depending on the region of spectral line formation, we consider two approaches for the radiative transfer: a) *Core emission*. The line forms only in the central layer of the structure, which can be more or less optically thick. We neglect absorption through the interface and corona. b) *Interface emission*. The region of the line formation is the transition zone of the features. This is considered optically thin and we allow absorption in the central region only.

3.   The Computation of the Statistical Parameters

The mean intensity for core and interface emission, respectively, is given by

$$\langle I\rangle = S\left(1 - e^{-Nq(\tau)}\right),\qquad (0.1)$$

$$\langle I\rangle = \varepsilon\Delta s\left[\frac{2 - q\left(\tau\right)}{q\left(\tau\right)}\left(1 - e^{-Nq(\tau)}\right)\right],\qquad (0.2)$$

where $q\left(\tau\right) = 1 - e^{-\tau}$. S and τ are the source function and the optical thickness of the central layer, ε and Δs are the line emissivity and the geometrical thickness of each interface, and N is the Poisson mean of the line-of-sight number of structures. The RelMSD has the same expression in both cases and is given by

$$\delta = e^{-2Nq(\tau)}\frac{e^{Nq(\tau)^{2}} - 1}{\left(1 - e^{-Nq(\tau)}\right)^{2}}.\qquad (0.3)$$

We calculated theoretical functions $\langle I\left(N,\tau\right)\rangle$ (Figure 1) and $\delta\left(N,\tau\right)$ (Figure 2), assuming arbitrary values for the number of layers in the line of sight (N) and the optical thickness of the core (τ). Concerning the RelMSD, we see
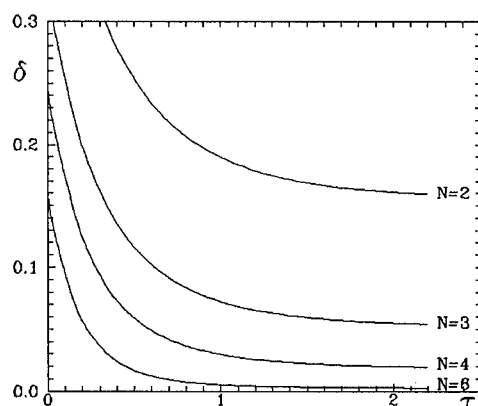
Figure 2. Theoretical relative mean square deviation, $\delta(N, \tau)$.

that it is decreasing with increasing N and τ. For large τ values, δ becomes insensitive to τ variations ($\delta = 1/\left(e^N - 1\right)$ for $\tau \gg 1$), and tends to 0 with growing N. If the central layer is optically thin ($N\tau \ll 1$), then $\delta = 1/N$.

4. The Statistical Parameters from Observations

The observations we used were produced by the Harvard College Observatory spectrometer on ATM aboard Skylab. For relatively quiet regions, the observational values of the mean intensity, $\langle I_{\mathrm{obs}} \rangle$, and RelMSD, δ_{obs}, were measured. Table 1 gives δ_{obs} values for some typical prominence regions.

Table 1. Typical values for the RelMSD in the observed prominences.

Spectral line	Bright regions	Normal regions	Faint regions
Ly-α 1216	0.045-0.06	0.055-0.075	0.075-0.09
Ly-β 1026	0.05-0.065	0.06-0.085	0.075-0.1
Ly-γ 972	0.07	0.07-0.1	-
CII 1336	0.1-0.25	0.25-0.3	0.3-0.4
OVI 1032	0.15-0.25	0.1-0.15	0.2-0.25
CIII 977	0.1-0.13	0.065-0.1	0.1
OIV 554	0.35-0.4	0.35-0.5	0.5-0.6

For the mean intensities of the studied areas, we generally find a factor of approximately 1.4 between bright and normal and between normal and faint regions, respectively.

The optically thick lines such as Ly-α and Ly-β exhibit smaller dispersion compared to other lines. The lowest values of δ_{obs} are found in the brightest parts of the prominences. Slightly greater values of δ_{obs} are observed for the optically thin lines that are emitted by hot regions and exhibit only a small

absorption in the core (CII 1336Å, CIII 977Å, OVI 1032Å). The RelMSD decreases as we move from the faint regions to the more intense ones, except for the brightest parts where large values occur. Higher dispersion occurs for the lines with wavelengths shorter than the Lyman limit, for instance the OIV 554Å line where the absorption in the core is high.

5. Number of Structures on the Line of Sight

In the optically thick limit δ does not depend on τ and enables us to estimate, from the observed values, the expected number of inhomogeneities along the line of sight. For the Ly-α and Ly-β lines, $\delta = 0.05 - 0.09$ provides N from 3.2 to 2.5. The relative fluctuations in the Ly-β line, and mostly in the Ly-γ line ($\delta \cong 0.1$), are slightly greater than those for the Ly-α line, which implies that – assuming the same number of structural elements – a smaller optical thickness in these lines is required to fit the observational value of δ.

For optically thin lines (CII 1336Å, CIII 977Å, OVI 1032Å), the central absorbing part of the structures becomes transparent ($\tau \to 0$) and the interface emission model gives $\delta \cong 1/N$. A value of the RelMSD of $0.1 - 0.25$ implies $N = 4 - 10$. However, for the OVI and CIII lines, the observational values of δ in the brightest regions are higher than expected. This could be due to the presence of another source of fluctuations beside the supposed one. The relatively large differences between the observational values of δ for different lines could be explained by: a) $\delta \cong 1/N$ does not hold, or b) the possible existence of a different number of independent structural elements with various temperatures. A number of structures in the same range is also obtained from the observed distributions of radiation intensity (Pojoga et al. 1998).

6. Conclusions

The above results allow us to assume the existence of a small number of structures in the line of sight. More precisely, for the same prominence region a number of approximately three cool absorbing cores and 4–10 emitting envelopes are found, when the optically thick and thin lines, respectively, are involved. The difference may be due to the existence of more complicated structures than the modeled ones.

References

Engvold, O., Jensen, E., Zhang, Y. and Brynildsen, N. 1989, Hvar Obs. Bull., 13(1), 205

Nikoghossian, A. G., Pojoga, S. and Mouradian, Z. 1997, A&A, 325, 813

Orrall, F. Q. and Schmahl, E. J. 1980, ApJ, 240, 908

Pojoga, S., Nikoghossian, A. G. and Mouradian, Z. 1998, A&A, to be submitted

Zirker, J. B. and Koutchmy, S. 1990, Sol. Phys., 127, 109

Small-Scale Structure in Loops and Prominence Threads

P. Rudawy

Astronomical Institute of the Wroclaw University, 51-622 Wroclaw, ul. Kopernika 11, Poland

M. S. Madjarska

Institute of Astronomy, 72 Trakia Blvd., 1784 Sofia, Bulgaria

Abstract. Preliminary results of the morphology of prominence fine structure are presented. Long time series of three post–flare loops, a spray and an eruptive prominence were digitalized and analyzed. The length-to-width ratio of the blobs was determined and, in some threads, a continuous movement of separate blobs of matter was detected.

1. Introduction

The photo–archive of the Large Coronagraph of Wroclaw University consists of many high resolution (better than 1 arcsec) observations of various types of prominences. On the basis of digitization of this material, we analysed the morphology of small–scale prominence structures. In this paper we present preliminary results concerning prominence fine structures.

2. Observational Material

For our analysis we chose a long time series of Hα filtergrams of three post–flare loops (August 18, 1990, June 27, 1992 and July 6, 1991), one spray (October 8, 1991) and one eruptive prominence (June 29, 1994). The observational material was digitized with the Joyce Loebl microdensitometer of the National Astronomical Observatory at Rozhen, Bulgaria. The two-dimensional scans were taken with a pixel size of 25×25 μ^2 and a step of 25 μ between the pixels in both directions.

3. Morphological Analysis

The analysis of the filtergrams shows that all analyzed prominences have a thread–like structure. The diameters of the threads vary from a few arc sec to less than the resolving power of the observations (≈ 0.5 arc sec). The prominence matter is organized inside the threads in blobs of dense matter separated by less dense matter and nonuniformly spread along the threads (Figure 1). Following the blobs' positions with respect to the solar limb, a continuous movement of the blobs was observed. The more precise analysis of these motions is

Figure 1.   Top: Thread-like structure of the loop prominence on August 18, 1990. Bottom: Enlarged part of the top image with overplotted contours of the blobs and lines marking the blobs' length and width.

under way.

As a parameter to describe the shape of a separate blob we chose its length (L) to width (W) ratio. The filtergrams are not calibrated, but the L/W ratio of the more or less oval blobs may be defined from the optical density contours taken for the middle value of the whole density range. We measured the well-separated blobs only, carefully avoiding the emission enhancements caused by crossing or overlapping of the loops or threads. Even inside the densest parts of some loops, we found some discontinuities of the brightness, which may be signatures of blobs or may be caused by the overlapping of some unresolved, very thin loops. The blobs of the eruptive prominence of June 23, 1994 were measured in the outer parts of the prominence only, because the individual threads were packed too tightly in the central part of this prominence. In Table 1 the minimum, maximum, mean and standard deviations, σ, of the L/W ratios are presented.

Table 1.   L/W ratio determined for different types of prominences

Date	Time [UT]	Type	No. of blobs	L/W ratio			
				min	max	mean	σ
Aug. 18, 1990	06 40 20	Loops	26	1.6	5.3	3.1	1.2
	06 52 48	Loops	53	1.1	7.4	2.8	1.1
Oct. 8, 1991	08 48 31	Loops	58	1.2	5.7	2.4	0.9
Oct. 8, 1991	14 24 23	Spray	37	1.1	6.8	22	1.2
	14 35 47		35	1.1	6.9	2.1	1.4
June 27, 1992	08 09 08	Loops	46	1.1	3.8	2.0	0.7
	08 17 19		44	1.0	4.9	1.8	0.7
June 29, 1994	10 20 27	Eruptive	30	1.1	4.5	2.0	0.5
	11 44 25		27	1.1	3.2	1.8	0.5

The L/W ratios vary from nearly 1:1 (round blobs) up to 7:1 (very elongated blobs). The mean L/W ratios were between 1.8:1 and 3:1. The loops and spray blobs have generally a higher L/W ratio than in eruptive prominences.

4. Discussion

The present achievements of multi-dimensional modelling of non-LTE radiation transfer make it possible to build new, more accurate models of post-flare loops. In the framework of this new approach, the loops should be considered as inclined, elongated, rope-like structures instead of over–simplified models of one-dimensional, plane–parallel slabs placed over the solar surface. One of the most crucial problems in post–flare loop modelling is an accurate description of the internal structure of the individual loops.

It is generally known that loops and threads of prominences are filled by the "blobs", separated by some less dense matter. This means that the calculations of radiation transfer and the physical parameters of prominences should be performed for the very complicated, three-dimensional structure of many threads filled with relatively dense blobs and less dense interblob space.

Eclipse Polarimetric Research of Prominences

A.N. Lebedev, I.A. Belenko, O.I. Bougaenko, I.S. Kim

*Sternberg State Astronomical Institute, Moscow State University
Universitetsky pr. 13, 119899 Moscow, Russia*

O.T. Matsuura, E. Picazzio

*Instituto Astronomico e Geofisico Universidade de São Paulo,
Av. Miguel Stefano, 4200 CEP 04301-904, São Paulo, SP, Brasil*

R.P. Livi, Silvia H.B. Livi

*Instituto de Fisica UFRGS, Campus do Vale, Av. Bento Goncalves, 9500
CEP 91501-970, Porto Alegre-RS, Brasil*

Abstract. A polarization analysis of E–limb prominences on November 3, 1994 is presented. Photometry and data reduction of 24 prominence pictures based on IDL software and Stokes–vector presentation and applied to H_α emission resulted in an accuracy of 1–1.5% in determination of the polarization degree and of 1.5–2.0° in the polarization direction. Distributions of polarization degree (polarization images) for prominences and the "white light" corona are presented. A polarization degree of 2–5% for prominences and 10–25% for the nearby white light corona are found. The polarization direction is found to be tangential to the solar limb. It is noted that eclipse observations can provide a powerful method for deriving the magnetic field at high altitudes in the coronal volume.

1. Introduction

Polarimetric research of prominences is very important for knowledge of the magnetic field structure which is the main parameter determining the prominence phenomenon. Until now prominence magnetic measurements based on the Zeeman and on the Hanle effects are very complicated even if a large coronagraph is used as the optics feed. Significant improvement of the signal–to–noise ratio is needed. Below, an attempt of polarimetric observations of prominences during totality of a solar eclipse is presented.

An eclipse color index polarization wave experiment carried out in Brazil (town of Criciuma) during the total solar eclipse of November 3, 1994 was aimed at polarization research within the innermost regions of the corona including prominences. Details of a portable coronagraph–polarimeter (D=55mm, 1:6) attached by a rotating polarizer placed in the plane of the Lyot stop have been given elsewhere (Kim et al. 1997). 1250 color negatives were obtained during the totality of 244 sec.

Below, the results of data reduction made by PDS through the color fil-

ter (λ_{max}=440nm, FWHM=20nm) of 24 frames exposed just after the second contact are presented. Photometry through the above–mentioned filter selects mainly densities caused by "red" emission. Digitizing was made with a pixel size corresponding to 6 × 6 arc sec on the film. The smoothing based on a moving-average method resulted in an angular resolution better than 18 arc sec for densities of 0.3 and more, and an accuracy of 1–2% for the polarization degree.

It is known that color eclipse pictures of the white light corona show prominences as red in slides or green in negatives. The color is caused by the prominence spectrum consisting of HI, HeI, HeII, etc. lines. As a rule the color of prominence images is mainly caused by dominant H_α emission. A detailed description of one of the eclipse color white light corona and prominence pictures was given by Leroy (1966). Employment of color film results in filtration due to the 3 layers sensitive to the blue, green and red emissions. Let S_λ be the spectral sensitivity of the "red" layer of the film used, $B_\odot$–the brightness of the Sun's center, B_{wc} –the brightness of the "white light" corona, $B_{H\alpha}$–prominences brightness in the H_α line. The spectral sensitivity S_λ of the "red" sensitive layer may be approximated by a Gaussian with a FWHM of 750Å. On average $B_{wc} \approx 10^{-6} B_\odot$ at distances R less than $1.2 R_\odot$. The prominence brightness in the H_α line is $(10^{-2} - 10^{-1})$Å$\cdot B_\odot$. Then the contrast (C) of "prominence–to–corona" images recorded by the "red" sensitive layer may be described by the expression

$$C = \frac{B_{H\alpha}}{\int\limits_{550nm}^{710nm} B_{wc}(\lambda) S_\lambda \, d\lambda} \approx 13 - 130.$$

The polarization degree of the white light corona does not exceed 25% at $R < 1.2 R_\odot$ while the prominence brightness equals 13–130 of the corona one. That means that the input of the "white light" corona in polarization degree measurements at the location of prominence does not exceed 2–0.2%, respectively.

2. Data Reduction

Details of the photometry, data reduction and the algorithm of the statistical processing were presented recently (Kim et al. 1996, Belenko et al. 1997). Stokes–vector presentations and IDL software were used for the analysis. After coaligning the 24 frames, the averaged density image $\mathbf{D} \equiv D(i, j)$ is created, where i, j are integer rectangular coordinates of pixel images while the point of reference is at the center of the Sun. The distribution of densities in this frame is used as a noise level indicator in statistical procedures of the polarization map of the object under study. $\mathbf{S}_k$–intensity frames resulting from density images contain information about the distribution of polarization parameters, which could be extracted as a result of statistical processing.

24 equations for every (i, j) pixel can be written using the 24 consecutive frames

$$S_k \equiv S_k(i, j) = I + Q' \cos \frac{\pi k}{12} + U' \sin \frac{\pi k}{12}, k = 0, 1, \ldots, 23,$$

where vector $(\mathbf{Q'},\mathbf{U'})$ is related to $(\mathbf{Q},\mathbf{U})$ by a $2\alpha_0$ rotation, where α_0 is the position of the plane of polarization in the first frame.

3.   Results

Figure 1 shows a computer half–tone "polarization image" (distribution of polarization degree) of E–limb prominences imposed on the white light corona. It looks similar to a conventional coronal image revealing a high polarization of the white light corona and the regions of prominences near the Moon's limb, where the degree of polarization varies from 2 to 5% in the prominences. The polarization for the prominences is found to be tangential to the solar limb within the limits of errors.
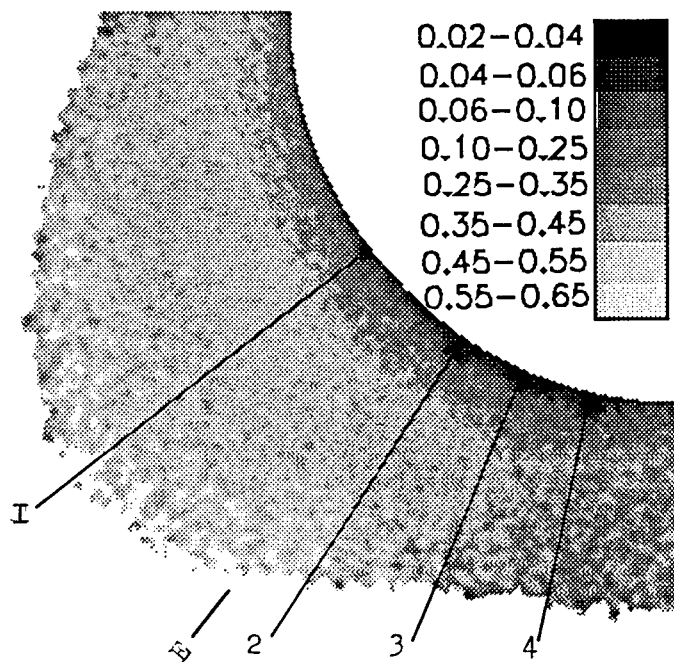
Figure 1.   A computer half–tone "polarization image" (distribution of polarization degree) of E–limb prominences imposed on the white light corona.

The averaged value of the polarization degree and deviations within the prominences are presented in Table 1.

4.   Conclusions

The polarization degree for the E–prominences of November 3, 1994 are found to be 2–5%. Within the limits of errors the polarization direction is tangen-

Table 1.

N	Position Angle	Height	Polarization Degree
1	74.9^0	$26''$	$4 \pm 2\%$
2	93.5^0	$34''$	$3 \pm 2\%$
3	105.3^0	$32''$	$4 \pm 2\%$
4	116.8^0	$52''$	$5 \pm 3\%$

tial to the solar limb. It should be noted, that the above–mentioned analysis was applied to non–filtered, low–resolution, and small–scale prominence images. During totality of solar eclipses the sky brightness is reduced by 2-3 orders of magnitude, resulting in a significant improvement of the signal–to–noise ratio. A polarization analysis of filtered, high–resolution, and large–scale eclipse prominence images in the light of different lines (H_α, H_β, ... and D_3 or 10830Å) [Bommier et al. 1985, Leroy 1985, Landi Degl'Innocenti 1986] could provide reliable polarimetric data to deduce the magnetic fields at high altitudes in the coronal volume.

References

Belenko, I., Bougaenko, O., Kim, I., Koutchmy, S, Matsuura, O. and Picazzio, E. 1997, in Z. Mouradian and M. Stavinschi (eds.), NATO ARW Proc., Theoretical and Observational Problems Related to Solar Eclipses

Bommier, V., Leroy, J. L. and Sahal–Brechot S. 1985, in Measurements of Solar Vector Magnetic Fields, M. J. Hagyard (ed.), NASA Conf. Publ. 2374, p. 375

Kim, I. S., Bougaenko, O. I., Belenko, I. A., Guetman, F. I., Koutchmy, S. and Matsuura, O. T. 1997, Solnechnye Dannye, Papers of 1995–1996, 145.

Kim, I. S., Bougaenko, O. I., Belenko, I. A. and Matsuura, O. T. 1996, Radiofizika, 10, 1298

Landi, Degl'Innocenti 1986, in Coronal and Prominence Plasmas, A. I. Poland (ed.), NASA Conf. Publ. 2442, p. 203

Leroy, J. L. 1985, in Measurements of Solar Vector Magnetic Fields, M. J. Hagyard (ed.), NASA Conf. Publ. 2374, p. 121

Leroy, J. L. 1966, Bulletin de la Société Astronomique de France, 80, 271

On the Bright Rims of Hα Filaments

F. Paletou

Observatoire de la Côte d'Azur, Département Cassini, BP 4229, F-06304 Nice Cedex 4, France   E-mail: paletou@obs-nice.fr

Abstract. Heinzel et al. (1995) have proposed that diffusive penetration of the incident chromospheric Hα radiation could explain the bright rims of filaments. We examine this suggestion with the help of new 2D radiative models of filaments and show that our computations do not support this explanation.

1. Introduction

Bright rims of filaments have been observed for decades. Early observations made in Hα at Kodaikanal Observatory were reported by Royds (1920). A systematic investigation based on the study of 271 filaments can be found in the 1948 *mémoire* of D'Azambuja and d'Azambuja. However, this feature of filaments is not yet well understood. Several scenarios have been used in order to explain bright rims: local heating due to magnetic reconnection at the footpoints (Engvold 1988, Kononovitch et al. 1994), increased Hα chromospheric emission in the filament channel because of a lack of "dark structures" (Heinzel et al. 1990), radiative interaction between the prominence and the underlying chromosphere (the so–called "prominence blanketing" effect; see Kostik and Orlova 1975, Zirin 1988) or diffusive penetration of the incident Hα chromospheric illumination into the filament body (Heinzel et al. 1995).

Using a 1D *horizontal* slab model, Heinzel et al. (1995) showed that a "bump" in the Hα source function, S(Hα), can be produced at the bottom of the slab and they interpreted it as the location of the bright rim. Basically, their explanation is that the rather large amount of chromospheric radiation penetrating the slab from below and scattered out could be seen as a bright contrast feature over a limb–darkened Hα chromosphere.

We discuss this latter tentative explanation from the standpoint of two–dimensional (2D) radiative modelling of prominences and filaments.

2. 2D Models: Results and Discussion

Our 2D models use a 5–level hydrogen atom plus a continuum. Lyα and Lyβ resonance lines are formed with partial frequency redistribution, and realistic incident radiation has been used (Paletou 1995, 1996). We have computed five different homogeneous 2D slab models with the same input parameters as in Heinzel et al. (1995), i.e., temperature (8000 K), gas pressure (0.3 dyn cm^{-2}), vertical (geometrical) extension (3200 km) and height above the solar surface
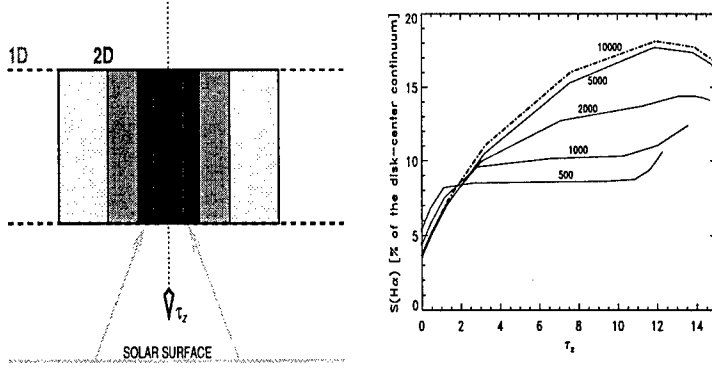
Figure 1.   Left: Sketch of the different 2D model geometries we used. Only the geometrical width of the structure was changed from one model to another. Right: Source function variations along the vertical symmetry axis displayed for different geometrical widths in km.

(10,000 km).

However, unlike in the 1D case we used different geometrical widths for the filament, namely: 10,000, 5000, 2000, 1000 and 500 km (Figure 1). The slab with the largest width is optically thick enough in the horizontal direction to reproduce along the vertical symmetry axis the 1D S(Hα) variations (cf., Heinzel et al. 1995, Figure 5). Hereafter, the source functions and emergent intensities will be expressed as a percentage of the disk–center continuum (4.077×10^{-5} cgs).

In Figure 1 (right) we show how the vertical variations of S(Hα) differ when the width of the 2D slab is reduced; each curve is labelled with the corresponding width in km. S(Hα) ranges between the 1D solution and the optically thin limit (S(Hα) $\approx$ 8% at all heights).

We also calculated what is actually emerging from the slab for a line of sight (LOS) close to the horizontal direction. Obviously, not only vertical variations but also *horizontal* ones will drive the emergent line intensity. Needless to say it is impossible to evaluate this using a 1D horizontal slab model, simply because the latter is *infinite* along the LOS of interest! In Figure 2 (left) we plot the full 2D variations of S(Hα) together with (right) the line center emergent intensity I_c(Hα) for a LOS parallel to the horizontal direction. It is important to note that in Figure 2 (right) the height is expressed in *geometrical* units.

We do not find any pattern in the I_c(Hα) vertical variations which reproduce a bright rim, i.e., a *local* peak of Hα emission at low altitude. Pushing the investigation further, we computed another set of 2D slab models for higher temperatures, gas pressures, heights and lower altitudes above the surface. Our results are displayed in Figure 3, and from these we conclude that, instead of showing a bright rim, it shows unrealistically bright prominences.
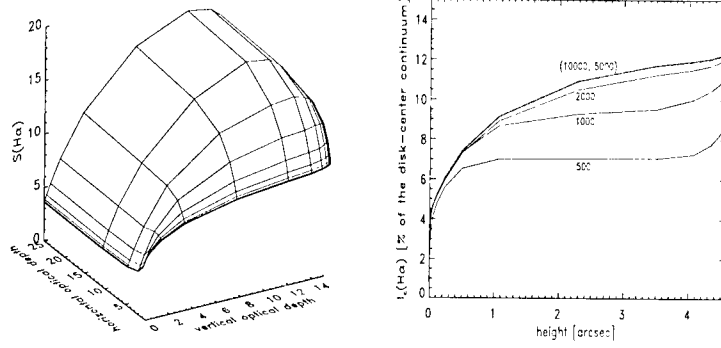
Figure 2.   Left: Full 2D variations of the source function; only the half–slab is displayed for symmetry reasons. Right: Vertical variations of the emergent line center intensity along the symmetry axis: results for different geometrical widths in km.
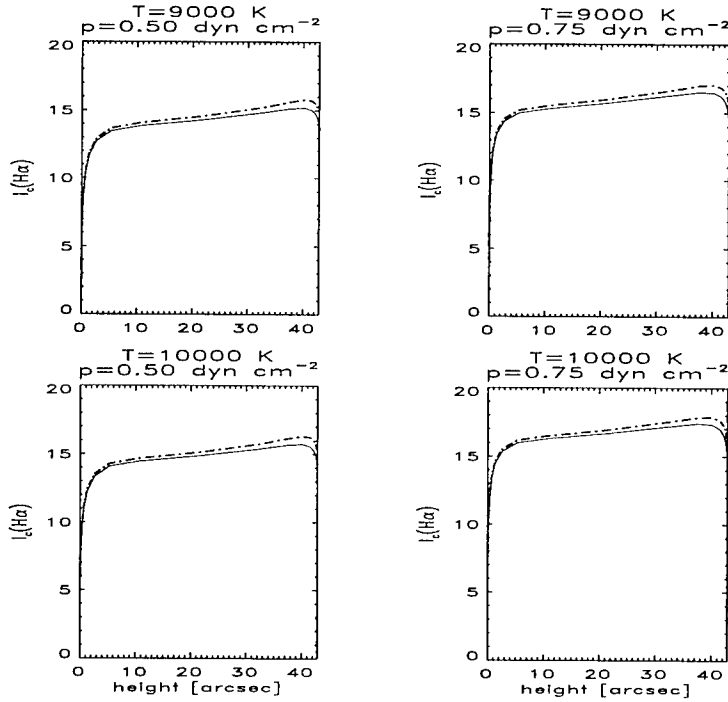
Figure 3. $I_c(H\alpha)$ vertical variations obtained with higher slab heights, gas pressures and temperatures. We also considered lower altitudes of the 2D slab above the solar surface (in km, 1000: dashed lines and 5000: solid lines).

3. Conclusion

We showed how the explanation of an Hα bright rim due to diffusive penetration of the incident radiation – a pure radiative transfer effect – seems to be insufficient when considering isothermal and isobaric 2D models of filaments.

Other explanations such as prominence blanketing should be investigated further by considering in some detail the radiative interaction between a 2D filament and the chromosphere that lies beneath it. It is also very likely that the existence of fine structure elements favour the penetration of the incident radiation to deep layers of the prominence. These two issues can be addressed further in multidimensional geometry.

Here we have demonstrated that significant geometrical effects can occur for a spectral line of moderate optical thickness such as Hα. More generally, we consider that diagnostics relying on radiative models need to be improved upon by using results from multidimensional models.

References

D'Azambuja L. and d'Azambuja M. 1948, Ann. Obs. Paris–Meudon 6, 7

Engvold O. 1988, in Dynamics and Structures of Quiescent Solar Prominences, E.R. Priest (ed.), Kluwer Acad. Pub., Dordrecht, Holland, p. 47

Heinzel P., Kononovich E. V. and Smirnova O. B. 1990, Debrecen Obs. 7, 172

Heinzel P. et al., 1995, Solar Phys., 160, 19

Kononovich E.V. et al. 1994, in Solar Coronal Structures, V. Rusin et al. (eds.), Astr. Inst., Slovak Republic, p. 365

Kostik R.I. and Orlova T.V. 1975, Solar Phys. 45, 119

Paletou F. 1995, A&A 302, 587

Paletou F. 1996, A&A 311, 708

Royds T. 1920, Kodaikanal Obs. Bull. 63, 289

Zirin H. 1988, Astrophysics of the Sun, Cambridge Univ. Press, Cambridge

A Large Filament and Flares in Active Region NOAA 5669 on September 2, 1989

G. A. Porfir'eva and G. V. Yakunina

Sternberg Astronomical Institute, 119899 Moscow B-234, Russia

and Z. Mouradian

Observatoire de Paris-Meudon, URA 326, France

Abstract. The behaviour of extended filaments in the vicinity of a new emerging magnetic flux site has been investigated during the 2N/M5.8 flare on September 1 and several flares on September 2, 1989.

1. Introduction

The behaviour of flare-associated filaments might be complex and the observational picture becomes complicated for different Doppler velocities along the filament channel. Filtergrams, obtained simultaneously in the center and wings of the H_α line up to $\lambda = H_\alpha \pm 3\overset{\circ}{A}$, permits us to better understand the filament behaviour and its relation with the flare situation in the active region (AR). The analysis of the evolution of extended filaments helps us to investigate large magnetic arches. In this paper we try to follow the behaviour of the long-lived large filament and filament-like structures in AR NOAA 5669 with a complex magnetic field on September 2, 1989 during the 2N/M5.8 flare and four consecutive subflares, one of which was accompanied by a M1.1-class X-ray burst.

2. Observations and Description of the AR

Observations were obtained at the High Altitude Station of Sternberg Astronomical Institute near Alma-Ata, Kazakhztan on a coude-refractor Opton using an H_α filter with a passband of 0.25 Å. We used also H_α filtergrams of the Meudon Observatory, photospheric (FeI 5324.19Å) and chromocpheric (H_β 4861.34Å) magnetograms, H_β Dopplergrams and H_β images, obtained at Huairou Solar Station (Table 1).

The AR NOAA 5669 was a large complex spot group stretching for about 30° from east to west. The leading spot, N1, had negative polarity and the following ones had mainly positive polarity, being surrounded by little spots and pores of both N and S polarities. The large-scale magnetic polarities interchanged as N-S-N-S-N-S. A schematic drawing of the AR (Figure 1a) is a result of the superposition of photos, obtained in red and blue wings of the H_α line, and H_β chromospheric magnetic charts, recorded at 0155 and 0239 UT (Zhang et al. 1992).

Comparing magnetograms (see Zhang et al. 1992) we notice that a good
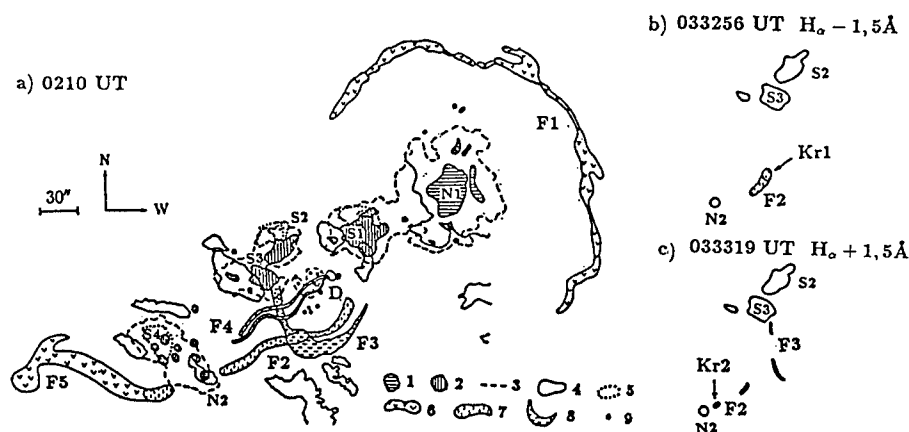
Figure 1. Drawings of events in AR5669: spots of N(1) and S(2) polarities, $(H_\alpha \pm 3\text{Å})$; penumbra (3); chromospheric fields of N(4) and S(5) polarities; filaments in center of H_α (6), in $H_\alpha - 0.75\text{Å}$ (7), in $H_\alpha + 0.75\text{Å}$ (8); little spots and pores (9).

similarity existed between the main magnetic features observed at the photospheric and chromospheric levels. Large-scale magnetic structures were relatively stable during several hours. Small-scale elements in the middle of the AR changed dynamically. Here in the vicinity of the D magnetic feature new emerging magnetic flux (EMF) was observed on September 2. Numerous little spots and pores were seen here on the H_α filtergrams, taken at $\lambda = H_\alpha \pm 3\text{Å}$ (Figure 1a). In this place the transverse magnetic field was noticeably sheared. Here at 2350 UT on September 1 the 2N/M5.8 flare occurred and for six hours after it H_α emission kernels of several subflares were located there. In the front the AR was encircled with a large quiet filament, F1, situated on the boundary of the large-scale magnetic field net. The F2 filament, having a length of about 3×10^5 km, was located beneath the AR along the boundary between the magnetic field regions of S and N polarities. The east end of F2 was near the N2 spot (Figure 1a). The loop-like H_α structure F3 was observed for several hours. It looked most striking at 0209:35 UT in $\lambda = H_\alpha + 0.75\text{Å}$. Later its intensity decreased and at 0530 UT it was not seen at all. In the middle of the AR filament-like structures, F4, were visible, located nearly parallel to the F2 filament and ending in the vicinity of the EMF near D. Behind the AR the large filament, F5, existed. One of its ends was anchored in the vicinity of the trailer spot group S4 (Figure 1a). The F2 filament was also observed in the H_β line but the F3 and F4 structures were not seen in the H_β line (Zhang et al. 1992).

3. Results and Discussion

The behaviour of the large H_α chromospheric features was investigated during several flares on September 2, 1989 and compared with the magnetic structures and Dopplergrams. The eastern parts of the H_β F2 filament, adjacent to the N2

Table 1.   Observational Data about NOAA 5669

Date	Magnetic field photosph.	Magnetic field chromosph.	Velocity field	H_β images	H_α filtergram (Alma-Ata)	Events in AR (SGD)
		Zhang et al. 1992				
1.IX				2250		
1.IX			2351	2354		2350-2502
2.IX	0002	0042	0032	0025		2N/M5.8
2.IX	0107	0154		0154	0150 0208-0210	0141-0156 SF/M1.1 0153-0227 SID
2.IX		0238	0235	0238		0231-0242 SF
2.IX		0300			0309-0315	H_α-brightening
2.IX	0335	0338	0325	0333	0330-0336	0330-0345 SN
2.IX	0544	0534	0527	0530	0524-0536	0522-0546 SF

spot, were seen during the preflare phase, maximum and decay of the 2N/M5.8 flare on September 1, 1989 and were not observed in the vicinity of the flare site (Zhang et al. 1992). The large S-shaped F5 filament, located just behind the AR, had a similar behaviour (Porfir'eva and Yakunina 1995). It became active when flares occurred near the filament end in the vicinity of the singularity pivot-point, situated near the S4 spot group (Figure 1a). This pivot point in the AR was found by Mouradian and Soru-Escout (1991).

During the five hours after 0100 UT, the F2 filament was observed along its whole channel length both in the H_β line and the H_α line. Comparison of the H_α filtergrams with the H_β images has shown that there was a good match between the contours of the H_α and H_β F2 filament. The sites with the maximum H_α intensities corresponded to the places with the maximum H_β intensities. The H_α F2 filament was active during the observations (see Table 2, for the wavelengths of maximum intensities of the filaments). The topology of Doppler velocities

Table 2.   Events in the AR NOAA 5669 on September 2, 1989.

Universal time	Data about flares (SGD)	Filament F2	Loop structure F3	Filament F4	Flare locations
0208-0210	0154 M1.1 0153-0227 SID	$H_\alpha - 0.5\text{Å}$	$H_\alpha + 0.75\text{Å}$, $H_\alpha + 1\text{Å}$;	$H_\alpha - 0.5\text{Å}$	Emission kernels in
0309-0315	H_α-brightening	$H_\alpha - 0.75\text{Å}$; Kr1 in $H_\alpha - 1.5\text{Å}$ in east part of F2, Kr2 in $H_\alpha + 0.75\text{Å}$ near the spot S5	$H_\alpha + 0.75\text{Å}$; vestiges in $H_\alpha + 1\text{Å}$	H_α, $H_\alpha - 0.75\text{Å}$	back part of the AR and in
0330-0336	0330-0334-0345 SN 21S, 54E	$H_\alpha - 0.75\text{Å}$; Kr1 in $H_\alpha - 1.5\text{Å}$ in east part of F2, Kr2 in $H_\alpha + 0.75\text{Å}$ near the spot S5	$H_\alpha + 0.75\text{Å}$; vestiges in $H_\alpha + 1.5\text{Å}$	H_α, $H_\alpha - 0.75\text{Å}$	region of emergent magnetic
0534-0536	0522-0524-0546 SN 18S, 48E	$H_\alpha - 0.5\text{Å}$; Kr1 in $H_\alpha-1\text{Å}$ in east part of F2		$H_\alpha-0.5\text{Å}$	flux near D

along F2 was complex and changeable. A correlation between H_α filtergrams and H_β Dopplergrams existed. Preferential blue Doppler shifts were registered along the H_β filament at 0235, 0325 and 0527 UT. Before a subflare at 0330 UT red Doppler shifts were observed in F2 near the N2 spot (Zhang et al, 1992). The filament looked more intensive in the blue H_α wings, and it was seen along its whole length in $\lambda = H_\alpha - 1\overset{\circ}{A}$, which agrees in general with the H_β velocity. The maximum Doppler velocity was in kernel Kr 1 (Figure 1b, Table 2). At 0309–0336 UT a little site Kr 2, seen in the red wing of the H_α line from $\lambda = H_\alpha + 0.75\overset{\circ}{A}$ to $\lambda = H_\alpha + 2\overset{\circ}{A}$, existed near the N2 spot. Hence, we conclude that both in the H_α filtergrams and H_β Dopplergrams, red Doppler shifts existed in the eastern part of F2. At the same time blue shifts dominated the western parts of F2 (Figure 1b, c, Table 2).

Distinct filament-like structures P1, P2 and T are noticeable on the chromospheric magnetic charts at 0154 and 0534 UT (Zhang et al. 1992). The magnetic structures P1 and T coincided by their location with the eastern and western parts of the F2 filament. The third structure P2 is possible to compare with the H_α features F4 (Figure 1a). As was indicated by Zhang et al. (1992), the appearance of the magnetic structures P1, P2 and T likely reflected the magnetic field configuration inside the filaments F2 and F4.

The AR looked active when sudden ionospheric disturbances (Table 1) were observed. A distinctive feature in the AR was the large loop-like structure F3, having a shape of a flag in $\lambda = H_\alpha + 0.75\overset{\circ}{A}$ (Figure 1a). A leg was anchored in the S3 spot. The F3 feature remained visible until 0335 UT. This magnetic feature possibly existed before 0200 UT and was visible in the H_β flare.

4. Summary

The behaviour of the large filaments in the vicinity of the EMF in the middle of AR 5669 was analysed during several hours after the 2N/M5.8 flare on September 1, 1989 (2350 UT). The filaments were active during the entire time of the observations and had Doppler velocities equal to dozens of km s^{-1}. The contours of the H_α and H_β F2 filament and their locations were similar. A definite correlation between H_α Doppler shifts in the F2 filament and H_β Dopplergrams existed. The observed activation could be explained by a gradual decay of the 2N/M5.8 flare, accompanied by several subflares. The investigated filaments were long-lived features. The H_α Meudon filtergrams show that the filaments F2 and F3 stayed visible all during the AR's passage across the solar disk.

References

Mouradian Z. and Soru-Escout I. 1991, in Dynamics of Solar Flares, B. Schmieder and E. Priest (eds.), Observ. de Paris, DASOP, p. 139

Porfir'eva G.A. and Yakunina G.V. 1995, Izvestia Academia Nauk., 59, 181

Zhang H., Ai G., Li W. and Chen J. 1992, Sol. Phys., 146, 61

Magnetic Fields in Filaments

P. Démoulin

Observatoire de Paris, Section de Meudon, DASOP, URA 2080 (CNRS)
F-92195 Meudon Cedex, France

Abstract. Filaments are present in highly non-potential magnetic configurations. On one hand, the complexity of modeling such 3-D configurations makes a useful comparison between observations and models difficult. On the other hand such highly sheared regions are more interesting and challenging for understanding eruptive phenomena like flares and coronal mass ejections. Fortunately, the presence of cold plasma allows us to measure the magnetic field inside prominences. Together with photospheric field measurements and other morphological observations, these provide a large set of puzzling constraints for plausible models of the magnetic configurations. Models are reviewed in the framework of present observational constraints with the aim to clarify a piece of the mystery which surrounds the magnetic configuration of filaments.

1. Observational and Theoretical Constraints

The magnetic field plays a key role in all the processes involved in the corona as in prominences because the plasma beta is low (in the range 10^{-3}–10^{-1}). It channels both the plasma motions and the thermal conduction. It provides support against gravity of the prominence plasma one hundred times denser than the coronal plasma. This primary role is not always recognized at its right level because the majority of observations are focused on the plasma. Furthermore, evidences for importance of the magnetic-field are even less compelling in prominences than in other phenomena since the prominence plasma do not usually visualize field lines as it does in arch-filament systems, surges and coronal loops. Models for the magnetic configurations are also difficult to build, both because the configurations are strongly non-potential and because even the global shape (topology) of the configurations is unknown.

Under these circumstances the detective story, started few decade ago, is still alive. We have now many indices: photospheric magnetograms, magnetic measurements inside prominences as well as the pattern of chromospheric fibrils and coronal loops. Still there are several theoretical scenarios and some observations provide alibi for some accused magnetic configurations. As in every good detective story, some of the alibis should be false; but which ones? Below I present my personal and actual (!) view on this interesting story and try to glue together as many pieces of the puzzle as possible.

1.1. Results from Magnetic-Field Measurements

Prominences are thin structures consisting of cold plasma embedded in the hot corona. Their global shape has been known for a long time (e.g., d'Azambuja and d'Azambuja 1948). They are always found above inversion lines of the photospheric magnetic field in regions, called corridors or filament channels, which are nearly free of chromospheric fibrils (Martres et al. 1966). They are also characterized on either side by the presence of $H\alpha$ fibrils nearly aligned with the inversion line, indicating a high magnetic shear (Foukal 1971, Rompolt 1990). The corridor is nearly free of vertical magnetic field flux except small parasitic polarities (Martin 1990). A necessary condition for prominence formation is a low gradient, transverse to the photospheric inversion line, of the vertical field component (Shelke and Pande 1983, Maksimov and Ermakova 1985, Maksimov and Prokopiev 1995).

In prominences the Zeeman effect only allows the measurement of the longitudinal component of the magnetic field (see Kim 1990, and references therein). Radio wavelengths provide information on the field strength (e.g., Apushkinskii et al. 1990). The Hanle effect gives the three components of the field (and the electron density) from the polarization measurements in two spectral lines (e.g., Bommier et al. 1994). The compatibility of the results obtained by these three independent methods and by different groups of observers have strongly validated the results (see Leroy 1988, 1989, and Kim 1990).

One of the main results of Hanle measurements is that the prominence field has the opposite direction to that expected from extrapolation of photospheric measurements (e.g., Leroy et al. 1983). Not only the field component orthogonal to the prominence is opposite to the field of a simple arcade (referred to inverse configuration), but also the field component parallel to the prominence is opposite to those of an arcade that would have been sheared by differential rotation! This has been shown after a detailed analysis because twin solutions, symmetrical with regard to the line of sight, exist with optically thin lines and right angle scattering (known as the 180° ambiguity). In the majority of cases, one solution is normal and the other inverse. At the beginning of the studies only the normal solution was retained (before 1983). But it became increasingly clear that this was in fact the wrong solution. This ambiguity has been resolved in four different ways: by statistical studies, by selecting unambiguous cases, by following the perspective evolution during a few days and, recently, by using a marginally thick line. A large majority of prominences belong to the inverse type (75% in Leroy et al. 1984, 85% in Bommier et al. 1994 and greater than 90% in Bommier and Leroy 1998, these proceedings).

It is now well accepted that the magnetic field in prominences is nearly horizontal (since Athay et al. 1983), while compatible with a slight magnetic dip (Bommier et al. 1986, 1994). The magnetic field strength is nearly homogeneous (Leroy 1989) on the scale of a few arc seconds, but shows a statistical increase of strength with height which is compatible with a dip configuration (e.g., Leroy et al. 1983).

1.2. Why Is a Magnetic Dip Required?

The gravitational scale height of prominence material ($\approx$ 200–500 km) is much lower than the typical height of prominences ($\approx 10^4$–10^5 km). This implies

that plasma pressure cannot provide the mechanism of support. The observed velocities (few km s^{-1}) are much less important than the free-fall velocities (several 10 km s^{-1}) and, usually, the velocity pattern does not show a pattern similar to the one seen in arch filament systems where plasma is clearly seen flowing down (Schmieder 1990). Thus the cold prominence plasma should be supported by the magnetic field. If enough mass (i.e., a plasma beta greater than 0.05) can be brought exactly to the top of sheared magnetic arcade in less than one hour, the gravity force can bend down the top of the field lines, providing a stable support for the prominence plasma (Schmieder et al. 1991, Fiedler and Hood 1993). However prominence formation takes usually a few days (resp. few weeks) in (resp. outside) active regions (e.g., Malherbe 1989). This implies that the magnetic dip should be intrinsic to the magnetic configuration (rather than being formed by plasma forces).

1.3. Observed Evidence for Magnetic Dips

Finding observational support for the existence of magnetic dips in prominences is not trivial. But the dip is **not** incompatible with the observed vertical fine structures (see, for example, Poland 1990, Steele and Priest 1992). The cold plasma fills only the extreme lower part of the field lines (over a height typically one hundred times lower than the field line radius of curvature). Therefore, the effect is too shallow to be observed in the quiescent phase. Higher spatial resolution does not really help because one can only observe the mixing of several fine structures along the line of sight. In the quiescent phase, the presence of magnetic dips is only shown indirectly by the Hanle measurements (e.g., Bommier et al. 1994).

Observational evidence for dips is present directly only in some eruptions (e.g., Rompolt 1990). Several favorable conditions should be present together for direct observation of dips: First, a spatial resolution good enough to see individual filled-flux tubes; second, a quantity of cold plasma sufficient to observe it, but not too great so that there are not too many overlapping structures! Finally, the magnetic dip should change location, (which implies a plasma flow from the old to the new dip location), otherwise the prominence plasma should be accelerated along field lines (e.g., like in surges).

2. Magnetic Configurations Supporting Dense Plasma

The need of a magnetic dip for stable support was first pointed out by Kippenhahn and Schlüter (1957), however, the implications of such a condition were used only recently to select magnetic configurations suitable for prominence formation (see Priest et al. 1989).

2.1. Prominences Supported in Arcade-Like Configurations

A dip cannot be present in a force-free $2\frac{1}{2}$D arcade, since the field lines become flatter as the magnetic shear increases (Amari et al. 1991). This is however possible in 3-D with an overlaying arcade compressing locally the central-part of an underlying sheared arcade (Antiochos et al. 1994). The latter gives mostly an inverse-polarity prominence with a magnetic field nearly aligned with the photospheric inversion line.

2.2. Prominence Supported in Twisted-Flux Tubes

Another way to create a dip is to form a twisted magnetic configuration. It can be formed in several ways: by photospheric twisting motions (Priest et al. 1989), by converging motions in a sheared arcade with magnetic reconnection at the inversion line (van Ballegooijen and Martens 1989), by resistive instability in a sheared arcade (e.g., Inhester et al. 1992), by relaxation and accumulation of helicity (e.g., Démoulin and Priest 1989, Amari and Aly 1992, Rust and Kumar 1994), or by emergence from the convective zone (e.g., Low 1994 1996).

Many observations suggest a helical-like pattern during eruption of prominences: on the disk (e.g., Raadu et al. 1988) and more often at the limb (e.g., House and Berger 1987, Rompolt 1990, Srivastava et al. 1991, Vršnak et al. 1991). Twisted configurations are also identified in CMEs with in situ measurements from Ulysses (e.g., Bothmer et al. 1996, Weiss et al. 1996). Even in the quiescent phase, Filippov (1994) discovered a pattern typical of twisted flux tubes: a "fishbone" organization in $H\alpha$ fibrils on both sides of the inversion line. Low and Hundhausen (1995) show how a twisted-flux tube topology can bring together many of the $H\alpha$ and magnetic observations. Finally, the emergence of a twisted configuration is supported by recent vector field measurements (Leka et al. 1996, Lites et al. 1995).

2.3. Prominences Supported in Quadrupolar Configurations

Quadrupolar configurations naturally have a dip. Kippenhahn and Schlüter (1957, their section 4) first proposed these inverse configurations for stable support of dense plasma; curiously very few authors have referred to this part of their work. Then Uchida (1981) and Malherbe and Priest (1983) independently proposed this configuration; the community remained mostly skeptical. The model was further developed by Démoulin and Priest (1993), Drake et al. (1993), and Uchida (1998, these proceedings). The presence of a corridor free of significant field is needed to have a prominence extension reaching the chromosphere and converging motions to provide mass supply. The quadrupolar model has been extended to magnetic configurations typically found in active regions (Titov et al. 1993, Bungey et al. 1996) and in polar crown regions (Cartledge et al. 1996). Finally, the equilibrium of a twisted flux tube in a quadrupolar region gives a normal polarity prominence (Amari and Aly 1992, Démoulin and Raadu 1992, Lepeltier and Aly 1994), while all other models above have an inverse polarity.

The most important observational supports are the following. First, $\approx 65\%$ of prominences lie in between bipolar regions (Tang 1987). Second, the long-term effect of differential rotation on them leads to the observed magnetic direction in prominences (see Bommier and Leroy 1998, these proceedings). Finally the presence of "dual arcades" in Yohkoh observations is a signature of magnetic reconnection in quadrupolar configurations (Uchida 1998, these proceedings).

2.4. Common Features of Models with Dips

In the vicinity of prominences, models with magnetic dips have the following common and observed properties (see section 1.1):
- the field strength increases with height;
- a low vertical magnetic flux is present in the corridor;
- the field component crossing the prominence is inverse;

- the emergence of flux implies converging, canceling fluxes, and lift-up of dense plasma.

I then deduce that the latter should be realized in prominence feet; it is then natural that the feet are observed to form first (Martres et al. 1966). Moreover, magnetic reconnection is required to progressively liberate the magnetic configuration from its deep anchorage (Low and Hundhausen 1995).

3. Large-Scale Magnetic Field Organization

3.1. Magnetic-Field Observations

There is a global spatial organization and a temporal evolution in phase with the solar cycle of the field measured in prominences (Leroy 1989). In particular, the field orientation is generally continuous along inversion lines. The direction of the field reverses only if one goes to the next inversion line or if one changes hemisphere. Moreover, the tilt of field direction along the equator is nicely correlated with the differential rotation but with a sign opposite to a sheared arcade (see Bommier and Leroy 1998, these proceedings).

3.2. Chirality Patterns

The magnetic observations are coherent with a segregation of chirality by hemisphere. For the northern hemisphere:
- The magnetic helicity is negative (Seehafer 1990, Pevtsov et al. 1995);
- The filaments are dextral and right bearing (Martin et al. 1994);
- The overlaying coronal arcade is left-bearing (Martin and Mc Allister 1996); and the opposite for the southern hemisphere.

3.3. Proposed Scenarios

A natural way to explain that both magnetic field components (parallel and normal to the prominence) are inverse is to use a quadrupolar field sheared by the differential rotation. However, this gives a magnetic helicity dominance in each hemisphere opposite to observations. The right helicity sign is obtained with Coriolis forces acting on diverging supergranular flows. Since it is typically five times more efficient than differential rotation (Priest et al. 1989), it can lead to accumulation of helicity in twisted flux tubes. However, localized twisting motions give neutralized currents while a dominance of one polarity is observed in each hemisphere (e.g., Pevtsov et al. 1995). Van Ballegooijen and Martens (1990) instead proposed the effect of differential rotation in sub-photospheric layers. Then the sheared field becomes buoyant and emerges forming a twisted flux tube with both field components inverse at the dip locations. Recently, Kuperus (1996) proposed a coronal process in which the presence of discrete flux tubes is fundamental (together with converging motions and magnetic reconnection). In conclusion, while the field component orthogonal to the prominence is almost always inverse in models in which one imposes a dip (section 2.4), the fact that the field component parallel to the prominence is also inverse is not yet understood. It is likely that this is caused by the global dynamo (see Berger 1998, Seehafer 1998, both these proceedings).

4. What Is Next?

4.1. Some Suggestions for Future Observations

Looking at the observed fine structure in Hα, one would like to see fine spatial details in the magnetic field, thus, an obvious improvement in magnetic measurements would be an increase of spatial resolution. However, in my view, this is not a major one because it will only reveal a small modulation associated with fine structures. Of much greater interest is to improve the polarimetry to deduce not only the vector magnetic field but its matrix gradient. Only in this way can observations put further constraints on models, in particular by selecting from different models. For example, the vertical variation of the angle between the prominence axis and the magnetic field is different in quadrupolar and in twisted models (in the first case the absolute value of this angle increases monotonically with height, while in the second it has a maximum in the middle of the dip region).

4.2. Combination of Photospheric and Prominence Measurements

The main way to deduce coronal magnetic fields is via extrapolation from photospheric magnetograms. Measurements in prominences give more direct clues on coronal fields, but they are localized ones and are not sufficient for computing the whole coronal configuration. While these data are not co-temporal (disk and limb observations) one can still try to combine them because of the slow time evolution of the field supporting quiescent prominences ($\geq$ weeks, Leroy 1989). In this way one can expect to create a better model for the coronal field.

The above mixed-boundary problem was first introduced by Anzer (1972) for a massive and vertical current sheet embedded in the 2-D potential case. It models a prominence attached to the chromosphere. The generalization to a detached prominence was made by Démoulin et al. (1989). The presence of mixed-boundary conditions brings several problems. Aly et al. (1989) and Démoulin and Forbes (1992) removed both unphysical line current singularities and lack of support at the prominence bottom and top. Then two regularization procedures were proposed by Démoulin and Priest (1993) and Lepeltier and Aly (1995) to apply the method to real data. One extension is to have a finite prominence width by matching an internal solution to the global one (Cartledge and Titov 1996). Another extension to a constant-current (linear) force-free field was done by Ridgway et al. 1992 (Démoulin and Raadu 1992).

To extend the aforementioned work to more general fields looks realisable in $2\frac{1}{2}$-D (one step in this direction is the work of Low and Hundhausen 1995), but there is presently no known way to generalize this to 3-D configurations. The only promising way is the extrapolation of photospheric data (without taking into account the presence of prominence material). This is justified to a first approximation by the low plasma β. There are recent advances in the extrapolation methods: see Amari et al. (1997) and Jiao et al. (1997). One can then compare the extrapolated magnetic field to the one measured in the prominences present in the region. If there is a rough agreement, one then can add cold material, with the observed density, and see if it can improve the correspondence. This is obviously not an easy task, because of the limitations of the extrapolation methods but also because of noise present in the transverse field measurements.

We are hoping that new vector magnetographs, in particular the Franco-Italian THEMIS telescope (e.g., Molodij et al. 1996), will improve the measurements. Finally, the prominence field measurements will put important constraints on magnetic extrapolation and help to construct realistic coronal fields. This is important to understanding prominence physics but it also has an impact on the determination of the global solar magnetic field with direct implications on dynamo theories and solar activity.

References

Aly J.J., Amari T., Colombi S. 1989, in M.A. Dubois, F.Bely-Dubau, D.Gresillon (eds.), Les Editions de la Physique, p. 181

Amari T., Aly J.J. 1992, A&A, 265, 791

Amari T. et al. 1997, Solar Phys., 174, 129

Amari T., Démoulin P., Browning P., Hood A.W., Priest E.R. 1991, A&A, 241, 604

Antiochos S.K., Dahlburg R.B., Klimchuk J.A. 1994, ApJ, 420, L41

Anzer U. 1972, Solar Phys., 24, 324

Apushkinskii G.P., Nesterov N.S., Topchilo N.A., Tsyganov A.N. 1990, SvA, 34(5), 530

Athay R.G. et al. 1983, Solar Phys., 89, 3

Bommier V., Leroy J.L., Sahal-Bréchot S. 1986, A&A, 156, 79

Bommier V. et al. 1994, Solar Phys., 154, 231

Bothmer V. et al. 1996, A&A, 316, 493

Bungey T.N., Titov V.S., Priest E.R. 1996, A&A, 308, 233

Cartledge N.P., Titov V.S. 1996, Solar Phys., 169, 55

Cartledge N.P., Titov V.S., Priest E.R. 1996, Solar Phys., 166, 287

d'Azambuja L., d'Azambuja M. 1948, Annales de l'Observatoire de Paris, 6, 7

Démoulin P., Forbes T.G. 1992, ApJ, 387, 394

Démoulin P., Priest E.R. 1989, A&A, 214, 360

Démoulin P., Priest E.R. 1993, Solar Phys., 144, 283

Démoulin P., Raadu M.A. 1992, Solar Phys., 142, 291

Démoulin P., Malherbe J.M., Priest E.R. 1989, A&A, 211, 428

Drake J.F., Mok Y., van Hoven G. 1993, ApJ, 413, 416

Fiedler R.A.S., Hood A.W. 1993, Solar Phys., 146, 297

Filippov B.P. 1994, Astron. Letters, 20, 665

Foukal P. 1971, Solar Phys., 19, 59

House L.L., Berger M.A. 1987, ApJ, 323, 406

Inhester B., Birn J., Hesse M. 1992, Solar Phys., 138, 257

Jiao L., McClymont, A.N. and Mikić, Z. 1997, Solar Phys., 174, 311

Kim I.S. 1990, Dynamics of Quiescent Prominences, Springer-Verlag, (eds.) V. Ruždjak, E. Tandberg-Hanssen, p. 49

Kippenhahn R., Schlüter A. 1957, Zs. Ap. 43, 36

Kuperus M. 1996, Solar Phys., 169, 349

Leka K.D., Canfield R.C., McClymont A.N., van Driel-Gesztelyi L. 1996, ApJ, 462, 547

Lepeltier T., Aly J.J. 1994, Solar Phys., 154, 393

Lepeltier T., Aly J.J. 1995, A&A, 293, 906

Leroy J.L. 1988, in Solar and Stellar Coronal Structures and Dynamics, R.C. Altrock

(ed.), National Solar Observatory, Sunspot, NM, p. 422

Leroy J.L. 1989, in Dynamics and Structure of Quiescent Solar Prominences, E.R. Priest (ed.), Kluwer Acad. Publ., Dordrecht, Holland, p. 77

Leroy J.L., Bommier V., Sahal-Bréchot S. 1983, Solar Phys., 83, 135

Leroy J.L., Bommier V., Sahal-Bréchot S. 1984, A&A, 131, 33

Lites B.W. et al. 1995, ApJ, 446, 877

Low B.C. 1994, Plasma Phys., 1, 1684

Low B.C. 1996, Solar Phys., 167, 217

Low B.C., Hundhausen J.R. 1995, ApJ, 443, 818

Maksimov V.P., Ermakova L.V. 1985, SvA, 29(3), 323

Maksimov V.P., Prokopiev A.A. 1995, Astron. Nachr., 4, 249

Malherbe J.M. 1989, in Dynamics and Structure of Quiescent Solar Prominences, E.R. Priest (ed.), Kluwer Acad. Publ., Dordrecht, Holland, p. 115

Malherbe J.M., Priest E.R. 1983, A&A, 123, 80

Martin S.F. 1990, in Dynamics of Quiescent Prominences, V. Ruždjak, E. Tandberg-Hanssen (eds.), Springer-Verlag, New York, p. 1

Martin S.F., Bilimoria R., Tracadas P.W. 1994, in Solar Surface Magnetism, R. Rutten and C. Schrijvers (eds.), Kluwer Acad. Pub., Dordrecht, Holland, p. 303

Martin S.F. and Mc Allister A.H. 1996, in Magnetodynamic Phenomena in the Solar Atmosphere, (eds.) Y. Uchida, T. Kosugi and H. Hudson, Kluwer Acad. Publ., Dordrecht, Holland, p. 497

Martres M.J., Michard, R., Soru-Escaut, I., 1966, A&A, 29, 249

Molodij G., Rayrole J., Madec P.Y., Colson F. 1996, A&A Suppl. Ser., 118, 169

Pevtsov A.A., Canfield R.C. , Metcalf T.R. 1995, ApJ, 440, L109

Poland A.I. 1990, Dynamics of Quiescent Prominences, V. Ruždjak, E. Tandberg-Hanssen (eds.), Springer-Verlag, New York, p. 120

Priest E.R., Hood A.W., Anzer U. 1989, ApJ, 344, 1010

Raadu M.A., Schmieder B., Mein N., Gesztelyi L. 1988, A&A, 197, 289

Ridgway C., Amari T., Priest E.R. 1992, ApJ, 385, 718

Rompolt B. 1990, Hvar Obs. Bull. Vol. 14, 1, 37

Rust D.M., Kumar A. 1994, Solar Phys., 155, 69

Schmieder B. 1990, in Dynamics of Quiescent Prominences, V. Ruždjak, E. Tandberg-Hanssen (eds.), Springer-Verlag, New York, p. 85

Schmieder B., Raadu M.A., Wiik J.E. 1991, A&A, 252, 353

Seehafer N. 1990, Solar Phys., 125, 219

Shelke R.N., Pande M.C. 1983, Bull. Astr. Soc. India, 11, 327

Srivastava N., Ambastha A., Bhatnagar A. 1991, Solar Phys., 133, 339

Steele C.D.C., Priest E.R. 1992, Solar Phys., 140, 289

Tang F. 1987, Solar Phys., 107, 233

Titov S., Priest E.R., Démoulin P. 1993, A&A, 276, 564

Uchida Y. 1981, in Proceedings of the Japan-France Seminar on Solar Physics, (eds.) F. Moriyama, J.C. Hénoux, p. 169

van Ballegooijen A.A., Martens P.C.H. 1989, ApJ, 343, 971

van Ballegooijen A.A., Martens P.C.H. 1990, ApJ, 361, 283

Vršnak B., Ruždjak V., Rompolt B. 1991, Solar Phys., 136, 151

Weiss L.A. et al. 1996, A&A, 316, 384

3-D Twisted Flux-Tube in a Linear Force-Free Equilibrium

G. Aulanier and P. Démoulin

Observatoire de Paris, Section de Meudon, DASOP, URA 2080 (CNRS), 92195 Meudon Cedex, France

Abstract. It is now commonly accepted that prominence plasma is supported in magnetic dips, in particular in twisted flux tubes. But present two-dimensional models are unable to explain the observed presence and structure of prominence feet. This requires three-dimensional models. We modelled the field using linear force-free field equations. Combining a small number of harmonics, and using observational constraints, we have found the area in the parameter space where prominences are likely to be present. Then, adding 3-D harmonics, we show that feet appear periodically underneath the prominence body. For great helicity, the parameter space is mostly fulfilled by configurations which have feet alternating between both sides of the prominence axis, as observed. The lateral feet are formed by dips in the vicinity of small magnetic polarities, that are located in a low field corridor where the prominence stands. The modelled configurations show in a natural fashion many observational aspects of prominences, such as the vector magnetic field measurements in prominences and the chirality patterns.

1. Description of the Model

Prominences are formed of plasma sufficiently ionised that we can consider it frozen into the magnetic field. Furthermore, their long-time existence and the slow motions of the plasma inside them allow us to consider their global structure as quasi-static, to a first approximation. The plasma β is typically of the order of 0.01 to 0.1, so the field can almost be considered as force-free. We choose below a linear force-free field (*lfff*) because it provides a large class of 3-D equilibrium states permitting us to understand the presence of feet (Démoulin et al. 1989, Aulanier and Démoulin 1998). Then the *lfff* can be described analytically by the combination of periodic harmonics, that are solutions of:

$$\triangle \vec{B} + \alpha^2 \vec{B} = 0\,.\tag{1}$$

The main criterion for a magnetic configuration that can support a prominence is the existence of dips in the field lines (Démoulin 1998, these proceedings, and references therein). In the following we will suppose that cold material is present in such dips while we neglect its effect on the magnetic field.

2. Filaments in OF Twisted Flux Tubes

From a preliminary $2\frac{1}{2}$-D study of the location of prominence-like configurations in the parameter space, it appears that among the various topologies, only the OF and OBP are satisfying (see Figure 1). The first letter of the terminology refers to the top of the prominence, and the following one(s) to its bottom. O is given for an O-point (i.e., a twisted flux tube), F for a flat field line, and BP for a bald patch. The signature of a bald patch is the presence of field lines whose dip is tangent to the photosphere (Titov et al. 1993). Hence, the underlying feet of the prominence are expected to have such a configuration in 3-D.
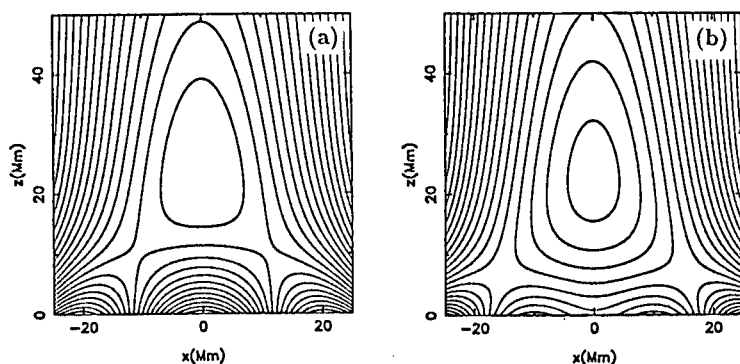
Figure 1.   Topologies for the field in $2\frac{1}{2}$-D satisfying the conditions for a prominence. The configuration is OF in (a) and OBP in (b).

3. Observables for a 3-D Prominence

For a given set of parameters, one can find a configuration which is satisfying for many observed aspects of prominences. The photospheric field has a quasi-
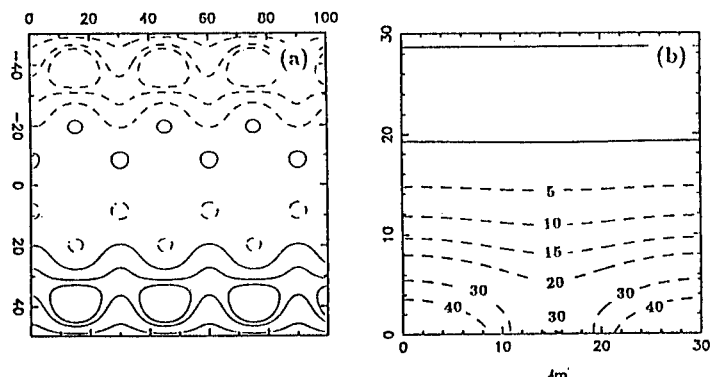
Figure 2.   The vertical photosheric field is shown in (a). Full (resp. dashed) lines are given for $B_z > 0$ (resp. $B_z < 0$). The angle between the field and the prominence axis is shown in (b).

bipolar pattern and the prominence stands above a magnetic corridor containing only small parasitic polarities (see Figure 2). Despite a high helicity, the combination of harmonics permits a large angle between the field and the prominence axis, as measured by the Hanlé effect (Bommier et al. 1994).

4.   The Natural Presence of Lateral Feet

We compute the magnetic field in a 3-D cube, and we look for the dips everywhere in this region. The main prominence body and its underlying feet appear naturally. The feet reach periodically the photosphere, every 30 Mm, which is imposed as the mean size of supergranulation cells. A remarkable feature is the presence of dips aside from the prominence, forming a lateral dip structure. These features join the underlying feet and reach the photosphere, forming bald patches. Their presence is related to small parasitic magnetic polarities in the low field corridor around the inversion line. It is noteworthy that they can be guessed from the $2\frac{1}{2}$-D OF topology (see Figure 1).

Then, assuming that the shape of the prominence is characterized by the presence of cold plasma contained in magnetic field lines at the dip locations, we only draw the portion of these which is likely to be filled with matter. We suppose that for each field line, the plasma can be observed on a few typical height scales above each dip. So we only draw the field lines at a given height of 1 Mm. The result is shown in Figure 3.
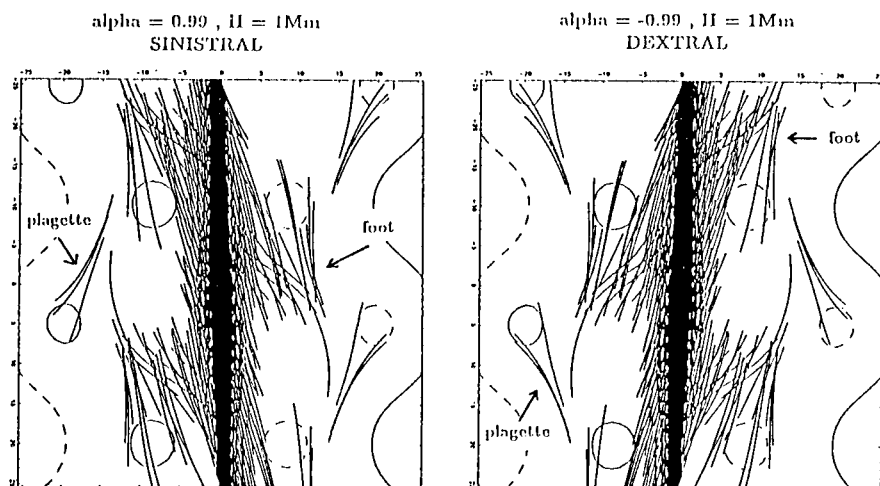
Figure 3.   Field lines computed for the same parameters as Figure 2; they are only drawn at the dip locations at a given height of 1 Mm.

Viewed from above, the lateral feet structures are composed of some portions of field lines that look like what has been introduced as barbs by Martin et al. (1994). These structures match quite well those of observed regular filaments. They naturally appear periodically by pairs, alternating between both sides of the prominence. The orientation, shape and proximity of the represented field

lines give the first impression that some field lines can cross the prominence, from one lateral foot to another one. This is not so. These two lateral features are in fact composed of different groups of field lines.

It is obvious in Figure 3 that a simple reversal of the sign of α changes the orientation of the lateral feet: A positive value of α gives a sinistral and left-bearing prominence, with overlying arcades having a right skew, and a right-handed helical field for the flux tube that supports the prominence. A negative α gives a dextral and right-bearing prominence, with overlying arcades having a left skew, and a left-handed helical field twist for the flux tube. This naturally links together the observed different patterns of chirality, in relation to the hemispheric helicity segregation (Martin and McAllister 1996, Rust and Kumar 1994, Pevtsov et al. 1995).

5. Conclusions

The magnetic configurations suited for prominence support we derived in the present paper are based on only a few hypotheses. We assume that the *lfff* approximation is valid to zeroth order and that combining a very small number of harmonics is sufficient to describe them. This simplicity provides very good agreement with many observational aspects of prominences and their environments, in particular the photospheric magnetic field, the measurements of the field in prominences made by the Hanlé effect, and the chirality pattern of the feet and overlying arcades. Further developments of the model are reported in Aulanier and Démoulin (1998). Finally, we note how fundamental the three-dimensional nature of the model was for the present study. It is obviously important for comparison with observations but, moreover, it emphasizes the importance of the OF configurations.

References

Aulanier, G. and Démoulin, P. 1998 A&A, 329, 1125

Bommier, V., Landi Degl'Innocenti, E., Leroy, J.-L. and Sahal-Bréchot, S. 1994, Solar Phys., 154, 231

Démoulin, P., Priest, E.R. and Anzer, U. 1989, A&A, 221, 326

Martin, S.F., Bilimoria, R. and Tracadas, P.W. 1994, in R. Rutten and C. Schrijvers (eds.), Solar Surface Magnetism, Kluwer, Dordrecht, Holland, p. 303

Martin, S.F. and McAllister, A.H. 1996, in Magnetodynamic Phenomena in the Solar Atmosphere, (eds.) Y. Uchida et al., Kluwer, Dordrecht, Holland, p. 497

Pevtsov, A.A., Canfield, R.C. and Metcalf, T.R. 1995, ApJ, 440, L109

Rust, D.M. and Kumar, A. 1994 Solar Phys., 155, 69

Titov, S., Priest, E.R. and Démoulin, P. 1993, A&A, 276, 564

Concerning Magnetic Field Measurements in Prominences Using Zeeman and Hanle Methods

V.S. Bashkirtsev and G.P. Mashnich

Institute of Solar-Terrestrial Physics, Irkutsk, P.O. Box 4026, Russia

Abstract. A critical review is made of the results of magnetic field measurements in prominences obtained by the Zeeman and Hanle methods. By considering the example of three prominences, some discrepancies between the methods are shown. The authors consider that the magnetic field measurements by the Hanle method inadequately represent the actual magnetic field pattern. To overcome these discrepancies a comparative analysis of magnetic field measurements in prominences by both methods is required.

1. Introduction

Prominence magnetic fields are currently measured using the Zeeman and Hanle effects. While, however, the Zeeman method was put through adequate tests in its practical implementation for magnetic field measurements on the Sun and the results obtained are beyond question, the Hanle method has not been validated at all. Sahal-Brechot et al. (1977) did make estimates only, based on which they arrived at the conclusion that the effects of emission depolarization and of rotation of the vector of polarization observed in prominences are caused by the magnetic field alone. It should immediately be noted that diagnosing the magnetic field on the basis of the Hanle effect is built precisely on this conclusion. However, our subsequent short comparative analysis of observational data (Figures 1–3) obtained by both methods runs counter to this estimating conclusion. We now address the observational data.

2. Observations and Discussion

Results of polarimetric measurements (Hanle method) in a clearly defined giant arch-like prominence (Figure 1) observed on August 15–17, 1980 at the latitude $\varphi=-25°$ E at Sacramento Peak Observatory (Athay et al. 1983) are surprising: the magnetic field vector runs parallel to the solar surface throughout the entire arch-like prominence, traverses its body across the arch (at the angle of 86°) and is directed from the positive polarity of the photospheric magnetic field to the negative polarity. The height gradient of the magnetic field was not determined. In our magnetograph observations on August 15–17 (Zeeman method), we recorded a positive height gradient of magnetic field $B_\|$, an increase of $B_\|$ toward the arch top (Bashkirtsev and Mashnich 1987). This disagrees with data of polarimetric measurements but logically follows from the picture that the
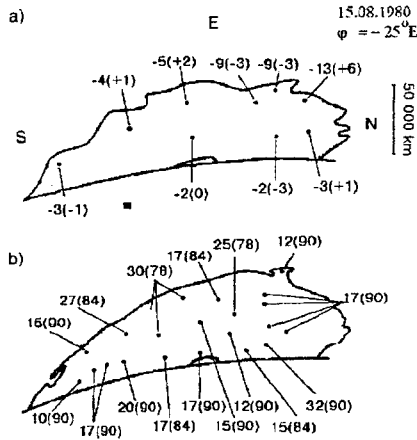
Figure 1.   Sketches of the prominence on August 15, 1980 ($\varphi= -25°$ E). a) Magnetograph measurements at the Sayan Solar Observatory: first numerals are the measured longitudinal magnetic field strengths $B_{\parallel}$ in G (minus = negative polarity); numerals in brackets = line of sight velocities in km s^{-1} (plus and minus signs denote, respectively, the direction from and to observer). b) Polarimetric measurements at Sacramento Peak Observatory: first numerals = the magnetic field strengths (modulus of B); numerals in brackets = the deviation of the magnetic field vector from the local vertical to the solar surface (in degrees).

magnetic field is directed along the prominence arch.

Another prominence, for which it is also possible to compare measurements obtained by both methods, was observed on August 5, 1980 at the latitude $\varphi=+22°$ E (Figure 2). It is remarkable that the emission features of this prominence were arranged along a path resembling a loop. From an interpretation of polarimetry data (Querfeld et al. 1985) it follows that, with increasing height, the magnetic field remains horizontal, i.e., parallel to the solar surface, quasi-perpendicular to the neutral line of the photospheric magnetic field and has a normal polarity. At the same time, according to our observations (Bashkirtsev and Mashnich 1987), both the longitudinal component of the magnetic field and the line-of-sight velocity of mass motion in the prominence increases with the height. Thus, we find that the magnetic field clearly changes with height, which cannot be said based on polarimetric measurements. The following comparison of magnetograph measurements with polarimetry data (courtesy J.L. Leroy) can be made for the prominence $\varphi=+75°$ E (Figure 3) observed on August 13, 1980 (Bashkirtsev and Mashnich 1987). The presence of two polarities in this prominence according to our observations indicates that the magnetic field has a more complicated configuration compared with the interpretation of polarimetric measurements: the magnetic field is unipolar, the magnetic field vector is parallel to the solar surface and quasi-perpendicular to the prominence long axis. On the whole, analysis of the polarized emission in terms of the Hanle
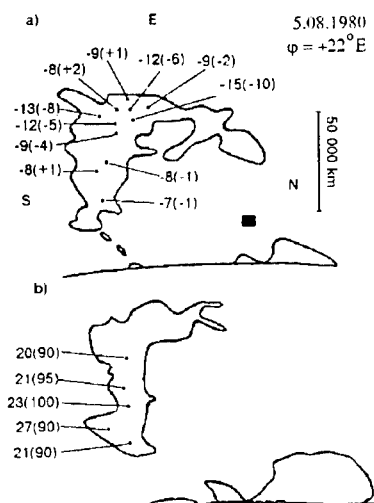
Figure 2.   Sketches of the prominence on August 5, 1980 ($\varphi=+22°$ E). a) Magnetograph measurements at the Sayan Solar Observatory. b) Polarimetric measurements at Sacramento Peak Observatory. For the other designations see Figure 1.
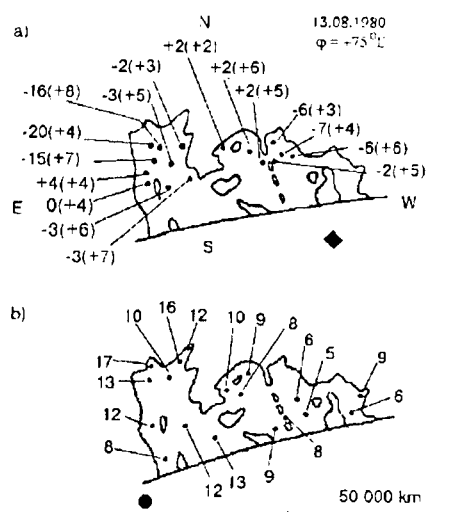
Figure 3.   Sketches of the prominence on August 13, 1980 ($\varphi=+75°$ E). a) Magnetograph measurements at the Sayan Solar Observatory. Dark box = spectrograph aperture. For other designations see Figure 2(a). b) Polarimetric measurements at the Pic du Midi Observatory. Numerals = magnetic field strength (modulus of B) in G. Dark circle = spectrograph aperture.
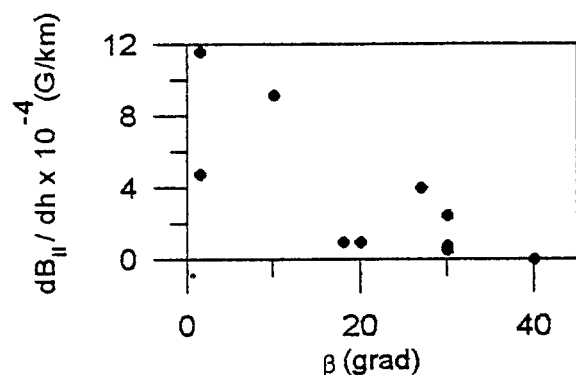
Figure 4.   Dependence of the height gradient of the longitudinal magnetic field, $dB_{\parallel}/dh$, in prominences on the β angle between the line of sight and the prominence (filament) long axis.

effect shows that the magnetic field in quiescent prominences is always invariably horizontal: the deviation from the horizontal (solar surface) does usually not exceed 10–15°. Our data are in conflict with this inference, however. The non-horizontal arch-like magnetic field is favoured by the following fact. If the magnetic field has a arch-like character, then the height gradient of the longitudinal field, $dB_{\parallel}/dh$, must depend on the angle β between the line of sight and the filament long axis and must increase with decreasing β. Such a dependence (taken from Bashkirtsev and Mashnich (1987)) is presented in Figure 4, and one can see that the expected behaviour of the height gradient $B_{\parallel}$ is indeed observed. Hence, the view of a arch-like spiral prominence magnetic field is supported by Zeeman observations, as well as by other observational evidence which, unfortunately, cannot be included here because of lack of space, but such a view is inconsistent with results obtained using the Hanle effect. To make sure that the Hanle method is valid when applied to prominences, it is necessary to carry out a further detailed comparison of observational data obtained by both methods.

References

Athay, R.G., Querfeld, C.W., Smartt, R.N., Landi Degl' Innocenti, E. and Bommier, V. 1983, Solar Phys., 89, 3

Bashkirtsev, V.S. & Mashnich, G.P.. 1987, in The Magnetographic Observations of Prominences at the Sayan Observatory, Irkutsk: preprint, 1987, p. 52

Querfeld, C.W., Smartt, R.N., Bommier,V., Landi Degl' Innocenti, E. and House, L.L 1985, Solar Phys., 96, 277

Sahal-Brechot, S., Bommier, V. and Leroy, J.L. 1977, A&A., 59, 223

Hidden Manifestations of Inverse Polarity in Filaments

Boris P. Filippov

Institute of Terrestrial Magnetism, Ionosphere and Radio Wave Propagation, Russian Academy of Sciences, Troitsk, Moscow Region, 142092, Russia

Abstract. Some aspects of inverse polarity of transverse magnetic fields in filaments are presented following from their fine structure and structure of the chromosphere underneath.

At present magnetic field strength and direction in filaments can be only inferred from prominence (limb) field measurements. The complexity of measurements and ambiguity of interpretation hardly raise hopes that the magnetic configuration of filaments will be determined in the near future. Perhaps the fine structure of filaments in Hα and the arrangement of nearby chromospheric fibrils can tell us more about the magnetic configuration of filaments than direct measurements of magnetic fields therein, though the interpretation of these data is not a simple problem.

In Hα images filaments look like long thin threads running along a polarity inversion line. Threads are not infrequently twisted in ropes. The direction of threads reveals a direction of magnetic field which, hence, makes a small angle with the axis of the filament, in agreement with the field measurements in prominences. Though the transverse component of the filament field is less than the axial one, it is of great importance for the problem of filament equilibrium.

Martin et al. (1994) have studied in detail 150 filaments observed during 1989–1992 at Big Bear Solar Observatory. Their attention was concentrated basically on the field component directed along the axis of a filament but some conclusions from the results of their research can be made about the transverse component as well.

First, the plagette "tails" near a filament always tip away from the neutral line which is to say that the transverse field here is opposite to the large scale photospheric field. Second, Martin et al. (1994) pay attention to 'legs' or barbs of filaments. They divide all filaments into right-bearing and left-bearing. As the barbs represent bunches of threads extended from the main body of a filament, their orientation is specified by a direction of transverse field about the axial component. In so far as all dextral filaments have right-bearing barbs and sinistral filaments have left-bearing ones, both types are of inverse polarity. Lastly, the legs of filaments are never anchored in places of concentration of the background magnetic flux. In contrast, they avoid them.

To these facts it is possible to add one more following from the existence of structures noticed by us in the chromosphere (Figure 1) which look like fishbones with the symmetry axis parallel to the filament (Filippov 1995). Such structures arise near the boundary of the inversion zone where the transversal to the filament axis component changes its sign and only the component along
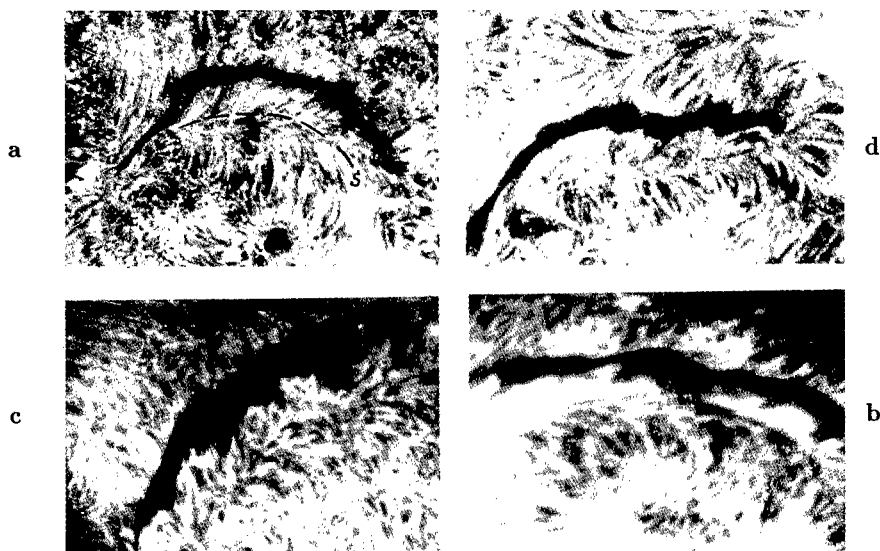
Figure 1.   Hα filtergrams of the filament vicinities in the chromo-
sphere. a) March 29, 1971 (courtesy of A. Bhatnagar), the dotted line
S is the axis of fish-bone structure, b) (courtesy of V. Makarov), c)
June 18, 1989, d) June 11, 1980 (courtesy of V. Ishkov).

the filament remains on the boundary. The change of the direction of transverse
field below a filament is the direct consequence of realization of equilibrium
conditions in the model of inverse polarity.

Field lines of an inverse polarity filament should have a helical structure
if the axial component is dominant. Many of the filaments actually look like
well-defined helices. Everyone is familiar with the helical structure of eruptive
prominences.   There is the separatrix surface in the configuration of inverse
polarity which separates the helical field lines of the filament current from the
lines of the background field. The intersection of the separatrix surface with the
chromosphere is the line S (Figure 2).

It should be noted that in practice it may not be easy to determine whether
an observed filament is a right-handed or left-handed helix. In fact, we observe
only one projection of the real three-dimensional magnetic structure filled by
matter very inhomogeneously. Depending on whether we see the top or bottom
part of the right-handed helix, it reveals itself as threads deviated clockwise or
counterclockwise from the axis of the filament. Rust and Kumar (1994) indicate
that from the stability condition, at least for quiescent filaments, Hα-absorbing
material that makes the filament visible should rest on the underside of the helix
where field lines have a U-like form. In eruptive filaments, opposite parts of a
helix can display opposite Doppler shifts (Figure 3).

One of the arguments being put forward against inverse polarity models is
the presumed absence of observed U-shaped structures in prominences. However,
sometimes such structures are visible when a filament is activated and the helix
is lifting and untwisting (see examples in Valníček et al. 1968, Webb et al. 1994,
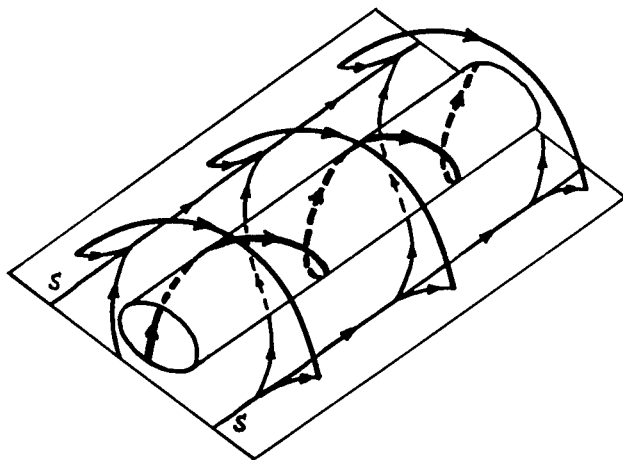
Figure 2.   A sketch of the three-dimensional geometry of the inverse polarity magnetic configuration. Helical field lines of a filament screwing on a cylindrical surface are enclosed into the arch system of a background field. Integral lines of the tangential field in the chromosphere are shown by thinner lines, and the lines, S, are the fibril separatrices.

Figure 3.   Filtergrams showing helical threads in the filament on June 27, 1980 06:20 UT. Left : $H\alpha - 0.5$ Å, the threads are deflected counterclockwise to the axis of the filament; right: $H\alpha + 1.0$ Å, the threads are deflected clockwise to the axis of the filament (courtesy of V. Ishkov).

6:55 UT, Hα - 1 Å   7:05 UT, Hα

7:05 UT, Hα - 2 Å   7:05 UT, Hα - 1 Å
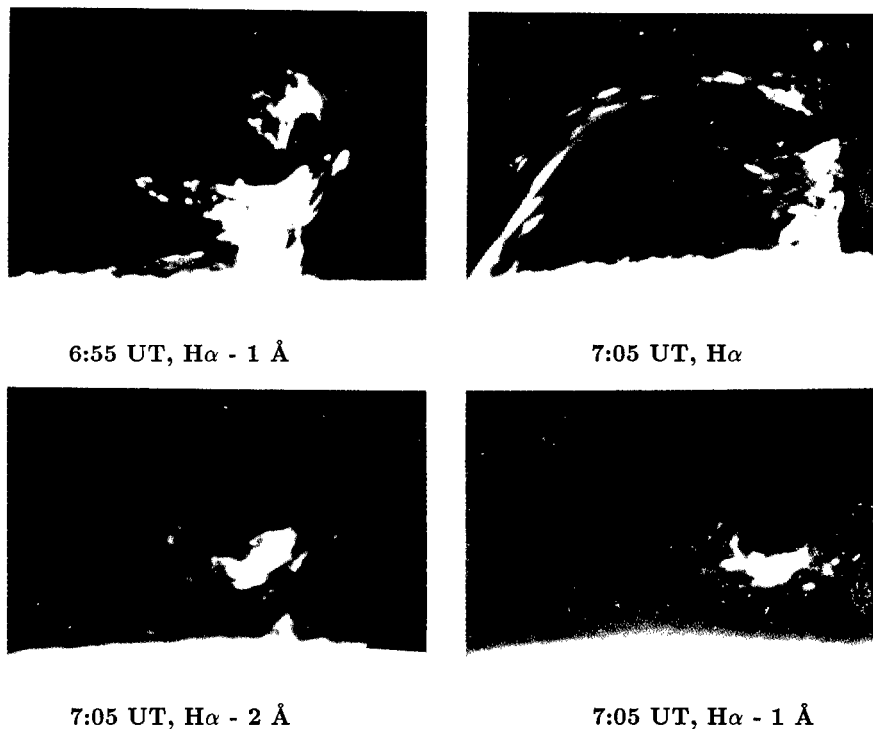
Figure 4.   U-shaped structures in a prominence on July 4, 1989 (courtesy of N. Shilova).

and in Figure 4) . In quiescent prominences they are possibly shaded by the large-scale arch structure of a rope with anchored in the chromosphere ends.

References

Filippov, B.P. 1995, A&A, 303, 242

Martin, S.F., Bilimoria, R., and Tracadas, P.W. 1994, in Solar Surface Magnetism, (eds.)   R.J. Rutten and C.J. Schrijver, New York: Springer-Verlag, p. 303

Rust, D.M. and Kumar, A. 1994, Solar Phys., 155, 69

Valniček, B., Godoli, G., and Mazzucconi, F. 1968, in Annals of the IQSY, A.C. Stickland, Cambridge, MA: The M.I.T. Press, p. 113

Webb, D.F. et al. 1994, Solar Phys., 153, 73

Vector Magnetic Fields at the Base of Filaments and the Filament Environment

Jingxiu Wang and Wei Li

Beijing Astronomical Observatory, Chinese Academy of Sciences, Beijing 100080, China

Abstract. Based on an analysis of three active filaments in AR 6891, we find that vector magnetic fields at the base of filaments and the filament environment is characterized by the following: (1) The transverse field is parallel along the magnetic neutral line for most of the filaments. The average transverse field beneath the filaments is more than 400 G. (2) The horizontal gradient of the line-of-sight field crossing the neutral line is, more or less, constant along the major fraction of a filament, but very steep at the two ends. The average gradient is 0.06 G/km. (3) For each of the filaments there is a *squeezing magnetic structure* which represents an intrusion of a satellite bipole into the main flux system. The neutral line for a squeezing magnetic structure has a large curvature, a strong sheared transverse field of more than 1 KG, and a steep field gradient of approximate 0.3 G/km. (4) The transverse field and field gradient are clearly enhanced before the filament eruption.

1. Introduction

Almost 10 years ago, Leroy (1989) stressed the urgent need of better knowledge of the photospheric magnetic neutral line hosting a filament. So far the situation he mentioned remains that *the photospheric field around the neutral line is rather poorly known*. As he emphasized, to learn the actual magnetic structure of the neutral line is a compulsory step to improving our understanding of the filament magnetic field.

In this report we present the first effort made at the Huairou station of Beijing Astronomical Observatory to determine the actual structure of the vector magnetic field under the filament and the filament environment. The sample we chose for this study consists of three active filaments in active region (AR) 6891 in October 1991. All three filaments erupted after hours of evolution.

The data base for this study is vector magnetograms taken in the FeI 5324Å line and Hβ filtergrams. The spatial resolution for the data is about 2 arcsec, the temporal resolution is minutes for filtergrams, tens of minutes for vector magnetogram. The noise level is less than 20 G for the line-of-sight magnetogram, and 150 G for the transverse field measurement. The calibration and data reduction have been described by Wang et al. (1996).
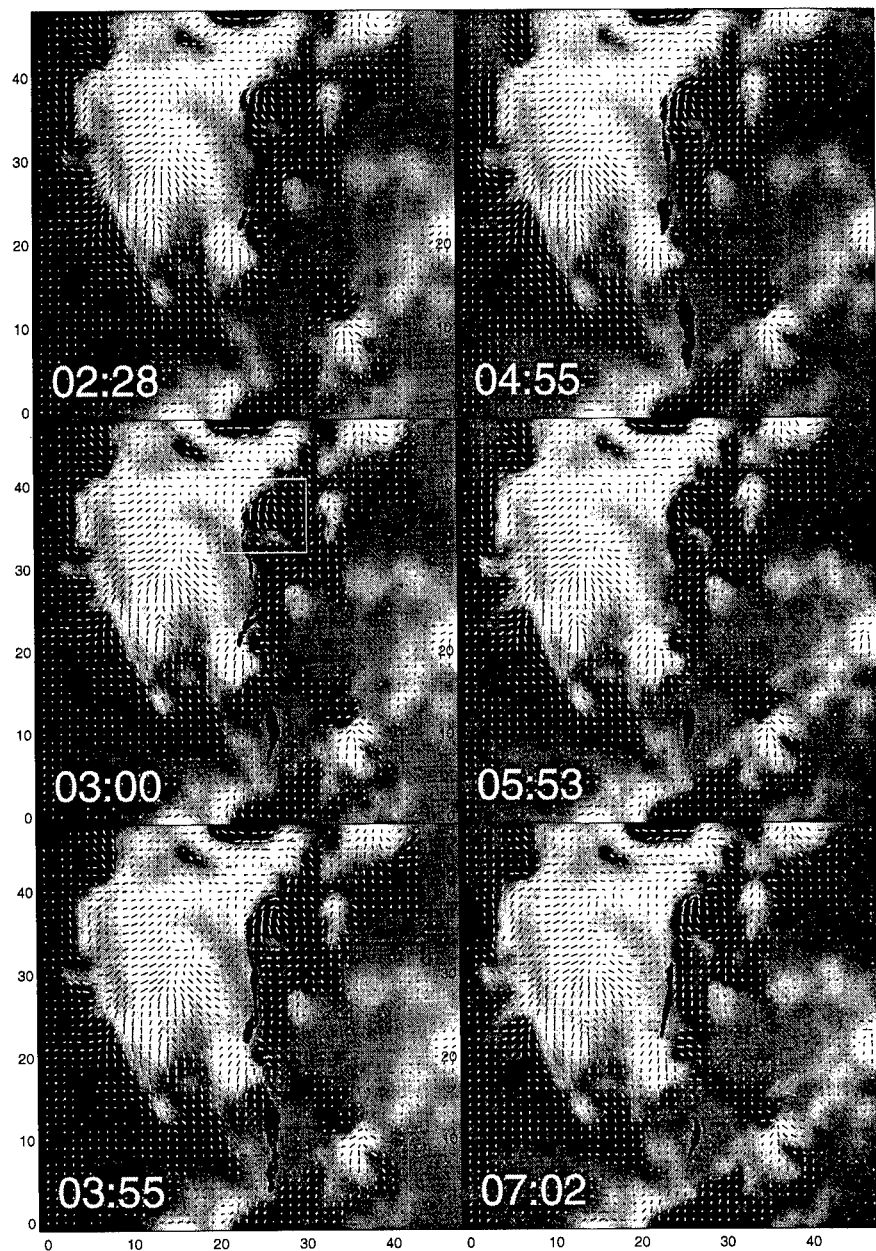
Figure 1.   Time sequence of vector magnetograms superposed on the filament morphology observed at the same time.

2. Data Analyses and Results

Figure 1 is a time sequence of vector magnetograms superposed on the H'β filament as dark fringes for the filament on October 27, 1991 (Filament 1). This filament consists of two pieces, one active piece located in the northern part (top of the figure) and the quiet piece in the southern part. The line-of-sight field is shown by brighter (darker) patches for positive (negative) polarity. The transverse field is shown by bars with length proportional to the field strength, and orientation parallel to the field direction with a 180 deg. ambiguity.
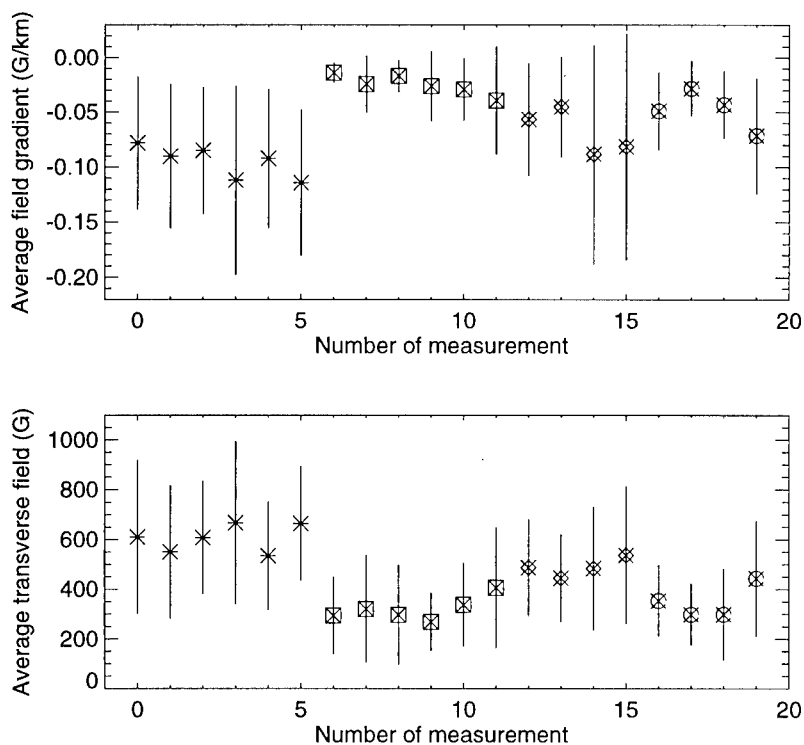
Figure 2.   Measurements of average field gradient and transverse field. Asterisks and squares are for the active and quiet pieces of Filament 1, respectively; diamonds for Filament 2; circles for Filament 3.

It is unexpected that the transverse field beneath the filament is rather strong, particularly at the northern end of the filament. The transverse field is parallel to the magnetic neutral line over most of the filament. The active piece of filament ends in the south where the transverse field runs across the neutral line. The average transverse field is 600 G along the active piece of the filament and 300 G for the quiet piece (see Figure 2 for details). It is astonishing to see that at the northern end, the transverse field is more than 1 KG, and exactly parallel to the curved neutral line. The general pattern of transverse field for two

other filaments on October 28 and 30 (Filament 2 and 3) is the same as described above, but the field strength varies among different filaments (see Figure 2).

The horizontal gradient of the line-of-sight field crossing the neutral line (referred to as field gradient) is measured within a distance of 4 arcsec from positive to negative polarity. The field gradient for the centralized major fraction of a filament is almost constant, approximately 0.06 to 0.07 G/km. However, it is very steep at the two filament ends, at least 0.3 G/km.

A common element of the vector field structure of all three filaments is a characteristic field pattern which we called as a *squeezing magnetic structure.* It consists of two flux patches which come from different flux systems, with one flux patch squeezing into the other, forming a curved neutral line. The neutral line shows a strong sheared transverse field of more than 1 KG, and a steep field gradient of approximately 0.3 G/km. The impacting flux comes from a newly emerging satellite bipole. An example of squeezing structure is shown in the small box in Figure 1 for Filament 1.

In Figure 2 we summarize all the measurements for these three filaments. The measurements at different times show the vector field evolution which is associated with the destablization of the filament. The last measurement for each filament is referred to as the time of filament eruption. The tendency is clear that the transverse field and field gradient are obviously enhanced before the filament eruption.

3. Summary

We have explored the vector field structure beneath filaments and the filament environment for the first time. It is characterized by a strong sheared transverse field and a certain range of field gradient. The squeezing magnetic structure at the far end of each filament is identified to be a common element for all three filaments.

We note that the filaments studied can be classified to be of A-type magnetic boundary (Tandberg-Hanssen 1974), i.e., they form within an active region. However, they do appear to separate the main flux system and the satellite bipoles. Thinking about Tang's (1987) discovery, we tentatively suggest that all filaments may, in fact, represent an environment of the interface of different sources of flux systems.

References

Leroy, J-L. 1989, in Dynamics and Structure of Quiescent Solar Prominences, E.R. Priest (ed.), Kluwer Acad. Publ., Dordrecht, Holland, p. 77

Tang, F. 1987, Sol. Phys., 107, 233

Tandberg-Hanssen, E. 1974, Solar Prominences, D. Reidel, Dordrecht, Holland

Wang, J., Shi, Z., Wang, H. and Lü, Y. 1996, ApJ, 456, 861

Magnetic Helicity and Filaments

M. A. Berger

Mathematics, University College London, London WC1E 6BT, U.K.

Abstract. Some of the most dramatic images of prominences show helical structure. Helical structure, as well as other structural features such as twist, shear, and linking, can be quantified using helicity integrals. This paper reviews how the calculation of helicity may be applied to prominence models. Recent observations indicate that the sign of helicity in an active region depends on which hemisphere the region is in. The source of this asymmetry is an important problem in solar physics. The total helicity of each hemisphere obeys a Poynting-like theorem which describes how helicity is transferred across the photosphere and the equator. Estimating this helicity transfer may help us in understanding the helicity balance of the sun.

1. Introduction

Some four decades ago, the problems of geomagnetism (Elsasser 1956) and solar magnetism (Woltjer 1958) motivated the discovery of magnetic helicity as a conserved quantity in MHD. Unfortunately, magnetic helicity has often been perceived to be difficult to calculate. Section 2 will try to show that the calculation of helicity for many coronal geometries is not difficult: in many cases the helicity reduces to a sum of terms which only involve measures of twist, shear, and flux. Helicity has several nice properties which make its calculation worthwhile: it is conserved in ideal MHD and approximately conserved during reconnection, it quantifies structural features of the field such as twist, shear, kinks, and linking, and it can be computed in any geometry. Section 3 gives an example calculation, showing where the helicity resides in a simple model of a twisted prominence.

Helicity allows us to compare models of fields in different geometries. Thus, a model of a sheared arcade might use its own special parameter to measure the net shear, while models of twisted flux tubes may have their own special parameters to measure net twist. The situation becomes even worse if different authors working on the same basic geometry define their parameters differently. Helicity integrals provide a single universal parameter to measure structural features like twist and shear, thus avoiding the use of parameters specific to one model. Also, if a magnetic system is described in terms of interacting parts (e.g., the solar field as subphotospheric + coronal, or a prominence system as filament + barbs + overlying arcade), then one can describe changes in structure in terms of how helicity is transferred from one part to another.

Helicity is approximately conserved in high magnetic Reynolds number plas-
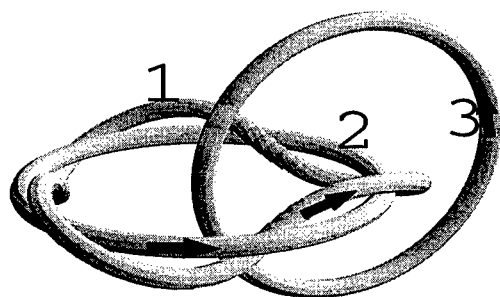
Figure 1.   A set of three linked tubes with linking numbers $L_{12} = 3$, $L_{13} = L_{23} = -1$.

mas (Berger 1984, Freedman and Berger 1993). Approximate helicity conservation provides a valuable constraint on the evolution of a reconnecting field. Of course, one can do physical calculations without worrying about conserved quantities; just let the evolution equations (e.g., Navier-Stokes and magnetic induction) do their work. One might think of calculating orbits of planets about the sun. This can be done numerically without invoking energy and angular momentum; however, these two quantities are essential for understanding the orbits (as well as for finding analytic solutions). Similarly, consideration of where magnetic helicity and magnetic energy come and go can provide shortcuts to solutions of MHD problems as well as checks on numerical calculations. In a confined volume, widespread reconnection may reduce the field to its minimum energy state, given the amount of helicity. This state is a linear force-free field (Heyvaerts and Priest 1984, Dixon et al. 1989). Insufficient reconnection will leave the field in a higher energy state, e.g., a nonlinear force-feee field.

The build-up of helicity in active regions can influence the structure of prominences both before and after eruption; helicity build-up may even be the cause of eruptions (Low 1994, Rust 1994). Furthermore, recent observations (Seehafer 1990, Martin et al. 1992, Pevtsov et al. 1994, Rust and Kumar 1994, 1996) have suggested that the *sign* of helicity in active regions is primarily negative in the Northern hemisphere and positive in the Southern hemisphere. The source of this asymmetry may arise below the photosphere in the solar dynamo (van Ballegooijen and Martens 1990, Rust 1996, Ruzmaikin 1996, Seehafer 1996). Section 4 shows how observations of differential rotation of open flux may be useful in understanding where the helicity comes from.

2.   A Primer on Calculating Magnetic Helicity

In 1833 Carl Gauss introduced the idea of linking number. More recent discoveries by Faraday and others had revealed close relations between electric currents and magnetic fields; Gauss became intrigued by the mathematical problems raised by inductance (where the net electric force around a circuit equals the rate of change of the magnetic field *linked* by the circuit). The linking number L (see Figure 1) is a topological number describing two closed curves. Each curve is given a direction; reversing one of the directions multiplies L by -1. No matter how the curves are distorted, L does not change unless the curves pass through each other. Gauss showed that L could be expressed as a certain line integral along the curves (see, for example, Moffatt 1969). While this integral is rarely used in practice to calculate L, it is useful in proving theorems about L, and provides a bridge between the intuitive world of geometrical pictures such as Figure 1, and the analytic world of integrals and vector calculus.

The linking of closed curves may at first seem irrelevant to the geometry of coronal loops. Note, however, that curves 1 and 2 in Figure 1 twist about each other – their linking number L_{12} measures how much twisting. The twist of two filaments about each other can sometimes be seen in erupting prominence images
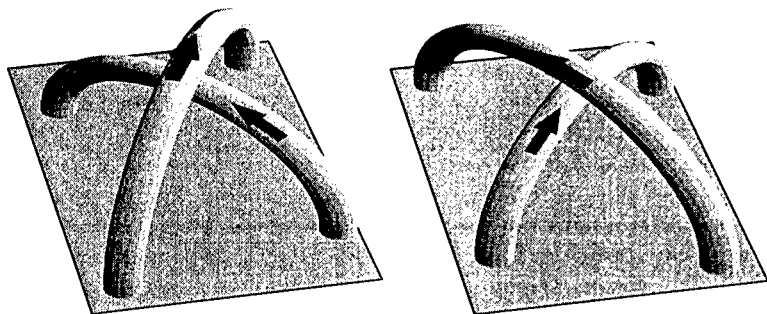
Figure 2.   A crossing can be either positive (left) or negative (right).

(House and Berger 1987, Vršnak et al. 1991). Furthermore, in any diagram or image involving curves or filaments there will be special points where two curves are seen to cross over each other. For example, the lines of force in an overlying arcade may cross over the lines in the prominence filament. The topology of both closed curves and open curves (i.e., curves with endpoints on a boundary such as the photosphere) can be examined using the notion of crossings.

In fact, crossings provide a nice way of calculating linking numbers while avoiding doing line integrals. Each crossing of the curves in Figure 1 has a sign $+1$ or -1 (see Figure 2). The linking number of closed curves is precisely half

the sum of signed crossings. This sum does not vary with either viewing angle of the curves or deformation of the curves. You do not need to carry Figure 2 with you whenever you feel the need to calculate L – there are some simple rules for finding the sign. First, the blades in ordinary right-handed scissors orient themselves to make a positive crossing; if you wish to purchase good quality left-handed scissors, make sure the crossing is negative. Alternatively, imagine two one-way roads which cross at a bridge. Let traffic flow in the direction of the arrows. For a positive crossing, the traffic on the upper road goes to the right as seen by drivers approaching the bridge on the lower road. A third method consists of the right hand rule. This is perhaps easiest looking at the complete closed curves as in Figure 1. Curl the fingers of your right hand along one of the curves (say curve 2) in the direction of its arrow. Now look at one of the places where curve 2 crosses over curve 3. If the crossing is positive, then the thumb will point in the direction of curve 3.

The concept of the linking of curves extends to the linking and twisting of magnetic field lines (Moffatt 1969). The magnetic helicity, very crudely, is the sum over linking numbers over all pairs of field lines. Field lines, of course, are difficult to work with: they are infinitesimally thin and there are infinitely many of them. It is far better to think of the net linking of magnetic flux. The magnetic helicity integral is a double volume integral similar in form to the Gauss integral. As applied to Figure 1, it gives a total helicity of

$$H = T_1\Phi_1^2 + T_2\Phi_2^2 + T_3\Phi_3^2 + 2L_{12}\Phi_1\Phi_2 + 2L_{13}\Phi_1\Phi_3 + 2L_{23}\Phi_2\Phi_3. \qquad (1)$$

Here Φ_1 is the net flux of tube 1 and T_1 refers to the net linking of field lines within tube 1. For a uniformly twisted circular tube, T measures the net number of turns (through 2π) that a field line makes about the central axis. We can call $T_1\Phi_1^2$ the self helicity of tube 1 and $2L_{12}\Phi_1\Phi_2$ the mutual helicity between tubes 1 and 2, in analogy with self and mutual induction.

So far we have discussed closed flux tubes. But coronal fields are rooted at the photosphere and do not form closed curves. In general, helicity integrals (like electrical voltage) require a ground state which sets the zero. The potential field ($\nabla \times \mathbf{B} = 0$) fits this role well: given the distribution of flu x at the boundary ($\mathbf{B}\cdot\hat{n}$), the potential field minimises the energy. With the helicity of the potential field set to 0, the helicity is always uniquely specified (Berger and Field 1984, Jensen and Chu 1984, Finn and Antonsen 1985).

Figures 3 and 4 show the magnetic helicity of various configurations with a plane boundary. First, consider a single twisted tube, Figure 3 (left). In general, the interior of a flux tube may not be uniformly twisted. In this case the helicity provides a measure of overall twist. Suppose the tube consists of a set of nested flux surfaces. Let ϕ be the axial flux within a particular surface. Thus, the central axis has $\phi = 0$, while the outermost surface has $\phi = \Phi$, the total axial flux. Also let $T(\phi)$ equal the twist (number of turns about the axis) at the flux surface labelled by ϕ. Then

$$H = 2\int_0^\Phi T(\phi)\phi d\phi. \qquad (2)$$

Dividing H by Φ^2 gives a dimensionless twist parameter. A highly twisted tube may begin to kink (Hood and Priest 1979, Velli et al. 1997). The amount of
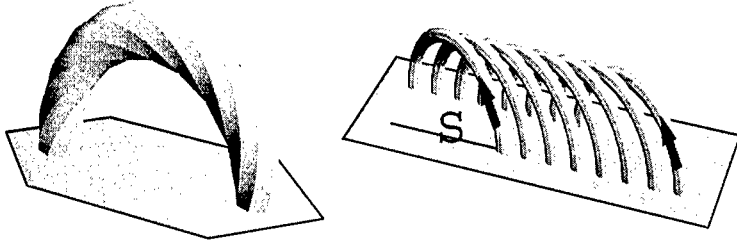
Figure 3.   A twisted flux tube and a sheared arcade.
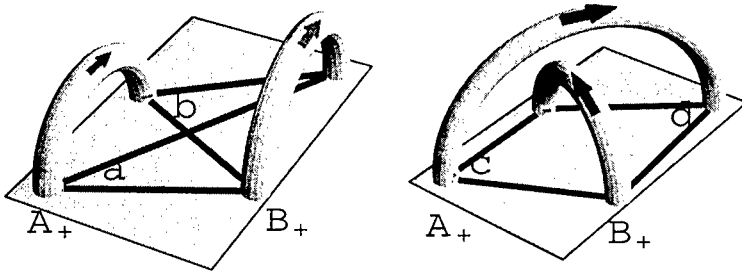
Figure 4.   Mutual helicity. For the tubes on the left, the mutual helicity is $H_{AB} = (a-b)\Phi_A\Phi_B/\pi$. On the right, $H_{AB} = (c+d)\Phi_A\Phi_B/\pi$.

kinking of the central axis can be quantified by the *writhing number* (Moffatt and Ricca 1992). In general the self helicity of the tube can be described as equalling the sum of the writhing number due to the shape of the axis, plus additional twist of field lines about the axis.

Next consider the arcade in Figure 3. This arcade has infinite extent, so we must calculate the helicity per unit length, $\tilde{H}$. The arcade has flux per unit length, $\tilde{\Phi}$, and has been sheared by the length, S. Then

$$\tilde{H} = S\tilde{\Phi}^2. \tag{3}$$

Figure 4 shows two examples of pairs of coronal arches. We assume that the footpoints of the arches are small compared to the distance between the footpoints. Let arch A have positive footpoint A_+ and negative footpoint A_-, and similarly for arch B. To calculate the mutual helicity between A and B, find the angles $\angle B_+ A_+ B_-$ and $\angle B_+ A_- B_-$. The mutual helicity is

$$H_{AB} = (\angle B_+ A_- B_- - \angle B_+ A_+ B_-)\Phi_A \Phi_B / \pi. \tag{4}$$

The plane boundary can be easily replaced with a spherical boundary; simply replace ordinary angles in Figure 4 by a spherical angle. (Consider 3 points P, Q, R on a sphere. The spherical angle $\angle PQR$ at vertex Q can be found by rotating the coordinates so that Q is at the North pole; then $\angle PQR$ equals the difference in longitude between P and R.)

3. Example: A Sheared Arcade Reconnecting to Form a Twisted Prominence

Many authors have suggested that twisted flux tubes can support prominence material (Hood and Priest 1979, Pneuman 1983, van Ballegooijen and Martens 1989, Priest, Hood and Anzer 1989, Ricca 1997). Here we consider a simple model where an initially sheared arcade partially reconnects (Figure 5). The part that does not reconnect can be called the overlying arcade (region 1). The reconnecting flux transforms into a twisted tube and an underlying arcade (regions 2 and 3). The fields are assumed invariant in the x direction. We choose the initial flux at the photosphere, $z = 0$, to be linear,

$$B_z = -B_0 y / a, \qquad |y| \leq a \tag{5}$$

with no flux entering the corona outside $|y| = a$. The shear profile is also linear: footpoint displacements occur in the x direction with magnitude

$$\Delta x(y) = -\frac{sy}{2a}. \tag{6}$$

Thus, for example, a field line starting at $(x, y, z) = (x_0, -y_0, 0)$ re-enters the photosphere at $(x_0 - sy_0/a, y_0, 0)$.

The helicity per unit length of this initial configuration can be computed using equation (3):

$$\tilde{H} = \int_{-a}^{a} \int_{y}^{a} B_z(y) B_z(y') \left(\Delta x(y') - \Delta x(y)\right) dy' dy. \tag{7}$$

The result is $\tilde{H} = 2B_0^2 s a^2 / 15$.

We suppose that only the photospheric flux within $|y| = \epsilon a$ reconnects, where ϵ is some number between 0 and 1. In the final configuration, the flux inside $|y| = \epsilon a$ belongs to the underlying arcade, while the outer flux goes into the overlying arcade. By an integration similar to equation (7), the self helicity (per unit length) of the overlying arcade is

$$\tilde{H}_{11} = (1 - 5\epsilon^3/2 + 3\epsilon^5/2)\tilde{H}. \tag{8}$$
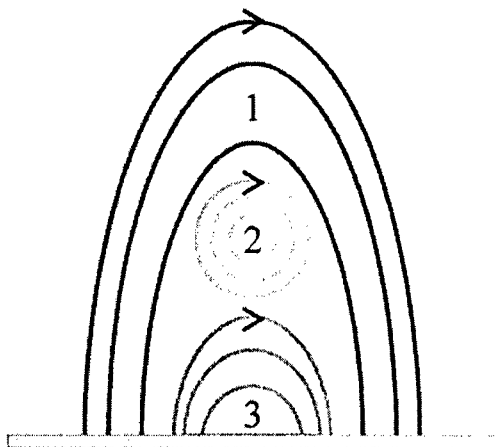
Figure 5.   A twisted prominence model.

Meanwhile the underlying arcade no longer contributes any helicity. Its self helicity $\tilde{H}_{33} = 0$ by the assumption of zero final shear. Its mutual helicities with the overlying arcade and the central flux tube also vanish.

The central tube (region 2) has self helicity

$$\tilde{H}_{22} = \epsilon^5 \tilde{H}; \tag{9}$$

this can be calculated using equation (2). Also the tube has flux $\Phi_2 = \epsilon^3 B_0 sa/3$. The mean twist parameter (per unit length again) is $\tilde{H}_{22}/\Phi_2^2 = 6/(5\epsilon s)$.

Finally, the azimuthal (y direction) flux in the overlying arcade is $\tilde{\Phi}_1 = B_0(1 - \epsilon^2)/2$. This flux links the axial tube flux; thus the mutual helicity is

$$\tilde{H}_{12} = 2\tilde{\Phi}_1\Phi_2 = 5(\epsilon^3 - \epsilon^5)/2. \tag{10}$$

Note that

$$\tilde{H} = \tilde{H}_{11} + \tilde{H}_{12} + \tilde{H}_{22}. \tag{11}$$

For example, if $\epsilon = 3/4$, then

$$\tilde{H}_{11} \ = 0.30\tilde{H}, \tag{12}$$

$$\tilde{H}_{12} \ = 0.46\tilde{H}, \tag{13}$$

$$\tilde{H}_{22} \ = 0.24\tilde{H}. \tag{14}$$

Thus the helicity is shared between shear $\tilde{H}_{11}$, linking $\tilde{H}_{12}$, and twist $\tilde{H}_{22}$. Any additional reconnection, for example at the initiation of a mass ejection, could change these ratios.

4. Helicity Balance in the Northern Hemisphere

Ruzmaikin (1996) and Seehafer (1996) explore the possibility that the α effect in dynamo theory causes the observed asymmetry in active region helicity in the two hemispheres of the sun. The α effect does not create any net helicity; instead it creates opposite signs of helicity in the mean field and the fluctuating field. Classically the mean field in the North should get positive helicity. If this is indeed happening below the photosphere, then the negative helicity seen in active regions must come from the fluctuating field. This scenario may be seen as a consequence of helicity conservation during reconnection. If two flux tubes reconnect deep below the photosphere, they will change their mutual helicity with an equal and opposite change in self helicity (Song and Lysak 1989, Wright and Berger 1989). The self helicity is stored in twist internal to the flux tubes, which in mean field theory would appear in the fluctuating part of the field.

On the other hand, the net helicity of the North may be negative. Let H_N be the total magnetic helicity of all magnetic fields in the solar interior north of the equator. Ignoring the small resistive dissipation term, the time derivative of H_N can be shown to a surface integral (Berger 1984):

$$\frac{dH_N}{dt} = \frac{1}{2\pi} \int \int_{surface} B_r(\mathbf{a}) B_r(\mathbf{a}') \frac{d\varphi(\mathbf{a},\mathbf{a}')}{dt} d^2a\, d^2a'$$
$$- \frac{1}{2\pi} \int \int_{equator} B_z(\mathbf{x}) B_z(\mathbf{x}') \frac{d\theta(\mathbf{x},\mathbf{x}')}{dt} d^2x\, d^2x' \tag{15}$$

where $\mathbf{a}$, $\mathbf{a}'$ are points on the surface and $d\varphi(\mathbf{a}, \mathbf{a}')/dt$ is the angular velocity of the field line at $\mathbf{a}$ about the field line at $\mathbf{a}'$ due to fluid motions. Similarly, $\mathbf{x}$ and $\mathbf{x}'$ label points on the equatorial plane below the surface; these rotate about each other with angular velocity $d\theta(\mathbf{x}, \mathbf{x}')/dt$. This Poynting-like equation describes transfer of helicity into and out of the Northern hemisphere.

Part of the transfer comes from differential rotation (Rust 1996). Open field lines in Northern coronal holes rotate, sending negative helicity into the Parker spiral. Conservation of helicity implies that an equal and opposite positive helicity goes downwards into the sun (this contributes to the first term in equation 15). But the net open flux leaving the Northern hemisphere must equal the amount of flux entering through the equatorial plane (mostly at the base of the convection zone). This flux also rotates, sending negative helicity upwards (second term in equation 15), and positive helicity downwards. If rotation is faster at the equator, then negative helicity will build up in the Northern hemisphere. This helicity may then find its way into active regions, eventually to be released in coronal mass ejections. Of course, during the solar cycle, toroidal flux crosses the equator cancelling out some of the helicity buildup. Both observations of the distribution of open flux and theoretical studies of the solar dynamo will be needed to understand the helicity balance of the sun.

References

Berger, M.A. and Field, G.B. 1984, J. Fluid Mechanics, 147, 133

Berger, M.A. 1984, Geophys. Astrophys. Fluid Dynamics, 34, 265

Dixon, A., Berger, M.A., Browning, P. and Priest, E.R. 1989, 225, 156

Elsasser, W.M. 1956, Rev. Modern Phys., 28, 135

Finn, J.H. and Antonsen, T.M. 1985, Comments Plasma Phys. Contr. Fusion, 9, 111

Freedman, M. and Berger, M.A. 1993, Geophys. Astrophys. Fluid Dynamics, 73, 91

Heyvaerts, J. and Priest, E.R. 1984, A&A, 137, 63

Hood, A. and Priest, E.R. 1979, Solar Phys., 64, 303

House, L. and Berger M.A. 1987, ApJ, 323, 406

Jensen, T. and Chu, M.S. 1984, J. Plasma Phys., 25, 459

Low, B.C. 1994, Phys. Plasmas, 1, 1684

Martin, S.F. et al. 1992, in The Solar Cycle, (ed.) K.L. Harvey, ASP Conf. Ser. Vol. 27, San Francisco, p. 53

Moffatt, H.K. 1969, J. Fluid Mechanics, 35, 117

Moffatt, H.K. and Ricca, R.L. 1992, Proc. Royal Soc. Lon. A, 439, 411

Pevtsov, A.A., Canfield, R.C. and Metcalf, T.R. 1994, ApJ, 440, L109

Priest, E.R., Hood, A.W. and Anzer U. 1989, ApJ, 344, 1010

Pneuman, G.W. 1983, Solar Phys., 88, 219

Ricca, R.L. 1997, Solar Phys., 172, 241

Rust, D. 1994, Geophys. Res. Lett., 21, 241

Rust, D. 1997 in Coronal Mass Ejections, (eds.) N. Crooker, J. Joselyn, and J. Feynman, AGU G.M. 99, Washington, D.C., p. 119

Rust, D. and Kumar, A. 1994, Solar Phys., 155, 69

Rust, D. and Kumar, A. 1996, ApJ, 464, L199

Ruzmaikin 1996 Geophys. Res. Lett., 23, 2649

Seehafer N. 1990, Solar Phys., 125, 219

Seehafer N. 1996, Phys. Rev. E, 53, 1283

Song, Y. and Lysak, R.L. 1989, J. Geophys. Res., 94, 5273

van Ballegooijen, A.A. and Martens, P.C.H. 1990, ApJ, 361, 283

Velli, M., Lionello, R. and Einaidi, G. 1997, Solar Phys., 172, 257

Vršnak, B., Ruždjak, V. and Rompolt, B. 1991, Solar Phys., 136, 151

Woltjer, L. 1958, Proc. Natl. Acad. Sci. USA, 44, 489

Wright, A. and Berger, M.A. 1989, J. Geophys. Res., 94, 1295

On the Relationship Between Current and Magnetic Field in Ring-Filaments

Dirk K. Callebaut

Physics Dept. UIA, University of Antwerp, B-2610 Antwerp, Belgium

Valentine I. Makarov

Pulkovo Observatory, 196140, St. Petersburg, Russia

Abstract. There is a type of filament that forms closed contours encircling regions of one polarity of magnetic field, while the surrounding region has the opposite polarity. One distribution of ring-filaments has sizes 2R = 40,000 to 160,000 km with the maximum around 100,000 km; the other distribution (with filaments and filament channels) has bigger sizes, with a maximum around 300,000 km. At low and mid latitudes the radial component B_{rs} (radial for the Sun) in the region outlined by filaments varies from 50 to 100 gauss, while the longitudinal component B_ϕ varies from 10 to 30 gauss. The total current inside the filament is $10^{10} - 10^{11}$ A, the ratio $R/a \approx 5$ to 10, the magnetic flux crossing the surface is $\approx 10^{21} - 10^{22}$ Mx; the magnetic energy is $\approx 10^{29} - 10^{31}$ erg. Polar ring-filaments at latitudes $60° - 80°$ are related to the polar magnetic field reversal and the quasi-flare processes at the poles during the field reversal. Correlation between B_{rs} and B_ϕ for the polar filament bands cannot be satisfactorily explained. A theoretical model using the conservation laws is used to study the relations between the various fields, currents, etc. of shrinking polar ring-filaments and their evolution. According to this theory ring-filaments should rise higher above the photosphere when shrinking. However, observations show that the height lowers. Presumably the discrepancy is due to the lack of dissipation in the model.

1. Introduction

The filament and filament channels (weak prominences, dense low chromospheric features, multi-channel systems of matter flow between two nearby prominences) sometimes form a continuous closed contour and outline regions of one polarity. There are two distributions of filament structures: one is a Gaussian distribution (for the sizes from 4–$16 \cdot 10^4$ km with maximum around 10^5 km) – these are pure filament structures; the other one is a Pearson distribution (for the sizes from 10^5 to $6 \cdot 10^5$ km, with maximum around $3 \cdot 10^5$ km (Makarov et al. 1986)) – these consist of pure filaments and filament channels. The structures belonging to the Pearson distribution are formed from those of the Gaussian distribution by merging (the diffusion factor is $\nu \approx 1.5 \cdot 10^{14}$ cm^2 s^{-1}). Most of the structures of the Gaussian distribution are more or less circular ring-filament systems.

2.   Low-Latitude Ring-Filaments

Ring-filaments have been detected as closed contours on Hα spectroheliograms at the Kislovodsk Solar Station during 1960–1980 (Makarov and Fatianov 1980) and in the Kodaikanal Observatory plate collection of spectroheliograms in the Hα and CaII-K lines during 1905–1975 (Makarov et al. 1982).

We studied the ring-filament on June 7, 1980 with reference to the magnetic field using Mount Wilson data, Kitt Peak magnetograms and Leroy's data (Leroy 1985, private comm.). We found that the circular filament outlines an island of "+" polarity with the parameters: big radius R = 50,000 km and small radius a = 5,000 km, radial component $B_{rs} \approx 60$ gauss, magnetic field inside filament $B_\phi \approx 18$ gauss. It has clockwise orientation and shows inverse polarity. The magnetic flux crossing the surface S is $F \approx 4 \cdot 10^{21}$Mx. The total current through S is $J_{rs} \approx 2 \cdot 10^{11}$A. The magnetic energy is $W = LJ_{rs}^2/2c^2 \approx 2 \cdot 10^{31}$erg, where $L = 2\pi R \ln(8R/a - 7/4)$. See Landau and Lifshitz (1982).

3.   Polar Ring-Filaments

According to the Hα magnetic charts (1910–1995) one observes ring-filaments at the latitudes $60° - 80°$ of the N and S hemispheres, about 2 to 3 years before polar magnetic field reversal. According to Leroy's data (Leroy 1978, 1985, private comm.) the field in polar prominences was oriented from West to East in the North hemisphere before the reversal in the 21st cycle. The field vector and the axis of the filament form a small angle, about 25°. In the South hemisphere the situation was opposite. The field of the prominences is opposite to the background field. Passing from the polar ring-filament to the next neutral line at middle latitude, the longitudinal component of the field, B_ϕ, changes sign and the entire pattern reverses from one cycle to the next. Let us consider the contour created by the polar ring-filament,

$$\oint \vec{B}\vec{dl} = \frac{4\pi}{c}\int \vec{j}\vec{dS} = \frac{4\pi}{c}J_{rs}$$

where dl is an element of the contour, dS is an element of the surface surrounded by the contour. In our case $B_\phi < 0$ and $J_{rs} < 0$ (i.e., the current enters the Sun). But the magnetic flux crossing the surface S is positive

$$\Phi(r) = \int_s \vec{B}\vec{dS} > 0$$

and

$$\alpha = 4\pi J_{rs}/cF(R) < 0$$

When the radial component of the photospheric magnetic field, B_{rs}, in the polar region reverses in the succeeding solar cycle, the longitudinal component, B_ϕ, in filaments reverses as well.

Thus, if $B_{rs}(\Theta \geq 60°) > 0$, then $B_\phi(\Theta \approx 60°) < 0$
and, if $B_{rs}(\Theta \geq 60°) < 0$, then $B_\phi(\Theta \approx 60°) > 0$.
Thus the parameter α does not change. However, at the same time we have

$$rot\ \vec{B} = \alpha\vec{B}$$

(they are approximately force-free fields) (Makarov and Molodensky 1985). $\alpha(t)$ is such that it never changes its sign; this is connected with the question of stability. We may ask ourselves the following questions:

1. Are there magnetic stars with $\alpha > 0$?
2. What is the difference between the Sun and those stars?

4. Model of Ring-Filaments

The ring-filament is in equilibrium, for certain situations (Figure 1):
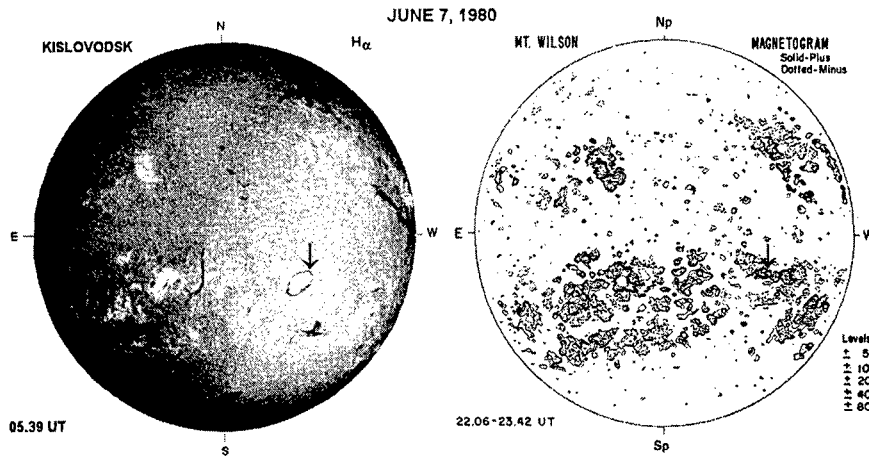
Figure 1.

1. Toroidal and poloidal flux conservation in ring-filament:
$\pi a^2 B_\phi \approx 10^{19}$Mx.

$\pi a R B_\Theta \approx 10^{19}$Mx, if $B_\Theta(r) = r B_\Theta / a$ with r the radial coordinate in the torus $(0 < r < a)$

We do not use flux conservation of $F(R) \approx \pi R^2 B_{rs} \approx 10^{21}$Mx. In fact, as observations show that the field strength inside the ring-filament does not change much when the enclosed surface decreases, it is clear that part of the field and the flux must disappear. How this happens is another matter which is related to the currents, J_{rs} and J_ϕ, (see point 4 below) which suffer losses (due to, e.g., eruptions) which are not taken into account in the present model. But it is clear that flux conservation for $\pi R^2 B_{rs}$ can not be used straightforwardly.

2. Magnetic energy in ring-filament is proportional to R:
$a^2 R(B_\phi^2 + B_\Theta^2) \approx 10^{29} - 10^{31}$erg.

3. Mass of ring-filament $a^2 R \rho \approx 10^{15}$g, with ρ the (average) density.

4. From Maxwell's equations:
$J_{rs} = cRB_\phi/2$ and $J_\phi = (c/2)aB_\Theta \tan \delta$ with δ the pitch angle (Figure 1).

5. Usually if $B_\phi > B_\Theta$, then, according to point 2 above $a^2 R B_\phi^2 \approx constant$. Dividing by the mass of the ring-filament (point 3) yields $B_\phi^2/\rho \approx const$. It may

be noted here that observations show that B_Θ is rather small after an eruption and then increases gradually. $B_\phi^2/\rho \approx const$ means that the Alfvén speed along the filament is nearly constant, but it may be higher in the filament channels than in the filaments.

6. We have shown that there is an internal consistency among the various relations indicated here, provided that flux conservation for $F(R)$ is not used.

7. Using the mirror current concept for the vertical force exerted by J_ϕ is $J_\phi^2/2hc^2$, where h is the height above the solar surface. Equilibrium requires that this equals the total weight of the ring. It follows that $h \approx R^{-2}$, thus the height of the ring-filament increases when the ring-filament shrinks (R decreasing). However, including losses may allow for a decrease of height.

5.   The Height of the Ring-Filaments at Middle and High Latitudes

The maximum amount of matter in a prominence is proportional to the density of the magnetic energy of the field and the degree of the curvature of its lines of force. The height of the prominence decreases with a decrease of the energy of the supporting magnetic field. Using the data for cycles 14–19 (Makarov 1994), we reason as follows. If h' is a height, b' is a base, Θ is the latitude, then we have from observations $S_m(\Theta = 45°) = h'_m \cdot b'_m \approx 5.9 \cdot 10^3$ and $S_p(\Theta = 85°) = h'_p \cdot b'_p \approx 2.0 \cdot 10^3$. Usually $b'_p = 0.7b'_m$, then $h'_m/h'_p = 2$. The height of the polar prominences is half the height of middle latitude prominences. However, according to the theoretical model above the height should increase when the ring-filament shrinks. However, in the model we have not yet taken into account dissipation, which probably explains the discrepancy since the total energy and, thus, the current, J_l, decrease due to dissipation.

References

Landau, L. and Lifshitz, E. 1982, Electrodynamics of Solid Bodies, Nauka, Moscow

Leroy, J. L. 1978, A&A, 64, 247

Makarov, V. I. 1994, Solar Phys., 150, 359

Makarov, V. I. and Molodensky, M. M. 1985, Soln. Dann. Bull., 5, 78

Makarov, V. I. and Fatianov, M. P. 1980, Soln. Dann. Bull., 10, 96

Makarov, V., Stoyanova, M. and Sivaraman, K. 1982, J. Astrophys. Astr., 3, 379

Makarov, V., Tavastcherna, K. and Sivaraman, K. 1986, Astron. Zhurn. (Russian), 63, 534

Formation of Thin Current Sheets in the Solar Atmosphere

C. Z. Cheng and G. S. Choe[1]
Princeton Plasma Physics Laboratory, Princeton University, Princeton, NJ 08543, USA

Abstract. In a two-dimensional quadrupolar magnetic field geometry, it is demonstrated that various magnetohydrostatic equilibrium field configurations containing current sheets can be formed either by changes in thermal properties or by footpoint displacement. The shape of current sheets depends on the mass distribution in flux tubes. If the mass per flux tube is maximum at the center of the low-lying bipolar arcades, a current sheet is formed between these two arcades along the separatrix line as the plasma temperature (or the shearing footpoint displacement) is increased above a critical value. If the mass per flux tube is higher in the outer tubes of the bipolar arcades than in the inner ones, a current sheet with a sharp downward-pointed tip hanging at a distance above the bottom boundary is formed when the temperature is decreased below a critical value. Resistive magnetic reconnection in the latter type current sheet results in a magnetic island wrapped in dipped field lines, which is regarded as a plausible prominence field configuration.

1. Introduction

It is widely believed that magnetic reconnection processes are involved in solar eruptive phenomena, coronal heating and prominence formation. Due to a large magnetic Reynolds number ($\sim 10^{12-14}$) in the solar atmosphere, a very thin current sheet is considered as a necessary condition of magnetic reconnection. Except during dynamic phases related to instabilities or magnetic reconnection, the solar plasma is in a near-equilibrium state because the wave transit time in coronal magnetic structures is short compared to the time-scale of external disturbances. When a system parameter is changed continuously in space and in time, the corresponding equilibrium may not exist in the initially given field topology, but may be found in a different topology. Under the ideal MHD conditions, such a transition of topology is inhibited and thus some field lines collapse to form a current sheet (see, e.g., Parker 1994). In this paper, we have constructed a sequence of 2D magnetohydrostatic (MHS) equilibria under the constraint of topology invariance and demonstrated the unavoidability of current sheet formation as system parameters, such as the plasma temperature and the footpoint displacement, are varied across critical values. In such current sheet configurations magnetic reconnection can be triggered by plasma dissipation to

---

[1] Presently at Tongmyong University of Information Technology, Pusan, Korea

116   C. Z. Cheng and G. S. Choe

form either magnetic islands or an X-point magnetic field topology.

2. Current Sheet Formation by Temperature Change

In the solar corona, the pressure change in a flux tube is more likely to come from a temperature change than a change in the mass content because the photosphere is considered to be quite rigid. Thus, we take the invariance of the mass per flux tube as a constraint and choose the temperature as the control parameter. A magnetofrictional method (Chodura and Schlüter 1981, Choe and Lee 1996) is used to to find 2D equilibrium solutions for a given topology.

2.1. Temperature Increase

A quadrupolar potential field solution by Low (1992) is adopted as the initial configuration so that the density is a function of height only and the mass per flux is maximum at the center of the low-lying bipolar arcades. We obtained equilibrium solutions as the temperature is uniformly increased. Since the expansion of plasma is more effective in the outer flux tubes than in the inner ones, the resulting pressure profile at the base has a pressure maximum at the center of each bipolar regions. As the temperature is increased above a critical value, the plasma pressure gradient pushes out the field lines of each bipolar region so that a current sheet of a finite length is formed where the field lines from each bipolar region come into contact (see Figure 1). The lower tip of this current sheet touches the origin and the current sheet extends along the separatrix.
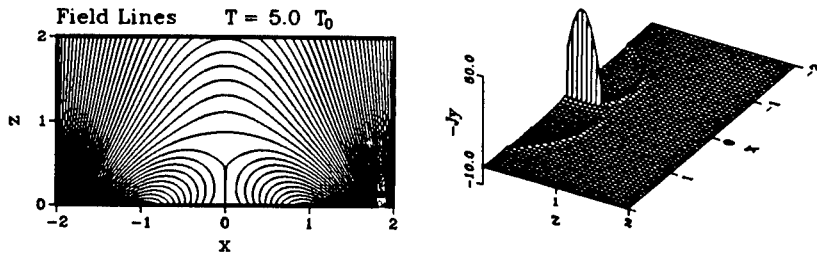
Figure 1.   Formation of a current sheet by temperature increase. The field lines and the current density are shown.

2.2. Temperature Decrease

In this case, the pressure is higher in the outer tubes than in the inner ones in the initial equilibrium. While the potential field subject to the same boundary condition has an X-point, the initial equilibrium field has none because the higher mass in the outer flux tubes depresses the system (Low 1992). As the temperature becomes uniformly lower in the whole atmosphere, the pressure scale height decreases, and the magnetic field pressure dominates the plasma

pressure in the upper part of the flux tubes. As the temperature is decreased below a critical value, the subsequent expansion of field lines creates a tangential discontinuity. The topology of the current sheet in this case is different from that in the former case in that a sharp-pointed tip of the current sheet hangs a distance above the bottom boundary (see Figure 2).
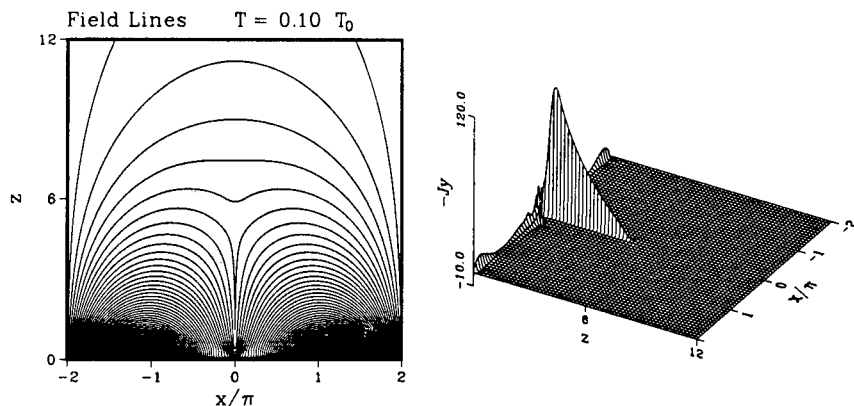
Figure 2.   Formation of a current sheet by temperature decrease. The field lines and the current density are shown.

Starting with an equilibrium obtained with the temperature reduced to 1/4 of the initial temperature, we performed resistive MHD simulations while lowering the temperature. Magnetic reconnection takes place in the current sheet and a vertically elongated magnetic island is formed in a thin current layer as shown in Figure 3. The density in the island is found higher than that in the surroundings. Although the study is based on a 2D isothermal model, it shows for the first time how a magnetic island can be formed between two bipolar regions. Such a field configuration was suggested by Malville (in a discussion reported by Anzer 1979) as a plausible model of prominence magnetic fields.

3.   Current Sheet Formation by Footpoint Displacement

We have also studied the current sheet formation by a shearing footpoint motion. In a complex field topology, the footpoint displacement may not be continuous even though the shearing velocity profile is continuous. To avoid this trivial case, we make sure that the footpoint displacement is everywhere continuous. As the shear is increased in a low β plasma, the two low-lying bipolar arcades expand outward and expel the magnetic flux belonging to the upper arcade. Above a critical amount of shear, a current sheet is formed between those two arcades and also along the separatrix field lines similar to that shown in Figure 1.
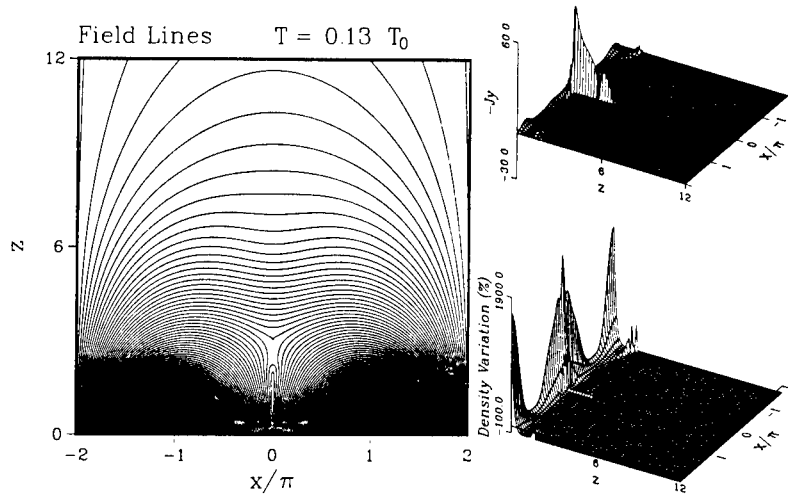
Figure 3.   The field configuration, current density and density varia-
tion resulting from atmospheric cooling with nonzero resistivity. The
magnetic island residing in a current layer should be noted.

4.   Conclusion

In this paper, we have shown that formation of a current sheet can be quite
common and ubiquitous in the solar atmosphere with a quadrupolar field geom-
etry. Due to footpoint displacements and thermodynamic changes the system
can evolve to form a current sheet. In addition to the possibility of a current
sheet tied to the bottom boundary, a current sheet can also be suspended above
the bottom boundary as long as a large enough mass exists around its tip. Mag-
netic reconnection in this current sheet can lead to a magnetic field configuration
favorable for prominence formation.

References

Anzer, U. 1979, in Physics of Solar Prominences, E. Jensen, P. Maltby and F.
        Q. Orrall, Institute of Theoretical Astrophysics: Blindern–Oslo, p. 322
Chodura, R., and Schlüter, A. 1981, J. Comp. Phys., 41, 68
Choe, G. S., and Lee, L. C. 1996, ApJ, 472, 360
Low, B. C. 1992, A&A, 253, 311
Parker, E. N. 1994, Spontaneous Current Sheets in Magnetic Fields, Oxford
        University Press: Oxford

Plasma Electric Field Measurements as a Diagnostic of Neutral Sheets in Prominences

P. Foukal

CRI, Inc., Cambridge, MA 02139, USA   E-mail: pfoukal@world.std.com

Abstract.
    Measurements of plasma electric fields offer, in principle, a direct test for the presence of neutral sheets in prominences. Macroscopic electric field intensities of order 1–10 V cm^{-1} are an essential element of MHD models of prominences containing neutral sheets. These fields should be detectable with our electrograph techniques using the high Paschen-series lines in the NIR, and the 15–9 and 16–9 transitions of H I around 10.5 μ. We discuss the upper limits of 1 V cm^{-1} we have achieved so far, and their implication for our ability to distinguish prominence models of the ideal-MHD type (e.g., Kippenhahn-Schluter 1957), from those fundamentally different models (e.g., Kuperus and Tandberg-Hanssen 1967, Martens and Kuin 1989) in which neutral sheets play a central role.

1. Introduction

Ideal MHD models of prominence support (e.g., Kippenhahn and Schluter 1957) predict very small E ($\leq 10^{-8}$ V cm^{-1}) for classical or even anomalous resistivity values. Such values of E would be completely undetectable. Current sheet models (e.g., Kuperus and Tandberg-Hanssen 1967, Martens and Kuin 1989) predict a very large drop along the current sheet ($\geq 10^8$ V). An electric field of order 1–10 V cm^{-1} should be detectable either i) within the prominence (i.e., around the current sheet); or ii) within the resistance of the cool legs of the prominence; or iii) in the upper photosphere, where the circuit should be completed (Foukal and Behr 1995). Table 1 summarizes previous electric field measurements in prominences.

2. Ongoing Electrograph Observations

The 16–9 transition of H I at 925.6 cm^{-1} (10.8 μ) was identified recently in our Fourier transform spectrometer (FTS) spectra of quiescent prominences by E. Chang (1996, private communication). One of our FTS spectra is shown in Figure 1, with this line marked. Calculations by R. Casini (Figure 2) show the sensitivity (mÅ/V cm^{-1}) of this line to electric fields directed perpendicular and parallel to the prominence magnetic field. Our first FTS spectra polarimetry on this line (Figure 3) indicates a sensitivity of about 1–2 V cm^{-1} should be achievable on bright quiescent prominences. Future observing runs at Kitt Peak will focus on electric fields in the prominence body and legs.

Table 1.   Previous Electric Field Measurements in Prominences

Technique	Limits on E	Type of Structure	Reference[a]
Total E-field from n-dependence of Balmer, Paschen line fwhm.	$170(\pm100)$V cm^{-1}	p-f loops, active proms	(1)
Plasma E-field from difference of total field and Holtsmark field (measured from line ratio diagnostics of Ni).	$\lesssim$5-10 V cm^{-1} $\lesssim 10^2$ V cm^{-1}	eruptives, p-f loops	(2) (3)
Electrograph measurements (spectrapolarimetry) of high-n Balmer, Paschen lines.	$\lesssim$5-10 V cm^{-1} $\lesssim$2-5 V cm^{-1}	quiescents	(9) (4)
Spectral profile analysis of H I 15-9.	$\leq$10 V cm^{-1}	quiescents	(5)

[a]numbers refer to ordering in the Reference section of this paper.
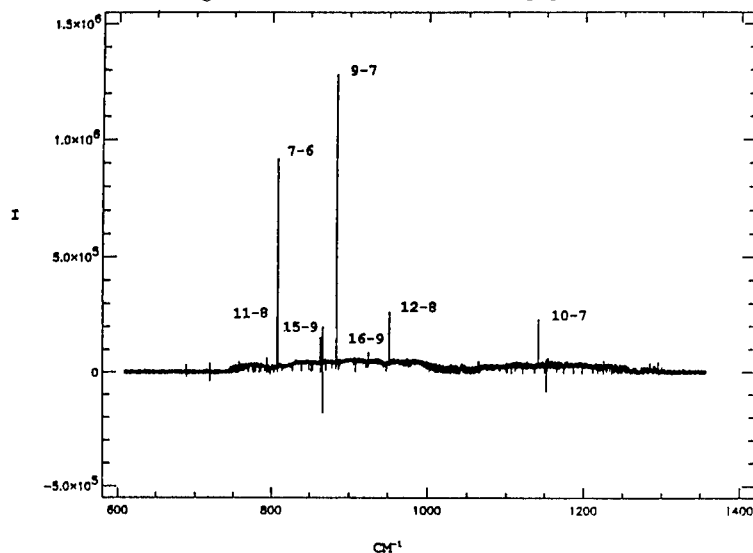
Figure 1.   Spectrum of a quiescent prominence, over the wavenumber range 600–1400 cm^{-1}, obtained with the FTS at the McMath telescope, Kitt Peak.

16-9 Transition (B=10 G — FWHM=0.7 Å)
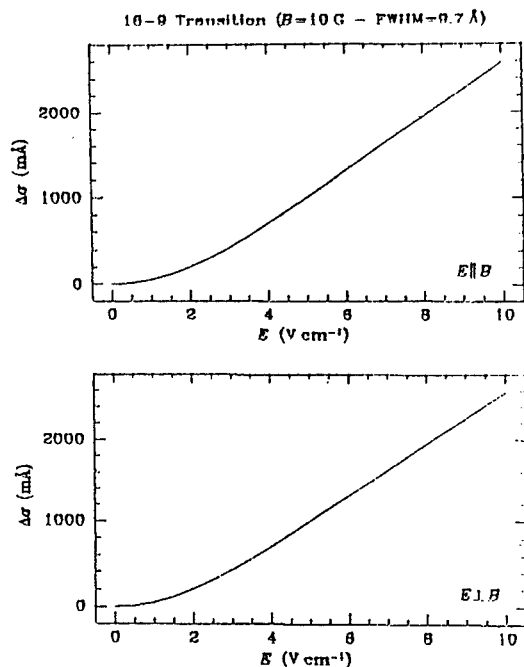
Figure 2.   Plots of the difference in full-width half-maximum of the
H I 16–9 transition, when only π and only δ-components of the Stark
profile are observed. The ordinate is line width modulation in mÅ; the
abcissa is electric field intensity in V cm^{-1}.
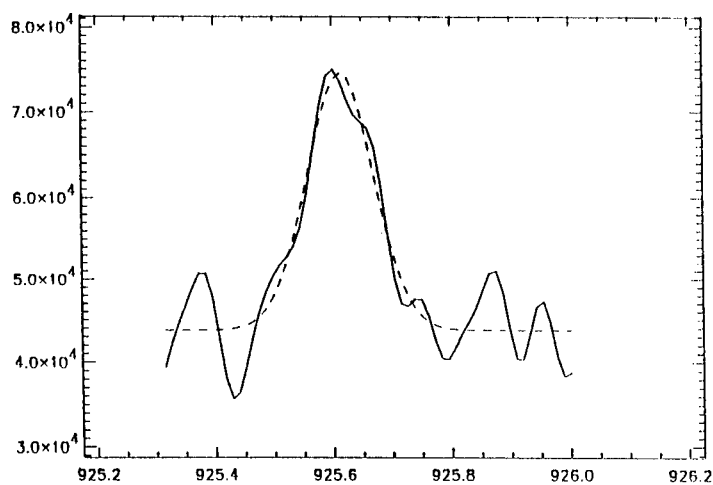
Figure 3.   Line profile of H I 16–9 observed (-) and gaussian fitted
(—). FTS spectrapolarimetry on April 15, 1997.

Electric fields associated with completion of the prominence circuit through the photosphere might be measurable using a Stark-sensitive photospheric absorption line. The most interesting candidate is the H I Paschen transition 7–3 at λ 10049. We are collaborating with R. Casini in estimating the Stark sensitivity of this absorption line.

3.   Conclusions and Future Directions

1. Spectrapolarimetry using Balmer and Paschen series lines has so far revealed no plasma electric fields in quiescent prominences, at a sensitivity level reaching 2–5 V cm^{-1}, which is comparable to the electric fields expected in the body and/or legs of the prominence if an extended neutral sheet is present. Ongoing FTS spectrapolarimetry using the highly Stark-sensitive 16–9 transition should yield sensitivity of 1–2 V cm^{-1}, in the body and legs of these structures.

2. Spectrapolarimetry using the Paschen 7–3 photospheric absorption line may enable us to determine if a significant part of the "missing potential drop" in a neutral-sheet associated prominence, might actually occur in the photospheric portion of the prominence's equivalent circuit.

3. Detection of electric fields within the prominence body, legs, or associated photosphere would provide a unique test of neutral sheet existence in the solar atmosphere. Absence of detectable E would call into question neutral sheet models of quiescent prominences. However, it is unlikely that even the sensitivity increase achieved with the 16–9 line will be sufficient to detect the (model-independent) motional electric field due to ionized particles collisionally crossing the magnetic field lines. This anisotropic, microscopic electric field must be present in the prominence plasma at the 0.5 V cm^{-1} level (Moran and Foukal 1991).

References

Foukal, P., Miller, P., and Gilliam, L. 1983, Solar Phys. 83, 83

Foukal, P., Hoyt, C., and Gilliam, L. 1986, ApJ, 303, 861

Foukal, P., Little, R., and Gilliam, L. 1988, Solar Phys. 114, 65

Foukal, P. and Behr, B. 1995, Solar Phys. 156, 293

Foukal, P. and Casini, R. 1996, BAAS, 28, 876

Kippenhahn, R. and Schlüter, A. 1957, Z. f. Astrophys., 43, 36

Kuperus, M. and Tandberg-Hanssen, E. 1967, Solar Phys., 2, 39

Martens, P.C.H. and Kuin, N.P.M. 1989, Solar Phys., 122, 263

Moran, T. and Foukal, P. 1991, Solar Phys. 135, 179

Nonstationary Electric Drifts in the Solar Atmosphere

I.S. Veselovsky

Institute of Nuclear Physics, Moscow State University

Abstract. Induced electric fields and nonstationary drift motions are considered. Nonstationary electric drifts may be important in erupting prominences, rising and shrinking coronal loops, and other phenomena in the solar atmosphere. Theoretical limitations are indicated for the concept of dominant plasma motions along magnetic field lines.

1. Introduction

Electric fields are difficult to measure in the solar atmosphere and are poorly known. Electric fields are generated in two ways: the solenoidal part depends on the electric current time variations and the potential or polarization part is due to electric charging. Electric charges and polarization fields are not invariant against coordinate system transformations. Because of this, the quasi-neutrality of the current carrying medium is dependent on the reference frame. The preferred reference system, where it is valid, should be always indicated to avoid confusion. The neglect of these facts and improper handling of electric fields and "frozen-in conditions" may sometimes lead to physically wrong general conclusions about slow plasma motions across magnetic fields in the solar atmosphere.

The purpose of this paper is to show that solenoidal electric fields are especially important when considering nonstationary motions in the solar atmosphere. Solenoidal electric fields are also termed nonpotential or induced electric fields.

2. Induced Electric Fields and Drifts

Eddies in the electric field $E(\vec{r}, t)$ are generated by time dependent magnetic fields $B(\vec{r}, t)$ according to Faraday's law

$$rot\vec{E} = -\frac{1}{c}\dot{\vec{B}}. \qquad (0.1)$$

Equation (1) leads to the expression for the induced electric field

$$\vec{E}_{ind} = -\frac{1}{4\pi c}\int [\dot{\vec{B}}(\vec{r}, t) \times \vec{R}]R^{-3}d^3r', \qquad (0.2)$$

where $\vec{R} = \vec{r} - \vec{r}'$. The induced electric field (2) may be represented using the vector-potential $\vec{A}(\vec{r}, t)$ by the formula $\vec{E}_{ind} = -\frac{1}{c}\dot{\vec{A}}$ because of $\vec{B} = \vec{\nabla} \times \vec{A}$. Induced electric fields are often (but not always) dominant in space plasma

conditions because of the strong magnetic fields which are varying with time. Potential electric fields $\vec{E}_{pot} = -\nabla\varphi$ are completely determined by the charge density distribution $\rho(\vec{r}, t)$ in space according to the equation $\varphi = \int \rho R^{-1} d^3 r'$. Because of this, potential electric fields are important when free charges are separated at sufficiently small spatial scales. The total electric field is equal to the sum of the two parts, the induced and potential ones: $\vec{E} = -\frac{1}{c}\dot{\vec{A}} - \nabla\varphi$.

We will consider the case of small electric potentials and large quasistationary varying magnetic fields in the laboratory frame. Magnetic fields in this case are completely determined by the electric currents $\vec{j}(\vec{r})$ according to the Bio-Savart law:

$$\vec{B} = \frac{1}{c}\int[\vec{j}(\vec{r}') \times \vec{R}]R^{-3}d^3r', \tag{0.3}$$

which follows from the second Maxwellian equation

$$rot\vec{B} = \frac{4\pi}{c}\vec{j} + \frac{1}{c}\dot{\vec{D}} \tag{0.4}$$

in the nonrelativistic approximation ($v \ll c$) when displacement currents are negligible $|\dot{\vec{D}}| \ll 4\pi\vec{j}$ and the corresponding wave lengths are large compared with the characteristic length scales (Landau and Lifshits 1983).

Electromagnetic and mechanical quantities are related to each other by material equations. The simplest example of such a relation is represented by Ohm's law

$$j_i = \sigma_{ik}(E_k - \frac{1}{c}e_{klm}v_l B_m) \tag{0.5}$$

with a scalar conductivity $\sigma, \sigma_{ik} = \sigma\delta_{ik}$, which is valid only for sufficiently frequent collisions and will be used for illustration purposes. In this case

$$\vec{j} = \sigma(\vec{E} + \frac{1}{c}[\vec{v} \times \vec{B}]) \tag{0.6}$$

and the drift velocity of the medium across the magnetic field is equal to

$$\vec{v}_\perp = c\frac{[\vec{E} \times \vec{B}]}{B^2} - \frac{c}{\sigma}\frac{[\vec{j} \times \vec{B}]}{B^2}. \tag{0.7}$$

Drift motions are completely determined when the electric and magnetic fields are known together with the electric currents and conductivity distributions in space.

For example: a) $\vec{j} = 0, \sigma \neq 0$. In the current-free medium with a finite conductivity from (7) and (8) immediately follows

$$\vec{v}_\perp = c\frac{[\vec{E} \times \vec{B}]}{B^2}, \qquad \vec{E} = -\frac{1}{c}[\vec{v} \times \vec{B}]. \tag{0.8}$$

b) $\sigma \to \infty, \vec{j} \neq \infty$. The well known frozen-in conditions (9) are valid only in this limiting case. c) $\vec{v} = 0$. Ohm's law in this case has the form $\vec{j} = \sigma\vec{E}$.

d) It is interesting to note that $\vec{v}_\perp = c\frac{[\vec{E}\times\vec{B}]}{B^2}$ only if $|\vec{j}| \ll |\sigma\vec{E}|$. Moreover, $\vec{v}_\perp = 0$ if $|\vec{j}| = |\sigma\vec{E}|$, and $\vec{v}_\perp = -\frac{c}{\sigma}\frac{[\vec{j}\times\vec{B}]}{B^2}$, when $|\vec{j}| \gg |\sigma\vec{E}|$. We do not consider here more complicated material equations (anizotropic conductivity, generalized Ohm's law, etc.)

The frozen-in condition is often met in the solar atmosphere. Because of this drift velocities can be estimated from Equations (9) using Equation (2) as follows

$$v_\perp \simeq 10^3 \tilde{N} r t^{-1}, \tag{0.9}$$

where $v_\perp$ (km/s), r (Mm), $t(s)$, $\tilde{N} = \tilde{B}/B_{tot}$. Here r and t are the characteristic space-time scales of the magnetic field variations. The total magnetic field B_{tot} is represented as a sum of the background stationary field B_0 and the time variable part $\tilde{B}(t)$: $B_{tot} = B_0 + \tilde{B}(t)$. For an active region on the Sun with $r \sim 10$–100 Mm, $t \sim 10^4$ s, $\tilde{N} \sim 1$ one obtains drift velocities $v_\perp \sim 1$–10 km/s.

Our considerations indicate that drift velocities are generally increasing with the distance from a source of quasistationary varying magnetic perturbations. Ascending prominences, coronal transients, expanding or contracting loops in the solar atmosphere often show the regularity of the same kind: larger loops are moving faster (Tandberg-Hanssen 1974, Illing and Hundhausen 1986). Expanding loops represent quasistationary structures with the plasma drift motions governed by the strong magnetic fields which are increasing with time. Contracting loops, according to this explanation, are driven by the decaying magnetic fields.

3. Discussion and Conclusions

Space-time correlations in the solar atmosphere are sufficiently large and allow us to distinguish individual structures like loops, ropes, arcades, threads, jets, rays, sheets, etc. The anisotropy introduced by the magnetic fields produces elongated structures with characteristic length scales $r_\perp \ll r_\parallel$. For nearly incompressible (subsonic) regimes one obtains from the continuity equation $v_\parallel \sim \frac{r_\parallel}{r_\perp}v_\perp$, which means the visible dominance of parallel motions. More numerous regimes of compressible motions depend on the ratio of time scales $\frac{t_\perp}{t_\parallel}$; where $t_\perp^{-1} = v_\perp/r_\perp, t_\parallel^{-1} = v_\parallel/r_\parallel$ are the characteristic times of flight across and along the field. Different solutions were described for large and small values of the duration of the nonstationary processes under consideration (flows along the magnetic tubes, local contractions and rarefactions) (Veselovsky 1991). Nonstationary drift motions and density enhancements in a time-variable dipole magnetic field were investigated under several assumptions in the three-dimensional and two-dimensional cases (Syrovatskii 1969, Gorbachev and Kellner 1988, Filippov 1996).

The results show that the concept that motions of the plasma in the regions of the solar atmosphere with appreciable magnetic fields are taking place mainly along magnetic field lines which was introduced about half a century ago (Cowling 1953, 1957) has theoretical limitations and contradicts observations in many instances: erupting prominences, twisted ropes, rising and shrinking

coronal loops, the solar wind flow across Archimedian spirals of the magnetic field, especially in the outer heliosphere.

We conclude that the popular idea that plasma can not move freely across magnetic fields is tenable only in the cases when there are no electric drifts.

References

Cowling, T.G. 1953, in The Sun, G.P. Kuiper (ed.), The University of Chicago Press, Chicago, p. 532

Cowling, T.G. 1957, Magnetohydrodynamics, Interscience: N.Y

Gorbachev, V.S. and Kellner, S.R. 1988, Sov. Phys. JETP, 94, 89

Filippov, B.P. 1996, A&A, 313, 277

Illing, R.M.E. and Hundhausen, A.J. 1986, J. Geophys. Res., 91, 10951

Landau, L.D. and Lifshits, E.M. 1982, Electrodynamics of Continuous Media, Nauka: Moscow (in Russian)

Syrovatskii, S.I. 1969, Astrophys. Space Sci., 4, 240

Tandberg-Hanssen, E. 1974, Solar Prominences, D. Reidel: Dordrecht, Holland

Veselovsky, I.S. 1991, Solnechnye Dannye, 11, 89 (in Russian)

A Model of Plasma Sheets in Equilibrium

S. Koutchmy

Institut d'Astrophysique de Paris–CNRS, 98 Bis Bd Arago, F–75014 France

M. Molodensky

IZMIRAN, Moscow region, Troitsk 142192 Russia

D. Vibert

Laboratoire d'Astronomie Spatiale, BP 8, F–13376 Cedex 12, Marseille France

Abstract. We consider large coronal streamers as confined thin plasma sheets overlying the filament and/or the magnetic polarity inversion lines. Confirmation is found in recent synoptic LASCO/SOHO data and simulations. We discuss the 3D axi-symmetric consistent MHD solution which provides the necessary properties of confinement and equilibrium by including gravity forces in the Grad-Shafranov equation.

1. Introduction

It has been known for a long time (Lockyer 1931, Vsekhsvjatsky 1963) that a connection exists between filaments and large coronal streamers. Both good resolution photometric data and a simple magnetic structure have been worked out by Koutchmy (1971) to interpret eclipse data and later, balloon data by Bohlin and Garrison (1974). Radially extended blades or sheets overlying the magnetic polarity inversion line (MPIL) were considered. Projection effects are of fundamental importance in interpreting white light (WL) images, so numerical models greatly help in removing ambiguities. Independently, resistive MHD models with increased sophistication have been proposed to explain the behavior of coronal streamers, especially when the physics of CMEs is considered. Among the latest work that follow the lines originally proposed by Pneuman and Kopp, we note the papers by Mikic and Linker (1994) and by Wu, Guo and Dryer (1997). Usually it is implicitely assumed that the WL coronal structures exactly match magnetic field lines computed by the model. However, from the analysis of prominence fine structures at least, this is not the case. We have the same difficulty when dealing with WL fine loop structures. In this short contribution we do not imply plasma structures are identical to magnetic lines but rather consider the confinement of these structures as well as the equilibrium of the coronal plasma (against gravity) at large scales, without considering the dynamical aspects.

2.   Observations

a) Many high-quality eclipse images show convincingly the direct links between prominences and coronal structures. Their 3D geometry is usually not easy to guess. Stereoscopic viewing helps identification (see Koutchmy and Molodensky 1992, Molodensky et al. 1996).

b) An extended new data set is available after the first year of operation of the SOHO mission. WL images of the corona are now collected at a high rate and good resolution is routinely achieved. We selected images taken during one solar rotation to look at the corona from different points of view, assuming rigid rotation. Images were taken at the time of the deep solar minimum in 1996, from April 11 to 28. The corona was particularly quiet, showing sometimes a very narrow equatorial sheet, at least on one side of the limb. A model was designed to represent the rather narrow distribution of plasma densities across the sheet (Vibert 1997). The shape of the sheet was taken as a radial extension of the MPIL at r = 2.5, computed using the potential field approximation and the available photospheric magnetographic data. Integration along the line of sight was performed taking into account the 3D geometry. Representative results of both the observed coronal structures and of the close agreement in the images given by the model, were shown at the meeting and can be found, e.g., in Vibert (1997). Even more convincing is the movie assembled using this material.

c) It is clear that this simple model confirms the importance of geometrical effects including fold-like configurations and the sheet-like nature of the streamer belt. A definite density enhancement occurs inside the sheet defined by the MPIL. This confinement of the plasma in a narrow sheet is quite similar to what is known to occur in the case of a large prominence ('curtain-type'). Accordingly, we developed an analytical model partly inspired by the classical model of prominences by Kippenhahn and Schluter (1957).

3.   Theoretical Modeling

We make several assumptions: axisymmetry, negligible dynamical effects, and a simple magnetic configuration. We looked further at fully consistant MHD solutions of the well known Grad-Shafranov equation (Landau et al. 1984) where forces due to gravity are taken into account. The parameters are chosen in such a way to guarantee that the plasma density in the equatorial sheet well exceeds the density of the surrounding corona. The plasma temperature can be determined from the equilibrium equations determining the pressure and density. The measured temperature of the corona sets stringent constraints on the free parameters. The configuration of the resultant magnetic field is then different from that proposed by Pneuman and Kopp (1971) and Alexeev et al. (1982). The equilibrium configuration in spherical coordinates of a plasma in a magnetic and gravitational field can be written as:

$$\nabla p - \frac{j^*}{cr\sin\theta}\nabla\Psi + \rho\nabla\Phi = 0 \, , \tag{1}$$

where Φ is the gravitational potential and Ψ is the flux function of the magnetic field satisfying the following relation:

$$\Delta^*\Psi + II'(\Psi) = \frac{4\pi}{c}j^*r\sin\theta,\tag{2}$$

where

$$\Delta^*\Psi = \frac{\partial^2\Psi}{\partial r^2} + \frac{\sin\theta}{r^2}\frac{\partial}{\partial\theta}\left(\frac{1}{\sin\theta}\frac{\partial\Psi}{\partial\theta}\right).\tag{3}$$

The variable j^* denotes that electric currents may exist besides j_ϕ. When $\Phi = 0$, eq. (2) reduces to the well known equation of Grad-Shafranov for the function Ψ.

Details of the treatment and the discussion of different solutions that we have obtained will be given in a more extended forthcoming paper. Figure 1 is an illustration of the set of magnetic field lines we obtained for the two cases which are deduced, depending of the thickness of the sheet we want to have: i) at left is the classical solution of the Pneuman and Kopp type which is coming from this treatment; ii) at right is the new solution we propose here that gives a well confined thin equatorial sheet.
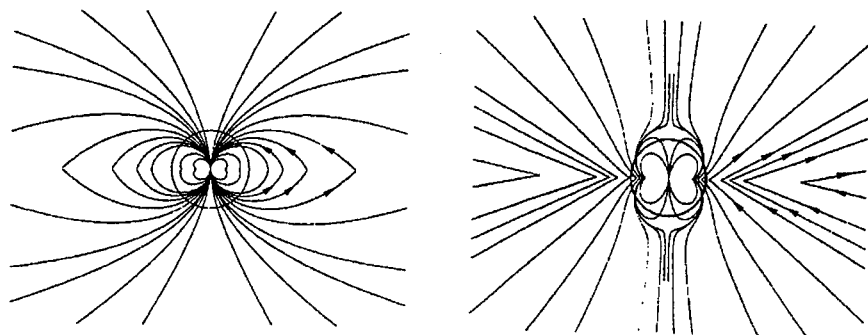
Figure 1.   The set of magnetic field lines corresponding to the two solutions we deduced to describe the equatorial plasma sheet in equilibrium. Only the solution at right gives a well confined thin sheet.

4.   Conclusions

a) The narrow distribution of densities inside an equatorial sheet can be in equilibrium provided the coronal magnetic field corresponds to the solution we show at right on Figure 1 (we call it 'concave current sheet'). Note that the classical solution of the Kopp-Pneuman type ('convex current sheet') cannot provide such confinement and would evacuate the region of the equatorial sheet, where the cusp forms.

b) A narrow heliospheric sheet is observed in the interplanetary medium out to very large distances as illustrated by the Ulysses results. We can then speculate

on the rather minor effect that the dynamics (wind) would play in our model.
c) Our model predicts some peculiar structures inside the equatorial sheet: magnetic lines across it show a concave shape. Features like this are now well observed in the equatorial flow of the wind seen on SOHO/LASCO movies.
d) A quite similar magnetic structure was calculated by Uchida and Low (1981) for the magnetosphere of a star with an accreted magnetized mass. We, however, noticed a fundamental difference with what we are proposing: in the case of an accretion disk, a uniform outer magnetic field is postulated. We do not have such a constraint in our model.
e) Finally, it could be useful to look more carefully at the magnetic structure of polar regions where prominences are usually absent. We plan to work soon on that.

References

Alexeev, I. I., Kropotkin, A. P. and Veselovsky, I. S. 1982, Solar Phys., 79, 385

Bohlin, J.D. and Garisson, L.M. 1974, Solar Phys. 38, 165

Kippenhahn, R. and Schlüter, A. 1957, Zeit. für Astrophys., 43, 36

Koutchmy, S. 1971, A&A, 13, 79

Koutchmy, S. and Molodensky, M.M. 1992, Nature, 360, 717

Molodensky, M. M., Starkova, L. I., Koutchmy, S. and Ershov, A. V. 1996, in Solar Drivers of Interplanetary and Terrestrial Disturbances, (eds.) Balasubramaniam et al., A.S.P. Conf. Ser. Vol. 95, San Francisco, p. 385

Landau, L. D., Lifshits E. M. and Pitaevskii, L. P. 1984, Electrodynamics of Continuous Media, 2nd edition, Translated by J. B. Sykes, J. S. Bell and M. J. Kearsley, Pergamon Press, Oxford

Lockyer, W.J.S. 1931, MNRAS, 41, 7, 801

Mikic, Z. and Linker, J.A. 1994, ApJ. 430, 898

Pneuman, G. W. and Kopp, R. A. 1971, Solar Phys. 18, 258

Uchida, Y. and Low, B.C. 1981, J. Astrophys. Astr. 2, 405

Vibert, D. 1997, These Dr es Sc., Marseille Univ., St Charles, France

Vsekhsvjatsky, S.K. 1963, in The Solar Corona, (ed.) J.W. Evans, Academic, San Diego, p. 271

Wu, S.-T., Guo, W. P. and Dryer M. 1997, Solar Phys., 170, 265

Latitudinal Variations of Line-of-Sight Velocity Oscillations in the Photosphere, Chromosphere and Prominences

G.P. Mashnich and V.S. Bashkirtsev

Institute of Solar-Terrestrial Physics, Irkutsk, P.O. Box 4026, Russia

Abstract. By studying line-of-sight velocity time variations in prominences, we found that velocity oscillations with a period over 40 min have a reasonably well-marked dependence of the period length with heliolatitude. Simultaneous observations of line-of-sight velocities in the photosphere and chromosphere showed that quasi-hourly oscillation periods at these levels in the solar atmosphere and in prominences have a similar latitudinal behavior.

1. Introduction

While speculating concerning the origin of oscillations in prominences, we tried to identify some peculiarities of oscillation parameters depending on the phase of solar activity cycle, and on the position of prominences relative to zones of activity. As a result, the study revealed a reasonably clear-cut heliolatitudinal dependence of the value of the line-of-sight velocity oscillation period in prominences (Bashkirtsev and Mashnich 1993). Line-of-sight velocity observations in prominences covering the period 1981–1991 were used in our investigation.

Whenever the issue concerns fundamental problems of the solar interior and differential rotation, of significant importance are reliable experimental data on latitudinal variations of physical plasma parameters, the geometrical size of solar features, and on their behaviour within the course of the evolution of a solar cycle. Directly or indirectly, observational data make it possible to get closer to realistic models. By investigating the line-of-sight velocity time variations in prominences, we defined the oscillations with periods over 40 minutes as the forced ones and supposed that the source of such oscillations resides in layers of the solar atmosphere below the prominence. If this is so, then the latitudinal peculiarities in quasi-hourly oscillations must be revealed, at least in the visible layers of the solar atmosphere. We present results derived by investigating the heliolatitude dependence of oscillation parameters in the photosphere and chromosphere.

2. Observations

The observations were made at the Sayan-Mountain Solar Observatory during August–September 1995 and in July 1996 at the horizontal solar telescope. Velocity variations were measured using a high-precision differential method of measuring line-of-sight velocities which has been used with the solar magneto-

graph. The concept of the instrument for differential measurements of the line-of-sight velocity and its implementation were detailed in a paper of Kobanov (1983). Using an additional photomultiplier we carried out measurements simultaneously in the photosphere (λ 485.97 nm) and the chromosphere (λ 486.13 nm), with the 2"× 8" entrance slit and with the spectrograph dispersion in V of the order of 0.32 Å/mm. The solar image was kept on the spectrograph slit by means of the photoelectric guider; solar rotation was automatically compensated. With allowance made for distorting factors, line-of-sight velocity measurements were made to an accuracy no worse than 20 m s^{-1}. Areas to be investigated were chosen in the light reflected from the spectrograph mirror slit and passed through a Halle Hα filter. It is known that short-period oscillations (of about 3.7 μHz) are vertical ones; therefore, the amplitude of such oscillations decreases from the center to the solar limb. The behaviour of the quasi-hourly oscillations of the chromosphere is the reverse (Bashkirtsev and Mashnich 1987): at the center of the solar disk they are virtually nonexistent, and with increasing distance from the center to the limb their amplitude increases. Taking these factors into account, we chose, for the observation, regions of the quiet Sun in longitude about 40° near the latitudes 0° 25° 50° and 65°. It is at these latitudes that we detected deviations from the mean values of the line-of-sight velocity, quasi-hourly oscillation period in prominences. The length of one recording was typically not less than 120 minutes; hence, during the daytime we were able to take one recording for each of the latitudes, provided that weather conditions allowed. Such a recording length gives sufficient resolution in the spectrum. The accuracy of determining the period, P, as shown by Djurovich and Pâquet (1994), is no worse than $P^2/2T$, where T is the length of a time period. For example, when $T = 2P$, the error in determining the period does not exceed $P/4$. Time sequences were pretreated; after that, the method of correloperiodogram analysis was used to calculate the line-of-sight velocity oscillation spectra for the frequency region less than 1 μHz. Of the spectra obtained, we picked components with the largest amplitude, at a significance level ≥ 0.99, whose values were plotted on the "period-latitude" diagram.

Proceeding in this way, we obtained heliolatitudinal dependences of the value of the quasi-hourly oscillation period. Figure 1 shows the latitudinal variations of the value of the period for the photosphere and Figure 2 for the chromosphere. For comparison, Figure 3 shows the latitudinal variations for the photosphere (dashed line), the chromosphere (dash-dotted line), and prominences (solid line). Even with small statistics, all dependences reveal deviations from the mean value of the period to maximum values at latitudes about 25°, and to minimum values at latitudes 45°-50°.

3. Discussion

The quasi-hourly oscillations observed in prominences are interpreted in some papers (Balthasar et al. 1988) as eigen-oscillations caused by the geometry and physical conditions of the prominence itself. However, the coincidence of the latitudial dependences of the oscillation period at different levels of the solar atmosphere, as is evident from Figure 3, permit the quasi-hourly oscillations in prominences to be treated as forced ones. The photosphere, the chromosphere
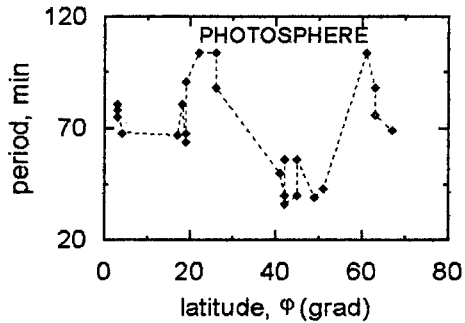
Figure 1.   Latitudinal variations of the quasi-hourly oscillation period
for the photosphere.
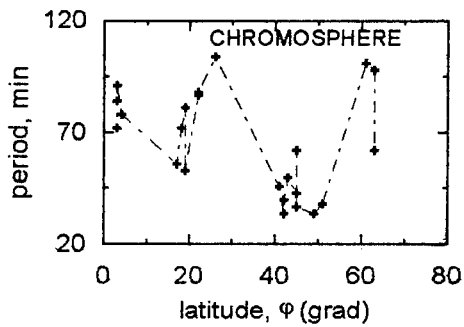
Figure 2.   Latitudinal variations of the quasi-hourly oscillation period
for the chromosphere.
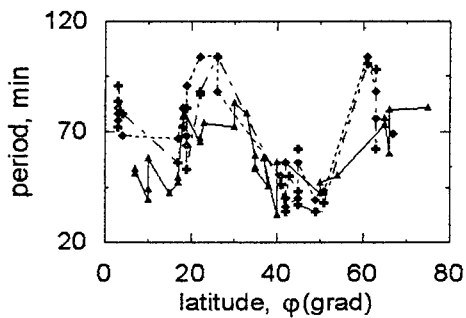
Figure 3.   Comparison of the latitudinal variations of the oscillations
in the photosphere, chromosphere and prominences.

and the prominence should be regarded as a unified oscillatory system for

frequencies less than 1 μHz.

It is not our intent here to provide an explanation for the presence of maxima and minima of the quasi-hourly oscillation period at certain latitudes, because of the small amount of observational data. It should be noted that some investigations detected variations of different physical parameters of solar plasma with latitude. A few examples are given below.

It is known that the solar magnetic field in the corona has a latitudinal zonal structure. Using data on the structure of the coronal magnetic field, Makarov (1983, 1984) showed that at maximum activity each solar hemisphere exhibits two global magnetic neutral lines at latitudes 20° and 40° and one line near the equator. In a series of papers addressing the observed frequency splitting of the p-modes, variations in the internal angular rotation velocity were calculated depending on the latitude and solar radius. Rhodes et al. (1990) carried out a comparison of the variations in inner angular rotation velocity depending on latitude and solar radius from observational data obtained at different observatories. A good agreement of results was found, and it was shown that the variations in inner angular velocity for $R = (0.6 - 0.95)R$ of the Sun behave differently for the equatorial, middle and near-polar latitudes. Rimnele and Schroter (1989), based on maps of line-of-sight velocities of the photosphere on the solar limb, found that the mean size of supergranulation cells varies with heliolatitude, showing a statistically significant minimum at the middle latitudes.

Our obtained result on the latitudinal variations of the value of the oscillation period in the photosphere, chromosphere and prominences is important not only for understanding the origin of prominences but, along with the above mentioned experimental data, is of interest when solving experimental problems of differential rotation and the solar interior.

References

Balthasar, M., Stellmacher, G. and Wiehr, E. 1988, A&A, 204, 286

Bashkirtsev, V.S. and Mashnich, G.P. 1987, Sol. Phys., 109, 399

Bashkirtsev, V.S. and Mashnich, G.P. 1993, A&A, 279, 610

Djurovich, D. and Pâquet, P. 1994, Sol. Phys., 152, 497

Kobanov, N.I. 1983, Sol. Phys., 82, 237

Makarov, V.I. 1983, Solnechnye Dannye, No.10, 93

Makarov, V.I. 1984, Solnechnye Dannye, No. 9, 52

Rhodes, E., Cassiani, A., Korzenik, S., Tomczyk S., Ulrich R. and Wooard, M. 1990, AJ, 351, 687

Rimnele, T. and Schroter, E.H. 1989, A&A, 221, 137

Velocity Fields of a Filament Region Observed with Ground-Based Telescopes and from SOHO

P. Mein, B. Schmieder[1] and J.-M. Malherbe

Observatoire de Paris, Section de Meudon, 5 Place Janssen, F-92195 Meudon, France

J.E. Wiik, O. Engvold, P. Brekke

Inst. Theoret. Astrophys., University of Oslo, P.O. Box 1029, Blindern, N-0315 Oslo, Norway

J.B. Zirker

NSO, NOAO, Sunspot, New Mexico 88349, USA

A.I. Poland

NASA/Goddard Space Flight Center, Greenbelt, Maryland, USA

J.-P. Delaboudinière

Inst. d'Astrophysique Spatiale, Université Paris XI, F-91405 Orsay Cedex, France

J. Staiger

K.I.S., Schöneckstrasse 6, D-79104 Freiburg, Germany

Abstract. We present preliminary results on solar filaments observed from the ground and from SOHO in September 1996. Motions in the network and close to the filament "barbs" are shown at different levels of the chromosphere and the transition region.

During the International Campaign of September 1996 several large filaments were observed simultaneously from the ground (MSDP of the German VTT, Tenerife, and Swedish Vacuum Solar Telescope [SVST], La Palma) and from SOHO (JOPs 17 and 29, SUMER, CDS and EIT). The observations on September 25, 1996 covered a large filament with well defined *barbs* (feet). We present a few combined results from these instruments. The MSDP produced H_α and CaII 8542Å line profiles covering two strips of 170×600 arc sec^2. High resolution H_α filtergrams were obtained with the SVST. Spectral scans with SUMER and CDS on SOHO produced dopplergrams in the temperature range from 3×10^4 K to several 10^5 K. The data show the connections between small-scale velocities and thread structures of the filament "barbs".

---

[1]Inst. Theoret. Astrophys., University of Oslo, P.O. Box 1029, Blindern, N-0315 Oslo, Norway
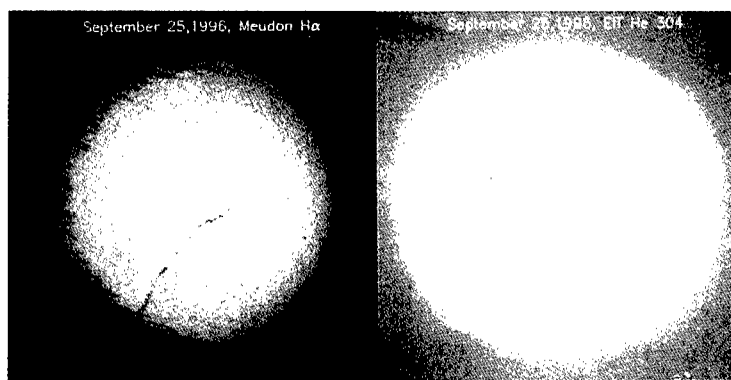
Figure 1. H_α Meudon spectroheliogram and EIT He 304 Å image, showing the full filament channel across the southern hemisphere. The following figures (2 to 4) concern only the northern part of the filament, close to the disk center.
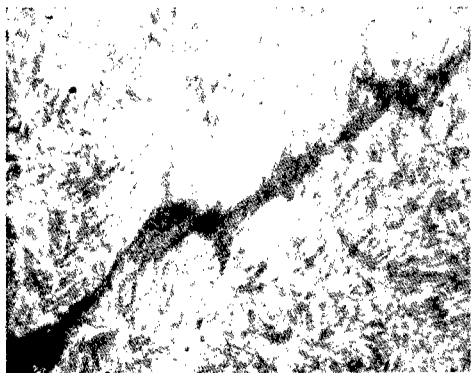
Figure 2.   High resolution H_α image of the filament at 12:03:25 UT (SVST, La Palma).
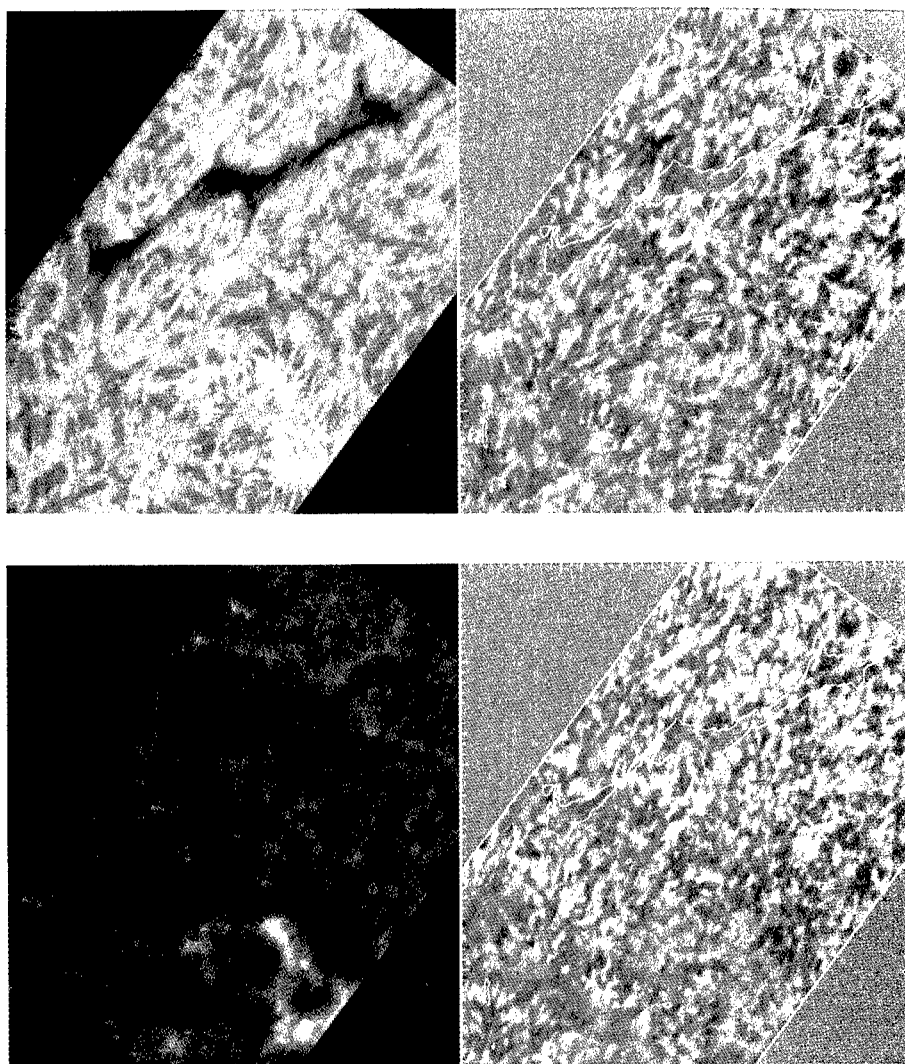
Figure 3.   MSDP data obtained at 12:23–12:28 UT (German VTT, Tenerife): *top left:* H$_\alpha$ intensity; *top right:* H$_\alpha$ velocities (bright = redshift); *bottom left:* CaII 8542 Å intensity; *bottom right:* CaII velocities. The brightness of the network is visible in CaII; in the filament body, velocities are generally upward, especially in H$_\alpha$; close to the "barbs" downward velocities are frequent in CaII (see, for example, the southern foot in the middle part of the filament).
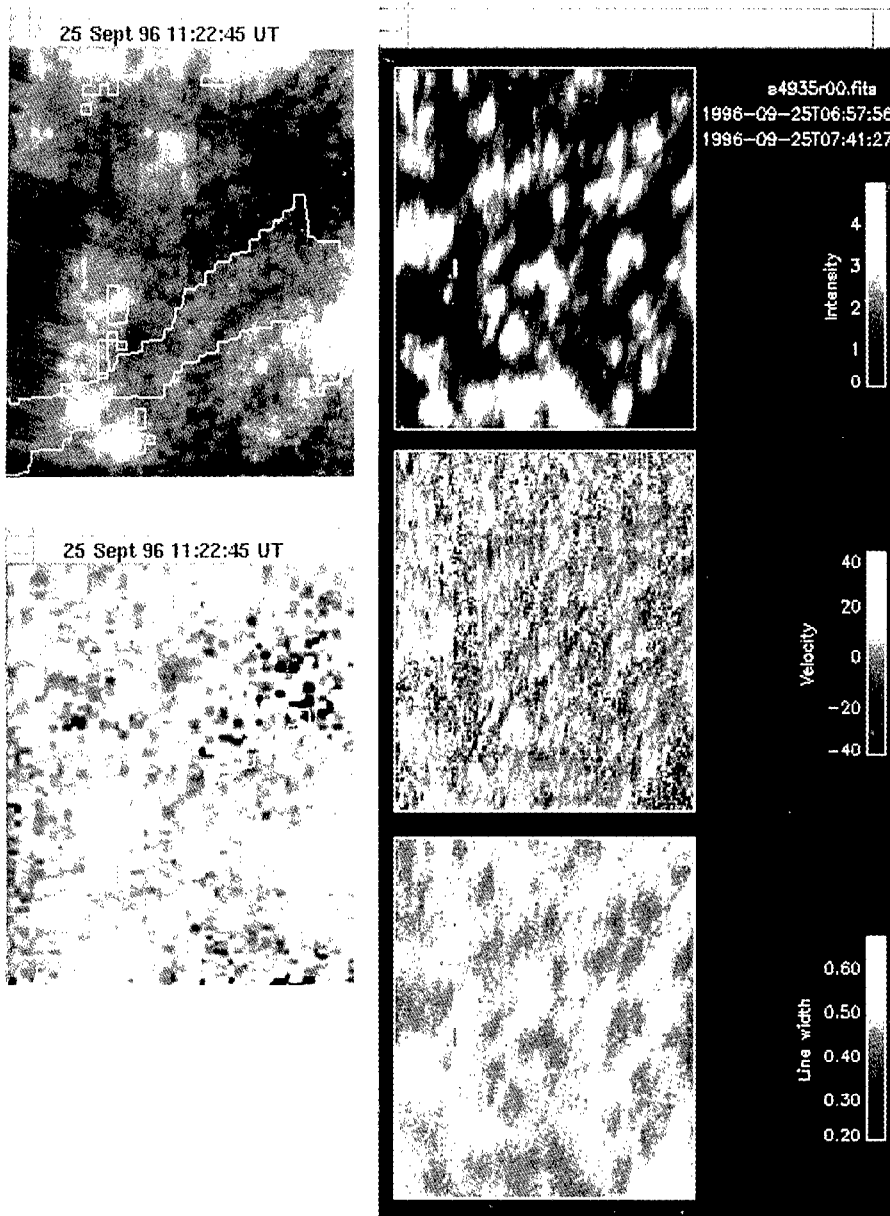
Figure 4.   *Left:* example of SUMER data: Si IV 1394 Å (top: intensities, bottom: velocities, bright = redshift); *Right:* example of CDS data: OV 629 Å (the scale is smaller than in the SUMER data; the central part includes the full field of Figure 2; bottom; the bright regions correspond to the network visible in CaII (Figure 3)).

Infrared Doppler Oscillations in a Solar Filament

R. Molowny-Horas
Observatoire de Paris, Section de Meudon, 5 Place Janssen, F-92195 Meudon, France

R. Oliver and J. L. Ballester
Departament de Física, Universitat de les Illes Balears, E-07071 Palma de Mallorca, Spain

F. Baudin
National Solar Observatory, National Optical Astronomy Observatory, P.O. Box 26732, Tucson, AZ 85726, USA

Abstract. We present the results of a high spatial resolution investigation of Doppler oscillations in a solar filament, using the He I 10830Å infrared line. Fourier power spectra of Doppler shifts reveal the presence of periodic signals. Two features, showing oscillations at 2.7 min and 12.5 min, have been studied. The use of the so-called wavelet analysis enables us to estimate the size of both features at 2.7 arc sec and 4.75 arc sec, respectively. Their approximate lifetimes are 10 min and 20 min.

1. Observations and Data Processing

A time series of CCD spectra of a solar filament (S44°, CM0.0) was recorded on October 15, 1996 in the infrared line He I 10830Å at the VTT (Vakuum-Turm-Teleskop) telescope of the Observatorio del Teide on the Canary Islands. The time interval between consecutive images was 7 sec, and the observations started at 10:31 UT and lasted for 72.3 min, giving a total of 620 CCD frames.

The slit of the spectrograph was placed approximately along the major axis of the filament. The slit width of the spectrograph was 150 μm, corresponding to 0.69 arc sec on the Sun. After a 2 × 8 spatial × spectral on-line binning was performed, the final scale per frame was 0.19 arc sec and 0.027Å respectively. During the acquisition, the IAC-KIS correlation tracker (Ballesteros et al. 1996) was operated simultaneously.

Line bottom position was calculated via a 6th-degree polynomial fit to the line profile, which included some continuum on both sides. Following Gheonjian et al. (1989), we have restricted our analysis to the investigation of oscillatory signals in Doppler velocities only.

2. Results

A temporal Fourier periodogram at each spatial location is plotted in Figure 1. At position **a** power is seen at a frequency of ≈ 6.2 mHz (2.7 min). A Lomb-Scargle analysis demonstrates the high significance (≥ 99.99%) of this power peak. At the **b** location, significant power is also observed at a frequency of ≈ 1.33 mHz (12.5 min). We have restricted our investigation to points around slit positions marked **a** and **b**, although other slit points also show significant power at various frequencies.
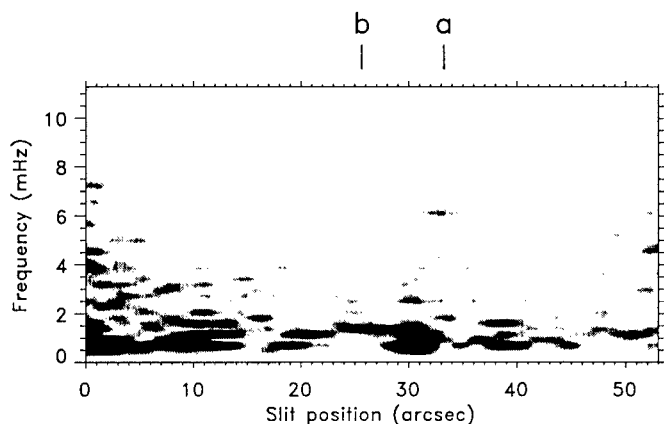
Figure 1.   Fourier periodogram at points along the slit. Notice that the colour gray table has been reversed, i.e. darker areas define higher power. Labels **a** and **b** at the top refer to slit positions as explained in the text.

Time/frequency diagrams of the signal at the slit location **a**, calculated with the so-called wavelet analysis (used for example by Bocchialini and Baudin 1995), are shown in Figure 2. We especially notice the evolution of the 2.7 min signal, starting at T≈ 40 min, and ending at T≈ 50 min.

The wavelet diagrams in Figure 2 allow us to estimate the size of feature **a** at ≈ 2.67 arcsec. For the perturbation **b**, we estimate from the wavelet analysis (not shown) a size of ≈ 4.75 arcsec.

From the wavelet diagrams it is also straightforward to infer a typical lifetime for the perturbations **a** and **b**, which are ≈ 10 min and ≈ 20 min, respectively. This is in good agreement with a previous similar study (Molowny-Horas et al. 1997).

The relative Fourier phase of the signals labelled **a** and **b** in Figure 1 are shown in Figures 3a and b, respectively. Both signals are seen to vary approximately linearly along the slit.

From the phase diagrams, we can set an upper limit to the actual wavelength of the perturbation, assuming a plane wave propagating in the filament (for details, see Molowny-Horas et al. 1997). For feature **a** we obtain $\lambda \leq 46,000$ km, whereas for feature **b** our estimate yields $\lambda \leq 31,000$ km.
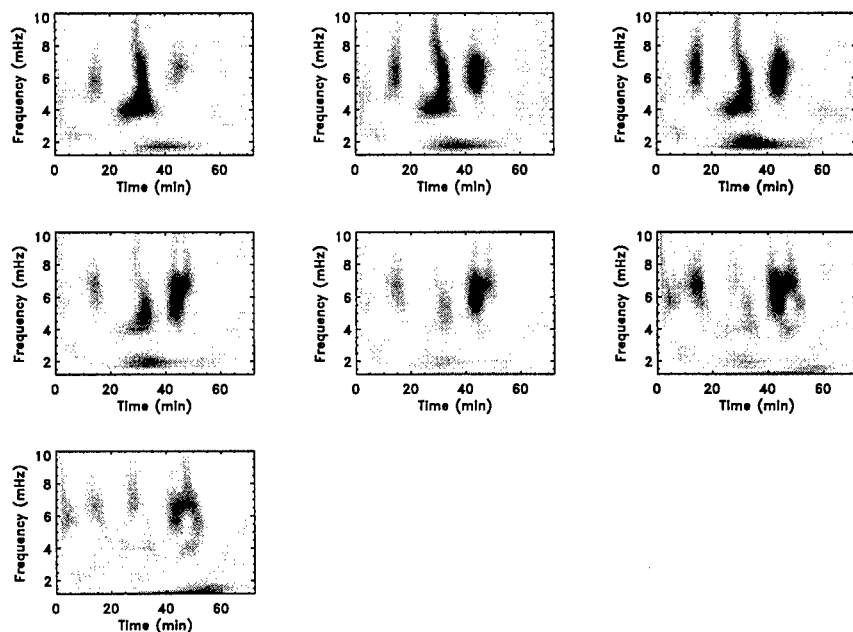
Figure 2.   The wavelet diagrams above correspond to consecutive points within the region of the slit labelled **a** in Figure 1. The colour scale has been reversed, i.e., darker colour tones mean greater power.
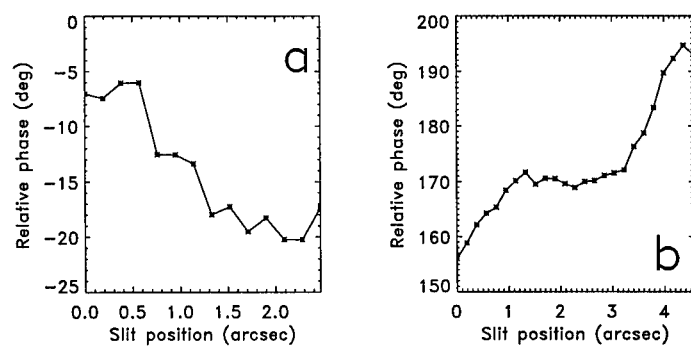
Figure 3.   Relative phase difference corresponding to slit locations **a** (upper plot) and **b** (lower plot) of Figure 1.

3.   Conclusions

Evidence has been found of the existence of oscillatory plasma motions in a solar filament. Our work agrees with previous investigations (Zhang et al. 1991; Thompson and Schmieder 1991).

Two signals with periods 2.7 min and 12.5 min have been studied. It should be noticed, however, that other signals, which may also represent periodic perturbations, have been observed. With the aid of the wavelet analysis it has been shown that the oscillations occur during limited time intervals. The present results also demonstrate the advantages of the use of an on-line image stabilizer (in this study, the IAC-KIS correlation tracker) to reduce image motion.

Future work will include a comparison of the present results with previous observational and theoretical calculations. The spatial orientation of the observed filament, however, may make it difficult to determine the MHD mode responsible for the reported periodic signals (see Oliver and Ballester 1998, these proceedings, and Joarder et al. 1997).

References

Ballesteros, E., Collados, M., Bonet, J.A., Lorenzo, F., Viera, T., Reyes, M., and Rodríguez Hidalgo 1996, A&AS, 115, 353

Bocchialini, K., and Baudin, F. 1995, A&A, 299, 893

Gheonjian, L.A., Klepikov, V.Yu., and Stepanov, A.I. 1989, Hvar Obs. Bull. 13 No. 1, pp. 147

Joarder, P.S., Nakariakov, V.M. and Roberts, B. 1997, Solar Phys., 176, 285

Molowny-Horas, R., Oliver, R., Ballester, J.L. and Baudin, F. 1997, Solar Phys., 172, 181

Thompson, W.T. and Schmieder, B. 1991, A&A, 243, 501

Zhang, Y., Engvold, O., and Keil, S.L. 1991, Solar Phys., 132, 63

The Prominence-Corona Transition Region and the Problem of Prominence Oscillations

R. Oliver and J. L. Ballester

Departament de Física, Universitat de les Illes Balears, E-07071 Palma de Mallorca, Spain

Abstract. Recent theoretical investigations of prominence oscillations indicate that the prominence-corona transition region (PCTR) may have a great influence on the magnetohydrodynamic modes of the whole system. We here consider an isothermal prominence embedded in an isothermal corona with a thin PCTR providing a smooth temperature transition between prominence and corona. The effect of the PCTR on the oscillations of the prominence body are investigated.

1. Introduction

Many of prominences' physical features still remain enigmatic – questions regarding the formation, long-term equilibrium, dynamic evolution and eventual eruption of quiescent prominences are yet to be answered. *Prominence seismology*, i.e., the constructive interaction between the modelling of prominence equilibrium, the theoretical study of the vibrations of their structure (normal modes) and direct observation (e.g., Molowny-Horas et al. 1998, these proceedings), is a way of improving our knowledge of these objects.

Most models used to investigate the magnetohydrodynamic (MHD) modes of a prominence-corona structure rely on a *discontinuous* temperature profile, with the isothermal prominence embedded in the isothermal corona (e.g., Joarder and Roberts 1992, Oliver et al. 1993). This approximation allows a simplified treatment of the equilibrium model and the wave problem.

On the other hand, Oliver and Ballester (1995) studied the propagation of MHD waves in the Low and Wu (1981) configuration, in which a very thin prominence is linked to the corona by an extended PCTR with a smooth temperature variation. They concluded that the nature of modes undergoes radical changes, and proposed the smooth variation of the temperature in the PCTR to be the reason for those changes.

Prompted by the last result, we consider a thin, non-isothermal PCTR between the isothermal prominence and corona and address the question "Are the modes of oscillation of a two-temperature system with a sharp temperature increase at the interface between the prominence and the corona different from the modes of a system with a smooth temperature variation from the isothermal prominence to the isothermal corona?" This, of course, may have important implications on the models that should be used in future investigations of this kind.

2. The Poland-Anzer Equilibrium Solution

The 1-D model put forward by Poland and Anzer (1971) is chosen to repre-
sent the equilibrium state of the system (Figure 1). This is a solution of the
Kippenhahn and Schlüter (1957) type that incorporates temperature gradients
across the prominence sheet. The temperature profile can be freely imposed,
without the need of solving the rather complicated energy equation coupled to
the mechanical equilibrium equation.

An analytical expression for $T/\tilde{\mu}$ (with T the temperature and $\tilde{\mu}$ the mean
atomic weight) is chosen as follows (Figure 2),

$$\frac{T}{\tilde{\mu}}(x) = \frac{1}{2}\left(\frac{T_c}{\tilde{\mu}_c} + \frac{T_p}{\tilde{\mu}_p}\right) + \frac{1}{2}\left(\frac{T_c}{\tilde{\mu}_c} - \frac{T_p}{\tilde{\mu}_p}\right)\tanh\left(\frac{x - x_{PCTR}}{\Delta}\right), \qquad (1)$$

for $x \geq 0$ and a symmetric function for $x \leq 0$. Subscripts 'p' and 'c' correspond
to prominence and corona. Moreover, the quantities $\Delta_{PCTR} \simeq 6\Delta$ and x_{PCTR}
are the PCTR width and position of PCTR centre.
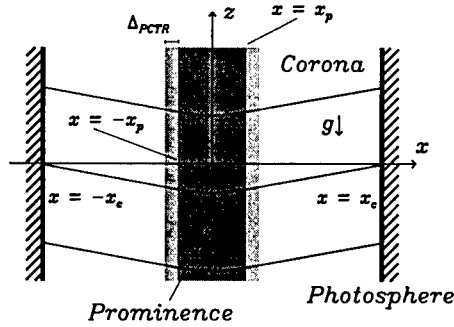
Figure 1.   Sketch of the Poland-Anzer prominence solution for a
prominence of width $2x_p$ (dark-grey region) surrounded by a thin
PCTR of width Δ_{PCTR} (light-grey region), embedded in the solar
corona. Support against gravity is achieved by the curvature of mag-
netic field lines (shown as solid lines) inside the prominence. The length
of field lines is of the order of the system width, $2x_c$.

3. Equations of Linear MHD Waves

The equations of ideal MHD are linearised about the equilibrium state for adia-
batic perturbations of the form $f(x)\exp(i\omega t - ik_z z)$. The slow and fast magne-
toacoustic modes are decoupled from the Alfvén mode. They are described by
a pair of equations of the form,

$$\frac{d^2 v_x}{dx^2} = q_1 \frac{dv_x}{dx} + q_2 \frac{dv_z}{dx} + q_3 v_x + q_4 v_z, \qquad (2)$$
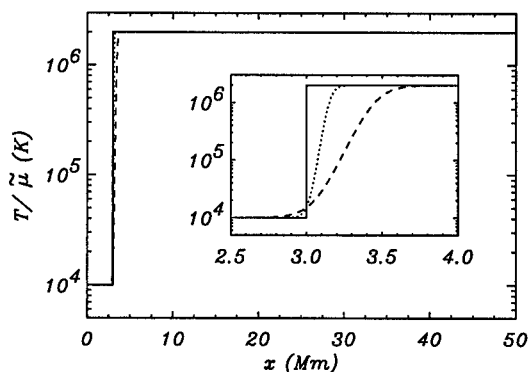
Figure 2.   Poland-Anzer temperature profile used in this work ($x > 0$ only). Solid, dotted, dashed lines: $\Delta_{PCTR} = 0$, $\simeq 300$ km, $\simeq 900$ km, respectively.

$$\frac{d^2 v_z}{dx^2} = q_5 \frac{dv_x}{dx} + q_6 \frac{dv_z}{dx} + q_7 v_x + q_8 v_z, \tag{3}$$

where $q_i = q_i(x; \omega, k_z)$ are complex coefficients.

The two magnetoacoustic modes are coupled together and so in this system there are no pure slow or fast MHD modes. However, owing to the small value of the plasma β in prominences, the two waves are effectively independent.

The two ordinary differential equations (2) and (3) constitute an eigenvalue problem that has been solved numerically. Line-tying boundary conditions are imposed on the eigenfunctions: $v_x = 0$ and $v_z = 0$ at the photosphere ($x = \pm x_c$).

4.   Results

Previous work used 1-D equilibrium solutions with a temperature discontinuity at the boundary between prominence and corona (e.g., Joarder and Roberts 1992, Oliver et al. 1993). It was found that three different types of MHD modes can propagate in such configurations: internal and external modes have properties determined by the isothermal prominence and corona, respectively, whereas the features of hybrid modes are determined by the two isothermal media. These equilibrium models can be reproduced by setting $\Delta_{PCTR} = 0$ in our temperature profile (see Figure 1). Hence, the question posed above can now be rephrased as, "Are there also internal, external and hybrid modes in a configuration with a PCTR ($\Delta_{PCTR} \neq 0$)?"

A comparison between the dispersion diagrams of the two equilibria (with a sharp temperature discontinuity and with a profile made of two temperature plateaus joined by a smooth transition) reveals that the shape of the magnetoacoustic modes is mostly unchanged, although their frequencies are modified (Figures 3a and b). The frequency change is larger for high harmonics than for low ones, the reason being that low harmonics possess long wavelengths in the x-direction so they do not "feel" the presence of the thin PCTR, while the
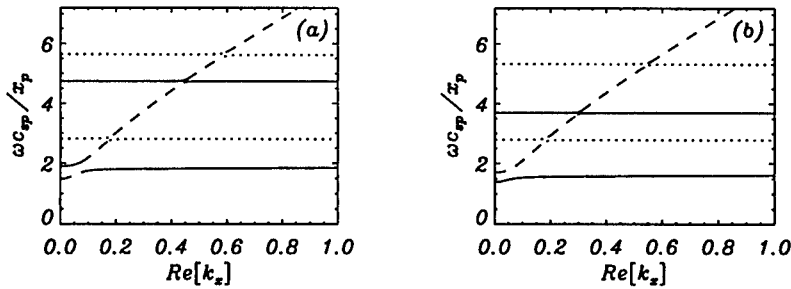
Figure 3.   Sausage mode dimensionless frequency $(\omega c_{sp}/x_p)$ vs. the real part of the vertical wavenumber. (a) $\Delta_{PCTR} = 0$ and (b) $\Delta_{PCTR} = 9,000$ km. Solid, dotted and dashed lines correspond to internal, external and hibrid modes, respectively.

shorter wavelengths of high harmonics makes them adjust their frequency and eigenfunctions $(v_x$ and $v_z)$ so as to accomodate to the PCTR.

An important feature of internal, external and hybrid modes in a two-temperature system $(\Delta_{PCTR} = 0)$ is that their frequencies evolve in a very different manner as the half-width of the system (x_c) is varied. Internal modes are characterized by a constant ω, external modes have $\omega \sim x_c^{-1}$ and hybrid modes have $\omega \sim x_c^{-1/2}$. This is also observed in the present case, even for a relatively thin promienence $(2x_p = 6,000$ km) embedded in a thicker PCTR $(\Delta_{PCTR} = 9,000$ km), so we can conclude that the presence of the PCTR does not eliminate the three types of modes.

So the question now is why there are no internal, external and hybrid modes in the Low–Wu model. The prominence width in this solution is rather small (a few hundred km only); we thus lower x_p in the Poland–Anzer model and look at the modes' features. It turns out that when the prominence region is destroyed (by setting x_p close to 0), the three types of modes disappear and their properties are governed by the dominating coronal medium. Obviously the same happens with the Low–Wu model.

References

Joarder, P. S. and Roberts, B. 1992, A&A, 261, 625

Kippenhahn, R. and Schlüter, A. 1957, ZAp, 43, 36

Low, B. C. and Wu, S. T. 1981, ApJ, 248, 335

Oliver, R., Ballester, J. L., Hood, A. W. and Priest, E. R. 1993, ApJ, 409, 809

Oliver, R. and Ballester, J. L. 1995, ApJ, 448, 444

Poland, A. and Anzer, U. 1971, Solar Phys., 19, 401

Prominence Oscillations and the Influence of the Distant Photosphere

N.A.J. Schutgens, M. Kuperus and G.H.J. van den Oord

Astronomical Institute Utrecht, Utrecht University, the Netherlands

Abstract. We model vertical prominence dynamics, describing the evolution of the magnetic field in a self-consistent way. Since the photosphere imposes a boundary condition on the field (flux conservation), the Alfvén crossing time $\tau_0/2$ between prominence and photosphere has to be taken into account. Using an electrodynamical description of the prominence we are able to compare two basic prominence models: Normal Polarity (NP) and Inverse Polarity (IP).

The results indicate that for IP prominences, the stability properties are sensitive to $\omega\tau_0$ (ω: oscillation frequency of prominence). For $\omega\tau_0 \gtrsim 1$ instability results. Forced oscillations of five minutes are efficiently excited in IP prominences that meet certain criteria only. NP prominences on the other hand, are insensitive to the Alfvén crossing time. Forced oscillations of five minutes are difficult to excite in NP prominences.

1. Introduction

For typical quiescent prominence heights ($z_0 \approx 30,000$ km) and coronal Alfvén speeds ($v_A \approx 100 - 10,000$ km/s), the Alfvén crossing time is $\tau_0/2 = z_0/v_A \approx 0.1 - 10$ min., which is of the same order as observed short oscillation periods in prominences (Yi Zhang et al. 1991, Thompson and Schmieder 1991). If the photosphere is instrumental in the support of a prominence, the Alfvén crossing time has to be taken into account when studying such oscillations (van den Oord and Kuperus 1992). Basically, the time-scale $\tau_0/2$ is the shortest time-scale on which photosphere and prominence can 'communicate'. It represents the delay with which the photospheric boundary condition influences the prominence dynamics.

Kuperus and Raadu (1974) suggested that the supporting force on a prominence stems from flux conservation at the photospheric level. The field due to the prominence current cannot enter the photosphere and the filament is effectively repelled. For a bipolar region, the Kuperus-Raadu model is the typical example of an Inverse Polarity (IP) prominence. Kippenhahn and Schlüter (1957) proposed a more local support mechanism: a small dip in the field lines of a coronal arcade would be sufficient to trap matter and support it against gravity. The resulting field topology is known as Normal Polarity (NP). Flux conservation at the photospheric level plays only a minor role in the support of NP prominences.

An equation of motion for an IP prominence, that takes the delayed photospheric boundary condition into account, has been derived and solved in the

linear approximation (Schutgens 1997a). We present here a summary of a comparative study into the vertical dynamics of IP and NP prominences (Schutgens 1997b).
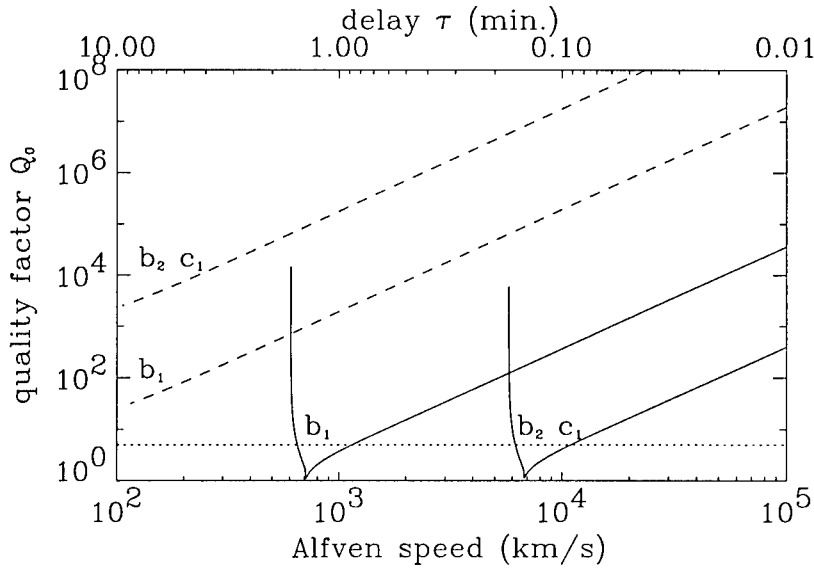
Figure 1.   The quality factors of stable (!) IP (solid lines) and NP (dashed lines) prominence oscillations as a function of the Alfvén speed. The assumed values for the prominence longitudinal density m and the arcade field strength B_0 are b_1) $m = 3.1 \times 10^4$ kg/m, $B_0 = 0.001$T; b_2) $m = 3.1 \times 10^2$ kg/m, $B_0 = 0.001$T; c_1) $m = 3.1 \times 10^4$ kg/m, $B_0 = 0.01$T.

2.   Free Oscillations

Consider a prominence in equilibrium, which experiences an impulsive perturbation and starts to oscillate. Our model allows us to study frequency and stability properties of IP and NP prominences as a function of the Alfvén speed. It turns out that the oscillation frequency ω depends only weakly on the Alfvén crossing time, and is fairly accurately approximated by the frequency found in the quasi-stationary approximation ($\tau_0 = 0$): $\omega \approx \omega_{stat}$. Also, the frequencies of NP prominences are usually one or more orders of magnitude smaller than those of IP prominences of the same longitudinal mass density.

    The effect of the crossing time $\tau_0/2$ on IP and NP stability properties can be analysed using the quality factor $Q_0 = \omega/2\nu$, where ω is the frequency and ν the damping rate of the oscillation. A small Q implies a strongly damped oscillation. Note that we do not apply any mass friction or wave emission; the damping

results solely from the inclusion of a delayed photospheric boundary condition. Figure 1 shows that the oscillations in IP prominences become strongly damped ($Q \lesssim 1$) for specific values of v_A. Also, left of the vertical asymptote present in each IP graph, the IP prominence is *unstable*. This instability occurs for $\omega \tau_0 \approx 1$. NP prominences are only weakly damped and almost marginally stable ($Q \gtrsim 100$).
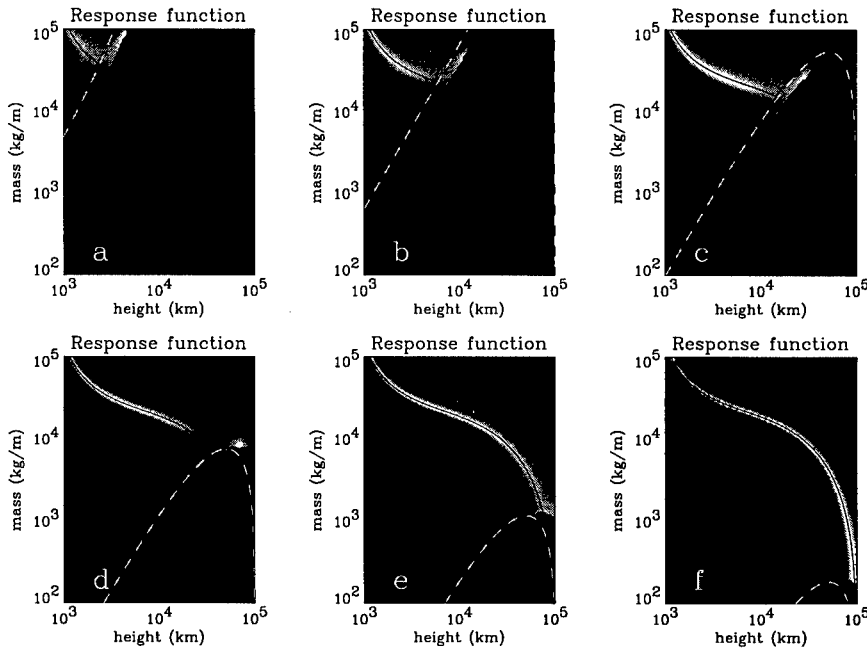
Figure 2. Gray-scale plot of the response function of forced oscillations in IP prominences for a driving period of 5 min, for different Alfvén speeds; *a)* $v_A = 100$ km/s; *b)* $v_A = 251$ km/s; *c)* $v_A = 631$ km/s; *d)* $v_A = 1585$ km/s; *e)* $v_A = 3981$ km/s; *f)* $v_A = 10{,}000$ km/s. The black area shows prominences that are unstable. The response function is plotted as a gray-scale, with white denoting the largest response.

3. Forced Oscillations

Typical oscillation periods for IP and NP prominences are 1–10 min. and 10–100 minutes, respectively. As a consequence, harmonic forcing with a period of five min. can possibly excite IP prominences, but not NP prominences. The response of an IP prominence to such forcing (the amplitude of oscillation) is plotted in Figure 2, for different values of the Alfvén speed v_A. Here the black area represents an unstable, growing oscillation, while the white area denotes stable prominences that are very strongly excited by five min. forcing. The elongated white curve extending from the upper left corner, corresponds to filaments whose

quasi-stationary oscillation period is equal to five min. Actually, the strongest response is obtained for those prominences that are associated with the bright little dot in Figure 2a, b, c and d, just at the border of stable and unstable oscillations. Apparently prominences with a specific combination of height z_0, longitudinal density m and coronal Alfvén speed v_A show a very strong response.

4. Conclusions

We show that the Alfvén crossing time-scale $\tau_0/2$ is an important time-scale for short period prominence oscillations in the vertical direction. Basically, this is the shortest time-scale on which photosphere and prominence can 'communicate'.

The oscillation frequencies depend only weakly on the Alfvén crossing time-scale, they are fairly accurately approximated by the frequency in the quasi-stationary approach ($\tau_0 = 0$ or $v_A \rightarrow \infty$). The stability properties of these oscillations, however, are sensitive to the Alfvén crossing time-scale. For $\omega\tau_0 \ll 1$ we approximate the quasi-stationary solution, which is marginally stable. For $\omega\tau_0 \approx 1$ the oscillations become strongly damped, while for $\omega\tau_0 \gtrsim 1$ the oscillations grow in time.

For typical parameter values of prominence and corona, NP prominences are well described in the quasi-stationary approximation and weakly damped (close to marginal stability, $\omega\tau_0 \ll 1$). Since their periods are much longer, forced oscillations of five min. are hard to excite in NP prominences. IP prominences show a strong dependence of the stability properties on the Alfvén crossing time and can even loose stability ($\omega\tau_0 = 0.1$–10). An IP prominence can only be forced to oscillate with a five min. period for specific combinations of mass, height and Alfvén speed. This can serve as a diagnostic for prominence and/or coronal parameters.

The case of horizontal oscillations is currently under investigation.

References

Kippenhahn, R. and Schlüter, A. 1957, ZAp 43, 36

Kuperus, M. and Raadu, M.A. 1974, Sol. Phys., 31, 189

Schutgens, N.A.J. 1997a, A&A, 323, 969

Schutgens, N.A.J. 1997b, A&A, 325, 352

van den Oord, G.H.J. and Kuperus, M. 1992, Sol. Phys., 142, 113

Thompson W.T. and Schmieder B. 1991, A&A 243, 501

Yi Zhang, Engvold O. and Keil S.L. 1991, Sol. Phys., 132, 63

Nonlinear Waves in Force-Free Fibrils

Y.D. Zhugzhda

Kiepenheuer-Institut für Sonnenphysik, Schöneckstr 6, D–79104 Freiburg, Germany   E-mail: yuzef@kis.uni-freiburg.de

V.M. Nakariakov

School of Mathematical and Computational Sciences, University of St. Andrews, St. Andrews, Fife KY16 9SS, Scotland

Abstract. Korteweg-de Vries equations for slow body and torsional weakly nonlinear Alfvén waves in twisted magnetic flux tubes are derived. Slow body solitons appear as a narrowing of the tube in a low β plasma and widening of the tube, when $\beta \gg 1$. Alfvén torsional solitons appear as a widening ($\beta > 1$) and narrowing ($\beta < 1$) of the tube, where there is a local increase of tube twisting. Two scenarios of nonlinear dissipation of strongly nonlinear waves in twisted flux tubes are proposed.

1.   Introduction

A treatment of prominence dynamics has to account for their fine structure and currents. Linear and nonlinear waves in structured magnetized plasma with currents differ fundamentally from MHD waves in a uniform magnetic field. The theory of waves in structured atmospheres is based on the theory of waves in thin flux tubes, which is well developed for linear waves in flux tubes without currents (see Roberts (1991) and references therein). The first steps in the theory of linear waves in force-free flux tubes have been done by Zhugzhda (1996, 1998, these proceedings). Nonlinear waves in current-free flux tubes have been considered by Roberts (1991) and Zhugzhda and Nakariakov (1997a, b). We present here preliminary results on nonlinear waves in force-free flux tubes, while details of the treatment are in Zhugzhda and Nakariakov (1997).

2.   Basic Equations

The general set of equations for force-free flux tubes (see Eqs. (1-8) in Zhugzhda (1998, these proceedings – hereafter Paper 1) is reduced to the following KdV equation by the method, which is described by Zhugzhda and Nakariakov (1997a, b). The KdV equation is obtained

$$\frac{\partial B}{\partial \tau} - \delta \frac{\partial^3 B}{\partial \xi^3} - \varepsilon B \frac{\partial B}{\partial \xi} = 0, \qquad (1)$$

where the coefficients δ and ε are rather cumbersome functions of modified Alfvén and sound velocities $C_\pm$ (Eq. (13) of Paper 1). The explicit expressions

for $\beta \ll 1$ are written below. The KdV equation (1) is valid for long wavelength slow body and torsional weakly nonlinear Alfvén waves in twisted flux tubes. Besides, the KdV equation (1) is valid for torsional waves of arbitrary wavelength in weakly twisted tubes.

3. Slow Body Solitons

The KdV equation (1) describes nonlinear body waves, when the phase velocity, C_+ (Eq. (13) of Paper 1), is substituted in δ and ε. In the limiting case of an untwisted flux tube, $K = 0$ (Eq. (15) of Paper 1) reduces to the KdV equation, which have been derived by Zhugzhda and Nakariakov (1997a, b). If $K \ll 1$ and $\beta \ll 1$, the coefficients of the KdV equation for slow body waves are

$$\delta = \frac{\mathcal{A}_0}{8\pi}(1 + 4K)\beta^{1.5}C_A, \quad \varepsilon = \frac{(\gamma + 1)(1 - 3K)C_A}{2B_0\beta^{0.5}} \tag{2}$$

and the soliton solution of the KdV equation (1) is

$$B = B_a \cosh^{-2}\left(\frac{\xi + V\tau}{L}\right), \tag{3}$$

where

$$L = 2(3\delta/B_a\varepsilon)^{1/2}, \quad V = \varepsilon B_a/3, \tag{4}$$

is the wavelength and speed of the soliton in the moving frame. The amplitude of soliton $B_a > 0$. The soliton is retarded, because its speed in the laboratory frame is less then the speed of the linear waves, C_-. According to expression (3), the soliton involves a narrowing of the magnetic tube, which is accompanied by an increase of the magnetic field, a decrease of the gas pressure and density, and an acceleration of the plasma in the soliton throat. The velocity and wavelength are not noticeably affected by a weak twisting, $K \ll 1$ in the case of strong magnetic field $\beta \ll 1$. In the case of sufficient twisting, the nonlinear coefficient ε could change sign. This occurs for slight twisting in the case of weak magnetic fields, when $\beta \gg 1$. For example, the sign of ε changes for $K = 0.1$ ($\alpha\mathcal{R}_0 = 0.28$), if $\beta = 15$, and $K = 0.001$ ($\alpha\mathcal{R}_0 = 0.09$), if $\beta = 50$. When the coefficient of nonlinearity is negative, the solution (3) has to be rewritten as

$$B = -B_a\cosh^{-2}\left(\frac{\xi - V\tau}{L}\right), \tag{5}$$

and the absolute value of ε has to be used in expressions (4) for the velocity and wavelength of the soliton. In this case nonlinear slow body waves widen the tube, which runs in the laboratory frame with a velocity larger than the modified tube velocity, C_-. The plasma is compressed and heated in the tube.

4. Alfvén Torsional Solitons

In the case of $\beta < 1$, the KdV equation for torsional Alfvén waves is

$$\frac{\partial B}{\partial \tau} - \delta\frac{\partial^3 B}{\partial \xi^3} + \varepsilon B\frac{\partial B}{\partial \xi} = 0, \tag{6}$$

where parameters δ and ε are defined in the case of a weakly twisted tube ($K \ll 1$) by

$$\delta \approx \frac{\mathcal{A}_0 C_A \beta^2 K^2}{2\pi}[1 - \beta + K(3 - 4\beta)(1 - 2\beta)(1 + \beta)] \qquad (7)$$

$$\varepsilon \approx \frac{C_A}{(1 - \beta)B_0}\left[1 + \beta K\left(3\beta + \gamma - \frac{2}{1 - \beta}\right)\right] \qquad (8)$$

The function (5) is the solution of the KdV equation (6). In the case of a weakly twisted tube, the tube wavelength and phase velocity of the Alfvén torsional soliton equal approximately

$$L \approx \sqrt{6}\mathcal{R}_0 K \beta(1 - \beta)\left(\frac{B_0}{B_a}\right)^{1/2}, V \approx \frac{C_A B_a}{3(1 - \beta)B_0} \qquad (9)$$

Thus, the Alfvén soliton involves a widening of the tube. The velocity of the soliton in the laboratory frame exceeds the modified Alfvén velocity, C_+. The Alfvén soliton could produce strong twisting in a weakly twisted flux tube, when the full ϕ-component of magnetic field on the surface of the tube equals

$$B_\phi \approx B_\phi^{(0)} - \frac{4BB_0}{(1 - \beta)B_\phi^{(0)}}, \qquad (10)$$

where $B_\phi^{(0)}$ is the ϕ-component on the surface of an undisturbed tube and B is defined by solution (5) of the KdV equation (6). If the twisting of the tube is very small, $B_\phi^{(0)} \ll B_0$ or $\beta \approx 1$, the soliton produces strong twisting of the tube. The twisting is accompanied by fast rotation of the plasma in the soliton. The azimuthal component of the plasma velocity on the surface of a weakly twisted tube equals approximately

$$V_\phi \approx -\frac{4C_A}{1 - \beta}\frac{B}{B_\phi^{(0)}}. \qquad (11)$$

The temperature, density and gas pressure drop in the soliton.

Both parameters δ and ε become negative when $\beta > 1$. In this case the solution of the KdV equation (6) is (3), where absolute values of parameters (7) and (8) have to be used for calculations of the wavelength and velocity of the soliton. In this case, the Alfvén soliton appears to involve narrowing, where twisting increases in accordance with (10) and rotation appears in accordance with (11), while pressure and density drop. However, the change of sign of δ and ε do not happen exactly at $\beta = 1$ and, moreover, do not happen at the same values of β. This means that there is a rather small range of parameters, β and K, when the parameters, δ and ε, of the KdV equation (6) for Alfvén torsional waves have different signs. In this case, the hyperbolic functions in the "soliton" solution of the KdV equation should be replaced by trigonometric functions, which have singularities. It seems to us that the stationary solution should contain discontinuities. At least it is clear that in the case of nonlinear wave propagation along the tube with varying parameters of β and K, the crossing of the region, where $\beta \approx 1$ has to be accompanied by some special effects. This is the region where twisting due to solitons could increase strongly and a narrowing wave transfers to a widening wave, or vice versa.

5.　Discussion

From the point of view of the dynamics of prominences, it is important to understand what happens with nonlinear waves of rather large amplitudes, when dispersive effects cannot balance nonlinear effects and nonlinear dissipation has to appear. The scenario of nonlinear dissipation of slow body waves in untwisted flux tube has been proposed by Zhugzhda and Nakariakov (1997a, b). The main point of this scenario is the transfer from subsonic to supersonic flow in the throat of a narrowing tube, as happens in a de Laval nozzle. The twisting of the tube does not change significantly the temperature of the plasma and flow velocity in the narrowing throat. There is some relative decrease of flow velocity and increase of temperature in a twisted tube compared to an untwisted one, if the amplitudes of solitons are the same. Thus, the scenario of nonlinear dissipation of slow body solitons in twisted and untwisted tube is the same.

The Alfvén torsional soliton causes a drop of pressure and temperature, when it appears as tube narrowing for $\beta < 1$. Consequently, the transfer from subsonic to supersonic flow in the narrowing throat is possible without shock formation. A shock has to be appear at the end of the jet because the tube does not widen infinitely. However, the alternative scenario of nonlinear dissipation of Alfvén torsional waves is possible. The drop of density and temperature in the Alfvén soliton decreases the number of electric charge carriers, while the increase of twisting follows the increase of the induction electric field. If the velocity of electrons in the Alfvén soliton are at about the ion temperature or higher, plasma instabilities or acceleration of energetic particles can occur. This scenario may be considered as a discharge in a flux tube with current. In this case, dissipation of magnetic energy takes place while dissipation of kinetic energy of plasma flow occurs in the alternative scenario.

Dissipation of nonlinear slow body and Alfvén torsional waves could both be responsible for an appearance of supersonic flows in prominences. The peculiarities of these flows is that they started from the regions of cool plasma.

References

Roberts, B. 1991, in Advances in Solar Magnetohydrodynamics, (eds.) E.R. Priest and A.W. Hood, Cambridge University Press, Cambridge, p. 105

Zhugzhda, Y.D. 1996, Phys. Plasmas, 3, 10

Zhugzhda Y.D. and Nakariakov V.M. 1997a, Phys. Lett. A, in press

Zhugzhda Y.D. and Nakariakov V.M. 1997b, Solar Phys., 175, 107

Linear Waves in Force-Free Fibrils

Y.D. Zhugzhda

Kiepenheuer-Institut für Sonnenphysik, Schöneckstr 6, D–79104
Freiburg, Germany
E-mail: yuzef@kis.uni-freiburg.de

Abstract. The advanced thin flux tube approximation for force-free thin magnetic flux tubes is used to derive a dispersion relation for linear waves. All wave modes appear to be coupled in a twisted flux tube. In the case of a weakly twisted flux tube, it has been found that torsional Alfvén waves have dispersion and produce pressure and temperature fluctuations. The effect of tube rotation is pointed out. These properties of linear waves have an impact on prominence oscillations.

1. Introduction

Theoretical treatments of oscillations of solar quiescent prominences are based on the well-developed theory of linear waves in current-free flux tubes and magnetic sheets. But the magnetic field of the prominences is not likely potential, because the helicity of filaments is observed. Thus, there is a need to examine the models of force-free magnetic filaments. The theory of linear waves in force-free flux tubes has not been developed up to the present time. The advanced thin flux tube approximation for force-free magnetic flux tubes, derived by Zhugzhda (1996) made it possible to obtain the dispersion equation for torsional, fast and slow body waves in twisted flux tubes. The distinctions of the linear waves in twisted and untwisted magnetic filaments are outlined. The effects of the twisting on the oscillations of the prominence filaments are discussed.

2. Basic Equations

The governing set of equations is the thin tube approximation for a straight, vertical, axisymmetric, force-free magnetic flux tube, which allows us to consider axisymmetric perturbations of the tube, and has been derived by Zhugzhda (1996). The dependent variables of the problem are the longitudinal component of the plasma velocity, u, the longitudinal component of the magnetic field, B, plasma density, ρ, and pressure, p, tube cross section, $A = \pi R^2$, ϕ-components of the magnetic field, $B_\phi = Jr$ and velocity, $v_\phi = \Omega r$, and the radial component of velocity, $v_r = vr$, where the radius coordinate, r, varies within the tube, $0 \leq r \leq R$. The set of the governing equations in these variables is

$$\rho \left(\frac{\partial u}{\partial t} + u \frac{\partial u}{\partial z} \right) + \frac{\partial p}{\partial z} = 0, \tag{1}$$

$$\frac{\partial}{\partial t}\left(\frac{\rho}{B}\right) + \frac{\partial}{\partial z}\left(u\frac{\rho}{B}\right) = 0, \tag{2}$$

$$\frac{\partial}{\partial t}\left(\frac{\Omega}{B}\right) + u\frac{\partial}{\partial z}\left(\frac{\Omega}{B}\right) = \frac{B}{4\pi\rho}\frac{\partial}{\partial z}\left(\frac{J}{B}\right), \tag{3}$$

$$\frac{\partial}{\partial t}\left(\frac{J}{B}\right) + \frac{\partial}{\partial z}\left(u\frac{J}{B}\right) = \frac{\partial\Omega}{\partial z}, \tag{4}$$

$$\frac{d}{dt}\left(\frac{p}{\rho^\gamma}\right) = 0, \tag{5}$$

$$\frac{\partial A}{\partial t} + u\frac{\partial A}{\partial z} - 2Av = 0, \tag{6}$$

$$\frac{\partial B}{\partial t} + u\frac{\partial B}{\partial z} + 2Bv = 0, \tag{7}$$

$$p + \frac{B^2}{8\pi} - \frac{A}{2\pi}\left[\rho\left(\frac{\partial v}{\partial t} + u\frac{\partial v}{\partial z} + v^2 - \Omega^2\right) + \frac{J^2}{4\pi} + \frac{B}{8\pi}\frac{\partial^2 B}{\partial z^2} - \frac{1}{16\pi}\left(\frac{\partial B}{\partial z}\right)^2\right] = p_{ext}, \tag{8}$$

where the condition of the constant external pressure, p_{ext}, is imposed. The consideration is restricted by the case of uniform atmospheres without gravity. The set of equations is valid for thin flux tubes of finite diameter. In the limit of the infinitely thin flux tube, the variables of the problem, B_ϕ and v_ϕ, tend to zero and the equations (3) and (4) for them are dropped out of the set, as well as the terms in the boundary conditions (8), which are proportional to the cross section of the tube. If equations (6) and (7) are written as a flux conservation condition, $BA = const$, the set of equations (1)–(8) is reduced to the well-known thin-flux-tube approximation of Roberts and Webb (1978). The treatment of linear and nonlinear waves in force-free flux tubes is not possible in the framework of this approximation.

3. Linear Waves in Force-Free Flux Tubes

After linearization and introducing the exponential dependence of perturbations on time and coordinate, $B \sim \exp(i\omega t - ikz)$, the equations (1)–(8) are reduced to a dispersion equation,

$$\frac{A_0}{4\pi(C_S^2 + C_A^2)}[\omega^6 + (0.5\alpha^2 C_A^2 - 4\Omega_0^2 - k_z^2(2C_A^2 + C_S^2))\omega^4 + 2\Omega_0\alpha C_A^2 k_z\omega^3 +$$
$$+k_z^2[2(\alpha^2 C_S^2 C_A^2 + C_S^2\Omega_0^2 - 0.25\alpha^2 C_A^4) + k_z^2 C_A^2(C_A^2 + 2C_S^2)]\omega^2 - \tag{9}$$
$$-4\alpha C_A^2 C_S^2 k_z^3\Omega_0\omega + k_z^4 C_S^2 C_A^2(2\Omega_0^2 + 0.5\alpha^2 C_A^2 - k_z^2 C_A^2)] -$$
$$-(\omega^2 - k_z^2 C_A^2)(\omega^2 - C_T^2 k_z^2) = 0,$$

where

$$C_A = \frac{B_{z0}}{(4\pi\rho_0)^{0.5}}, \quad C_T^2 = \frac{C_S^2 C_A^2}{C_S^2 + C_A^2}, \quad \alpha = \frac{2J_0}{B_{z0}}, \quad C_S^2 = \frac{\gamma p_0}{\rho_0}. \tag{10}$$

We restrict our consideration to a nonrotating tube ($\Omega_0 = 0$) when the dispersion equation (9) reads

$$(\omega^2 - C_T^2 k^2)(\omega^2 - C_A^2 k^2) - \frac{A_0}{4\pi}\frac{(\omega^2 - C_A^2 k^2)^2(\omega^2 - C_S^2 k^2)}{C_A^2 + C_S^2} -$$

$$- \frac{J_0^2 A_0 C_A^2}{2\pi B_{0z}^2}\frac{(\omega^2 - C_A^2 k^2)(\omega^2 - C_S^2 k^2) + 2\omega^2 k^2 C_S^2}{(C_A^2 + C_S^2)} = 0. \qquad (11)$$

The first term in the dispersion equation corresponds to the wave propagation in the infinitely thin, untwisted tube ($J_0 = 0$, $A_0 = 0$). The second term shows the influence of the finite cross-section. The third term shows the effect of the twisting. It is simple to show that dispersion appears only due to the second term. The dispersion equation (11) can be rewritten as

$$(C_A^2 + C_S^2 - KC_A^2)(\omega^2 - C_+^2 k^2)(\omega^2 - C_-^2 k^2) + \frac{A_0}{4\pi}(\omega^2 - C_A^2 k^2)^2(\omega^2 - C_S^2 k^2) = 0, \qquad (12)$$

where

$$C_\pm^2 = C_A^2 \frac{C_A^2 + 2C_S^2 + K(C_S^2 - C_A^2) \pm \sqrt{S}}{2(C_A^2 + C_S^2) - 2C_A^2 K}, \qquad (13)$$

$$S = C_A^4 + 2K\left(3C_A^2 C_S^2 + 4C_S^4 - C_A^4\right) + K^2(C_S^4 - 6C_S^2 C_A^2 + C_A^4). \qquad (14)$$

The parameter K is

$$K = \frac{J_0^2 A_0}{2\pi B_{0z}^2} = \frac{A_0 \alpha^2}{8\pi} = \frac{\alpha^2 R_0^2}{8}, \qquad (15)$$

where α is the well-known parameter of force-free magnetic fields and R_0 is the radius of the flux tube. If the parameter K tends to zero, the fast speed C_+ tends to the Alfvén speed C_A, and the slow speed C_- tends to the tube speed C_T. Alfvén torsional and slow magnetosonic sausage waves are modified by the twisting of the tube. The speeds C_+ and C_- may be considered as the *modified Alfvén speed* and *modified tube speed* respectively.

In the case of a weak dispersion, when $\omega \approx C_\pm k$ the dispersion equation (12) reduces to an approximate one

$$\omega^2 \approx C_\pm^2 k^2 \left(1 \pm \frac{A_0}{4\pi}\frac{(C_\pm^2 - C_A^2)^2(C_\pm^2 - C_S^2)}{C_A^2 \sqrt{S}}k^2\right), \qquad (16)$$

The case of weak dispersion has a long wavelength limit, when the wavelength is large in comparison with the tube diameter, $k^2 A_0 \ll 1$. A weak dispersion limit for torsional Alfvén waves appears also for the case of weakly twisted flux tubes, when $K \ll 1$ and the phase velocity is approximately

$$C_+^2 \approx C_A^2 \left(1 + \frac{K\beta}{2}\right). \qquad (17)$$

In this case the approximate dispersion relation reads

$$\omega^2 \approx C_+^2 k^2 \left(1 + \frac{A_0 K^2 \beta^2 (1 - \beta)}{16\pi}k^2\right) \qquad (18)$$

which is valid for any values of $k^2 A$, if the twisting is small enough.

4.   Discussion

Eq. (11) cannot be subdivided into the dispersion equations for Alfvén, tube, and other waves. This means that Alfvén, tube, and sausage body wave modes are coupled and pure simple wave modes do not exist. Each of the wave modes is a mixture of Alfvén, tube, and sausage modes. For the case of $K\beta \ll 1$ the wave modes appear to be weakly coupled and they do not differ significantly from the pure Alfvén, tube, or sausage modes in untwisted tubes. But the dispersion equation cannot be subdivided into the dispersion equations for pure MHD modes, as happens in a uniform atmosphere. Slow waves in the force-free magnetic field are accompanied by torsional disturbances, whereas torsional Alfvén oscillations in force-free magnetic fields are accompanied by pressure, density and temperature fluctuations.

The effect of a coupling of linear wave modes in force-free magnetic fields is essential for the dynamics of solar prominences. There has to be coupling between torsional and pressure oscillations of prominences. This makes possible the excitation of torsional oscillations by arbitrary shaking of the prominence legs. Even pure pressure fluctuations in the legs of prominences produce torsional oscillations as well if there are currents in the prominence. This easily makes the excitation of torsional oscillations of prominences.

The Alfvén torsional waves could be considered as an alternative current. If an alternative current exists along with a constant current, it produces fluctuations of optical emission, which is proportional to product of the strengths of those currents. Consequently, direct observations of alternative currents in prominences are possible.

The general dispersion relation (9) shows that the effect of tube rotation is similar to the influence of tube twisting on linear waves. The wave modes appear to be coupled in the rotating tube. The production of currents in prominences is the result of the twisting, which appears due to rotation of the flux tubes. Consequently, both twisting and rotation couple different modes of prominence oscillations.

The dispersion of Alfvén torsional waves is essential for nonlinear waves (see Zhugzhda and Nakariakov (1998, these proceedings)).

References

Roberts B. and Webb A.R. 1978, Solar Phys., 56, 5
Zhugzhda, Y.D. 1996, Phys. Plasmas, 3, 10

Observation of a Prominence Heating and the Heating Mechanism

L. Ofman

Hughes STX/NASA Goddard Space Flight Center, Code 682, Greenbelt, MD 20771, USA

Z. Mouradian

Observatoire de Paris-Meudon, DASOP-CNRS URA 326, F-92195 Meudon Cedex, France

T. A. Kucera

SAC/NASA Goddard Space Flight Center, Code 682, Greenbelt, MD 20771, USA

A. I. Poland

NASA Goddard Space Flight Center, 682, Greenbelt, MD 20771, USA

Abstract. An arch-shaped prominence was observed with SUMER-SOHO spectrometer on March 31–April 1, 1996. The observations were performed at three wavelengths in the Lyman continuum. Ten successive images were obtained at 41 minute time intervals. Based on the computed models of Gouttebroze-Heinzel-Vial we have determined the temperature distribution of the prominence using the intensity ratio of 876 Å and 907 Å. The observed time sequence shows that the prominence disappears by heating, i.e., ionization of hydrogen: a thermal DB. We model the heat input with the linearized MHD equations using a prescribed initial density and a broad-band spectrum of Alfvén waves and find a good qualitative agreement with observations. In the model the prominence is heated by the resonant absorption of Alfvén waves with frequencies that match the resonant condition for a particular flux tube structure that is determined by the magnetic field topology and density.

1. Introduction

We present the observations of an arch-shaped prominence obtained with the SUMER spectrometer on board the SOHO spacecraft on March 31–April 1, 1996. The observations were performed at three wavelengths in the Ly continuum. Ten successive images were obtained at 41 minute time intervals and show evidence of thermal sudden disappearances (DB) (see Mouradian et al. 1995). Based on computed models of Gouttebroze-Heinzel-Vial (GHV) (Gouttebroze, Heinzel, Vial 1993), we have determined the temperature distribution of the prominence
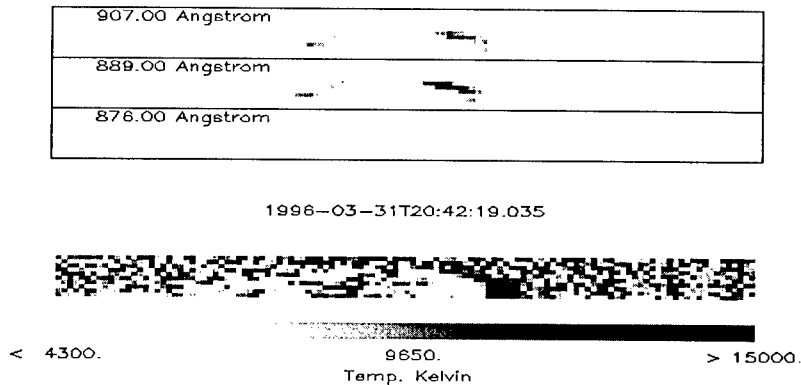
Figure 1.   The image of the prominence in 876 Å, 889 Å, and 907 Å of Ly-continuum obtained by SUMER on March 31, 1996 at 20:42:19.035 UT (top three panels). The temperature distribution obtained from the ratio of 876 Å and 907 Å images and the GHV model (bottom).

using the intensity ratio of 876 Å and 907 Å images.

Resonant absorption of Alfvén waves was first suggested by Ionson (1978) as a nonthermal heating mechanism for coronal loops and since then has been extensively studied (see Ofman et al. 1995, and references therein). This mechanism appears to be a good candidate for prominence heating due to its short dissipation length and high efficiency in converting the wave energy to heat (Ofman and Mouradian 1996).

We compare the heating time scale obtained from SUMER observations to the resonant absorption heating model and find good qualitative agreement. However, a more realistic model that includes the effects of coupling between the prominence plasma and the chromosphere/photosphere is needed to explain the heating and cooling near the foot points.

2.   Observations

An arch-shaped prominence was observed with the SOHO-SUMER spectrometer on March 31, 1996. Ten successive images in the Ly-continuum were obtained at 41 minutes with the resolution $1'' \times 0.83'' \approx 700 \times 600$ km. In Figure 1 we show the typical image of the prominence in 876 Å, 889 Å, and 907 Å of Ly-continuum taken on March 31, 1996 at 20:42:19.035 UT (top three panels). Based on the GHV model we have determined the temperature distribution of the prominence using the intensity ratio of 876 Å and 907 Å (lower panel). It is evident that regions of hotter and cooler material are concentrated near the footpoints with the hot material "on top" of the cool material above the limb.

The effects of heating and cooling are evident near the footpoints in regions of hot (>15,000K) and cool (~4000–7000K) prominence material. In Figure 2

Prominence footpoint temperature
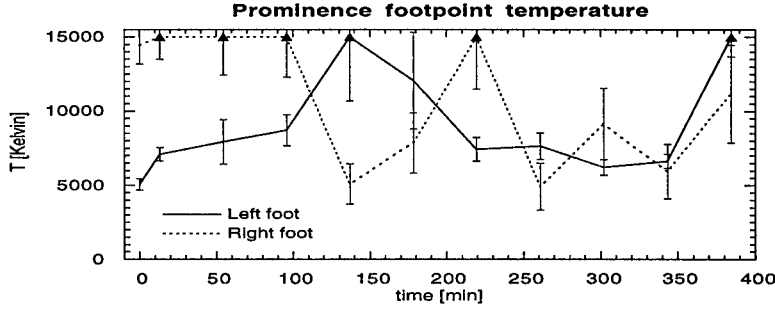
Figure 2.   The time dependence of the temperature near the promi-
nence footpoints determined from intensity ratio of 876 Å and 907 Å
images obtained by SUMER on March 31–April 1, 1996. The arrows
indicate temperatures above 15,000 K (outside the GHV model range).

we show the time dependence of the temperature near the prominence footpoints
obtained by SUMER on March 31–April 1, 1996. The temperature error bars
were calculated using the expression

$$\frac{\Delta T}{T} = \sqrt{\frac{1}{I_{876}} + \frac{1}{I_{907}}}, \tag{1}$$

where I_{876} and I_{907} are the photon counts at the corresponding wavelengths, and
we assumed Poisson statistics for the photons. Figure 2 was taken at particular
points and shows cooling and heating. However, the observed time sequence
of the full prominence image shows that parts of the prominence disappear by
heating, i.e. ionization of hydrogen which is a thermal DB. The arrows indicate
that temperatures above 15,000 K (outside the range of the GHV model) are
present. The footpoint temperature varies on a timescale of 1–2 hours, which
may indicate heating and cooling at this time scale. The temperature may also
change due to flow of hotter or cooler material into the footpoints.

3.   Alfvén Wave Resonant Absorption Heating Model

Here, we present a brief description of the Alfvén wave resonant absorption heat-
ing model for prominences. More details on the model can be found in Ofman
and Mouradian (1996). We model a single flux tube (thread) of a coronal promi-
nence by a slab of plasma (i.e., neglecting the effects of curvature) embedded
in a uniform magnetic field. The z direction is along the longitudinal magnetic
field of the flux tube, the y direction corresponds to the azimuthal direction of
the flux tube, and the density inhomogeneity occurs in the x direction, which
corresponds to the radial direction of the flux tube.

The Alfvén waves are driven by a broad band (random) driving term in the
momentum equation. In Figure 3 we show the temporal evolution of the heating
rate obtained from the above model with $\tau_A = 12.8$ sec. It is evident that the
heating varies in magnitude considerably due to the resonance effects of the

L. OFMAN ET AL.
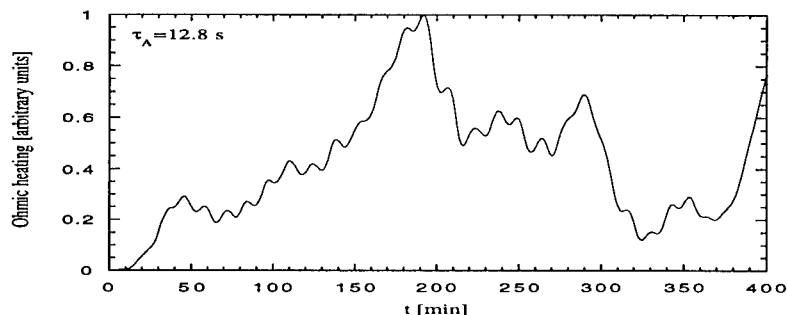
Figure 3.   The temporal evolution of the heating rate in the resonant absorption model.

various frequencies in the time-dependent Alfvén wave power spectrum with the flux tube structure. When there is more power in the narrow band of frequencies near the global mode frequency of the flux tube – the heating increases. When the available power shifts to other frequencies – the heating decreases. The time scale for the decrease and increase in heating is determined by the geometry of the flux tube, the plasma parameters, and the supplied Alfvén wave spectrum. The evolution of the model heating is similar to the observed evolution of the footpoint temperature.

4.   Summary and Conclusions

SUMER observations show that a quiescent prominence undergoes heating and cooling on time scales of 1–2 hours, and that the temperature distribution near the footpoints is different from the top of the prominence. Since the Alfvén waves would be trapped and reflected differently at the footpoints and at the top of the prominence, we suggest that the Alfvén waves supply the necessary heat to the prominence.

We apply the resonant absorption heating model to prominences by solving the linear low-β MHD equations and find that the heating time and global mode frequencies agree with the heating time and the wave frequencies observed in a typical quiescent prominence (Ofman and Mouradian 1996). We find that with a broad-band (random) Alfvén wave source the model prominence undergoes periods of high and low heat input, similar to the observed temperature evolution. However, chromospheric coupling, gravity and magnetic field geometry must be take into account to explain heating and cooling near the footpoints.

References

Gouttebroze, P., Heinzel, P. and Vial, J. C. 1993, A&AS, 99, 513
Ionson, J. A. 1978, ApJ, 226, 650
Mouradian, Z., Soru-Escaut, I. and Pojoga, S. 1995, Solar Phys., 158, 269
Ofman, L., Davila, J.M. and Steinolfson, R.S. 1995, ApJ, 444, 471
Ofman, L. and Mouradian, Z. 1996, A&A, 308, 631

Yohkoh Observations of Coronal Structures Surrounding Dark Filaments

Yutaka Uchida

Physics Department, Science University of Tokyo, Shinjuku-ku, Tokyo, Japan

Abstract. We describe in this paper some of the findings of the Yohkoh satellite about the coronal structure surrounding dark filaments in the pre-event and initial phases of high latitude arcade formation events. The knowledge of pre-event structure and its change is essential for the proper understanding of the arcade flaring process from the causality point of view. The wide dynamic range and high sensitivity obervations by Yohkoh allow us to look into the faint structures and their changes with the use of a faint-feature-enhancing technique in the image analysis.

1. Introduction

The topics covered in this paper are soft X-ray observations of the part of the coronal structure that has not been easy to see, namely, the coronal structure surrounding dark filaments, and their greater environment. The wide dynamic range of Yohkoh observations, however, have made it possible for us to look into those, with the use of some faint-feature-enhancing techniques in the image analysis.

The motivation to look into these came from our finding that typical arcade flares observed at the limb showed the presence of some features that are not expected in the widely-accepted "classical flare model(s)" (Sturrock 1966, and others). The well-known February 21, 1992 arcade flare (Tsuneta et al. 1992), and the December 2, 1991 event (Tsuneta 1993), both seen on axis, showed the same type of bright "cusped arcade" and a dark tunnel below it at the center of the flaring region, and Tsuneta claimed in his initial reports that the "classical flare model was observationally validated". We, however, noted that this was too hasty a conclusion since (i) there existed in both of these cases two high loop structures connecting the top of the "cusped flare core" back to the photosphere at some distance on both sides of this flare core, and (ii) that both of these flares had similar small but strong brightening at the axis of the dark tunnel below the "cusped flare core" in their initial phase (Uchida 1996). There was furthermore (iii) a faint blob rising before the initiation of both of these flares from the top part of the "pre-flare cusp" which is the bottom of the valley of the high connections mentioned above. The blob, probably the heated part of the rising dark filament, seemed to rise *without* dragging and producing antiparallel parts by pulling the overlying magnetic arcade outwards as assumed in the classical model. All these are different from the assumptions in the classical model(s).

163

In the following, we try to see what the corresponding situation is like in the larger scale X-ray arcade formation events in the high latitude regions. These are considered to be of the same category as arcade flares, but occurring in larger scale, weaker field regions. We examine the still fainter pre-event structure of them in the corona where the responsible dark filament is located, and where the X-ray arcade formation is to occur later. We also investigate the behavior of the arcade formation process from the still faint very initial phase to the later phase of the develpment. Scrutinization of these is essential for the true understanding of the process of arcade formation (and, therefore, of arcade flares in active regions), but has not been performed before.

2. Coronal Structure Prior to X-ray Arcade Formation, and Its Relation to the Hα Filament and the Photospheric Magnetic Field

The pre-event corona in such high latitude regions in which a quiescent dark filament is located is generally dark without marked activity, and the structure in these regions have not been studied much. In order to look into those dark areas, we, therefore, have to use the frames taken with the thinnest filter and the longest exposure time which saturates brighter zones of the CCD pixels. Furthermore, we use the so-called "unsharp-image masking" method for enhancing the faint features in the regions of our concern.

We use Hα pictures from Big Bear Solar Observatory and magnetograms from Kitt Peak National Observatory. The times of the Hα and magnetic field observations are generally not coincident, but hours and even a few days apart from the time of the relevant X-ray images in the pre-event period of X-ray arcade formation. Fortunately, however, our targets and their environment are very quiet, and we may use the following way to compare the relative locations of X-ray, Hα, and magnetic field (Uchida et al. 1998): (a) Find a magnetogram frame nearest in time and assign heliographic coordinates to the pixels. Then we rotate the pixels on the solar surface to the time of the X-ray frame by taking the tilt angle of the solar rotation axis and appropriate law of differential rotation into account. (b) Find likewise an Hα frame nearest in time, and draw the locus of the top parts of the Hα dark filament. We map this locus *on a sphere with a radius, $R_o + h$,* where R_o is the solar radius, and h is the assumed height of the top of the dark filament (for simplicity, assumed to be constant along the length of the filament). Here, h is determined as follows: The locus of the top of the dark filament mapped on the sphere of radius $R_o + h$ is rotated to the exact time of the X-ray observation as before, and then the rotated locus is down-projected to the solar surface to compare with the magnetogram. Try to find an h that allows the best matching of the down-projected locus to the field polarity reversal line in the magnetogram rotated in (a), with an assumption that the dark filaments are lying above the field polarity reversal lines. (c) Using this determined h, the locus of the top of the dark filament, rotated to the time of X-ray observation is compared with the X-ray structures.

We present one typical result in Figure 1 (from Uchida et al. 1998. Several cases have been analysed, and essentially similar results have been obtained for each). It is clearly seen in this case for the arcade formation event of February 24-25, 1993, that: (a) the faint-feature-enhanced X-ray image shows a struc-
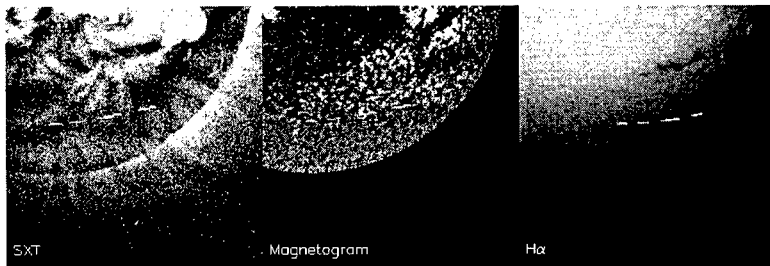
Figure 1.   Pre-event features of the February 24-25, 1993 arcade for-
mation event. (a) Pre-event coronal structure on Feb. 23, 1993, 11:16 UT,
showing "dual arcades" with the inside legs crossing. (b) Kitt Peak magne-
togram taken at a closest-available time, Feb. 22, 1993, 17:33 UT, and rotated
to the exact time of the soft X-ray loop picture to examine precise positional
relationship. (c) Hα picture from Big Bear Solar Observatory at Feb. 25,
1993, 17:33 UT, in which the locus of the top part of the dark filament was
drawn. This white locus is rotated to the exact time of the X-ray picture,
with an assumed height h, where h is determined so that its down-projection
on the photosphere best coincides with the polarity reversal line in (b).

ture of "overlapped dual arcades" whose inside legs cross with the others, quite
different from the simply-connected bipolar arcade with the top sagged at the
dark filament as expected from the classical picture; and (b) the locus of the
top of the dark filament mapped on the sphere of radius $R_o + h$, and rotated
to the time of the X-ray picture, coincides well with the region of the crossed
legs, and (c) its down-projection coincides with the polarity reversal line of the
(smoothed) photospheric field, with $h=1 \times 10^4$ km in this case.

Finding the "overlapped dual arcades" was significant because it was quite
different from what the classical model assumed, and we naturally wondered
what the physical reason for this was. By examining the magnetogram, we
found that the photospheric magnetic field under the region of these crossed
legs was highly mixed with considerable number of patches of wrong polarity
on both sides of the polarity reversal line (of the smoothed photospheric field)
(Martin 1980), instead of cleanly bordered bipolar regions. These opposite-
polarity patches on the other side of the polarity reversal line (of the smoothed
field) seem to play an important role, and may be responsible for the "overlapped
dual arcades" structure: The loop-like features in the "overlapped dual arcades"
coming from a distant part in the region of one polarity seems to be connected
to the patches of the *same polarity* transported to the opposite sides! This is,
of course, not possible if the loop-like features are normal magnetic flux tubes.
A natural solution to this paradoxical situation is to identify the "overlapped
dual arcades" with the "separatrix surface" in a quadrupole magnetic source
model proposed by Uchida and Jockers (1979). The "separatrix surface" in the
quadrupole source model takes a form similar to the observed one (Figure 1),
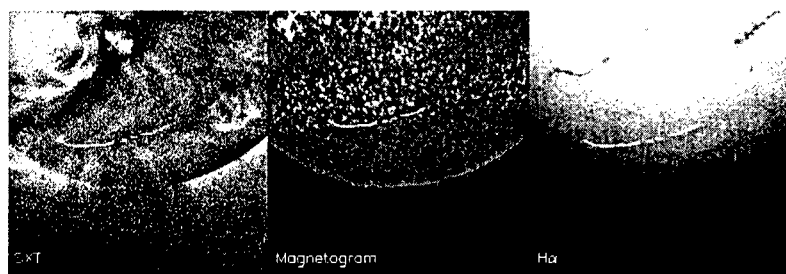
Figure 2.   X-ray structure surrounding a dark filament on March 19,
1993. The angle which the legs of "dual arcades" makes is very large, so that
it is not possible to attribute this structure to a sagged-top simple arcade
connecting bipolar regions. (The height h determined is 7×10^4 km.)

and is likely to have high density and high temperature gas along them because
the crossing line of the two leaves of the "separatrix surface" is the neutral line
(neutral sheet if squeezed from the sides) where a minor but continuous release
of energy is expected even before the flaring, and thus the "separatrix surface"
may show up in X-rays.

In the case of the dark filament which leads to the formation of the "Giant
Cusp" event of January 24-25, 1992, all the characteristic features mentioned
above, namely, the "overlapped dual arcades", the presence of the mixed polarity
belt below the region of crossed legs, the coincidence of the locus of the top of the
dark filament with the region of crossed legs, etc., are confirmed (with $h=1.2\times10^5$
km, see Uchida et al. 1998).

Also in the case of the long dark filament found in the northern hemisphere
during the same period, a very clear "overlapped dual arcades" type structure
exists, as well as other features described above. This case is important because
the viewing angle is quite different from those already described, and we can
confirm that it is actually an "overlapped dual arcades" type structure in 3D
(with $h=7\times10^4$ km, see Uchida et al. 1998).

The case of March 19, 1993 shown in Figure 2 is a case by which the classical
hammocking configuration is excluded, because the angle which the legs of the
two "arcades" make is about 60 degrees. The lines of force in a sagged simple
arcade can not make such angle without landing in the middle.

Some remarks should be made on other possible interpretations. One ques-
tion is whether the southern side of one of the "dual arcades" is really a closed
"arcade" shape structure, or part of the open polar field. The answer is that it is
a closed structure since it has enhanced density on it. Therefore, we regard the
structure as "dual arcades". Next, can not we interpret the structure as a much
larger single arcade? Only the legs of the large distorted loops would be visible
in a specially favorable perspective to give us an impression of "dual arcades".
This is not likely because the down-projected dark filament would be along the
locus of footpoints of only one side of such a large arch, or we have to admit that
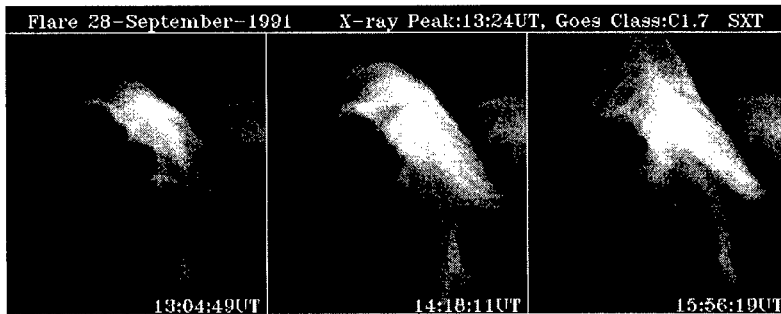
Figure 3. Time development of the September 28, 1991 arcade formation event. A bright region appeared near the crossing point of two loop systems, and that turned out to be a bundle of arches (arcade) with a few pre-existing longitudinal threads perpendicular to them. The "spine" (consisting of *multiple* bright threads that can not be the locus of reconnecting points as supposed in the classical models of arcade flarings) rose, and this rising bundle of threads seemed to push up the arcade from below into the form of a triangular tent (from McAllister et al. 1992).

we see a large arch in which the furthest part of one polarity region is connected to the part closest to the polarity-reversal line in the opposite polarity region, *and not* vice versa. Since we have found the above configuration in many cases, attribution of this to a specially favorable perspective seems unlikely.

3. X-ray Arcade Formation Events and Some Remarks on CME Connections

The first observation of the arcade formation process by Yohkoh was the September 28, 1991 arcade formation event (McAllister et al. 1992). This event was considered to be an exceptional case, because it was quite different from the idea about arcade flarings based on the "classical" model. But this event turned out to be *not* exceptional, but rather, a canonical one, since many of the observed arcade formation events show essentially similar characteristics as we will see.

In the September 28, 1991 event, the arcade formation started from the point at which two systems of arches crossed. As a bright knot grew in size, it turned out to be an arcade consisting of loops perpendicular to the axial structure which was composed of a few pre-existing longitudinal threads (that we called the "spine") rising from *below* the arcade (Figure 3). It seemed that the "spine" continued to rise and pushed up the arcade from below to make it into a triangular "tent"-like structure at the northern part toward the end of the period of observation (McAllsiter et al. 1992). The model counterpart in the "classical model" for the rising "spine" would be the "locus of reconnection appearing *above* the X-ray arcade", but the "spine" here could not be that,
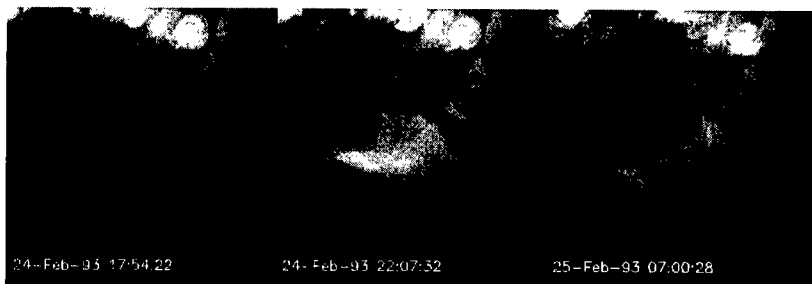
Figure 4.   Time development of the February 24-25, 1993 arcade for-
mation event. A bright bundle of threads ("spine") appeared above the
region where the dark filament existed. The "spine" consisting of multiple
bright threads rose, and this rising bundle ballooned up at its western part,
and finally formed a protruding large arch similar to the "Giant Cusp" of
January 25, 1992.

since it consisted of *multiple pre-existing threads* connecting the opposite polarity
regions in skew with the polarity-reversal line, and seemed to come up from *below*
(or be a part of) the X-ray arcade.

A second example we show in Figure 4 is the X-ray arcade formation event
of February 24-25, 1993 (Fujisaki et al. 1997), whose pre-event coronal structure
was described in section 2 above. In this event, the "spine" rose from the location
where the dark filament existed (but the dark filament had erupted some time
before that, although we can not tell the exact time). Foot-connections (arcade
structure) appeared on the north side of the western part of the "spine", and
the system formed a shape like a toothbrush with the "spine" as its stem. The
westernmost part of the "spine" rose further, pulling up the foot-connections
with it, and finally evolved into a large arch that reminded us of the "Giant
Cusp" event on January 25, 1992.

The example of the "Giant Cusp" formation event of January 24-25, 1992
(whose pre-event structure has already been described in section 2 as a case
with a very clear "overlapped dual arcade" structure in its pre-event phase) has
been believed to be a good example of the classical "reclosing of an opened-up
magnetic arcade" occurring on a gigantic scale. Hiei and Hundhausen (1996)
found that, while the "Giant Cusp" increased the width and height of the whole
structure, a small substructure inside peeled off and moved downward. They
interpreted this as evidence of the classical model. It is, however, necessary to
point out that the reclosing cusp in the classical model is not the only explanation
for such peeling-off structure. It is also possible in the "spine ballooning" process
in the quadrupole source model mentioned above.

Another more pronounced case indicating the "ballooning spine" is the ar-
cade formation on the west limb on October 5, 1996 (Watari et al. 1997). This
case shows very clearly the rise of the "spine", eventually ballooning up in the
shape of an "inchwarm". It "pulls up" the arcade of loops, in an even clearer

manner than the case of February 24-25, 1993, and shows that there exists such a process as an "arcade of magnetic loops being pulled up by a ballooning magnetic spine" without cutting it, or without "annihilation" at their contact points! A physical explanation has not yet been given.

We now add some comments on the relation of the arcade formation events with CMEs (coronal mass ejections). Observing the CME production process from the X-ray arcade formation is not necessarily suited for Yohkoh, because of the limited field of view, but the Yohkoh observations can help the interpretations of SOHO/LASCO data. Associations of X-ray arcade formation observed by Yohkoh and CMEs evidenced by SOHO/LASCO or with other satellites like Ulysses, should be pursued to better understand what is occurring in the production of CMEs. One of the greatest interests in this context is where exactly the mass of CMEs comes from. Hudson and Webb (1997) noted the dimming of the corona above arcade flares, which they identified with the escape of the coronal mass ahead of the dark filament. Watari et al. (1997), on the other hand, noted that there existed a very long connectivity in the event of October 5, 1996, the long "spine" pulling up the X-ray arcade. It should be stressed that the "spine" comes up much later than the dark filament eruption itself, and does not have a counterpart in the classical model. We are proposing a model in which the dark filament splits (Tang 1987) into a rising dark filament and an S-shaped structure remaining below, and the major shedding of the mass and energy is triggered and comes from the region of high mass density and magnetic stress (Hirose et al. 1997).

4.   Conclusion

It is seen that the "classical model", which has been the most widely accepted model for the last thirty or so years, does not have counterparts for some of the key characteristic features found by Yohkoh in the faint pre-event and initial phases of arcade flaring processes. Those features found in the faint pre-event or initial phases are extremely important for the true understanding of the process from the causality point of view, but have not been examined before. A model capable of explaining the newly found key characteristics was given based on the quadrupole magnetic source configuration (Uchida 1980), and turned out to be appropriate in explaining the observed key characteristics (Uchida et al. 1998, these proceedings, Hirose et al. 1997).

References

Fujisaki, K., Uchida, Y., Morita, S., Hirose, S., and Cable, S. 1997, Publ. Astron. Soc. Japan, submitted

Hiei, E. and Hundhausen, A. 1996, in Magnetodynamic Phenomena in the Solar

Atmosphere–Prototypes of Stellar Magnetic Activity, (eds.) Y. Uchida et al., Kluwer Academic Publ., Dordrecht, Holland, p. 125

Hirose, S., Cable, S.B., Uemura, S., and Uchida,Y. 1997, in preparation

Hudson, H.S., and Webb, D. 1997, in Geophysical Monographs No. 99, Coronal Mass Ejections, (eds.) N. Crooker et al., AGU, p. 27

Martin, S. 1990, in Dynamics of Quiescent Prominences, Lecture Note in Physics, Vol. 363, (eds.) V. Ruzdjak and E. Tandberg-Hanssen, Springer-Verlag, New York, p. 1

McAllister, A.H. et al. 1992, Publ. Astron. Soc. Japan, 44, L205

Sturrock, P.A. 1966, Nature, 221, 695

Tang, F. 1987, Solar Phys., 107, 203

Tsuneta, S., Hara, H., Shimizu, T., Acton, L.W., Strong, K.T., Hudson, H., and Ogawara, Y. 1992, Publ. Astron. Soc. Japan, 44, L63

Tsuneta, S. 1993, in The Magnetic and Velocity Fields of Solar Active Regions, (eds.) H. Zirin, G-X, Ai, and H. Wang, ASP Conf. Series No. 46, p. 239

Uchida, Y. and Jockers, K. 1979, Max Planck Institute for Astrophysics Preprint

Uchida, Y. 1980, in Solar Flares, (ed.) P.A. Sturrock, Univ. of Colorado Press, Boulder, p. 67 and p. 110

Uchida, Y. 1996, Adv. Space Res., 17, 4/5, p. 19

Uchida, Y., Fujisaki, K., Morita, S., Torii, M., Hirose, S., and Cable, S.B. 1998, Publ. Astron. Soc. Japan, submitted

Watari, S., Watanabe, Ta., Acton, L., and Hudson, H. 1997, in The Corona and Solar Wind Near Minimum Activity, ESA SP-404, Oslo, p. 725

Axial Soft X-ray Brightening Associated with Hα Filaments

Frank C.R. Solberg

Institute of Theoretical Astrophysics, University of Oslo, Norway

Alan McAllister

Helio Research, NCAR/HAO, Boulder, CO 80307, USA

Abstract. We have studied coronal soft X-ray (SXR) arcades around filament channels, as observed with the Yohkoh Soft X-ray Telescope (SXT). We have found about a dozen events (1991–1993). Comparisons with Hα filaments have revealed an association between some SXR structures and filaments. These bright thread-like SXR structures (often) appear to be *parallel* to and *co-spatial* with Hα filaments. The SXR structures are occasionally maintained for days, although transient brightening of axial structures is more common.

1. Introduction

Covered here are the events on March 10, 1992 and March 24-26, 1992. Full-disk Hα images are from Big Bear Solar Observatory, and the 868.8 nm FeI magnetograms are from Kitt Peak National Observatory. The Hα images were resized and de-rotated to fit full disk SXT images, spatially (to an accuracy of about one pixel) and temporally. The boxes on the full-disk SXT images indicate the location of the partial images. These have been extracted from full-disk SXT images and are shown with Hα contour overlays in Figures 1 and 2. All SXT images were enhanced using a special sharpening routine (McAllister et al. 1992). The thinnest SXR structures approach the resolution of the SXT images. Higher cadence (~0.5–1 hour) Hα images (recently supplied from Sacramento Peak Observatory by Haosheng Lin) were used to check the stability of the filaments.

2. The Events

- **March 10, 1992** (Figure 1): Located near Sun center, between two active regions. The western active region is an emerging flux region (EFR) which seems to have triggered the event (Note: Hα flaring occurred here at 10:33 UT and 14:50 UT). The overall lifetime of pronounced axial SXR structures was about 6 hours (~14:00 UT to ~20:00 UT). The filament seemed to be fairly undisturbed during the axial X-ray events on the 10th. The filament even grew in size from about 16:00 UT, while there was still high axial SXR activity.
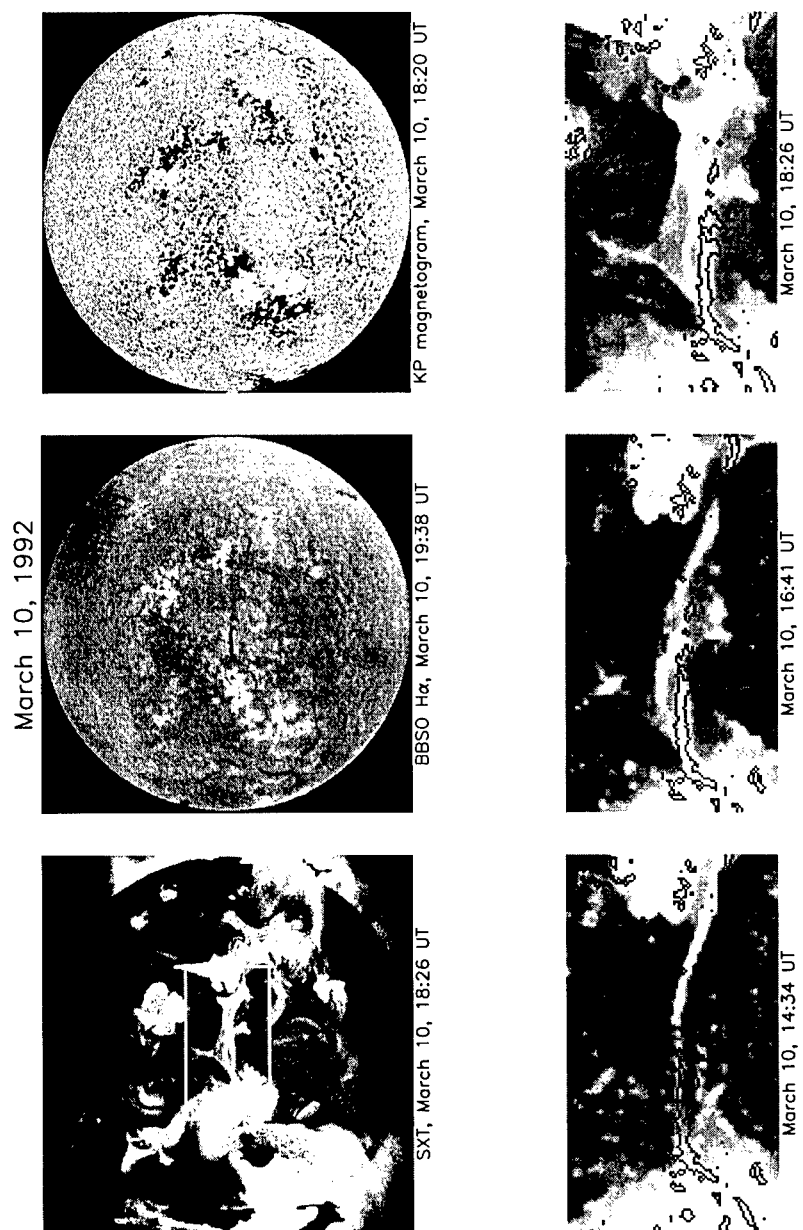
Figure 1.
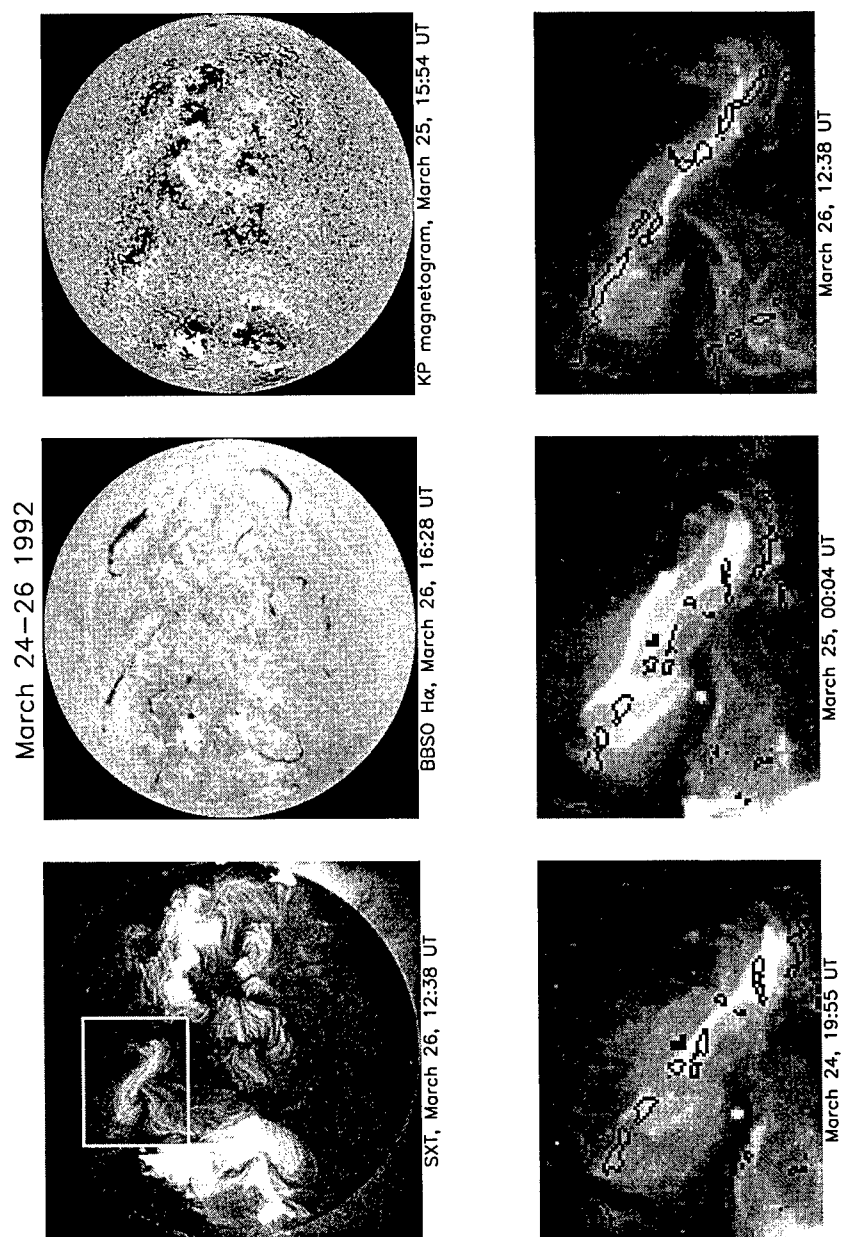
Figure 2.

This suggests that there is a significant height difference between the Hα filament and the axial X-ray structures. The Hα contours on the partial images are from the 19:38 UT BBSO image.

- **March 24-26, 1992** (Figure 2): Long-lived axial event situated in the northeast quadrant (not an EFR). Locally, the SXR structures showed transient axial activity and flickered with time-scales down to minutes. Pay special attention to the middle partial frame, where both the axial *and* the transverse SXR loops are bright. Higher cadence Hα images show that the filament was not stable throughout the event. The filament did not disappear completely and it more or less resumed its original state after some time. Contours on the first two partial images are from the Hα image taken at 19:03 UT, March 24, whereas the right partial image has contours from the image taken at 16:28 UT, March 26.

3. Interpretation

The axial SXR structures owe their existence to some dynamical energization. In this low-β plasma, the energization must result from a need to readjust the magnetic field. Movement of magnetic anchor points in the photosphere, or emergence of new flux in the region, can then be the driving force. The movements cause loops of the complex system of filament and filament channel to interact, creating stress and pressure gradients to drive sufficient reconnection to produce the observed X-ray emission.

4. Conclusions

- We have found axial soft X-ray signatures associated with Hα filaments and filament channels. They appear to be parallel and co-spatial with the filaments. We also see axial SXR structures in filament channels without observing any Hα filament.

- The Hα filaments appear fairly stable during some periods of axial soft X-ray brightening, but disappear temporarily in others. When the Hα filaments are stable during axial X-ray activity it suggests that the cool filament plasma is separated (and insulated) from the heated X-ray plasma.

- The axial SXR structures have varying lifetimes, from a few hours to several days. On shorter time-scales (minutes), the structures often show a flickering behavior.

References

McAllister et al. 1992, Publ. Ast. Soc. Jap., 44(5), L205

Solar Prominence Diagnostics

J.-C. Vial

Institut d'Astrophysique Spatiale, CNRS/Université Paris XI, Bâtiment 121, 91405 Orsay Cedex, France

Abstract. This paper reviews the diagnostic techniques currently used to establish estimates of the physical properties of prominences. Most often the fine structure of prominences cannot be resolved. Because of this and the complex structures and the varied forms of prominences, it is difficult to establish definitive values for temperature, density, magnetic field, electric field, differential emission measure, mass flows, etc. Nevertheless, there are many useful techniques ranging from spectroscopic analysis to measurements of prominence oscillations. Most of the major techniques are reviewed in this paper, with examples of the results and an extensive bibliography. Special attention is paid to the potential diagnostic value of optically thick lines. Suggestions are made for further progress based on SOHO and other observations.

1. Introduction

For the last extensive review of this subject, we refer to the book "The Nature of Solar Prominences" by Tandberg-Hanssen (1995) (hereafter ETH), especially his Chapter 3. We want to stress three features from it:
i. There is no such thing as a canonical prominence (see the different classifications in ETH).
ii. No structure is really isolated (it has interfaces with the chromosphere and the corona).
iii. No prominence has an uniform structure.
    These three features have two consequences:
i. A large range of values within a prominence and from prominence to prominence (which may also be due to the diagnostic techniques used).
ii. The difficulty of the diagnostic, which is nevertheless necessary for building MHD models, in describing and explaining the formation and disappearance of prominences. We now describe the techniques commonly used to determine thermodynamic parameters.

2. Diagnostic of Thermodynamic Parameters

In order to understand the very existence of cool material in the corona, it is essential to precisely measure its temperature and the variation of temperature within the structure, especially at the interface regions.

2.1. Temperature

We refer here to the electron temperature since the density is sufficient to provide equal temperatures for the different species.

The first technique consists in the measurement of the profile shape of at least two lines of different elements which leads to the separation of temperature (5000–8000K) and associated "microturbulence" (5–8 km/s). See ETH and the Hvar Reference Model (Engvold et al. 1990). The above range of temperatures corresponds to the coolest material, although Hirayama et al. (1979) reported 4300K and 3 km/s for temperature and "microturbulence", respectively. It must be noted that the technique assumes an optically thin plasma and neglects sources of broadening other than Doppler: pressure, electric fields, etc..

The color temperature of the Lyman continuum has been shown by Heasley and Milkey (1983) to represent the electron temperature, at least for layers that are not too thin. From Skylab observations, they derived values around 6500K. Higher temperatures exist in Active Region Prominences and, of course, in the Prominence Corona Transition Region (PCTR).

As for radio observations, the derived parameter is the brightness temperature, T_b. At $l < 1$cm, T_b of the cool material is 8000K; limb measurements performed with the JCMT (Harrison et al. 1993) indicate a *very* low temperature if a "reasonable" density is assumed. At $l > 1$cm (VLA observations), T_b of the PCTR goes up to 80,000K, a value which is much lower than the one deduced from EUV measurements (Engvold 1989). This disagreement has been discussed in terms of magnetic field orientation vs. height by Chiuderi-Drago et al. (1992) and could provide evidence of different PCTRs at the sides and top of filaments (see Chiuderi-Drago et al. 1998, these proceedings). We note that the Nobeyama telescope (17 GHz) has proven to be very useful for locating filaments and filament channels.

2.2. Densities

According to the Hvar Reference Atmosphere of Quiescent Prominences, the electron density is in the range $10^{10} - 10^{11}$ cm^{-3} in the cool part, down to 10^8 in the PCTR. This range is larger, because of the variety of methods used.

The most direct method (Stark effect in high Balmer lines) has been used recently by Hirayama (1990) who found about $n_e \sim 10^{11}$ cm^{-3}. On the other hand, line ratio techniques have been used in the visible (e.g., Na I to Sr II resonance lines ratio shown to be proportional to n_e) by Landman (1985, 1986). They indicate that n_e is larger than 10^{11} cm^{-3}. Foukal et al. (1986) find n_e of the order of 10^{11} cm^{-3}. The line ratios technique in the infrared (Fe XIII 10747/10798Å) employed with the Pic-du-Midi Coronagraph provides evidence of a coronal cavity, although the density is not lower everywhere around the prominence (Wiik, Schmieder and Noens 1992). With the opportunity of an eclipse, Stellmacher, Koutchmy, and Lebecq (1986) measured the Hβ line to continuum ratio and derived a density of about 3×10^9 cm^{-3}. In the UV, line ratios such as O IV (1401/1404Å) lead to $n_e \sim 10^{11}$ cm^{-3} (Wiik et al. 1993).

An interesting by-product of the work on the Hanle effect consists in measurement of the depolarization in two lines, one, such as D_3, being depolarized by the magnetic field only, the other, such as Hβ or Hα, depolarized by both magnetic field and collisions. In this way, the effect of collisions can be evaluated

and the electron density derived. Bommier et al. (1986, 1994) found n_e in the range $3 \times 10^9 - 4 \times 10^{10}$ cm^{-3}).

Radio prominence measurements performed in the mm range with the VLA (Bastian et al. 1993) and the JCMT (Harrison et al. 1993) also point to low values (about 10^{10} cm^{-3}). Of course, the very existence of such low densities implies large effective thicknesses, as noted by Hirayama (1990).

2.3. Ionization Degree (ID)

As shown by Poland et al. (1971), the cool parts of prominences are ionized by the H and He Lyman incident radiation. The ionization degree (ID) is a crucial parameter for the determination of pressure, flows, and balance of forces (mass to current ratio). Here, we define ID by the ratio of proton density to neutral hydrogen density. It is roughly equal to the ratio of electron density (the helium ionization is reduced) to the density of the level 1 population n_e/n_1. In the Hvar Reference Atmosphere, the ionization is described by the ratio X of electron density to the **total** hydrogen density. Between the two quantities, we have the relation: ID $= 1/(X^{-1} - 1)$. Assuming we know n_e we must determine n_1. There is no direct technique: the idea is to determine the opacity at the head of the L_∞: Landman (1983, 1984) found ID $<< 1$. According to ETH, "the best range of values for quiescent prominences is probably: $0.05 <$ ID < 1". In a loop prominence, Heinzel and Vial (1992) found ID $= 0.9$. Measuring obscuration effects in the EUV (Skylab), Schmahl and Orrall (1979, 1986) derived larger IDs in the range 2–10. Let's also mention that by deriving a proportionality between the ratio of intensities Lα/CaK and ID^2, Vial (1982) could bracket, from OSO8 observations, the ID between 1 and 10.

The NLTE modelling of Gouttebroze et al. (GHV 1993) and Heinzel et al. (HGV 1994) lead to an ID of about 10 for low densities (Figure 1). As shown by Figure 1, the ionization (measured here by the X parameter) does not change much with temperature as long as the densities are low. This reflects the domination of radiation in the ionization process.

With the large range of values of ID goes a large range of gas pressures with P_g (cgs) $\sim$ 0.1–1 (0.02 at the edges). Let's say that the NLTE models (discussed in Section 3) favor low pressure values. From the He singlet/triplet, Stellmacher and Wiehr (1997) could measure the total hydrogen density (3×10^{10} cm^{-3}) and conclude that the pressure P is about 0.02 dyn cm^{-2}.

2.4. Differential Emission Measure (DEM) in the PCTR

The DEM as defined by n_e^2 $(dT/dz)^{-1}$ is similar in the PCTR to the DEM in the CCTR. This shape is well explained at temperatures higher than 10^5K where radiative losses balance conduction energy gain. But for temperatures lower than 10^5K, no real explanation has been provided. Engvold (1989) refers to flows and enthalpy flux. Rabin (1986) proposes perpendicular conductivity which can only work if many thin layers constitute the PCTR. Chiuderi and Chiuderi-Drago (1991) and Chiuderi-Drago et al. (1992) studied the effect of a large angle between the temperature gradient and the magnetic field vector and its effect on the perpendicular conductivity. Still, an extra energy input is needed at low T which could be the dissipation of Alfven waves (see also Chiuderi-Drago et al. 1998, these proceedings).
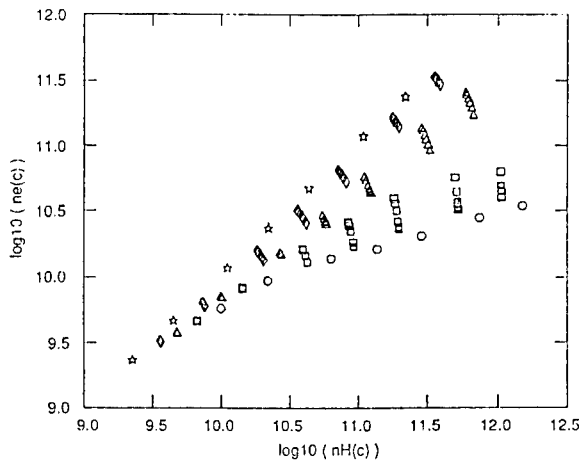
Figure 1.   Logarithmic plot of the variation of electron density with total hydrogen density at the center of different slabs with different pressures, widths and temperatures ranging from 4300 K (circles) to 15,000K (stars). From HGV.

2.5. Velocities (Flows)

We must distinguish between the cases of quiescent and active prominences. In quiescent prominences, both upward and downward vertical motions have been found (see Schmieder 1990 and ETH). *Downflows* of about 0.5 kms^{-1} have been observed both at the limb (apparent motions) and on the disk (Doppler). *Upflows*, usually less than 5 kms^{-1}, have been observed on the disk (Doppler), e.g., above filament feet. As for horizontal motions (only measured at the limb with the Doppler technique), values of about 10–20 kms^{-1} can be found at all temperatures (up to 60 kms^{-1} in active region prominences), especially at the edges. This leads to the rather surprising result that horizontal velocities are seemingly larger than vertical ones. However, from systematic limb-to-limb measurements performed in the C IV line observed with UVSP/SMM, Simon et al (1986) showed that at 10^5K, vertical velocities are larger than horizontal ones. They interpret these results as flows occurring within small loops. The non-visibility of vertical velocities at temperatures lower than 10^5K certainly tells something about the heating/cooling processes within prominences. Moreover, helical and rotational motions have been detected (Liggett and Zirin 1984, Vrsnak 1990, Schmieder et al. 1998, these proceedings). Perhaps, prominence fine structures are more unstable than commonly believed as evidenced by "impulsive brightenings/velocity transients" seen in Hα by Toot and Malville (1987).

In activated prominences (Disparition brusques, etc.) which lead to Coronal Mass Ejections, one finds very high values (larger than the liberation speed). In the diagnostic lines, the Doppler dimming/brightening effect (e.g., in Hα, Rompolt 1969) should not be forgotten.

2.6. Oscillations

Oscillations are better (and more surely) detected in velocities (Balthasar and Wiehr 1994, Molowny-Horas et al. 1997). The last authors distinguish three cat-

egories of periods: short (< 5 min); intermediate (6–20 min); and long (40–90 min) periods. Hβ measurements indicate a strong power at 7.5 min, a propagation over less than 20,000 km, and a lifetime of about 12 min. These results raise the issue of Alfven waves and their role in heating, an idea also proposed by Yi and Engvold (1992). Measurements also point at the coupling of the prominence with the chromosphere and the corona. Energy inputs can be studied via intensity and velocities fluctuations.

3. Optically Thick Lines and Modelling

Diagnostics with optically thick lines are complex and involve the most plasma parameters (densities, temperature, filling factors, etc.). It is nevertheless necessary, even for optically thin lines which are influenced by optically thick lines in the atom (ion) system. Since the pioneering works by Heasley, Mihalas, Milkey, Morozhenko, Poland, Yakovkin, improved computations with "true" (OSO8) incident radiation profiles and PRD (Heinzel, Gouttebroze and Vial 1987) have been made. No match was found for the computed ratio Lα/Lβ, still higher than the observed one (the problem is more severe than in the chromosphere).

GHV initiated the construction of a wide set of empirical models, with the triple objective of: 1) Predicting observable lines, deriving physical quantities from observed spectra, and finding to what physical parameters lines are sensitive; 2) Drawing some laws that may help to understand what physical processes are at work; and 3) Providing benchmarks for the validation of more sophisticated models, e.g., two-dimensional codes (Paletou 1995). GHV prominence models consist of isothermal, isobaric slabs standing vertically above the solar surface. The hydrogen atom model consists of twenty levels and the continuum. 140 panels corresponding to the 140 models have been produced (see GHV). Correlation plots have been obtained by HGV, e.g., Hα vs. Hβ and Hα vs. Emission Measure (n_e^2 D) (Figure 2).

Coupling the last correlation plot with an independent measurement of the electron density, n_e, leads to the determination of the (effective) thickness, D, of the structure (Heinzel et al. 1996): 100 to 30,000 km (Figure 3). However, these values are in contradiction with Kippenhahn-Schlüter (KS) models derived from the same set of measurements (Heinzel and Anzer 1998, these proceedings). KS models have smaller thicknesses and higher pressures.

Other relations obtained by GHV and HGV include: Lyman continuum vs. column mass, T_{color} of the Lyman continuum vs. T_e, Lα vs. pressure, Lα/Lβ vs. pressure, n_e^2 vs. n_2, etc. Similar computations have been performed in Ca II by Gouttebroze et al. (1997 GVH). GVH computed exactly the ionization of Ca I and Ca II for different temperature and pressure models. Correlations between Ca II lines and Ca II/hydrogen lines have been obtained. Figure 4 shows K (3933Å) and infrared (8542Å) Ca II profiles for various conditions.

Let's mention the technique of the cloud models which Mein et al. (1996) improved noticeably, since it is now possible to take into account a varying Hα source function and velocity gradients within the filament. This fast technique is efficient for deriving velocity fields from MSDP data.
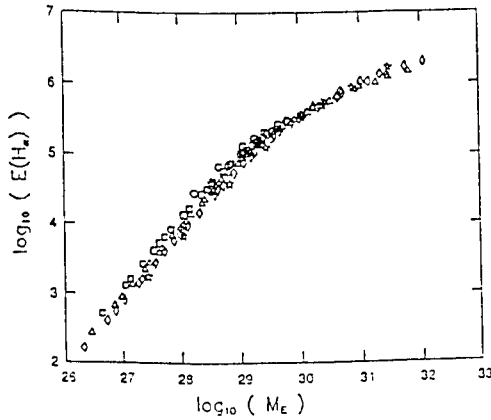
Figure 2.   Correlation plot between Hα intensity and Emission Measure obtained from the set of 140 models of GHV. (From HGV).
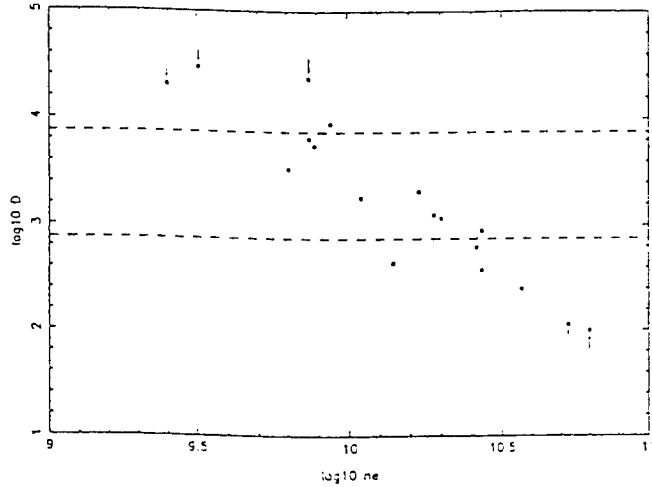
Figure 3.   Geometrical thickness (in km) versus electron density for the set of prominences studied by Bommier et al. (1994). The two dashed lines show the thickness of 1 and 10 arcsec, respectively. (From Heinzel et al. 1996).

3.1. Effect of Radial Velocities

The above mentioned NLTE techniques must be modified in order to take into account the Doppler dimming/brightening in a moving atmosphere. The first non-LTE and transfer computations were performed by Heinzel and Rompolt (1987). More recently, modelling with Partial Frequency Redistribution (PRD) has been done by Gontikakis et al. (GVG1 and GVG2 1997). Basic results are as follows:

Taking account of PRD leads to higher Lα, Lβ, and even Hα intensities and intensified ionization. The coherent scattering produced by PRD gives lines asymmetries, especially in the Lα line (Figure 5). One notices line profiles and
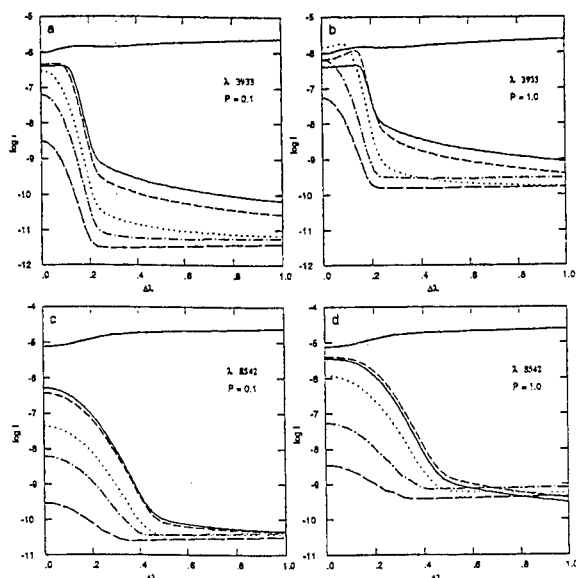
Figure 4.   Ca II line half-profiles emitted by prominence models for different temperatures and pressures. The flat upper curve represents the intensity at disk center, for comparison. For the other curves, the solid line corresponds to 4300K, short dashes to 6000K, dots to 8000K, dot-dashes to 10,000K, long dashes to 15,000K. Panel (a): K line, P = 0.1 dyn cm^{-2}. (b): K line, P = 1 dyn cm^{-2}. (c): 8542Å, P = 0.1 dyn cm^{-2}. (d): 8542Å, P = 1 dyn cm^{-2}. (From GVH)

intensity variations with the thickness of the layer. The correlation between Hα and Emission Measure is also modified. A diagnostic of eruptive prominences is now possible, including the determination of the true velocity vector, V.

4.   Magnetic Field

As summarized by Leroy (1989) and updated by Bommier et al. (1994), the magnetic field has different properties in quiescent and active prominences.

In quiescent prominences, the field is horizontal and has a large shear angle, α (the angle betwen the field and the filament is about 25°) (see Figure 6). As confirmed by Bommier and Leroy (1998, these proceedings), they mostly have an inverse configuration. The field strength seems to increase with height, but the field is homogeneous and slowly varying. Its magnitude is in the range 3–30 G. ETH suggests an average value of 8 G. Because of the large range of gaseous (see above) and magnetic pressures, the plasma β may vary from about 0.001 to 3. The ambiguity in the direction has been solved using different techniques (see Leroy 1989). In active region prominences, the average field is in the range 20 to 70 G according to ETH. The magnetic configuration is mostly normal.
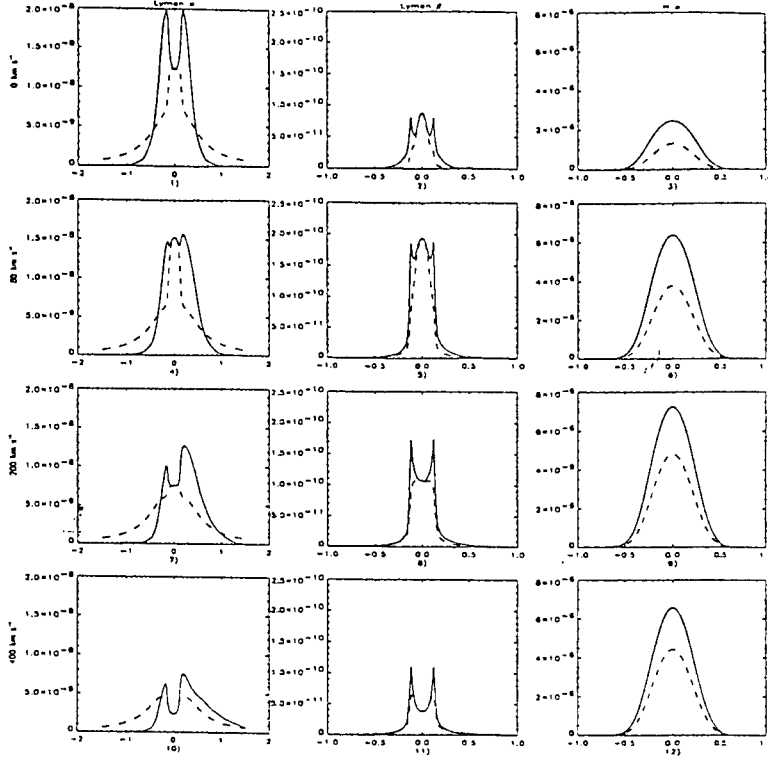
Figure 5.   The profiles of Lα, Lβ and Hα (columns 1, 2, 3) for four
velocities: 0, 80, 200 and 400 km/s (rows 1, 2, 3 and 4). The model has
a temperature of 8000K, a thickness of 2000 km and a pressure of 0.1
dyn cm^{-2}. PRD corresponds to the solid line and CRD to the dashed
line. The intensity is in ergs^{-1}cm^{-2}sr^{-1}Hz^{-1} and the abscissa is in Å .

4.1.   Electric field

Stark-polarized line profiles of hydrogen Paschen lines 18–3 allow us to detect
electric fields perpendicular to the line-of-sight (Casini and Foukal 1996). Nine
bright prominences have been observed by Foukal and Behr (1995) who found
that 5 V/cm is an upper limit for the electric field. These authors raise the issue
of the validity of KR model for low latitude prominences.

5.   Prominence Fine Structure

There is direct evidence of small-scales in intensity and velocity images (Heinzel
and Vial 1992), such as the vertical threads in Dunn's movie along which the
material flows. Such evidence questions the compatibility between small-scale
downflows and uniform *horizontal* magnetic field. This may be the indication
that the core of small structures is dense and not very ionized. There are many
indirect evidences of small-scale structure. For instance, Engvold et al. (1980)
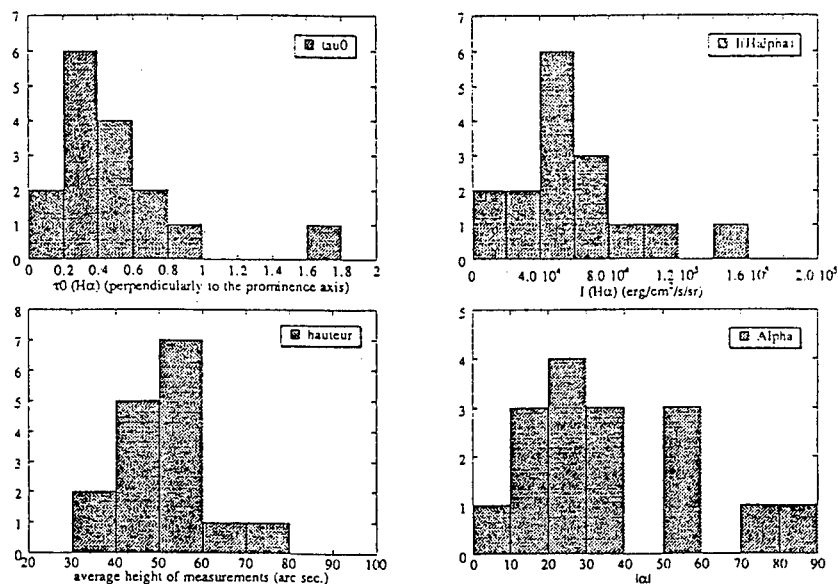
Figure 6. Histogram of tau0 (optical thickness in Hα), I(Halpha) (measured intensity in Hα), hauteur (height of observations, in arcsec) and Alpha (angle between the field vector and the prominence long axis). From Bommier et al. 1994.

studied the influence of the spatial resolution on line broadening, $< v >$, and line shift, v: they found that $< v >$ decreases and v increases with better spatial resolution.

There also is much information in the distributions of Hα intensities, line shifts and widths, as measured on the disk (Mein and Mein 1991) or at the limb (Zirker and Koutchmy 1991). The presence of about 10 to 20 structures along the line of sight have been derived. According to Mein (1994), this is a lower limit since one should distinguish three characteristic lengths: L_T (characteristic of temperature and density fluctuations), L_V (velocities) and L_B (magnetic field) with $L_T < L_V < L_B$. This means that one may have clusters of threads with the same velocities or magnetic field. Poland and Tandberg-Hanssen (1983) and Cheng (1980) found evidence of different threads at different temperatures at medium scales. Small filling factors (0.01–0.1) have been found in the PCTR which imply that the density in these threads may be two orders of magnitude larger than the "average" density.

At high spatial and temporal resolution, we have a "chaotic picture" (Jensen 1990). The problem of support is now the one of supporting material on individual tubes of force on very short time-scales (minutes). A possible candidate has been advanced by Jensen (1990): Alfven waves, generated in the convective zone, become non-linear and are trapped in prominences; in the dissipation process, momentum is transferred from waves to material. In the area of fine
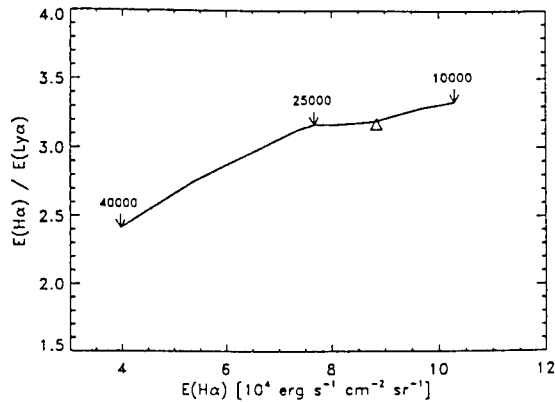
Figure 7.   Variation of the ratio of Hα/Lα intensities with Hα intensity at different altitudes in the prominence slab. From Paletou (1996).

structure, optically thick lines have recently proven to be very useful.

5.1. Optically Thick Threads and Modelling

a. In the two-dimentional modelling of Paletou, not only two-dimentional effects are taken into account (from the point of view of illumination and photon escape), but the filament emission can be properly computed and the backscattered radiation of the filament towards the chromosphere included (Paletou 1995). Figure 7 shows the variation of the ratio Hα/Lα with the Hα emission along the filament height (Paletou 1996). Paletou (1998, these proceedings) also addressed the issue of the visibility of bright rims ("marges"); he found no major increased excitation at the bottom of the filament/slab, contrary to Heinzel et al. (1995).
b. In the multi-thread modelling of Fontenla et al. (FRVG 1996), the thread (replaced by a slab) is defined by the balance between radiative losses and conduction and is constructed from a fixed central temperature to a coronal temperature. FRVG take into account the PRD and the ambipolar diffusion but no radiative interaction between threads (see Heinzel 1989). The ionization degree (ID) is never less than 2.5. The radiative losses increase by more than an order of magnitude below 10^5 K, as compared with Cox and Tucker. FRVG computed the variations of lines profiles with the pressure and the number of threads. They need about 100 threads to match the Lα, Lβ and Hα intensities and profiles (Figure 8). The Lα/Lβ ratio is closer to the observed one, but agreement with observations is only obtained with a cool core in the model.
c. Other techniques take into account randomly distributed inhomogeneities (e.g., Nikoghossian et al. 1997).

6. Prospects

We anticipate progress on the following issues:
1. Better measurements of the magnetic field in prominences and better connec-
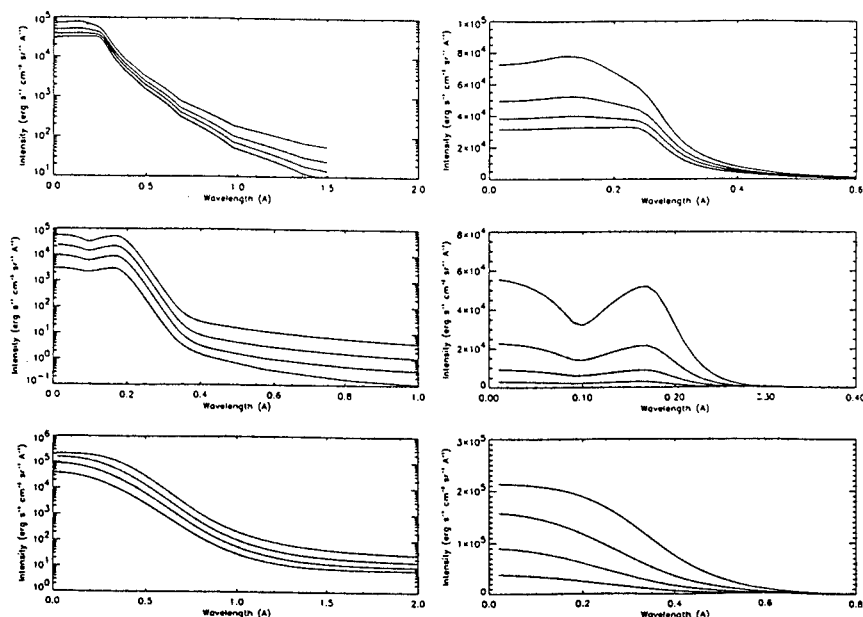
Figure 8.   Computed half-profiles of Lα (first row), Lβ (second row), and Hα (third row) for four different pressures. The first column is a semi-log plot to better see the far wing; the second column is a linear plot. (From FRVG 1996).

tion with the photospheric magnetic structure, a major task to which THEMIS is devoted. One can also expect major progress in field extrapolation. One could say that prominences are the testbed of all techniques of field extrapolations.

2. Better spectroscopic diagnostics: SOHO provides increased temperature coverage, good time resolution, and continuous observing sequences. The IR (1.6 m, continuum, He) may prove to be very useful for detecting the lowest temperatures (Hirayama et al. 1979).

3. When possible, *simultaneous* spectroscopic and magnetic measurements that can provide the β of the plasma.

4. Modelling: studies should include non-LTE transfer combining a multilevel atom, partial frequency redistribution *and* realistic geometries. They should be done in as many lines and continua from different atoms and ions as possible.

5. Energy and mass budget (magnitude and location): detailed radiation budgets (with lines spanning temperatures of $10^4 - 10^6$K) are possible with SOHO.

6. Oscillations: their measurements in different lines provide information on the connection of the prominence and its environment. We may well be *en route* towards prominence seismology.

7. Fine structure: If one wants to have direct evidence, what are the required spatial and temporal resolutions? If one relies on indirect evidence (measurements of filling factors), how reliable is the density diagnostic? What is the impact of flows on the departure from ionization equilibria?

References

Balthasar, H. and Wiehr, E. 1994, A&A, 286, 639

Bastian, T.S., Ewell, M.W. Jr. and Zirin, H. 1993, ApJ, 418, 510

Bommier, V., Leroy, J.L., Sahal-Brechot, S. 1986, A&A, 156, 79

Bommier, V. et al. 1994, Sol. Phys., 154, 231

Casini, R. and Foukal, P. 1996, Sol. Phys., 163, 65

Cheng, C.-C. 1980, Solar Phys., 65, 347

Chiuderi, C., and Chiuderi-Drago, F. 1991, Sol. Phys., 132, 81

Chiuderi-Drago, F., Engvold, O. and Jensen, E. 1992, Sol. Phys., 139, 47

Engvold, O., Wiehr, E. and Wittmann, A. 1980, A&A, 85, 326

Engvold, O. 1989, in Dynamics and Structure of Quiescent Solar Prominences, (ed.) E.R. Priest, Kluwer Acad. Publ., Dordrecht, Holland, p. 47

Engvold, O. et al. 1990, in Dynamics of Quiescent Prominence, Ruzdjak, V. and Tandberg-Hanssen, E. (eds.), Springer-Verlag, New York, p. 294

Fontenla, J., Rovira, M., Vial, J.-C. and Gouttebroze, P. 1996, ApJ, 466, 496

Foukal, P., Hoygt, C., and Gilliam, L. 1986, ApJ, 303, 86

Foukal, P. and Behr, B. B. 1995, Sol. Phys., 156, 293

Gontikakis, C., Vial, J. and Gouttebroze, P. 1997, Sol.Phys., 172, 189 (GVG1)

Gontikakis, C., Vial, J. and Gouttebroze, P. 1997, A&A, 325, 803 (GVG2)

Gouttebroze, P., Heinzel, P. and Vial, J.-C. 1993, A&AS, 99, 513

Gouttebroze, P., Vial, J.-C., and Heinzel, P. 1997, Solar Phys., 172, 125

Harrison, R.A. et al. 1993, A&A, 274, L12

Heasley, J.N. and Milkey, R.W., 1983, Ap.J., 268, 398

Heinzel, P. and Rompolt, B. 1987, Solar Phys., 110, 171

Heinzel P., Gouttebroze P. and Vial J.-C. 1987, A&A, 183, 351

Heinzel, P. 1989, Hvar Observatory Bull., 13, p. 317

Heinzel, P. and Vial, J.-C. 1992, in Proc. of ESA Workshop on Solar Physics and Astrophysics at Interferometry Resolution, ESA SP-348, p. 57

Heinzel P., Gouttebroze P. and Vial J.-C. 1994, A&A, 292, 656

Heinzel P., Kotrc, P., Mouradian, Z. and Buyukliev, G. 1995, Sol. Phys., 160, 19

Heinzel P., Bommier V. and Vial J.-C. 1996, Solar Phys., 164, 211

Hirayama, T., Nakagomi, Y. and Okamoto, T., 1979, in Physics of Solar Prominences, (eds.) E. Jensen, P. Maltby, and F.Q. Orrall, Oslo, p. 48

Hirayama, T. 1990, in Dynamics of Quiescent Prominences, Ruzdjak, V. and Tandberg-Hanssen, E. (eds.), Springer-Verlag, New York, p. 187

Jensen, E. 1990, in Dynamics of Quiescent Prominences, Ruzdjak, V. and Tandberg-Hanssen, E. (eds.), Springer-Verlag, New York, p. 129

Landman, D.A. 1983, Ap.J., 269, 728

Landman, D.A. 1984, Ap.J., 279, 438

Landman, D.A. 1985, Ap.J., 290, 369

Landman, D.A. 1986, Ap.J., 305, 546

Leroy, J.-L. 1989, in Dynamics and Structure of Quiescent Prominences, (ed.)
    E.R. Priest, Kluwer Acad. Publ., Dordrecht, Holland, p. 77

Liggett, M. and Zirin, H. 1984, Solar Phys., 91, 259

Mein, P. and Mein, N. 1991, Solar Phys., 136, 317

Mein, P. 1994, in Solar Coronal Structures, (eds.) V. Rusin, P. Heinzel and J.-C.
    Vial, Tatranska Lomnica, Slovakia, p. 289

Mein, N. et al. 1996, A&A, 275, 283

Molowny-Horas, R. et al. 1997, Solar Phys., 172, 181

Nikoghossian, A.G., Pojoga, S. and Mouradian, Z. 1997, Solar Phys., 325, 813

Paletou, F. 1995, A&A, 302, 587

Paletou, F. 1996, A&A, 311, 708

Poland, A.I et al. 1971, Solar Phys., 18, 391

Poland, A.I. and Tandberg-Hanssen, E. 1983, Solar Phys., 84, 63

Rabin, D. 1986, in Coronal Prominence Plasmas, NASA CP-2442, A. Poland
    (ed.), p. 135

Rompolt, B. 1969, Acta Universitatis Wratislaviensis, 77, 117

Schmahl, E.J. and Orrall, E.Q. 1979, ApJ, 231, L41

Schmahl, E.J. and Orrall, E.Q. 1986, in Coronal Prominence Plasmas, NASA
    CP-2442, A. Poland (ed.), p. 127

Schmieder, B. 1990, in Dynamics of Quiescent Prominences, Ruzdjak, V. and
    Tandberg-Hanssen, E. (eds.), Springer-Verlag, New York, p. 85

Simon, G., Schmieder, B., Démoulin, P. and Poland, A.I. 1986, A&A, 166, 319

Stellmacher, G. and Wiehr, E. 1997, A&A, 319, 669

Stellmacher, G., Koutchmy, S. and Lebecq, C. 1986, A&A, 167, 351

Tandberg-Hanssen, E. 1995, The Nature of Solar Prominences, Kluwer Academic
    Press, Dordrecht, Holland

Toot, G.D. and Malville, J.M. 1987, Solar Phys., 112, 67

Vial, J.-C. 1982, Ap.J., 254, 780

Vrsnak, B. 1990, Sol. Phys., 129, 295

Wiik, J.-E., Schmieder, B. and Noens, J.C. 1992, Solar Phys., 149, 51

Wiik, J.-E., Dere, K.P. and Schmieder, B. 1993, A&A, 273, 267

Yi, Z. and Engvold, O. 1992, Sol. Phys., 134, 235

Zirker, J.B. and Koutchmy, S. 1991, Solar Phys., 131, 107

Lyman Lines in Prominences and Filaments: NLTE Modelling Strategies

P. Heinzel

Astronomical Institute, Academy of Sciences of the Czech Republic
CZ–25165 Ondřejov, Czech Republic

Abstract. We briefly summarize the most important aspects of NLTE formation of hydrogen Lyman lines in prominences and filaments. A modified MALI code of Heinzel (1995) is described and its applicability to the interpretation of SOHO/SUMER data is discussed.

1. Introduction

A sophisticated NLTE modelling of the first few hydrogen Lyman lines ($L\alpha$ to $L\delta$) in isothermal and isobaric slabs has been performed, taking into account the partial redistribution (PRD) scattering physics, multilevel transitions and realistic incident radiation fields. In 1D, prominences are modelled as finite *vertical* slabs (Gouttebroze et al. 1993) and filaments as *horizontal* slabs (e.g. Mein et al. 1996). For 2D models see Paletou (1995) and Gorshkov (1997). Typically a 5-level plus continuum hydrogen model atom was used. Only Gouttebroze et al. (1993) have considered up to 30 levels, but Lyman transitions higher than $L\delta$ have been put into detailed radiative balance. In this contribution we summarize the strategies of how to extend such modelling to higher or even very high members of the Lyman series.

2. Higher Lyman Lines

Detailed study of NLTE line formation of higher Lyman lines requires an effective treatment of a multilevel hydrogen atom with a large number of explicit transitions for which the transfer equation must be solved. For example, to compute the intensity profiles of the four Lyman lines recently detected in a filament by SUMER, i.e., $L\delta$ to L-7 (see Schmieder et al. 1998, these proceedings), we have used a 12-level hydrogen model atom with 78 transitions including the continua (note that all subordinate continua are considered to be optically thin with radiative rates fixed by the incident radiation fields). As shown by Heinzel et al. (1997), for higher Lyman lines in prominences and filaments, the Stark broadening dominates the natural one. On the other hand, the importance of PRD is substantially lowered and one can treat higher members in the complete redistribution (CRD). Such multilevel treatment also requires an adequate routine to evaluate the collisional rates (Gouttebroze - private communication) and the full set of realistic incident radiation fields. The latter one has been taken from SOHO/SUMER measurements (for details see Heinzel et al. 1997).

3. MALI Code for Multilevel Problems

Current MALI (Multilevel Accelerated Lambda Iterations) techniques are capable of treating a large number of atomic levels and explicit transitions self-consistently (Rybicki and Hummer 1991, Heinzel 1995, Paletou 1995), thus replacing the assumption of detailed radiative balance in higher Lyman lines. For very high members, the line ovelapping must be properly taken into account. For higher densities, the level-occupation-probability formalism has to be considered when dealing with Lyman lines close to the series limit (Hubený et al. 1994). We have modified our prominence/filament MALI code in order to include an arbitrary number of hydrogen levels. For all corresponding transitions we specify the incident radiation fields (boundary conditions). Stark broadening parameters for higher Lyman lines are estimated according to Gouttebroze et al. (1978). NLTE simulations proceed in two steps. First, the linearized statistical-equilibrium equations are solved for a 5-level model atom in order to determine the ionization structure (depth variations of the electron density). Next, we use the full number of levels and solve the linear MALI problem for prescribed electron density.

4. Temperature Structure

As demonstrated by Schmieder et al. (1998, these proceedings) and Heinzel et al. (1997), SOHO/SUMER data do indicate that the prominence-corona transition region (PCTR) must be considered when interpreting higher Lyman lines, particularly in the case of filaments where no incident radiation falls on their top. To account for a temperature gradient in PCTR, we have replaced our previous isothermal models with new ones considering the temperature variations with depth (column mass). This automatically requires that a depth-dependent PRD must be accounted for, and we thus evaluate the redistribution matrices at each particular depth. However, a realistic determination of the PCTR temperature structure is rather difficult (i.e., using trial and error), and we plan to apply an effective optimization technique to ensure the best fits to all observed lines.

References

Gorshkov, A.B. 1997, in Science with Themis, (eds.) N. Mein and S. Sahal-Bréchot, Observatoire de Paris, p. 273

Gouttebroze et al. 1978, ApJ, 225, 655

Gouttebroze, P., Heinzel, P. and Vial, J.-C. 1993, A&AS, 99, 513

Heinzel, P. 1995, A&A, 299, 563

Heinzel, P., Schmieder, B. and Vial, J.-C. 1997, in The Corona and Solar Wind Near Minimum Activity, ESA-SP 404, p. 427

Hubený, I., Hummer, D.G. and Lanz, T. 1994, A&A, 282, 151

Mein, N. et al. 1996, A&A, 309, 275

Paletou, F. 1995, A&A, 302, 587

Rybicki, G.B. and Hummer, D.G. 1991, A&A, 245, 171

NLTE Model of a Quiescent Filament

E. V. Kononovich, A. B. Gorshkov, O. B. Smirnova
Sternberg Astronomical Institute, 119899 Moscow, Russia

P. Kotrč
Astronomical Institute, 25165 Ondřejov, Czech Republic

Abstract. The Sacramento Peak Observatory VTT Echelle Spectrograph was used to obtain high resolution spectrograms of the filament at W06° S27° observed on April 9, 1991 in hydrogen Hα, Hβ, and CaII H and λ 8498 lines. The line profiles were measured and digitized. A numerical code based on the MALI approach with partial frequency redistribution (PRD) in resonance lines was applied to obtain theoretical profiles of hydrogen and CaII lines. As a result of fitting the observed and calculated profiles, the physical parameters of the filament plasma were obtained. They include temperature, gas pressure, electron density and turbulent velocity.

1. Introduction

In spite of the existence of a large number of treatments of the spectral line transfer problem for the solar chromosphere and prominences, a variety of improved observations stimulates further refinement of the existing models and codes. The first NLTE prominence models were of a one-dimensional (1D) slab type (Jefferies 1955, Jakovkin and Zeldina 1964). Sobolev (1962) considered a much more difficult case of a spherical configuration. The whole 1D problem has been fully examined during the last few decades. However, before 1985 mostly the complete frequency redistribution approximation (CRD) was used and even rather sophisticated multi-slab models were elaborated (for references see Heinzel et al. 1987). In their paper a large set of 1D models for the hydrogen atom with standard PRD lines were presented. The basic ideas of NLTE prominence modeling were summarized by Heinzel (1991) together with various departures from classical finite 1D homogeneous slab models.

All these treatments are restricted to the case of only one chemical element – presumably hydrogen (e.g., Heinzel et al. 1987) or CaII (e.g., Gouttebroze et al. 1997). On the other hand, it is necessary to include several elements to make the prominence plasma diagnostics less ambiguous. In this work the NLTE PRD code similar to that described by Heinzel (1995) is adopted for simultaneous analysis of hydrogen and Ca II lines in filaments observed on the solar disk, in contrast to the usual interpretation of prominence observations on the solar limb. The validity of such an approach was demonstrated in our previous analysis of the July 6 filament (Kotrč et al. 1994) by means of the cloud
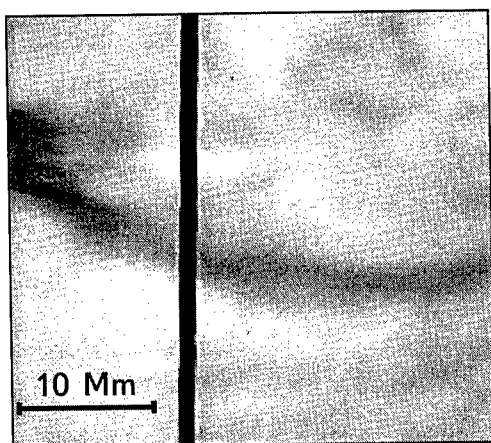
Figure 1.   The Hα slit-jaw picture of the Sac Peak Echelle Vacuum
Spectrograph with filament W06° S27° on April 9, 1991.

model applied to hydrogen and Ca II lines.

2.   Observations

In this work we use the high resolution spectrograms of a quiescent filament
obtained on April 9, 1991 under excellent atmospheric conditions. The observa-
tions were performed by one of us (P. Kotrč) at Sacramento Peak Observatory,
operated by NSO, and the parameters of the VTT Echelle Spectrograph were
given by Kotrč et al. (1994). The filament under investigation was at W06°
S27°, i.e., at the distance about 30° from the solar disc center. Figure 1 presents
the Hα slit-jaw image. The dark vertical line is the position of the spectrograph
entrance slit. The hydrogen Hα, Hβ, Ca II H and λ8498 lines were chosen for
further analysis.

       Accurate microphotometry was performed at Sternberg Astronomical In-
stitute of Moscow State University. The digital AMD-1 densitometer was used.
The photometric slit was of $50\,\mu \times 50\,\mu$ size. The scanning step was the same
$(50\,\mu)$, i.e., one step (pixel) corresponds to the distance of 126.5 km or 0.175 arc
sec on the Sun. The photometric calibration was done by fitting the reference
profiles to the standard profiles for the quiet Sun (Kurucz 1990).

       Figure 2 shows the obtained photometric cross sections of the filament (i.e.,
mean profile along the slit) for all considered lines, and Figure 3 presents spectral
line profiles for 5 distances from the filament channel. The central line intensities
are given in Table 1.

3.   Modeling

The filament line profiles definitely differ from the undisturbed chromospheric
profile as is seen in Figure 4. The difference is not large and it is smaller for more
transparent lines. This demands a higher accuracy of photometry and model
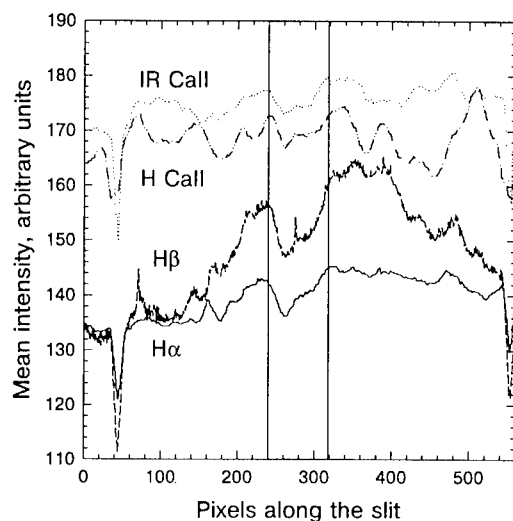
Figure 2. Photometric profiles of the April 9, 1991 filament averaged over the central parts of the corresponding lines. The filament is between the two vertical lines.

Table 1. Central line intensities in % of the nearby continuum

Line	Quiet Sun	Filament Channel
Hα	16	12
Hβ	14	6
CaII H	5	2
CaII λ8498	28	18

Table 2. The Filament Model

$T = 9500\ K$	$P = 0.13\ din/cm^3$	$V_{turb} = 8\ km/s$

Line	τ_0	$J,\ 10^6\ erg/(s \cdot ster \cdot cm^2)$
Hα	7.8	6.1
Hβ	1.1	4.4
CaII H	20.1	1.3
CaII λ8498	0.1	26.6

Figure 3.   Line profiles at different points along the slit: a) Hα, b) Hβ, c) H CaII, and d) λ8498 CaII, in % of the nearby continuum.

calculations. Nevertheless, even the cloud model used in our previous treatment (Kotrč et al. 1994) has led to a rather good agreement between observed and calculated intensities. In this work we apply the 1D NLTE PRD code. It is similar to that described by Heinzel (1995) but adopted to simultaneous analyses of H and Ca II lines. The model parameters were searched using the method of trial and error beginning from the hydrogen lines to obtain a value of the electron density. Then the calcium lines were calculated.

The resulting filament model is summarized in Table 2 with temperature $T = 9500\ K$, $P = 0.13\ din/cm^3$, $V_{turb} = 8\ km/s$ and electron density in the filament center $n_e = 4.2 \cdot 10^{10}\ cm^{-3}$.

4.   Discussion

For the first time we present results concerning the PRD transfer problem solution for the case of joint spectroscopy of two different atomic species, namely, hydrogen and Ca II. The procedure was applied to the filament spectral lines λ 6563, 4861, 3968, 8498 of both of these elements. The resulting physical parameters, T, P, P_e, and V_{turb}, obtained by fitting the observed and calculated line profiles are in good agreement with other prominence models. The accuracy of the fitting procedure for the four lines varies from 1 to 5%. The best fit is for the Hβ and Ca II H lines. We suggest that such a good agreement for both lines
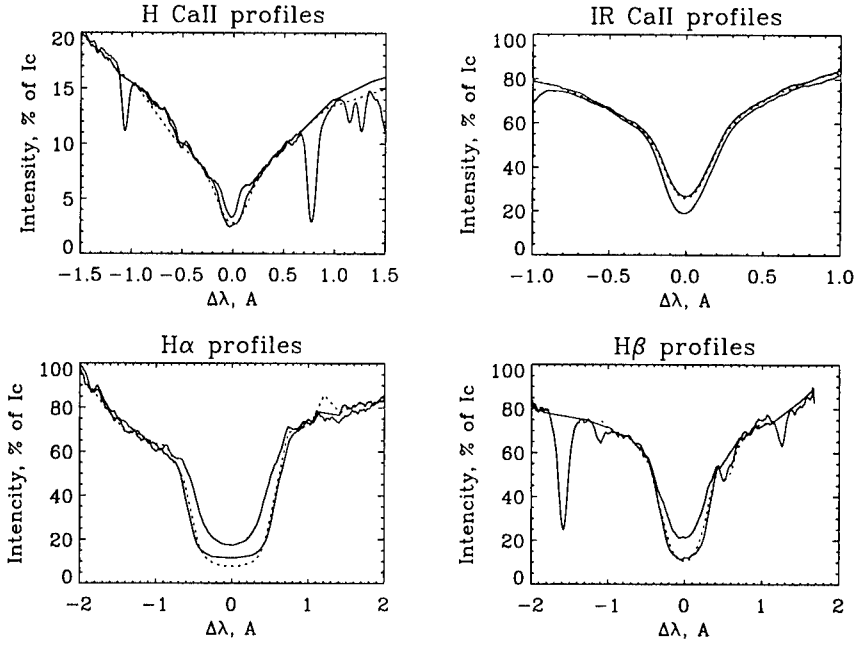
Figure 4.   Calculated line profiles (dashed) in comparison to the observed ones (lower full lines). Upper full lines are the incident radiation profiles used in the calculations.

is due to their intermediate value of the corresponding total optical thickness in the line center $1 < \tau_c < 10$. That means that the observed emission originates along the whole filament thickness. Concerning the optically thick Hα line one may suggest the existence of some unconsidered transition process in the upper border of the filament, where the line core is forming.

We still do not understand the large discrepancy for the infrared Ca II line. Cloud model calculations led to a rather small ratio (~ 5, see Kotrč et al. 1994) of optical depths between the resonance H line and subordinate $\lambda 8498$ line. Meanwhile NLTE calculations gave a much larger value, ~ 200. This contradicts the qualitative result that the filament is clearly seen on the original $\lambda 8498$ spectrogram; according to the model calculation it is not expected to be seen. A possible explanation may be found in terms of inhomogenious structure of the filament consisting of "hot" and "cold" small fibrills. This may be possible if the IR calcium line source function depends mostly on the temperature values, but not on the density.

References

Gouttebroze, P., Vial, J.-C. and Heinzel, P. 1997, Sol. Phys., 172, 125

Heinzel, P., Gouttebroze, P. and Vial, J.-C. 1987, A&A, 183, 351

Heinzel, P. 1991, Preprint 122, Astron. Inst. Czechosl. Acad. Sci.

Heinzel, P. 1995, A&A, 299, 563

Jakovkin, N. A. and Zeldina, M. Yu. 1964, AZh, 41, 914 (Russian)

Jefferies, J. T. 1955, MNRAS, 115, 617

Kotrč, P., Heinzel, P., Gorshkov, A. B., Kononovich, E. V., Kupryakov, Yu. A.
    and Smirnova, O. B. 1994, in Solar Coronal Structures, (eds.) V. Rusin,
    P. Heinzel and J.-C. Vial, VEDA Publ. Comp., Bratislava, p. 361

Kurucz, R. L. 1990, in The Solar Interior and Atmosphere, (eds.) A. N. Cox,
    W. C. Livingston and M. Matthews, Univ. of Arizona Press, Tucson, AZ,
    p. 663

Sobolev V. V. 1962, AZh, 39, 632 (Russian)

Prominence Emission Lines Observed With SUMER and Two Ground-based Telescopes

C. R. de Boer

Max-Planck-Institut für Aeronomie, D-37191 Katlenburg-Lindau, Germany

G. Stellmacher

Institut d'Astrophysique, 78bis Boulevard d'Arago, F-75014 Paris, France

E. Wiehr

Universitäts-Sternwarte, Geismarlandstr 11, D-37083 Göttingen, Germany

Abstract. Two sets of H, He, and Ca^+ emission lines were observed in a quiescent prominence simultaneously with the VTT and the Gregory telescope on Tenerife. At the same time, SUMER took two scans of low-ionized EUV emission lines.

The emission ratios of Ca^+–to–Balmer lines from ground vary little in the prominence, indicating a largely constant gas-pressure. In contrast, the ratio of He–to–Balmer from the ground shows the (known) increase toward the prominence borders, indicating higher temperature there. Similarly, the two-dimensional distributions of the ratios S IV/N II and C III/He I show pronounced bright prominence rims.

The reduced He 537Å and He 584Å line widths are 2.6 and 3.6 times larger, respectively, than those of He D_3 and He 3888Å. Explaining this by the optical thickness yields $\tau_0 = 10^4$ and $\tau_0 = 2 \cdot 10^5$ for the two EUV lines. The total He 584 emission amounts to 13 watt/m^2 ster in the main prominence body where the D_3 line yields 4 watt/m^2 ster; existing models, however, predict a factor 0.18.

The widths of simultaneously observed optical lines with different atomic weights yield thermal and non-thermal broadening parameters of $T_{kin} \approx 8000$ K and $2.5 < \xi < 6.5$ km/s. The EUV lines, however, show line widths which correspond to much higher temperatures and non-thermal velocities. Assuming for each ion the corresponding ionization temperature, the line widths require non-thermal velocities of 15–40 km/s which is similar to values for the quiet corona.

1. Introduction

The transition between cool prominences and hot coronal material is not yet satisfactory explained. Cooling by Lyman radiation, ('cooling trap', Unsöld 1956), would 'rarefy' the surrounding corona. A smooth transition between cool

prominence and hot corona, however, might cause a hot 'skin'. The known structuring of prominences offers the picture that either cool inner 'threads' are surrounded by hotter outer threads, or that each individual thread has a hot 'skin'. Such problems can be treated by EUV observations using the SUMER instrument along with ground based observations.
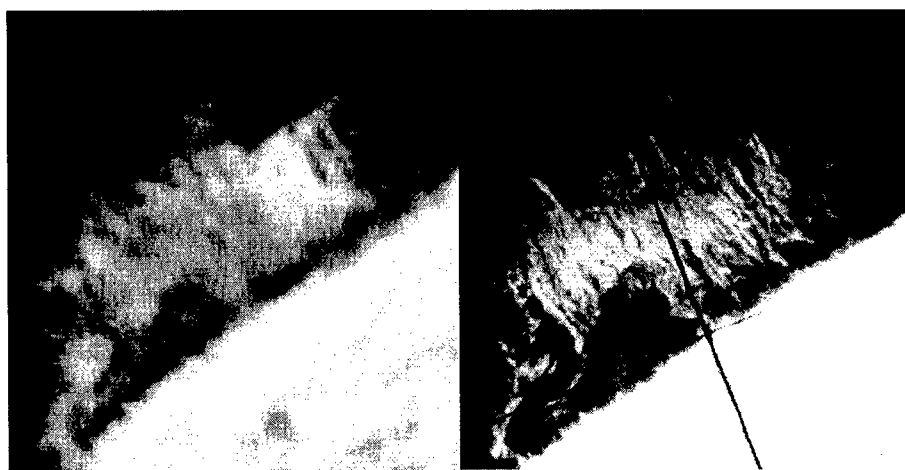
Figure 1.   He I 584Å composite image from SUMER (left) and an H$_\alpha$ image from the ground on June 28, 1996.

2.   Observations

A quiescent hedgerow-type prominence at E20°S was observed on June 28, 1996 with both German solar telescopes on Tenerife and with SUMER. The evacuated Gregory Coudé Telescope (GCT) was used to monitor the emission lines He 3888Å and H$_8$ 3889Å simultaneously with Ca$^+$ 8498Å on two CCD cameras integrating for 12 s. With the Vacuum Tower Telescope (VTT), H$_\beta$, He–D$_3$, and Ca$^+$ 8542Å were simultaneously observed with three CCD cameras integrating for 3 s. A fourth CCD took H$_\alpha$ slit yaw images. The slit widths for both telescopes corresponded to 1.5 arcsec. The influence of wavelength-dependent refraction was avoided by orienting the slits in a direction perpendicular to the horizon. At the same time, SUMER was used to observe in a first scan the He I 584Å emission simultaneously with O I 1152Å C I 1158Å, and C III 1175Å. In a second series, SUMER took He I 537Å simultaneously with N II 1085Å, S III 1077Å and S IV 1062Å. Figure 1 shows a He I 584Å composite image from SUMER together with an H$_\alpha$ slit jaw image from the VTT.

All CCD images were corrected for dark current and the gain matrices. For the ground-based spectra, the straylight aureole spectrum was subtracted. Finally, all prominence emissions were calibrated in units of the disc center intensities (Labs and Neckel 1970). The obtained emission lines were fitted by Gaussian profiles, from which shifts, widths, central intensities and integrated total emissions were determined.

Scatter plot diagrams of the shifts of simultaneously observed lines from SUMER were used to verify that the lines originate from the same prominence regions in agreement with Wilk et al. (1993). Highest velocities up to 30 km/s mainly occur in peripheral prominence regions. This is also found in the ground based spectra.

3. Line Widths

The widths of the emission lines from the ground based observations were used to separate thermal and non-thermal line broadening parameters. The ratio of the reduced 1/e-widths of H_β / Ca^+ 8542 indicates a narrow temperature regime, $7500 < K < 8000$ K, but varying non-thermal velocities, $2.5 < \xi < 6.5$ km/s.

The line widths observed with SUMER indicate much larger broadening. In particular, He 584Å has reduced widths which are 3.5 times larger than those of He D_3. Interpreting this as a saturation effect gives for the optical thickness at line center $\tau_0 = 2 \cdot 10^5$ for He I 584 and $7 \cdot 10^3$ for the fainter He I 537 line. Another explanation may be a different excitation mechanism for the various Helium lines as shown by Andretta and Jones (1997).

Also the other SUMER lines are much more broadened than expected from the optical lines. Assuming as kinetic temperature the corresponding ionization temperature, one obtains non-thermal velocities of 15–40 km/s. The range of non-thermal velocities would be smaller if the O I line is assumed 'hotter' than 18,000 K and the C III line 'cooler' than 70,000 K, in agreement with Seely et al. (1997) for the quiet corona.

The line widths depend slightly on the total emission E_{tot}, but the largest widths do not necessarily occur at the largest E_{tot}. Instead, we find significantly broad lines for faint emissions, in contrast to Wilk et al. (1993). This might arise from Doppler-shifted superposed faint emissions.
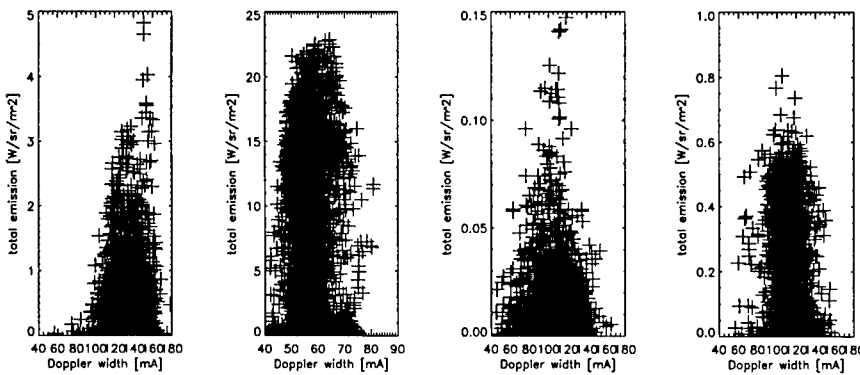
Figure 2.   Dependence of the line width on the integrated emssion. From left: C III, He I 584, S IV, N II.

4.   Integrated Line Emissions

Among the integrated line emissions E_{tot}, the ratio Ca^+/Balmer is mostly sensitive to the gas-pressure. The almost constant ratio indicates small variations of the gas pressure in the prominence. The temperature-sensitive relation of the He D_3 versus the H_β emission (from the VTT spectra) shows the known branching (Stellmacher and Wiehr 1995) caused by an easier penetration of the ionizing and exciting UV radiation at peripheral prominence regions. In the spectra from the Gregory telecope, the two violet lines He 3888 and H_8 show a ratio of 1.6 which fit the relation by Stellmacher and Wiehr (1994) for $T_{kin} \approx 8000$ K. The mean ratio of the total emissions of He 3888 (from GCT) and He D_3 (from VTT) is 0.06, being nearly half of the calculated value 0.125 by Heasley et al. (1974). The Ca^+ 8498 line shows a mean prominence emission of 0.13 of that of Ca^+ 8542, which is in good agreement with Landman and Illing (1977).

The SUMER lines show brightenings at the prominence periphery for the ratios of the C III/He I and S IV/N II emissions This brightening is only marginally
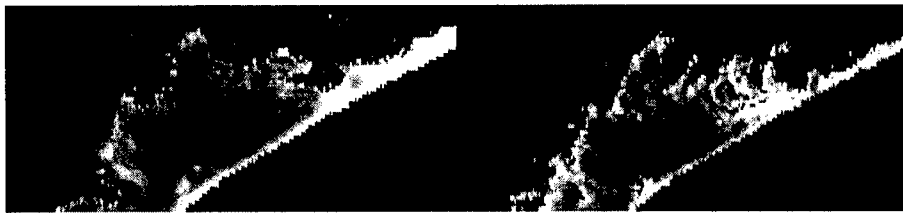
Figure 3.   Total emission ratios of C III/He I 584 (left) and S IV/N II.

caused by broader lines but essentially due to an increased emission, similar to the larger He D_3/H_β ratio at the prominence borders.

For the total emissions of He I 584 and He D_3 we find in the main body of the prominence mean values of 13 and $4 \cdot 10^3$ watt/m^2 ster. The ratio of 3.25 is 18 times higher than that calculated by Heasley et al. (1974).

References

Andretta V. and Jones H.P. 1997, ApJ, 489, 375
Heasley J.N., Mihalas D. and Poland A.I. 1974, ApJ, 192, 181
Labs D. and Neckel H. 1970, Sol. Phys. 17, 50

Landman D.A. and Illing R.M.E. 1977, A&A, 55, 103

Seely J.F., Feldman U., Schühle U., Wilhelm K. and Curdt W. 1997, ApJL 484, L87

Stellmacher G. and Wiehr E. 1994, A&A, 286, 302

Stellmacher G. and Wiehr E. 1995, A&A, 299, 921

Unsöld A. 1956, Physik der Sternwatmosphären, Springer/Heidelberg, p.700

Wilk J.E., Dere K.and Schmieder B. 1993, A&A, 273, 267

Solar Prominence Diagnostics From the November 3, 1994 Eclipse

B.H. Foing [1], J.E. Wiik, L. Duvet, N. Henrich, S. Cravatte, F. David, B. Altieri, T. Beaufort, L. Ligot

ESA Space Science Department, ESTEC, The Netherlands

E. Maurice

Marseille Observatory, France

Abstract. We report results on solar prominences from our observations of the November 3, 1994 total solar eclipse from the North Chile alteplano. From the military base at Putre, we used our transportable CCD camera and telescope, as well as support photographic digitised observations from Putre and Parinacota volcano. The variation of density and equivalent temperature were derived in coronal holes (plumes and interplumes) and in equatorial streamers. We obtained images from the inner to the outer corona, as well as low-resolution spectra of prominences and of the inner corona. We present the analysis of images and spectra of prominences in the Balmer, He I and Ca II lines, and in the Thomson scattered continuum.

1. The Total Solar Eclipse of November 3, 1994 and SSD Experiments

The total solar eclipse of November 3, 1994 was observed with ESA Solar System Division (SSD) experiments from the Putre, Chile military base, situated on the central line of totality. The totality band was 173 km, and the eclipse magnitude was 1.046, due to the apparent semidiameter of the Sun of 16'07.43" and of the Moon 16'43.07". The motion of the Moon relative to the Sun was 0.446 arc-sec/s.

The aim of our observing campaign was to obtain images of the inner corona, and to measure spectra of the inner corona and protuberances on the observed limb (Foing et al. 1995, 1996a, b). The CCD experiment developed at the ESA SSD included a transportable automatic 25 cm aperture Meade LX200 telescope, used with a focal reducer from f/10 to f/6.3 in order to include a full diameter on the length of our detector, a Peltier-cooled Photometrics scientific CCD camera. The detector is a 1284x1024 pixel array of 16 micron pixels, with Multi Pinned Phase technology yielding very low dark current noise. The data were read through a controller at high rate up to 2 Mb/s, and transferred to a Macintosh memory. Automatic scripts were developed and tested before the

---

[1] Also at: Institut d'Astrophysique Spatiale, CNRS, France

eclipse to be triggered 20 s before second contact of totality, in order to measure optimally different phases from last limb photospheric emission, chromospheric flash variations, and deeper exposures of the inner and middle corona.
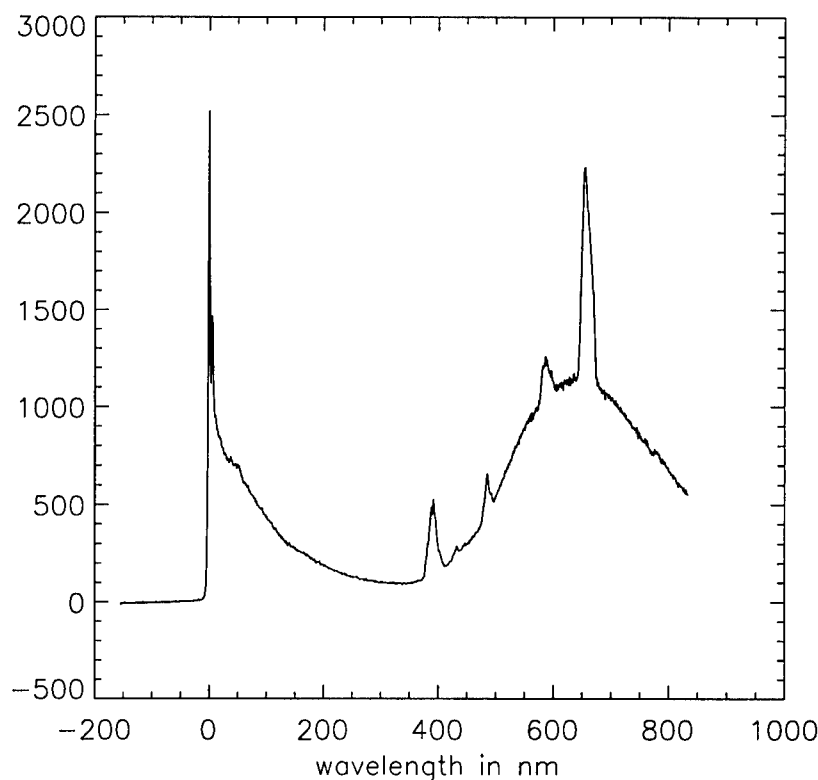
Figure 1.   One frame obtained with our CCD and transportable tele-
scope experiment.   The zero order image (below) shows equatorial
streamers, prominences and radial plume structures in the polar coro-
nal hole. The objective grating first order (above) permits us to mea-
sure the spectrum of the inner corona, and monochromatic images of
prominences in the lines of Ca II, Hγ, Hβ, He D and Hα.

We used a transmission objective grating with 200 grooves/mm blazed at 10° for 476 nm. This permits us to measure simultaneously an image in zero order and a low resolution spectrum of the innner corona. The spectral dis-persion was determined consistently using the constructor parameters and the distance from the spectro-imager to the detector, leading to a dispersion of 0.95 nm/pixel.

2. Data Acquisition and Reduction

For the intensity calibration of the image we estimated the areas free from over-lapping from the spectral orders, made corrections for the opening of the mechanical shutter at very fast exposures, made corrections for the flat field response, and estimated the straylight correction. A bias correction from a median of several biases in order to avoid cosmic rays was done. The flat field variations due to the vignetting of the optical system and the grating support were corrected for (Duvet 1996).
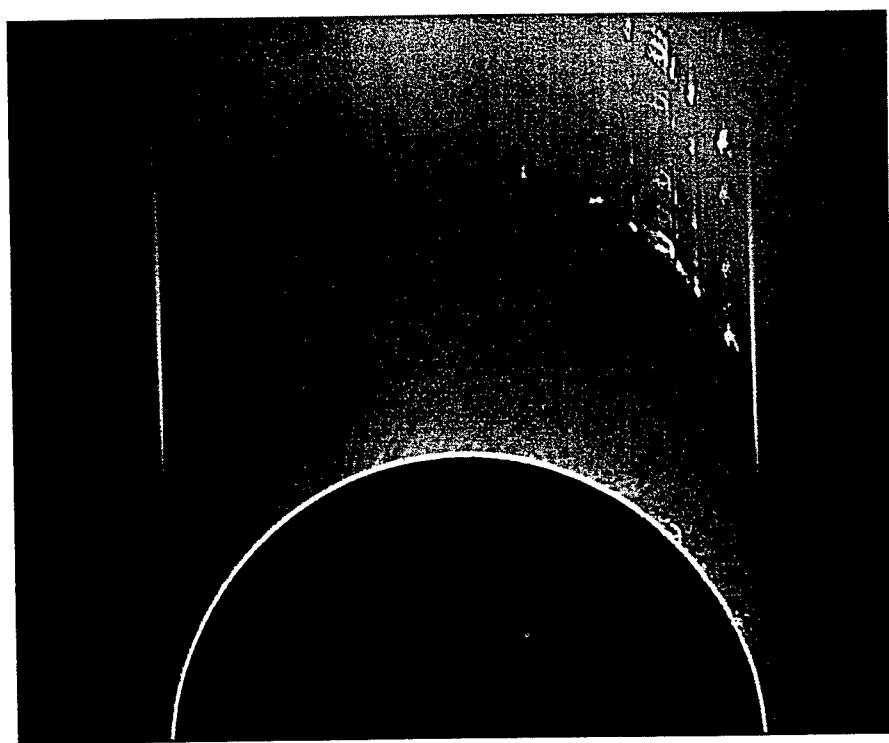
Figure 2.   CCD cross section through a prominence along the axis of wavelength dispersion. The signal below 320 nm comes from the zero order image and permits mapping of the Thomson diffusion. This allows us to distinguish the vertical extent of the prominence and to measure the decay of electron density with height. The 1st order spectrum above 390 nm shows the line emission in Ca II, Hγ, Hβ, He I D3, and Hα, respectively.

3.   Solar Prominence Observations

A preliminary analysis of the CCD images shows several coronal characteristics. First, the respective centers and cardinal axes of the Moon and the Sun were determined. From the larger apparent diameter of the Moon and limb contour we determined exactly the moon's center. For the Sun, the parameters of the second contact were used. Also, observations of prominences in Ca II K from Meudon and Coimbra on the eclipse day (Mouradian et al. 1995) allowed us to identify and locate five prominences measurable on our frames. The second contact could then be confirmed as well as the center and orientation of the Sun. In projection we could determine for the larger arch prominence a height of 37,000 km. We also detected two other prominences, not specifed by Mouradian et al. Structures at larger scale are also visible on the image. At the pole one notices almost radial lines, which are polar plumes. A comparison with an image taken by the Yohkoh satellite shows their link with polar coronal holes. To the east one notices a streamer visible in the low corona. Large-field photographic images show at the moment of the eclipse a typical configuration of solar minimum, with polar coronal holes and two near-equatorial streamers. Spectra of the prominences show the dominate lines from Ca II, Hγ, Hβ and, especially, He D3 and Hα. High resolution monochromatic images of the prominences were extracted in these lines. They show different structures than the continuum (electron Thomson scattering) indicating optical thickness and 3D radiative transfer effects in the prominences.

References

Duvet, L., D.E.A. June 1996, Thesis report, ESTEC/Univ. Paris, 6

Foing, B.H. 1995, Total Solar Eclipse of 3rd November 1994: Observations and Preliminary Results, Ann. Geophys., 13, Part III, C664

Foing, B.H. et al. 1996a, Solar Eclipse and Transition Region Camera Results, Ann. Geophys., 14, Part III, C735

Foing, B.H. et al. 1996b, Results from 3 November 1994 Solar Eclipse, Proc. IAU Coll., Kluwer Acad. Pub., Dordrecht, Holland, p. 415

Mouradian, Z. et al. 1995, Solar Phys. 158, 379

SUMER/SOHO Filament Observations in Selected Lyman Lines

B. Schmieder[1]

Observatoire de Paris, Section Meudon, F 92195 Meudon, France

T. Kucera[2]

NASA, GSFC, MD 20771, USA

P. Heinzel

Astronomical Institute, CZ 25165, Ondřejov, Czech Republik

J.-C. Vial

Institut d'Astrophysique Spatiale, CNRS/Université Paris XI, Bât. 121, 91405 Orsay Cedex, France

Abstract.
    On September 21, 1996 a filament located in a region close to an enhanced network was observed with the SOHO SUMER and CDS instruments. Four Lyman lines have been detected ($L\delta$, $L\epsilon$, L-6, L-7) by SUMER in the raster mode. We have corrected the spectral data for flatfield and destreching and made wavelength and absolute intensity calibrations. In all these lines we detect a central absorption and an asymmetry in the intensity of the two peaks. Preliminary NLTE computations indicate that these Lyman profiles and their absolute intensities can be reproduced with the existing models provided that we take into account a prominence-corona transition region (PCTR).

1. Introduction

The diagnostic potential for quiescent prominences of Lyman lines has been evidenced in the works of Gouttebroze et al. (1993) and Heinzel et al. (1994). These authors have shown, for instance, how the Lyman alpha and the Lyman beta lines (differently radiatively dominated) could be indicators of temperature and pressure (at higher values).
    In the case of (radially) moving prominences, Gontikakis et al. (1997a, b) have shown evidence that the Lyman beta profile is still sensitive to Doppler effects, even if less so than Lyman alpha.

[1]Institute of Theoretical Astrophysics, P.O. Box 1029, Blindern, N-0315 Oslo, Norway

[2]Applied Research Corporation, 8201 Corp. Drive, Landover, MD 20785, USA
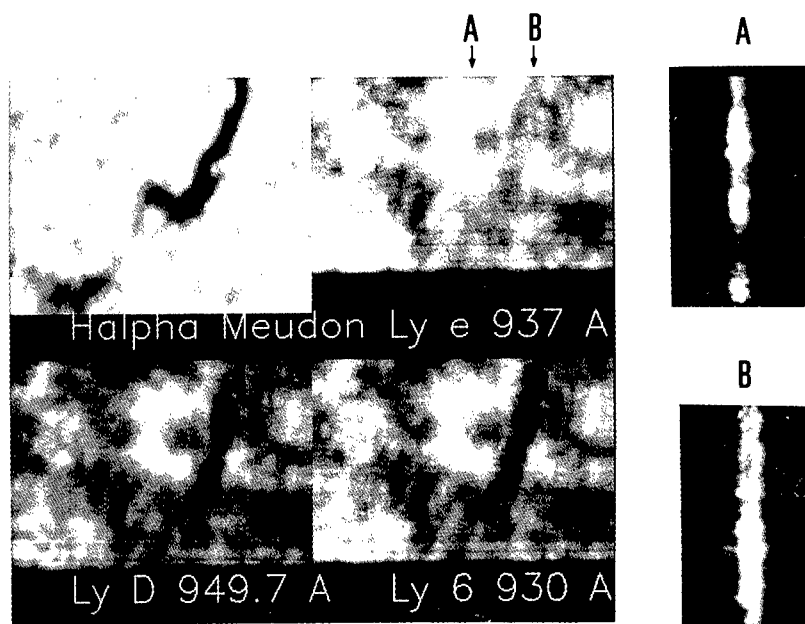
Figure 1.   Left panels (a): Observations of the filament on September 21, 1996: at Meudon in Hα and with SUMER on SOHO in Lyman lines (only 100 pixels along the slit are used in these images). The Lyman line intensities are averaged over 3 pixels at the profile center. The arrows indicate the positions A and B of the spectra shown in the right panels (b): examples of Lyman spectra observed by SUMER in A through the network and in B in the filament.

Going higher in the Lyman series, we expect that the shapes and intensities of these optically thick lines can provide information on the temperature, radial velocity and density across the observed structure. We stress that this information is not limited to low temperatures only.

2.   SUMER Observations and Data Reduction

The target of SUMER on board the SOHO satellite was part of a North-South filament (S6-12, E5), close to a bright network cell (see Hα spectroheliogram from Meudon, Figure 1a). SUMER has been described by Wilhelm et al. (1997). SUMER was rastering a region 120 by 150 arc sec with a raster-step of 3 arc sec. The exposure time was 60 sec with the slit-width being 1 arc sec. In the wavelength range 920 to 950 Å, seven windows of 50 × 120 pixels each were displayed on the detector A, with one window (949.7 Å) being on the bare part of the detector. Seven lines have been observed: S VI at 944.54 and 933.380 Å, N IV at 923.220 Å and four lines of the Lyman series: Lδ (949.74), Lε (937.80), L-6 (930.75) and L-7 (926.23 Å).

We first corrected the observations by a flat-field image obtained on Septem-
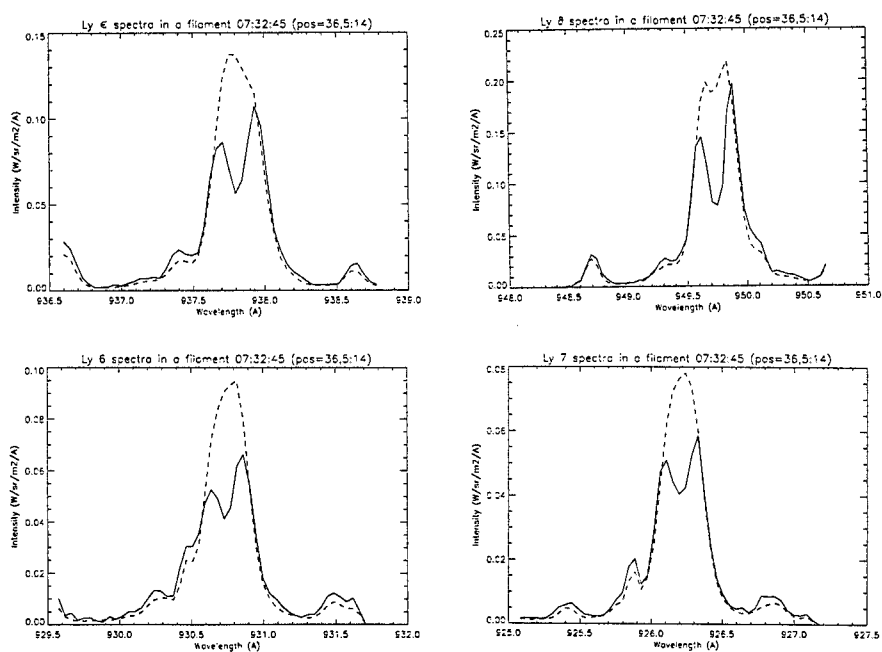
Figure 2.   Examples of profiles in the Lyman series. The dashed profiles correspond to the background emission, obtained by suming 5 spectra. The solid ones correspond to the filament (average profile over 10 pixels along the slit).
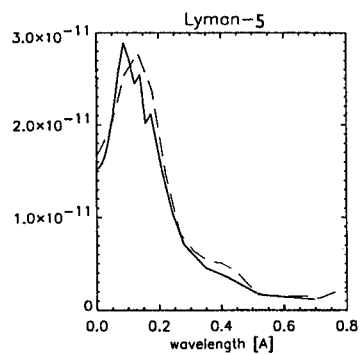
Figure 3.   Fit of the observed Lε profile (dashed line) with the theoretical one (solid line).

ber 24, 1996. The curvature of the lines ('inverse-cushion' distortion) depends on their position on the detector. The 'destretching' of the spectra was done with the SUMER analysis software procedure **destrech.pro** provided by T. Moran.

Wavelength calibration was done by using the Lyman lines observed on the quiet Sun nearby. The profiles were fitted by gaussians. We derived the mean dispersion: 0.04445 Å/pixel. We found that the measured wavelengths are shifted relative to the standard wavelengths by quantities less than 0.015 pixel, a value which corresponds to one third of a pixel (4 km/s).

For the intensity calibration we used the procedure of Wilhelm et al. (1997) called **radiometry-a**. Our results are consistent with the spectra obtained by Wilhelm for the quiet Sun but our values of the line maxima are higher by a factor 1.3, a discrepancy that we explain by the presence of a network boundary in the field (Figure 1a, b).

3.   Comparison of Observed and Theoretical Profiles

In Figure 2 we give examples of the four Lyman lines that were observed in the filament. All filament profiles of Lyman lines have central reversals because of self absorption. They also are asymmetrical (Schmieder et al. 1998). NLTE computations (see Heinzel 1998, these proceedings) show that an isothermal model cannot reproduce profiles of all lines. Using a 1D horizontal slab model and the NLTE tranfer code based on the MALI-method, we show that a reasonable fit for $L\epsilon$ can be obtained with a PCTR model ($T_c = 7000$ K and $T_s = 14000$ K, $D = 20000$ km, $p = 0.1$ dyn cm^{-2}, $v_t = 10$ km s^{-1}) (Figure 3). However, to reproduce all lines simultaneously one has to apply an optimization technique to construct the filament model.

References

Gouttebroze, P., Heinzel, P. and Vial, J.-C. 1993, A&AS, 99, 513

Heinzel P., Gouttebroze P. and Vial J.-C. 1994, A&A, 292, 656

Gontikakis, C., Vial, J.-C. and Gouttebroze, P. 1997a, Solar Phys., 172, 189

Gontikakis, C., Vial, J.-C. and Gouttebroze, P. 1997b, A&A, 325, 803

Schmieder, B., Heinzel, P., Kucera, T. and Vial, J.-C. 1998, Solar Phys., in press

Wilhelm K. et al. 1997, Solar Phys. 170, 75

2-D Radiative Transfer Simulations with Angle-Dependent Partial Frequency Redistribution

A. B. Gorshkov

Sternberg Astronomical Institute, 119899 Moscow, Russia

P. Heinzel

Astronomical Institute, 25165 Ondřejov, Czech Republic

Abstract. We demonstrate how the angle-dependent redistribution function can be incorporated into the 2-D transfer modelling of solar prominences. Some preliminary numerical simulations have been performed and we present their results by comparing the emergent hydrogen Lα line profiles computed with the angle-averaged and angle-dependent redistributions.

1. Introduction

Standard angle-averaged redistributions are currently used for Lyman lines in prominences and prominence-like structures, both in 1-D (Gouttebroze et al. 1993, Heinzel 1995), as well as in 2-D cases (Paletou 1995). Since 2-D transfer computations can explicitly account for strong anisotropies of the incident solar radiation, the angle-dependent approach seems to be more appropriate in such cases. In the present contribution we investigate this problem and demonstrate the differences between angle-averaged and more rigorous angle-dependent 2-D simulations for the case of prominences.

To achieve this, we have applied a 2-D code of Gorshkov (1996) to the problem of radiative transfer in solar prominences (Figure 1) for the case of a 4-level plus continuum HI atom. The main features of the code are: Multilevel Accelerated Lambda Iterations (MALI) scheme with Partial Frequency Redistribution (PRD) in resonance lines; modified long-characteristics method (timing is linearly proportional to the number of grid points) for 2-D solution of Radiative Transfer Equation (RTE); an ability to calculate angle- and height-dependent boundary conditions based on observational data.

2. Basic Formulae

2.1. Angle-Dependent PRD

In our calculations we used the redistribution function in the form:

$$R(\nu', \nu, \Theta) = \gamma R_{II}(\nu', \nu, \Theta) + (1 - \gamma)\phi(\nu)\phi(\nu'),$$
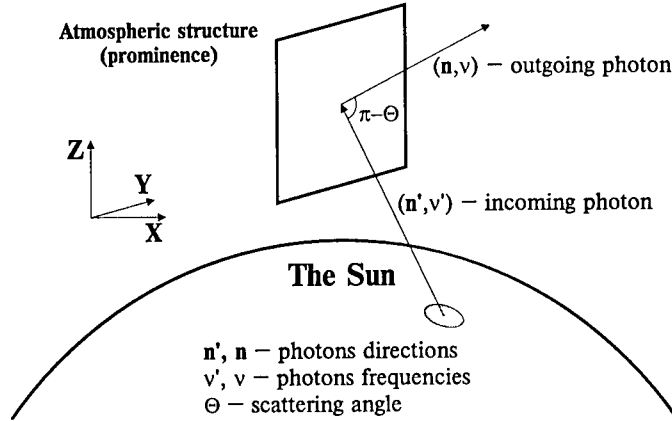
Figure 1.   Photon scattering geometry.

where γ is the coherence parameter, Θ is the scattering angle between directions of the incoming and the outgoing photons ($\mathbf{n}'$ and $\mathbf{n}$, correspondingly), and R_{II} represents Hummer's (1962) function for the case of purely coherent scattering in the atom's frame.

Similarly to the angle-averaged case, PRD effects are taken into account by introducing the ratio of emission and absorption coefficients for a given line transition ij ($i < j$):

$$\rho_{\nu n} \equiv \frac{\psi_{\nu n}}{\phi_\nu} = 1 + \gamma \frac{n_i}{n_j} \frac{B_{ij}}{P_j} (\bar{R}_{II}(\nu, n) - \bar{J}),$$

where n_i and n_j are the populations of atomic levels i and j, B_{ij} is the Einstein coefficient for absorption, P_j represents a probability for an atom to leave the level j; $\bar{J} = (4\pi)^{-1} \int_0^\infty \int_0^{4\pi} I_{\nu' n'} \phi_{\nu'} d\nu' d\Omega'$ is the mean integrated intensity and $\bar{R}_{II}$ stands for the scattering integral (see Hubený 1985). Contrary to the *standard* PRD, ρ now depends on the angle Θ because $\bar{R}_{II}$ has the following form:

$$\bar{R}_{II}(\nu, n) = (4\pi\phi_\nu)^{-1} \int_0^\infty \int_0^{4\pi} R_{II}(\nu', \nu, \Theta) I_{\nu' n'} d\nu' d\Omega', \qquad (*)$$

where the redistribution function is (x, x' are frequencies counted from the line center and expressed in Doppler units):

$$R_{II}(x', x, \Theta) = \begin{cases} \frac{g(\Theta)}{\pi \sin \Theta} \exp\{-[\frac{1}{2}(x - x')]^2 \csc^2 \frac{\Theta}{2}\} H[a \sec \frac{\Theta}{2}, \frac{1}{2}(x + x') \sec \frac{\Theta}{2}] \\ \qquad\qquad\qquad\qquad\qquad\qquad\qquad\qquad 0 < \Theta < \pi \\ \frac{1}{\sqrt{\pi}} H(a, x') \delta(x - x') \qquad\qquad\qquad\qquad \Theta = 0 \\ \frac{a}{2\pi^{3/2}} exp\left\{-(\frac{x-x'}{2})^2\right\} \left[(\frac{x+x'}{2})^2 + a^2\right]^{-1} \qquad \Theta = \pi \end{cases}$$

Here $H(a,x)$ is the Voigt function and a the damping parameter. Examples of the function $R_{II}(x',x,\Theta)$ are shown in Figure 2. Since the function varies very sharply with Θ and x', we used appropriate Θ- and x'-dependent frequency quadratures for the evaluation of the scattering integral (*).
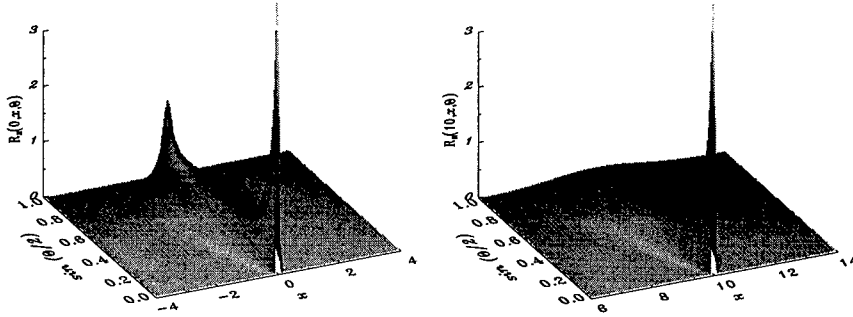
Figure 2.   Function $R_{II}(x',x,\Theta)$ for $x' = 0$ (left) and $x' = 10$ (right).

2.2.   Changes in the Formal Solution of RTE

Since we need to know specific intensities I_ν to calculate the integral (*), the following changes in a standard Feautrier scheme of the formal solution of RTE are necessary:

$$d^2u/d\tau^2 = u - \bar{S} + d\Delta S/d\tau,$$
$$d^2v/d\tau^2 = v - \Delta S + d\bar{S}/d\tau$$

Here $u = (I_\nu^+ + I_{-\nu}^-)/2$ and $v = (I_\nu^+ - I_{-\nu}^-)/2$ are Feautrier variables; $\bar{S} = (S_\nu^+ + S_{-\nu}^-)/2$ and $\Delta S = (S_\nu^+ - S_{-\nu}^-)/2$ represent averaged sum and difference of source functions in positive $(+)$ and negative $(-)$ directions. The scale of optical depths τ is calculated in a positive direction. To solve these transfer equations, we introduced corresponding changes in an improved Feautrier method of Rybicki and Hummer (1991).

3.   Results and Conclusion

Using the above-described approach, we have computed 2-D transfer for the prominence model having the following parameters: dimensions $\Delta Z = 2\,000$ km, $\Delta Y = 2\,000$ km, low boundary at the height $H = 10,000$ km above the solar surface, temperature $T = 8\,000$ K, gas pressure $P_{gas} = 0.05$ dyn/cm^2 turbulent velocity $V_{turb} = 5$ km/s. The angle-dependent incident radiation field was used similarly as in Gorshkov (1996), where other details of our numerical procedure are described. As a result of preliminary simulations, we present a comparison of emergent Lα line profiles (taken in the center of the slab) for the cases of angle-averaged and angle-dependent PRD (see Figure 3). The main effect seen here is a lowering of the intensity in the line core. As a next step in
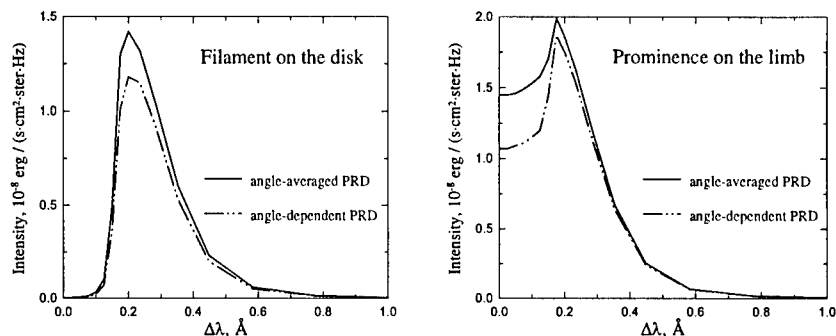
Figure 3.   Calculated emergent profiles for the Lα line as seen on the disk (left) and on the limb (right).

this work we intend to demonstrate the influence of the angle-dependent PRD on spectral diagnostics of prominence plasmas.

Acknowledgments.   A.B.G. greatly appreciates the support from the colloquium organizers which enabled him to attend the meeting. Travel expenses were covered from grant GACR 1199.

References

Gorshkov, A. B. 1996, in N. Mein and S. Sahal-Brechot (eds.), Science with THEMIS, Proc. Forum THEMIS, Observatoire de Paris-Meudon, p. 273

Gouttebroze, P., Heinzel, P. and Vial, J.-C. 1993, A&AS, 99, 513

Heinzel, P. 1995, A&A, 299, 563

Hubený, I. 1985, Bull. Astron. Inst. Czech, 36, 1

Hummer, D. G. 1962, MNRAS, 125, 21

Paletou, F. 1995, A&A, 302, 587

Rybicki, G. B. and Hummer, D. G. 1991, A&A, 245, 171

Modelling of Non-Uniform Prominence Slabs

P. Heinzel

Astronomical Institute, Academy of Sciences of the Czech Republic CZ–25165 Ondřejov, Czech Republic

U. Anzer

Max-Planck-Institut für Astrophysik, Postfach 15 23 D–85740 Garching, Germany

Abstract. We present new slab models for quiescent prominences in which both the condition of magnetohydrostatic equilibrium as well as NLTE are fulfilled. Using the Kippenhahn-Schlüter model, a unique relation between the components of the magnetic field on one hand and the gas pressure and width on the other is established for a given uniform temperature. We construct a grid of such NLTE models and compare them with the set of isothermal-isobaric models of Gouttebroze et al. (1993).

1. Introduction

An up-to-day study of NLTE properties of prominences has been recently performed by Gouttebroze et al. (1993 – GHV). For each of their 140 isothermal-isobaric models they calculated the emergent spectrum in various hydrogen lines and the Lyman continuum. They also derived correlations between prominence plasma parameters and the emitted radiation (Heinzel et al. 1994 – HGV). These isobaric slabs, however, cannot be in static equilibrium with their surroundings since: a) the vertical pressure scale-height for prominence material is a factor 100 smaller than that of the corona, and b) all high-density prominences would require unreasonably large values of the coronal pressure to confine them in the horizontal direction. Therefore, magnetic fields are definitely needed to support and confine the prominence plasma. In order to demonstrate how physical and optical properties of non-uniform models compare to those for isobaric ones, we perform here NLTE calculations for Kippenhahn-Schlüter (K-S) type prominences with the gas pressure varying according to the magnetohydrostatic equilibrium.

2. Pressure Equilibrium

The simplest magnetic equilibrium configuration which one can consider is the isothermal K-S-like configuration (see Anzer 1995). Such 1D magnetic slab configurations can also be described in terms of the column-mass coordinate, m,

as done by Heasley and Mihalas (1976). With

$$dm = -\rho dx \tag{1}$$

one gets the pressure variations inside the slab in the form

$$p(m) = 4p_c \frac{m}{M}(1 - \frac{m}{M}) + p_0, \tag{2}$$

where p_0 is the gas pressure at the outer boundary (coronal pressure) and ρ is the plasma density. This formulation has the advantage that slabs with finite width which extend from $m = 0$ to $m = M$ can be treated quite naturally; in addition, it is valid for arbitrary temperature structure. Moreover, the column-mass scale represents a standard coordinate system for radiative transfer calculations. The magnetic field components must then satisfy the relations

$$p_c = \frac{B_{z1}^2}{8\pi} \tag{3}$$

and

$$M = \frac{B_x B_{z1}}{2\pi g} \tag{4}$$

where B_{z1} represents the vertical field-component at the prominence surface, which is defined by $x = x_1$. p_c is the central gas pressure (see Anzer 1995).

In the present investigation we want to compare physical and radiative properties of isobaric slabs with those of K-S type which have the same total column mass and the same mean gas pressure (in order to see clearly the effect of various pressure profiles, we consider here only isothermal slabs). We shall define the mean pressure by the relation

$$\bar{p} = \frac{1}{M} \int_0^M p \, dm, \tag{5}$$

which gives

$$\bar{p} = \frac{2}{3}p_c + p_0. \tag{6}$$

The thickness of the slab, which is given by $D = 2x_1$, can also be obtained from (see Heasley and Mihalas 1976)

$$D = \int_0^M \frac{dm}{\rho} \tag{7}$$

once $\rho(m)$ has been calculated from the constructed NLTE model. For the comparison of isobaric and K-S type configurations we also evaluate mean values of the gas pressure, hydrogen density and electron density using Eq. (5). To compute the emission measure, we use here the definition

$$EM = \int_0^M n_e^2 \, dm/\rho. \tag{8}$$

3. Statistical Equilibrium

Both isobaric and K-S type models are assumed to satisfy the statistical equilibrium, i.e., the hydrogen excitation and ionization is computed consistently with the radiation fields in all relevant transitions (for description of our NLTE treatment see Heinzel 1995). We use a five-level plus continuum hydrogen model atom which is accurate enough to evaluate the ionization structure, gas density and the emergent radiation in the Lα, Lβ, L-cont and Hα transitions. We use a depth-dependent PRD treatment of Lyman lines as in GHV. We evaluate both isobaric and K-S models with the same NLTE code which allows us to make internally consistent comparisons.

4. Model Calculations

We have performed NLTE calculations for different isobaric and K-S slab configurations with temperature $T = 8000$K, and microturbulent velocity $v_t = 5$km/sec (used only for the line broadening). The mean gas pressure was set to be $\bar{p} = 0.05, 0.1, 0.5$ dyn/cm^2 and M was chosen in such a way as to give us the geometrical thickness $D = 500$ and 5000 km. Isobaric models with these parameters are those considered by GHV. To evaluate K-S models, we just replace the mean gas pressure by $p(m)$ according to Eq. (2), with $p_0 = 0.01$ dyn/cm^2 and with $p_c = 3(\bar{p} - p_0)/2$; the values of $\bar{p}$ and M are then taken from the corresponding isobaric slab model.

5. Results and Conclusions

For each model we have computed the relative deviations (in %) of mean values of all physical and optical quantities. The deviations between individual parameters are defined as

$$\Delta[\%] = \frac{par(KS) - par(isobar)}{par(isobar)} \times 100. \tag{9}$$

All these parameters as evaluated for the K-S configuration differ only slightly from those computed with corresponding isobaric models. The differences are typically smaller than 5%. Only the mean density of the hydrogen first-level population differs by about 10%, and also the intensity of the Lyman continuum at its head is rather different for models with high pressure and large width (but still not exceeding 16%). Very important is the fact that the deviation of the emission measure, EM, is negligible. We demonstrate this in Figure 1 which compares the previously-found correlation of GHV and the newly computed one for K-S-type, non-uniform slabs. This result means that neither EM nor the Hα integrated intensity are sensitive to the pressure (density) variations in K-S slabs. And since the mean electron densities agree quite well, one can also use the correlation curve of GHV or HGV for K-S-type models and get the *mean* electron density. Alternatively, for a given mean electron density, D can be obtained from EM. However, this value of D is smaller than that defined by Eq. (7). To be more consistent with isobaric models (and to get about the same D), one has to define D for K-S models as $D = M/\bar{p}$.

Finally, our analysis suggests an interesting possibility to derive the magnetic field which is needed for a K-S-type magnetic equilibrium directly from the mean value of gas pressure, M and p_0, using the formulae of Section 2. $\bar{p}$ and M have to be determined from spectral diagnostics, where one can use – to a high degree of accuracy – the simple isobaric models.
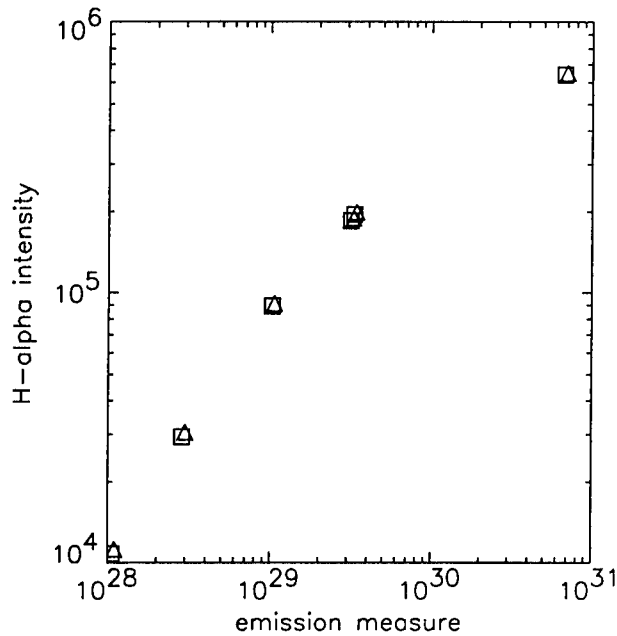
Figure 1.   Integrated Hα intensity vs. emission measure EM (in CGS units). Squares – K-S models, triangles – isobaric models.

References

Anzer, U. 1995, Solar Phys., 161, 49

Gouttebroze, P., Heinzel, P. and Vial, J.-C. 1993, A&AS, 99, 513

Heasley, J.N. and Mihalas, D. 1976, ApJ, 205, 273

Heinzel, P. 1995, A&A, 299, 563

Heinzel, P., Gouttebroze, P. and Vial, J.-C. 1994, A&A, 292, 656

Spectroscopic Study of a Quiescent Prominence

Y. D. Park

Korea Astronomy Observatory, San 36-1, Whaam-dong, Yuseong-gu, Taejeon 305-348, Korea

H. S. Yun

Department of Astronomy, Seoul National University, Seoul 151-742, Korea

K. Ichimoto

Solar Physics Division, National Astronomical Observatory of Japan, Mitaka, Tokyo 181, Japan

K. J. Sim and Y-J. Moon

Korea Astronomy Observatory, San 36-1, Whaam-dong, Yuseong-gu, Taejeon 305-348, Korea

Abstract. We have analyzed a set of spectra of Hα and CaII H & K lines taken from a quiescent prominence with the G1 CCD camera attached to a 25 cm coronagraph at the Norikura Coronal Station, the National Astronomical Observatory of Japan. From these lines we have determined temperature, turbulent velocity and electron density at various locations on the prominence. The final analysis shows that the averaged temperature of the prominence is about 8600K with mean turbulent velocity of 7.5 km/s and with a mean electron density of $< n_e > = 2.4 \times 10^{10}$ cm^{-3}.

1. Introduction

Spectroscopic studies of prominences have been made by numerous workers (e.g., Hirayama 1971, 1979; Engvold 1978, 1981; Heasley et al. 1974; Landmann 1981, 1985; Zhang et al. 1987). To understand their physical and morphological characteristics, it is desirable to know the detailed distribution of physical parameters of individual prominences.

In the present paper, we present two dimensional distributions of temperature, non-thermal velocity and electron density determined from a quiescent prominence.

2.   Observation and Data Analysis

Observations were made with the G1 CCD camera attached to a 25 cm cor-
onagraph/Littrow type spectrograph at the Norikura Coronal Station of the
National Astronomical Observatory of Japan. The observed prominence was of
the hedgerow type, which appeared on August 16, 1992 with a position angle
of 110°. The prominence kept the same shape during the observation and its
maximum projected height was more than 40,000 km. A set of spectra of Hα
(6562.81Å), CaII H (3933.68Å) and K (3968.47Å) have been taken of the promi-
nence with spectral resolution of 0.0115Å/pixel at the 2nd order of the Hα line
and spatial resolution of 0.3 arc sec/pixel. In taking these spectra the slit was
placed in parallel to the solar limb at 6 different heights on the prominence, each
being separated by 10 arc sec. The individual spectra were taken 30 seconds
apart for about half an hour, during which time the slit was kept fixed. In order
to determine physical parameters of the prominence, the observed spectra were
analyzed in detail.

   We have measured the observed line widths of Hα, CaII H and K to estimate
the temperature and have utilized the Goldberg-Unno method for determination
of the Doppler width of the Ca II H and K lines (Gallegos and Machado 1973).
In this way we derived non-thermal velocity, temperature and column density of
neutral hydrogen and Ca II atoms at various locations in the prominence traced
by the slit. For this analysis we excluded the spectra closest to the solar limb
because these spectra were strongly affected by the photospheric light.

3.   Results and Discussion

Table 1 shows mean values of physical parameters derived from the observed
prominence. The non-thermal velocity ranges from 6 km/s to 10 km/s with a
mean value of 7.5 km/s (Figure 1a). The temperature ranges from 4000K to
12,000K with a mean value of 8600 K (Figure 1b). Figure 1 (c) and (d) show the
column density distributions of Ca II and hydrogen in the observed prominence.
The mean electron density of the prominence is found to be $< n_e > = 2.4 \times 10^{10}$
cm^{-3} with a hydrogen ionization ratio of $n_{HII}/n_{HI} = 0.5$ and with an effective
thickness of $l = 1000$ km, in good agreement with those of Gallegos and Machado
(1973), Engvold (1976) and Hirayama (1990).

   The mean temperature of our prominence turns out to be a little higher
than generally favored 5000K $\sim$ 7500K. This could be accounted for by the
following two considerations. First, our observed spectra of various lines had
to be recorded at different times, because the CCD camera and spectrograph
covered only a limited range in wavelength. Second, as Kubota (1980) reported,
about 12.5% of prominences reveal a central reversal in the Ca II K line due
to absorption of light coming from the surface layer of prominences. Hirayama
(1990) demonstrated that the self-absorption effect should be taken into account
in the determination of prominence temperatures when using Hα and/or Ca II K
lines. In the present work, however, the self-absorption effect did not need to be
taken into consideration since none of the spectral lines showed central reversal.
We plan to continue our studies of quiescent prominences by two dimensional
spectroscopy which will allow us to include also more optically thin lines.
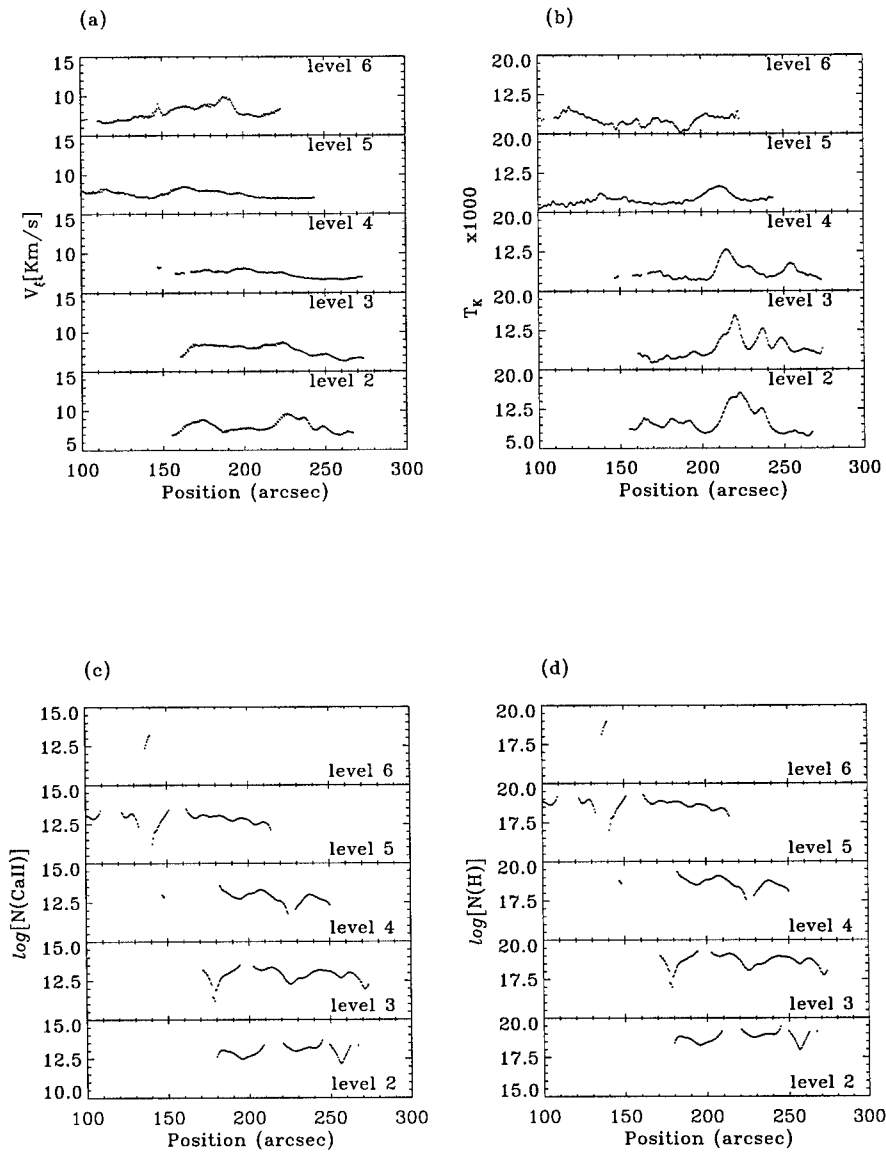
Figure 1. Distributions of (a) turbulent velocity, (b) kinetic temperature, (c) Ca II column density, and (d) hydrogen column density at different heights.

Table 1.   Averaged values of physical parameters of our observed quiescent prominence deduced from Hα and Ca II H & K line widths and the intensity ratio of CaII H & K line center.

Physical parameters	Averaged values
T_k	$8600 \pm 1200\ K$
V(Doppler)	$3.5\ km/s$
$V_\xi{}^a$	$7.5 \pm 0.6\ km/s$
$\tau_K{}^b$	1.0
log [N(Ca II)]	$12.88(\ \pm 0.41\ )\ cm^{-2}$
log [N(H)]	$18.66(\ \pm 0.41\ )\ cm^{-2}$
n_e	$2.4 \times 10^{10}\ cm^{-3}$

[a]Non-thermal velocity
[b]Optical depth of Ca II K

References

Engvold, O. 1976, Solar Phys., 49, 283

Engvold, O. 1978, Solar Phys., 56, 87

Engvold, O. 1981, Solar Phys. 70, 315

Gallegos, H. G. and Machado, M. E. 1973, Solar Phys., 31, 427

Heasley, J. N., Mihalas, D. and Poland, A. I. 1974, ApJ, 192, 181

Hirayama, T. 1971, Solar Phys., 19, 384

Hirayama, T. 1979, Physics of Solar Prominences, E. Jensen et al. (eds.), Oslo, p. 4

Hirayama, T. 1990, in Dynamics of Quiescent Prominences, V. Ruzdjak and E. Tandberg-Hanssen (eds.), Springer-Verlag, New York, p. 187

Kubota. J. 1980, Publ. Astron. Soc. Japan, 32, 359

Landman, D. A. 1981, ApJ, 251, 768

Landman. D. A. 1985, ApJ, 290, 369

Zhang, Q. Z., Livingstone, W. C., Hu, J. and Fang, C. 1987, Solar Phys., 114, 245

Evolution of Complex Filaments

Cristiana Dumitrache

Astronomical Institute of Romanian Academy, 75212 Bucharest, Str. Cutitul de Argint 5, Romania

Abstract. This study focusses on the less studied aspects of filaments evolution: the coupling of two or more filaments to form a complex filament and also the split of one such filament into many components. This phenomenon was first observed by d'Azambuja – we apply statistical mathematical methods to obtain evolutionary sequences and detect the complex filaments.

1. Introduction

During its life a filament may joint with others and later separate from them, each one following its peculiar evolution. In their work d'Azambuja and d'Azambuja (1948) revealed this kind of phenomenon and called it complex filaments, "des filaments complexes" in French. He also explained the difficulties in studying such phenomena from an observational point of view. It is very difficult to know, after the junction followed by a separation of the filaments, which part of which filament goes in one direction or in another.

By applying a cluster analysis method we can detect, in a computational way, the coupling and splitting of filaments and reveal the aspects linked to photospheric and chromospheric activity. We focus on these less studied aspects of the filament activity. We think that the evolution of a complex filament could be an example of magnetic reconnection and we may also learn new aspects about the prominences' magnetic field.

2. Data and Method

A computation based on a cluster analysis method led us to find the evolutionary sequences of filaments (see Dumitrache, Dinulescu and Priest 1994 or Dumitrache 1997) and then to detect the sequences that contain complex filaments. This method of computation strongly depends on the differential rotation laws of filaments. We have used d'Azambuja's law:

$$\omega = 1.22 - 1.40 \sin^2\phi - 1.33 \sin^4\phi$$

from which we have subtracted the synodical differential rotation (13.2°/day).

The data on filaments, extracted from the Solnechnyie Dannye Bulletin (1989), are given by the coordinates of their end points (latitude and Carrington longitude). In order to study their evolution, we have also computed for each

221

filament the length (the angular distance between the ends), denoted by y, and the inclination made with the solar parallel – the tilt angle x. This angle is positive for filaments oriented '/' and negative for filaments oriented '\ '.

We have analyzed many cases of complex filaments for the period 1987–1989, taking into account the synoptic maps and the daily observations maps provided by the same catalogue.

3.   Results

The analysis of particular sequences containing complex filaments has revealed the following general conclusions.

Filaments join as a result of sudden changes of differential rotation velocity: one filament accelerates, while the other decelerates (Figure 1). One filament splits in two or more parts when each part reaches a change of the differential rotation, with very different values of one to the other.

As a continuation of the sudden changes of the differential rotation velocity, sudden changes of the tilt angle x also take place. This could indicate local magnetic reconnections in the photosphere or below.

Many times, when the filaments come together, they undergo sudden disappearances (DB) and, after a period, can reform separately or not at all.

The complex filaments tend to be localized at latitudes between 40° and 58°. There are very few complex filaments at latitudes less then 40° and those that are there are linked to the rising of active centers after the filament apparition. The active centers seem to attract the contiguous filaments, producing simultaneously the juncture. After the disappearance of the active center, the complex filament splits again.

There are many complex filaments linked to pivot-point evolutionary sequences. The filaments with pivot points (discovered by Mouradian and Soru-Escaut 1989) also attract neighboring filaments to produce complexes.

The polar filaments join together to form one complex, but usually they link to their ends as a longer filament, as their tilt angle decreases in time. After a DB, a long filament may reform as other small separate filaments.

4.   One Particular Case

We describe here the evolution of four filaments observed in the northern hemisphere, which joined and split in a very complicated process, during their evolution. There are two sequences (denoted S1 and S2) with pivot points, one sequence is the migrator type (S3) and the other is the retrograde type sequence (S4), according to the classification of Dumitrache (1997).

After a sudden disappearance, S1 formed much later connected to S2. They evolved together, as one filament, during one rotation and suffered a DB, when the tilt angle x changed in a dramatic way (from negative to positive values). After two rotations, S2 reformed (in rotation no. 1796) and its length elongated very much, being connected with filament S4 (observed one rotation before). It disappeared again for three days, after which it arose located at two degrees of latitude less then before, together with S1, as a single huge filament. The

sequence S3, evolved independently at the beginning, but in rotation 1796 it joined the complex S1+S2+S4 in the last day of apparition.

Figure 1 displays the variations of the filaments' differential rotation velocity in time, while Figure 2 shows the variations of the tilt angles, x.
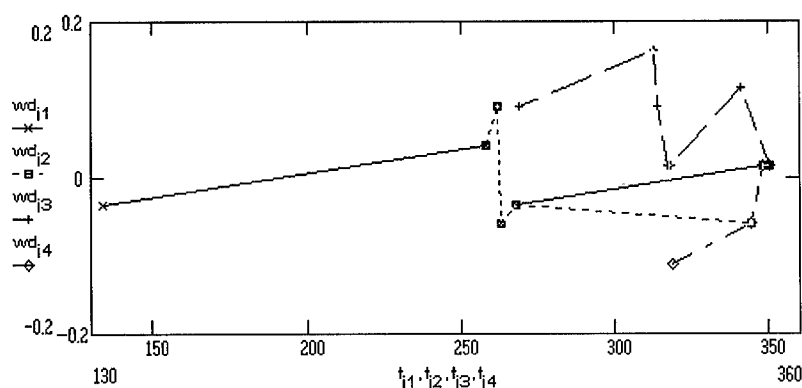
Figure 1.   Variation of the differential rotation velocity of filaments with time in days.
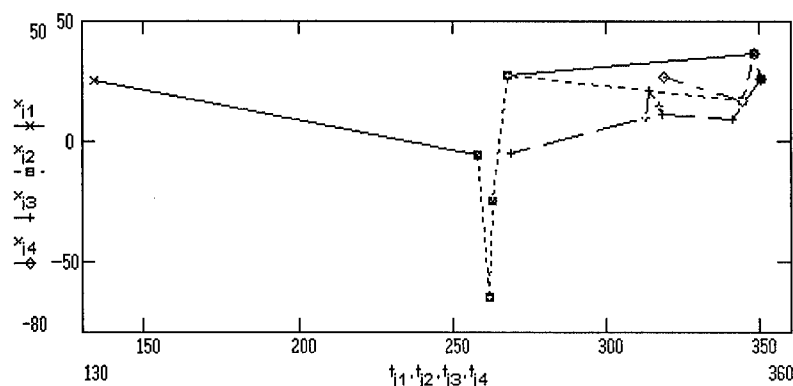
Figure 2.   The tilt angle variation with time (days).

The evolution of the filaments' lengths, y, is displayed in Figure 3. Figure 4 shows the evolution of the coordinates of these filaments. The filaments' migration in latitude, especially when coupled in a complex, which also have led to the differential velocity changes, are certainly due to the emergence of photospheric magnetic flux. This process is accompanied by magnetic reconnections, indicated also by the change of filament orientations, which have produced DBs.

We suggest that complex filaments are caused by the emergent magnetic flux producing the juncture. The split of filaments may be a consequence of photospheric magnetic field fragmentation.
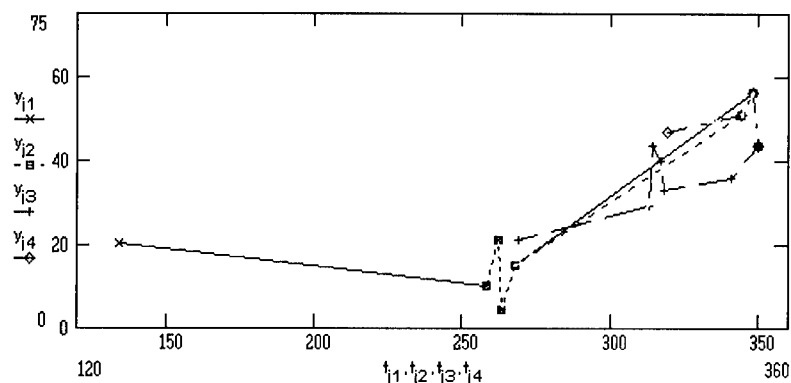
Figure 3. Variation of the filaments' lengths with time (days).
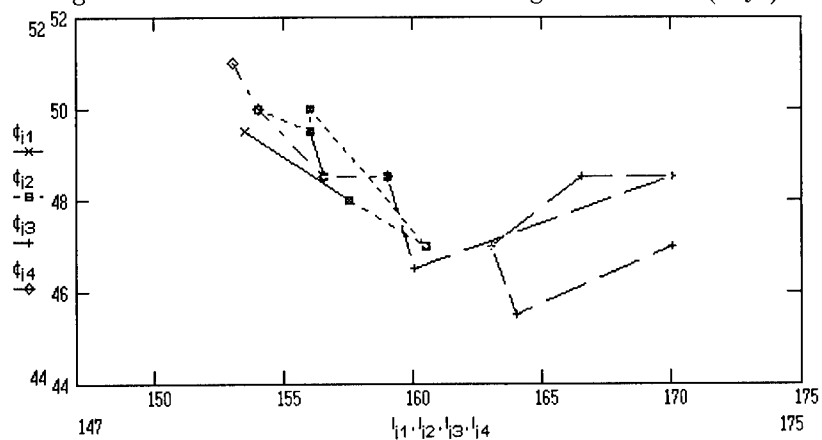
Figure 4. The evolution of the filaments' central coordinates with time (days).

References

d'Azambuja, L. and d'Azambuja, M. 1948, Ann. Obs. Paris, tome 6, fascicule 7

Dumitrache, C., Dinulescu, S. and Priest, E.R. 1994, in G. Belvedere et al. (eds.), Publ. Obs. Astrof. Catania, Special Volume, p. 65

Dumitrache, C. 1997, Solar Phys., 173, 281

Mouradian, Z. and Soru-Escaut, I. 1989, A&A, 210, 410

Solnechnyie Dannye Bulletin of the Pulkovo Observatory, 1987–1989

Stellar Filaments

Evidence of Prominences on Cool Late-type Stars

P.B. Byrne[1], M.T. Eibe

Armagh Observatory, College Hill, Armagh BT61 9DG, N. Ireland

G.H.J. van den Oord

Sterrekundig Instituut, Postbus 80.000, 3508 TA Utrecht, The Netherlands

Abstract. We review the observed characteristics of co-rotating clouds of neutral hydrogen recently detected in rapidly rotating, chromospherically active late-type stars and commonly termed "stellar prominences". Their observed properties are placed in an overall interpretive framework and compared to standard solar prominences.

1. Introduction

Solar chromospheric phenomena are widely repeated among stars of solar spectral type and later. The corresponding stellar phenomena range in scale (physical dimensions, energy content, etc.) from a little less than solar to orders of magnitude greater. In general, at any given spectral type, this activity level correlates inversely with rotation period reflecting its origin in magnetic field energy generated via dynamo action. Thus starspots may occupy $\sim$10-20% of the stellar disk (Byrne 1996), while stellar flares release up to 10^6 times the energy of the largest solar flares (Byrne 1995).

Solar prominences are intimately associated with magnetic fields on the Sun (Tandberg-Hanssen 1995) and are characterised by cool (chromospheric temperature, i.e. $\sim 10^4$K) material embedded in the otherwise multi-million degree corona. They are seen as dark features in solar monochromatic images taken in chromospheric bright lines, such as CaII H&K or Hα, due to scattering of the underlying chromospheric radiation. Their projected areas are, in general, a small fraction of the area of the solar disk.

Stellar disks are not usually resolved. Therefore, the detection of solar-like prominences on stars presents severe observational difficulties. Nevertheless, recent investigation has indicated analogous structures on the most active late-type stars under favourable circumstances. A comparison of some important properties of four well studied examples of these stars are given in Table 1. The individual stars are discussed more fully in the sections which follow.

---

[1]Deceased, September 1997

Table 1.   Some parameters of prominence stars. Note that R_{Sp} is the radius derived from the star's spectral type (Allen, 1973).

Star	AB Dor	HK Aqr	BD+22°4409	RE1816+541
Spectral type	K0V	M1V	K5-7V	M1-2V
P_{rot} (dy)	0.517	0.431	0.424	0.459
$v\sin i$ (km/s)	91	69	60	61
$R\sin i/R_\odot$	0.93	0.59	0.50	0.55
$R_{Sp}/R_\odot$	0.89	0.60	0.65	0.57
$\sin i$	1.04	0.98	0.77	0.96

2.   AB Dor

Stellar prominences were first invoked to explain the Hα variations of the field K0V dwarf star, AB Dor (Cameron and Robinson 1989a, b). Absorption features were seen to cross the rotationally broadened Hα profile in times $\sim$1 hr from blue to red. Since this crossing time is very much less than half the rotation period of AB Dor (P_{rot}=12.4 hr) Cameron and Robinson concluded that they could not be due to surface features, e.g. plages or spots. Instead they invoked cool clouds of neutral hydrogen magnetically suspended high above the stellar photosphere and in forced co-rotation with it. When such clouds transit the stellar disk they scatter the underlying chromospheric Hα radiation giving rise to an absorption feature. The line-of-sight velocity of the resulting absorption reflects the velocity of the obscured portion of the stellar disk. Because the material is at least partially neutral and yet magnetically contained, the analogy with solar prominences is obvious.

Cloud height is related to disk crossing time and Cameron and Robinson's analysis of the crossing times for AB Dor suggested that these clouds lay at or above the co-rotation radius, i.e., the radius at which the centrifugal force equals the local gravity. They suggested that, as "normal" hot coronal loops evolve to larger radii, their apices eventually extended beyond the co-rotation radius and experienced reversed effective gravity. In a star such as AB Dor the co-rotation radius is very close to the photosphere (because of the rapid rotation) and magnetic fields are systematically stronger than solar, enabling loops to survive under these conditions. Pooling of material at the apex would then produce enhanced plasma density which could cool radiatively to produce the observed neutral material.

The condensed neutral material would be tied to the field lines only through collisions with the hot, ionised component and would eventually diffuse from it and disperse. The pressure of the hot gas in the loop legs would, however, continue to replenish the gas for some period. Cameron and Robinson pointed out that such a mechanism would remove angular momentum from the parent star. Their estimates of cloud masses and lifetimes suggested that these "coronal condensations" could be responsible for the rapid braking of young solar-type, rapidly rotating cluster stars which are thought to brake on a timescale of $\sim$10^8 yr (Stauffer 1987).

For some time however AB Dor remained a unique object. Further examples of rapidly rotating late-type stars should, in principle, exhibit similar

phenomenology.

3. HK Aqr

HK Aqr is a rapidly rotating (P_{rot}=10.34 hr) early M dwarf in the field and, like AB Dor, its Hα profile is rotationally dominated. Byrne et al. (1996) made a detailed study of the behaviour of its Hα line and concluded that it too has disk-crossing neutral hydrogen clouds. Their analysis of cloud heights, however, suggested they were not at or beyond the co-rotation radius. Indeed, some of the clouds appeared to lie at altitudes more typical of large solar prominences. Thus, the condensation mechanism invoked by Cameron and Robinson could not operate in this case.

To make a more rigorous examination of allowed heights of the observed clouds van den Oord et al. (1998a, 1998b these proceedings) considered in detail the dependence of derived cloud height on all of the relevant parameters, i.e. stellar inclination, cloud latitude, etc. When applied to the observations of HK Aqr this analysis confirmed fully the earlier conclusions of Byrne et al. (1996) concerning cloud heights. How then are we to understand the earlier conclusions relating to AB Dor and the tendency for its clouds to occur near the co-rotation radius?

Van den Oord et al. pointed out the critical effect of stellar inclination on the range of allowed cloud heights. The smaller the inclination the less constrained cloud height is. Furthermore, relatively modest inclinations ($i \sim 60°$) resulted in cloud height being poorly constrained (Figure 1). They examined the supporting arguments for the inclination used by Cameron and Robinson ($i \sim 60°$) and concluded that a value of 90° was also acceptable, if not even more likely (Table 1). When this value of inclination was used, many of the clouds observed by Cameron and Robinson lay below the co-rotation radius (Figure 1b). Recent consideration of the value of AB Dor's inclination by Cameron and Foing (1997) also admits a value of 90°.

What of the mechanism for producing cool, neutral clouds in the absence of the co-rotation condensation effect? Van den Oord and Zuccarello (1998) pointed out that, cool apex loops can be created when coronal heating decreases at or near the loop apex. This can occur when a loop becomes stellar-sized and heating becomes less efficient.

Van den Oord et al. (1998a) also considered the balance of magnetic and mechanical forces on plasma in extended loops. They point out that, at larger distances, the low-level multipole active region fields resolve into a global field which is approximately dipolar. In this configuration clouds would be stable only near the equatorial plane and above a critical height unless there is a dip in the field lines. Below this critical height stability is impossible and material released from magnetic containment may flow along the dipole field lines towards the magnetic poles. Evidence for such a poleward flow of cool material should be sought in a rapid rotator with a high inclination.

AB Dor clouds Gaussian fits for i=60°

AB Dor clouds Gaussian fits for i=90°
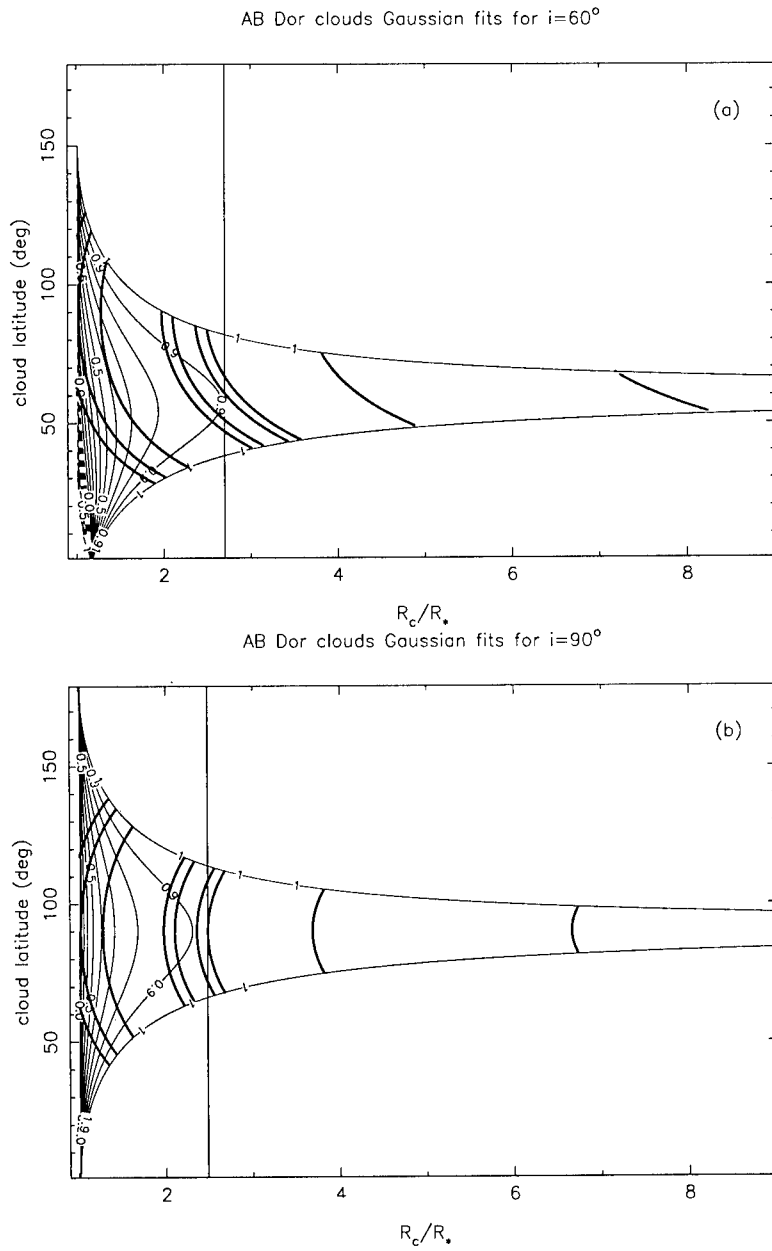
Figure 1.   Visibility diagrams for observed clouds on AB Dor for assumed inclinations of (a) 60° and (b) 90° (van den Oord et al. 1998a). The heavy lines represent allowed heights.
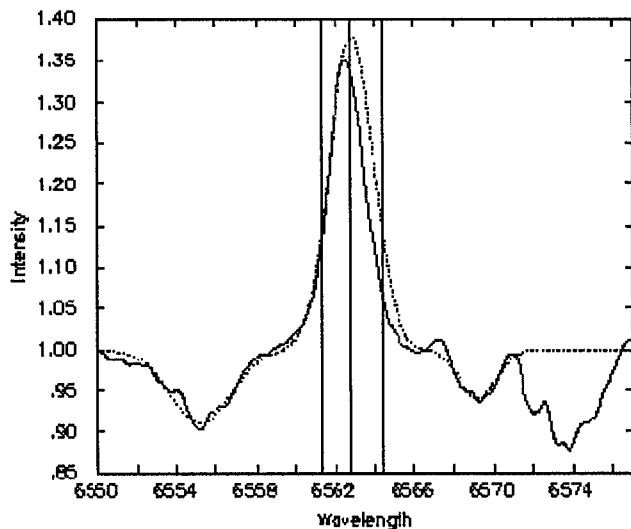
Figure 2.   Mean Hα profile for the K5V star, BD+22°4409 (Eibe et al.
1998a). The three vertical lines indicate the photospheric rest wave-
length of the Hα line ±$v\sin i$, while the dotted line is a symmetric profile
constructed by reflecting the blue wing in the central wavelength.

4. BD+22°4409

BD+22°4409 is such a star. It is a K5-K7 field dwarf which rotates with a
period of ~11.17 hr and $v\sin i$ ~60 km/s. Combining these two measurements
suggests $R\sin i$ ~0.5 $R_\odot$, considerably less than that expected for a ~K6V star,
and suggesting $\sin i$ ~0.77 (Table 1). Although the derivation of $\sin i$ from $v\sin i$
and rotational period, combined with radius from the observed spectral type,
R_{Sp}, is subject to uncertainties in the determination of both $v\sin i$ and R_{Sp}, it
is probably accurate to ~10%.

   Eibe et al. (1998a) analysed BD+22°4409's Hα line seeking evidence of
discrete clouds. Figure 2 shows the time-averaged Hα profile which results.
It is displaced to the blue with respect to the rest velocity determined from
photospheric lines and has a FWHM appreciably less than that expected from
a uniformly bright star rotating with $v\sin i$ ~60 km/s. These anomalies are
constant with time. We take this as evidence of continuous absorption on the
red wing of Hα indicative of continuous inflow of neutral hydrogen as predicted
in the van den Oord et al. scenario.

   Taking into account the higher angle of inclination this is interpreted as
evidence for cool material falling along the lines of the large-scale global field,
originating either in regions where stability is not possible, or having diffused
from closed field structures.
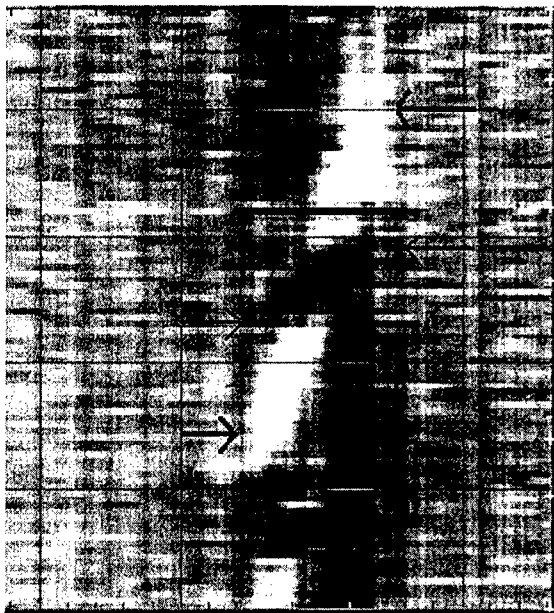
Figure 3.   Each line of the above image is a grey-scale representation of a single Hα spectrum of RE1816+541. The entire image is constructed from an entire night's data with time running from bottom to top. All have been ratioed to a mean Hα spectrum before display. Note the bright (emission) feature crossing the disk between the heavy arrows and the dark cloud intersecting it between the lighter arrows (Eibe et al. 1998b).

5.   RE1816+541

RE1816+541 is almost a duplicate of HK Aqr in terms of spectral type and rotation period (Table 1). Its Hα behaviour has been studied in detail by Eibe et al. (1998b). They found clear evidence for clouds similar to those around HK Aqr. Furthermore, they also recorded the passage of a plage-like, Hα-bright region across the stellar disk at or near the photosphere. The cloud passed over the plage region and absorbed it fully (Figure 3). This confirms nicely the fact that the clouds are indeed suspended above the stellar photosphere.

6.   Clouds in Other Stars?

Rapid rotation provides conditions in which individual clouds can be identified and tracked across a stellar disk. However, most active late-type stars are rotating too slowly to permit an approach similar to those described above. What would we expect to see when clouds transit the disk of an active slow rotator? Van den Oord et al. (1998a, 1988b these proceedings) have shown that, even in
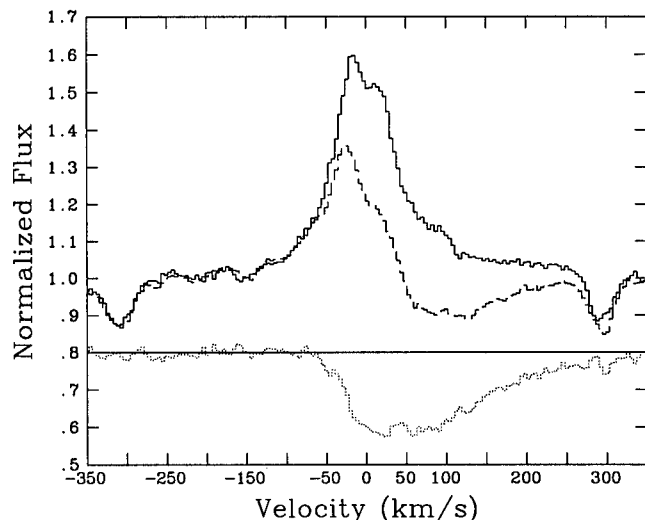
Figure 4.   Hα for the RS CVn star, II Peg, at two different epochs
(Byrne et al. 1995).

the case of moderately fast rotators, all spatial resolution is lost for a wide range
of cloud conditions. Thus all that will be seen in most cases will be short-term
reductions in line flux.

If, however, there are flows present, due, for instance, to internal cloud
motions or if one is viewing the star along a line-of-sight at high latitude, the
symmetry of the absorbed line will be affected. Evidence of asymmetry in the
Hα emission of active late-type stars has been remarked on. In Figure 4 we
show both the mean Hα emission profile of the active RS CVn star, II Peg,
and, superimposed, a type of profile which is seen from time to time. The
mean profile is asymmetric in the sense that there is more flux to the blue side
of line centre. Furthermore the reversal at line peak is similarly asymmetric.
The dashed profile shows an almost unaffected blue wing while the red wing is
massively cut away. Similar effects are seen in HeI λ10830Å (Byrne et al. 1998).

This gives the clear impression that all these asymmetries arise from the
same root cause, i.e. absorbing material superimposed on the global chromo-
spheric Hα emission, which is variable in its absorbing power. We interpret these
phenomena as evidence for the existence of infalling neutral material similar in
nature to that seen in the rapidly rotating late-type dwarf stars.

7.   Conclusions

The unique circumstances of extreme rapid rotation have aided the discovery of
stellar analogues of solar prominences. However, as is so often the case, there are
important differences between the phenomenon as seen in active stars and the
solar case. These include scale, support mechanism and, probably, mass. Their

study is still in its infancy, however, and we look forward to rapid progress in the next few years.

References

Allen, C.W. 1997, Astrophysical Quantities, University of London Press

Byrne, P.B. 1995, in Flares and Flashes, Proc. IAU Coll. 153, (eds.) J. Greiner, H.W. Deurbeck and R.E. Gershberg, Springer-Verlag, New York, p. 14

Byrne, P.B. 1996, in Stellar Surface Structure, (eds.) K.G. Strassmeier and J.L. Linsky, Kluwer, Dordrecht, Holland, p. 299

Byrne, P.B., Panagi, P.M., Lanzafame, A.C., Avgoloupis, S., Huenemoerder, D.H., Kilkenny, D., Marang, F., Panov, K.P., Roberts, G., Seiradakis, J.H. and van Wyk, F. 1995, A&A, 299, 115

Byrne, P.B., Eibe, M.T. and Rolleston, W.R.J. 1996, A&A, 311, 651

Byrne, P.B., Sarro, L.M. and Lanzafame, A.C. 1998, in Cool Stars, Stellar Systems and the Sun, (eds.) J. Bookbinder and R. Donohue, ASP Conf. Ser., in press

Cameron, A.C. and Foing, B.H. 1997, Observatory, 117, 218

Cameron, A.C. and Robinson, R. 1989a, MNRAS, 236, 57

Cameron, A.C. and Robinson, R. 1989b, MNRAS, 238, 657

Eibe, M.T., Byrne, P.B., Jeffries, R.D. and Gunn, A.G. 1998a, in preparation

Eibe, M.T., Byrne, P.B. and Robb, R.M. 1998b, in Cool Stars, Stellar Systems and the Sun, (eds.) J. Bookbinder and R. Donohue, ASP Conf. Ser., in press

Stauffer, J.R. 1987, in Cool Stars, Stellar Systems and the Sun, (eds.) J.L. Linsky and R.E. Stencel, Lecture Notes in Physics, No. 291, Springer-Verlag, New York, p. 182

Tandberg-Hanssen, E. 1995, The Nature of Solar Prominences, Kluwer Acad. Publ., Dordrecht, Holland

van den Oord, G.H.J., Byrne, P.B. and Eibe, M.T. 1998a, A&A, submitted

van den Oord, G.H.J. and Zuccarello, F. 1998, A&A, submitted

Prominences on Rapidly-Rotating Solar-Type Stars

M. Jardine, J. Barnes, Y. Unruh and A. Collier Cameron

Department of Physics and Astronomy, University of St. Andrews, North Haugh, St. Andrews, Fife, KY16 9SS U.K.

Abstract. We present Hα observations of two rapidly-rotating G2 dwarfs in the Alpha Persei cluster and of AB Dor, a young K0 dwarf. All three stars have projected rotational velocities of about 90 km s^{-1} and axial rotation periods ranging from 11 to 15 hours. He 520 and AB Dor show very clear transient features that move through the profile. The most likely explanation for these features is that they are huge prominences in co-rotation with the star. We also use the recently developed technique of *least squares deconvolution* to present simultaneous dynamic profiles of the stars' photospheric lines which show the locations of the surface spots. This technique has allowed us to extend our studies to a greater range of stars.

1. Introduction

Prominences on rapidly-rotating solar-like stars have been observed now for nearly 13 years (Collier Cameron and Robinson 1989a, b). They are observed as transient absorption features that move through the Hα profile. From the rate at which these features move we can find the distances of the prominences from the stellar rotation axis. Significantly, in contrast to the Sun, we find that most prominences are located at great distances (typically 2 to 6 stellar radii) from the stellar rotation axis. While similar in their temperatures and formation times to solar prominences, these prominences are larger and more massive (by two orders of magnitude) than their solar counterparts. They are also much shorter-lived, surviving for only a few days. The surface positions of the spots on these stars can also be found using the technique of Doppler Imaging (Vogt and Penrod 1983), although it is still an open question as to how stellar prominences are linked to the surface magnetic fields and star spots. On AB Dor (the most consistently-observed example) we find that spots appear in two active latitudes, one at about 30° and one at about 80°. Recently, Donati and Collier Cameron (1997) have used the least squares deconvolution of approximately 1500 photospheric lines to produce Doppler maps both of the surface spots on AB Dor and of the radial and horizontal components of the magnetic field in the bright regions. Using data obtained on the 7th and 11th of November 1995 they have also derived the surface differential rotation which is very similar to that for the Sun (in that the equator laps the pole in 120 days rather than 110 days for the Sun). This result not only places severe constraints on dynamo mechanisms for this star, but also on the possible means of destabilising the prominences.

2. The Observations

Observations of the α Persei stars were taken using the Utrecht Echelle Spectrograph at the 4.2m William Herschel Telescope on October 25–26, 1996 and November 24–26, 1996. The magnitude of both He 699 and He 520 (i.e., $m_v \approx 11.5$) necessitated exposure times of 900 s for each observation. This allowed a signal to noise ratio of 40–60 to be obtained in the raw spectra while keeping the effects of rotational blurring to a minimum. The AB Dor data were obtained using the UCL spectrograph at the Anglo Australian Telescope. This star is much brighter ($m_v \approx 7$), thereby allowing a greater time resolution (i.e., shorter exposure times). In both cases, data reduction was carried out using standard Starlink packages. The resolution of both sets of Hα dynamic spectra is 6 km s^{-1} per pixel and 3 km s^{-1} for the photospheric dynamic spectra.
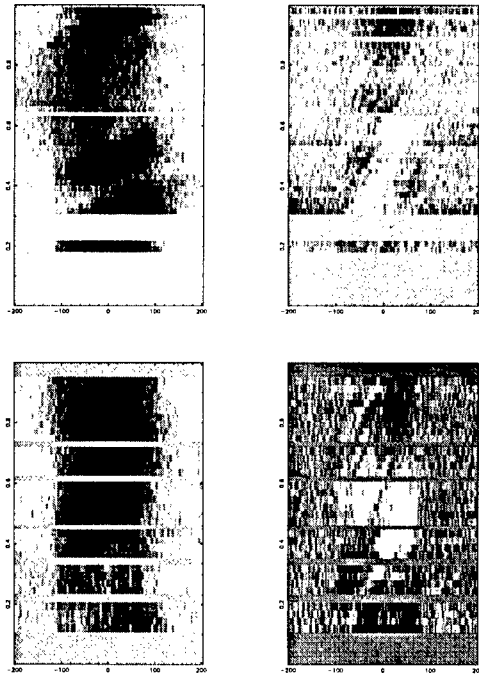
Figure 1.   Phase plotted against $v\sin i$. Top and Bottom Left: He 520 and He 699 Hα dynamic spectra, Top and Bottom Right: He 520 and He 699 photospheric dynamic spectra. Half-profile widths are $v\sin i = 86$ km s^{-1} (He 520) and $v\sin i = 94$ km s^{-1} (He 699).

3. Prominence Positions

The Hα observations give us the distances of the prominences from the rotation axis which is inclined at some angle to the observer's line of sight. For a group
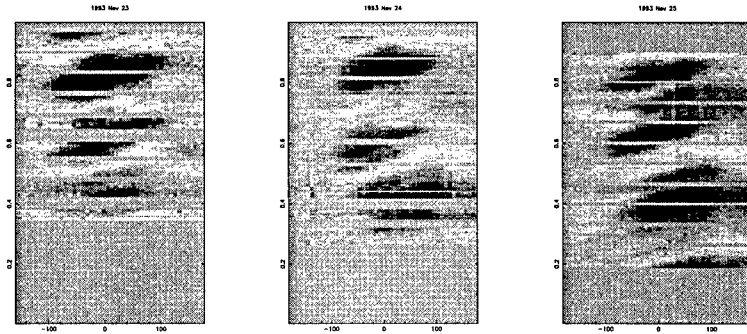
Figure 2. AB Dor, Hα dynamic spectra, November 23–25, 1993. Note that individual features are repeated, and show evolution from night to night ($v\sin i = 91$ km s^{-1}). This suggests that they are prominences, and not shorter lived features such as stellar flares.

of stars in the one cluster the inclination angle can be determined using the technique of Hendry et al. 1993 and O'Dell et al. 1994. Table 1 summarizes the prominence positions and inclinations (ranging from 60° to 90°) for four G dwarfs in the young (50 Myr) open cluster, α Persei. The age of the cluster tells us that the G dwarfs should lie on the zero age main sequence. Because prominences can only be observed when they cross in front of the stellar disk, for those stars with a lower inclination (where the observer is looking in at high latitudes), any prominences that are observed far from the rotation axis must be confined at high latitudes well out of the equatorial plane. This suggests that the footpoints of the magnetic field lines confining these prominences must both lie in the same hemisphere (see Ferreira 1998, these proceedings).

TABLE 1 - Alpha Persei and AB Doradus data

Parameters		He 520	He 699	He 373	He 622	AB Dor
P	[d]	0.6079	0.4908	0.333	0.804	0.5148
$v\sin i$	[km s^{-1}]	86 ±2	94 ±4	140	61	91
R_c	[$R_\odot$]	3.0	2.6	2.0	3.64	2.5
R_p (CW92)	[R_*]	3.7 - 5.1	3.8 - 6.0	2.0 - 2.8	5.4	-
R_p (1996)	[R_*]	2.8 - 3.0	1.7; 1.3 - 2.4	-	-	-
R_p 23 Nov	[R_*]	-	-	-	-	3.1 - 3.4
R_p 24 Nov	[R_*]	-	-	-	-	2.6 - 2.9
R_p 25 Nov	[R_*]	-	-	-	-	3.5 - 4.3
i		90°	62°	61°	70°	60°

For comparison, prominence positions for several Alpha Per stars were calculated from the paper by Collier Cameron and Woods (1992) (CW92). The new (1996) data allow both prominence and spot positions to be calculated for He 520 and He 699. The dynamic Hα spectra in Figure 1 show that for He 520, dark absorption features cross the profile at a rate which shows that they lie close to the co-rotation radius, R_c. He 699 appears to show lower lying features, and

we cannot exclude that they are at the photosphere. We, therefore, conclude that these features may indeed be active regions, rather than prominences. The dynamic photospheric spectra in Figure 1 show the underlying photospheric features (note, spots appear bright) produced by the least squares deconvolution of approximately 1000 metal lines. The deconvolution process yields a combined profile with sufficient S:N to give significant deviations of profile distortions produced by surface inhomogeneities such as cool spots. The dynamic spectrum of He 699 shows spot features that do not cross the whole profile, indicating high latitude or polar features. He 520 seems to indicate a high latitude region of spots also. By comparison, high latitude features are also seen on AB Dor. Figure 2 shows Hα observations of AB Dor for three successive nights. These show between three and five prominences in the observable part of the corona, some of which are clearly seen forming from night to night. The similarity in crossing times of the transients shows the prominences to be at similar distances from the rotation axis.

4. Conclusions

The ability to observe both the surface magnetic field and the positions of the prominences trapped high in the corona gives us a unique insight into the complex nature of the magnetic fields of rapidly-rotating stars. In the past, the ability to map surface features on single main sequence stars has been limited to nearby K stars. The use of *least squares deconvolution* presented here has allowed the sample of stars that can be studied in this way to be extended to G stars which have shallower convective regions. The use of these observations to produce surface maps of these G stars will be the subject of further study.

References

Collier Cameron, A. and Robinson, R.D. 1989a, MNRAS, 256, 57
Collier Cameron, A. and Robinson, R.D. 1989b, MNRAS, 238, 657
Collier Cameron, A. and Woods, J.A. 1992, MNRAS, 258, 360
Donati, J.-F. and Collier Cameron, A. 1997, MNRAS, 291, 1
Hendry, A., O'Dell, M.A. and Collier Cameron, A. 1993, MNRAS, 265, 983
O'Dell, M.A., Hendry, A. and Collier Cameron, A. 1994, MNRAS, 268, 181
Vogt, S.S. and Penrod, G.D., 1983, PASP, 95, 565

Stability of an Idealised Equilibrium Model of Prominences in Rapidly-Rotating Stars

Miguel Ferreira

School of Physics and Astronomy, University of St. Andrews, St. Andrews, Fife KY16 9SS, Scotland

Abstract. We study the stability of an idealised model of stellar prominences. We find that surface fields of a few hundred gauss are required to hold them in a stable equilibrium.

1. Physical Considerations

Prominence-like clouds have now been observed in many stars other than the Sun. These stars are invariably very rapid rotators and exhibit a strong magnetic activity. In contrast to their solar counterparts, there is a class of stellar prominences that do not lie close to the surface but rather at heights of several stellar radii. In particular, they are inferred to form close to, or beyond, the *corotation radius* (R_k). This is the point at which the centrifugal force and gravity are in balanc e at the equatorial plane in a co-rotating atmosphere.

Let us first consider the simple problem of determining the locations where material could, in principle, accumulate to form a prominence in a prescribed magnetic field. This is illustrated in Figures 1 and 2 where we calculate the points at which the combine d effects of gravity and centrifugal force (that we denote as effective gravity, $g_{eff} = -GM_*/r^2 + \omega^2 r$) are in a stable balance along the direction of the field.
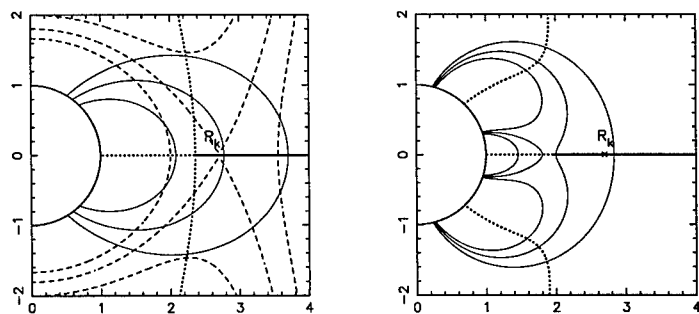
Figure 1. Equilibrium points for a dipole and a combined dipole and sextupole fields. Shown are the equipotential lines (dashed), field lines (light full), the unstable equilibrium points (dotted) and the stable equilibrium points (thick full).
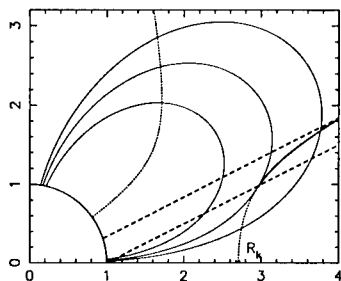
Figure 2. Equilibrium points for a quadrupolar field. The parallel dashed lines contain the part of stellar surface occulted by a prominence formed in the stable equilibrium region, as seen by a distant observer along that direction.

From these simple examples we infer that stable equilibrium along the direction of the field is possible with simple potential fields. Not so obvious is the fact that this can occur below R_k even in the absence of a dipped configuration (Figure 1 a), while in other cases stable equilibrium is only possible further way from R_k (Figure 2). Assuming that prominences form on some of these equilibrium surfaces, then, with the exception of the field configurations symmetric with respect to the stellar equator, they will in general have a curved shape.

If we make the analogy with solar prominences, we expect these stellar clouds to be thin structures along the direction of **B**. If so, how can they be observed? This crucial question was raised during this conference by U. Anzer. Naturally, one can not rule out the possibility that stellar prominences are very different from their solar counterparts (e.g., Could they be evolving, cool post-flare loops?). Nevertheless, if we assume this analogy, the question can be answered by the fact that the area of the prominence projected on the stellar surface along the direction of the observer is a substantial fraction of the total stellar surface area, therefore absorbing a significant fraction of the chromospheric flux (Figure 2). Also, noticing that in the region where stellar prominences form the pressure scale-height is about one order of magnitude larger than the solar value, we predict that stellar promine nces have a greater width than solar ones.

Let us now turn our attention to the equilibrium and stability of the prominence material in the direction perpendicular to the field. The ratio of the gas pressure gradient force to the effective gravity in the radial direction is

$$\frac{\frac{dP}{dr}}{\rho g_{eff}(r)} \approx \frac{p}{l_0 \rho g_{eff}} = \frac{RT_p}{l_0 g_{eff}} \tag{1}$$

where l_0 is the typical radial extent of the prominence and T_p its temperature. At the corotation radius $g_{eff} = 0$ and pressure is the only non-magnetic force present. However, if prominence material forms even a fraction of a stellar radius away from R_k and for typical parameters ($T_p = 10^4$K, $l_0 \approx 10^8 - 10^9$m), effective gravity dominates over pressure gradient and the above ratio is much smaller than one. We then neglect the gas pressure gradient force in the equi-

librium equation and only look at the balance between the Lorentz force and effective gravity. It is reasonable to consider that stable equilibrium can occur in the prominence if the local magnetic energy is greater than the generalized gravitational potential energy:

$$\frac{B^2}{2\mu} \geq \rho \left[\frac{GM_\star}{r'} + \frac{\omega^2 r'^2}{2} \right]_{r'=R_k}^{r'=r_p} . \tag{2}$$

If the prominence lies sufficiently away from R_k this condition is similar to imposing $v_A \geq \omega r_p$. Writing the unknown prominence mass density in terms of the mass density of solar prominences, $\rho = (\rho/\rho_\odot)\rho_\odot$, and taking $\rho_\odot = 1.6 \times 10^{-13} \mathrm{g\,cm}^{-3}$, we obtain a minimum field strength, $B(r_p)$

$$B(3) = 5 \left(\rho/\rho_\odot\right)^{1/2} \mathrm{G} \; ; \quad B(4) = 20 \left(\rho/\rho_\odot\right)^{1/2} \mathrm{G}, \tag{3}$$

which is similar to the field strength measured for solar prominences. Assuming a dipolar field one obtains a surface field of $B_s(r_p = 3) = 135\mathrm{G}$ and $B_s(r_p = 4) = 1.3\,\mathrm{kG}$, respectively.

2.   Axisymmetric Massive Current Sheet Model

In this model prominences are represented by an equatorial axisymmetric massive current sheet supported by a dipole field. After prescribing the surface current distribution, $\sigma(r) \equiv -[B_r]/\mu = -2B_r^+/\mu$, the total magnetic field is computed by assuming that either the field is closed everywhere or it opens up at a given radius in order to simulate the effect of a wind (Figure 3). The surface mass density is then determined using the equilibrium equation, $m = -2B_r^+ B_\theta/\mu g_{eff}$.
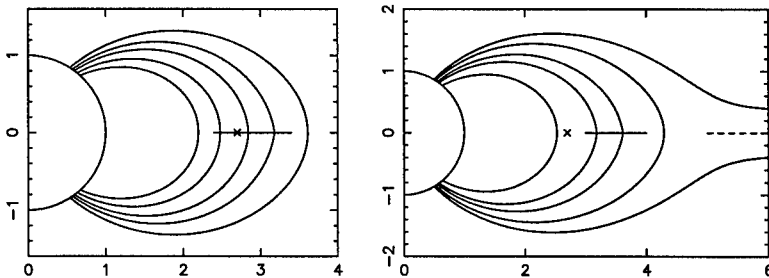
Figure 3.   Prominences as massive current sheets. Left: The prominence extends from $r = 2.4$ to $r = 3.4$ and the field is closed everywhere. Right: The prominence extends from $r = 3.0$ to $r = 4.0$ and the field opens up at $r = 5.0$. The represented configurations are stable.

In a rotating system there is no energy principle because of the Coriolis force. Nevertheless, by simply substituting gravity for g_{eff} and neglecting the Coriolis force one can still apply the energy method of Bernstein et al. (1958) to obtain sufficient, though not necessary, linear and ideal stability conditions:

$$- B_r^+ \frac{\partial (r B_\theta)}{\partial r} - m \frac{\omega^2}{r} \leq +C \tag{4}$$

$$\frac{\partial B_r^+}{\partial r} - \frac{1}{g_{eff}}\frac{\partial g_{eff}}{\partial r}B_r^+ \geq -A \quad \Leftrightarrow \quad \frac{\partial}{\partial r}\left(\frac{m}{|B_\theta|}\right)g_{eff} \geq -A. \tag{5}$$

The functions A and C represent the stabilizing effect of line-tying (Lepeltier and Aly 1996) and are such that $A, C \geq 0$. The above conditions are written assuming $B_\theta \leq 0$, $B_r^+ > 0$ ($r > R_k$). These stability criteria are similar to the ones derived for solar prominences (Anzer 1969). Condition (4) is related with the field curvature and is easily obeyed by the equilibrium models. The term $m\omega^2/r$ is stabilizing and allows for stable equilibrium to be possible for $r < R_k$ without the presence of a dip at the loop top (Figure 1a). Condition (5) states that the mass per unit flux cannot decrease outwards very fast and this can be associated with the magnetic Rayleigh-Taylor instability. While solar promin ences are most unstable to the interchange mode at their lower end, these stellar counterparts are most unstable at their upper end where the magnetic field strength is weaker and therefore less capable of stabilizing the equilibrium. A normal mode analysis restricted to short wavelength perturbations yields necessary stability conditions (Spruit and Taam 1990). In the particular case considered, with the equilibrium at the equatorial plane, conditions (4) and (5) are found to be both necessary and sufficient.

Masses of stellar prominences have been estimated to be of the order of $2-6\times10^{17}$g (Collier-Cameron et al. 1990). Although the model is axisymmetric, we consider that the prominence mass is concentrated in a region of dimension L in the azimuthal direction. We find that the minimum surface field strength necessary for a stable equilibrium is given by

$$B_s = B_0\left(\frac{M_p}{5\times10^{17}g}\right)^{1/2}\left(\frac{r_p}{4L}\right)^{1/2}\text{G},$$

where B_0 depends on the following: the prominence location (r_p), its radial extent, the mass distribution profile along it and also how close the prominence is to the open field region. Making sensible choices one obtains $B_0 = 200-800$G. The kinetic energy of these prominences is of the order of $10^{32} - 10^{33}$ erg while the free magnetic energy calculated using stable equilibrium models is almost one order of magnitude lower. The energy of the flares observed on these stars can be as high as 5×10^{34} erg. We conclude that in these prominences there is enough energy to explain the low and medium energetic flares but probably not the very energetic ones.

References

Anzer, U. 1969 Solar Phys., 8, 37

Berstein, I. B. et al. 1958, Proc. Roy. Soc., A244, 17

Collier-Cameron, A. and 7 other authors 1990, MNRAS, 247, 415

Lepeltier, T. and Aly, J. J. 1996, A&A, 306, 645

Spruit, H. C., and Taam, E. R. 1990, A&A, 229, 475

Prominences and Circumstellar Emission Around FK Comae Berenices: Balmer Lines Diagnostics from MUSICOS Spectra[1]

J. M. Oliveira[2], B. H. Foing[3], Ph. Gondoin, H. C. Stempels and T. Beaufort

ESA Space Science Department, SO/ESTEC, PB299, 2200 AG Noordwijk, The Netherlands

R. S. Le Poole

Leiden Observatory, The Netherlands

J. A. de Jong

Astronomical Institute "Anton Pannekoek", The Netherlands

Abstract. We present results from the analysis of spectra of the fast rotating active giant star FK Comae Berenices. The extended emission is interpreted as arising in giant active loops and prominences. The absorption is due to a shell of cold and dense gas (like solar filaments).

1. Introduction: Solar-like Activity in FK Com

Solar-like activity manifests itself in stars where chromospheres, spots, active regions, coronae and flares are observed. Only recently stellar prominences have been detected by their clear spectroscopic signature, as they transit the stellar disc of fast-rotating dwarfs (Collier Cameron and Robinson 1989). Fast rotating giants are another interesting case for searching for the equivalent of prominences in different gravity and magnetic configurations than in the solar case.

FK Comae Berenices is a rapidly rotating, single G5II type giant. One of its most striking peculiarities is its extreme rotational velocity, $v \sin i \sim 162.5 \pm 3.5$ kms^{-1} (Huenemoerder et al. 1993), for a single star. The rotational period is P=2.4 days (Bopp and Stencel 1981.

Its spectra exhibits an Hα emission feature, very broad and erratically variable (e.g., Bopp and Stencel 1981), with an asymmetric, double peaked appearance (Ramsey, Nations and Barden 1981). The emission is attributed to giant structures extending to several stellar radii (Huenemoerder et al. 1993).

Some spectral characteristics found in FK Com are common to the RS CVn binary systems: CaII H&K (Bildeman 1954) and Hα emissions, quasi-sinusoidal optical light curves (Holtzman and Nations 1984), and radio and X-ray emissions (due to an active corona). These similarities indicate a very enhanced solar-like activity.

We present new spectroscopic observations of FK Com. The Balmer absorption and emission are analysed in the frame of extended structures, confined in corotation with the star. The absorption component is interpreted as due to the obscuration by the star and by a near-stellar cool gas shell. The emission is attributed to giant structures, similar to active loops or prominences.

2.   ESA-MUSICOS Spectra Acquisition and Reduction

The data were obtained in May 1996 with the 2.5 m Isaac Newton Telescope (INT), La Palma, Spain during the commissioning campaign of the (fiber-fed) ESA-MUSICOS spectrograph. The specific performances and experimental set-up of this spectrograph on INT are given in Foing et al. (1998). The frames were obtained with the "red" operating mode, in the range 4700 to 8100Å. The resolving power of these spectra is $R = 23,000$. For the data reduction we used the MIDAS Nov94 echelle reduction package.

3.   Results

Artificially broadened spectra of the low-activity star HD145001 (G8 III) were subtracted from the Balmer lines spectra of FK Com (Figure 1) to remove the photospheric contribution and to derive the effect of its extreme activity.

3.1.   Circumstellar Balmer Emission and Prominences

The difference spectrum shows an emission extending to $\sim$ 780 kms^{-1} in Hα. Both in Hα and Hβ, the wings of the extended emission, outside $v \sin i$, can be adjusted by gaussian profiles, Figure 2. The FWHM of the gaussian fitted profiles are FWHM (Hα)=642 ± 12 kms^{-1} and FWHM (Hβ)=381 ± 20 kms^{-1}.

Assuming corotating material, we derive as a maximum extent of the emission $\sim$ 4.75$R_* \sin$ i for Hα and $\sim$ 2.66$R_* \sin$ i for Hβ ($R_* \sin$ i is the projected stellar radius). The ratio between the total fluxes for these two Balmer lines is approximately 8.3, reminiscent of solar-like active prominences.

We modelled the emission wings profile by taking a 3D gaussian distribution of source material around the star (Oliveira et al. 1997). If we assume an effectively thin, corotating emission, the measured FWHM relate directly to the emission scale height. Such a 3D distribution represents well the profile wings but differs strongly in the central absorption profile.

3.2.   Model of the Near-Stellar Shell of Filament-like Absorption

The central absorption can partly be interpreted as the effect of projected obscuration by the star itself. As this absorption is in fact slightly broader than $2v \sin i$, it indicates the presence of a near-stellar shell of absorbing material
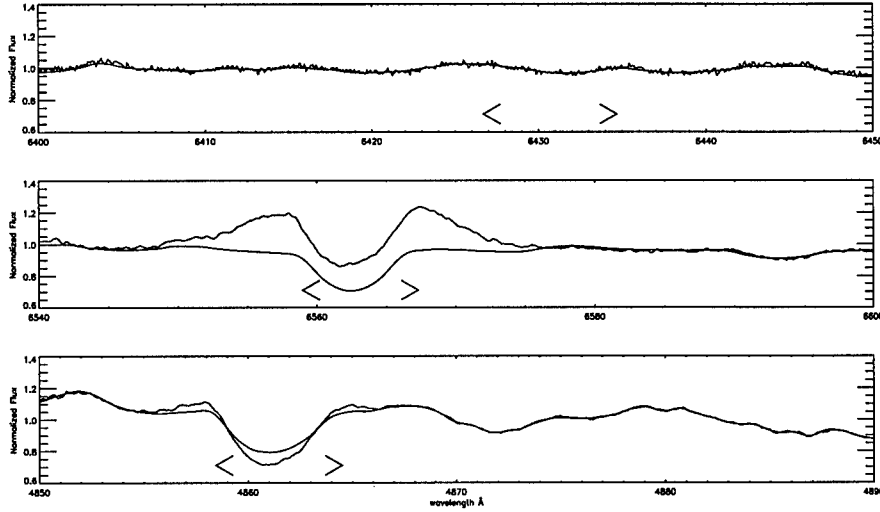
Figure 1.   FK Com and reference star broadened spectra are shown
for photospheric lines around 6430Å (for comparison) and for Hα and
Hβ (from top to bottom). Note the good adjustment for the photo-
spheric lines, and the strong difference in the core and the wings of the
Balmer lines (Oliveira et al. 1997). The marks <> indicate $2v \sin i$.

(Oliveira et al. 1997). This shell also absorbs the background photospheric
profile by a factor ε, to be adjusted.

The numerical integration of the 3D gaussian emission is computed at a
given velocity, considering the obscuration effect by the star. This modelled
profile is then corrected for the extra absorption by subtracting the function
$\varepsilon * I_{phot}$, where I_{phot} is the photospheric spectrum. The resulting profile is com-
pared with the difference spectrum in Figure 2. The values for the parameters
that give the best agreement between the two profiles are $R_{abs}^{H\alpha}=1.25$ $R_* \sin i$,
$R_{abs}^{H\beta}=1.1$ $R_* \sin i$, $\varepsilon=0.225 \pm 0.02$. The residuals are interpreted as inhomoge-
neous active regions at, or near, the stellar surface and denser than the circum-
stellar environment, accounting for $\sim 10\%$ of the total emission.

4.   Differences with Solar Active Loops and Prominences

In FK Com, the surface gravity and photospheric scale height are, not account-
ing for the fast rotation, $g \leq 0.025 \sin^2 i g_\odot$ and $H \geq 40 \sin^{-2} i H_\odot$, respectively,
where $g_\odot$ and $H_\odot$ are the solar values and i is the inclination. The low effec-
tive gravity and fast rotation create conditions for loop structures extending to
large height, magnetically confined in corotation and filled with emitting mate-
rial. These loops could be responsible for the very broad Balmer emission. This
is reminiscent of circumstellar structures observed in RS CVn stars which, at
times, undergo exceptional flaring (Foing et al. 1994).

These same combined effects can cause the hot coronal loops to undergo
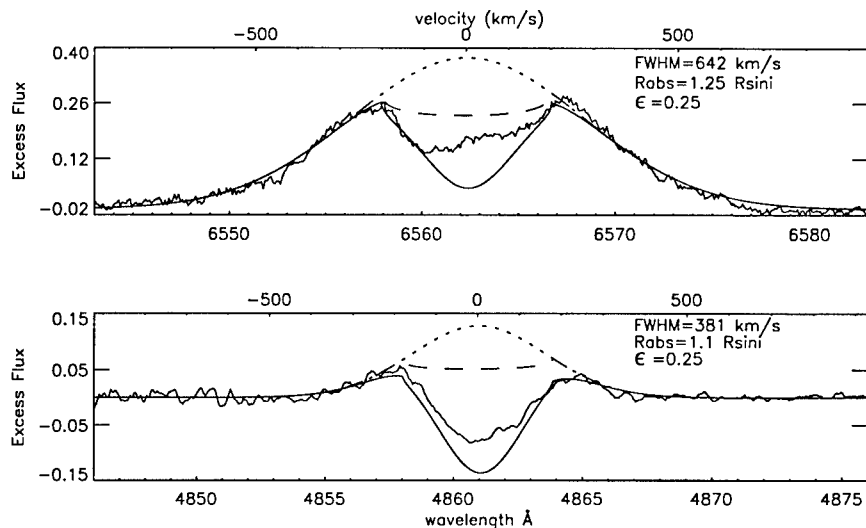
Figure 2.   The Hα (top) and Hβ (bottom) average difference spectra, as well as the gaussian profiles (dotted line), fitting the wings of the extended emission. The obscuration by the star and the absorption of the near-stellar shell are displayed (dashed line) and also the effect of the extra absorption of the background photospheric profile (full line) (Oliveira et al. 1997).

thermal instabilities and condense into cool loops. According to our model, the near-stellar shell of absorbing material is just beyond the break-up radius, $R = 1.12R_*\sin i$, therefore consistent with this very unstable region.

References

Bildeman W.P. 1954, ApJS, 1, 175

Bopp B.W. and Stencel R.E. 1981, ApJ, 247, L131

Collier Cameron A. and Robinson R.D. 1989, MNRAS, 236, 57

Foing B.H., Stempels H.C. and Oliveira J.M. 1998, A&A, in preparation

Foing B.H. et al. 1994, A&A, 292, 543

Holtzman J.A. and Nations H.L. 1984, AJ, 89, 391

Huenemoerder D.P. et al 1993, ApJ, 404, 316

Oliveira J.M. et al. 1997, A&A, submitted

Ramsey L.W., Nations H.L. and Barden S.C. 1981, ApJ, 251, L101

A Fibril Structure Model for Stellar Prominences

R. Oliver and J. L. Ballester

Departament de Física, Universitat de les Illes Balears, E-07071 Palma de Mallorca, Spain

Abstract. Extensive observational background exists about the presence of cool material clouds embedded in the stellar coronae of rapidly rotating, late-type stars. Observations of such clouds in HKAqr (Gliese 890) and HD197890 suggest that the clouds are at heights smaller than the star's corotation radius and could be looked at as a phenomenon similar to that of solar prominences. Recent observations of solar prominences have reinforced the evidence about their fibril structure made of many long, thin magnetic flux tubes making angles about 25 degrees with the direction of the filament channel, with only the central 10–20% of the magnetic flux tubes filled with cool matter, which can produce a depression at the summits of the flux tubes. Then, assuming a similar structure for the stellar cool clouds, we have looked for the physical characteristics of such stellar prominences, i.e. the size of the flux tube depression, the density, temperature, half-width and supported mass of the cool region, taking into account gravity variation with height and centrifugal acceleration, since such clouds have been detected at great heights within stellar coronae belonging to rapid rotators.

1. Introduction

Recently, claims about the discovery of cool, prominence-like material embedded in hot stellar coronae of late-type stars have been made. Collier-Cameron and Robinson (1989a, b), using spectra of the Hα profile in the active, rapid rotator K0 dwarf AB Doradus, suggested that such features originate in cool, dense clouds embedded in and corotating with the hot corona. The observations indicate that the clouds form in a region just outside the Keplerian corotation radius having a projected extension between 3 and 20% of the stellar surface area. The temperatures are in the range 4500-14,000 K and densities could be between $10^9 cm^{-3}$ and $10^{13} cm^{-3}$. The clouds seem to be forced to corotate with the star, thus indicating the presence of closed magnetic loops reaching great heights in the stellar atmosphere. Doyle and Collier-Cameron (1990) made observations of the M dwarf Gliese 890, concluding that the spectral features were consistent with the existence of a cloud of neutral hydrogen with a projected area of 0.25-0.40 times that of the stellar disc. In this case, the cloud seems to be close to but below the corotation radius. Collier-Cameron and Woods (1992) found evidence for prominence-like circumstellar material in four rapidly rotating G – K stars of the α Persei cluster. In this case, the observations suggest that the clouds lie preferentially outside the Keplerian corotation radius. Jeffries

(1993) obtained Hα spectra of the rapid rotator HD197890. The behaviour of the absoption transients is consistent with the model of cool clouds of material trapped in corotating, closed magnetic structures above the star's surface. Also, it seems that some of the clouds are located outside the Keplerian corotation radius while others can be located within the corotation radius. Byrne et al. (1996) and Byrne (1996) have reported the discovery of cool, prominence-like material embedded in the corona of the rapid rotator HKAqr (Gl890). The observations suggest that such features form well below the co-rotation radius and that their dimensions lie between 3 and 20 times those of solar prominences. Further evidence has been obtained by Byrne et al. (1997) who have used visibility plots to show that most of the clouds are located near the equatorial plane, below the corotation radius.

From the theoretical point of view, van den Oord (1988) used a current line model to investigate the possibilities of filament support in binary stars. Collier-Cameron (1988) studied the properties of coronal loop structures with lengths comparable to or greater than the stellar radius and the classes of solutions, hot and cool, which can be found. He suggested that an explanation for neutral hydrogen clouds is that they can be formed by thermal collapse of large X-ray loop structures, whose summits extend beyond the Keplerian corotation radius, with centrifugal acceleration providing support against the Rayleigh-Taylor instability. Ferreira and Jardine (1995) have presented a model, using a massive circular line current, describing the equilibrium of a stellar filament in the equatorial plane of a rapidly rotating, late-type star. Recently, Byrne et al. (1997) have studied the equilibrium of prominence-like clouds in late-type rapid rotators, presenting arguments with respect to the nature of the clouds, i.e. whether they are filamentary-like structures or coronal loop-like structures. They conclude that the filamentary hypothesis can be ruled out since filaments can only have stable equilibria up to 0.63 times the corotation radius and most of the detected clouds are located at larger heights. Then, an interesting possibility is that the clouds are of coronal loop-like nature with a temperature inversion near the apex. Van den Oord and Zuccarello (1996) showed that, below the corotation radius, such temperature reversals can be created when there is insufficient heating near the apex of the loops or when the cross-section increases towards the apex.

2. Basic Model

Observations of quiescent solar prominences have shown very fine structures in the body of the filament, suggesting they are composed of small-scale structure aligned with the magnetic field and anchored at many different foot-points. Such fibrils have been well-resolved by Yi et al. (1991) and Yi and Engvold (1991) in their observations of the HeI $\lambda10830\mathring{A}$ in quiescent filaments. From such observations these authors conclude that the prominence matter is contained in many long, thin magnetic flux tubes making angles of about 25 degrees with the direction of the filament channel. Also, it seems that only the central 10-20% of the magnetic flux tubes is filled with cool matter.

Ballester and Priest (1989) developed a model to explain the observed fibril structure of solar prominences. They assumed that the fibril structure of a

prominence is composed of flux tubes containing hot plasma ($T_i \sim T_c$) over most of their length and cool plasma ($T_i \ll T_c$) near their summits representing the cool prominence body. They start with a hot flux tube and assume that a cool condensation appears near the top of the flux tube, which produces a downward anti-buoyancy force which must be balanced by other forces acting on the flux tube. The magnetic field is assumed to be in equilibrium and the plasma is in a state of hydrostatic equilibrium along the magnetic field lines.

This model was further developed by Degenhardt and Deinzer (1993) by including a simplified energy equation without a conduction term. Schmitt and Degenhardt (1998) extended this model by solving, numerically, the full energy equation together with the equilibrium equations, which improves the temperature gradient between the prominence and the corona, without modifying substantially the obtained values for the rest of parameters (density, temperature, size of the depression) characterizing the prominence region.

Here, we assume that cool clouds, observed below the corotation radius in late-type stars, are stellar prominences having a fibril structure like solar ones, and our aim is to obtain the physical characteristics (density, temperature, size of the depression, half-width, supported mass) of the cool part of such fibril structure. To this end, we have adapted the model by Degenhardt and Deinzer (1993) to the stellar case by taking into account gravity variation with height and centrifugal acceleration, since such clouds have been detected at great heights within stellar coronae belonging to rapid rotators.

3. Rapid rotators: HKAqr (Gl890) and HD197890

Cool clouds have been observed in these stars with the common feature that they seem to be located below the corotation radius. HKAqr is a dM2Ve star with a radius about $0.56R_\odot$, mass about $0.4M_\odot$ and a rotation period of 10.34 hr. HD197890 is a K0V star with a radius about $0.85R_\odot$, mass about $0.75M_\odot$ and a rotation period of 8.04 hr. Since the physical characteristics and rotation periods are different, we have performed separate calculations for HKAqr and HD197890.

To know the influence of different parameters on prominence characteristics, we have varied the coronal temperature, the heating constant, the coronal base pressure and the critical coronal height. In all cases, the values of three parameters have been kept constant and we have modified the fourth one.

The most important parameter affecting prominence characteristics is the height of flux tube summit, since when it is increased the size of the dip grows spectacularly. On the other hand, the rest of parameters are still consistent with the existence of cool material at the dip.

We have also studied, for a solar-type star, the influence of the centrifugal acceleration on prominence characteristics. To this end, we have varied the angular velocity between one and a hundred times the solar value, finding that the increase of the angular velocity does not substantially affect prominence characteristics.

Two important quantities to be determined are the mass in the cool region and the half-width of the cool region. The half-width of the cool region has been taken as the horizontal distance from the dip position to the point where the

internal pressure becomes equal to the central pressure divided by e. Once we know the height at which the above condition is matched, we can compute the contained mass. These calculations have been done for HKAqr and HD 197890 and the obtained mass is similar to the mass of a well developed quiescent solar prominence. Assuming a cool cloud 800,000 km long, 30,000 km high and 20,000 km wide, the mass is about 10^{13} kg.

In summary, this fibril structure model for stellar prominences located below the corotation radius indicates that the most important parameter affecting prominence characteristics is the height of the flux tube summit while the angular velocity has no importance. The critical coronal height determines the depth of the depression, where the cool material is located, influencing, at the same time, the half-width of the prominence and the amount of mass contained within it.

References

Ballester, J. L. and Priest, E. R. 1989, A&A, 225, 213

Byrne, P.B. 1996, in Magnetodynamic Phenomena in the Solar Atmosphere, Y. Uchida, T. Kosugi and H. S. Hudson (eds.), Kluwer Acad. Publ., Dordrecht, Holland, p. 139

Byrne, P.B., Eibe, M.T. and Rolleston, W.R.J. 1996, A&A, 311, 651

Byrne, P.B., Eibe, M.T. and van den Oord, G. H. J. 1997, in preparation

Collier-Cameron, A. 1988, MNRAS, 233, 235

Collier-Cameron, A. and Robinson, R.D. 1989a, MNRAS, 236,57

Collier-Cameron, A. and Robinson, R.D. 1989b, MNRAS, 238, 657

Collier-Cameron, A. and Woods, J.A.. 1992, MNRAS, 258, 360

Degenhardt, U. and Deinzer, W. 1993, A&A, 278, 288.

Doyle, J.G. and Collier-Cameron, A. 1990, MNRAS, 244, 291

Ferreira, J.M.T.S. and Jardine, M. 1995, A&A, 298, 172

Jeffries, R.D. 1993, MNRAS, 262, 369

Schmit, D. and Degenhardt, U. 1998, in G. Klare (ed.) Rev. Mod. Astron., Springer-Verlag, Berlin (in press).

van den Oord, G.H.J. 1988, A&A, 205, 167

van den Oord and G.H.J., Zuccarello, F. 1996, in Stellar Surface Structure, Strassmeier, K. G. and Linsky, J. L. (eds.), Kluwer Acad. Publ., Dordrecht, Holland, p. 433

Yi, Z., Engvold, O. and Keil, S. L. 1991, Solar Phys, 132, 63

Yi, Z. and Engvold, O. 1991, Solar Phys, 134, 275

Prominence-like Clouds Near HK Aqr

G.H.J. van den Oord

Sterrekundig Instituut, Postbus 80.000, 3508 TA Utrecht, The Netherlands

P.B. Byrne and M.T. Eibe

Armagh Observatory, College Hill, Armagh BT61 9DG, N. Ireland

Abstract. A time series of H_α spectra of the rapidly rotating star HK Aqr has been analyzed. Evidence is found for the presence of cool clouds which are in co-rotation with the star. The cloud velocities, as derived from the clouds' absorption features, can be used to put constraints on the clouds' co-latitudes and their distances from the star using a so-called visibility diagram. For HK Aqr most clouds are at distances of 2–3 stellar radii and do not extend beyond the co-rotation radius. By using a simple radiative transfer model, we demonstrate that for most stars the presence of clouds affects the whole H_α profile and does not result in discrete absorptions. Only clouds near rapidly rotating stars, with an inclination close to 90°, will cause discrete absorption features. The cool cloud plasma can form when a temperature inversion is created at the apex of a stellar-sized coronal loop because of reduced coronal heating at large distances from the star. It is likely that the cloud condensations are related to inverse polarity filaments because, near rapidly rotating stars, the axial current in normal polarity filaments decreases with height and has to change sign at the co-rotation radius.

1. Introduction

Observations of the H_α profile of the rapidly rotating M1.5 dwarf star HK Aqr ($P_{rot} = 10.34$ h) indicate the presence of cool clouds which are forced into co-rotation by the stellar magnetic field. These clouds cause absorption features which transit the underlying H_α profile from blue to red. Observations of HK Aqr have previously been reported by Byrne et al. (1996). In van den Oord et al. (1997, VDOBE) we present a further analysis of the cloud phenomenon.

2. Detection of the Clouds

When a point-like cloud is in front of the stellar disk it causes an absorption at velocity

$$v_{abs} = \Omega R_c \sin \theta_c \sin i \sin \varphi \qquad (0.1)$$

with $\Omega = 2\pi/P_{rot}$ the angular velocity of the star, R_c the distance of the cloud to the center of mass of the star, θ_c the co-latitude of the cloud, i the inclination
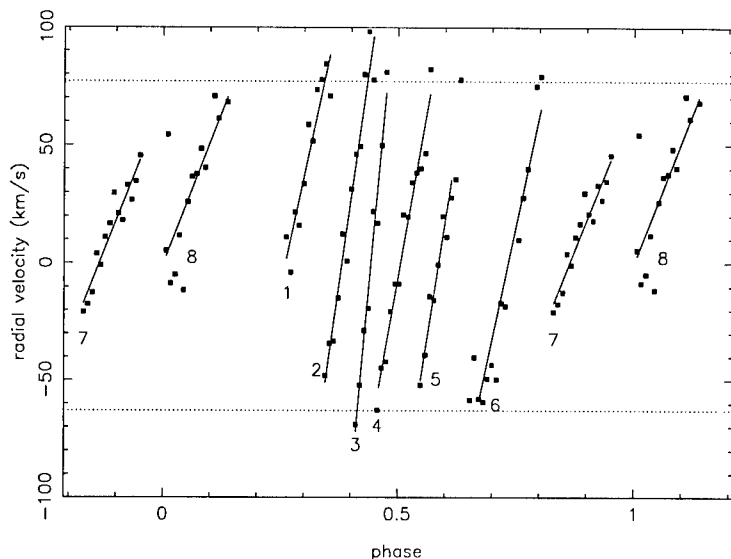
Figure 1. Observed radial velocity tracks for HK Aqr's clouds as a function of orbital phase. The observing conditions for clouds 7 and 8 were affected by the occurrence of a flare. Cloud 1 was already crossing the disk when the observations started.

of the star and $\varphi = \Omega t$ the phase angle of the cloud. At central meridian crossing $(\sin \varphi = 0)$ Eq. (1) gives

$$\frac{R_c \sin \theta_c}{R_*} = \frac{1}{\Omega} \frac{1}{v_* \sin i} \left. \frac{dv_{abs}}{dt} \right|_{\sin \varphi = 0} \tag{0.2}$$

where $v_* = \Omega R_*$ is the intrinsic equatorial rotation speed of the star. The right hand side of Eq. (2) can be determined from observations, thus providing information about $R_c \sin \theta_c / R_*$. The phases of in- and egress of a cloud ($\varphi \equiv \pm \Psi$) are given by

$$\cos \Psi = \left(\sqrt{1 - R_*^2/R_c^2} - \cos \theta_c \cos i \right) / (\sin \theta_c \sin i) . \tag{0.3}$$

Because Eqs. (2) and (3) depend on R_c/R_* and on the cloud's co-latitude θ_c, it is possible to construct a so-called visibility diagram depicting contours of $R_c \sin \theta_c / R_*$ and $\cos \Psi$. In Figure 1 we show the observed radial velocity tracks of eight clouds which have been identified in the H_α spectra of HK Aqr. In Figure 2 we show the positions of the clouds in the visibility diagram. Most clouds are located below the co-rotation radius.

Subtracting the observed spectra from a template spectrum gives the absorbed flux. This flux can be written as

$$F_{abs}(\Delta\lambda) = \int_{-1}^{1} \mathcal{K}(\Delta\lambda - \Lambda y) Z(y) dy \tag{0.4}$$
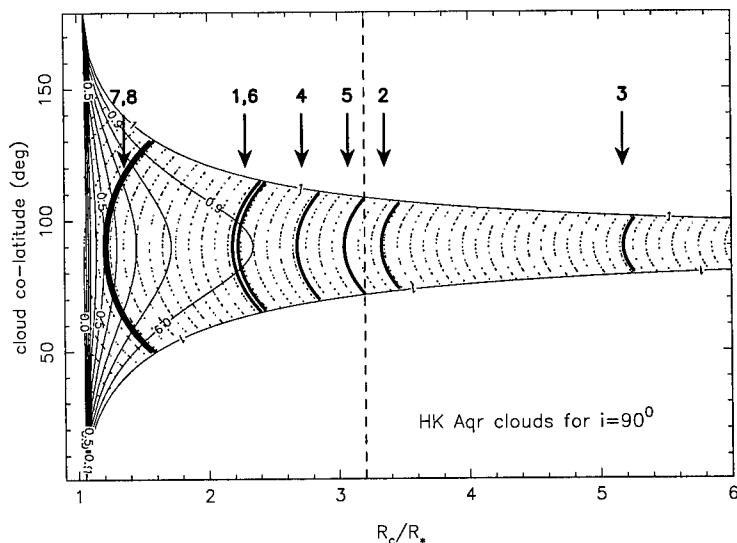
Figure 2.   Visibility diagram for the clouds observed on HK Aqr. The thick solid lines indicate the possible locations of the clouds. The labels correspond to the numbers in Figure 1. The dashed line indicates the location of the co-rotation radius. The thin solid contours indicate $\cos\Psi = $ constant and the dotted contours $R_c \sin\theta_c/R_* = $ constant. Clouds in the blank area are off the disk and do not result in absorptions.

where $\Delta\lambda = \lambda - \lambda_c$, λ_c is the central wavelength of H_α, $\Lambda = |v_* \sin i|\lambda_c/c$, $\mathcal{K}(\Delta\lambda) = I_*(\Delta\lambda)[1 - \exp\{-\tau(\Delta\lambda)\}]$, I_* is the stellar line-of-sight intensity and $Z(y)$ is a function describing the distribution of the clouds on the projected stellar disk. Lines $y = $ constant correspond to a specific line-of-sight velocity. The total cloud area is given by $\int Z(y)dy$. Eq. (4) shows that the absorbed flux is given by a convolution of $Z(y)$ with the kernel $\mathcal{K}$. The accuracy with which $Z(y)$ can be recovered depends on the width of the kernel $\mathcal{K}$ (see VDOBE). When the absorption profile is dominated by thermal Doppler broadening, the resolution Δy which can be achieved on the disk is given by

$$\frac{\Delta y}{2R_*} = 1.28 \frac{\sqrt{T_4}}{|v_{*,10}\sin i|} f(\tau_0) \qquad (0.5)$$

where T_4 is the cloud temperature in units of 10^4 K and $v_{*,10}$ is the intrinsic equatorial rotation speed of the star in units of 10 km/s; $f(\tau_0)$ is a slowly varying function of the central optical depth τ_0 (for $\tau_0 \ll 1$ $f = 0.83$ and for $\tau_0 = 10$ $f = 1.63$). For clouds to show in- and egress requires that $\Delta y/2R_* < 1$. This condition is only fulfilled for rapidly rotating stars, like HK Aqr and AB Dor, and for stars for which the inclination is not too low. It could well be that the cloud phenomenon is not restricted to fast rotators, but that only for fast rotators can it be identified because of the presence of discrete absorptions. In other stars it will show up as variations of H_α affecting the whole line profile.

3.   The Nature of the Clouds

In the previous section we showed that, based on spectral diagnostics, clouds do not necessarily have to be an exclusive phenomenon for rapid rotators. Clouds were first detected on the rapidly rotating star AB Dor (Cameron and Robinson 1989a, b). Based on the technique of skew-mapping these authors found evidence of clouds beyond the co-rotation radius. In that case fast rotation could be important for cloud formation and Cameron and Robinson suggested that the clouds form in loops with temperature inversions. These can be created when the effective gravity changes direction in a loop, e.g., at the co-rotation radius. We note that the AB Dor clouds found with the more traditional technique of gaussian fitting are mainly below the co-rotation radius. The clouds near HK Aqr are also mainly found below the co-rotation radius but still at some considerable distance of the star. Because these clouds cannot be formed by gravity reversals, it is likely that they arise because of insufficient coronal heating near the apex of loops, leading to a temperature inversion. To suppress the Rayleigh-Taylor instability a dip is required in the magnetic field making the clouds resemble filament-like structures. We can consider two possible topologies. In the normal polarity model (NP) the Lorentz force of the background magnetic field balances the effective gravity while in the inverse polarity model (IP) the Lorentz force of the background field is balanced by the Lorentz force due to a surface current distribution on the star. If we assume that the clouds form between the star and the co-rotation radius, and then move slowly outward, then the NP model has the undesired property that the filament current has to decrease as the filament moves outward and has to change sign as the cloud passes through the co-rotation radius. For the IP model this problem does not exist because the current increases as the cloud moves outward. Also, NP prominences are unstable to radial perturbations while IP prominences are not. If the clouds are related to IP prominences then there is no reason why their presence should be restricted to rapid rotators, since for IP prominences mechanical forces are unimportant for the equilibrium. For weakly ionized clouds the typical life time of a cloud is $\tau \approx 21.6(\ell_c/R_*)^2 n_{n,10}$ hours and the velocity of the cloud with respect to the field is $v_\perp \approx 5(\ell_c/R_*)^{-1} n_{n,10}^{-1}$ km/s. Here ℓ_c is the typical dimension of the cloud and $n_{n,10}$ is the density of the neutrals in units of 10^{10} cm^{-3}.

References

Byrne, P.B., Eibe, M.T. and Rolleston, W.R.J. 1996, A&A, 311, 651
Cameron, A.C. and Robinson, R. 1989a, MNRAS, 236, 57
Cameron, A.C. and Robinson, R. 1989b, MNRAS, 238, 657
van den Oord, G.H.J., Byrne, P.B. and Eibe, M.T 1997, A&A, submitted

Birth and Death of Filaments

Filament Channels: Essential Ingredients for Filament Formation

V. Gaizauskas

Herzberg Institute of Astrophysics, National Research Council of Canada,
100 Sussex Drive, Ottawa, K1A 0R6 Canada

Abstract. Channels share with their filaments in a hemispheric dependance for the orientation of their axial magnetic fields. This property has significant implications for models of filaments. In support of new model-building exercises, this review examines known signatures of channels, presents evidence that emerging flux plays a key role in creating a new filament channel, and compares channels which form in the belts of active latitudes with those formed closer to the poles.

1.   Introduction

Solar filaments form in filament channels, seen in the cool chromosphere as long narrow voids overlying polarity inversions between plages of opposite magnetic polarity – hence 'plages couloirs' (Martres et al. 1966). Spicules or fibrils rooted in enhanced magnetic elements are suppressed, even absent, inside channels. Foukal (1971) concluded that the characteristic orientation of Hα fibrils to either side of a filament channel denotes a magnetic field with a predominantly horizontal component along, and not across, the axial direction of the channel. The dominant horizontal direction of fields in filaments themselves was confirmed by the observations of many prominences at the limb using the Hanle effect (reviewed by Leroy 1989).

Radiation originating in hotter plasma is characteristically weakened above polarity inversions with filaments or filament channels – as in He I 10830 (Harvey 1996) or at mm wavelengths (Bastian et al. 1993), or is completely absent – as in the UV (Dere et al. 1986) or in X-rays (Serio et al. 1978) where the filament channel is equated to the filament cavity (Engvold 1994; Moses et al. 1994). The relationship between these radiative signatures and those revealed by the morphology of the underlying chromosphere is unclear.

Not every filament channel contains a filament, nor does every polarity inversion develop an associated channel. Convergence of magnetic flux, leading to flux cancellation at a polarity inversion, is a necessary condition for producing a filament channel and filament (Martin 1990).

Martin et al. 1994 discovered a hemispheric asymmetry for quiescent filaments and their underlying channels: when quiescent filaments/channels are viewed from the positive polarity side, a majority in the northern (southern) hemisphere have fields directed to the right (left). Thus the filament/channel field has a definite orientation – either "dextral" or "sinistral" – which predom-

257

inates in the northern and southern hemispheres, respectively. Channels with a common orientation can join to form very long and very persistent structures. Channels can exceed in length and duration any filament which forms in them.

Figure 1.   Filament channels in McMath 14726 on April 18, 1977: (a) Hα filtergram; (b) cospatial filtergram at Hα + 0.6 Å with voids between plages at channels C1, C2, C3; (c) cospatial NSO/KP B$_\parallel$ magnetogram with contours of 3 filaments superposed. S1 and S2 are both p-polarity spots (black is negative). Top N; right W in all figures.

Polarity inversions and the channels that outline them are basic ingredients of the Sun's global magnetic topology. McIntosh (1972, 1992) used Hα images for two decades to locate channels and to follow their evolution against a backdrop of continually evolving active regions. Filament channels may be implicated in coronal mass ejections (CMEs). Huge soft X-ray arcades, seen with the Yohkoh SXT to form suddenly over extended polarity inversions, followed: (i) a CME in the absence of a filament eruption (McAllister et al. 1996); (ii) 'X-ray blowouts' at polarity inversions near the borders of coronal holes but without any corresponding chromospheric disturbance (Bhatnagar 1996).

This review presents data which show that the visibility of channels depends on local field strengths, that emerging flux plays a key role in creating a new channel, and that channels in the belts of active latitudes are related to those formed closer to the poles.

2.   Signatures of Filament Channels

The Ottawa River Solar Observatory (ORSO) acquired many large-scale images of filaments and filament channels in raster scans, made daily whenever possible from 1978 to 1992, of the entire Sun with a 0.25 Å bandwidth Hα filter displaced 0, ± 0.6 Å, ± 1.0 Å at each of 102 overlapping positions on the disc. Images at ± 0.6 Å are especially useful to detect voids in fibril patterns and to find reversals in the streaming direction of fibrils on opposite sides of a polarity inversion − basic signatures of a chromospheric filament channel. Samples presented here from the ORSO archive illustrate a range of channel environments.

2.1. In Active Latitudes

The clearest channels are located on the boundaries of active regions where a spot and plage, evolving together as a unit of bipolar flux, are separated by a polarity inversion from pre-existing flux. Of three filaments in an activity complex comprising two closely packed bipoles (Figure 1a), two have channels (C1 and C3, Figure 1b) at polarity inversions isolating the flux inside the complex from surrounding plages. They are wider than channel C2 which separates older p-polarity spot S1 from the f-polarity plage associated with its younger p-polarity neighbor, S2 (Figure 1c). Contrary directions of streaming fibrils on opposite sides of broad channel C3, indicated by arrows in Figure 1b, brand C3 as a sinistral channel. C3 is less voided than C1 or C2: besides the still-visible spine of the filament, faint dark threads cross C3 diagonally in Figure 1b.

Activity complexes are at times spaced almost regularly around the active belts of the Sun (Gaizauskas et al. 1983); polarity reversals between adjacent complexes, typically inclined diagonally across the belt of active latitudes, are often marked by the long quiescent filaments called the 'intermediate' type. Figure 2 compares in the same field of view an intermediate filament near the E limb with a boundary filament surrounding active region (AR) 7163, a so-called 'anemone' region in an adjacent coronal hole. The void in the channel of the intermediate filament is not yet evident at a wavelength offset of $+ 0.4$ Å (Figure 2a). Instead, numerous low-lying fine dark structures inside the channel are coaligned with the axis of the filament – not across it – over its entire length, similar to the axial alignment of Hα fibrils seen alongside filaments in the core of the line in strong channels (F3 in Figure 1a and F1 in Figure 3). For the boundary filament of AR 7163, however, a void is already evident at this wavelength (Figure 2b).
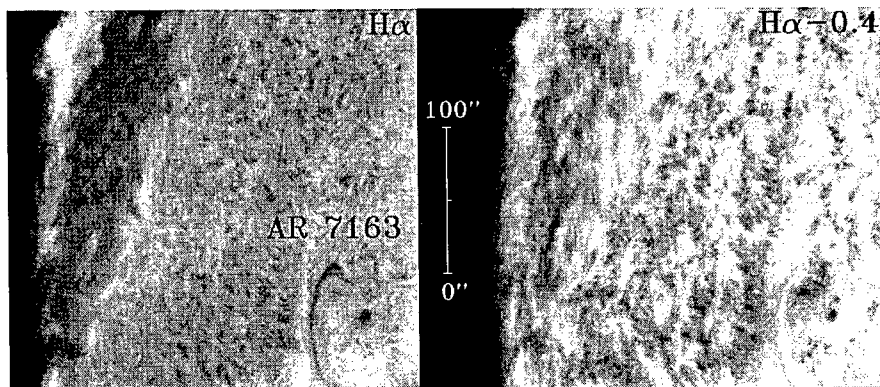
Figure 2.   Intermediate and boundary filaments on May 10, 1992.

2.2. In Quiet Equatorial Regions

Of three filaments depicted on the same day in Figure 3 only the channel for F1 is obvious, from: coaligned Hα fibrils next to the Hα filament; a strong void at
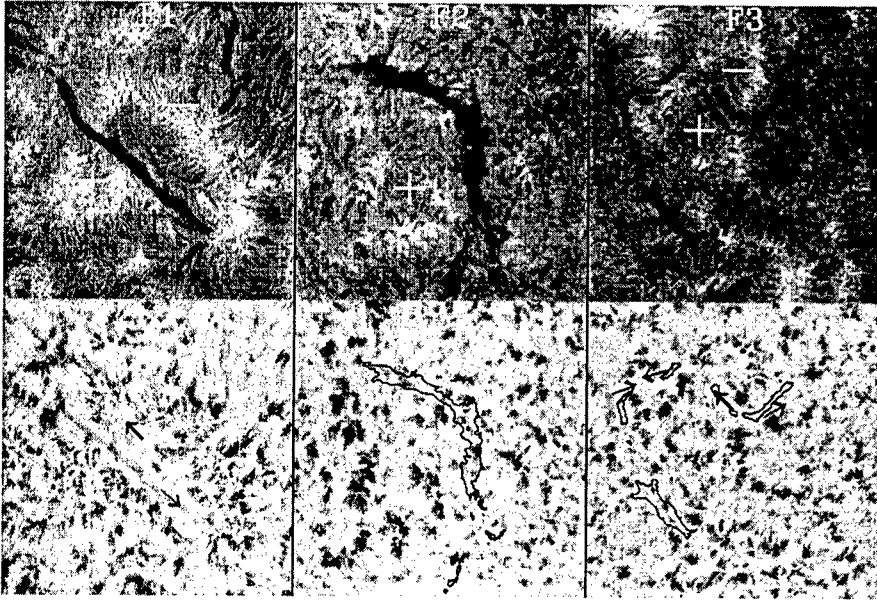
Figure 3.   Upper row (filaments) Hα filtergrams; lower row (channels) Hα + 0.6 Å filtergrams with filaments superposed as black contours. ORSO images on July 24, 1992. +/− signs denote magnetic polarity.

Hα + 0.6 Å; and counter-streaming fibrils on the edges of the channels (black arrows) which brand F1 as a dextral filament. It was stable during its disk passage.

All of these signs are absent for multi-barbed F2; most of its many barbs indicate that F2 is sinistral. The lack of a channel may be related to the fact that F2 altered markedly each day and vanished before reaching central meridian. A channel is barely traceable at fragmented filament F3 from counter-streaming fibrils marked by arrows in the coaligned Hα + 0.6 Å filtergram.

These 3 filaments are superposed as contours against the full-disk SXT image in Figure 4. The arcade of loops overlying dextral filament F1 is a stable feature during this disk transit. Coronal loops over either F2 or F3 are invisible. Only the filament lying between the strongest magnetic fields has both a chromospheric void and an arcade visible with these exposures of Yohkoh/SXT.

2.3. In Quiet Regions at High Latitude

Channels for polar crown filaments (PCFs) are indistinct or invisible in Hα . Sub-polar crown filaments, which form along the high-latitude fringe of active latitudes, can have conspicuous Hα channels. Both kinds were present in July 1979 (see Figure 1 of Harvey and Gaizauskas 1998, these proceedings) as a single long structure outlining a large-scale unipolar pattern of negative (trailing) polarity flux transported poleward from the northern belt of active latitudes and sheared by differential rotation, to form a 'switchback'. This channel is remark-
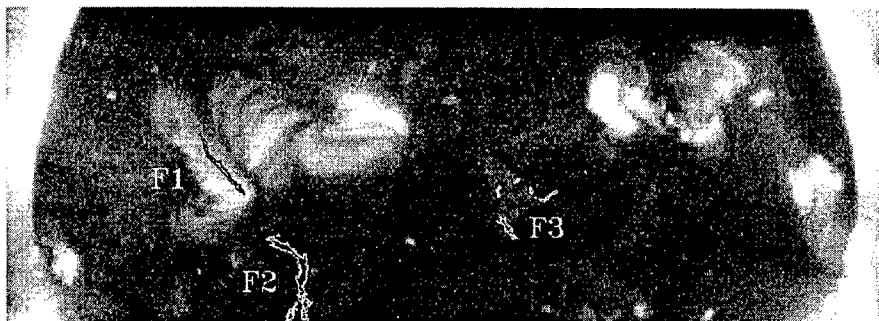
Figure 4.   SXT(Yohkoh) image for July 24, 1992 with Hα filaments superposed as black (F1) or white (F2, F3) contours.

ably continuous in the He I 10830 image as a path with weakened absorption and reduced contrast in the network. Fragments of filaments overhang the entire channel. In the polar crown portion, Hα fibrils lack systematic alignments; but in the sub-polar crown portion, many Hα fibrils are axially aligned along the axis of the channel.

In summary, Hα channels are clearest (anti-parallel fibrils, clear voids) at polarity inversions embedded in strong magnetic fields; they are vague in weak fields. Where magnetic fields are weakest, as in polar regions, He I 10830 remains a sensitive indicator of filament channels.

3.   Creation of Filament Channels

(a)   (b)   (c)
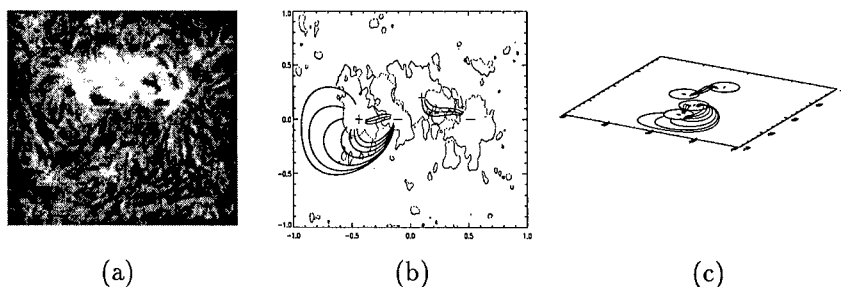
Figure 5.   Field lines in a filament channel (Courtesy D.H. Mackay)

It follows that the best place to find an Hα filament channel in the act of formation should be among strong fields. A successful search for such an event is described by Gaizauskas et al. (1997). Because flux emerged in an undisturbed background, it was possible to trace the detailed evolution of Hα fibrils surrounding the new small activity complex. A channel formed in a few hours but a stable filament did not form in it for another 4 days. Key to the formation of the channel was the close emergence of two bipoles, not one alone, resulting in

a sharply non-potential magnetic field close to the surface. A force-free model constructed by Mackay et al. (1997) for this example is shown in Figure 5.

On the left side of Figure 5a the aligned coarse fibrils are seen a day after the channel formed; force-free field lines modeled for $\alpha = 3.0$ are plotted in panel (b) to show their close fit to the direction of the Hα fibrils in the channel; the oblique view in panel (c) emphasizes how flat and shallow the field lines are in this situation. The filament forms when flux from the newly arrived concentration of flux converges onto an old diffuse region and the magnetic connectivity of field lines in the channel changes due to magnetic reconnection (see Galsgaard and Longbottom, these proceedings).

Figure 6.   Sunspot filament in AR 3804 on July 15, 1982. Fibrils stream in directions of arrows: white/black = +/− polarity. Mosaic of 15 ORSO images at Hα + 0. 6 Å.

Filaments inside activity complexes are at one extreme of flux concentration. Figure 6 shows one anchored in the large δ -type spot of the most flare-active

region of Cycle 21, AR 3804, within a long-lived ($\geq$ 20 solar rotations) complex of activity. The channel is defined by anti-parallel fibrils (between the curved black and white arrows) at the edges of enhanced network on opposite sides of the void partially filled with a strongly Doppler-shifted segment of the filament. Fibrils are also aligned over a much broader area radiating away from AR 3804 and away from the polarity inversion containing the long filament. From their directions we can infer that a huge arcade overlies the narrow portion of the filament. The randomly oriented fibrils underneath the broad northern portion of the filament give no hint there of a channel or an overlying arcade.

The enhanced network arose from the dispersion of earlier flux emergences in the same activity complex. In two more rotations, enhanced network of both polarities had migrated up to the coronal hole covering the polar cap. During that migration, the filament channel depicted in Figure 6 first elongated and then fragmented as the supply of flux in the core of the activity complex weakened. By September 1982 the filament and channel of Figure 6 had disappeared; a newer and longer one had formed between the fluxes diffusing poleward from the complex containing AR 3804 and from its eastern companion, AR 3810 and AR 3812 combined (Figure 6). Furthermore, the huge switchback formed by these rapidly evolving patterns now had fragments of a PCF between the advancing enhanced network and the polar coronal hole. The steps – major flux eruption to formation of a PCF – were completed in just 3 or 4 solar rotations.

4. Discussion

A relationship between chromospheric voids in channels and overlying coronal cavities has been long suspected (Section 1). A recent Yohkoh/SXT observation at the limb (Figure 2 of Harvey and Gaizauskas, these proceedings) supports this conjecture. An exceptionally sharp outer boundary of an X-ray cavity terminates precisely at the outer edges of a channel defined by a void in He I 10830 enclosing a filament. This is the first direct evidence that a 'coronal' cavity, terminating at the surface, could result in reduced density surrounding a filament at chromospheric heights. The reduced visibility in channels of off-band Hα and He I 10830 fine structure may thus be due simply to a lack of sufficient matter to illuminate low-lying field lines at these wavelengths. This suggestion is consistent with the increasing visibility reported in Section 2 of chromospheric voids with increasing magnetic flux density surrounding channels, which in turn is consistent with the findings about coronal X-ray arches and filament channels by Davis and Krieger (1982). They found that the arches were brightest above filament channels with little or no filamentary matter in strong fields on the fringe of active regions, but were absent above strongly absorbing filaments located beneath X-ray cavities typical for quiescent filaments.

A density reduction alone in the channel cannot account for the He I 10830 signature in the absence of an Hα one in large quiescents such as PCFs. Coronal cavities above these tall structures reduce the downward flux of radiation and hot electrons, thereby weakening the He I 10830 absorption in the channel. Any axial field in the filament will further inhibit downward thermal conduction.

The behaviour of PCFs with the solar cycle has often been represented as a secular trend and linked to the solar dynamo (review by McIntosh 1992).

The preliminary case study based on Figure 6 shows instead that PCFs and their channels can occur in a highly episodic fashion and are more likely driven by the transport to high latitudes of large quantities of surface flux originally concentrated in activity complexes at much lower latitudes.

References

Bastian, T.S., Ewell, M.W., Jr., and Zirin, H. 1993, ApJ, 418, 510

Bhatnagar, A. 1996, in Solar and Interplanetary Transients, (eds.) S. Ananthakrishnan and A. Pramesh Rao, Astrophys. and Space Sci. Vol. 243, Kluwer Acad. Publ., Dordrecht, Holland

Davis, J.M. and Krieger, A.S. 1982, Solar Phys., 80, 295

Dere, K.P., Bartoe, J.-D.F., Brueckner, G.E. 1986, ApJ, 305, 947

Engvold, O. 1994, in Solar Coronal Structures, (eds.) V. Rusin, P. Heinzel, and J.-C. Vial, VEDA, Slovakia, p. 207

Foukal P. 1971, Solar Phys., 19, 59

Gaizauskas, V. et al. 1983, ApJ, 265, 1056

Gaizauskas, V., Zirker, J.B., Sweetland, C., and Kovacs, A., 1997, ApJ, 479, 448

Harvey, K.L. 1996, in Solar Wind Eight, (eds.) D. Winterhalter et al., AIP Conf. Proc. 382, AIP:Woodbury, NY, p. 9

Leroy, J.L. 1989 in Dynamics and Structure of Quiescent Prominences, (ed.) E.R. Priest, Kluwer:Dordrecht, p. 77

Mackay, D.H. et al. 1997, ApJ, 486, 534

Martin, S.F. 1990, in Dynamics of Quiescent Prominences, (eds.) V. Ruzdjak and E. Tandberg-Hanssen, Springer:Berlin, p. 1

Martin, S.F., Bilimoria, R., and Tracadas, P.W. 1994, in Solar Surface Magnetism, (eds.) R. Rutten and C. Schrijver, Dordrecht:Kluwer, p. 303

Martres, M.-J., Michard, R., and Soru-Iscovici, I. 1966, A&A, 29, 249

McAllister, A.H. et al. 1996, J. Geophys. Res., 101, 13,497

McIntosh, P.S. 1972, Rev. Geophys. and Space Sci., 10, 837

McIntosh, P.S. 1992, in The Solar Cycle, (ed.) K.L. Harvey, ASP Conf. Ser. Vol. 27, p. 14

Moses, D. et al. 1994, ApJ, 430, 913

Serio, S. et al. 1978, Solar Phys., 78, 65

Magnetic Flux Transport and Formation of Filament Channels

A. A. van Ballegooijen

Harvard-Smithsonian Center for Astrophysics, 60 Garden Street, Cambridge, MA 02138, USA

N. P. Cartledge and E. R. Priest

Mathematical and Computational Sciences Department, University of St. Andrews, KY16 9SS Scotland, UK

Abstract. We present a model of the transport of photospheric and coronal magnetic fields with the aim of explaining the observed global pattern of dextral and sinistral filaments on the quiet sun. The model is based on the assumption that the axial field in a filament channel originates in the surrounding coronal arcade. The model predicts that switchbacks in the polarity inversion line have opposite chirality on the two arms of the switchback: the higher latitude "lead" arm has sinistral (dextral) orientation in the North (South), while the lower latitude "return" arm has dextral (sinistral) orientation. This is in conflict with prominence observations which show that the chirality is the same on the two arms of a switchback. The model predicts the wrong sign of the axial field in polar crown filaments. This suggests that axial field in quiescent filaments are not produced by differential rotation acting on the surrounding coronal arcades.

1. Diffusion Model

Measurements of magnetic fields in solar prominences (Leroy 1978, Leroy, Bommier and Sahal-Bréchot 1983, 1984, Bommier and Leroy 1998, these proceedings) and observations of Hα filaments on the solar disk (Martin, Marquette and Bilimoria 1992, Martin, Bilimoria and Tracadas 1994) show that the "axial" component of magnetic field (i.e., the component along the polarity inversion line) exhibits a large-scale organization: quiescent filaments in the northern hemisphere predominantly have *dextral* orientation (i.e., axial magnetic field pointing toward the right when viewed from the positive polarity side), while those in the southern hemisphere have *sinistral* orientation. In this paper we consider a model of the formation of filament channels which assumes that these axial fields are produced by differential rotation acting on the surrounding coronal arcades. Then the axial field in the filament channel should have the same sign as the axial field in the surrounding arcade.

The transport of radial magnetic field in the solar photosphere can be described in terms of a diffusion model (e.g., Leighton 1964, Sheeley et al. 1987).
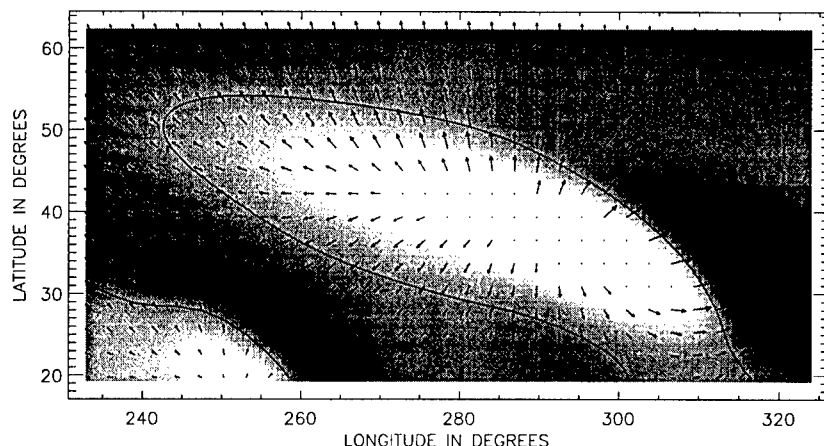
Figure 1.   Magnetic field near a switchback in CR 1791. Grey levels indicate radial magnetic field in the photosphere ($|B_r| < 15$ Gauss); vectors indicate the horizontal magnetic field at $r = 1.1R_\odot$.

We extended this model to include not only the radial field at the photosphere but also the horizontal field, both in the photosphere and higher up in the corona (van Ballegooijen, Cartledge and Priest 1998). The model includes differential rotation, meridional flow and supergranular diffusion (photospheric diffusion constant $D = 450$ km$^2/s$). We assume that fluid motions in the corona are purely horizontal, and we artificially suppress the vertical diffusion of horizontal magnetic fields. The magnetic induction equation is solved numerically by decomposing the magnetic field into spherical harmonics ($l_max = 63$). For the initial conditions we use potential fields computed from synoptic magnetic field data obtained at NSO/Kitt Peak[1]. The magnetic field from one Carrington Rotation (CR) is evolved over a period of 27 days, and the result is compared with the observed field for the next rotation. Figure 1 shows the simulated magnetic field near a switchback in the polarity inversion line in CR 1971 (July 1987).

2.   Analysis

We simulate the magnetic fields for four Carrington Rotations (CR 1791, 1816, 1849 and 1876) and deduce the orientation of the axial field over the polarity inversion lines. Figure 2 shows histograms of the predicted number of dextral and sinistral channels as a function of latitude (compare with Martin et al. 1994). We assume that filament channels form preferentially in locations where

---

[1]The NSO/Kitt Peak data used in this study are produced cooperatively by NSF, NASA/GSFC and NOAA/SEC.
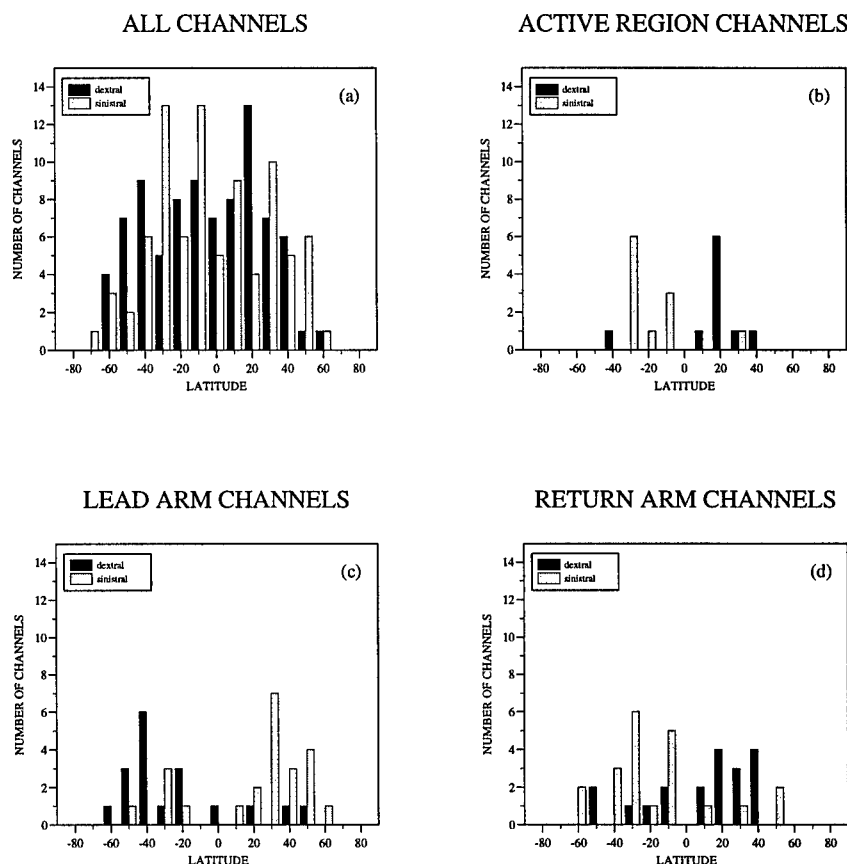
Figure 2.   Histograms of predicted number of filament channels.

some magnetic shear is already present in the surrounding arcade, so we define a "channel" as a region where the computed magnetic field is sheared over a substantial section along the polarity inversion line (minimum length $0.15R_\odot$; minimum shear angle 30°). Note that there is no clear hemispheric pattern: the model predicts that dextral and sinistral channels occur in about equal numbers in each hemisphere (see Figure 2a). The subset of channels located within relatively young active regions (Figure 2b) are mostly dextral in the north and sinistral in the south, which is due to differential rotation acting on initially north-south oriented polarity inversion lines in these regions. Figures 2c and 2d show the latitude distribution of channels located on the "lead" and "return" arms of switchbacks. The lead arms are predicted to have sinistral (dextral) channels in the north (south), and the same is true for the polar crowns. This is due to differential rotation acting on coronal arcades overlying nearly east-west oriented polarity inversion lines (van Ballegooijen and Martens 1990). The

return arms of switchbacks have dextral (sinistral) channels in the north (south), which can be traced to the influence of the polar magnetic field. Hence, the chirality of the field is predicted to be different on the two arms of a switchback, as shown in Figure 1. Since the lead arms occur at higher latitude than the return arms, there is a slight excess of sinistral (dextral) channels in the north (south) above latitudes of 40° (see Figure 2a).

Filaments are known to occur on both "lead" and "return" arms of switch-backs. Therefore, on the basis of the present model one would expect to find a mixture of both dextral and sinistral channels in each hemisphere. This is in conflict with observations which show a clear preference for dextral channels in the north and sinistral channels in the south (see Bommier and Leroy 1997, Martin et al. 1994). We conclude that the present model (filament axial field originating in the surrounding coronal arcade) does not reproduce the observed global patterns of dextral and sinistral channels on the quiet sun. However, the flux transport model may be successful in describing the build-up of magnetic shear in coronal arcades.

It has been proposed that the axial field in filament channels originates in the solar convection zone: differential rotation acting on subsurface fields can produce the correct sign of the axial field (e.g., Priest, van Ballegooijen and MacKay 1996). However, there is as yet no direct observational evidence for the emergence of such axial fields through the photosphere. Therefore, the origin of the observed global patterns is still unclear.

References

Leighton, R. B. 1964, ApJ, 140, 1547

Leroy, J. L. 1978, A&A, 64, 247

Leroy, J. L., Bommier, V. and Sahal-Bréchot, S. 1983, Solar Phys., 83, 135

Leroy, J. L., Bommier, V. and Sahal-Bréchot, S. 1984, A&A, 131, 33

Martin, S. F., Bilimoria, R. and Tracadas, P. W. 1994, in Solar Surface Mag-netism, (eds.) R. J. Rutten and C. J. Schrijver, Dordrecht: Kluwer, p. 303

Martin, S. F., Marquette, B. and Bilimoria, R. 1992, in The Solar Cycle, (ed.) K. Harvey, ASP Conf. Ser. Vol. 27, San Francisco, p. 53

Priest, E. R., van Ballegooijen, A. A. and MacKay, D.H. 1996, ApJ, 460, 530

Sheeley, N. R., Jr., Nash, A. G. and Wang, Y.-M. 1987, ApJ, 319, 481

van Ballegooijen, A. A., Cartledge, N. P. and Priest, E. R. 1998, ApJ, submitted

van Ballegooijen, A. A. and Martens, P. C. H. 1990, ApJ, 361, 283

Filament Channels: Contrasting Their Structure in Hα and He I 1083 nm

Karen L. Harvey

Solar Physics Research Corporation, 4720 Calle Desecada, Tucson, AZ 85718, U.S.A.

Victor Gaizauskas

Herzberg Institute of Astrophysics, National Research Council, 100 Sussex Drive, Ottawa, Canada, K16OR6

Abstract. From a direct comparison, we find that filament channels are more easily detected in He I λ1083 than in Hα, particularly for polar crown filaments. He I 1083 nm filament channels appear to coincide with the outer boundaries of *Yohkoh*/SXT X-ray cavities.

1. Filament Channels in He I λ1083

Filament channels occur along polarity inversions that separate magnetic fields of opposite magnetic polarity. They may or may not have a filament within their boundaries, but their existence is a necessary condition for the formation of a filament. In He I λ1083 nm images, filament channels are observed as brighter, elongated structures. As shown in Figure 1, they are easily distinguished from the similar-appearing coronal holes by the characteristics of the underlying magnetic field.

This paper compares the properties of He I 1083 nm filament channels in relation to those in Hα and to coronal cavities that surround filaments/prominences. We make use of five data sets: the National Solar Observatory at Kitt Peak (NSO/KP) daily high-resolution (1–2 arc-sec pixels), full-disk observations of the line-of-sight photospheric (λ868.8 nm) and chromospheric (λ854.2 nm) magnetic fields and He I λ1083 nm equivalent width; the Ottawa River Solar Observatory (ORSO) daily center-line and off-band Hα high-resolution ($\leq$ 0.5 arc-sec pixels), limited-field surveys of the entire solar disk; the *Yohkoh*/Soft X-ray Telescope (SXT) full-disk X-ray images taken in the thin Al and AlMg filter with a pixel size of 5 arc-sec.

2. Comparison of Filament Channels in He I λ1083 and Hα

A comparative study of filament channels in He I λ1083 nm and Hα was made for several days in 1978, 1979 and 1992. Figure 1 shows one example of an area of the northern hemisphere on July 14, 1979. This area of the Sun includes a polar-crown filament (N47E41 to N67W22) and two segmented filaments in the latitude range N20 to N30. Several smaller filaments are also seen in the Hα
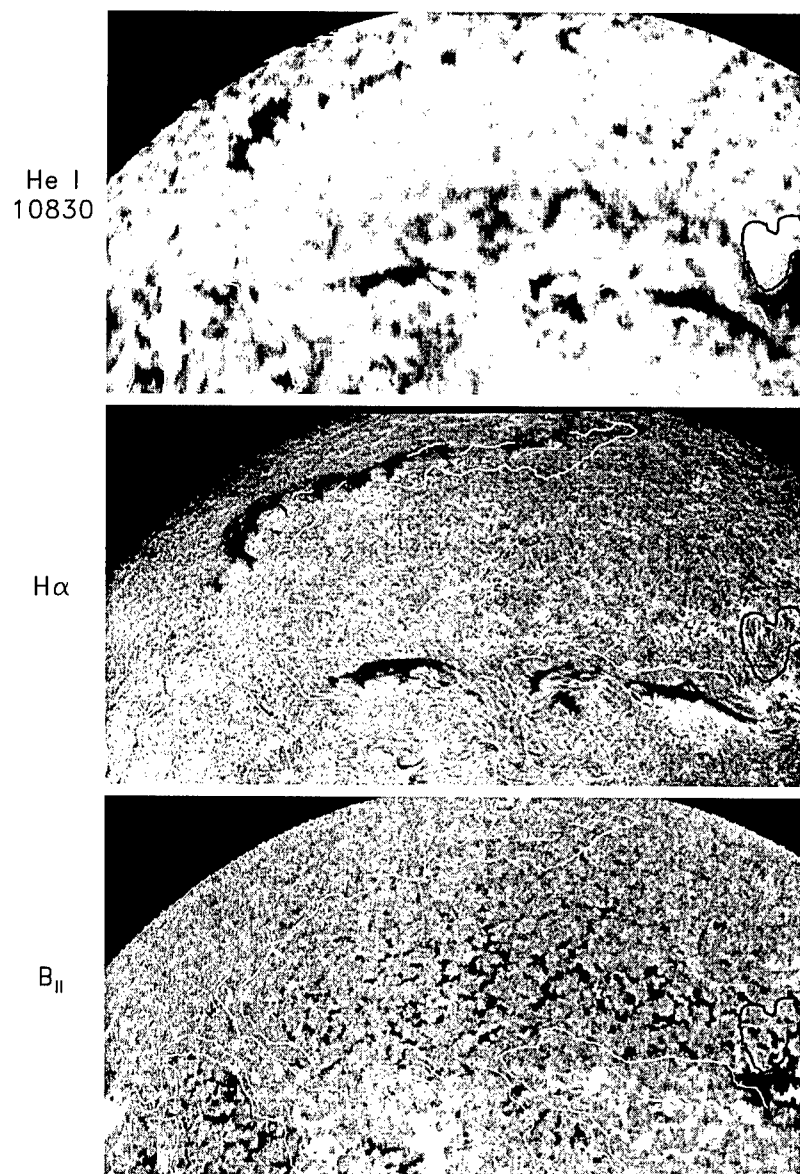
Figure 1.   *Top:* NSO/KP He I λ1083 nm spectroheliogram on an inverse equivalent width scale (1741 UT). *Middle:* ORSO Hα filtergram (1412 UT). *Bottom:* NSO/KP magnetogram (1630 UT) of a portion of the northern hemisphere on July 14, 1979. The He I 1083 filament channels are outlined in *white* and a coronal hole in *black* in all three panels. North is at the top and East to the left.

filtergram.

The He I 1083 nm filament channels, outlined in Figure 1 and as described above, are elongated structures along almost every polarity inversion in Figure 1. The mean equivalent width of the channels is 29–35 mÅ, comparable to that of the interiors of supergranular cells, which are partially or completely enclosed by enhanced He I 1083 nm absorption associated with magnetic network fragments at the edges of the cells, and to that of coronal holes.

Many of the He I 1083 filament channels located in stronger magnetic flux of decaying active regions exhibit a corridor of Hα fibrils that are nearly aligned with the polarity inversion (Figure 1, middle panel), an Hα characteristic first noted by Foukal (1971) and later by Martin, Bilimoria and Tracadas (1994). The width of the He I 1083 filament channel across the polarity inversion corresponds to the width of the pattern of aligned Hα fibrils. These properties are observed whether or not the channel is occupied by a filament.

In the area of the polar-crown filament at higher latitudes, there is no obvious alignment of the Hα fibrils along the polarity inversion, although the polar-crown filament channel is easily detected in the He I 1083 image. Since polar-crown filaments extend to a greater height than those filaments in stronger fields, it may be that the alignment of Hα fibrils along a polarity inversion is related to the height of a filament or its corresponding magnetic structure.

3.   Comparison of a Filament Channel in He I λ10830 and an X-ray Prominence Cavity

A persistent coronal cavity was observed by *Yohkoh*/SXT on several successive limb crossings during June–August 1997 (Hudson, Acton and Harvey 1998). This X-ray cavity is compared on July 4, 1997 in Figure 2 with the corresponding NSO/KP He I 1083 spectroheliogram. The filament associated with this cavity can be seen on the disk and at the limb in both He I 1083 nm and Hα extending to 59,000 km above the limb at 0100 UT. Although there is a 15-hour time difference between the He I 1083 and X-ray observations, we do not expect the relative positions of the channel and the X-ray emission to change, because of the east-west orientation of the filament channel. It appears from this comparison, as well on other limb crossings, that the boundaries of the filament channel coincide with the outer boundaries of the X-ray cavity. This correspondence hints that the appearance of the He I 1083 channel may be related to the lower density and X-ray emission that is typically observed in the overlying cavity (Tandberg-Hanssen 1974 and references therein, Serio et al. 1978).

The prominence, similar in height and structure in Hα, He I 1083 nm, and the SOHO/EIT He II 30.4 nm images, is centered below the enhanced X-ray emission structure located within the cavity. The top of the prominence at the time of the X-ray image extends just inside of the bottom of this structure, as shown in Figure 2.

4.   Conclusions

He I λ1083 nm filament channels, which appear bright and almost devoid of structures, correspond to the corridor of Hα fibrils aligned along polarity in-
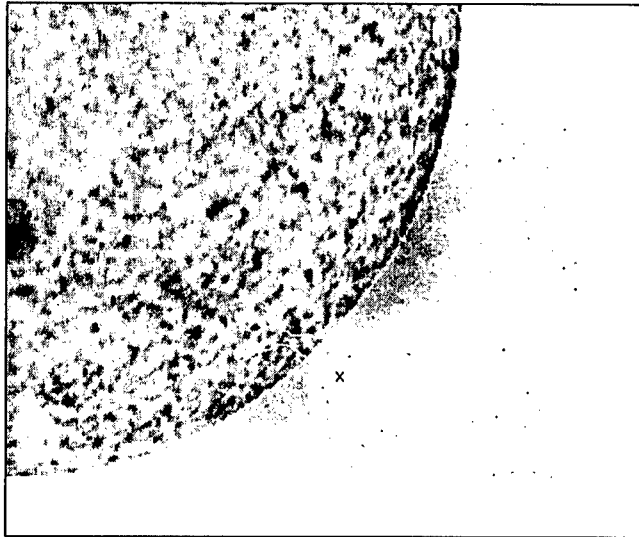
Figure 2.   The southwest quadrant of the NSO/KP He I λ1083 nm spectroheliogram (1520 UT) superimposed on a *Yohkoh*/SXT image (0002 UT) on July 4, 1997. The filament channel at the base of the X-ray cavity is outlined in white. An × marks the top of the prominence observed on the limb at 0108 UT.

versions in stronger magnetic field regions. However, in weaker field regions, such as the polar crown, filament channels are clearly visible in He I 1083 nm images, but generally not in Hα. This result suggests that He I 1083 nm is a more sensitive indicator of a filament channel. The fibril alignment seen in Hα may be related to the height of a filament and its magnetic structure; the higher the filament, the less evidence of fibrils aligned with the polarity inversion. The boundaries of the He I 1083 nm appear to coincide with the outer boundaries of *Yohkoh*/SXT X-ray cavities.

References

Foukal, P. 1971, Solar Phys., 19, 59
Hudson, H.S., Acton, L.A. and Harvey, K.L. 1998, to be submitted
Martin, S. F., Bilimoria, R. and Tracadas, P. W. 1994, in Solar Surface Magnetism, (eds.) R. J. Rutten and C. J. Schrijver, Kluwer Acad. Publ., Dordrecht, Holland, p. 303

Serio, S, Vaiana, G.S., Godoli, G., Motta, S., Pirronello, V. and Zappala, R.A. 1978, in Proceedings of the Open Meetings of the Working Groups on Physical Sciences, Tel Aviv, Israel, Oxford, Pergamon Press, p. 337

Tandberg-Hanssen, E. 1974, Solar Prominences, D. Reidel Publishing Co., Dordrecht, Holland, p. 132

Force-Free Models of Filament Channels

A. W. Longbottom

Mathematical Institute, University of St. Andrews, Fife KY16 9SS, U.K

Abstract. A fast multigrid method to calculate the linear force-free field for a prescribed photospheric flux distribution is outlined. This is used to examine an idealized model of a filament channel. The magnetic fields, for a number of different field strengths and positions, are calculated and the height up to which field lines connect along the channel is examined. This is shown to strongly depend on the value of the helicity of the system. A possible explanation, in terms of the global helicity of the system, is suggested for the dextral/sinistral hemispheric pattern observed in filament channels.

1. Introduction

Two of the prerequisites for the formation of solar prominences are that, first, an initial arcade structure must have already been formed above the polarity inversion line (PIL) and, second, that there must be a substantial component of the magnetic field along the PIL (Martin et al. 1994). Such a configuration is described as a filament channel. The overall magnetic field topology of these structures can be examined by the construction of force-free equilibria for given magnetic flux distributions at the photosphere. Such models, using the linear force-free approximation, are developed below allowing the global nature of filament channels to be explored.

2. Linear Force-Free Fields and the Numerical Method

In general a force-free equilibrium can be described by the equation

$$(\nabla \times \mathbf{B}) \times \mathbf{B} = 0,$$

where $\mathbf{B}$ is the magnetic field. This may be rewritten as

$$\nabla \times \mathbf{B} = \alpha \mathbf{B}, \qquad (1)$$

where α is a function of space and, in some sense, measures the helicity of the system. If $\alpha = 0$ then the resulting equilibrium is current-free (or potential). If $\alpha = $ constant the equilibrium is linear force-free, and if α is a true function of space it is nonlinear force-free. The linear force-free field retains much of the detail of the nonlinear solution while being far easier to calculate. This approximation allows a substantially more realistic representation of the true equilibrium field than the current-free case.

It must, however, be pointed out that the magnetic field may only be locally modelled by linear force-free equilibria, over regions of space where α is constant. Indeed, the linear solution is dependent on the size of the domain within which it is calculated. A number of theorems reguarding linear force-free fields are well established (Berger 1985): 1. For a given size of domain and boundary conditions a series of resonance points occur, as α is increased/decreased from zero, where the helicity and magnetic energy go to infinity. 2. For a given helicity (α) the linear force-free field is the lowest energy equilibrium compatible with the fixed boundary conditions. 3. All solutions with α less than the value of the first resonance point are linearly stable to ideal MHD modes.

Here the linear force-free equation is solved numerically by the method of Finn et al. (1994) rewriting (1) as

$$\nabla^2 \mathbf{A} = \alpha \nabla \times \mathbf{A}, \tag{2}$$

where

$$\mathbf{B} = \nabla \times \mathbf{A}.$$

The numerical box is a cube with normalized dimensions $-1 < x, y < 1, 0 < z < 2$ and has a resolution of up to 129^3 grid points. For a given vertical component of magnetic field prescribed on the base of the box (the photosphere) a Poisson equation is solved, on the base, to give the values of $\mathbf{A}$ on that face. The elliptic equation (2) is then solved directly within the three-dimensional domain. The boundary conditions on the faces, other than the photospheric base, are that the normal component of magnetic field vanishes and $\nabla \cdot \mathbf{A} = 0$. The second of these guarantees that when (2) is solved with the given boundary conditions $\nabla \cdot \mathbf{A} = 0$ everywhere within the computational domain.

If classical iterative methods (such as SOR) are used to solve the equations, convergence towards the solution quickly saturates once short wavelength errors are smoothed. In fact, the number of iterations to gain a given accuracy scales like the square of the number of grid points. Thus, doubling the resolution requires 64 times the number of iterations.

Here linear multigrid methods (Longbottom et al. 1998) are used to speed up the rate of convergence of the classical scheme. Multigrid methods smooth all wavelength errors simultaneously so convergence does not saturate. The number of iterations to gain a given accuracy scales independently of the grid size.

3. Results

In trying to model a filament channel an idealized flux distribution is used. This consists of two elongated regions of equal and opposite flux emerging from the photosphere, forming the overlying arcade, together with two concentrated regions of flux at either end of the arcade, representing an underlying component of the field directed along the length filament channel. This geometry together with a typical calculated field is shown in Figure 1. Ratios of concentrated to elongated flux per unit area between 2 and 24 have been taken, with ratios a/b of separation of concentrated to elongated flux regions of 1 or 2.

A. W. LONGBOTTOM
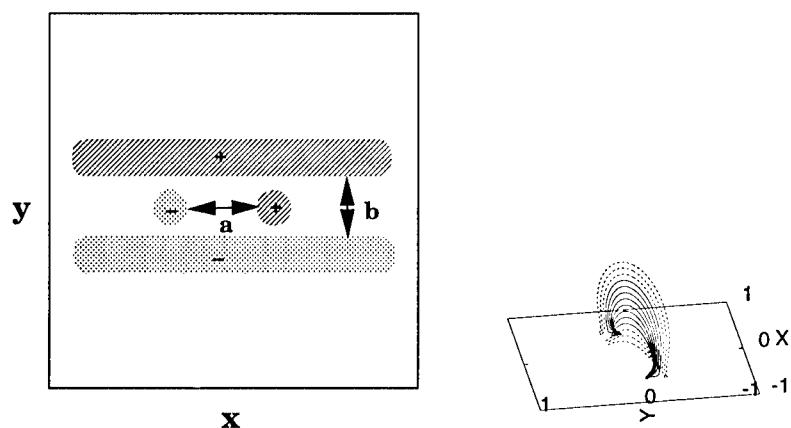
Figure 1.   (a) The flux distribution on the photospheric base. (b)
Field lines for the case $a/b = 2$, flux ratio $= 12$, $\alpha = -2$.

For each case the linear force-free field between the the first (positive and
negative) values of the resonant α have been calculated. An examination of
the field line topology then gives distinct regions of field line connectivity. The
separatrix surface enclosing all field lines that connect the two concentrated
sources can be calculated. The maximum separatrix height (always along the
line rising vertically from the centre of the base) as a function of α, is plotted
in Figure 2.
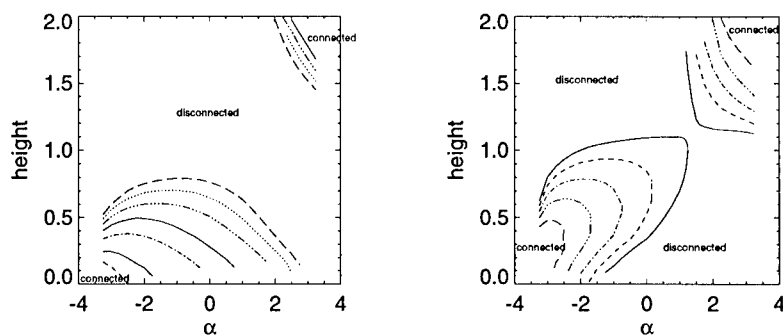
Figure 2.   The height of the separatrix surface for (a) $a/b = 1$ and
(b) $a/b = 2$.

The results for $a/b = 1$ are shown in Figure 2a. This represents the case
where the concentrated flux sources are separated by the width of the filament
channel. With increasing height, the curves represent flux ratios of 2, 4, 8, 12, 16,
20 and 24. The curves for large α and height are due to the boundary conditions
on the top and sides of the computational domain and do not represent physically
relevant solutions. For this flux distribution a value of helicity (α) may always

be found for which field lines will connect the two concentrated flux sources, forming a component of field along the channel.

For the potential case ($\alpha = 0$) considered by MacKay and Priest (1998) this would not be the case. Only when the concentrated flux becomes large with respect to the arcade flux do field lines connect the two concentrated sources.

Figure 2b shows the equivalent results for the case $a/b = 2$ (the concentrated flux sources are separated towards the ends of the filament channel). The curves from left to right represent flux ratios of 8, 12, 16, 20 and 24. Again the curves for large α and height are due to the top and side boundary conditions. In most cases for a given α, there is now both a lower and upper bound to the separatrix surface giving a closed volume above the photospheric boundary within which field lines connect the concentrated sources along the filament channel. It can also be noted that, as the concentrated sources are now further separated, greater strengths are required to connect them.

A plot of the field lines for the case $a/b = 2$, flux ratio $= 12$, $\alpha = -2$ is shown in Figure 1b. Field lines connecting the two concentrated sources are shown solid and those connecting the arcade dashed. It is interesting to note that this represents a dextral filament channel which is preferentially observed in the northern hemisphere. Figure 2b shows that this topology (Figure 1a) has a bias towards negative values of α. Similarly sinistral filament channels (observed preferentially in the southern hemisphere) show a bias towards positive values of α. This agrees with the corresponding hemispheric variation of α observed by Pevtsov et al. (1995). For further details see MacKay and Longbottom (1998).

4. Conclusions

This paper outlines a method for the fast generation of linear force-free equilibria for a given magnetic flux distribution at the photospheric boundary. This has been used to model the global topology of a filament channel. It is shown that both the strong component of field along the channel and dextral/sinistral hemispheric pattern can be reproduced by the appropriate choice of helicity, this choice agreeing with the observed hemispheric pattern of helicity.

References

Berger, M. 1985, ApJS, 59, 433

Finn, J., Guzdar, P., and Usikov, D. 1994, ApJ, 427, 475

Longbottom, A., Fiedler, R. and Rickard, G. 1998, A&AS, submitted

MacKay, D. and Priest, E. 1997, Solar Phys., 167, 281

MacKay, D. and Longbottom, A. 1998, ApJ, in preparation

Martin, S., Bilimoria, R. and Tracadas, P. 1994, in Solar Surface Magnetism, R. Rutten and C. Schrijver, Springer-Verlag, New York, 303

Pevtsov, A., Canfield, R. and Metcalf, T. 1995, ApJ, 440, L109

Simulation Studies of Solar Prominence Formation

G. S. Choe[1]

Tongmyong University of Information Technology, Pusan 608-080, Korea

C. Z. Cheng

Princeton Plasma Physics Laboratory, Princeton University, Princeton, NJ 08543, USA

Abstract. A series of numerical simulations are presented for formation of solar prominences. We have investigated the dynamic and thermodynamic evolution of coronal plasma in response to photospheric horizontal motions. In three different setups of field configurations and footpoint motions, different types of prominences are found to be formed by thermal instability.

1. Introduction

Solar prominences are always observed above polarity inversion lines and this indicates that magnetic fields play an important role in subsistence of prominences. Martin (1990) discussed the conditions for prominence formation observable in the optical wavelengths, which can be summarized by two phrases: *sheared magnetic fields* and *converging motions* toward the polarity inversion lines. Although the origin of magnetic shear is not clearly known, it can be attributed to shearing and converging motions at the field line footpoint level as observed by Rompolt and Bogdan (1986).

Based on these observations, we have investigated the dynamic and thermodynamicevolution of the coronal plasma and magnetic fields employing shear-increasing footpoint motions as boundary conditions. In our numerical models, the field-aligned heat conduction, the radiative cooling and a phenomenological form of the coronal heating are taken into account to explore the thermal instability (for details see Choe and Lee 1992, Choe 1995). Bipolar (Cases A and B) and quadrupolar (Case C)field configurations, respectively, are considered in three different cases.

2. Case A: Formation of a Kippenhahn-Schlüter Type Prominence

In this case, a shearing footpoint motion is applied to a single magnetic arcade. The first stage of the evolution is almost adiabatic and the temperature is decreased over the whole domain by the expansion of the arcade. The radiative

---

[1]Also at Princeton Plasma Physics Laboratory, Princeton, NJ 08543, USA

cooling is gradually enhanced by the adiabatic cooling and finally a thermal instability is effected. At $t \sim 7500\,\text{s}$ the temperature drops quickly to about $10^4\,\text{K}$ in a small patch and the material in the vicinity is sucked into it along field lines. Above and below this region, thermal instability takes place successively upward and downward. Consequently, the condensed material forms a sheet-like structure, in which the peak density reaches about 70 times the initial value. The field lines are pressed down by the prominence mass and form a dip structure, which is a typical signature of the Kippenhahn-Schlüter prominence model (see Figure 1). Above a certain height, the cooled material contracts at the edges of the cooled region and the condensed material slides down along field lines. This process evacuates the flux tubes and creates a coronal cavity as shown in Figure 1.
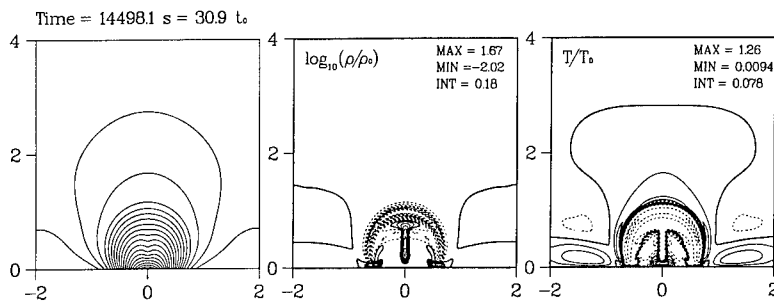
Figure 1. Case A: A Kippenhahn-Schlüter type prominence with a coronal cavity. Field lines and contours of density $(\log{(\rho/\rho_0)})$ and temperature (T/T_0) are shown. The dotted lines refer to decrease of the quantities from the initial values.

3. Case B: Formation of a Kuperus-Raadu Type Prominence

In Case B, a converging motion toward the polarity inversion line is applied to a sheared bipolar arcade to increase the magnetic shear more effectively. In the expanding arcade, a thermal instability develops as in Case A, but the condensed material slides down along field lines because the field line curvature in the cool region is higher than that in Case A. As the footpoints converge, a current layer develops in the lower part of the arcade where magnetic reconnection takes place. The highly enhanced density in the magnetic island triggers another thermal instability and the condensed material is accumulated at the bottom of the looped field lines, finally forming a sheet-like structure. About 92% of the mass in the island is concentrated in the prominence and the rest of the island volume constitutes a low pressure cavity (see Figure 2). In Case B, an inverse polarity prominence of Kuperus-Raadu type is attained.

Time = 2.68×10⁴ s
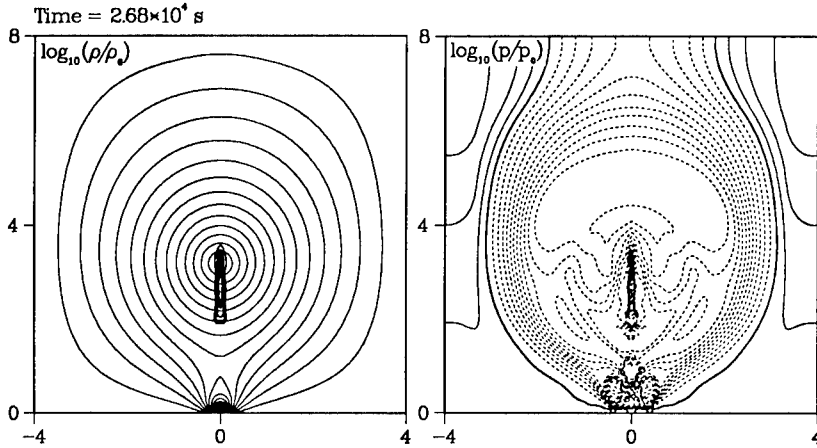
Figure 2.   Case B: Density and pressure profiles of a Kuperus-Raadu type prominence. On the left, contours of $\log(\rho/\rho_0) \geq 0$ are super-imposed on the magnetic field lines. The corresponding contours of $\log(p/p_0)$ are shown on the right.

4.   Case C: Prominence Formation Between Two Bipolar Regions

In this case, two adjacent bipolar regions are mimicked by a quadrupolar field without an X-point initially. As the footpoint shear increases, both arcades individually expand and form a current sheet between them, where magnetic reconnection takes place. The expansion of arcades induce a quasiadiabatic cooling except near and below the X-line. The density is decreased within the two expanding arcades except near the X-line, but is increased in the overlying arcade. Thus, a thermal instability takes place in the overlying arcade and the upward and downward propagation of condensation results in a vertical sheet structure of the prominence (Figure 3). Although the field lines supporting the prominence material are topologically similar to those in the Kippenhahn-Schlüter model, the prominence field will be observed to have an inverse polarity. Therefore, a Kippenhahn-Schlüter type cannot always be equated with a normal polarity prominence.

5.   Discussion

In our models, prominences are formed by condensation of coronal plasma. However, we cannot exclude the possibility that the cool prominence material may be directly transported from the chromosphere without any cool seed in the corona. Our simulations not only suggest some condensation mechanisms of the hot plasma, but also show that cool material of whatever origin can survive in

Time = 3.89×10⁴ s
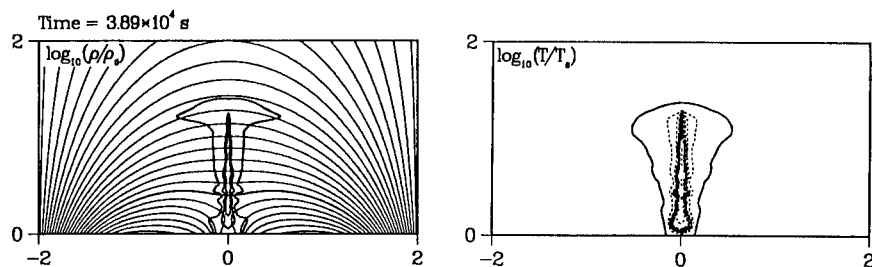
Figure 3. Case C: Formation of a prominence between two bipolar arcades. The density ($\log(\rho/\rho_0) \geq 0$) contours are shown in the left panel superimposed on the magnetic field lines. In the right panel, the temperature ($\log(T/T_0)$) contours are plotted.

the corona under certain conditions of the magnetic fields.

Besides the field geometries shown in this paper, Malville (in a discussion reported by Anzer 1979) proposed another field geometry as a plausible model of prominence magnetic fields. In Malville's model, a magnetic island is wrapped by Kippenhahn-Schlüter type field lines. In relation to this, the simulation study by Cheng and Choe (1998, these proceedings) has shown that Malville's configuration can be realized by magnetic reconnection in a current sheet whose lower tip lies above the bottom boundary.

References

Anzer, U. 1979, in Physics of Solar Prominences, E. Jensen, P. Maltby and F. Q. Orrall, Institute of Theoretical Astrophysics, Blindern:Oslo, p. 322

Choe, G. S. 1995, Ph.D. Thesis, University of Alaska: Fairbanks

Choe, G. S. and Lee, L. C. 1992, Solar Phys., 138, 291

Martin, S. F. 1990, in Dynamics of Quiescent Prominences, (eds.) V. Ruždjak and E. Tandberg-Hanssen, Springer-Verlag:Berlin, p. 1

Rompolt, B. and Bogdan, T. 1986, Coronal and Prominence Plasmas, (ed.) A. Poland, NASA CP 2442, Washington, D.C., p. 81

Are Prominences Formed by Flux Convergence?

K. Galsgaard and A. W. Longbottom

Department of Mathematical and Computational Sciences, University of St. Andrews, St. Andrews, North Haugh, KY16 9SS, Scotland

Abstract. Numerical 3D resistive MHD experiments are used to investigate the dynamical properties of a quadrupolar magnetic field, as the two dipolar regions are pushed together. A current concentration is formed between the approaching flux concentrations and, when reconnection starts, material is lifted against gravity. As it rises the material spreads out along the polarity inversion line and forms a prominence-like structure.

1. Introduction

Quiescent prominences have been observed intensely for decades. Despite much effort into understanding them they are still mysterious phenomena, providing many unanswered questions. One such question relates to their method of formation. At present there are no comprehensive observations that provide detailed information about how prominences form. However, indirect quantities have been extracted from the huge observational material. Martin (1990) analysed regions where prominences had formed, prior to their formation, and found three necessary criteria for prominence formation. These are: 1) the presence of a magnetic arcade overlying a polarity inversion line; 2) the convergence of flux towards the polarity inversion line under the arcade; 3) the cancellation of opposite flux in the vicinity of the polarity inversion line. The first two points provide clear information about topology and flow dynamics, but the third point, the cancellation of flux, is by no means clear. The observations have not been able to distinguish between flux emergence/submergence of bipolar regions close to the polarity inversion line, and annihilation of magnetic flux due to magnetic reconnection. The difference is important and will, when resolved, put strong limitations on models describing this important phase of prominences life.

To put forward a simple model for prominence formation, a quadrupolar magnetic field is taken as the initial magnetic field configuration. This magnetic field topology contains the first of Martin's (1990) criteria, and has a simplified topology similar to the one example discussed by MacKay et al. (1997). The topology of the magnetic field is shown in Figure 1. The sources contain the same amount of flux, though their surface areas are different. The magnetic field is divided into four topologically distinct regions by the separator surfaces defined by two 3D null points located at the photospheric boundary. The magnetic field in the Cartesian box is found by solving for the potential solution to the imposed boundary conditions (Longbottom et al. 1997), assuming that magnetic flux is only penetrating the bottom boundary. As magnetic field is only penetrating
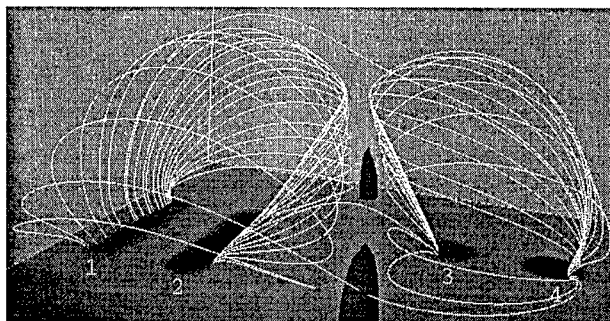
Figure 1.   The initial magnetic field line topology. The shading at the bottom plane indicates the locations of the penetrating flux. Field line traces outline the location of the separator connecting the two nulls. The null point locations and the start of the separator line, that divides space into four magnetically independent flux regions, is indicated by the isosurfaces.

the "photospheric" boundary at the four source locations and then immediately becomes space filling, the magnetic field strength changes dramatically over a short distance close to the sources. To get time-scales in different parts of the numerical domain that are not too different, a model atmosphere with a density stratification with up to 12 scale heights and a constant plasma temperature is used.

To fulfill the second criteria of Martin (1990) a smooth step function velocity profile is imposed on the lower boundary. This moves the two sets of dipolar regions (1–2, 3–4 in Figure 1) toward each other without distorting their individual separation. The dynamical evolution is followed numerically by solving the full set of MHD equations (Nordlund and Galsgaard 1995, URL: http://www-solar.dcs.st-and.ac.uk/~klaus) without a proper treatment of heat conduction and plasma condensation.

2.   Results

Experiments with different parameter values have been conducted, representing different magnetic field strengths and number of density scale heights. This paper only discusses the general features of the experiments, without giving details of the dependence on specific parameters (see Galsgaard and Longbottom 1998).

As the magnetic flux distributions are forced together by the boundary motion, the magnetic field between the two approaching flux concentrations is compressed. Initially, the connections from the strong circular flux distribution (3) connect to a thin line along the straight edge of the elongated flux distribution (2) with almost straight field lines when projected onto the bottom boundary. When the distance between sources 2 and 3 decreases, the field lines connecting them change shape. Close to the sources this change is minor while the weaker parts higher up in the atmosphere accumulate nearly all of the horizontal change
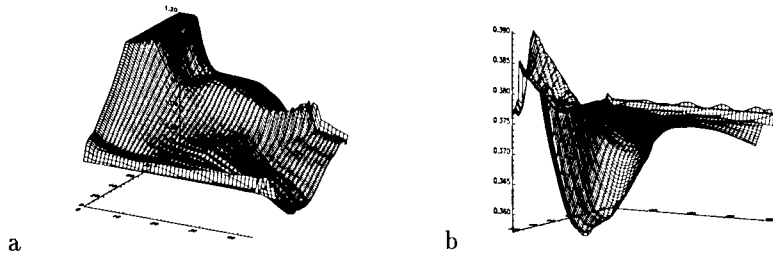
Figure 2.   Left, the change in density (relative to the initial density) as a function of height and time measured on a line of data points located at the convergence line between the two approaching sources. Right, a similar plot for the plasma temperature.

along the convergence line between the footpoints and, therefore, become almost parallel to this line.

As the field between the two sources (2, 3) is compressed, magnetic field with different horizontal components approach each other and a current concentration is slowly built up between them. As the current magnitude increases, it eventually reaches a strength where the resistive and advective contributions to the induction equation become comparable, and the field line connectivity starts to change in the current sheet region. Half of these reconnected field lines have an upward directed tension force that is strong enough to lift dense plasma against gravity. As the field lines move away form the reconnection site, and the field line dip broadens, the captured dense plasma spreads out along the field line above the polarity inversion line. This decreases the absolute density, but maintains a density enhancement relative the surrounding plasma, a possible first step in a prominence formation.

Figure 2a shows the change in density relative to the initial distribution as a function of height and time for a line of points between the two approaching flux sources that are located on the center of the convergence line. Here it is seen that the density close to the base grows almost linearly with time until about t=15, when the reconnection starts. The buildup of density in the initial phase is due to the fact that the plasma is trapped on field lines that are slowly shortened and that the plasma is not allowed to exit the box through the boundaries. After t=15 a flat density plateau is formed above a certain height – the "prominence" location – while the density below increases rapidly because the field lines are now much shorter and are simultaneous being compressed by the dominating downward directed tension force. At the base the large density enhancement is not spread out in the horizontal direction, because the magnetic field is strong enough to confine it. Despite the Joule heating in the current sheet, it is found that the lifted plasma decreases in temperature as it is lifted. The material is lifted almost adiabatically and, therefore, has to adjust to the lower surrounding plasma pressure by decreasing it's plasma density (spreading out along the field lines) and decreasing the temperature. This mechanism forms a low temperature blob, Figure 2b, which for a long period of time is the easiest way of identifying the field lines that have changed connectivity.

3. Conclusion

The experiments have shown that it is possible to lift plasma against gravity by magnetic field lines that reconnect close to the bottom boundary as a part of the process of flux convergence. They also show that the lift height and the density enhancement increases with decreasing magnetic β, a natural consequence of the increasing influence of the magnetic forces on the plasma dynamics. The lift velocity of the plasma is always found to peak around the Alfvénic Mach one just above the location of the peak tension force. One would expect to find similar lift velocities on the sun, if this process is important for any phase of a prominences' life. The experiments do not have realistic values of magnetic β, nor do they include a transition region which we expect is required to be located between the reconnection site – in the lower chromosphere – and the prominence – in the corona – to obtain a significant density enhancement relative to the plasma surrounding the prominence. It is found that the density enhancement starts to decrease as soon as the driving of the system is turned off. Therefore, to maintain the prominence for a long time, there has to be a continued flux convergence beneath it that can provide a continued mass input. When the mass supply stops, the density plasma slowly drains away from the prominence region. This occurs because practically none of the field lines passing through the prominence are spiralling along the prominence axis. The majority of field lines supporting dense plasma pass through the prominence region, having summit points on either side of the prominence before connecting back to the sources on the bottom boundary. It is found that the height difference between the summit and the dip supporting the dense plasma decreases with time. The plasma therefore slowly slips over the lowest of the summit points and drains down towards the bottom boundary.

Our expectation is, therefore, that to maintain a prominence, built by the principle of flux convergence for a long period of time, there must be a continued mass supply replacing the plasma that is slowly draining down. The life of a prominence must therefore be a highly dynamical phenomena that will only be fully understood when investigated under this assumption. To obtain such insight it is of vital importance that high resolution observations of plasma motions – velocities, masses – and magnetic fields are obtained. Only such observations can provide the information required to understand the life of prominences.

References

Galsgaard, K. and Longbottom, A. W. 1998, ApJ, in preparation

Longbottom, A. W. et. al. 1997, A&AS, submitted

Martin, S. F. 1990, in Dynamics of Quiescient Prominences, (eds.) V. Ruzdjah and E. Tandberg-Hansen, Springer-Verlag, New York, p. 1

MacKay, D. et al. 1997, ApJ, 486, 534

Force-Free Models of a Filament Channel In Which a Filament Forms

D.H. Mackay, V. Gaizauskas[1] and E.R. Priest

School of Mathematical Sciences, University of St. Andrews, St. Andrews, Fife KY16 9SS, U.K.

Abstract. Over the years few examples of the formation of filament channels or filaments have been observed. One such example was recently seen by Gaizauskas et al. (1997). This paper constructs force-free models of the main stages of formation.

1. Introduction

The formation of the filament channel and filament occurred when a small activity complex emerged near to and interacted with an old remnant region. One day after the complex emerged a system of curved fibrils surrounded it (Figure 1a). The alignment signified the formation of the channel. On the fifth day of development flux from the complex cancelled with flux from the remnant region and a filament formed (Gaizauskas et al. (1997), Figures 2–4). Force-free models of the main stages of formation are now constructed (Mackay et al. 1997).

2. Fibrils Around the Activity Complex

To model the fibrils around the activity complex a numerical, constant-α, force-free field will be constructed from the magnetogram of the complex. A contour plot of the magnetogram is shown in Figure 1b. In the area considered there is good flux balance ($\sim 0.1\%$). Since there is such good flux balance and the patches of flux emerged together, this suggests that the activity complex in its early stages of development may be an isolated system. The initial modelling will, therefore, not include the remnant region. The best comparison between the field lines and fibrils (Figure 1b) was obtained for $\alpha = 3.0$. On the left-hand side the field lines bend around from the positive region to the negative region in a north-south direction and give a very good comparison to the fibrils. This topological agreement shows that the C-shaped arc of fibrils and, therefore, the filament channel is aligned with, and due to, the extended non-potential field of the complex. The channel is of sinistral type, since the magnetic field points to the left (when viewed from the +ve polarity side). The formation of a sinistral channel is due to currents that are parallel to the field (α +ve). If

---

[1] Herzberg Institute of Astrophysics, National Research Council of Canada, Ottawa, Canada
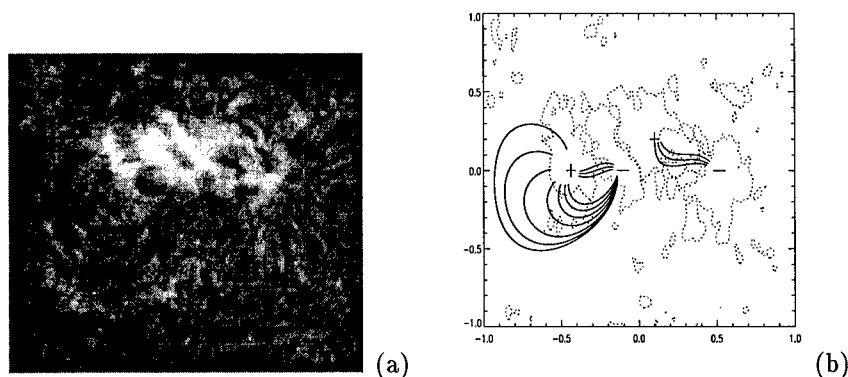
Figure 1.   (a) Fibrils around activity complex in Hα. (b) Field lines deduced by model plotted on a contour of the magnetogram.

α had been negative the fieldlines would have closed south-north and a dextral channel produced.

3.   Magnetic Structure of the Filament

On the fifth day of formation the remnant region and new region interacted. To model the magnetic structure of the filament, both of the regions are included. The field lines in the channel are computed for various values of α and the best representation of the filament is for $\alpha = 2.3$ (Figure 2(a)). The field lines that represent the filament form a thin straight structure that runs down the channel parallel to the polarity inversion line. Near one end there is a steep bend to the right as they enter a region of negative plage. The separatrix surface that encloses the flux connecting regions 2 and 9 is shown in Figure 2(b). The flux that represents the path of the filament forms a thin vertical sheet structure. Near source 2 the sheet is inclined at an angle to the vertical and becomes more vertical as it reaches further down the channel. It fattens out near the neutral point at $x = 0.12, y = 0.02$. Since the angle of inclination of the sheet changes, this gives the appearance of twist of the field lines. However, this is a projection effect and there is no twist in the structure.

The remnant region forms a necessary boundary on the east side of the channel on the day the filament forms. To show this only the activity complex and small plage region where the filament ends are included for this day. For no values of α do field lines connect between areas 2 and 9 along the path and height of the filament (Figure 3, $\alpha = 2.3$). The field lines have a geometry that represents the type of fibril structure that was seen on earlier days of formation. This suggests that the filament could not have formed in the channel with this same topology if the two regions had not interacted. Therefore, the remnant region and reconnections have an important role in the evolving topology of the channel on later days of formation.

(a)   (b)
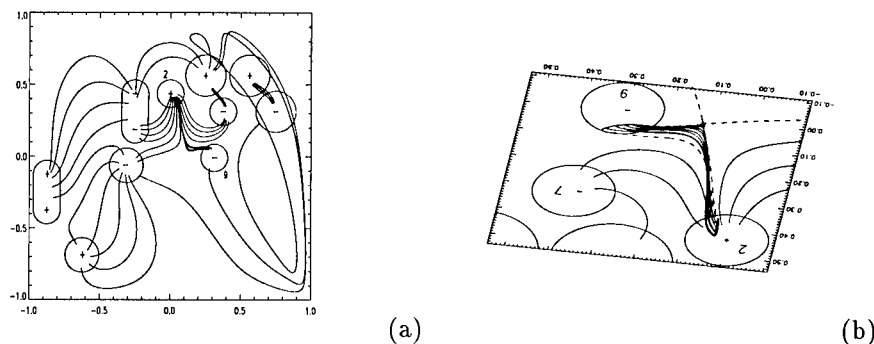
Figure 2.   (a) Field lines in channel for $\alpha = 1.5 \times 10^{-8} m^{-1}$. (b) Separatrix surface of flux representing filament.

4. Hemispheric Pattern

The net helicity of the complex plays an important role in determining the chirality of the channel. A positive sign of α gave a sinistral channel. In the northern hemisphere 76% of active regions have net negative helicity (α -ve) and in the southern hemisphere 69% have net positive helicity (α +ve) (Pevstov et al. 1995). The channel analysed herein is now considered when the flux emerges on both the east and west side of the remnant region in each hemisphere. The sign of α is changed until a filament-type structure can be obtained as before. The results are shown in Figure 4. If the flux regions emerge to the west of the remnant region, a positive value of α is required to give the correct connectivity in the southern hemisphere and a negative value in the northern. Sinistral channels are produced in the southern hemisphere and dextral in the northern. If the opposite value of α is used in each case, a transverse structure is obtained across the channel and no filament channel created. On the east side a negative value of α is required in the southern hemisphere and gives a dextral channel; a positive value is required in the northern hemisphere to give a sinistral channel. Emergence on the west side needs the dominant sign of α in each hemisphere to get the correct structure while emergence on the east side needs the minority sign of α. The minority values of α give the wrong chirality, while the dominant values give the correct chirality for each hemisphere. Thus, statistically there is a much higher chance of having dextral filaments in the northern hemisphere and sinistral filaments in the southern hemisphere (Mackay et al. 1998).

5. Conclusions

In this paper force-free models of a filament channel and filament formation have been constructed. The modelling suggests that the formation of the filament channel is due to the emergence of the complex in a sheared state. Force-free models then give a good representation of the filament. The field lines that gave the best fit formed a thin vertical sheet of flux that connected down the channel.
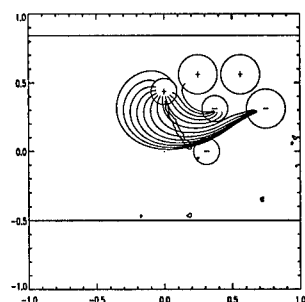
Figure 3.   Field lines of filament channel when remnant region excluded.

A hemispheric pattern was then deduced, with dextral filaments dominating in the northern hemisphere and sinistral filaments in the southern. Helicity may, therefore, have an important effect on the hemispheric patterns of filaments.
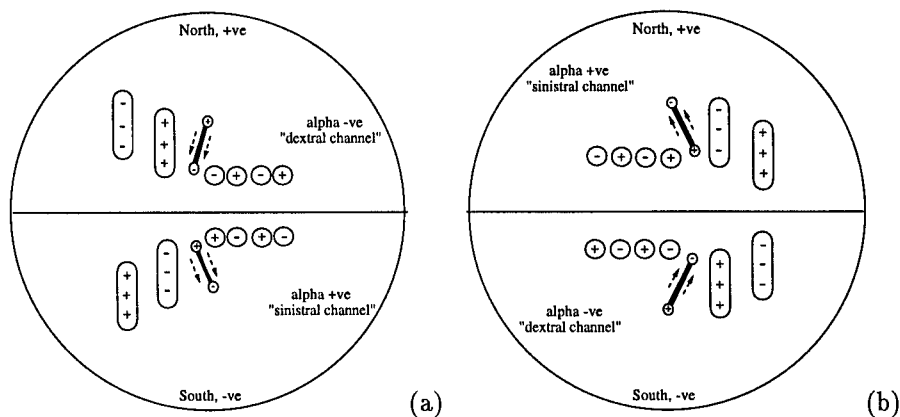
Figure 4.   Filament channel formation (a) west and (b) east of remnant region.

References

Gaizauskas, V., Zirker, J., Sweetland C. and Kovacs A. 1997, ApJ, 479, 448

Mackay, D.H., Gaizauskas, V., Rickard, G.J. and Priest, E.R. 1997, ApJ, 486, 534

Mackay, D.H., Priest, E.R., Gaizauskas, V., van Ballegooijen, A.A. 1998, Solar Phys., submitted

Pevstov, A.A., Canfield, R.C., Metcalf, T.R. 1995 ApJ, 440, L109

Analysis of Hα Observations of High Altitude Coronal Condensations

U. A. Allen, F. Bagenal

University of Colorado, Boulder, Colorado 80309

A. J. Hundhausen

High Altitude Observatory, National Center for Atmospheric Research, Boulder, Colorado 80301

Abstract. Preliminary analysis of Hα images of high-altitude coronal condensation known as "coronal spiders" is presented. The kinematics of material seen draining from the coronal spiders are also studied. An estimate of the mass of the object for a range of electron temperatures and electron densities is obtained.

1. Introduction

Coronal spiders are suspended plasma visible in Hα approximately $0.1R_\odot$ above the solar limb, and which may last for hours or days. In the descending phase of the solar cycle, they are quite common, occurring on average once every ten days. Some of the more remarkable observed features of coronal spiders include their height above the limb, the span of the footpoints, and the lack of an observable mechanism of support for the central mass. These characteristics raise interesting questions concerning the topology of the magnetic field in the corona where coronal spiders are observed.

The coronal spiders studied in this paper were seen in Hα images of the High Altitude Observatory's Prominence Monitor. An example of one of the coronal spiders studied is shown in Figure 1. A quantitative description of some of the spiders observed is given in Table 1.

The work presented here is principally descriptive and diagnostic, and has been pursued in the hope that these results will be useful in studying the origin and role of suspended mass in coronal structures. Observations of coronal spiders raise several questions concerning their nature and relevance to coronal dynamics. In particular, one would like to know what the magnetic field structure is like, and if it is possible to use the falling mass to trace the field lines. To this end, an investigation into the kinematics of small knots of material seen draining from the central mass of the spider is discussed in Section 2. Further, since no upwelling of mass from the chromosphere into the spiders has been observed, the question arises of where the emitting plasma originates. As a first approach to this question, Section 3 presents a mass estimate for the coronal spider of January 24, 1992.
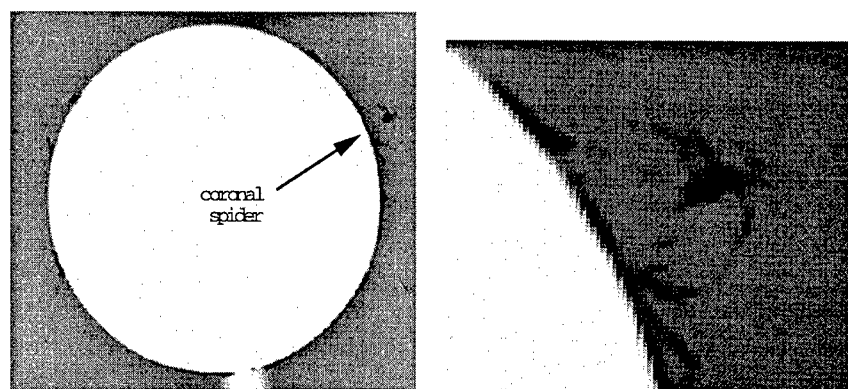
Figure 1.   (a) Hα image of the coronal spider (arrow) of January 24,
1992. (b) A close-up of the same coronal spider.

Table 1.   Descriptive statistics for seven coronal spiders.

Event	Duration	Height above limb	Width	Length	Footpoint Span
2 January 92	1 day	70,000 km	14,000 km	55,000 km	150,000 km
3 January 92	30 minutes	70,000 km	14,000 km	35,000 km	140,000 km
12 January 92	3 hours	14,000 km	30,000 km	40,000 km	none visible
18 January 92	1 day	83,000 km	20,000 km	70,000 km	180,000 km
24 January 92	1 day	70,000 km	20,000 km	40,000km	180,000 km
29 January 92	2 days	30,000 km	40,000 km	70,000 km	150,000 km
1 March 92	1 day	55,000 km	85,000 km	30,000 km	165,000 km

2.   Kinematics

The kinematics of a small knot of falling material were examined in order to as-
certain whether the fall might be along a magnetic field line. The event studied,
chosen to minimize projection effects, was the January 31, 1997 "tower" event,
which looks similar to an earlier stage of some of the spiders described in Sec-
tion 1. In a movie made from digital Prominence Monitor images taken at three
minute intervals, the draining material seemed to be in free-fall, and movement
was primarily vertical. Edge-enhanced images of the selected event were used
to better indicate the position of the knot of material. The radial position of
the falling mass is shown in Figure 2. The estimated error included in the plot
is due to the motion of the occulting disk with respect to the limb, as well as to
the change in shape of the falling material. Figure 2 shows that the data are fit
well by a quadratic. In particular, free-fall in solar gravity with an initial down-
ward velocity of 41.76 km/s fits the data well within the observing error. Such
an initial velocity, while large, is not unreasonable, and could be due to a force
imparted to the falling mass before it becomes visibly separate from the central
mass. Alternatively, had the mass started falling from rest 100 seconds earlier
from several thousand kilometers higher, a velocity of 42 km/s could easily have
been attained by the time its motion became discernable. These results suggest
that, for this event, the mass may be falling along a magnetic field line.
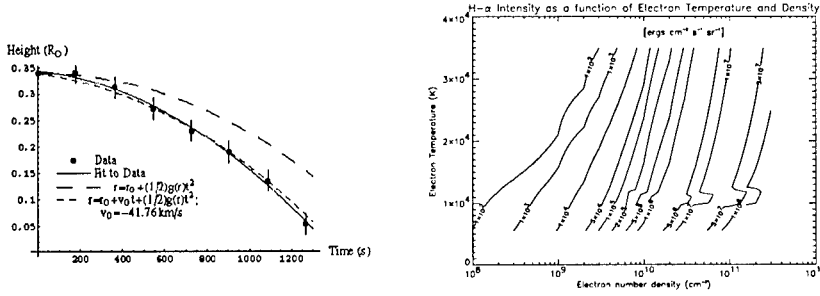
Figure 2.   Left: Draining material in January 31, 1997 event. Error bars indicate measurement error due to observational problems such as motion of the occulting disk.

Figure 3.   Right: Contour plot showing Hα intensity as a function of electron density and electron temperature (deviations near 10^4K are due to slow convergence of the code and should be ignored).

3.   Mass Estimate

In order to better understand the formation of coronal spiders, it is desirable to obtain an estimate of the mass. From the Hα intensity observed in the Prominence Monitor data, the population of the n=3 level of hydrogen can be obtained, assuming a suitable length dimension and optical thinness. A radiative transfer code is then used to determine what range of electron temperatures and electron densities could produce the observed Hα intensity, following the method of Athay and Illing (1986). A mass estimate for the spider is obtained from the total density, the two observed dimensions of the spider, and the unobserved third dimension which is assumed comparable to the two observed dimensions.

The radiative transfer code used to predict the n=3 population for various electron temperatures and electron densities was developed by P. Judge at the High Altitude Observatory. The model consists of a uniform layer 30,000 km thick of neutral and ionized hydrogen. Hydrogen is modeled as a six-level atom, with five bound states and a continuum. The statistical equilibrium equations are then solved numerically to obtain ratios of bound state populations to protons.

For the January 24, 1992 coronal spider, the intensity observed in the Hα image was $2.19 \times 10^9\,erg\,cm^{-2}\,sr^{-1}\,s^{-1}$. If a linear dimension of 30,000 km is assumed, then the observed intensity yields a value for the n=3 population of 6.87 cm^{-3}, since

$$I(H\alpha) = \left(\frac{h\nu_{32}}{4\pi}\right) n_3 A_{32} L \tag{1}$$

where L is the linear dimension of the spider, and $A_{32} = 4.4 \times 10^7\,s^{-1}$ is the transition rate out of the n=3 level.

A contour plot (Figure 3) shows the range of electron densities which can give rise to the observed Hα intensity for electron temperatures between 5,000 K and 40,000 K. Electron densities between 3×10^9 cm^{-3} and 2×10^{10} cm^{-3} will

produce the observed Hα intensity for electron temperatures in this range. To constrain the temperature or density range, measurements in other wavelengths would be necessary. Electron densities of this range yield a range of estimated masses of approximately 10^{13} g to 5×10^{14} g for the dimensions of the January 24, 1992 coronal spider.

4. Discussion

This study of coronal spiders has been carried out in order to examine the structure of the coronal magnetic field and the origin and support of mass density enhancements in the corona from a novel perspective.

While the observational difficulties involved in the field-tracing technique described in Section 2 limit its applicability to other events, it is hoped that such a technique will permit the magnetic field topology to be more confidently traced. In addition, the draining of mass from the central body of the spider is of interest in establishing the source of the spider mass, as well as the reasons for its disappearance.

The mass estimate of the coronal spider shows that a significant mass – approximately one-hundredth of the mass involved in a typical coronal mass ejection – is suspended high in the corona for an extended period of time. Ten to one hundred times more dense than the surrounding corona (Athay 1976), the plasma would require 10^{28} erg to be raised from the photosphere to a height typical of spiders. Observation seems to suggest, however, that mass of chromospheric temperature and density is not lifted to the spider, but that coronal plasma condenses to form the spider. Questions yet to be answered in the study of coronal spiders include what kind of magnetic field structure might support them, and what kind of conditions in the corona favor their formation.

References

Athay, R. G. and R. Illing 1986, J. Geophys. Res., 91, 10961

Athay, R. G. 1976, The Solar Chromosphere and Corona: Quiet Sun, D. Reidel, Dordrecht, Holland, p. 329

MHD and Plasma Interpretation of a Prominence Eruption Observed by SOHO

P.C.H. Martens

ESA Space Science Department, SOHO Experiment Operations Facility Code 682.3, GSFC, Greenbelt, MD 20771, USA

Abstract. Data on the May 1, 1996 prominence eruption, jointly observed by CDS, SUMER, and EIT, aboard SOHO, Yohkoh-SXT, and Kitt Peak and Meudon observatories are analyzed to obtain information on the plasma temperature, density, and velocities, as well as the magnetic field topology and strength. It is found that the 'standard' model of an erupting helical flux tube probably applies, although questions arise on the MHD stability of the prominence flux tube. The prominence is observed to remain relatively cool during its eruption ($\leq 5 \times 10^5 K$), while the density and velocity vary considerably on scales down to the limit of resolution. It is found that the high density, high velocity plasma blobs can be contained by the relatively weak magnetic field, as is indeed observed.

1. Introduction

In May and June 1996 several filaments/prominences were observed in an international campaign among SOHO, Yohkoh-SXT, and a whole array of ground based observatories in Eurasia: Pic du Midi, Meudon, Debrecen, Wroclaw, Ondrejov, Izmiran, Irkutsk, Crimea, Ratan, and Hida. For SOHO the observational sequences are written up as Joint Observations Programme 12 (JOP012; see http://sohowww.nascom.nasa.gov/~soc/JOPs/), with data from CDS, SUMER, EIT, LASCO, and MDI. This data set is probably the most comprehensive ever obtained for filaments/prominences.

In this review I will concentrate on the best event from these observations, curiously enough a test-run of the program on May 1, 1996. Observations were made by SUMER, CDS, EIT, and LASCO aboard SOHO, Yohkoh-SXT, and on the ground by the Observatoire de Meudon, and Kitt Peak National Solar Observatory.

I will present observations of an erupting filament on the limb, and describe the conclusions that can be drawn from them in terms of topology, density, temperature, motions, and magnetic field strength and stability. The novel aspect of these observations is the clear delimitation on plasma parameters through the high resolution spatial and spectral images of CDS and SUMER. These results indicate the presence of fine structure at and below the limit of resolution, with a wide variety in densities and velocities, in an otherwise uniformly cool prominence.

2. Time Line of the Prominence Eruption

SUMER and CDS obtained excellent spectroscopic data of the eruption of a
filament from the SE limb on May 1, 1996, between 07 and 09 UT. These data
have been described in detail by Wiik et al. (1997) and by Kucera et al. (1998,
these proceedings). Experience during later runs of JOP012 has shown that it is
extremely difficult to pinpoint the exact time and location of a filament eruption
and, therefore, the data from the May 1 test run have become extremely valuable.

   In this review the CDS/SUMER spectroscopic data will be analyzed in a
wider context. Using available magnetograms, UV, and soft X-ray data for April
30, and May 1, I have compiled the time line in Table 1 which summarizes the
main events and data availability.

Table 1
Time Line for the May 1, 1996, Prominence Eruption and CME

Time	Event/Observation	Reference
30 April, 10:05 UT	Yohkoh-SXT Image with a Clear Dark Filament Channel and Off-limb Keyhole	Figure 1a
30 April, 21:21 UT and onward	High Prominence on SE Limb in EIT 304 Å	Figure 2
30 April 14:10–15:05 UT	Kitt Peak Magnetogram, with EW Polarity Inversion Line at SE Limb	Figure 1b
1 May, 01:17 UT & 01:29 UT	EIT 284 and 195 Å Images show Filament Channel but no Keyhole	Figs. 1c & 1d
1 May, 07:21 UT	Filament Channel in Yohkoh-SXT has straightened	Figure 3a
1 May, 07:25 UT	Meudon CA II K3 Spectroheliogram, with CDS (box) and SUMER FOV (crosses in CDS box)	Figure 3b
1 May, 07:13–09:55 UT	Spectroscopy of Filament Eruption by CDS and SUMER	see Kucera et al. these proc., and Wiik et al. 1997
1 May, 10:00–18:00 UT	LASCO C3 Observations of CME from E Limb	Wiik et al. 1997

P. C. H. MARTENS
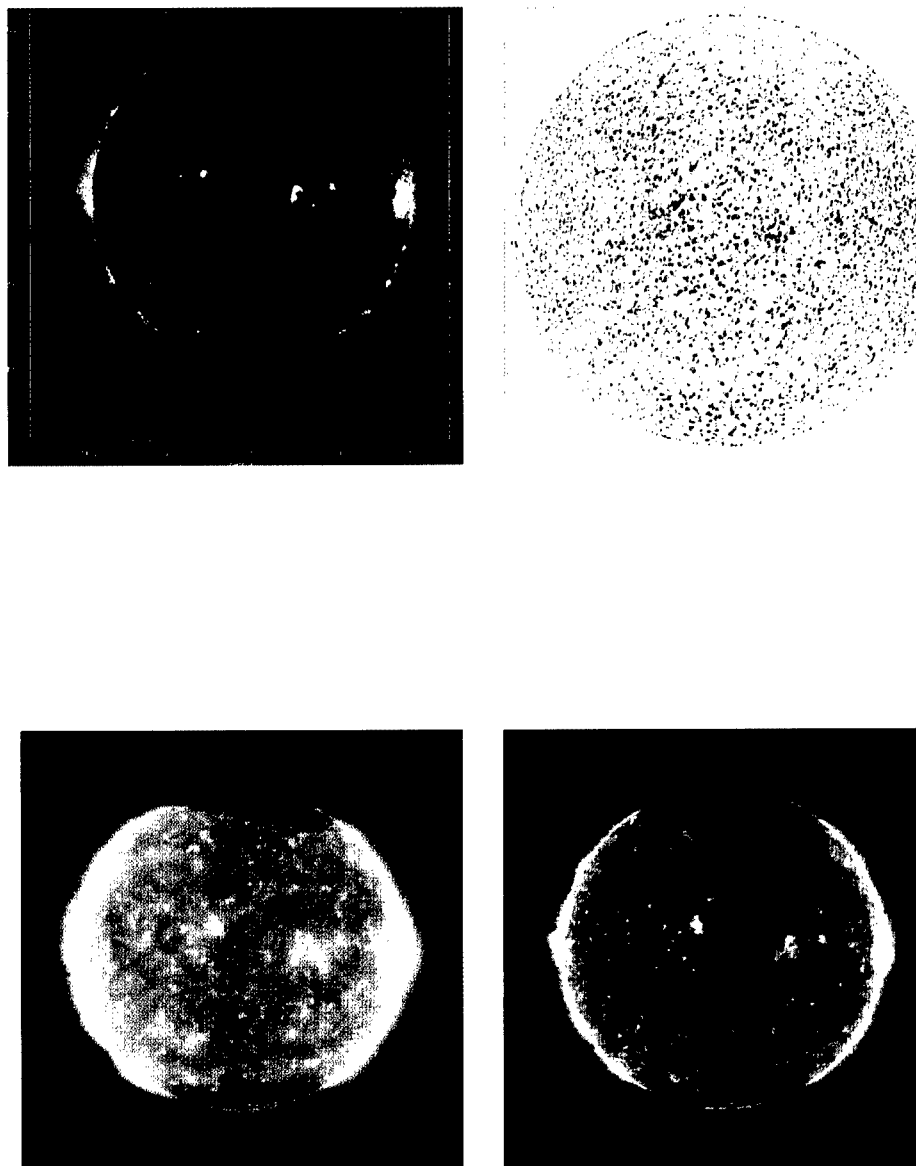
Figure 1.   Four full disk images on April 30, 1996. Clockwise from top left: (a) Yohkoh-SXT at 10:05 UT, (b) Kitt Peak Magnetogram at 14:10 UT, (c) SOHO-EIT, 284 Å, at 01:17 UT, and (d) SOHO-EIT, 195 Å, at 01:29 UT. Note the polar coronal hole polarity inversion line and filament channel in the SE quadrant, and the "keyhole" in the SXT image, at the east extension of the filament channel.

30-Apr-1996 21:21   1-May-1996 02:13   1-May-1996 11:06   1-May-1996 19:45   2-May-1996 03:23
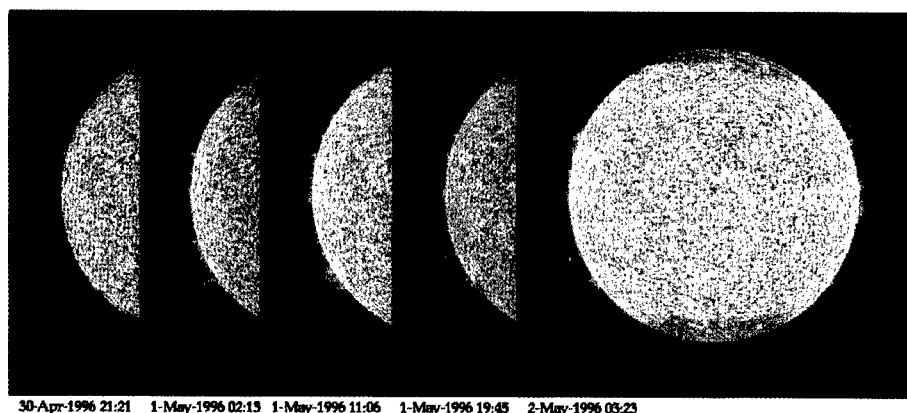
Figure 2.   A time series of EIT 304 Å observations of the development of a prominence on the SE limb. The EIT 304 Å images consist of a blend of He II and Si XI line radiation; for prominences this is dominated by He II at about 60,000 K.
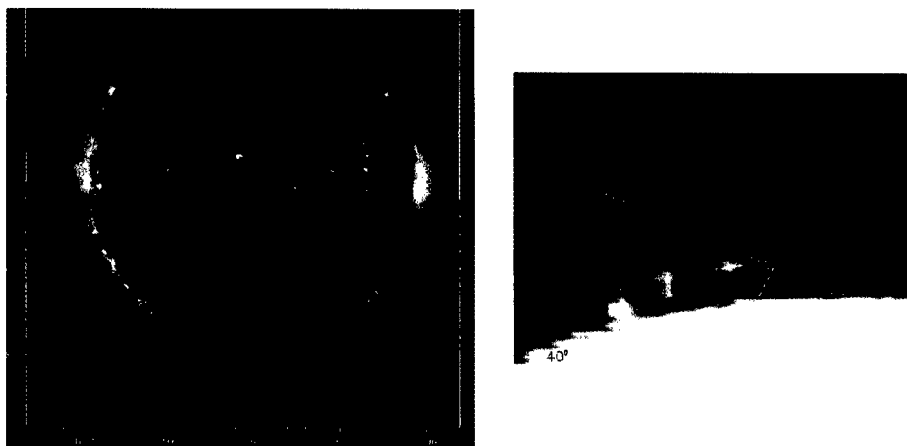
Figure 3.   Left (a): A Yohkoh-SXT full disk image on May 1, 07:21 UT, during the partial prominence eruption on the SE limb. Right (b): Meudon Ca II K3 Spectroheliogram, taken at 07:25 UT, with CDS field of view delineated by the box and SUMER by the crosses.

3. Plasma Environment: Interpretation

The Kitt Peak full-disk magnetogram (Figure 1a) demonstrates an absence of large-scale organized magnetic features, except for the polar coronal hole magnetic polarity inversion lines, both north and south. The dark prominence channel seen by Yohkoh-SXT (Figures 1a and 3a) can clearly be identified with the polarity inversion line, and with the prominence observed by Meudon (Figure 3b), and EIT, CDS, and SUMER aboard SOHO.

The Yohkoh-SXT images also show the so-called "keyhole" feature, a darkening in the X-ray intensity just off the limb at the extension of the polar crown polarity inversion line. This "keyhole" has always been interpreted as absence of X-ray emission from the helical magnetic flux tube that constitutes the filament. This flux tube, according to many models for filaments (e.g., Martens and Kuin 1989), is suspended above the polarity inversion line, with its axis parallel to it. Thus, just off the limb, where the axis is parallel to the line-of-sight, one would indeed notice an absence of soft X-ray emission, in the form of a cross-section of the filament flux tube.

This interpretation is supported here by the clearly visible filament channel on the disk. The Yohkoh-SXT observations for this filament thus suggest a relatively "cool" filament, with temperatures less than 1 million K. The SUMER and CDS observations below will confirm this. "Cool" filament channels are relatively rare among the Yohkoh-SXT observations of filaments; more often one sees the "spine" of the filament quite clearly in soft X-rays, in particular just before and during an eruption. What causes the absence of soft X-ray emission in this case, is not known.

The height above the limb of the prominence at the onset of the eruption ($\approx$ 07 UT) is 100,000 km, very high in comparison with most other filament eruptions. In the Martens and Kuin model (1989) this requires that the photospheric magnetic field below the filament is uniform over about the same scale-size. This is consistent with the Kitt Peak magnetogram.

The SUMER and CDS observation show that the middle part of the prominence erupts, well within their field of view. Both instruments see an expanding loop that heats up somewhat (from 100,000 K to just under 500,000 K), but no soft X-ray emitting plasma is produced, as Yohkoh-SXT observations confirm. The EIT data (see Figure 2) demonstrate that the prominence has reformed by 11 UT, although its detailed structure is quite different.

Wiik et al. (1997) interpret the most southern leg as the continuation of the filament onto the disk, along the filament channel. There is also a small loop between the southern legs, which in the CDS and SUMER observations is seen to be the one that erupts. These observations exclude the possibility of a thermal DB, since the loop is clearly seen moving upward in subsequent images and remains visible in line spectra. Thus, it appears that only the middle part of the prominence, with its continuation onto the disk, erupts and reforms very quickly.

The fact that the prominence reforms so quickly – it is observed by EIT at 11:06 UT in He II/Si XI at 304 Å, at a temperature of about 60,000 K, and also by CDS in a much smaller field-of-view at 11:00 UT – makes one wonder whether the prominence middle section really erupted. Is it possible that what

we are observing is merely the disconnection and retraction of one of the feet of the prominence, the inner southern one at about S33°? The retraction of the feet of a prominence during its evolution is a well known phenomenon from Hα movies of prominences. However, the simultaneous occurrence of a CME observed by LASCO at about the same position angle (see Wiik et al., for a detailed description) might be taken as an indication of a real eruption, although it is certainly not a sure sign.

If there was indeed a partial eruption of the filament within the field of view of SUMER and CDS, then this can be interpreted within the now more or less standard model of an erupting flux tube, with reconnection just below it; see, for example, Figure 1 in Hirayama (1974). We note that the Meudon image (Figure 3b) gives the impression of a flux tube with many coils around it, and this is reinforced by careful inspection of the SUMER and CDS rasters.

Stability against the kink mode for a flux-tube attached at both ends has been investigated by Kadomtsev (1966) for the Tokamak case, and by Hood and Priest (1979, 1981) for solar coronal flux tubes. Their results suggest that only one, or at most a few, turns are permitted before instability sets in; the exact number being determined by the details of the model and the boundary conditions. In the case of filaments the mass loading at the lowest points in the coils by the filament material will have a stabilizing influence, but I am not aware of any studies to quantify this. In the absence of such studies, and given the generally low plasma β in the solar corona, one would not expect this mass loading to change the stability criteria appreciably. Hence, if we maintain the interpretation of the prominence as a helical flux tube, we are faced with the problem that this flux tube should be MHD-unstable according to our theoretical knowledge. The observations do not show the development of a kink, however. Indeed the same prominence is observed almost intact one day later by EIT (Figure 2). The same phenomenon has been observed in several other prominences by SOHO. I conclude that it is time to perform detailed MHD stability calculations for flux tubes with mass loading, and if the contradiction persists, for a reexamination of current prominence models.

The detailed analysis of the CDS and SUMER observations with respect to the plasma parameters of the prominence has been reported upon in detail by Wiik et al. (1997). Here I will just summarize the most salient conclusions:

- $T \approx 2 \times 10^4$ K – 5×10^5 K (highest in erupting part)

- $n \approx 3 \times 10^9$ cm^{-3} – 3×10^{11} cm^{-3} (large dispersion)

- $\Delta v \approx 100$ km/sec ($\geq c_s \approx 40$ km/sec $\sqrt{T_5}$)

The density determinations from density-sensitive line ratios show a large pixel by pixel (1 arcsec) variation along the slit, indicating the presence of unresolved (filamentary?) fine structure in the erupting loop. The observed Doppler shifts are predominantly red in the northern leg of the loop and blue in the other, and of the order of 40 km/sec, consistent with large scale downdrafts, as one might expect in an erupting loop. SUMER, due to its higher spectral and spatial resolution, sees velocities up to about 100 km/sec, with sometimes several structures along the line-of-sight with a large velocity dispersion. Such high velocities are unusual (Schmieder 1989). We note that for this relatively

cool prominence the Doppler shifted velocities are of the order of, or larger than, the sound velocity (see the equation in the third bullet above) and horizontal. Hence, the motion must be driven by a magnetic force, rather than pressure or gravity. Perhaps we are seeing jets from the reconnection region below the erupting part of the prominence, as, for example, modeled by Shibata et al. (1992).

Finally, we note that for a polar crown prominence of such large height, a magnetic field strength of at most about 10 G can be expected. This is borne out by measurements of the magnetic field in other polar crown prominences through the Hanle effect by Bommier and Leroy (1998, these proceedings, and references therein). On the other hand, the observed Doppler shifts can be interpreted as plasma motions along the helical magnetic field lines that make up the prominence. Since the prominence flux tube preserves its integrity, even while it erupts, its magnetic field must be strong enough to contain the plasma motions inside. This implies that the centrifugal force from the plasma motions must be smaller than the tension force in the flux tube, i.e.,

$$\frac{\rho v^2}{2R} \leq \frac{B^2}{4\pi R},\tag{1}$$

where ρ is the mass density, v the plasma velocity, B the magnetic field strength, and R the radius of the prominence flux tube. Using the maximum value for the observed particle density given above, and a plasma velocity of 100 km/sec, it is found that the magnetic field strength must be larger than 12.5 G, of the same order as the field strength expected for these types of prominences. Since the plasma velocity is of the order of, or larger than the sound velocity in this cool prominence, the plasma β is of the order of unity for the observed density and a field of around 10 G. Hence, it appears that the high density parts of the fine structure have the highest density that can be accommodated in this type of prominence.

4.   Conclusions

The data from the joint observations described in this paper have allowed us to derive the plasma parameters for an erupting prominence in unprecedented detail. Prominence eruptions, and the frequently accompanying flares and CMEs, are complex phenomena, involving a large scale reconfiguration of the magnetic field, with plasma effects on all scales, from giant arcades to small reconnection flows and jets. No single instrument can provide a complete data set including all these effects and, therefore, well coordinated multi-observatory campaigns, followed up by joint data analysis efforts, are necessary to enhance our understanding of prominences and their eruptions. SOHO has been the central element in a series of prominence campaigns, and its continued operations through solar maximum will provide the solar physics community with a unique opportunity for further study of prominences. The catalog of SOHO coordinated observations is available on the Web for anyone interested (http://sohodb.nascom.nasa.gov/cgi-bin/soho_campaign_search), and the campaign data enter the public domain after one year.

References

Hood, A. W and Priest, E. R. 1979, Solar Phys., 64, 303

Hood, A. W and Priest, E. R. 1981, Geophys. Astrophys. Fluid Dyn., 17, 297

Hirayama, T. 1974, Solar Phys., 34, 323

Kadomtsev, A. A. 1966, in Reviews of Plasma Physics, Vol. 2, M. A. Leontovich (ed.), Consultants Bureau: New York, p. 153

Martens, P. C. H. and Kuin, N. P. M. 1989, Solar Phys., 122, 263

Shibata, K., Nozawa, S. and Matsumoto, R. 1992, Publ. Astron. Soc. Japan, 44, 265

Schmieder, B. 1989, in Dynamics and Structure of Quiescent Prominences, E. R. Priest (ed.), Kluwer: Dordrecht, Holland, p. 15

Wiik J. E., Schmieder, B., Kucera, T., Poland, A., Brekke, P. and Simnett, G. 1997, Solar Phys., 175, 411

Prominence Eruptions

B. Vršnak

Hvar Observatory, Faculty of Geodesy, Kačićva 26, HR-10000 Zagreb, Croatia

Abstract. The kinematics and dynamics of prominence eruptions are reviewed and different phases of the eruption are identified. The properties of the equation of motion in these phases are shown. The morphology of the prominence prior and during the eruption is described and the implications to the MHD description of the process are discussed.

1. Introduction

The evolution of prominences over their lifetime is characterized by several stages (Rompolt 1988) during which the internal structure gets more and more complex. When the structure becomes too intricate, the prominence becomes unstable and erupts (Rompolt 1990, Ballester 1994). The typical dimension of the system prior to the eruption is of the order of 10^5 km but can vary from several 10^4 km up to dimensions comparable to the solar radius. The time scale of an event is several hours, during which the prominence reaches the height in the range from several 10^5 km up to 10 solar radii (Valniček 1968, Tandberg-Hanssen et al. 1980, Athay and Illing 1986, Illing and Hundhausen 1986, Rompolt 1990). In the late phases of the eruption the prominence plasma becomes invisible in the Hα line either because of heating, or due to the decrease of the density caused by volume expansion or the mass loss through the legs of the prominence (Athay and Illing 1986, Illing and Hundhausen 1986, Vršnak et al. 1993). The velocity of the ejected prominence ranges from several tens of km/s up to several hundereds of km/s (Rompolt 1990). It is of the order of the intrinsic Alfvén velocity, revealing the magnetic nature of the process. Finally, let us stress that the 'frozen-in' condition is fulfilled (Vršnak 1992) so the morphology of the fine structure discloses the prominence's magnetic field skeleton and its evolution.

2. Kinematics

In Figure 1 the typical behaviour of an eruptive prominence is presented. The process of the eruption develops in several phases. In the pre-eruptive phase (denoted as phase 1 in Figure 1a) the prominence slowly rises with an approximately constant velocity in the order of 1–10 km/s. The internal structure gradually transforms from an intricate and chaotic structure into a simpler one, frequently characterized by helical-like patterns (Vršnak et al. 1991) sometimes also revealed by helical trajectories of the internal mass motions (Rušin and Ry-
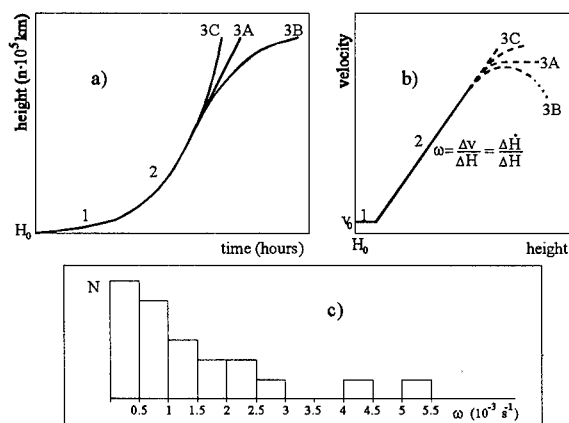
Figure 1.   a) A typical dependence of the prominence height versus time. b) The graph (a) represented as the prominence velocity versus the height. c) The distribution of the growth rates $\omega = \dot{H}/H$ obtained from a sample of 20 prominences exposing $\dot{H} \propto H$ phase.

banský 1982). In the eruptions of the flare-spray type, the pre-eruptive phase is most often not observed (Tandberg-Hanssen 1974, Tandberg-Hanssen et al. 1980).

At some critical height (usually it is comparable with the prominence's foot-point half-distance), the prominence suddenly starts to accelerate (denoted as phase 2 in Figure 1a) and the velocity increases up to several hundreds of km/s. After the acceleration phase, the velocity often becomes constant (denoted as phase 3A in Figure 1a). Sometimes, the prominence continues to accelerate until it becomes invisible (phase 3C) and sometimes a deceleration phase occurs (phase 3B). In one case it was observed that the prominence reached an upper equilibrium position and relaxed there as a damped oscillator (Vršnak et al. 1990).

In Figure 1b the kinematics of the eruption is presented in the velocity-height graph $v(H)$, providing better insight into the dynamics of the process (Figure 2). The graph reveals that during the acceleration phase the velocity $v = \dot{H}$ is proportional to the height H. Out of 23 cases taken as illustrative samples, 20 prominences showed $\dot{H} \propto H$ phase with $\omega = \dot{H}/H \approx 10^{-3}$ s^{-1} (Figure 1c). In 9 cases the velocity reached $\dot{H} = const.$ phase (phase 3A), in 8 cases the velocity was continously increasing ($\dot{H} \propto H$) untill the end of observations (phase 3C), and in 3 cases the velocity was decreasing $\Delta\dot{H} < 0$ (phase 3B). In the remaining three cases the phase 2 has not been identified.
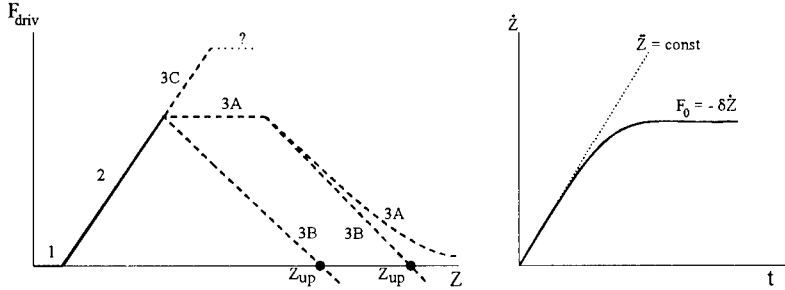
Figure 2.   a) Properties of the driving force as inferred from the kinematics of the eruption. b) The behaviour of the velocity in the $F = const$ phase with the viscous drag of the form, $F_v \propto \dot{Z}$.

3.   Equation of Motion

Figures 1a and 1b reveal the basic properties of the equation of motion and the behaviour of the forces driving the eruption (Figure 2). Let us consider the equation of motion in the simplest form:

$$\ddot{Z} = F(Z) - \delta\dot{Z} \ . \tag{1}$$

Here, the dimensionless parameter $Z = H/D$ is introduced, i.e., the height is normalized with respect to the prominence's footpoint half-separation (Figure 3); the driving force (per unit mass) is denoted by $F(Z)$, and the term $\delta\dot{Z}$ represents the viscous drag (assumed to be proportional to the velocity). The value of the damping constant δ is of the order of $\delta \approx 10^{-3}$ s^{-1} as inferred from the observations of prominence oscillations (Ramsey and Smith 1966, Kleczek and Kuperus 1969, Tandberg-Hanssen 1974, Vršnak 1984, Vršnak et al. 1990, Vršnak 1993).

The pre-eruptive phase is characterized by $F(Z) \approx 0$ and $\delta\dot{Z} \approx 0$, so that the acceleration $\ddot{Z} = 0$ (i.e., the velocity $\dot{Z} = const$) and the prominence evolves through a series of equilibrium states. The second phase is characterized by $\dot{Z} \propto Z$. This implies that the viscous drag is still negligible and that $F(Z) \propto Z$ so that the equation of motion can be written in the form:

$$\ddot{Z} = \omega^2 Z \ , \tag{2}$$

where we denoted $\omega = \Delta\dot{Z}/\Delta Z$ (Figure 1b). The solution of Eq. (2):

$$Z \propto e^{\omega t} \ , \tag{3}$$

shows that the acceleration phase has the characteristics of a linear instability. The parameter, ω, represents the growth rate of the instability and in the sample of 20 eruptive prominences having $\dot{Z} \propto Z$ it was most often close to the value of 10^{-3} s^{-1} (Figure 1c).

The phase 3A characterized by $\dot{Z} = const$ can be comprehended in two ways. First, the driving force could be ceasing, as well as the viscous drag
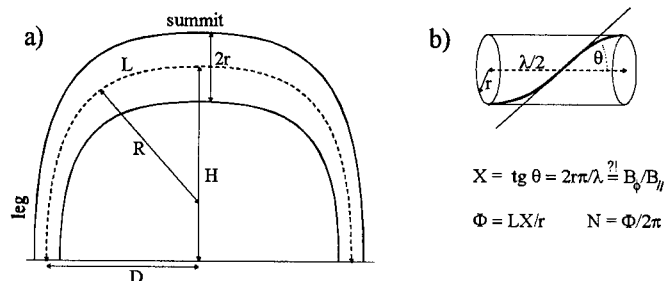
Figure 3.   a) Schematic drawing of an erupting prominence. b) Parameters defining a fine structure helical thread.

(due to the decrease of the coronal density), and so $\ddot{Z} \to 0$, meaning that the velocity becomes constant ($\dot{Z} = 0$). Another possibility is that $F(Z)$ becomes approximately constant and then, after a sufficiently high velocity is reached, the viscous drag balances the driving force (Figure 2b). Assuming that $F(Z)$ becomes constant ($F(Z) = F_0$), the asymptotic solution of Eq. (1) gives $F_0 = \delta \dot{H}$. Taking $\delta = 10^{-3}$ s^{-1} (Kleczek and Kuperus 1969, Vršnak et al. 1990) and the velocity of the value $v = \dot{H} = 100$ km/s one obtains $F_0 = 100$ N/kg. Taking for the density of the prominence $n = 10^{16}$m^{-3} one gets the force per unit volume of the order of $f_0 = 10^{-9}$ N/m^3, which is comparable with the 'magnetic forces', $f_B = B^2/2\mu_0 R \approx 10^{-9} - 10^{-8}$ N/m^3, proving that the eruption is of MHD origin. On the other hand, the deceleration of the prominence implies that the driving force has ceased and that the drag slows down the eruption.

Finally, there is a possibility that $F(Z)$ has such a shape that there exists an upper equilibrium position (denoted as Z_{up} Figure 2a). Then the prominence should relax at this position as a damped oscillator if $\omega_{up} > \delta$ or should monotonically approach it if $\omega_{up} < \delta$ (Vršnak et al. 1990)

4. Morphology

Eruptive prominences usually have a shape of an arch with legs anchored in the dense photosphere (Figure 3a). The parameters defining the arch are footpoint distance ($2D$), the height of the prominence axis summit (H) the radius of the curvature (R), the length of the axis (L) and the prominence width ($2r$) which is usually larger at the summit than in the legs (Figure 3a). It is useful to normalize these parameters with respect to the footpoint half-distance, D, which is the only parameter constant during the process of eruption (e.g., $Z = H/D$, $l = L/D$, etc.). The internal structure frequently shows helical-like patterns (especially well exposed in the prominence legs) indicating that the prominence could be described in cylindrical geometry as a twisted magnetic flux tube of curved axis, with its footpoints anchored in the photosphere. In Figure 3b the pitch angle, θ, the pitch length, λ, the parameter, $X = \mathrm{tg}\theta$, the radius of the tube, r, as well as an effective twist, Φ, are defined, and the parameter, N, represents the number of turns of a helical thread from one footpoint to the

another. Taking into account that the 'frozen-in' condition is fulfilled (Vršnak 1992), one can relate the parameter, X, to the ratio of the azimuthal and the longitudinal component of the prominence magnetic field as $X = B_\phi / B_{||}$.

In the pre-eruptive phase an initially intricate internal structure simplifies and in this stage the first signs of helical-like patterns appear (Rušin and Rybansky 1982, Vršnak et al. 1993). Usually the patterns are twisted more at the summit than in the legs (i.e., $X_{summit} > X_{leg}$) which reveals that the twist was transported into the expanded part of the tube (Jockers 1978, Browning and Priest 1983).

During the eruption, the ascending motion (causing streching of the prominence axis) is accompanied by the radial expansion of the tube (Ruždjak and Vršnak 1981) and the so-called 'detwisting' (Vršnak 1990a, Roša et al. 1993). This is not a proper term really, as the footpoints are anchored in the photosphere, so the total twist, Φ, should remain constant if no internal reconnection of the magnetic field occurs. However, the parameter, X, decreases $\Delta X < 0$, implying that the stretching dominates over the radial expansion (Roša et al. 1993). The process of stretching of the helical patterns proceeds in such a way that the twist within an element of the tube (Φ') remains roughly constant (Vršnak 1990a, Vršnak et al. 1993, Roša et al. 1993), implying that the process of the transport of the twist into the expanding part of the prominence (at its summit) is too slow to be effective during the eruption. Sometimes, it is observed that the prominence axis screws, as expected from the screw mode instability (Sakurai 1976) implying that the internal twist is partly transported into the twist of the prominence axis. This can be significant when the dynamics of the eruption is considered, since it decreases the radius of the curvature at the summit of the prominence (Vršnak 1990b, c).

The eruption is usually accompanied by mass loss (draining of the material downwards along the legs) which can be as large as 90% of the initial mass (Vršnak et al. 1993). The rate of mass loss is highest in the phase of acceleration, indicating that it is initiated by the inertial force at the prominence summit, and then controlled by gravity when draining along the prominence legs.

5.   Onset and Dynamics of the Eruption

In an order of magnitude approach (Vršnak 1990b, c, Chen 1996) the forces per unit length, acting in the prominence and driving the eruption, could be represented in a rather simple form: $F_m = \mu_0 I^2 / 4\pi H$ (the force due to the 'mirror current effect', Kuperus and Raadu 1974); $F_k = \mu_0 I^2 / 4\pi R$ (the 'kink effect' term, Vršnak 1990b,c); $F_t = -\mu_0 I^2 / 2\pi R X^2$ (the 'tension effect' term, Vršnak b,c); $F_g = -mg$ (gravity); $F_0 = \pm I B_0$ (the force due to an external field, Van Tend and Kuperus 1978); $F_v = -m\delta \dot{Z}$ (viscous drag). Here the current flowing along the axis of the prominence is denoted by I and m stands for the mass per unit length of the prominence ($m = r^2 \pi \rho$). Neglecting the dependence of the gravity force on the height and neglecting the viscous drag (approximation valid in the early stages of the eruption) the equation of motion can be written in the form:

$$\ddot{Z} = A\left(\frac{L}{H} + \frac{L}{R} - \frac{2L}{RX^2}\right) , \tag{4}$$
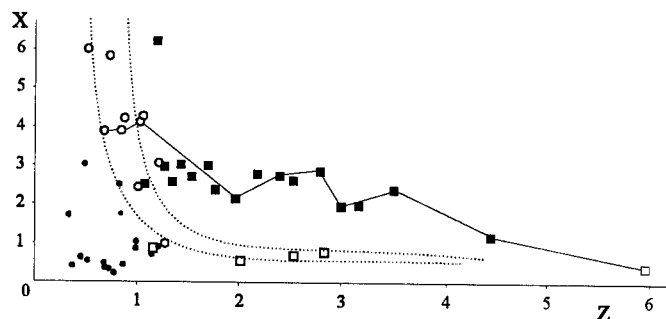
Figure 4.   Stability diagram.   Dotted lines represent the band in which the instability should occur. Dots represent the observed stable prominences, circles – the prominences at the onset of the eruption, black squares – prominences in the eruption, squares – the prominences in the post-acceleration phase. Full line represents the evolution of the eruptive prominence of August 18, 1980.

where:

$$A = \frac{\mu_0 I^2}{4\pi M D} = \frac{B^2_\phi}{\mu_0 \rho L D} \approx \frac{v_A{}^2}{LD} \approx \tau_A{}^{-2} \approx \omega^{-2} \, , \tag{5}$$

Here M is the total mass of the prominence $M = r^2 \pi L \rho$, and v_A and τ_A represent the Alfvén velocity and the Alfvén travel time along the axis of the prominence, respectively. Taking order of magnitude values for the magnetic field $B = 10^{-3}$, T and $\rho = 10^{-11} \mathrm{kg/m^3}$ for an average density, one finds the Alfvén velocity of the order of 100 km/s, i.e., the growth rate of the instability is of the order of $\omega \approx 10^{-3} \mathrm{s^{-3}}$, consistent with the observations.

Linearizing Eq. (4) in the vicinity of the equilibrium position, and taking into account the complete set of MHD equations governing the behaviour of the parameter I in various approximations (Vršnak 1990b, c, Chen 1996), one finds a set of curves, depending on the initial values of the relevant parameters (I, ρ, r, L, D), which define the band in the graph $X(Z)$ where the instability should occur (denoted by the dotted lines in Figure 4). To the left of the indicated band prominences should be stable, and to the right they should be in the phase of acceleration. In Figure 4 the values of the parameter, X, measured close to the summit of the prominence axis in 28 cases, is presented versus the parameter, Z. One finds a good agreement (within the errors of the measurements) with the expectations based on Eq. (4) (Vršnak et al. 1991).

The scenario for the onset of the eruptive instability could be inferred from Eq. (4). An increase of the parameter, A, in the pre-eruptive phase (caused by $\Delta B_\phi > 0$, i.e., $\Delta I > 0$, or by $\Delta M < 0$) shifts the equilibrium position to a larger height (Figure 5) and the whole function $\ddot{Z}(Z)$, given by Eq. (4), shifts upwards in the graph. The prominence is located at the height defined by the intersection of the curve $\ddot{Z}(Z)$ with the abcissa of the graph (Z) characterized by $\Delta \ddot{Z}(Z)/\Delta Z < 0$, meaning that for a small displacement from the equilibrium position the prominence should behave as an harmonic oscillator. For a larger displacement from the equilibrium (if it reaches the intersection characterized
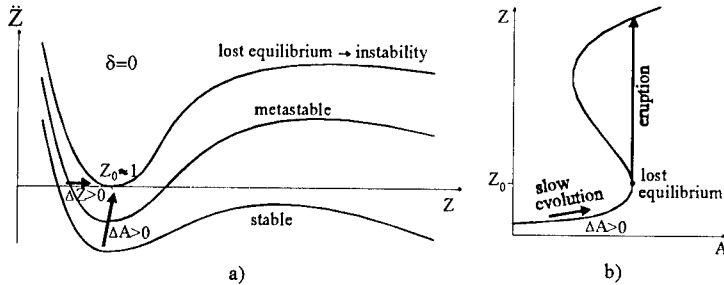
Figure 5.   a) Curves representing behaviour of the driving force as given by Eq. (4). b) Evolution of the prominence towards the eruption, caused by an increase of the parameter A.

by $\Delta \ddot{Z}(Z)/\Delta Z > 0$) it should erupt: the prominence is in fact metastable. As the parameter, A, increases and the curve, $\ddot{Z}(Z)$, is shifted above the abscissa so that the values of the acceleration $\ddot{Z}$ are always positive, the prominence can not find a neighboring equilibrium position, i.e., it looses equilibrium and erupts (Figure 5b). The shape of the curves in Figure 5a determines the behaviour of the acceleration, and so the dynamics of the eruption. Taking into account the possible reconnection of the magnetic field lines below the prominence and the mass loss through the legs, one can get different variations of the curves shown in Figure 5a (Vršnak 1990b, c). However, basic features remain the same, and are in agreement with the behaviour of the driving force shown in Figure 2a. The solutions of the equation of motion allow also a monotonical ceasing of the acceleration, as well as the existence of an upper equilibrium position (Z_{up}) at which the prominence should relax as a damped oscillator due to the viscous drag (Vršnak 1990b).

6.   Discussion and Conclusions

The kinematics of the eruption can be described by a rather simple equation of motion (Eq. (1)). The driving force is a result of several factors (Eq. 4). Substitution of Eq. (4) into Eq. (1) provides a comprehension of all basic features of the prominence eruption scenario. The agreement with the observations is good in the pre-eruptive phase, the onset of the eruption and the early stages of the eruption during which the prominence undergoes acceleration. Late phases of the eruption could be described in different ways, and the effects of mass loss and the reconnection of the magnetic field lines below the filament (like in the two-ribbon flare scenario) should be considered. The comprehension of the stability of prominences and transition to instability can be improved by analyzing their large scale oscillations (Vršnak 1993) in more detail. Finally, we stress that sometimes prominences relax to a lower energy state without eruption, i.e., by evolving through a series of equilibrium states (Vršnak and Ruždjak 1994).

References

Athay, R. G. and Illing, R. M. E. 1986, J. Geophys. Res., 91, 10951

Ballester, J. L. 1994, in Solar Dynamic Phenomena and Solar Wind Consequences, ESA SP-373, p. 13

Browning, P. K., and Priest, E. R. 1983, ApJ, 266, 848

Chen, J. 1996, J. Geophys. Res., 101, 27499

Illing R. M. E. and Hundhausen, A. J. 1986, J. Geophys. Res., 91, 10951

Jockers, K. 1978, ApJ, 220, 1133

Kleczek, J. and Kuperus, M. 1969, Solar Phys., 6, 72

Kuperus M. and Raadu, M. A. 1974, A&A, 31, 189

Ramsey, H. E., and Smith, S. F. 1966, AJ, 71, 197

Rompolt, B. 1988, in Dynamics and Structure of Solar Prominences, (eds.) J. L. Ballester and E. R. Priest, Universitat de les Illes Ballears, p. 125

Rompolt, B. 1990, Hvar Obs. Bull., 14, 37

Roša, D., Vršnak B., Ruždjak, V., Ozguc, A. and Rušin, V. 1993, Hvar Obs. Bull., 17, 15

Rušin, V. and Rybanský, M. 1982, Bull. Astron. Inst. Czechosl., 33, 219

Ruždjak, V. and Vršnak, B. 1981, in Solar Maximum Year 2, (ed.) V. N. Obridko, Acad. of Sci. of Russia, Moscow, p. 256

Sakurai, T. 1976, Publ. Astron. Soc. Japan., 28, 177

Tandberg-Hanssen, E. 1974, Solar Prominences, D. Reidel, Dordrecht, Holland

Tandberg-Hanssen, E., Martin, S. F. and Hansen, R. T. 1980, Solar Phys., 65, 357

Valniček, B., 1968, in Structure and Development of Solar Active Regions, (ed.) K. O. Kipenheuer, D. Reidel, Dordrecht, Holland, p. 282

Van Tend, W., and Kuperus, M. 1978, Solar Phys., 59, 115

Vršnak, B. 1984, Solar Phys., 94, 289

Vršnak, B. 1990a, Solar Phys., 127, 129

Vršnak, B. 1990b, Solar Phys., 129, 295

Vršnak, B. 1990c, Astrophys. Space Sci., 170, 141

Vršnak, B. 1992, Ann. Geophys., 10, 344

Vršnak, B. 1993, Hvar Obs. Bull., 17, 23

Vršnak, B. and Ruždjak, V. 1994, Hvar Obs. Bull. 18, 1

Vršnak, B., Ruždjak, V., Brajša, R. and Zloch, F. 1990, Solar Phys., 127, 119

Vršnak, B., Ruždjak, V. and Rompolt, B. 1991, Solar Phys., 136, 151

Vršnak, B., Ruždjak, V., Rompolt, B., Roša, D. and Zlobec, P. 1993, Solar Phys., 146, 147

Magnetic Field Reconnection in the Hα Eruptive Prominence on September 18, 1995

Marian Karlický, Pavel Kotrč, Stanislava Šimberová, Miloslav Knížek and Michal Varady

Astronomical Institute of the Academy of Sciences of Czech Republic, CZ-251 65 Ondřejov, Czech Republic

Abstract. A violent evolution of the September 18, 1995 eruptive prominence is studied. The fast changes of the prominence structure started immediately after a weak radio burst on 3 GHz indicating the presence of non-thermal processes. A comparison with *Yohkoh* soft X-ray pictures was made. A detailed analysis of observations indicates magnetic field line reconnection, mainly in the space below the rising Hα prominence. The reconnection processes are manifested by structural changes of the Hα prominence and X-ray loops and also by the character of Doppler velocities in the Hα spectrum formed close to the reconnection space.

1. Introduction

It is believed that solar flares and eruptive prominences are physically connected to magnetic field line reconnection (see Rompolt 1990, Švestka and Cliver 1992, Tandberg-Hanssen 1995, Tsuneta 1996). Several papers showing good evidence of the reconnection or loop interactions are in Sakai (1993). Also, Šimberová et al. (1993) found indications of the reconnection in a large coronal arch and Smartt et al. (1994) found indirect evidence of magnetic field reconnection in coronal loops. Recently, Pevtsov et al. (1996) studied the May 8, 1992 flare associated with an Hα filament eruption and found evidence of reconnection occurring just tens of minutes before the filament eruption. We analyse the September 18, 1995 eruptive prominence with fast structural changes similar to Pevtsov's et al. (1996) flare event. As this event was situated on the limb, the reconnection processes can be studied in more detail.

2. Observations

The September 18, 1995 eruptive prominence situated on the NE limb was observed by the Hα telescope and Optical Multichannel Spectrograph, equipped with a videosystem for monitoring the Hα spectrum and slit-jaw pictures (Kotrč et al. 1993), and the Radiospectrograph in Ondřejov. The prominence activation started at about 09:15 UT with a slow rise of Hα loops followed at 09:40 UT by much faster processes. In the period 09:39 UT to 09:41 UT a weak radio burst on 3 GHz was observed. The GOES instrument registered a B4.3 soft

09:41:53 UT

09:44:36 UT
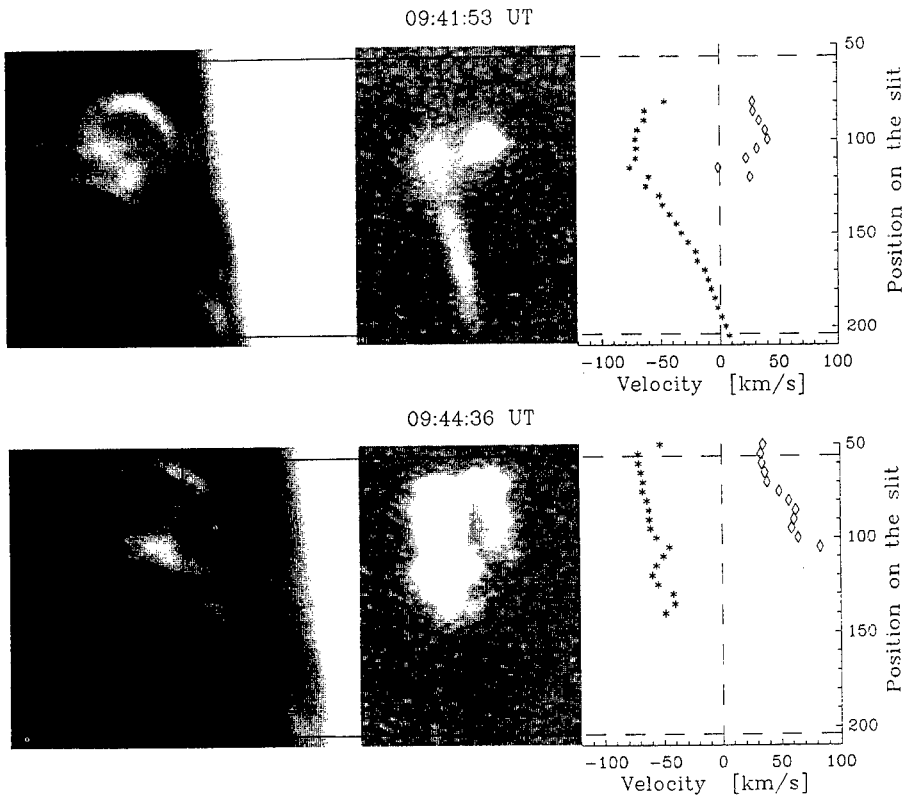
Figure 1.   Slit-jaw pictures of the eruptive prominence are on the left side; corresponding Hα spectra are in the center while charts of evaluated Doppler velocities are on the right side.

X-ray flare starting at 09:33 UT with its maximum at 09:43 UT.

At 09:40 UT the Hα prominence consisted of two cusp-shaped structures (see the left hand side of Figure 1): a higher one was more open at the top, and the smaller one, which is shifted northwards seemed to be closed. This smaller structure formed a bubble-shaped loop at 09:41 UT. Simultaneously, the bottom ends of this bubble-shaped loop started to interact with the higher cusp-shaped structure. This loop interaction process continued from 09:42 to 09:43 UT, the northern side of the prominence rose higher into the corona and formed a circular structure at 09:44 UT and the open ends of the initially higher cusp-shaped structure on the opposite side of the prominence reconnected. Then, during a one-minute time interval a large chaotization of the circular structure occurred. In the following periods the prominence evolution became slower, but still its structure changed. Two Hα images and spectra are shown in Figure 1 where one can find a very crucial moment: At the places where the slit of the spectrograph cuts *the contacts of individual loops*, (i.e., at the bottom of the circular prominence structure) the Hα spectra show large brightening and substantial

splitting into two separated red- and blue-shifted and, at the same time, very
bright components. We fit the measured line profiles of the eruptive prominence

Figure 2.   Hα eruptive prominence and *Yohkoh* SXT flare loops at
10:04 UT. The arrow marks interacting soft X-ray loops.

by the sum of two gaussians to derive Doppler velocities of the individual com-
ponents. The *Yohkoh* soft X-ray instrument observed this phenomenon only in
its final phase from 09:59 UT. To show positions of both Hα and soft X-ray
structures, we made a superposition of the pictures (Figure 2). The interacting
X-ray loops are situated above the closed X-ray loop but below the Hα erupted
prominence material.
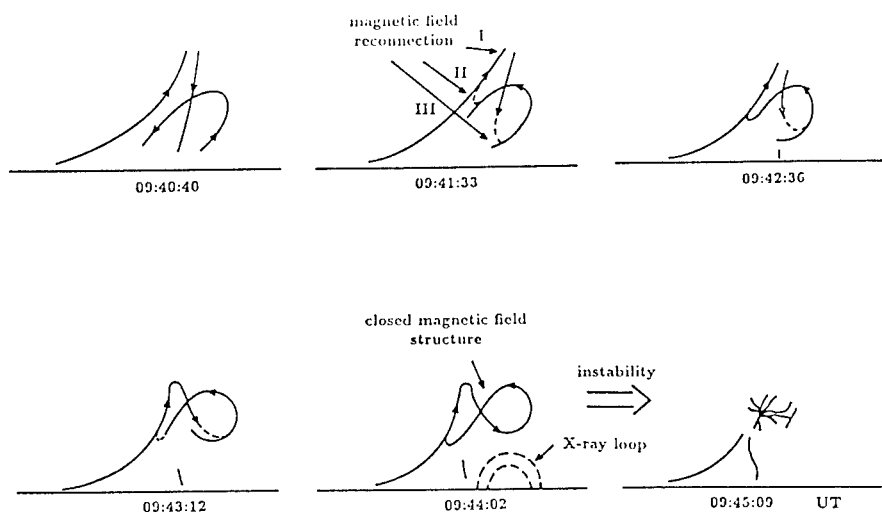
Figure 3.   Prominence evolution and magnetic field reconnection.

3. Interpretation

A simplified schematic of the prominence evolution with places of the magnetic field line reconnection is shown in Figure 3. We assume the magnetic field lines to be parallel to the shape of $H\alpha$ loops. Obviously, only their relative orientation is important for reconnection. At the beginning of the evolution the upper part of the $H\alpha$ prominence shows cusp-structures. We found three places (I, II, and III – see Figure 3), where the magnetic field reconnection is very probable. We think that only reconnection can explain the fast changes of the prominence structure. The most important reconnection process was probably at place III. Namely, the reconnection can explain not only changes of the prominence observed in $H\alpha$ (circular structure), but also the presence of closed X-ray loop observed below this reconnection place by *Yohkoh* (Figure 2, in Figure 3 this hot loop is expressed by dashed lines). The X-point of the magnetic field reconnection is expected just between both these structures.

This reconnection scenario can be also supported by the observation of the X-ray loop interaction between the closed X-ray loop and arising $H\alpha$ prominence (Figure 2). The $H\alpha$ line splitting into red and blue Doppler shifted components at place III represents further evidence of the reconnection process. Namely, as known from the magnetic field reconnection theory, a plasma with the magnetic field flows into the X-point where the reconnection process takes place. We suggest that just in these inflowing plasmas (in the direction from and towards an observer) the enhanced $H\alpha$ emission with line splitting is generated at place III. Consequently, the Doppler velocity components in the $H\alpha$ spectrum (typical values are of the order $\pm$ 50–100 km s^{-1}) we can interpret as the centerward velocity field of the inflowing plasma into the place of reconnection.

References

Kotr, P., Heinzel, P. and Knek, M. 1993, in JOSO Annual Report 1992, (ed.) A. v. Alvensleben, Freiburg, p. 114

Pevtsov, A. A., Canfield, R. C. and Zirin, H. 1996, ApJ, 473, 533

Rompolt, B. 1990, Hvar Obs. Bull., 14, 37

Sakai, J. (ed.) 1993, Proceedings of Symposium on Current Loop Interaction in Solar Flares, Toyama University

Smartt, R. N., Zhang, Z., Kim, I. S. and Reardon, K. P. 1994, in Solar Coronal Structures, V. Rušin et al. (eds.), VEDA Publ. Co., Bratislava, p. 219

Šimberová, S., Karlický, M. and Švestka, Z. 1993, Solar Phys., 146, 343

Švestka, Z. and Cliver, E. W. 1992, in Eruptive Solar Flares, (eds.) Z. Švestka, B. Jackson and M. Machado, Springer-Verlag, Berlin, p. 1

Tandberg-Hanssen, E. 1995, The Nature of Solar Prominences, Kluwer Acad. Publ., Dordrecht, Holland

Tsuneta, S. 1996, ApJ, 456, L63

Wave Activity and Prominence Eruption

F. Baudin, K. Bocchialini

Institut d'Astrophysique Spatiale/Univ. Paris XI Bât. 121, Campus d'Orsay, 91405 Orsay, France

C. Delannee, S. Koutchmy, G. Stellmacher

Institut d'Astrophysique de Paris/CNRS, 98 Bis Bd Arago, 75014 Paris, France

K. Shibata

National Astronomical Observatory, Mitaka 181 Tokyo, Japan

I.S. Veselovsky, O.A. Panasenko, A.N. Zhukov

Institute of Nuclear Physics, Moscow State University, Moscow 119899, Russia

Abstract. Observational evidence of 3 and 5 min vertical oscillations of a filament on the disk are recorded. Wave activity was observed before, during and after a filament disappearance, inside and around the filament. Both an H_α brightening and, later, a blowing out of a faint soft X-ray (Yohkoh) loop system occuring in connection with a flare were noticed. The wave activity seems to be a dynamically important ingredient of this erupting prominence.

Propagating MHD waves and convective structures bring their energy and momentum from the photosphere towards the chromosphere up to the coronal heights where they are partially reflected and/or dissipated. The transition from the laminar to the turbulent state of the whole prominence enhances the dissipation rate of the external waves inside this system, adding energy to produce the heating and lifting of the plasma. Internal plasma instabilities could trigger this transition in the framework of a prominence disappearance.

1. Introduction

Conditions for prominence formation are thought to be related to the arcade of coronal fields joining opposite-polarity photospheric fields with the convergence and cancellation of small patches of opposite-polarity magnetic flux (Martin 1990). The concept of "the ball in the air" supported in a statistical sense by nonlinear Alfvén waves has been developed for quiescent prominences (Jensen 1990). Nonlinear oscillations of the plasma near the tops of magnetic loops in the gravity field could make this configuration dynamically stable (Gorbachev and Kelner 1988). A connection between the filament and the chromospheric

network was suggested based on the observed up- or downward motions up to ~10 km/s at the footpoints (Schmieder 1990). MHD shock waves travelling along fibrils were suggested as a possible explanation of this connection (Sterling and Hollweg 1988).

Prominence oscillations have been reported in many papers (see, e.g., Bashkirtsev and Mashnich 1984, Wiehr et al. 1989, Molowny et al. 1997). The viscous friction or the wave emission are supposed to be important dissipative factors in the late phase of an erupting prominence. The aim of the present paper is to present new observations of oscillations in a disappearing filament on the disk and to discuss a possible role of small-scale processes in the phenomenon.

2. Observations

The observations were obtained at the Sacramento Peak Observatory Vacuum Tower Telescope (VTT). Sequences of images in the H_α red and blue wings (at 0.75Å from the line center) taken through the narrow UBF passband were obtained during 110 min with a sampling time of 1 min, an exposure time of 0.8 s, and a spatial resolution of 0.34 arcsec/px [see details in Baudin et al. (1997), who also made observations in the continuum and the MgI_{b1} line in the same field of view]. Here, we concentrate on the analysis concerning a filament lying between plages with opposite polarities.

We observed a very rapid temporal evolution of the filament, which moved over an apparent distance of 18,000 km in 12 min (between T_{obs}=42 and 54 min, leading to a minimum speed of 25 km/s, see Figure 1), which was followed by the eruption of a loop system observed in soft X-rays by the Yohkoh telescope about 2 hours later. We observed also oscillations in the 2–8 mHz range in the region of the filament over the whole time sequence, but stronger "pulses" of power (aroud 3 and 5.5 mHz) occurred at the beginning of the eruption of a large part of the filament (see Figure 1) in the time/frequency analysis of a time series extracted from a region at the center of the filament.

3. Discussion

Prominences show numerous manifestations of the mechanical and thermodynamical loss of equilibrium. Faint dissipative MHD and kinetic properties of the gas and electromagnetic radiation seem to be important in the regulation of the energy, momentum and mass flows associated with filaments and prominences. It is generally believed that MHD waves and explosive events are essential phenomena (Jensen 1990). Many important details are not known, so we can only guess about dominant MHD and kinetic processes.

For these purposes we used estimated parameters characterizing filaments. We distinguished three more or less arbitrary scales in filaments: the largest characteristic scales for the structure as a whole (L), substructures (M) and the smallest (S) observable scales (see Table 1). Several implications follow from the analysis of physical conditions. Both thermal and bulk motions can be essential in the prominence structure and dynamics. The corresponding MHD regimes can be nearly sonic because $M \sim 1$. The cool parts ($T < 10^4$) are
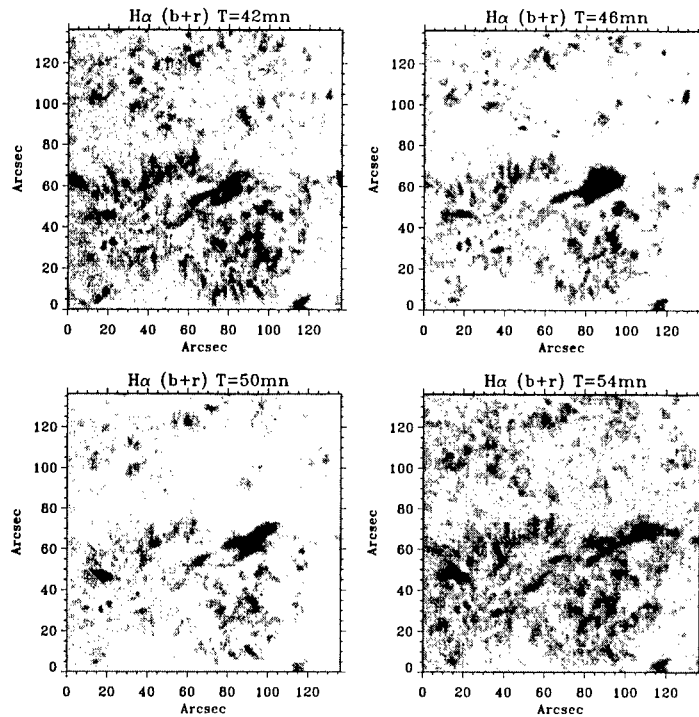
Figure 1.   Eruption of the filament as seen in frames with both H_α wings added together, during a period of time of 12 min.

probably dominated by radiation in the energy balance. Radiative H_α losses are comparable to the estimated MHD wave energy inputs. Viscous terms may be neglected because $Re \gg 1$. This means that flows are turbulent for these scales. The analysis of dimensionless parameters shows that L structures are quasistationary. This is not the case for M and S structures. High magnetic Reynolds numbers allow us to use the frozen-in approximation. Motions along magnetic fields in prominences and filaments are regulated by the combined action of the gas pressure and gravity forces with the inertia term due to the inhomogeneity of the drifts across the magnetic field. As a result, magneto-acoustic-gravity waves and convective structures appear.

Alfvén waves are nonlinearly damped in the low magnetic field, dense regions. Previous work (Suess et al. 1992) stated that 5 min Alfvén waves are not reflected in the solar corona up to heights of about 6 solar radii, but this could be different in the presence of sharp inhomogeneities. Small-scale structures inside filaments and prominences can reflect and scatter the waves coming from the bottom. An increase of the turbulence level due to the internal instability adds to the scattering and the dissipation of the external waves because of the appearance of new scattering and absorbing elements. We speculate that the transition to a more turbulent state of the prominence produces an enhancement of the overall dissipation of the external energy fluxes crossing the system

in the shape of quasi-stationary electric currents and mechanical motions, as well as waves (3 and 5 min oscillations). The enhanced dissipation probably leads to the brightening, heating, and proper oscillations of the prominence, and eruption when the lifting force is large enough.

Table 1.   The characteristic scales in filaments and prominences

		Dimension (Mm)			Lifetime
		Length	Height	Width	
L	Large scale ranges	60 – 600	15 – 100	4 – 15	weeks-months
M	Medium scale	30			2 – 12 hours
S	Small scale	0.3 – 1			$\leq$ 10 min

4. Conclusion

Our results lend some additional support to the view that the role of waves and small-scale convective structures in filaments and prominences may be twofold. First, they bring energy and momentum from the photosphere towards the chromosphere up to coronal heights where they are partially reflected and dissipated. Second, the fast transition from a quiescent to the eruptive state could be triggered by the switch of the extreme gas pressure gradient or the electric currents or by a rapid increase of internal small-scale plasma inhomogeneities, modifying the dissipative characteristics of the prominence/cavity plasma system.

References

Bashkirtsev V.S. and Mashnich G.P. 1984, Solar Phys., 91, 93

Baudin F., Molowny-Horas R. and Koutchmy, S. 1997, A&A, 326, 842

Gorbachev V.S. and Kelner S.R. 1988, Zh. Exp. Theor. Phys., 94 (9), 89

Jensen E. 1990, in Dynamics of Quiescent Prominences, V. Ruždjak and E. Tandberg-Hanssen (eds.), Springer-Verlag, New York, p. 129

Martin S.F. 1990, in Dynamics of Quiescent Prominences, V. Ruždjak and E. Tandberg-Hanssen (eds.), Springer-Verlag, New York, p. 1

Molowny-Horas R. et al. 1997, Solar Phys., 172, 181

Schmieder B. 1990, in Dynamics of Quiescent Prominences, V. Ruždjak and E. Tandberg-Hanssen (eds.), Springer-Verlag, New York, p. 85

Sterling A.C. and Hollweg J.V. 1988, ApJ, 327, 950

Suess S.T., Moore R.L., Musielak Z.E. and An C.-H. 1992, in Solar Wind Seven, E. Marsch and R. Schwenn (eds.), Pergamon Press, Oxford, p. 117

Wiehr E., Balthasar H. and Stellmacher, G. 1989, Hvar Obs. Bull., 13 (1), 131

Helical Structure in an Eruptive Prominence Related to a CME (SUMER, CDS, LASCO)

T. A. Kucera[1] and A. I. Poland

NASA/GSFC, Code 682, MD 20771, USA

J.E. Wiik [2] and B. Schmieder

Observatoire de Paris, 92195 Meudon Cedex, France

G. Simnett

University of Birmingham, Birmingham B15 2 TT, UK

Abstract. SOHO (SUMER/CDS) observed an eruptive prominence on May 1, 1996, associated with a CME observed by LASCO. We investigate the physical conditions of this prominence in order to quantify velocity, temperature, and density. SUMER spectra in Si IV and O IV lines are used to obtain Doppler-shift images of the prominence. The prominence shows large-scale red and blueshifted regions, revealing a large helical structure with a global twist. In addition, fine structure analysis shows multiple components in the line profile, suggesting integration of many threads along the line-of-sight with a large dispersion of velocities ($\pm$ 50 km s^{-1}).

1. SUMER Observations

One of the main objectives of SOHO is to study the dynamics of prominences and the prominence-corona interface. By analyzing the spectra of O IV and Si IV lines observed with SUMER and the spectra of 15 lines with CDS, Doppler shifts, temperatures, and electron densities were derived in different structures of the prominence (Wiik et al. 1997).

1.1. Calibrated Intensity

Wilhelm et al. (1997) give the calibration curve of SUMER Detector A and discuss a procedure to calibrate the SUMER spectra. Mean Si IV 1393.76Å profiles averaged along the slit are shown in Figure 1. Profiles from both the prominence and the disk are shown. The count rate in the prominence is low. As a result, the profiles of lines emitted in the prominence are rather noisy. The ratio between the emission in the prominence and that of the disk was

---

[1]Also st: Space Applications Corp., 901 Follin Ln., Vienna, VA 22180, USA

[2]Also at: University of Oslo, P.O. Box 1029 Blindern, N 0315 Oslo, Norway
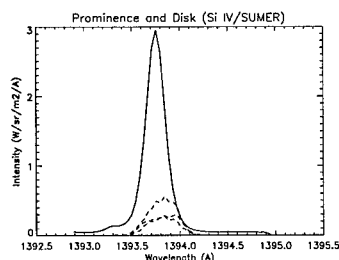
Figure 1. Calibrated mean profiles in the prominence (solid and dashed lines) and over the disk (dot-dashed line) close to the prominence.

low, 10% in the dense bubble and 5 to 8% in the rest of the prominence. The Si IV 1393.76Å emission reached 0.5 W/sr/m^2/Å in the dense bubble while the maximum 1401.51Å O IV line emission was only 0.07 W/sr/m^2/Å. The ratio between these two lines (around 2.5) is too low for us to use them to accurately determine electron density (Cheng et al. 1982). The ratio between the O IV 1401.51 and 1399.75Å lines is more useful and was used to derive electron density in different structures of the prominence (Wiik et al. 1997).

1.2. Dopplershifts

To determine quantitative values of Doppler shifts we have calibrated the lines in wavelength (Wiik et al. 1997). We use two methods to compute the velocity field: 1) fitting all points with a single Gaussian, and 2) fitting specific points in the helical structure with multiple Gaussians (using the procedure "xcfit" developed by S. Haughan). The maps displayed in Figure 2 were obtained with the single-Gaussian fits. Parallel to the axis of the loop, we see redshift on one side and blueshift on the other. We interpret this as helical motions around the axis of the loop, although it is difficult to determine how many coils there are. O IV 1399.74Å and Si IV 1393.76Å profiles yield similar results when fitted with multiple Gaussians. Here we show results from fitting the Si IV profiles. Figure 3 shows examples of profiles in the helical loop. Table 1 gives the characteristics in three different locations. The locations are indicated in Figure 2a.

We see that in addition to the global motion along the loop there are also individual pixels with blue- and redshifts. These structures appear consistently in the different lines observed. We interpret them as individual twisted threads and suggest that the global motion is, in fact, the combined motions of the individual threads.

2. Discussion and Conclusion

The eruptive part of the prominence observed by SUMER consists of a bubble (plasmoid) of material at transition region temperatures with redshifts of up
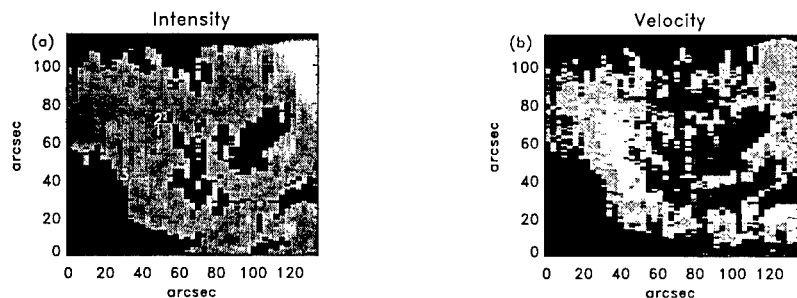
Figure 2.   SUMER intensity (a) and velocity (b) (black/white for blue/redshifts) images of the prominence of May 1, 1996 (08:16-08:50 UT) showing the large helical structure of the prominence in Si IV at 1402.77Å. The limb is in the upper right corner. The locations of the spectra described in Table 1 are shown by the numbers 1, 2, and 3.
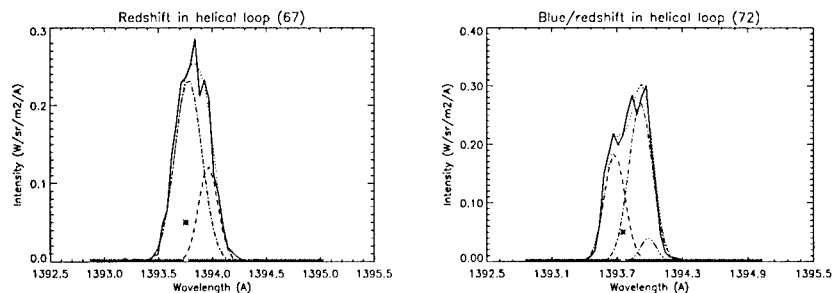
Figure 3.   Examples of multi-structure profiles in the helical struc-ture: observed profile in solid line, Gaussian components in dashed and dot-dashed lines, fitted profile in dotted line. The center of the line is indicated by an asterisk.

Table 1.   Characteristics of profiles in the helical structure. Doppler shifts are in km s^{-1}. Blueshifted values are negative, redshifted ones positive.

Location	Moments	Gaussian 1	Gaussian 2	Gaussian 3
1. redshifted region	intensity	9.35	4.8	
	Doppler shift	4.9	50	
	line width	0.29	0.209	
2. blue/ redshifted region	intensity	7.4	10.8	1.6
	Doppler shift	-16.6	34.6	50.0
	line width	0.22	0.25	0.17
3. blueshifted region	intensity	19.6	0.5	
	Doppler shift	-10.9	18	
	line width	0.25	0.29	

to 80 km s^{-1} and electron density of the order of 10^{10} cm^{-3}. This could be the signature of a reconnection point between magnetic field lines due to an instability. Material might be ejected from such a point in the form of jets or surges (Shibata et al. 1992). This could destabilize all the structures above and produce the CME.

The whole prominence was very active. It developed both a large helical loop and several smaller loops consisting of twisted threads or multiple ropes. The profiles of the SUMER lines in these loops show a large dispersion of velocities ($\pm$ 50 km s^{-1}) and the ratio of the O IV lines indicates a large dispersion in electron density (3×10^9 cm^{-3} to 3×10^{11} cm^{-3}). These variations are consistent with the idea that the prominence structure contains multiple threads.

The large helical structure of this prominence suggests that the event can be explained by an instability of the sort occurring in the model of van Ballegooijen and Martens (1989) for the formation and eruption of solar prominences based on canceling flux. In this model the magnetic flux is transferred from the arcade field, which supports the prominence, to a helical field. The magnetic field map (Kitt Peak) shows that the prominence lies in a corridor between two polarities. Based on the sign of the polarities and the sign of the velocities in the prominence we conclude that the helical loop is untwisted.

We observe transport of mass and no real heating of the prominence structure, indicating that the eruption is a purely dynamical phenomenon. The eruption looks like the ejection of a plasmoid, and the prominence loops are twisted.

The eruption of the prominence and the CME, spatially and temporally related, can be interpreted in terms of global destabilization of the magnetic field. The exact timing of the phenomena is difficult to estimate due to the low cadence of the SUMER and CDS observations so we have no evidence that one event triggered the other. However, it is clear that they are the result of the same magnetic instability.

References

van Ballegooijen, A.A. and Martens, P.C.H. 1989, ApJ, 343, 971

Cheng, C.-C., Bruner, E.C., Tandberg-Hanssen, E., Woodgate, B.E., Shine, R.A., Kenny, P.J., Henze, W. and Poletto, G. 1982, ApJ, 253, 353

Shibata, K., Nozawa, S. and Matsumoto, R. 1992, PASJ, 44, 265

Wiik J.E., Schmieder, B., Kucera, T., Poland, A., Brekke, P. and Simnett, G. 1997, Solar Phys., 175, 411

Wilhelm, K., Lemaire, P. and Curdt, W., 1997, Solar Phys., 170, 75

Hα Observations of the Dual Eruptive Prominences of June 29, 1994

L. Lenža

Astronomical Observatory, Vsetínská 78, 757 01 Valašské Meziříčí, Czech Republic

Abstract. Our results in the field of observing prominences at our observatory show dual eruptive prominences on June 29, 1994 obtained by a coronograph at our observatory at Valašské Meziříčí. We tracked the evolution of these eruptive prominences in time and morphology.

1. Data

The source of these observations was a prominence patrol running at Valašské Meziříčí Observatory. For taking pictures of active prominences (and also of the overview pictures) we use an H-alpha coronograph with Zeiss E 150/1950 mm objective with Šolc filter (passband 0.5 nm) and KODAK 2415 Technical Pan film or KODAK SO115 film (developer D-19 at 21°C).

Chromospheric observations made by colleagues from the Solar Department of the Astronomical Institute AV ČR at Ondřejov (Czech Republic) were also used in this paper. They used a refractor 210/3410 with a Daystar (0.06 nm) Hα filter and a CCD camera.

Other data were obtained from the Internet and Solar Geophysical Data.

2. Observations

On June 29, 1994 the prominence patrol started shortly after 07:00 UT. Along with a few small prominences, two larger ones were registered, the first of them at the position N11°E (Figure 1) and the second at S20°W (Figure 2).

During a few hours both prominences showed a lot of activity. and disparitions brusques occurred almost simultaneously. The global morphological evolution of both events can be seen in Figure 1 and Figure 2. In both events, at almost same time, a destabilisation occurred, the origin of which could be the emergence of new magnetic flux at the surface. The question is whether the coexistence of this couple of events is accidental or somehow has a global cause.

2.1. Eruptive Prominence – N11°E (Figure 1)

At 08:12:54 UT brightness variations were observed in this prominence at some points. Unfortunately, on the photographs that were taken nothing is visible, so we can not specify which area it was. Information about these brightness variations comes from the visual observation (notation in the observer's diary).
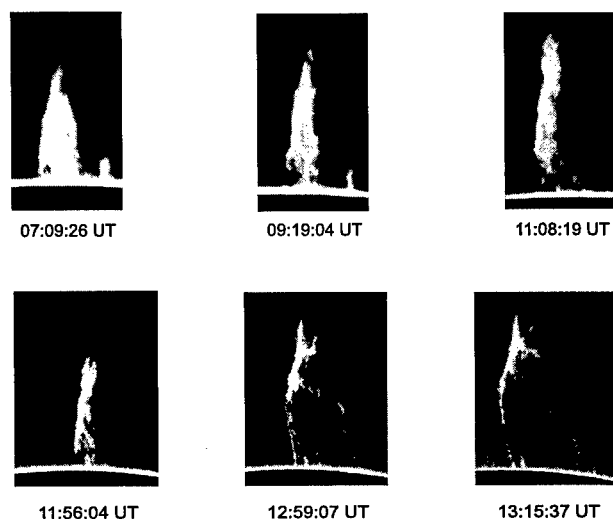
Figure 1.   The evolution of prominence E N11. Date: June 29, 1994;
Device: Hα coronograph with Zeiss E 150/1950 mm objective with Šolc
filter (passband 0.5 mm); Position: E N11; Scale of the original image:
1 mm=6500 km; Material: KODAK SO115; Observer: Libor Lenža.

The evolution of the prominence on Figure 1 can be compared to the in-
creasing height of the top of the prominence, measured relative to the solar limb
(Figure 3). The increasing speed of the prominence as projected on the sky was
rising from the values of kilometers per second to tens of kilometers per second.
Further observations were interrupted by cloudiness.

2.2.   Eruptive Prominence – S20°W (Figure 2)

After the beginning of the observation, a nervelike mass outflow, heading out
from the prominence to the nearby surroundings was observed. On the mosaic of
images in Figure 2 we can follow the evolution of the prominence. The morphol-
ogy of the prominence can be compared with its altitude in the sky projection
(Figure 3).

On the images taken after 10:00 UT we can find signs of fragmentation
into smaller arched formations, which as a whole, keep the original shape of the
prominence. It was probably caused by the emergence of new magnetic flux at
the surface.

The material from the rising prominence runs down along magnetic force
tubes connecting the top of the prominence with the chromosphere. In these
structures we can also see hints of twisting (Figure 2 – 13:04:44 UT).

3.   Discussion

We are not able to say anything objective about the interesting time coinci-
dence, which means we can not say whether both these events have the same

07:10:40 UT   11:09:26 UT   12:57:46 UT

12:59:45 UT   13:04:44 UT   13:13:37 UT
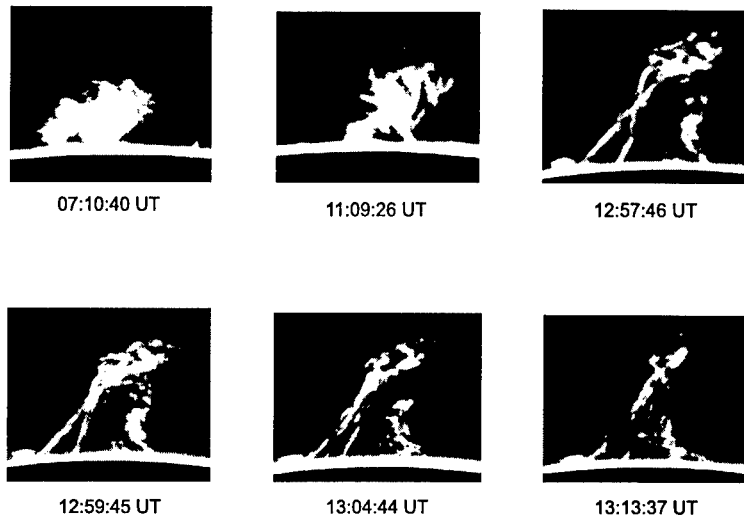
Figure 2.   The evolution of prominence W S20. Date: June 29, 1994;
Device: Hα coronograph with Zeiss E 150/1950 mm objective with Šolc
filter (passband 0.5 mm); Position: W S20; Scale of the original image:
1 mm=6500 km; Material: KODAK SO115; Observer: Libor Lenža.

cause, or whether they are unrelated results of some global event. Both promi-
nences were situated away from active regions (there were not many of them
on the sun at that time). This leads us to suppose, that the impulse for the
prominence activation was not flares, but rather new emergence of magnetic
flux. However, the possible eruption activity behind the limb could also cause
this effect. Surrounding the prominences on the western limb were old, decayed
active regions (NOAA 7736, 7737, 7740). On the eastern limb was NOAA 7746,
which appeared on the disc on July 2, 1994 (heliographic latitude N10°).

At the available radio frequencies no significant effect was found which could
have a definite connection with eruptive prominences.

4.   Conclusion

Observation of the two prominences on June 29, 1994, whose phase of activa-
tion was during the same time interval, was from time to time interrupted by
cloudiness. This is one of the reasons, why we can not say more about the whole
morphological evolution of these events.

It is very useful to compile and analyse all the available data about such
interesting double eruptive prominences (e.g., Koutchmy and Noëns 1994).

References

Koutchmy S. and Noëns J. C. 1994, in Solar Dynamic Phenomena and Solar
      Wind Consequences, ESA SP-272, p. 91

Solar-Geophysical Data 600 1994, NGDC, Boulder
Solar-Geophysical Data 601 1994, NGDC, Boulder
Solar-Geophysical Data 604 1994, NGDC, Boulder
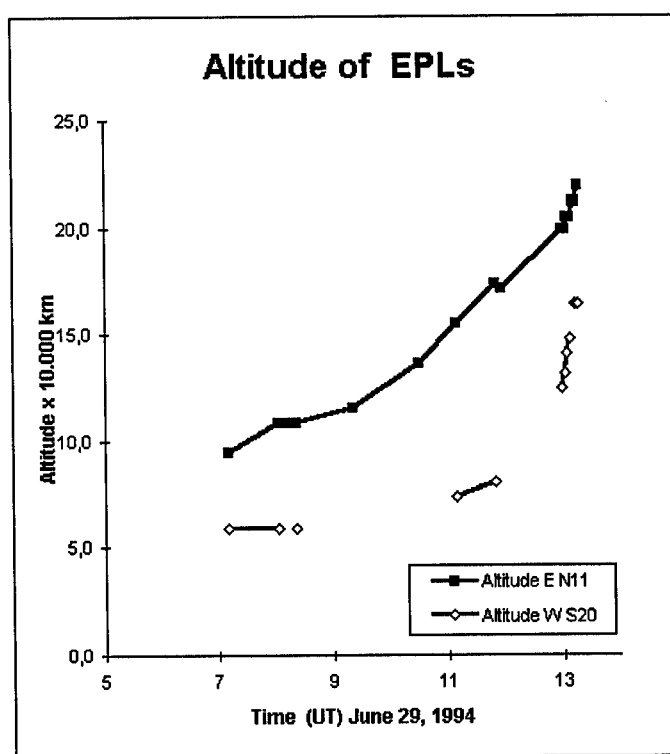
Figure 3.   Time evolution of altitude of EPLs.

Behaviour of Hα and H Ca II Emission Lines in a Prominence Before and During its Dynamic "Disparition Brusque"

M. S. Madjarska and V. N. Dermendjiev

Institute of Astronomy, 72 Trakia Blvd., 1784 Sofia, Bulgaria

Z. Mouradian

Observatoire Paris-Meudon, DASOP, URA 326, 92195 Meudon, France

P. Kotrč

Astronomical Institute of the Czech AS, 25165 Ondřejov Observatory, Czech Republic

Abstract. Hα and H Ca II emission lines in a limb quiescent prominence (QP) undergoing destabilization are studied. The temperature, line-of-sight velocity and micro-turbulence are obtained in one of the prominence legs, just before and during the prominence activation.

1. Introduction

On August 3, 1992 at the solar East limb ($\phi = -16°$, $l = 90°$), a prominence was registered by the Multicamera Flare Spectrograph (MFS) of the Ondrejov Observatory (described in Valníček et al. 1959). The prominence was observed in two series, from 13:25:45 to 13:30:15 UT and from 14:22:55 to 14:33:35 UT. The registration was made by all cameras of the MFS in different slit positions on the prominence body. During the first series of observations the prominence behaved as a quiescent one, whereas in the second one as a dynamic "disparition brusque" (DB). According to Solar Geophysical Data (1993) the activation started at 13:50 UT and finished at 17:05 UT, so that we have observations covering the late QP phase and the chance to follow the start of the destabilization and eruption. In this paper we present preliminary results concerning the basic plasma parameters in a prominence leg, just before and during the DB process.

2. Observational Material

During the first series of observations, which lasted 4m 30sec, 6 registrations were made in different slit positions. At 14:22:55 UT the observations were renewed and 10 spectrograms more were taken in different slit positions.

The spectrograms cover five spectral regions including the following emission lines – Hα, D3 He, Hβ, Hγ, H and K Ca II. The height of the slit is 50 mm which corresponds to 627,125 km and the working width is 0.0534 mm ≈

669 km. The focal image of the Sun has a mean diameter of 125.6 mm. In the different spectral regions, 1 mm of the vertical scale corresponds to 17.3 arc sec on the solar disc. The dispersion is in order of 1 Å/mm. The exposure time for the first series is 5 sec and for the second series is 6 sec.

3. Image Processing

The observational material was processed on the Joyce Loebl microdensitometer at the National Astronomical Observatory – Rozhen. The two-dimensional scans were taken with a diaphragm of 25×25 μ^2 and a step of 25 μ in both directions. The obtained spectra were corrected for ghosts as well as for scattered light.

4. Prominence Plasma Parameters

To study the physical conditions in the prominence at certain times of its quiescent and DB phases, we compared the slit positions of both series of observations. Two of them, in the south prominence leg (at 13:25:45 UT and 14:22:55 UT), nearly coincided. The location of the slit was almost perpendicular to the prominence leg which permitted us to follow velocity and temperature changes along the leg's cross section.

The line-of-sight velocity was determined by the equation

$$v_r = c\frac{\lambda - \lambda_0}{\lambda_0}$$

where c is the velocity of light, λ_0 is the real wavelength and λ is the registered one. The obtained results (Figure 1) show that just before the eruption (dashed line) in the periphery of the prominence leg $v_r > 0$, whereas in the central region $v_r < 0$, where v_r is in the range of –5 to 5 km s^{-1}. During the DB phase (continuous line) we determined $v_r = -14$ km s^{-1} for the left edge of the prominence leg, whereas in the central part and right edge the velocity did not change significantly.

In addition to thermal effects, the atoms possess a non-thermal velocity component (micro-turbulence) that influences the line profile and gives rise to the total Doppler width (Tandberg-Hanssen 1995), expressed by

$$\Delta\lambda_D = \frac{\lambda}{c}\sqrt{\frac{2kT}{m} + \xi_t^2}.$$

Both velocities could be separated by comparing the width of two spectral lines from atoms of different weight. We compute the temperature using Hα and H Ca II lines arising in the same portion of prominence volume by the formulae

$$T = 1.95 \times 10^{12}\left(\frac{1}{\mu_1} - \frac{1}{\mu_2}\right)^{-1}\left[\left(\frac{\Delta\lambda_{D_1}}{\lambda_1}\right) - \left(\frac{\Delta\lambda_{D_2}}{\lambda_2}\right)\right]^2,$$

where μ_1 and μ_2 are the atomic weights for Hα and H Ca II, respectively. The

M. S. MADJARSKA ET AL.
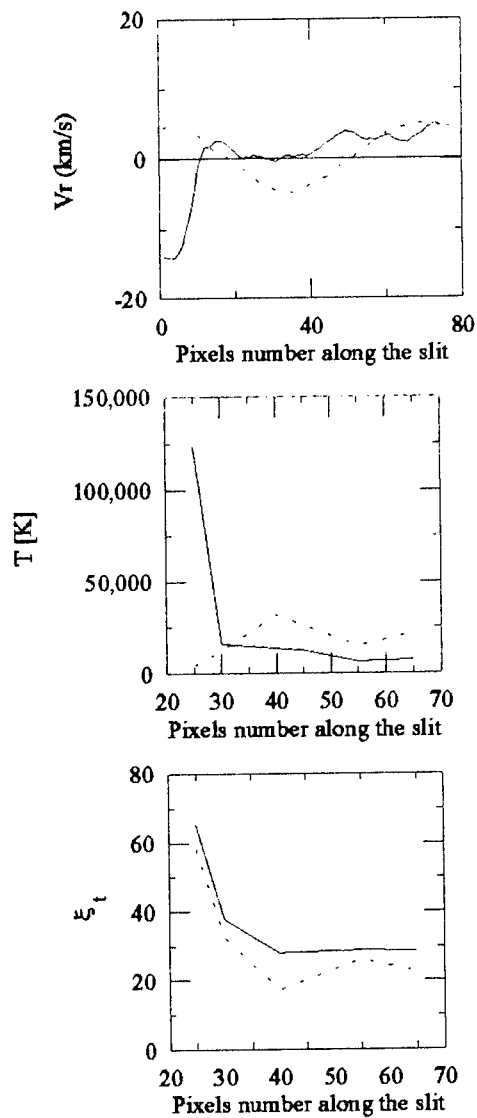
Figure 1.   The line-of-sight velocity (top), temperature (middle) and micro-turbulence (bottom) during the QP (dashed line) and active phase (continuous line).

micro-turbulence was determined by the equation (Jefferies and Orrall, 1962),

$$\xi_t = \left(c^2 \frac{\Delta\lambda^2}{\lambda^2} - \frac{2kT}{m} \right)^{1/2}$$

where k is the Boltzmann constant and m is the mass of unit atomic weight.

It is interesting to note that in the central part of the prominence leg, during the QP phase, ξ_t decreases (Figure 1, bottom). On the other hand the temperature (Figure 1, middle) slightly increases. Without additional observational information it is difficult to interpret the obtained results. One of the possible suppositions is that there was a slight down flow of hotter material. Such a downflow will increase to certain degree the horizontal (parallel to the disk) oscillations leading to the observed increase of $| v_r |$ (Figure 1, top).

5. Conclusion

The scenario sketched in this paper from these preliminary results is rather attractive. However, it needs further verification based on the entire series of registered emission lines.

References

Jefferies, J. T. and Orrall, F. Q. 1962, ApJ, 135, 109

Solar Geophysical Data 1993, WDC-A, Boulder, p. 580

Valnicek, B., Leftus, V., Blaha, M., Švestka, Z. and Seidl, Z. 1959, Bull. Astron. Inst. Czech., 10, No 5, 149

Tandberg-Hanssen, E. 1995, The Nature of Solar Prominences, Kluwer Academic Publ., Dordrecht, Holland

Horizontal Expansion of Eruptive Prominences

Bogdan Rompolt

Astronomical Institute of Wrocław University, 51-622 Wrocław, ul. Kopernika 11, Poland

1. Introduction

It is well known that quiescent prominences (QPs) as well as active region prominences (ARPs) occasionally undergo eruptions. The process of eruption of these prominences is caused by eruption of a huge magnetic system (HMS) associated with the prominence channel and the prominence itself (Rompolt 1984). Material of these prominences is frozen-into only a part of such a magnetic system – before as well as during the eruption. When an HMS erupts it simply lifts with it the frozen-in prominence material.

Usually during the eruption a large part of the prominence material is lifted high into the corona and/or into interplanetary space. Nevertheless, on some occasions during the eruption a significant part of the original prominence material flows down to the chromosphere (Rompolt 1990).

Eruption of the QPs and ARPs in more or less the vertical direction proceeds with increasing speed from several kilometers per second at the beginning phase of the eruption up to several hundreds of kilometers per second at the late phase of the eruption. A typical eruptive prominence [EP] of type I (classification according to Rompolt 1984, 1990) is shown in Figure 1a, and the corresponding typical height-time [H-T] curve one can find is shown in Figure 1b.

2. Horizontal Expansion

Besides the eruption in the vertical direction, some QPs as well as ARPs exhibit expansion in the horizontal direction with an average constant velocity of several tens of kilometers per second (Rompolt 1984). One classic example of such a horizontal expansion during the eruption of a QP on September 20, 1980 is shown in Figure 2. As the eruption proceeded, the southern extremity of the prominence was seen to be displaced more and more toward the south pole.

White arrows in Figure 2 in the panels labelled 08:07:01 UT and 10:36:12 (left) indicate the southern extremity of the prominence just before the eruption, whereas the right arrow in panel 10:36:12 UT shows the prominence's southern extremity at the end phase of the eruption in the light of the hydrogen Hα line. During the eruption the southern extremity of the prominence was displaced by 120,000 km with a constant velocity of 65 km/s. The displacement–time diagram [D-T] for five eruptive prominences showing horizontal expansion during their eruption is presented in Figure 3. Identify in this diagram the D-T dependence for the EP of September 20, 1980 and compare it with it's H-T dependence shown in Figure 1b.
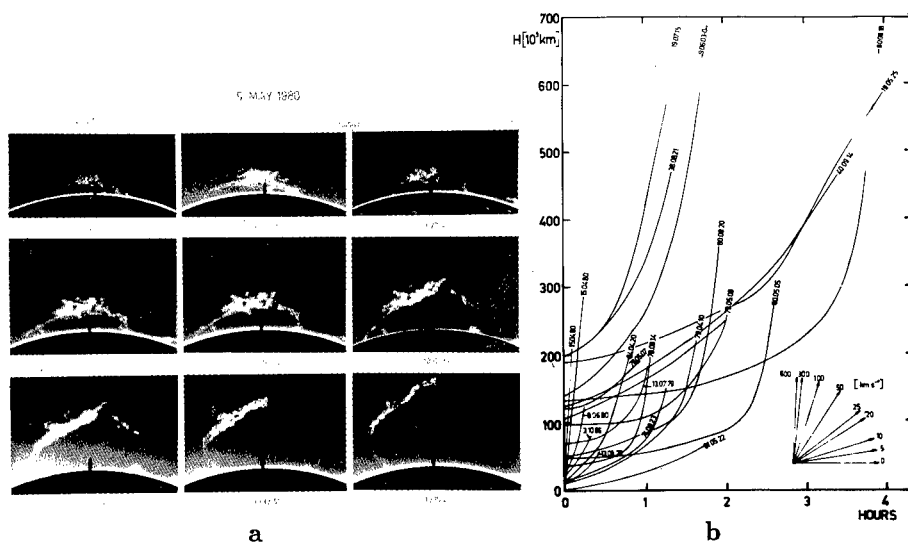
Figure 1. a: A typical example of an eruptive prominence [EP] of type I (taken with the SC), b: The height-time diagram for EPs - the zero level has been placed at the top of every prominence just before the eruption.
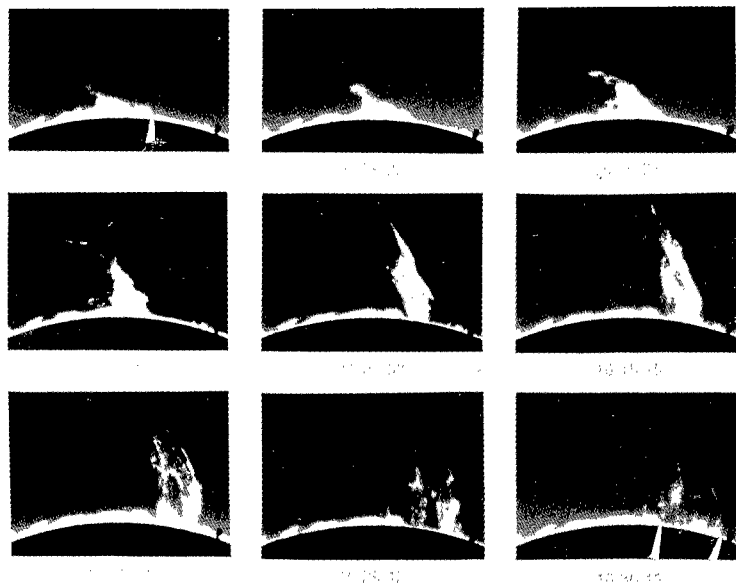
Figure 2. An eruptive prominence [EP] of type II on September 20, 1980 exhibiting during the eruption expansion in the horizontal direction (SC).

Horizontal Expansion of EPLs
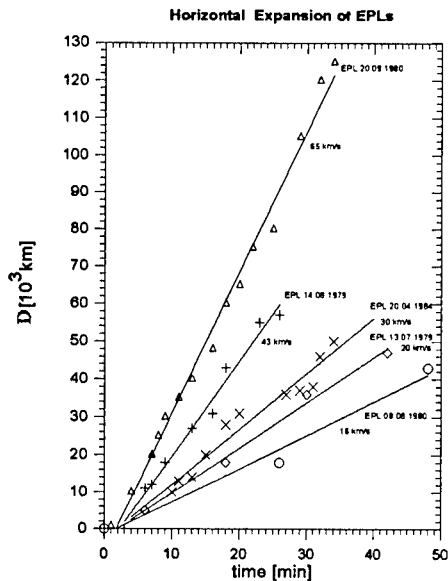
Figure 3.   The horizontal displacement–time diagram [D-T] for five eruptive prominences showing horizontal expansion.

In deriving the displacements and velocities of horizontal expansion of the eruptive prominences, the inclination of the main body of these prominences towards the line of sight, while in the quiescent phase, was taken into account. This inclination was measured for these Hα filaments which were identified with the corresponding limb prominences on the Meudon synoptic maps of the chromosphere.

Horizontal expansion has been measured in a dozen or so EPs observed mainly with the Small Coronagraph (SC) of the Wrocław Observatory. According to our measurements the velocities of horizontal expansion are in the range from 15 to 80 km/s. In one case, where the horizontal expansion was seen to spread out from the limb to a region on the disk close to the limb, the horizontal expansion of the prominence legs appeared to be about 160 km/s (Rudawy et al. 1994)!

3.   Conclusion

The horizontal expansion of an EP seems to be an effect of the eruption from the Sun of an associated HMS. In the course of this process the magnetic field is pulled out from the solar near-surface layers high into the corona and interplanetary space. In a later phase of the eruption when the bulk of the prominence material is lifted high into the corona, that part of the prominence material which flows down to the chromosphere is very likely gradually intercepted by a set of the prominence magnetic filaments being stretched out into the corona.

These magnetic filaments, not visible during the earlier phase of eruption, now become visible in Hα due to the intercepted prominence material being subsequently cooled. This mechanism is schematically explained in Figure 4.

Figure 4.   A drawing illustrating the mechanism of EPs' horizontal expansion.

The QPs as well as ARPs are formed by a system of intertwisted and/or interweaved fine filaments. During an eruption these prominences undergo untwisting into a system of fine loops (Rompolt 1984, 1990). In some cases, especially during a late phase of an eruption of the large, old QPs, one can identify several tens of fine loops.

References

Rompolt, B. 1984, Adv. Space Res., 4, No. 4, 357

Rompolt, B. 1990, Hvar Obs. Bull., 14, 37

Rudawy, P., Rompolt, B., Kotrč, P., Heinzel, P. and Knižek, M. 1994, in Solar Magnetic Fields, (eds.) M. Schlüsser and W. Schmidt, Cambridge University Press, p. 372

On the Eruption of Prominences and Disappearance of Quiescent Filaments

S.S. Gupta
Indian Institute of Astrophysics, Kodaikanal – 624103, India

Jagdev Singh
Indian Institute of Astrophysics, Bangalore – 560034, India

Abstract. The analysis of an eruptive prominence and disappearing quiescent filaments indicates that the prominence height on the limb increases after the filament develops a twist as seen in the Hα on the disc. The increase in prominence height, large change in the shear angle, and the appearance of filament as a U-shaped structure before the disappearance of the filament or prominence eruption can be explained by assuming that the middle portion of the filament rises above the solar surface with its edges anchored in the chromosphere. Further, the loop-like structure of the filament splits into two parts 2–3 days prior to its disappearance and the gap between the two increases with time. The increasing gap and simultaneous disappearance of both parts of the filament suggests that heating of the top of the loop-like structure begins about 2 days before its disappearance. The cause for this portion of the filament not being visible in Hα may be that it is heated to a high temperature.

1. Introduction

Detailed observations of quiescent prominences over a long period can provide a clue to conditions for the onset of the eruptive instability, as well as its development (Vrsnak 1990 a, b). To understand the mechanism and role of shear before the disappearance of quiescent filaments, we have investigated an eruptive prominence and two disappearing quiescent filaments, in the period December 1949 to April 1950, with a new technique for measuring the shear and orientation of the filament.

2. Observational Data and Measuring Technique

Data has been taken from the solar obsevational archives of Kodaikanal observatory, consisting of photoheliograms (image diameter of 200 mm), spectroheliograms in Hα, Ca +K and prominences (image diameter of 60 mm). For the three cases taken in this study, the positions of sunspots and sketches of the Hα filaments were marked on a 200 mm diameter sunchart. The coordinates of the different portions of the filament were measured from the sunchart and replotted on a linear graph to avoid the error in measurement due to foreshort-

334
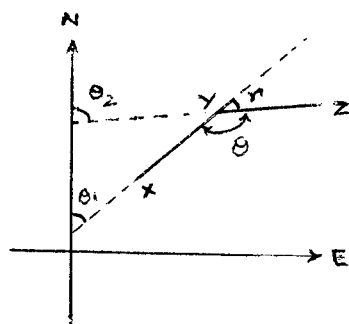
Figure 1.   Technique used to measure the shear angle in Hα filaments.

ening. To detect changes in the filament orientation with time, the angle made
by the filament or its each portion of the filament with the rotation axis of the
sun was measured from the linear graph from the north towards the east. The
total uncertainty in the measurement of angles due to pole marking, alignment
of different images and sketching of filament is ±2° near the centre of the image
and ±4° near the limb.

Consider a non-linear filament XYZ (Figure 1). The filament can be rep-
resented by two straight lines XY and YZ. Θ_1 and Θ_2 are the angles made
by these two portions with the rotation axis of the solar image, respectively.
The angle between these two portions of filaments, Θ, is given by the relation
$\Theta = \Theta_1 - \Theta_2 + 180°$. The shear angle $\gamma = 180° - \Theta$, is defined as the amount by
which the filament differs from a straight line. In the following we discuss the
development of each filament in detail.

3.   Eruptive Prominence of February 3, 1950

The prominence, mean location at 24°SW, before it erupted at the west limb
on February 3, was first visible as a filament on December 27, 1949. During
its second transit on January 25, a kink at location 'A' (Figure 2) developed
in the filament. The shear angle gradually increased until January 31 and then
rapidly on February 1 and 2. Another kink developed at point 'B' on January
28 (Figure 2) and the shear angle at this point also increased. At the time of
the first observation at 02:29:17 UT on February 3, this prominence was already
in the eruptive phase and lasted for more than six hours. The eruptive phase
ended with a part of the material falling back at a distant location in the vicinity
of sunspot group at 10°N.

4.   Disappearing Filament of February 1, 1950

This quiescent filament survived less than one solar rotation. The filament
located near the center of the solar disc at 10°N and 1°W disappeared between
08:36 UT on January 31 and 02:37 UT on February 1, 1950. It was first observed
on January 25, 1950, as a prominence having a height of 55 arcsec at a mean
position of 10°NE. The filament appeared sheared and broken at point 'C' on
January 28 (Figure 3). The shear angle remained 48°±6° with minor fluctuations
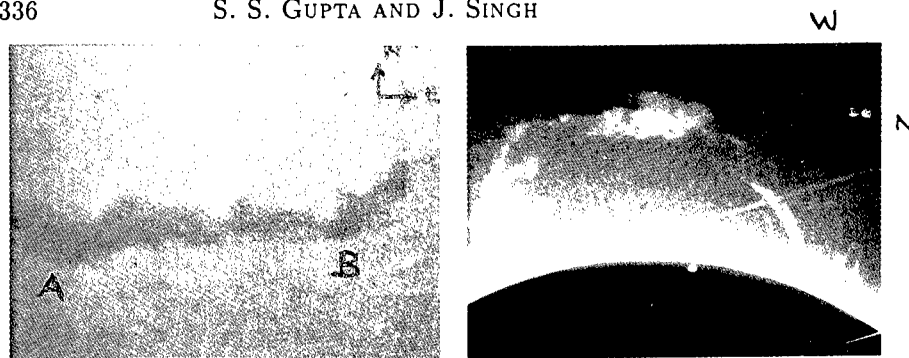
Figure 2.   Left, Hα filament on January 30, 1950 at 02:23:46 UT and, right, eruptive phase on the limb on February 3, 1950 at 04:16:00 UT.

until 02:56 UT on January 31. The gap between these two portions of the filament increased to about 5° on January 31. At 08:36 UT the shear angle became very large, 81°, and the filament very faint before disappearing.
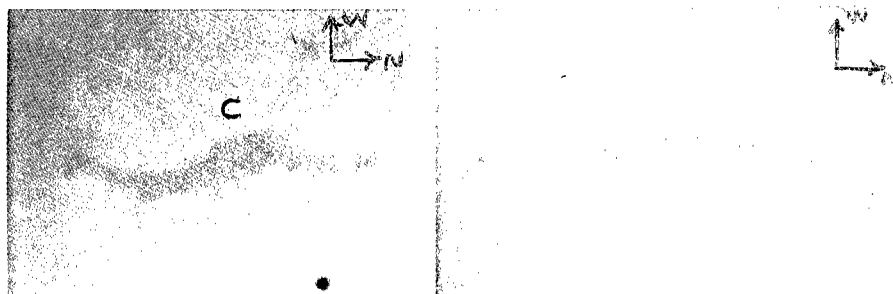
Figure 3.   Left, Hα filament on January 29, 1950 at 02:19:08 UT and, right, on January 31, 1950 at 02:56:08 UT.

5.   Disappearing Filament of April 15, 1950

This quiescent filament lived more than 5 solar rotations. An inverted U-shaped Hα filament located at 23° − 43°N, 06° − 43°E on April 14 at 02:45 UT disappeared before 02:36 UT on April 15, 1950. The filament was first seen as a prominence at 30°NE, on December 15, 1949. A small kink developed at point 'D' on January 16. The shear angle at this kink remained the same until February 19, 1950 with small variations of the order of ±7°. Correspondingly, it showed a small increase in height on the west and east limbs. A small portion on the west side of this filament disappeared on January 21. The kink at point 'D' developed from March 14 to 18, 1950 (Figure 4) and the shear angle during this period of 5 days was 42° ± 2°. Correspondingly, the prominence showed increase in height at the limbs.

In its fifth transit, the filament seen near the east limb on April 12 was highly sheared with a gap of about 5°. The filament took the shape of an inverted 'U' with the gap increasing to 12° on April 13, 17° on April 14, (Figure 4) and the
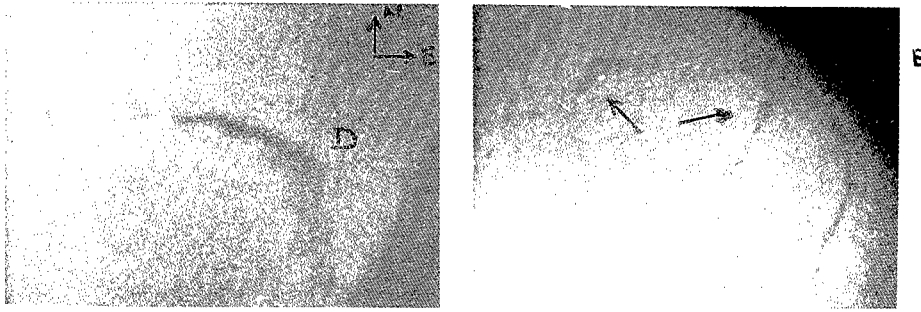
Figure 4.   Left, Hα filament on March 12, 1950 at 08:13:36 UT and, right, on April 14, 1950 at 02:40:10 UT.

shear angle became 74° and 103°, respectively. Between the afternoon of April 14 and morning of April 15 both portions of this filament disappeared.

6.   Discussion

In all the three cases, the shear angles became very large one or two days before the disappearance of the filament. A change in the orientation of the filament or development of a kink causing shear in the filament can be due to the rise of the middle part of the filament above the solar surface. The possibility of this part of the filament rising above the solar surface, due to heating or other instability, and appearing as an inverted U-shaped structure due to projection and line of sight effects seems to be real. Thus, it appears that the measured shear in the filament is due to rise of the part of the filament above the solar surface and the ends of the filament anchored in the chromosphere.

We have seen that the Hα filament split into two portions 2–3 days prior to its disappearance and the gap between the two parts increased with time. Also, both portions of the filament disappeared at the same time and the middle part of the filament rose into the corona far above the solar surface before its disappearance. Rust (1984) and Tang (1986) reported that a filament disappearance may be caused by heating or by dynamic processes. Considering these facts, one may assume that the top of the filament gets heated and thus is not seen in Hα pictures. Simultaneous observations with good photometric accuracy in different temperature-sensitive lines will yield clues to understanding the circumstances leading to the eruption of quiescent prominences and filament disappearances.

References

Rust, D.M. 1984, Solar Phys., 93, 75
Tang, F. 1986, Solar Phys., 105, 2
Vrsnak, B. 1990a, Solar Phys., 127, 129
Vrsnak, B. 1990b, Solar Phys., 129, 295

Eruption of a Twisted Filament and Associated Phenomena

Wahab Uddin and V. K. Verma

Uttar Pradesh State Observatory, NainiTal-263129, India

Abstract. In this paper we present CCD observations between February 14–20, 1994 and analysis of the giant twisted filament evolved in the active region NOAA 7671. The dynamic eruption of the filament was accompanied by a major flare (3B/M4), CME, long duration type II, IV radio bursts, great microwave bursts, a long duration soft X-ray burst, SIDs, strong geomagnetic storms and a very energetic proton flare. We analysed and estimated the twist, length, volume, mass and energy associated with filament system between February 14 and 20, 1994. The present study shows that the magnetic energy required for the solar flare came from the filament system associated with the solar flare and associated phenomena.

1. Introduction

The study of filament/prominence evolution and its subsequent eruption has great significance in the field of solar activity for understanding the process of magnetic energy storage and its later release. The morphology of the filament reflects the complexity of the magnetic field and the energy storage site in the active region. When an active region is born, there might be transient process of energy libration associated with the emergence of magnetic flux. After the initial relaxation is over, the flare productive active region continue to grow and develop a highly distorted or sheared magnetic field cofiguration. This energy buildup phase can be regarded as a slow evolution of magnetic equilibria. The capacity of energy storage depends on the stability of the magnetic field, i.e., the magnetic field must be stable for smaller perturbations so that a large amount of energy can be stored. This phase is followed by an explosive liberation of the stored magnetic energy when the magnetic field loses equilibrium. In this phase the phenomenon of sudden filament disappearance is a familiar one to observe in Hα. The disappearance of Hα dark filaments occurring over magnetic inversion lines is often associated with X-ray brightenings and sometimes with coronal mass ejections (CMEs). The disappearance may be caused by heating or by the dynamical processes similar in many respects to flares. The disparition brusque (DB) of an active filament often precedes the likely occurence of flares. It is widely assumed that flares draw their energy from the free energy of the magnetic field in the volume of the flare, the free energy being stored. For the occurrence of the large flares about 10^{32} ergs of energy is required. Such a large amount of energy is stored in an active region in which active region filaments play an important role in the occurence of violent flares. Keeping in mind these facts, the study of the morphological evolution of active region filaments is very

useful for understanding the energy storage process and its release during flares.

The present paper deals with observations of the evolution of a giant circular and twisted filament and its subsequent eruption on February 20, 1994 leading to a large solar flare and transient phenomena.

2. Observations, Analysis and Conclusions

The observations of the filament evolution in Hα emission between February 14 and 20, 1994 have been recorded with a 15 cm f/15 Coude' refractor and Peltier-cooled (-25°C) CCD camera system. The CCD camera system used for the observations has a chip size of 385 × 578 pixels, with a pixel size 22 × 22 microns and a 16 bit A–D system.

The shape of the filament kept on changing from February 14–19, 1994 and, ultimately, the filament's twisting, shearing and energy buildup reached a critical stage which led to eruption of the filament system on February 20, 1994. The eruption of the filament was not recorded at UPSO because it took place before sunrise at NainiTal, India. The filament eruption and flare were recorded at Hida Observatory, Japan (Kurakawa and Shinkawa 1995). We recorded the decay phase of the filament/flare eruption.

In Figure 1 we show a composite figure of the filament evolution with the spot group from February 14–20, 1994. As is clear from Figure 1, the twisting and shearing of the filament continuously increased from February 14–20. The twisting of the filament started on February 14 and continued up to February 20 before the filament eruption. The filament erupted out on February 20 and the decay phase of the filament/flare eruption is shown in Figure 1. From the observations of filament evolution from February 14–19, we estimated the twist, length, mass, volume and energy of the filament which are shown in Table 1. The spot group associated with the filament under study between February 14–20 was found to be rotating, which enhanced the twist in the filament. The emerging flux regions also increased the complexity of the magnetic field. The rotation of the sunspot group measured by us is shown in Table 1.

Table 1.   Estimated parameters of the filament

Date Feb. 1994	Twist of Filament (in π)	Rotation of Sunspots in degree	Length of Filament x10^5 km	Radius of Filament x10^3 km	Energy of Filament x10^{32} ergs	Volume of Filament x10^{28}cm^3	Mass of Filament x10^{16} gm
14	—	0	1.677	4.246	0.945	0.95	1.63
15	2	5	2.924	5.366	2.636	2.65	2.52
16	2.5	15	3.268	6.449	4.247	4.27	3.46
17	3.0	22	3.354	6.990	5.120	5.15	4.43
18	3.5	32	3.440	7.512	6.070	6.10	5.14
19	4.0	65	3.569	7.519	6.309	6.34	7.15
20	-	-	3.660	7.524	6.48	6.51	8.57

In the table the values of various parameters on February 20, 1994 are extrapolated values. The magnetic energy storage took place due to enhancement of twisting and shearing in the filament (Moore 1988 and Hagyard et al. 1990). This is a very dynamic, long duration event which occurred as the result of a

twisted giant filament erupting. This was the one of the most energetic events in the decay phase of solar cycle 22, because the event was associated with a major flare, 3B/M4, the third largest proton flare (10,000 pfu) of solar cycle 21 and 22, great wicrowave bursts, long duration type II (1400 km/s) and IV radio bursts, SIDs, strong geomagnetic storms, a CME and other related phenomena (SGD 1994 and 1996). This is a good example of a dynamic disparition brusque. It is also the observational manifestation of the flare models proposed by Carmichel (1964), Sturrock (1968), Hirayama (1974) and Kopp and Pneuman (1976) (CSHKP model).

Kurokawa and Shinkawa (1995) reported that the mass ejected after the filament eruption had a velocity >500 km/sec. We estimated the magnetic energy associated with filament system and the kinetic energy released after filament eruption using the following formulae:

$$\frac{B^2}{8\pi}V = 6.5 \times 10^{32} erg$$

$$\frac{1}{2}Mv^2 = 1.1 \times 10^{32} erg$$

assuming B= 500 Gauss, V= estimated volume of the filament, M= mass of the filament and v= 500 km/sec.

From the above it is clear that the magnetic energy associated with the filament system was greater than the kinetic energy released during the filament eruption. Therefore, we are of the view that the source of energy required for the flare was stored in the filament system associated with the flare.

References

Carmichael, H. 1964 in AAS-NASA Symposium on the Physics of Solar Flares, W. N. Hess (ed.), NASA SP-50, p. 451

Hagyard, M.J., Venkatakrishnan, P., and Smith, J.B. Jr. 1990, ApJS, 73, 159

Hirayama, T. 1974, Solar Phys., 34, 324

Kopp, R.A. and Pneuman, G.W. 1976, Solar Phys., 50, 85

Kurokawa, H. and Shinkawa, M. 1995, STEP GBRSC NEWS, 5/1, p. 3

Moore, R.L. 1988, ApJ, 324, 1132

Solar Geophysical Data 1994/1996, WDC-A, Boulder

Sturrock P.A. 1968, in Structure and Development of Solar Active Regions, K.O. Kiepenheuer (ed.), D. Reidel, Dordrecht, Holland, p. 471
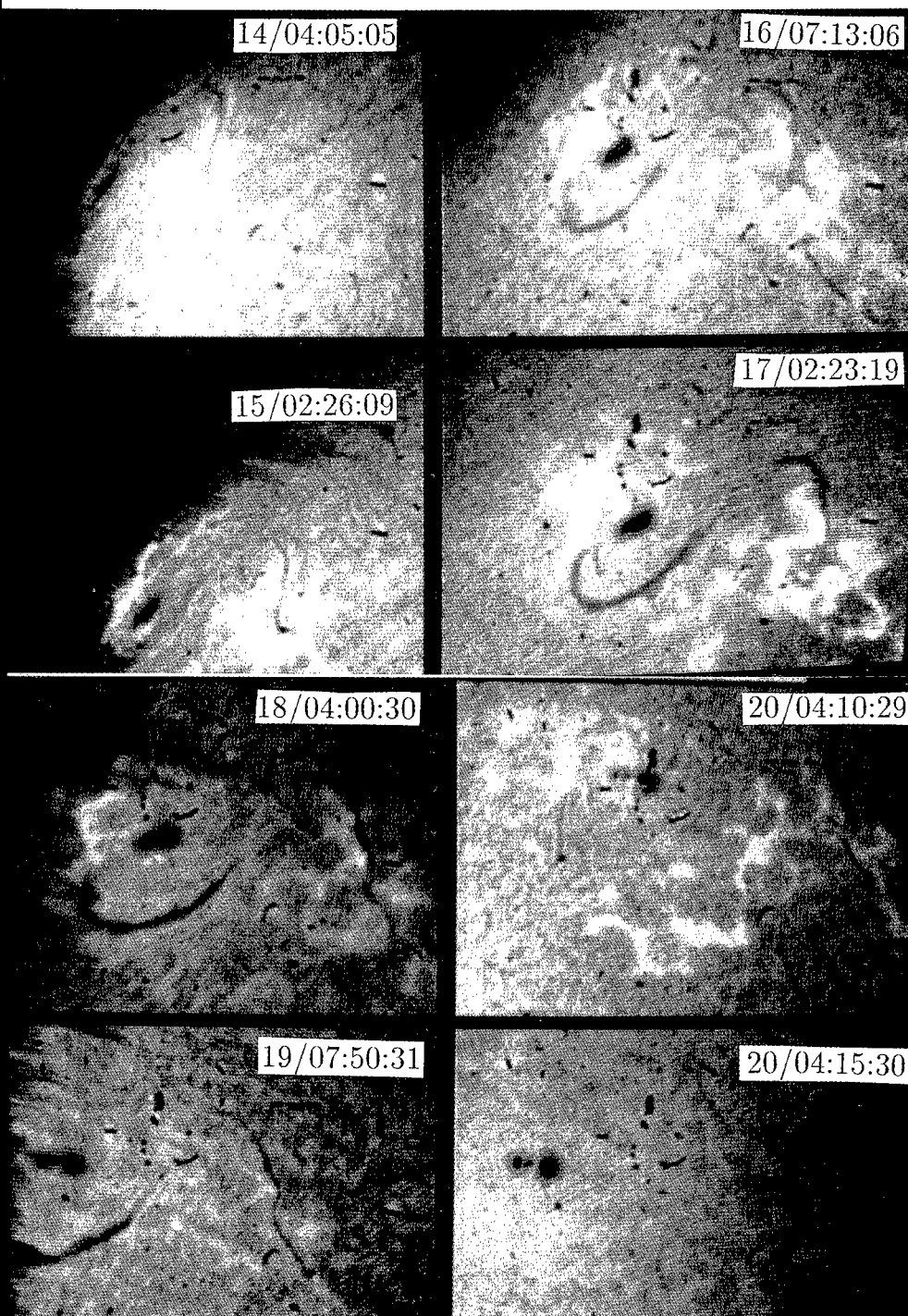
Figure 1.   Filament evolution from February 14–20, 1994.

Causes and Effects of Filament Eruptions

Boris P. Filippov

Institute of Terrestrial Magnetism, Ionosphere and Radio Wave Propagation, Russian Academy of Sciences, 142092, Troitsk Moscow Region, Russia

Abstract. Observational and theoretical aspects of filament destabilization are reviewed in light of the concept of filament eruption as catastrophic loss of equilibrium in a magnetic configuration of inverse polarity. Interrelations between eruptive prominences and other phenomena of solar activity such as flares, CMEs, and loop arcade are considered.

1. Energetics of Filament Equilibrium

In spite of the fact that filaments are perhaps the most long-lived and stable features in the solar atmosphere, at times they either demonstrate fast changes and motions, or disappear completely from view. Sometimes the activation of a filament is initiated by appreciable external events, for example by a remote flare or fast emergence of new magnetic flux nearby, but more often motion of a filament begins before other manifestations of energetic non-stationary processes in the atmosphere of the Sun. In the majority of cases, there is no reliable evidence in favor of an external source of filament destabilization.

The cause of eruption is more likely not in a strong external action but in properties of filament equilibrium itself, possibly in the rapid growth of instability. Since there appears to be little doubt that the prominence material is kept from falling by the magnetic field, the causes of eruption should be searched for in peculiarities of the magnetic configuration around the filament. In this connection it should be remembered that there are two possible directions of a filament current relative to the direction of the field of subphotospheric sources. The external field can support a current if the force is directed upwards, or press a current to the photosphere. In the latter case, the current in a filament should be so great that the currents induced by them on the surface of the photosphere and equivalent to a mirror current are able to generate a magnetic field stronger than the field of subphotospheric sources. This is the configuration of models of inverse polarity, while the former configuration corresponds to models of normal polarity (Priest 1990). The current magnitude is connected to the amount of magnetic energy stored in the corona which can be released and become apparent during the eruption. From the point of view of fast eruptions, the inverse and normal configurations are not equivalent. Simple force balance shows that for a filament of normal polarity the Lorenz force is equal to the weight of the filament

$$\frac{IB}{c} = mg, \tag{1}$$

and, in the case of the disturbance of equilibrium assuming reasonable conditions, $\Delta B \ll B, \Delta I \ll I$, the acceleration of the filament can reach only a small fraction of the free-fall acceleration, g. In inverse polarity models, an equilibrium is possible in which the weight of a filament is of minor importance

$$\frac{I^2}{hc^2} = \frac{IB}{c} \gg mg, \tag{2}$$

where h is the height of the filament above the photosphere. A small violation of equilibrium is able to create an acceleration large compared with g.

2. Changing of External Conditions Before and During an Eruption

The question arises what changes of magnetic field and photospheric displacements lead to current growth, twist increase, loss of stability and equilibrium of a filament, that is, to eruption. It is obvious that non-uniform vortical motions produce a growing current flow (Brandt et al. 1988, Browning 1991). Simon et al. (1986) provided evidence that the evolution of the small scale photospheric magnetic field near a filament, namely pore movement or a new pore birth, is at the origin of the destabilization of the filament. Feynman and Martin (1995) found from study of 53 filaments observed from September 1991 to February 1992 that there is a high probability that a filament will erupt when major new flux emerges within or adjacent to the unipolar magnetic fields astride a filament in an orientation favorable for reconnection. Flux concellation in the vicinity of a neutral line is assumed by Martin (1986) as a necessary condition for filament formation and eventually for its eruption. Expectations following from theoretical notions may at times make a pattern of observed motions seem more ordered than it actually is. One type of field deformation leading to instability most favorite by theorists is shear motion, or moving of the footpoints of arches parallel to a neutral line in opposite direction on both sides. Another type of motion is a converging motion which transports new magnetic flux tubes towards the neutral line to support the conditions for reconnection. Observations confirm, indeed, the presence of such motions near the neutral line (Martin 1986, Athay et al. 1986, Athay 1990), but it is unlikely that one can say with certainty that just these motions are responsible for the growth of the current and loss of filament equilibrium. It is a very telltale fact that the fine structure of filaments contradicts a pattern which would be expected from simple action of differential rotation on a coronal arcade. Although Priest (1996) and Kuperus (1996) proposed some new models of filament magnetic field generation due to differential rotation and flux concellation, these ideas hardly solve the problem completely.

Observational data on movements and magnetic field changes at the photospheric level and eruptive filament motions suggest that the discrepancy of the characteristic times of these processes is as much as two orders of magnitude. It is obvious that a simple linear relationship cannot exist between processes in these two layers. The mechanism which maintains the prominence equilibrium should offer sufficient nonlinearity for catastrophic process to be in progress under small and slow changes of the external conditions. Models of inverse polarity again meet this requirement to a greater extent. In the simplest two-dimensional model with a line current, as was noted by Van Tend and Kuperus

(1978), if the photospheric background field falls off with height faster than $1/h$, a critical value for a filament current exists. If the current is less than the critical value, a filament is in stable equilibrium. The equilibrium height increases with the growth of a current. When a current exceeds a critical value the equilibrium will be lost. Therefore, smooth evolution of a filament terminates and eruption follows. The characteristics of filament motion will no longer be determined by changes of the photospheric field and will depend only on the spatial distribution of magnetic field in the corona, the filament weight and properties of a circuit. In terms of potential energy, the process looks like gradual reduction of the depth of a potential well with the growth of a current, and its complete flattening when the current achieves the critical value.

A consideration of the third dimension adds helical and kink instabilities inherent in a straight current (Sakurai 1976). Measurements of magnetic fields in prominences (Rust 1967, Leroy et al. 1984) testify that the field vector makes a small angle with the axis of a filament. Therefore, a filament can be represented by a twisted flux tube extended along a neutral line. These flux rope or flux tube models correlate well with the observed internal fine structure of filaments. The helical structure of filaments most clearly manifests itself during eruptions. There are a lot of studies which have investigated the stability of cylindrical helical structures in various environments and at various deformations (Raadu 1972, Hood and Priest 1979, Kuperus and Van Tend 1981, Vrsnak 1990). The theory imposes limits on the maximum value of twist for a filament to be stable. These threshholds are confirmed roughly by the observed twists in quiescent and eruptive filaments (Vrsnak et al. 1991).

3.   Eruptions and Hα Flares

As a system in equilibrium, a filament should be sensitive to any changes of magnetic field. A filament can be activated by a flare at some distance away from it. The activation can be limited to several oscillations of a filament near the equilibrium position, if it is stable enough (that is its potential well is deep), or it can result in eruption of the filament. More intimate connections occur between eruptions and bright strands arising on both sides of the ascending filament. The connection is so close that both phenomena are, probably, different manifestations of a single process of the reconstruction of the magnetic configuration. Filament eruption begins before the appearance of bright ribbons so, in some sense, it can be considered as "primary".

Many people have outlined a scenario of the process using two-dimensional models of inverse polarity (Kaastra 1985, Martens and Kuin 1989, Priest and Forbes 1990, Forbes and Isenberg 1991, Forbes 1991). Sturrock (1989) has tried to conceive of a three-dimensional geometry of such a process. And his scheme finds some support in numerical calculations of the evolution of a stretchable current contour in external magnetic field (Filippov 1996a). It is possible that ascending filament current creates two factors which provide favorable conditions for energy release in the corona. First, an additional source of magnetic field, represented by filament current located high in the corona, creates readily a saddle structure which is the basic prerequisite for reconnection or builds up a helmet configuration with a current sheet when moving through the corona
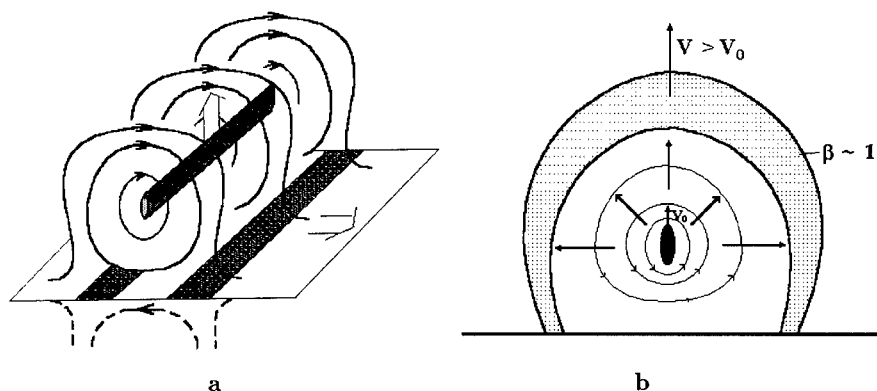
Figure 1.   Schematic representations of the magnetic configuration with flare ribbons therein (a) and of CME formation (b).

(Kopp and Pneuman 1976, Pneuman 1982). Second, fast movement of such a source produces fast changes in the surrounding magnetic field, which cannot be expected as a result of the relatively slow emergence of new magnetic flux in the photosphere.

In general, a broad spectrum of different effects would be expected during the fast changes of magnetic field with complex topology ranging from acceleration of particles to plasma heating. For example, emission in the ribbons (particularly outside of active regions) can arise as a result of heating of the chromospheric gas compressed by changing magnetic field in the regions where field lines diverge drastically (Filippov 1997). Such regions exist in inverse polarity models on both sides of the filament (Figure 1a).

4.   Eruptive Filaments as a Part of Coronal Mass Ejections

There is no doubt that an ascending filament current as a source of magnetic field should make an appreciable rearrangement of coronal density in large volume surrounding an eruptive filament. Investigations of coronal mass ejections (CMEs) have revealed eruptive prominences to be the best-correlated phenomena among the other manifestations of activity in low layers of the solar atmosphere (Munro et al. 1979, Webb and Hundhausen 1987, St. Cyr and Webb 1991). In many images obtained by orbital coronagraphs, an eruptive prominence is clearly visible as a bright core of a CME surrounded by a dark cavity of depleted material. The cavity is bordered by a bright loop of enhanced density (Sime et al. 1984, Hundhausen 1998). In these events, it is impossible to deny an interrelation between CMEs and eruptive prominences, but several empirical arguments have been used against the concept that the prominence eruption drives the CME (Hundhausen 1998): (i) There are CMEs which have no bright cores and there are no data on simultaneous filament eruptions or the disappearance of a dark filament from the visible solar disk. (ii) The average angular width of CMEs is about 50°. This scale size is larger than that of erup-

tive prominences $\sim 20°$. (iii) The top of the prominence observed in either Hα emission or scattered white light almost always moves outward more slowly than the top of the dark cavity or bright frontal loop.

The large scale of the phenomenon and the effects of projection favor, probably, a wide variety of observable forms of CMEs. But even if no CMEs are caused by eruptions of filaments, there can be little doubt that each eruption causes a CME if for no other reason than prominence material moving through the corona may be considered a CME.

In some models, there are no distinctions between a filament eruption and a CME (Mouschovias and Poland 1978, Anzer 1978, Van Tend 1979, Yeh and Dryer 1981, Sakai 1982, Browning and Priest 1984, Chen 1989). It may be justified if the internal structure of a CME is not accounted for. In other models (Pneuman 1980, Anzer and Pneuman 1982, Steele and Priest 1989) the motion of the outside part of a CME is considered separately and the driving force is the magnetic pressure created by the eruptive prominence. Three main parts of the internal CME structure are assumed to exist prior to the beginning of an eruption and, after loss of equilibrium, all parts interact with each other. After a rather short stage of acceleration, both the prominence and the loop move with a constant speed, with the speed of the loop being higher than the speed of prominence in accordance with observations.

Smith et al. (1992) investigated density variations of the coronal plasma when a filament is rising. They used vacuum field calculations based on the low value of β in the coronal plasma. They came to the conclusion that the magnetic configuration of a model of inverse polarity is not able to cause the observed plasma distribution in the CME. The problem is that the distance between neighboring field lines above the filament at the location of the CME loop is increasing as the current is rising. Hence, rarefaction of coronal matter should occur there instead of compression. Our approach (Filippov and Shilova 1995, Filippov 1996b) differs by taking into account the limited size of the low β region. Then, in the region where magnetic pressure is greater than gas pressure, plasma motion can be assumed as a drift motion. Its characteristic is such that the further one gets from the filament, the larger is the drift velocity of the plasma. This type of motion leads to a rarefaction of plasma and formation of a cavity around the filament in accordance with the results of Smith et al. (1992). Near the boundary $\beta = 1$, gas pressure begins to decelerate the plasma motion and, as a result, the coronal density increases. Plasma compression near the surface $\beta = 1$ leads to formation of a dense envelope which can be identified with the outer loop of a CME (Figure 1b).

Coming back to the objections of Hundhausen (1998), it seems that they can be rejected within the framework of an understanding of eruption as the loss of equilibrium of the magnetic configuration with coronal current flowing along a neutral line. The cold substance of a prominence only outlines this configuration, but it is not of crucial importance in the equilibrium conditions. Therefore, it is possible to imagine the eruption of an almost "empty" flux tube.

5. Post-Flare Loop Systems

In the wake of an eruption and a flare, systems of expanding loops arise which are visible both in Hα and soft X-rays. A few minutes after the initiation of a large flare, dense plasma loops appear in the corona above the neutral line which can be visible in emission or absorption for hours (Bruzek 1964, Rompolt 1993, Schmieder et al. 1994). The loops connect flare ribbons aligned with the neutral line along both sides of it. The system expands initially with a speed up to 50 km/sec which is gradually reduced to 1–2 km/sec. Observations in coronal lines (McCabe, 1973), in UV (Hiei and Widing 1979), in soft X-rays (Švestka 1987) and in radio wavelengths (Velusamy and Kundu 1981) have revealed the existence of hot coronal arcades over the Hα loops.

The relationship between the arcades and eruptive prominences was not originally noted, possibly because many sets of observations did not cover the initial phase of the phenomenon. Later, observational evidence showed that the system was growing in the space previously occupied by disappeared or erupted filament (Martin 1979). They are referred to as 'post-flare loop systems', though sometimes they are observed in the absence of flares and most of them are associated with sudden filament disappearances or eruptions (Rust and Webb 1977). An illustrative example is of a sequence of events on July 30–31, 1992 in simultaneous observations in radio (17 GHz), soft X-rays and Hα (Hanaoka et al. 1994).

Theoretical models of the phenomenon are based on the idea of continuous reconnection of open or greatly elongated field lines at the magnetic X-line which moves upward (Carmichael 1964, Sturrock 1966, Hirayama 1974, Kopp and Pneuman 1976, Forbes et al. 1989). The elongation and opening of field lines is due to the filament eruption. The released energy heats up coronal plasma and loops with temperatures approaching $3 \cdot 10^7$K. Heat conducted along field lines mapping from the reconnection region to the chromosphere ablates chromospheric plasma and creates associated flare ribbons. In loops leaving a zone of reconnection, plasma cools down to chromospheric temperatures and becomes visible in Hα. The plasma in the cool flare loops flows down the legs of the loops. As field lines are reconnected, the loops grow in size, and ribbons move away from one another.

6. Conclusions

Electric current above the polarity inversion line in the corona, visualized by filament matter, is a very energetic and mobile feature in the solar atmosphere. Filament equilibrium is realized in a nonlinear manner. So, a catastrophic process is possible under slow and smooth changes of external conditions. Filament eruption implies more or less large scale reconstruction of the magnetic configuration in the corona. It can create the field topology necessary for the action of energy release mechanisms and development of such phenomena as flare ribbons and post-flare loop systems. Rapid motion of filament current in the corona produces fast changes in the surrounding magnetic field. These changes are able to cause compression or rarefaction of plasma resulting in brightenings or CME formation.

References

Anzer, U. 1978, Solar Phys., 57, 111

Anzer, U., Pneuman, G.W., 1982, Solar Phys., 79, 129

Athay, R.G. 1990, Solar Phys., 126, 135

Athay, R.G., Jones, H.P., and Zirin, H. 1986, ApJ, 303, 877

Brandt, P.N., Scharmer, G.B., Ferguson, S., Shine, R.A., Tarbell, T.D., and Title, A.M. 1988, Nature, 335, 238

Browning, P.K. 1991, Plasma Phys. and Contr. Fusion 33, 571

Browning, P.K. and Priest, E.R. 1984, Solar Phys., 92, 173

Bruzek, A. 1964, ApJ, 140, 746

Carmichael, H. 1964, in AAS-NASA Symposium on Physics of Solar Flares, (ed.) W.N. Hess, NASA SP-50, p. 451

Chen, J. 1989, ApJ, 338, 453

Feynman, J. and Martin, S.F. 1995, J. Geophys. Res., 100, 3355

Filippov, B.P. 1996a, Astron. Reports, 40, 754

Filippov, B.P. 1996b, A&A, 313, 277

Filippov, B.P. 1997, A&A, 324, 324

Filippov, B.P. and Shilova, N.S. 1995, AZh, 72, 222

Forbes, T.G. 1991, Geophys. Astrophys. Fluid Dynamics, 62, 15

Forbes, T.G., Malherbe, J.M., and Priest, E.R. 1989, Solar Phys., 120, 285

Forbes, T.G. and Isenberg, P.A. 1991, ApJ, 373, 294

Hanaoka, Y. et al. 1994, Publ. Astron. Soc. Japan, 46, 205

Hiei, E. and Widing, K.G. 1979, Solar Phys., 61, 407

Hirayama, T. 1974, Solar Phys., 34, 323

Hood, A.W. and Priest, E.R. 1979, Solar Phys., 64, 303

Hundhausen, A.J. 1998, in The Many Faces of the Sun; Scientific Highlights of the Solar Maximum Mission, (eds.) K.T. Strong, J.L.R. Saba, and B.M. Haisch, Springer-Verlag, New York, in press

Kaastra, J. 1985, Solar Flares: an Electrodynamical Model, Thesis, University of Utrecht

Kopp, R.A. and Pneuman, G.W. 1976, Solar Phys., 50, 85

Kuperus, M. and Van Tend, W. 1981, Solar Phys., 71, 125

Kuperus, M. 1996, Solar Phys., 169, 349

Leroy, J.L., Bommer, V., and Sahal-Brechot, S. 1984, A&A, 131, 33

Martens, P.C.H. and Kuin, N.P.H., 1989, Solar Phys., 122, 263

Martin, S.F. 1979, Solar Phys., 64, 165

Martin, S.F. 1986, in Coronal and Prominence Plasmas, (ed.) A.I. Poland,

NASA CP-2442, p. 73

McCabe, M.K. 1973, Solar Phys., 30, 439

Mouschovias, T.Ch. and Poland, A.I. 1978, ApJ, 220, 675

Munro, R.H., Gosling, J.T., Hildner, E., Mc Queen, R.M., Poland, A.E., and
      Ross, C.L. 1979, Solar Phys., 61, 201

Pneuman, G.W. 1980, Solar Phys., 65, 369

Pneuman, G.W. 1982, Solar Phys., 78, 299

Priest, E.R. 1990, in Dynamics of Quiescent Prominences, (eds.) V. Ruzdjak
      and E. Tandberg-Hanssen, Springer-Verlag, New York, p. 150

Priest, E.R. 1996, in Solar Drivers of Interplanetary and Terrestrial Distur-
      bances, (eds.) K.S. Balasubramaniam, S.L. Keil, and N. Smartt, ASP
      Conf. Ser., Vol. 95, p. 229

Priest, E.R. and Forbes, T.G. 1990, Solar Phys., 126, 319

Raadu, M.A. 1972, Solar Phys., 22, 425

Rompolt, B. 1993, Solar Phys., 141, 1

Rust, D.M. 1967, ApJ, 150, 313

Rust, D.M. and Webb, D.F. 1977, Solar Phys., 54, 403

Sakai, J. 1982, ApJ, 263, 970

Sakurai, T. 1976, Publ. Astron. Soc. Japan, 28, 177

Sime, D.G., MacQueen, R.M., and Hundhausen, A.J. 1984, J. Geophys. Res.,
      89, 2113

Simon, G., Gesztelyi, L., Schmieder, B., and Main, N. 1986, in Coronal and
      Prominence Plasmas, (ed.) A.I. Poland, NASA CP-2442, p. 229

Schmieder, B. et al. 1994, Solar Phys., 150, 199

Smith, D.F., Hildner, E., and Kuin, N.P.M. 1992, Solar Phys., 137, 317

Sturrock, P.A. 1966, Nature, 211, 695

St. Cyr, O.C. and Webb, D.F. 1991, Solar Phys., 136, 379

Steele, C.D.C. and Priest, E.R. 1989, Solar Phys., 119, 157

Sturrock, P. 1989, Solar Phys., 121, 387

Švestka, Z. 1987, Solar Phys., 108, 411

Van Tend, M. 1979, Solar Phys., 61, 89

Van Tend, M. and Kuperus, W. 1978, Solar Phys., 59, 115

Velusamy, T. and Kundu, M.R. 1981, ApJ, 240, 1130

Vrsnak, B. 1990, Solar Phys., 129, 295

Vrsnak, B., Ruzdjak, V., and Rompolt, B. 1991, Solar Phys., 136, 151

Webb, D.F. and Hundhausen, A.J. 1987, Solar Phys., 108, 383

Yeh, T. and Dryer, M. 1981, Solar Phys., 71, 141

The Energetics of Flux-Rope Prominence Models in Axially Symmetric Systems

J. Lin
Yunnan Observatory, Kunming, Yunnan 650011, China

T. G. Forbes and P. A. Isenberg
University of New Hampshire, Durham, NH 03824, USA

P. Démoulin
Observatoire de Paris, Meudon, France

Abstract. We analyze a prominence model containing a flux rope which is completely detached from the photosphere. The maximum magnetic energy which can be stored in the configuration does not exceed the open-energy limit proposed by Aly and Sturrock. However, a loss of ideal-MHD equilibrium can occur and create a current sheet which is likely to undergo rapid reconnection.

1. Introduction

According to Aly (1984) and Sturrock (1991), the energy stored in an axially symmetric system cannot exceed the energy of the fully opened magnetic field for any model where all the field lines are simply connected to the surface of the Sun. Mikić and Linker (1994) have confirmed that a simply connected arcade system with axial symmetry evolves towards the open configuration as the footpoints of arcade are sheared. Here we consider a prominence model which has some field lines that are not connected to the solar surface in order to see if it is possible to store energy in excess of the energy of the fully opened field. The model is based on an axially symmetric flux rope and a Sun-centered dipole.

2. Evolution of the Model

The model consists of two-dimensional equilibrium solutions in a spherical system with axial symmetry and with $r = R_0$ being the photospheric boundary. The coronal region $r \geq R_0$ is assumed to be perfectly conducting, and the gas pressure there is assumed to be negligible. The ring-like magnetic flux rope is suspended in the corona by a balance among tension, compression, and curvature forces. Evolution of the system takes place in two stages: The first stage stores energy, while the second releases it. During the storage phase, the evolution is slower than the reconnection, so current sheets cannot form due to dissipation. During the eruptive phase, mechanical equilibrium is lost and the system evolves rapidly over an Alfvén time scale (i.e., ≤ 100 s). The flux rope jumps to

a higher altitude, releasing part of the magnetic energy stored in system, and a large-scale current sheet appears. This transition constitutes a catastrophe according to Thom (1972).
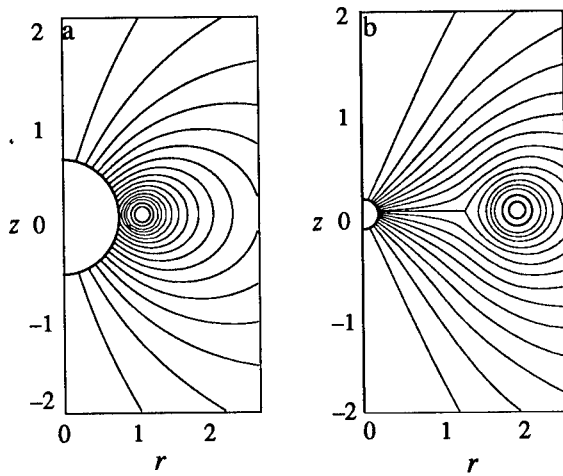
Figure 1.   Magnetic field configuration. (a) prior to eruption, and (b) after eruption.

Initally, the flux rope is the only magnetic field source above the photospheric surface at $r = R_0$. For the model, we use the Lundquist solution to describe the current desity within the flux rope (Lundquist 1950 and Miller and Turner 1981), but outside the flux rope, the field is prescribed by the solution of Poisson's equation with the boundary condition:

$$A_\phi(r = R_0, \ \theta) = \frac{m_0 \sigma(t) \sin \theta}{R_0^2}, \tag{1}$$

on the photospheric surface. Here m_0 is a normalized constant, and $\sigma(t)$ is a function which slowly decreases with time. This boundary condition corresponds to a Sun-centered dipole of strength $m_0 \sigma$ and, as σ decreases, the configuration reaches a point where the system loses equilibrium. The flux rope jumps upwards, and a current sheet attached to the surface forms (Forbes and Isenberg 1991 and Isenberg et al. 1993). Figure 1 shows the configurations before and after the system loses equilibrium, while Figure 2 shows the equilibrium height of the flux rope h as a function of σ for an initial flux rope radius of $r_0^o = 0.01 R_0$.

3.   Asymptotic Behavior and Energetics

After the system develops a current sheet, we cannot determine a general analytic solution due to the additional mathematical complexity which is introduced, but we can investigate the asymptotic behavior of the system when the current sheet becomes very large and the flux rope is far from the Sun. In this limit, both h and q, the height of the flux rope and the length of current sheet,
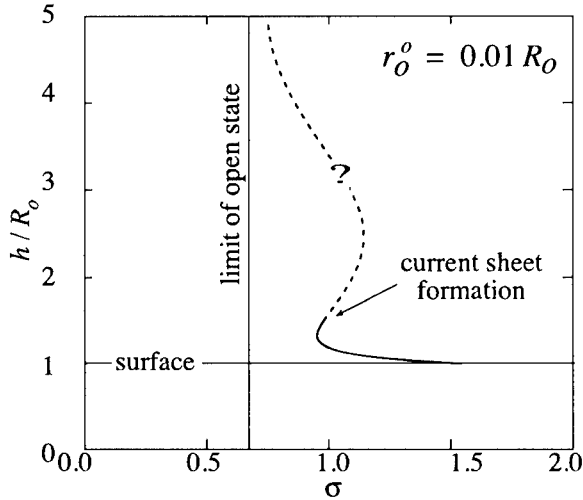
Figure 2.   Equilibrium height h as a function of dipole strength σ.

are much larger than R_0, and the Sun can be regarded as a point. This limit is in fact the open field limit, and it occurs at $\sigma = 0.741$, as shown by the vertical line in Figure 2. Thus, the configuration becomes open if the attractive force supplied by Sun's dipole falls below a certain value. This behavior is similar to that found by Mikić and Linker (1994) for the opening of an arcade when its shear exceeds a particular value. Due to lack of a complete solution for the configuration with a current sheet of arbitrary size, the complete $h - \sigma$ relation remains unknown (dashed portion of the curve in Figure 2).

The magnetic energy stored in the system before losing equilibrium can be obtained in the way described by Isenberg et al. (1993). The result is shown in Figure 3 which plots the ratio W_t/W_p against r_0^o/R_0, where $W_t = W + W_p$, W_t is the total magnetic energy, W is the free magnetic energy, and W_p is the potential energy at the critical point. The ratio decreases as the flux-rope radius, r_0^o, declines, which is the opposite of the behavior of the 2-D models with translational symmetry. The change in behavior is caused by the curvature force (Shafranov 1966) which becomes infinite as r_0 tends to zero unless the current, and hence the energy W, also tend to zero at the same rate. The maximum energy ratio is 1.62, which is just slightly smaller than 1.662 for the fully open field state.

4.   Conclusions

We have analyzed a two-dimensional model for solar eruptions in a spherical system based on an axially symmetric flux rope and a Sun-centered dipole. The results show the system has catastrophic behavior when r_0 is sufficiently large. Catastrophe leads to sudden current sheet formation, but does not lead to a fully open field. The energy which can be stored in the system increases with r_0^o, contrary to what happens in models where the curvature force is absent. The
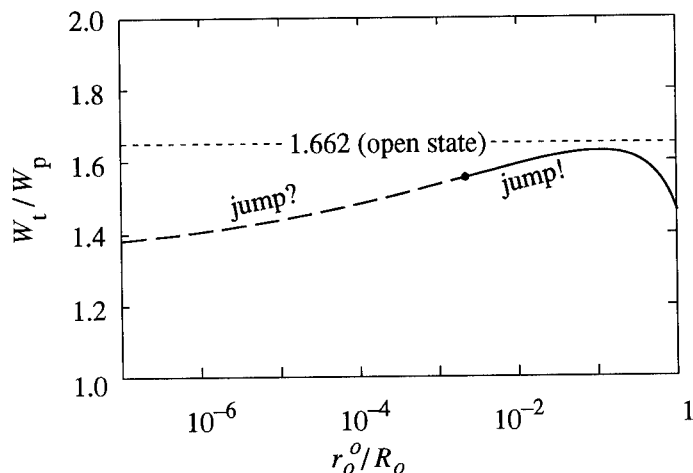
Figure 3. Magnetic energy W of equilibria at the critical points as a function of the flux-rope radius r_0^o. Note that it is not clear if there is any catastrophe when r_0^o is small (dashed curve), but catastrophe does occur for large r_0^o (solid curve), and the energy stored prior to eruption can be very close to that stored in the fully open field.

maximum of W_t/W_p is around 1.62, which is smaller than 1.662, the ratio for a fully open field. This result suggests that even for the models which have field lines that are not all connected to the surface, the theorem of Aly and Sturrock might still apply.

References

Aly, J. J. 1984, ApJ, 283, 349
Forbes, T. G. and Isenberg, P. A. 1991, ApJ, 373, 294 (Paper I)
Isenberg, P. A., Forbes, T. G. and Démoulin, P. 1993, ApJ, 417, 368
Lundquist, S. 1950, Ark. Fys., 2, 361
Mikić, Z. and Linker, J. A. 1994, ApJ, 430, 898
Miller, G. and Turner, L. 1981, Phys. Fluids, 24 (2), 363
Shafranov, V. D. 1966, Revs. of Plasma Phys., 2, 103
Sturrock, P. A. 1991, ApJ, 380, 655
Thom, R. 1972, Stabilité Structurelle et Morphogénése, Benjamin, New York

On a Possible Mechanism of Quiescent Prominence Destabilization

P. Nenovski

Geophysical Institute, Acad. G. Bonchev Str, 1113 Sofia, Bulgaria

V. N. Dermendjiev and M. S. Madjarska

Institute of Astronomy, 72 Trakia Blvd., 1784 Sofia, Bulgaria

J.-C. Vial

I.A.S., Université Paris XI-CNRS, Bâtiment 121, 91405 Orsay, France

Abstract. The possibility of multiple reflections generating standing surface wave modes carrying field-aligned current (FAC) in an arch-like prominence structure is studied. The conditions for enhancement of FAC leading to observable destabilising effects are specified.

1. Introduction

In this work we study the possibility that some surface MHD modes, generated in a simple arch-shaped prominence structure, can enhance the electric current along the magnetic field, named the field-aligned current (FAC). We try to derive a criterion determining the commencement of the prominence instability.

2. MHD Surface Wave Model of FAC Intensification

First attempts to construct a model of FAC carried by MHD surface modes were made by Nenovski and Momchilov (1987). Madjarska et al. (1996) studied a surface wave FAC intensification process relevant to quiescent prominences (QP). It was shown that nonaxial surface waves (SW) propagating obliquely to the ambient magnetic field carry FAC. Such an MHD surface mode "induces" an inertial term in the corresponding equation for the FAC. These FACs are located at the prominence boundaries.

According to Madjarska et al. (1996) the FAC intensification depends on the reflection coefficient, R, for SW modes in the prominence feet and the SW dissipation in the prominence body. The necessary condition for FAC enhancement in a prominence, with arch length L, can be given by the inequality

$$(L(A)/L)ln(1 - R) > 1. \qquad (1)$$

FAC can be intensified when both the reflection coefficient $R < 0$ and the FAC gain exceeds the SW dissipation. We express the SW dissipation by the characteristic damping length $L(A)$.

2.1. Reflection Conditions in the Prominence Feet

We examine a simple model of a prominence foot depending only on the z–coordinate, perpendicular to the solar limb. The calculation grid has a step Δz = 200 km and knots number $N_z = 10$. This corresponds to a 2000 km high prominence foot. The magnetic field is computed using the formula $B = B_0 \exp^{-2\pi z/L}$, where B_0 is a constant. Here we take two types of initial conditions: 1) plasma parameters similar to those of Hvar Reference Atmosphere of QP (Engvold et al. 1990) and 2) plasma parameters corresponding to the VAL network chromosphere model (Vernazza et al. 1981), i.e., supposing a plasma upflow in the prominence feet. The corresponding reflection coefficient R is given by

$$R = \frac{\sum_A - \sum_p}{\sum_A + \sum_p}, \tag{2}$$

where $\sum_p = \int \sigma_\perp dz$ is the height–integrated Pedersen conductivity, and $\sum_A = 1/\mu v_A$ is the Alfven wave conductivity. R is derived under the condition $div \vec{j} = 0$, which means that the FAC will be completely closed by the perpendicular Pedersen and Hall current flowing in the prominence feet at the prominence–chromosphere system. The perpendicular to the magnetic field conductivity $\sigma_\perp = \sigma_{\perp,i} + \sigma_{\perp,e}$ is computed taking into account the ion–neutrals, ν_{in}, and electron–neutrals, ν_{en}, collision frequencies under the assumption for pure Hydrogen plasma.

Setting the first initial condition in the computation procedure, we obtain R positive. However, under the second initial condition we obtain R negative, even $R = -1$. This should lead to FAC intensification at each reflection event.

In the computations of $\sum_p$, at each step we verify the inequality $\nu_{in} > \omega_{ci}$, where ω_{ci} is the cyclotron-ion frequency. The equality $\nu_{in} = \omega_{ci}$ marks the maximum height of the conductivity layers, where the FAC could be closed. In Figure 1 (top) the map represents the dependence of the quantity $(\nu_{in} - \omega_{ci})$ on Hydrogen concentration n_H and magnetic field B. The reflection coefficient R, computed for 5 different values of B is given in Figure 1 (bottom) as a function of the height (z–coordinate). The basic conclusion is that R will be negative (reflection of SW in the prominence feet will occur) when the plasma density increases in the prominence feet, and/or when the axial component of the ambient magnetic field is strongly weakened.

2.2. SW Dissipation in the QP Body

The intensification process of the surface wave FAC depends on the ratio $L(A)/L$. This means that the damping length $L(A)$ has to be large enough than L, so that the SW will be multiply reflected. We suppose that in prominence conditions the viscous losses dominate and we can use for the damping length the formula

$$L(A) = \langle s_z \rangle / Q, \tag{3}$$

where Q is the volumetric heating rate, and $\langle s_z \rangle$ is the time–averaged z–component (along the FAC direction) of the Poynting flux.

When $\omega_{ci} > \nu_{in}$ (this condition is fulfilled in the prominence body)

$$Q = \frac{P}{\nu_{in}} (\nabla . \vec{v})^2 / 3 \tag{4}$$

$$\langle s_z \rangle = \rho_0 [c_0^2 + v_A^2](\nabla . \vec{v})^2 k_\perp / \omega^3, \tag{5}$$

hence

$$L(A) = \rho_0 L^3 \omega_{ci} / (2\pi)^2 t_A \rho_n, \tag{6}$$

where c_0 is the sound velocity, ω is the SW frequency, P is the pressure, $k_\perp$ is the normal component of the wave vector. It is clear that the damping length is sensitive to the SW period, t_A, and the neutral density, ρ_n.

3.   Criteria for Destabilization of a Loop-Shaped QP

Starting from the inequality (1) we can obtain the following criteria for destabilization. When $R = -1$, then $ln(1 - R) = 0.7$ and we obtain

$$(L(A)/L) > 1.4. \tag{7}$$

From the ion collision damping condition $\nu_{in} < \omega_{ci}$ we obtain

$$\frac{n_H}{B} < a_1 \times 10^{23} \text{ (in SI units)}, \tag{8}$$

where a_1 is a constant of order of $0(1)$. Additional restrictions on n_H and magnetic field variation we obtain from the condition of the closure of the FAC

$$n_H \sqrt{n} / B k_\perp < 1.5 \times 10^{32} \text{ (in SI units)}, \tag{9}$$

The derived relationships (6, 7, 8 and 9) give all principal requirements for the intensification of FAC by standing SW and the possible consequent QP destabilization, and allow a direct observational verification even in the case when the magnetic field in the prominence body remains unknown.

4.   Conclusion

The inclusion of surface MHD modes as FAC carriers in a model of QP destabilization seems to have a good perspective. However, some details of the model need additional examination by means of numerical simulations.

References

Engvold, O., Hirayama, T., Leroy, J.-L., Priest, E. R. and Tandberg-Hanssen, E. 1990, in Dynamics of Quiescent Prominences, V. Ruždjak and E. Tandberg-Hanssen (eds.), Springer-Verlag, New York, p. 294

Madjarska, M. S., Dermendjiev, V. N., Mouradian, Z. and Nenovski, P. 1996, Astroph. Lett. and Comm, 34, 113

Nenovski P., Momchilov, G. 1987, Planet. Space Sci., 35, 1561

Vernazza, J., Avrett, E., Loeser, R. 1981, ApJS, 45, 635
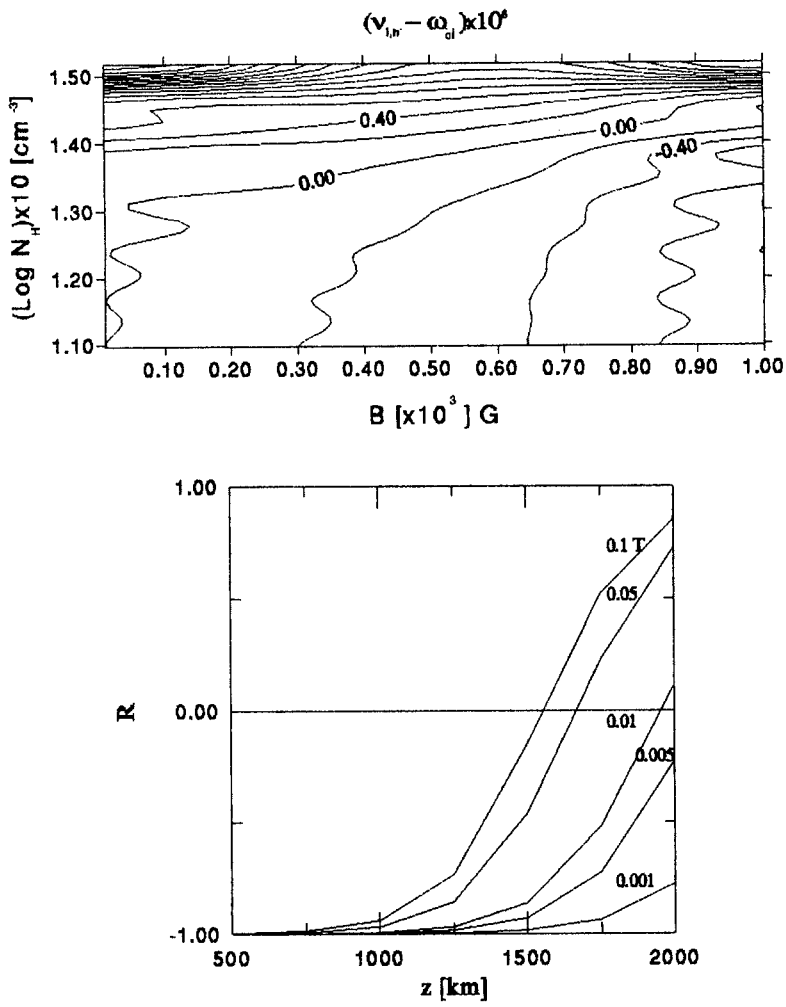
Figure 1.   Top: Isopleth map representing the quantity $(\nu_{in}-\omega_{ci})$ as a function of the H-concentration, N, and the magnetic induction, B. Bottom: The reflection coefficient, R, as a function of the height, z, for given values of the magnetic induction.

Radio and X-ray Investigations of Erupting Prominences

N. Gopalswamy

Physics Department, The Catholic University of America, Washington, DC 20064, USA

Y. Hanaoka

Nobeyama Radio Observatory, Minamisaku, Nagano-321, Japan

J. R. Lemen

Lockheed Martin Advanced Technology Center, Palo Alto, CA 90034, USA

Abstract. Prominence eruption is one of the most important solar phenomenon because of the possibility of using it as proxy of geoeffective solar disturbances. In a series of investigations using Nobeyama radio observations in conjunction with Yohkoh data we have found that there is more to a prominence eruption than the simple picture portrayed by Hα observations. The extent of coronal volume associated with the eruption is much larger than the prominence. We illustrate this with several examples and discuss the implication of the results for understanding the interplanetary manifestation of coronal mass ejections.

1. Introduction

Prominence eruption is the most common signature of coronal mass ejections (CMEs) near the solar surface. X-ray and microwave observations can provide information on eruptions close to the solar surface, which is difficult to obtain from coronagraphic observations. After the advent of the Yohkoh/Soft X-ray Telescope (SXT, Tsuneta et al. 1991) and the Nobeyama radioheliograph (Nakajima et al. 1994), it has become possible to study the near surface manifestations of CMEs in detail. Recent studies have shown that X-ray emission can originate from an arcade formed beneath the erupting filament (Hanaoka et al. 1994), the filament itself (McAllister et al. 1992) and from the CME frontal structure (Gopalswamy et al. 1996, 1997a). What seems to be a simple CME in white light seem to contain complex structures and multithermal plasmas with violent mass motions near the solar surface (Gopalswamy et al. 1997b). In radio, we can observe the cooler, optically thick structures such as prominences (in emission above the limb) and filaments (in absorption on the disk), in addition to the hot flare plasma. Thus, a combination of radio and X-ray observations can prove to be very powerful in studying the origin of CMEs. In this paper, we present a summary of a few such studies that combine radio and X-ray observations.

2. Radio Observations of Filaments and Prominences
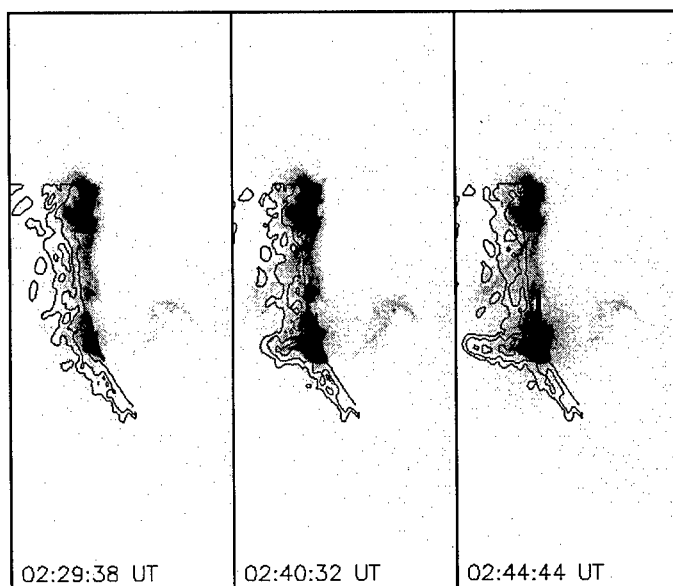
Figure 1.   Overlay of the 17 GHz contours of the November 23, 1992
prominence on Yohkoh/SXT images at three instances.   The X-ray
intensity is inverted so darker regions are brighter.

The prominence is a cool structure suspended in the corona with a typical tem-
perature of 8000 K and an electron density of about 10^{10}–10^{11} cm^{-3}. In order
to see how a prominence is observed in microwaves, let us estimate the free-free
opacity of the prominence material from the formula,

$$\tau_{ff} = 0.2 \int n_e{}^2 dl f^{-2} T^{-1.5}$$

where n_e is the electron density, f is the observing frequency, and T is the
temperature. For $T = 8000$ K, $f = 17$ GHz, and $n_e = 10^{11}$ cm^{-3}, the prominence
is optically thick for $L = 1$ km. Therefore, the observed brightness temperature
at 17 GHz is very close to the temperature of the prominence. Since the corona
contributes very little to the microwave emission, the prominence is observed in
emission above the limb against the cold sky background. The solar disk has a
brightness temperature of about 10,000 K at 17 GHz. Therefore, the prominence
appears dark on the disk as it absorbs the underlying quiet Sun emission similar
to Hα dark filaments. Typically, the filament shows up as a depression in the
range $(2 - 3) \times 10^3$ K below the quiet Sun.

The events presented in this paper were observed by the Nobeyama radio-
heliograph and the Yohkoh/SXT. The Nobeyama radioheliograph obtains the

visibility data of the sun for about 8 hours every day with a time resolution of 100 ms at two frequencies (17 and 34 GHz). Images can be made at any suitable time resolution above 100 ms. The typical spatial resolution of the images is about 10″ at 17 GHz and about 5″ at 34 GHz. The SXT images the Sun with a wide range of combinations of spatial and temporal resolutions. The full disk images used here have a spatial resolution of about 4″.92 and a temporal resolution of about 2 minutes.
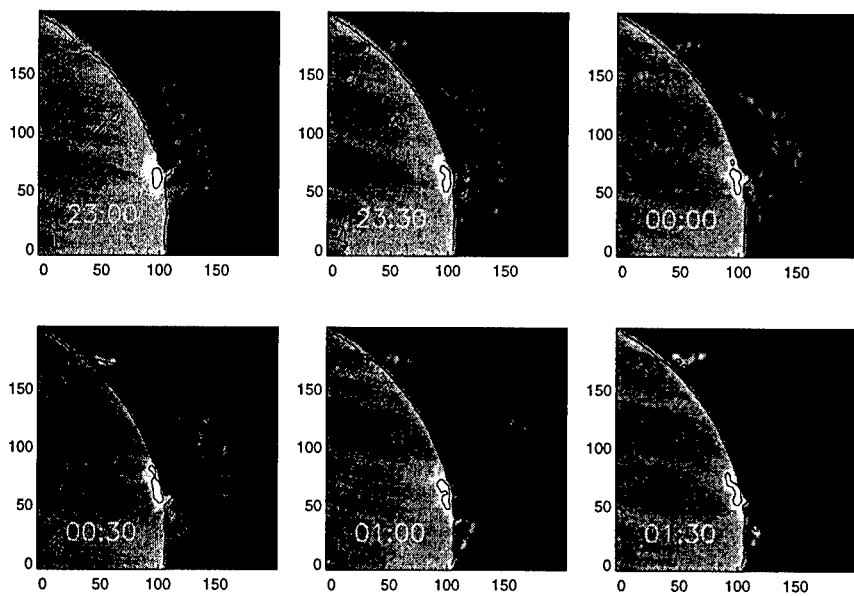
Figure 2.   Eruption of the April 4–5, 1994 prominence as observed at 17 GHz. The images are in pixel coordinates (1 pixel=4.92 arcsec).

2.1. The November 23, 1992 Compact Eruption

A gradual X-ray event took place close to the west limb on November 23, 1992 between 02:20 and 03:40 UT. An active prominence erupted from this flare site and moved into the corona about 1 $R_\odot$ above the limb. Figure 1 shows this eruption in X-rays (grey scale) and in microwaves (contours) at three instances: 02:29:38, 02:40:32 and 02:44:44 UT. In the first panel, there is no appreciable radio signature. In the next panel, the ejection is underway and has reached a height of about 0.2 $R_\odot$ above the limb. At the same time we can see a large faint X-ray structure overlying the erupting prominence. The width of the X-ray structure is about 5 times larger than that of the prominence. In the third panel, the prominence has moved to a larger height (speed $\sim$ 240 km s^{-1}) and part of the overlying X-ray structure seems to have opened up. In addition, we see

the outward movement of X-ray structures from under the prominence in the last two panels. Most of the GOES full-sun X-ray flux and the microwave flux came from the base of the prominence. The radio emission at the base of the prominence lasted for more than an hour, after the prominence had departed. This event clearly demonstrates that a coronal volume much larger than that of the prominence is affected during the eruption.

2.2. The Giant Quiescent Prominence Eruption of April 5, 1994

Quiescent prominences are large-scale cool structures lying along neutral lines separating opposite magnetic polarity regions. Eruption of these quiescent prominences can signal the start of a geoeffective solar disturbance (Joselyn and MacIntosh 1981). Some workers think that eruptive prominences might become magnetic clouds in the interplanetary medium (Bothmer and Schwenn 1994). Do the quiescent prominences show changes in the corona similar to the active ones? We show that large scale changes do take place in the corona ahead of the eruption. Figure 2 shows the eruption of a quiescent prominence during April 4–5, 1994. The prominence starts to rise around 23:00 UT (April 4) and slowly accelerates (11 m s^{-2}) to reach a speed of only about 70 km s^{-1} before reaching the edge of the field of view. The X-ray image taken around this time showed nothing spectacular. However, when we made a difference of the images at 00:04 UT (April 5) and 22:23 UT (April 4), we found a large depletion above the prominence (see Figure 3 left), similar to coronal dimming observed by Hudson et al. (1996). When we superposed the image of the erupting prominence on the contemporaneous X-ray difference image, we found that the depletion had a much larger radial extent and a comparable lateral extent. There was no depletion when we made differences of earlier X-ray images. The depletion was clearly ahead of the erupting prominence, and occupied a volume much larger than that of the prominence itself.

2.3. Prominence Eruption in a Quadrupolar Coronal Structure

On June 10, 1993 a loop-like prominence erupted from the east limb (Figure 4). In microwaves the prominence started from an initial height of 50,000 km and moved to about 300,000 km in about 45 min. The initial width of the prominence was about 300$''$ and remained roughly the same throughout the event. The X-ray coverage of this event was not very good, but was sufficient to understand the dynamics of the prominence environment. The top panel shows at two times the prominence overlain on simultaneous X-ray images. The prominence is located between two weak X-ray structures (marked N, S in Figure 4) above the west limb. In the bottom panel, we have shown the prominence at two later times superposed on X-ray difference images. The X-ray structures S, N on either side of the erupting prominence have expanded. The overall structure of the eruption seems to be quadrupolar, with one neutral line at the location of the prominence and the other two associated with the two X-ray structures. As in other events, we see a bright and compact arcade formation at the base of the filament located between the two X-ray structures. This was indeed a long-duration event (LDE; marked as ARCADE in Figure 5). The changes in the southern X-ray structure were correlated with the LDE (marked as SOUTHERN ARCADE). Although the prominence was observed in
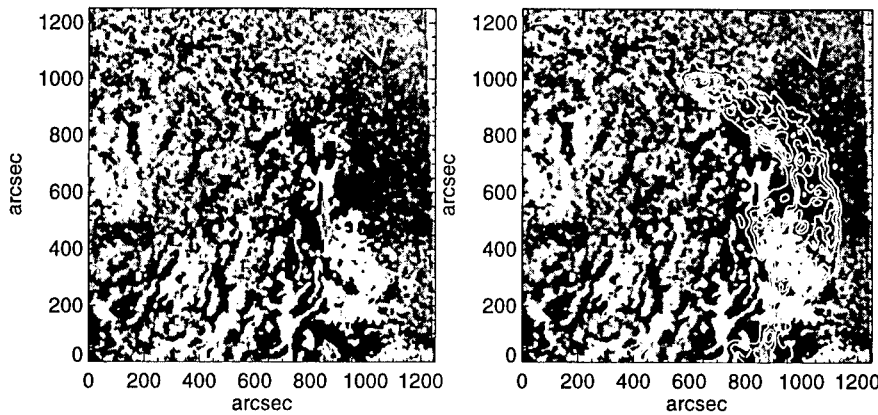
Figure 3.   Association between coronal depletion in X-rays (arrow) and the eruptive prominence (contours) above the northwest limb. The X-ray and radio data correspond to the same time. The X-ray depletion is clearly above the prominence. A preevent image was subtracted from the X-ray image. The X-ray image without the overlay is shown on the left for comparison.

projection against the plane of the sky, we think the prominence was of relatively small size compared to the large X-ray structures on either side. According to theoretical investigations, one needs reconnection of a structure overlying both the X-ray structures and the prominence (Antiochos 1997).

2.4.   Filament Eruption During the February 7, 1997 CME

We finally present an event on February 7, 1997 with complex filament eruption from the southern hemisphere. The filament eruption was associated with a spectacular partially Earth-directed CME observed by SOHO/LASCO (Gopal-swamy et al. 1997c). Figure 6 shows the superposition of a microwave image on a Yohkoh/SXT image. There was activity in the entire southern hemisphere along a long neutral line and the associated filament channel. A small fragment (P) from the northwest end of this activity channel erupted; it could be tracked beyond the limb and became the core of the CME. As soon as the filament started moving, an X-ray arcade started to form and spread to the southeast (see Figure 6). The horizontal portion (H) of the filament channel showed continuous activity even after the CME had moved to a height of several solar radii. In Figure 7, we have plotted the average radio brightness temperature in a box around the horizontal portion of the filament channel. The darkness of the filament increased for about two hours after the initial eruption and then the darkness slowly declined over several hours. The darkening corresponds to the enhanced absorption by optically thick material expanding out of the filament channel. There is evidence for the heating of the filament material when we compared the radio data with observations at other wavelengths. It is important to
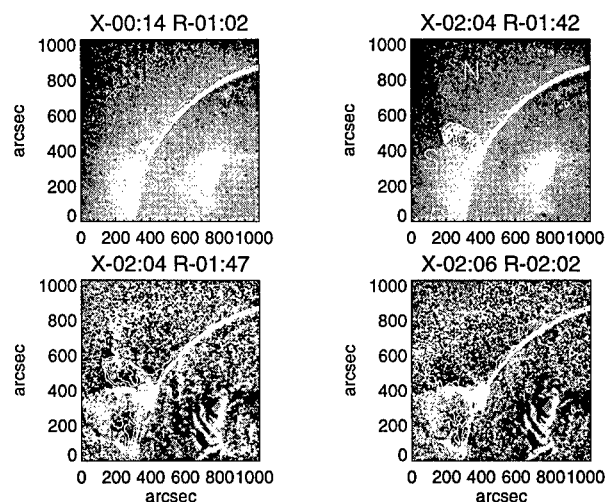
Figure 4.   (top): Radio prominence (contours) of June 10, 1993 superposed on Yohkoh/SXT images. The times of radio (R) and X-ray (X) images are given at the top of each image. S and N are the two X-ray structures on either side of the erupting prominence. (bottom): X-ray difference image at 02:04 and 02:06 UT showing the continued filament eruption and the X-ray structures.
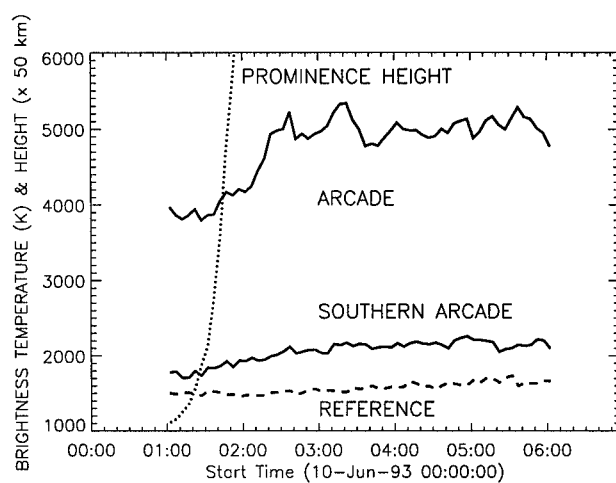
Figure 5.   Brightness temperature of the arcade and the southern X-ray structure compared to the height variation of the prominence (dotted line). We have also included the brightness temperature of an active region for reference (dashed line).

note that the X-ray arcade formation extended almost over the entire neutral line, although the tightly packed section was located only on the northwest to southeast section of the neutral line. If we had only white light observations, only the small northwest fragment of the filament would have been observed as the core of the CME and all the activity on the disk and the X-ray arcade formation would have been missed.
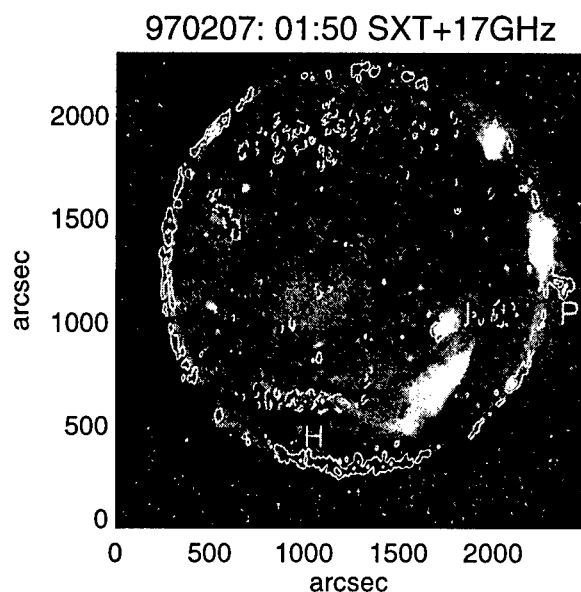
Figure 6.   Overlay of radio contours (solid for enhancement and broken for depression with respect to the quiet sun) on Yohkoh soft X-ray image showing the arcade formation in the southwest quadrant on February 7, 1997. P is the erupting prominence which moved from the location marked I near the active region. H is the horizontal section of the filament channel.

3.   Discussion and Conclusions

We have presented a representative set of observations which clearly demonstrate that prominence eruption is a small part of a large coronal change. X-ray images obtained simultaneously with the radio data show that a coronal volume much larger than the prominence is affected during the eruption. Therefore, prominence eruptions can be very useful predictors of geoeffective solar disturbances over a time scale of 2 days or more. Since the prominence eruptions can be observed on the disk, they are especially good indicators of Earth-directed CMEs. It must be remembered that the prominence itself lags behind the CME frontal structure and, hence, will be the last to arrive at the Earth. The implica-
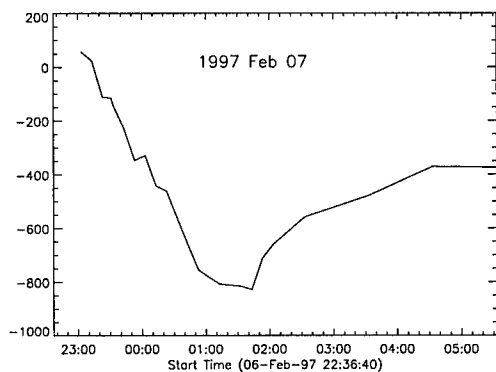
Figure 7.   Average brightness temperature with respect to the quiet sun from around the filament channel H on February 7, 1997.

tion is that magnetic clouds, the interplanetary manifestation of the CMEs, may not be due to the prominences as suggested by Bothmer and Schwenn (1994). The interplanetary counterparts of the prominences may be the pressure plugs sometimes observed at the rear of magnetic clouds (see, e.g., Burlaga et al. 1998, Gopalswamy et al. 1998).

Acknowledgments.   We thank H. Hudson for help in the analysis of the November 23, 1992 event. NG thanks the scientific organizing committee for their generous financial support to attend the IAU Colloquium 167. NG and JRL were supported by NASA contracts NAG-5-6139 and NAS-8-40801, respectively.

References

Antiochos, S. 1997, BAAS, 56, No. 3, 189

Bothmer, V. and Schwenn, R. 1994, Space Sci. Rev., 70, 215

Burlaga, L. et al. 1998, J. Geophys. Res., 103, 277

Gopalswamy et al. 1996, New Astronomy, 1, 207

Gopalswamy et al. 1997a, ApJ, 475, 348

Gopalswamy et al. 1997b, ApJ, 486, 1036

Gopalswamy et al. 1997c, BAAS, 29, No. 2, 908

Gopalswamy et al. 1998, Geophys. Res. Lett., in press

Hanaoka, Y. et al. 1994, PASJ, 46, 205

Hudson, H. S., Acton, L. W. and Freeland, S. 1996, ApJ, 470, 629

Joselyn, J. A. and McIntosh, P. S. 1981, J. Geophys. Res., 86, 4555

McAllister, A. et al. 1992, PASJ, 44, L205

Nakajima, H. et al. 1994, Proc. IEEE, 82, 705

Tsuneta, S. et al. 1991, Solar Phys., 136, 37

Filament Disparition Brusque and CME – September 25–26, 1996 Event

L. van Driel-Gesztelyi[1], B. Schmieder[2], G. Aulanier, P. Démoulin
Observatoire de Paris, DASOP, 92195 Meudon Cedex, France

P.C.H. Martens
ESA/SSD at GSFC, Greenbelt, MD 20771, USA

D. Zarro, C. DeForest, B. Thompson, C. St. Cyr, T. Kucera
NASA/Goddard SFC, Greenbelt, MD 20771, USA

J.T. Burkepile, O.R. White
High Altitude Observatory/NCAR, P.O. Box 3000, Boulder, CO 80307-3000, USA

Y. Hanaoka
Nobeyama Radio Observatory, NAOJ, Nobeyama 384-13, Japan

N. Nitta
Lockheed Martin Solar and Astrophysics Laboratory, Palo Alto, CA 94304, USA

Abstract.
    During the September 1996 campaign of multi-wavelength observations with the SOHO (SUMER, CDS, EIT, MDI, LASCO) and Yohkoh (SXT) spacecraft, the HAO Mauna Loa Solar Observatory Chromospheric Helium Imaging Photometer and the Nobeyama radioheliograph, a filament disparition brusque (DB) associated with a Coronal Mass Ejection (CME) was observed. The timeline of this complex event, which lasted for tens of hours, shows that the CME had started before the DB of a filament, while the main "bubble" of the CME was probably launched hours after the DB from the so-called "zipper" region. All these suggest that a general reorganization of large-scale fields was taking place on the Sun, and both the DB and the CME were symptoms of this.

---

[1]Konkoly Observatory, Budapest, Pf. 67, H-1525, Hungary

[2]University of Oslo, P.O. Box 1029 Blindern, N-0315 Oslo, Norway

DISPARITION BRUSQUE & CME ON SEPT. 25/26, 1996

(a) Sept. 26 01:05 UT

(b) Sept. 26 01:46 UT

(c) SOHO/EIT Fe XII 195 A Sept. 26 19:05 UT

(d) Yohkoh/SXT Sept. 26 19:18 UT
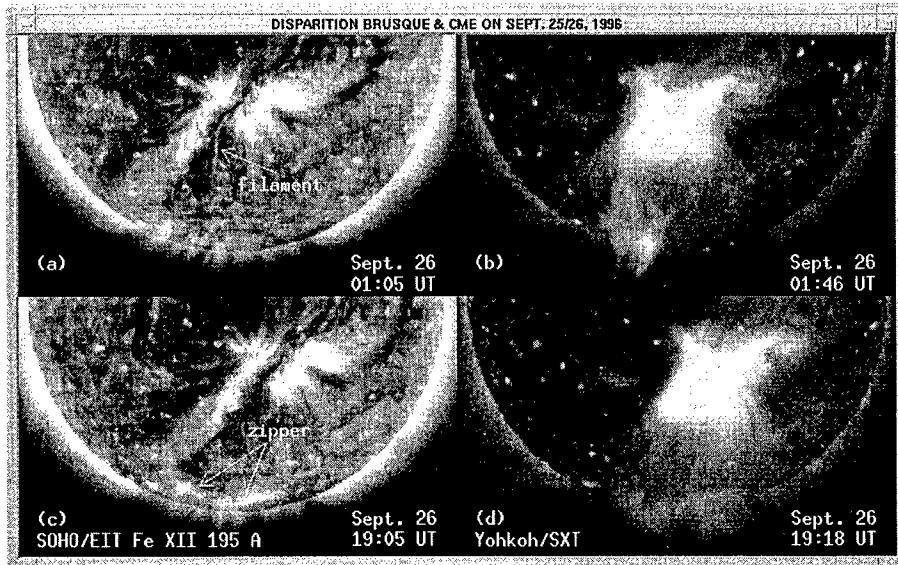
Figure 1. Partial images showing the (a, c) EUV and (b, d) soft X-ray images of the AR during the event including the DB of the filament and the evolution of the 'zipper' structure.

1. Observations

On September 25–26, 1996, a face-on CME event occurred (van Driel et al. 1998) in the dispersed bipolar remnant of active region (AR) NOAA 7986 during its central meridian passage. A long filament lay along the magnetic inversion line reaching South as far as the polar crown (Figure 1a). At the polar crown the inversion zone turned westward forming a so-called switchback, which is a favourable configuration for CME activity (McAllister et al. 1998). Linear force-free magnetic field line extrapolations (Figure 2) show that the coronal (X-ray) arcade overlying the filament channel was more sheared in the Northern part ($\alpha \approx 1.4 \times 10^{-2} Mm^{-1}$) than in the Southern part of the AR ($\alpha \approx 1.0 \times 10^{-2} Mm^{-1}$). During the hours prior to the DB, flux emergence and cancellation took place at different locations along the filament channel accompanied by coronal activity (X-ray bright points, loop brightenings, even cusp structures). Filament disturbances (movement at the Southern end) started after 21 UT on September 25, leading to the disappearance of the filament in He 10830Å by 23:45 UT (White et al. 1998). It is noteworthy that the filament was observed longer (20–30 min) in absorption in microwaves at Nobeyama.

In soft X-rays (SXRs) observed by Yohkoh/SXT a transient cusp-like structure appeared as early as 22:07 UT, when the filament disturbance had started, but the filament had not erupted yet. The X-ray cusp structure might indicate the presence of a primary reconnection involving larger-scale (e.g., polar crown) fields in the high corona prior to the filament eruption as suggested by Antiochos (1997, private communication).
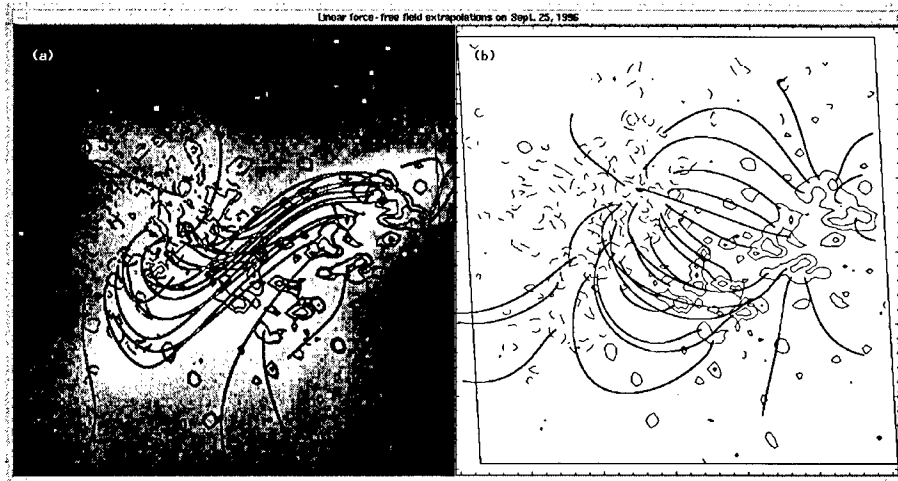
Figure 2.   (a) Linear force-free field extrapolations of a SOHO/MDI magnetogram (September 25, 01:41 UT) with α = $1.0 - 1.4 \times 10^{-2} Mm^{-1}$ (decreasing from N to S) show a good agreement with the observed coronal loops (Yohkoh/SXT, 01:43 UT), while (b) the potential field lines do not match the observations.
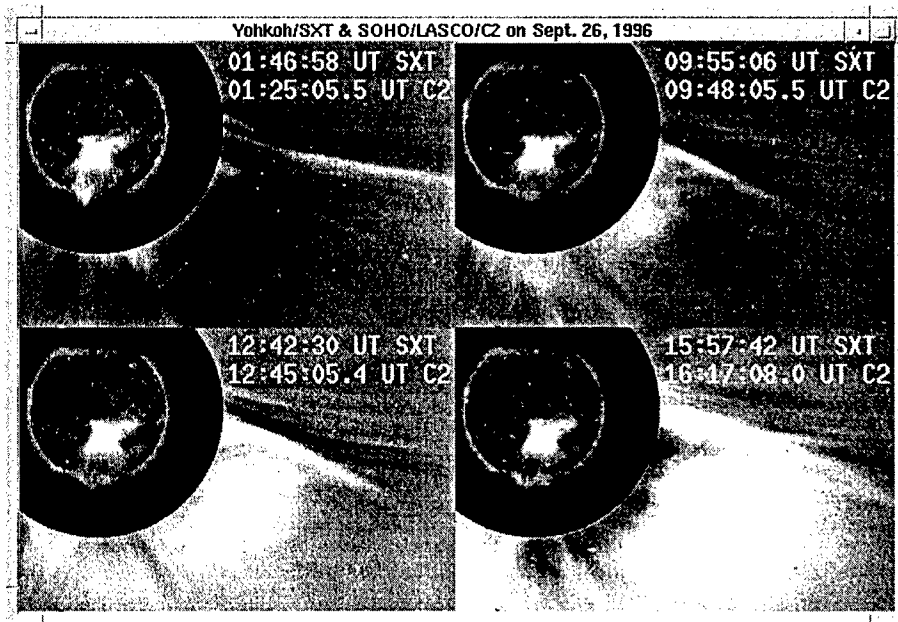
Figure 3.   Co-aligned Yohkoh/SXT and SOHO/LASCO C2 images show the evolution of lower coronal structures and the CME.

Only the southern part of the filament outside of the AR disappeared, while the filament inside the AR underneath the sheared coronal loops was only heated, thus appearing in emission in three SOHO/EIT wavelengths (in the Fe lines, cf. Figure 1a) and in SXRs (as observed between 00:24–01:46 UT, cf. Figure 1b). In SXRs cusped arcade formation started immediately after the DB (23:46 UT, Figure 1b) followed by an arcade formation along the polar-crown part of the switchback inversion zone (Figure 1d). The latter event was named 'zipper' and it was observed for tens of hours in all four EIT wavelengths as a growing chain of bright points, which were apparently the footpoints of an arcade of loops observed in SXRs (Figure 1c, d).

The SOHO/LASCO images (Figure 3) showed a CME moving outward over several days. The "primary" CME appeared as a "ragged front" between 23:25 and 01:25 UT. The CME spanned almost 140° in position angle (PA) and was centered at PA=205°. There were several dark and bright loops (non-concentric) embedded in the ragged front, and the height-time measurements for an early feature indicate a gradual acceleration through the C2 and C3 fields with a final speed measurement at 29 $R_\odot$ of about 420 km s^{-1}.

The latter "bubble" became visible in the C2 field of view only at about 09 UT, or nine hours after the DB of the filament (Figure 3). We should keep in mind, that this was a face-on CME event, therefore, projection effects may play an important role in this late appearance of the "bubble" believed to contain the erupted filament. On the other hand, the filament eruption along the N-S part of the switchback was followed by a coronal arcade formation along the connecting E-W part of the switchback inversion zone. Thus, it is possible that the main "bubble" of the CME was *not directly* linked to the filament DB, but to the "zipper" arcade along the polar crown. The filament eruption was more probably linked to the "primary" CME which appeared as a "ragged front" between 23:25 and 01:25 UT above the South pole.

2. Conclusion

This CME was a complex event lasting for tens of hours in which multiple events of activity appeared, suggesting that a general reorganization of large-scale fields was taking place on the Sun. Both the DB and the CME were symptoms of that.

References

McAllister, A.H., Hundhausen, A.J., Burkepile, J.T., McIntosh, P. and Hiei, E. 1998, J. Geophys. Res., to be submitted

van Driel-Gesztelyi, L. et al. 1998, Solar Physics, to be submitted

White, O.R. et al. 1998, in preparation

Ultraviolet Spectroscopy of a Coronal Mass Ejection

A. Ciaravella[1], J.C. Raymond, S. Fineschi, L. Gardner, J. Michels, R. O'Neal and J. Kohl

Harvard-Smithsonian Center for Astrophysics, 60 Garden St., Cambridge, MA 02138

M. Romoli and G. Noci

Dipartimento di Astronomia e Scienza dello Spazio, Università di Firenze, Largo E. Fermi 5, 50125 Firenze, Italy

C. Benna and S. Giordano

Università di Torino, I-10125 Torino, Italy

E. Antonucci

Osservatorio Astronomico di Torino, 10125 Pino Torinese, Italy

Abstract. A coronal mass ejection (CME) event was observed on December 23, 1996 with the Ultraviolet Coronagraph Spectrometer in both ultraviolet and visible light channels at 0.5 $R_\odot$ over the solar limb. The CME was followed during its evolution in the bright lines of Lyα (1216Å), Lyβ (1026Å), Lyγ (972Å), C III (977Å) and the OVI doublet (1032, 1037Å) and in several weaker lines. The Lyα peak intensity shows an excursion of two orders of magnitude during the CME evolution, and blue shifts up to 0.8Å ($\sim$200 km/sec). The data provide the emission measure in the Log T range 4.0–5.5 with a 0.3 sampling. Line intensities and profiles have been measured, providing important diagnostics for a detailed study of the CME's physical and dynamical parameters.

1. Introduction

Statistical analysis of Coronal Mass Ejection (CME) observations has shown a correlation of these events with prominence eruptions. This has been confirmed by the Solar and Heliospheric Observatory (SOHO–Domingo et al. 1996) which, for the first time, observes CMEs from the onset region into the extended corona in several spectral bands. In particular, the Ultraviolet Coronagraph Spectrometer (UVCS) (Kohl et al. 1997, Noci et al. 1997, Antonucci et al. 1997a) has observed, at ultraviolet wavelengths, several CME events. In this paper we describe one of the first UVCS observations of a CME with preliminary results of its analysis (Antonucci et al. 1997b, Ciaravella et al. 1997).

---

[1]Also at: European Space Agency, ESA/Estec, Noordwijk, The Netherlands

2. The Instrument

The Ultraviolet Coronagraph Spectrometer consists of two UV channels and a broadband visible light polarimeter designed to observe the solar corona from 1.4 to 11 $R_\odot$ (Kohl et al. 1995). The solar corona can be scanned through an entrance slit 40' long with a width variable in the range from a few to 84". The field of view of Visible light channel is a portion of 10x10" located at center of the entrance slit.

The visible light polarimeter detects the linearly polarised intensity of the solar corona in the wavelength band 4500–6000Å.

The UV channels are: the Lyα channel (LYA) optimised for measurement of Lyα 1215.67Å covers the range 1160–1350Å; and the OVI channel (OVI) optimised for OVI doublet 1031.91 and 1037.61Å covers the range 945–1123Å (473–561 in the second order). In this channel lines in the range 1160–1270Å (580–635 in the second order) can be also imaged. The dispersions are 0.1437 and 0.0993Å/pix in LYA and OVI detector, respectively.
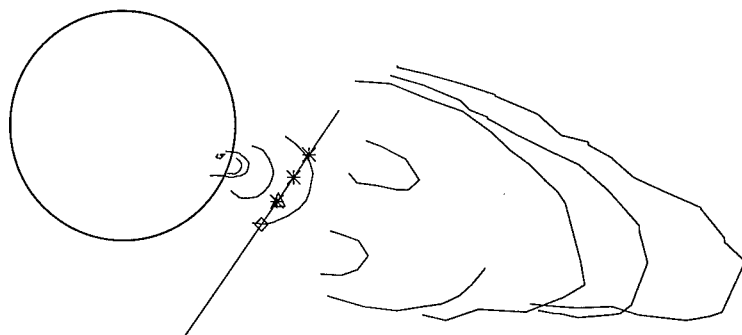
Figure 1. CME evolution through the field of view of EIT, C1 and C2/LASCO coronagraphs and the UVCS entrance slit position. The square marks the slit center and the asterisks mark the position of bright knots observed in the Lyα line.

3. Observations

The CME happened on December 23, 1996 in the Southwest. The event was observed with UVCS, the Extreme Ultraviolet Imaging Telescope (EIT) (Delaboudiniere et al. 1995) and the Large Angle Spectrometric Coronagraph (LASCO) (Brueckner et al. 1995). In Figure 1 is drawn the CME evolution as observed with EIT and LASCO and the UVCS entrance slit. The EIT 195Å images display the evolution of the prominence as the eruption causes a shock wave surrounding a dark void and the ejected plasma (Dere et al. 1997).

The UVCS observed at 235° PA at a fixed heliocentric height of 1.5 $R_\odot$ from 20:48:34 to 22:59:05 UT with 5 min exposures. In the LYA channel three spectral windows were imaged 1240.90–1243.49Å, 1210.51–1221.43Å and 1195.35–

1197.94Å binned to 0.29, 0.14 and 0.86Å, respectively. The grating position was 120000 and the entrance slit width 50 μm (14"). In the OVI channel we used four grating positions corresponding to 940–1040Å, 949–1049Å, 1017–1117Å, 1020–1120Å, wavelength ranges. The spectral binning was 0.2Å. The spatial binning was 3 pixels (21") in the LYA channel and 10 pixels (70") in OVI.

In Figure 2 the Lyα 1215.67Å line is shown for two stages during the observation. The vertical axis gives the coordinate along the entrance slit and the zero marks the heliocentric distance of 1.5 R$_\odot$.
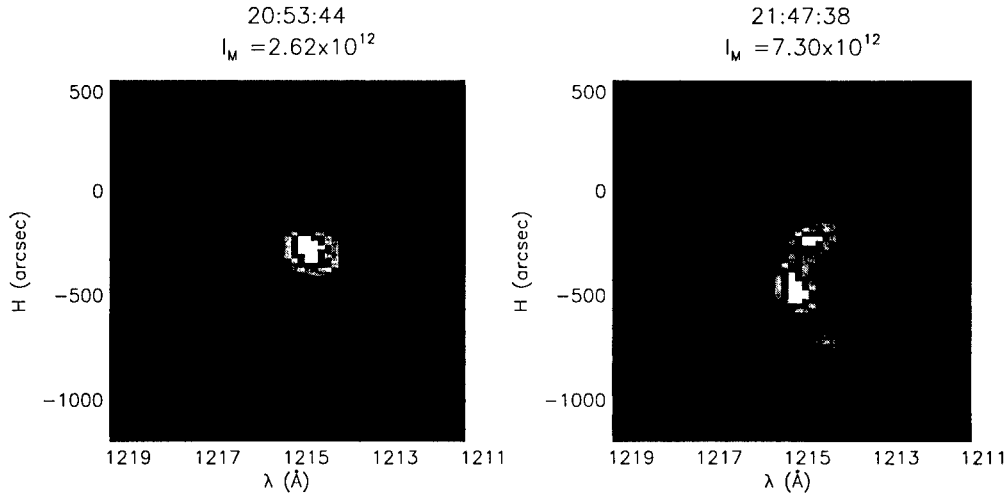
Figure 2.   Two panels show the Lyα line emission at two times during the observation. The initial UT time of each exposure and the line peak intensity are shown. The vertical axis is the spatial coordinate along the entrance slit. Each image is scaled to its brightest pixel.

The initial UT time of each exposure and the line peak intensity are shown. The event occured in a streamer region. The bright knots detected in the Lyα line correspond to the prominence material ejected into the corona as a consequence of the eruption detected with EIT (Dere et al. 1997). The first panel shows the first evidence of the CME, the bright spot slightly blue-shifted with respect to the underlying streamer emission. Fifteen minutes later, at 21:09:57 UT, the CME was at the peak if its emission, about 500 times the original streamer emission. After this time the CME started to fade, and in about 1 hr and 30 min the initial streamer conditions were almost recovered. During the observation several bright knots appeared in the UVCS field of view (second panel in Figure 2).

The spectrum observed in the OVI detector at the same time (21:47:38 UT) is shown in Figure 3. The O VI doublet, Lyβ , Si XII (499Å in second order), C III (977Å) and Lyγ can be seen. In spite of the coarse spatial binning used in this detector (70") the structure of CME material can still be seen. The three bright knots in C III show the same Doppler shifted structure as the Lyα line. The upper and lower knots are blue shifted as compared with the central one.
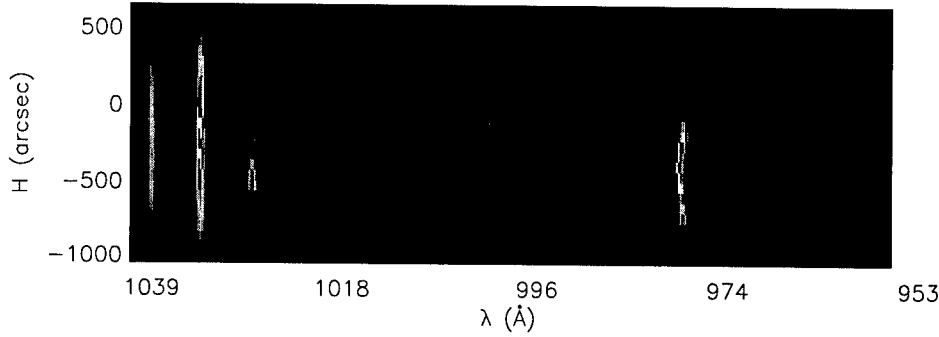
Figure 3.   Spectrum observed in the OVI detector at the same time as panel 2 in Figure 2.

4.   Results

4.1.   Emission Lines

Several emission lines were observed during the CME evolution and most of them are low temperature lines which are normally not observed in the solar corona. A list of the brightest is shown in Table 1.

Table 1.   Brightest Observed Lines

λ_{ID}	Identification
629.73	O V $2s^2\ {}^1S_0 - 2s2p\ {}^1P_1$
949.74	Ly δ
972.54	Ly γ
977.02	C III $2s^2\ {}^1S_0 - 2s2p\ {}^1P_1$
989.79	N III $2s^2\ {}^2P_{1/2} - 2s2p^2\ {}^2D_{3/2}$
991.58	N III $2s^2\ {}^2P_{3/2} - 2s2p^2\ {}^2D_{5/2}$
1025.72	Ly β
1031.91	O VI $2s\ {}^2S_{1/2} - 2p\ {}^2P_{3/2}$
1037.61	O VI $2s\ {}^2S_{1/2} - 2p\ {}^2P_{1/2}$
1084.56	N II $2s^2\ 2p^2\ {}^3P_1 - 2s2p^3\ {}^3D_{5/2}$
1215.67	Lyα
1242.80	N V $2s\ {}^2S_{1/2} - 2p\ {}^2P_{1/2}$

4.2.   Temperature Estimate

The spectral width of the bright knots observed in Lyα (Figure 2) is narrower than in the underlying streamer. We find in the bright knots of Lyα a Gaussian width narrower than in the streamer region, implying a temperature of ejected plasma at least six time lower than in the underlying streamer. Similar behavior has been found for the Lyβ , Lyγ and Lyδ lines.

Since C III 977.02Å and Lyβ show the same line widths, an upper limit to the plasma temperature of 7.4×10^4 K is obtained. On the other hand, using the

Lyman line ratios and the C II to Lyα ratio two independent estimates of the plasma temperature can be obtained. The two approaches give different values. This result suggests that the hypothesis of plasma optically thin to the Lyman lines is not appropriate (Ciaravella et al. 1997).

4.3. Velocity Structure

The velocity field in the CME region appears very structured. In Figure 2, panel 2, the lower and upper knots are blue shifted by 0.40 and 0.29Å with respect to the central one. During the observation we detected Lyα blue-shifts up to 0.8Å and red-shifts up to 0.2Å, corresponding to line of sight velocities of 200 km/sec and 50 km/sec, respectively. The CME extension along the slit increase from 200" at 20:53:44 UT to about 1000" at 21:47:38 UT implying expansion of about 200 km/sec. The bright knots have also a component of velocity along the UVCS slit. The average drift velocities are 70 and 50 km/sec for the upper and middle knot in Figure 2.

4.4. Emission Measure

Using the brightest spectral lines we estimate the emission measure:

$$\int n_e n_H \ dh = \frac{I_\lambda}{<P_\lambda>} \quad cm^{-5} \tag{1}$$

where

$$<P_\lambda> = \frac{P_{max}}{2} \quad phot \ cm^3 \ sec^{-1} \tag{2}$$

The emission measure as a function of temperature for four times during the CME evolution is shown in Figure 4.

Except for the initial rapid decrease between 4.1 and 4.5 in Log T, the distribution is relatively flat as a function of temperature. The emission measures at 1.5 $R_\odot$ are three or four orders of magnitude smaller than EUV spectra of prominences in the literature (Schmahl and Orrall 1979). The C III 972 Å and N III 991Å lines are formed at nearly the same temperature in ionization equilibrium, yet they imply emission measures differing by a factor of 3–4. An abundance anomaly related to the FIP effect (e.g., Meyer 1985) might cause such a discrepancy, as the material we observe was presumably well above the solar surface before the prominence erupted. Alternatively, the assumption of ionization equilibrium may be at fault.

5. Conclusions

A CME associated with a prominence eruption has been observed at UV wavelengths. The eruption occurred in a streamer region. Several low temperature lines were detected which are normally absent in a streamer region. The Lyman line widths suggest a temperature of ejected plasma at least six times lower than in the underlying streamer. The Lyα Doppler shifts give a diagnostic of the line of sight velocity structure. The Lyman line ratios suggest that the optically thin approximation is not valid to model the Lyman line intensities. Discrepancies in the emission measures of C III and N III lines were found.
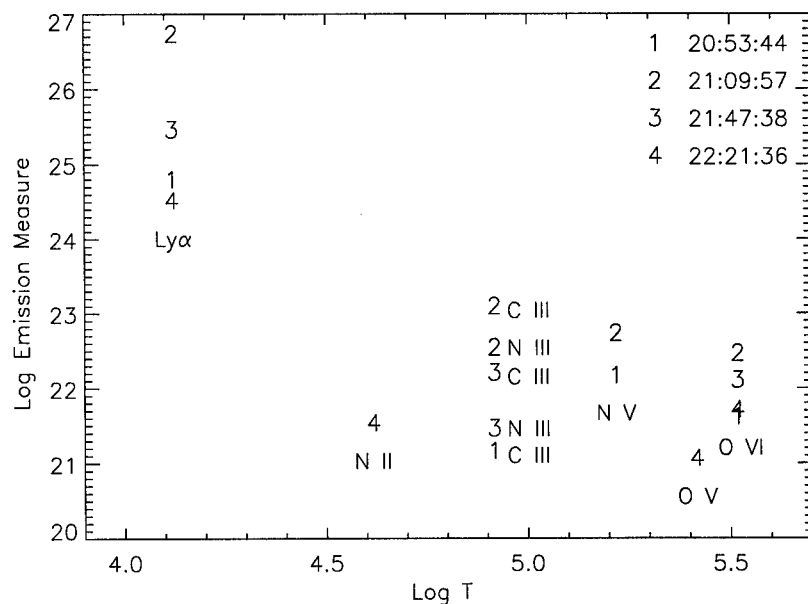
Figure 4.   Emission measure as a function of temperature. The four
symbols represent four stages of the CME evolution. At 21:09:57 (sym-
bol 2) the CME was at the peak of its emission

References

Antonucci, E. et al. 1997a, Adv. Space Res., in press

Antonucci, E. et al. 1997b, ApJL, 490, 183.

Brueckner, G.E. et al. 1995, Sol. Phys, 162, 357

Ciaravella, A. et al. 1997, ApJL, 491, 59.

Delaboudiniere, J.P. et al. 1995, Sol. Phys, 162, 291

Dere, K.P. et al. 1997, Sol. Phys., 175, 601

Domingo, V., Fleck, B. and Poland, A. 1996, Sol. Phys., 162, 1

Kohl, J.L. et al. 1995, Sol. Phys, 162, 313

Kohl, J.L. et al. 1997, Sol. Phys., 175, 613

Meyer, J.P. 1985, ApJS, 57, 173

Noci, G. et al. 1997, Adv. Space Res., 20 (12), 2219

Schmahl, E.J. and Orrall, F.Q. 1979, ApJL, 231, L41

Soft X-Ray Observations of Eruptive Prominences

T. Watanabe and M. Yamamoto
Ibaraki University, Mito 310, Japan

H. Hudson
Solar Physics Research Corp., Tucson, U.S.A. and ISAS, Sagamihara 229, Japan

M. Irie and K. Ichimoto
National Astronomical Observatory, Tokyo 181, Japan

H. Kurokawa
Hida Observatory, Kyoto University, Kamitakara 506-13, Japan

H. Yatagai
Fujitsu Co. Ltd, Tokyo, Japan

Abstract. Evolution of magnetic structures in the region around an eruptive prominence of August 28, 1992 are examined using soft X-ray images obtained by Yohkoh. The eruption was preceded by the appearance of a large-scale soft X-ray jet which was ejected from near the root of the southern end of the prominence. Changes of magnetic geometry at the southern end of the prominence appeared to trigger the eruption. In the course of prominence eruption, helically twisted soft X-ray loops were observed around the prominence. This indicates that magnetic reconnection of a sheared arcade took place underneath the erupting prominence.

1. A Case Study: The Eruptive Prominence of August 28, 1992

Many eruptive-prominence events have occurred since the launch of Yohkoh in 1991. Among them, some events showed very complicated soft X-ray structures during the course of their eruption. As an example, we discuss the event observed above the eastern solar limb on August 28, 1992. An example of an H_α image of the erupting prominence is shown in Figure 1. The latitudinal extent was 15° in projection onto the plane of the sky. According to the H_α synoptic map from the Solar-Geophysical Data (NOAA/SESC), the magnetic neutral line underneath the prominence was aligned nearly in the north-south direction, so that we have a side view of the prominence. The prominence did not show appreciable ascending motion when H_α observations at Boulder and Holloman were performed at 14–17 UT on August 28. The start time of the eruption must have been between 17 UT and 21 UT on August 28 (the latter time was that of

28 August 1992

Hα (21:24 UT)   Soft X-Ray (21:32:08 UT)   Hα + Soft X
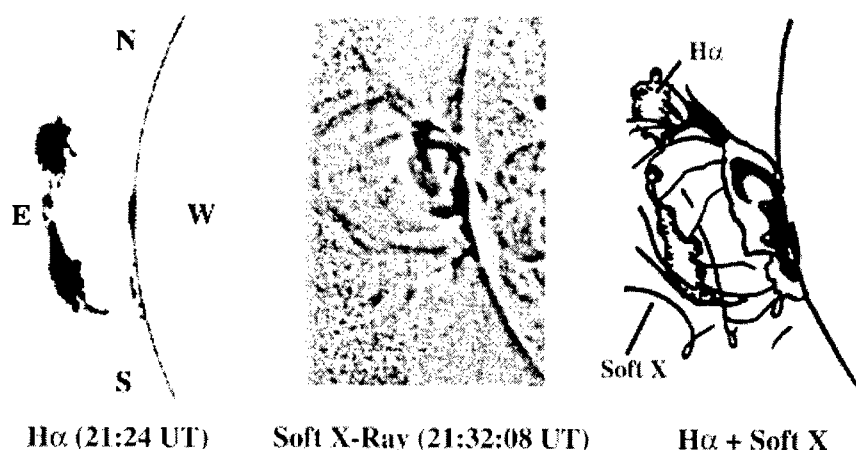
Figure 1.   Left: an H_α photograph (negative) of the eruptive promi-
nence of August 28, 1992 (21:24 UT) taken at Norikura Observatory.
Middle: an enhanced soft X-ray image (negative) taken by the Soft
X-ray Telescope of Yohkoh (21:32:08 UT). Right: a sketch of the soft
X-ray loop structures based on the middle flame. The approximate
geometry of the eruptive prominence is also shown in this sketch.

the first H_α observation in Japan on this date).

The most remarkable feature, which appeared immediately before the erup-
tion, is the large soft X-ray jet (Figure 2). This jet appeared to have been ejected
near the root of the southern end of the prominence at about 18:40 UT. The X-
ray intensity of a bright region seen underneath the prominence began to increase
after the appearance of the jet. We suggest that this jet, which was unusually
large (see Shimojo et al. 1996), marked a precursor event of the prominence
eruption. Since the eruption began shortly after the appearance of the jet, the
jet may reveal the start of the destabilization of the magnetic structures which
supported the prominence.

According to H_α observations performed at Mitaka and Hida, the ascend-
ing speed of the prominence was 30–60 km/sec. Highly complicated soft X-ray
structures, which were observed during the course of the prominence eruption
(21:32:08 UT), are shown in the middle frame of Figure 1. A composite sketch of
the prominence and soft X-ray loops is also shown in this figure for comparison.
The most interesting feature seen in Figure 1 is the presence of kinky loops,
which are interpreted as the projected images of helical flux ropes. Straighter
loops apparently passing through the center of the helical loops are seen also
around the erupting prominence. Although it is difficult to know the 3D config-
urations of these loops, a combination of helically twisted loops on the outside
and straight loops passing through the axis of the helical loops is consistent
with the projected view which we observed. This configuration is similar to that
proposed by van Ballegooijen and Martens (1989) to create twisted flux tubes

N

E

18:33:18   JET   18:58:54
                 18:41:50
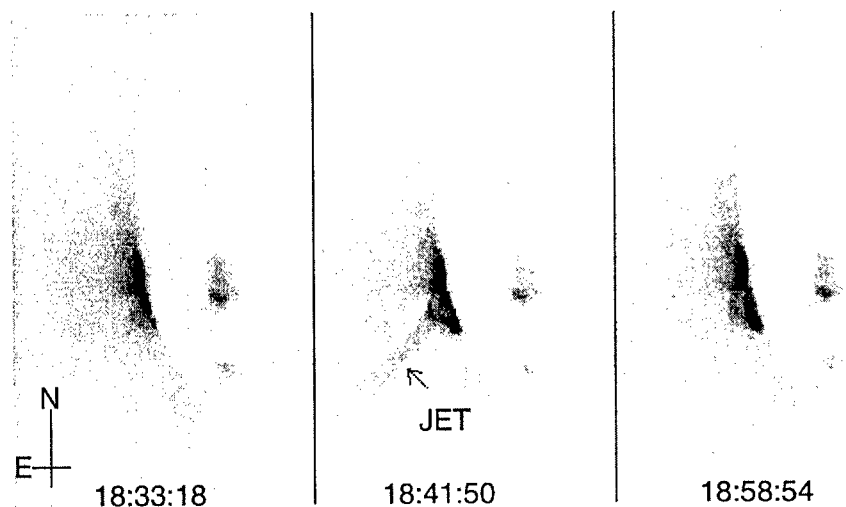
Figure 2.   A soft X-ray image (negative) of the jet (18:41:50 UT) which appeared about 3 hours before the prominence eruption. For comparison, soft X-ray images taken immediately before and after the appearance of the jet are also shown.

above the magnetic neutral line. They showed that twisted flux tubes are formed by development of sheared prominence-supporting field due to flux cancellation above the neutral line. They suggested also that prominence eruption can be caused by this process.

2.   Concluding Remarks

This event is one of the best examples of prominence eruptions observed by Yohkoh. Since the eruption took place shortly (< 3 hours) after the appearance of the jet, we suppose that the trigger action, required for the prominence eruption, was the change in magnetic structure near the root of the southern end of the prominence. Perhaps emerging flux could have produced this magnetic restructuring, as suggested by Feynman and Martin (1995). The presence of helical loops surrounding the erupting prominence and a bright soft X-ray arcade following it can be explained by magnetic reconnection underneath the erupting prominence (e.g., Hirayama 1974). Further detailed analysis is in progress.

References

Feynman, J. and S. F. Martin 1995, J. Geophys. Res., 100, 3355

Hirayama, T. 1974, Solar Phys., 34, 323

Shimojo, M., S. Hashimoto, K. Shibata, T. Hirayama, H. Hudson and L. Acton

1996, Publ. Astron. Soc. Japan, 48, 123
van Ballegooijen, A. A., and P. C. H. Martens 1989, ApJ, 343, 971

Prominence Disappearance Related to CMEs

E. Hiei

Meisei University, 2-1-1, Hodokubo, Hino, Tokyo 191, Japan

Abstract. DB (disparition brusque) events are associated with dynamic phenomena such as a CME, a flare, brightening of a soft X-ray arcade, and soft X-ray dimming, and probably a change of the coronal magnetic field on a large scale. The DB event observed on January 16, 1993 identified with a CME occurred on the solar disk.

1. Introduction

A DB (disparition brusque) is a signature of a change in the coronal magnetic field surrounding a prominence. A CME (Coronal Mass Ejection), a flare, brightening of soft X-ray arcade, and soft X-ray dimming may all be related to a change of the coronal magnetic field configuration. However, which is a cause of the other event is not known. Several examples of the observations of DB/CME/flare/soft X-ray brightening/dimming are discussed to find out which is the first event among the other ones.

2. Observations

We have studied a relation between the DB of a polar crown prominence and CME/soft X-ray brightening/dimming, and found that a CME and a DB occur almost simultaneously, but the brightening of a soft X-ray arcade occurs always after a DB event. It is important to determine which (CME or DB) starts first. However, it is difficult to determine a starting time of the event. A prominence is usually moving up slowly at the beginning and then shows an abrupt change of its upward velocity (Mouradian 1995). The behavior of a CME is also difficult to determine when the CME begins to move up. At the beginning of a CME, it moves up slowly and its intensity is seen to be very weak. The observation of a CME, however, shows that the front of the CME moves faster than that of the lifting prominence (Hundhausen 1998), so it is natural to think that a prominence may not push a CME, but rather a CME may be the cause of a DB.

A good example of a DB, a CME, and brightening of a soft X-ray loop was observed at the southwest limb. A polar crown prominence disappeared on April 30, 1993, and a lifting prominence and its related CME were observed with the K-coronameter at Mauna Loa in Hawaii, and soft X-ray brightening was observed with the soft X-ray telescope (SXT) on board the Yohkoh satellite. Figure 1 shows the observed height of the CME (cavity) and the prominence versus time. The velocity of the CME was higher than that of the prominence. A soft X-ray loop brightened up almost 2 hours later than the first appearance of

the lifting prominence. The SXT loop extended up along the trajectory of the lifting prominence.
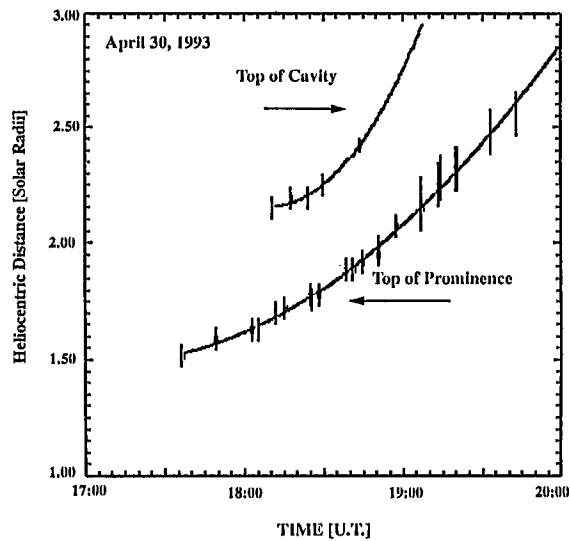
Figure 1. Height change of CME and prominence.

The soft X-ray intensity of the coronal region above the X-ray bright loop showed a dimming, which started at almost the same time as the first appearance of the CME. The X-ray intensity of the dimming region recovered 7 hours later. The dimming seemed to be due to the depletion of coronal matter associated with the CME.
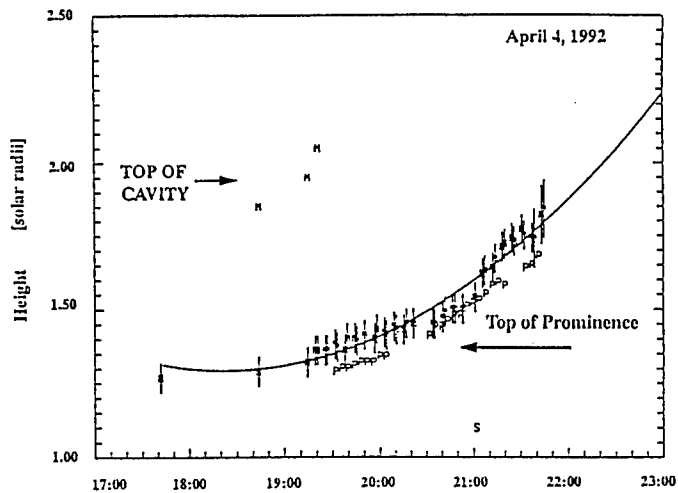
Figure 2. Height change of CME and prominence.

A large polar crown prominence erupted on April 4, 1992. The lifting promi-
nence and its related CME were observed at Mauna Loa. Figure 2 shows the
height variation of the top of the CME cavity and the lifting prominence versus
time. While the DB and CME were obvious in visible wavelengths, the only
significant feature detected in soft X-rays was a faint knot of enhanced emission
at approximately 0.11 solar radii above the limb about 3 hours later than the
appearance of the prominence. The soft X-ray emission thus occurred below the
location of the prominence, and after the acceleration phase of the eruption.
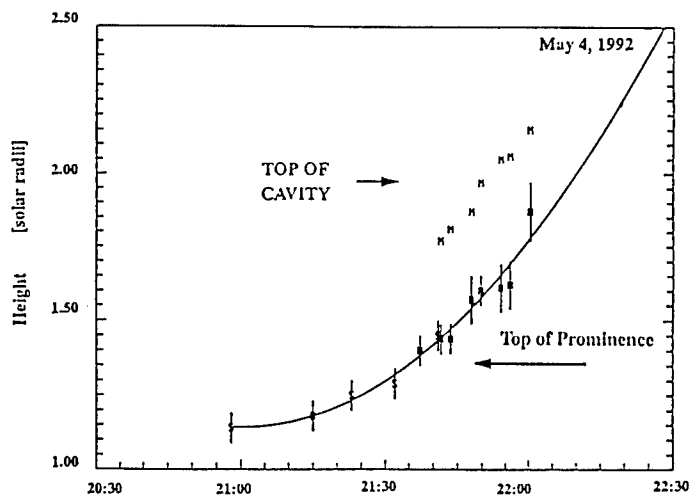
Figure 3. Height change of CME and prominence.

Figure 3 shows the height change of a CME and a prominence versus time on
May 4, 1992. The outer loop, cavity and central core of the CME were observed
with the K-coronameter at Mauna Loa. An outward motion of material was seen
in SXT data and might be identified as the front of the CME. Inspection of the
Hα data, however, reveals that the mass ejection appeared to arise from active
region 7154 near S27E54, and that the core of the ejected material was associated
with a very small filament which erupted from this region. The motion seen in
the soft X-ray images, thus, are those of the inner core of the CME and not the
outer loop or top of the CME.

A dimming event on January 16, 1993, associated with a DB and soft X-ray
brightening, provides good evidence of the CME event observed on the solar disk.
The disappearance of the DB was observed between 09:00 UT and 12:30 UT.
The dimming started at 12:00 UT and was greatest at 13:30 UT. The duration
of the dimming was not determined because the later phase of the dimming was
affected by the brightening of soft X-ray loops appearing after the DB.

A particle decrease at the earth, which indicates the presence of an inter-
planetary CME, was detected at 10:22 UT on January 19, 1993 (Cane 1996,
private communication) and, thus, the DB and its associated dimming of Jan-
uary 16 can be identified with a CME observed on the disk.

References

Hundhausen, A.J. 1998, Coronal Mass Ejections, in The Many Faces of the
Sun, (eds.) K.T. Strong, J.L.R. Saba, B.M. Haisch, and J.T. Schmeltz,
Springer-Verlag, New York

Mouradian, Z., Soru-Escaut, I. and Pojoga, S. 1995, Solar Phys., 158, 269

MHD Simulation of Dark Filament Eruption in the Quadrupole Source Model

Y. Uchida, S. Hirose, S. Cable, S. Uemura, K. Fujisaki, M. Torii and S. Morita

Physics Department, Science University of Tokyo, Shinjuku-ku, Tokyo, Japan

Abstract. A magnetohydrodynamic simulation in a 2.5D approximation is performed for the quadrupole source model for arcade flares treated years ago by Uchida (1980), and recently supported by the observations from Yohkoh. It is shown that this model can explain several key characteristic features of arcade flares found by Yohkoh, and can avoid some of the paradoxes existing in the "classical model".

1. Introduction

Recent observations by Yohkoh of the faint pre-event coronal structures of arcade flares and high latitude X-ray arcade formation events have revealed that there exist structures like the connections from the top of the flare cusp back to the photosphere on both sides (Uchida 1996), or "overlapped dual arcades" in the pre-event corona before arcade formations (Uchida et al. 1998), quite unexpected from the "classical model" for solar arcade type flares. The findings about the process of X-ray arcade formation itself (Fujisaki et al. 1998) also suggest that the observations are not compatible with what the "classical model" predicts.

In the present paper, we describe our results of 2.5D magnetohydrodynamic simulations in the quadrupole magnetic source model (Uchida 1980), and present a new interpretation for the dynamic eruption of dark filaments.

2. Magnetodynamic Simulations with the Quadrupole Source Model

Based on the new observational findings presented in our review (Uchida 1998, these proceedings), we assume: (i) a quadrupole array photospheric magnetic source (as in Figure 1) which may represent the bipolar field plus a belt of flux patches transported to the other sides, together with the presence of an overall longitudinal (parallel to the central neutral line) field component as found for arcade formations (Uchida et al. 1998), and (ii) a certain amount of gas (dark filament gas) loaded on the part of the longitudinal field in the region of the neutral sheet, and (iii) the photopheric footpoints are squeezed slowly and nearly homologously toward the central polarity-reversal line to prepare the state with energy stored in the form of magnetic stress (Figure 2).

In our model, the longitudinal field, $B_\parallel$, dominates in the neutral sheet because $B_\perp$ is zero there, and this $B_\parallel$ has a clear role in *separating* the oppositely-
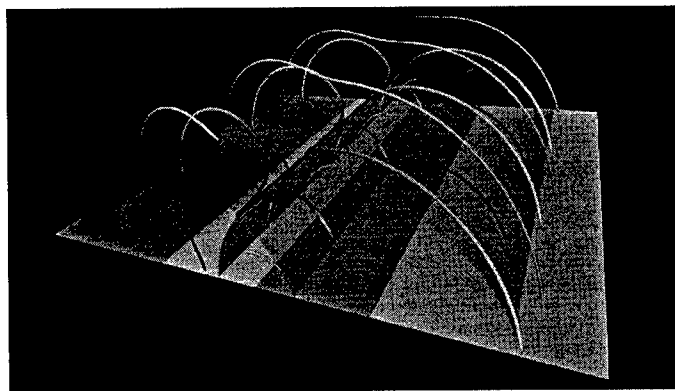
Figure 1.   A model magnetic field for quadrupole photospheric sources before squeezing. The separatrix surfaces of "dual arcades" shape is seen, just like the observed "overlapped dual arcades". $B_\parallel$ dominates in the region near the "neutral line" (the locus of the neutral points in $B_\perp$), and the lines of force there are parallel to the neutral line.

directed $B_\perp$ on both sides of the thin and vertical neutral sheet in our model, preventing the reconnection. The dark filament mass stabilizes this function. The dark filament here, however, is dynamically passive, and can be squeezed out by external perturbations, and the separation of the opposite-polarity fields $B_\perp$ can diminish, allowing the start of reconnection, leading to a reconfiguration by which the stress energy can be relaxed.

The observations by Yohkoh suggest that the region of high latitude dark filaments is very stable for a few solar rotations before destabilization. Therefore, they are likely to be in a relatively low-tension state, rather than something like a highly sheared state. In our model, the elongated form of the dark filament is due to the vanishing $B_\perp$ in the neutral sheet, rather than due to a strong shear.

Our interpretation for the destabilization is that there is an injection of current (twist in a small emerging loop may be transferred to our magnetic field system through reconnection) from the emerging flux pair right into the dark filament region. If the injected current has opposite direction to the current in the dark filament, then an expulsive force acts, pushing the upper part of the dark filament upward. At the same time, the lower part is pressed down and heated to make the S-shaped X-ray feature in the dark tunnel.

After the evacuation of the dark filament together with $B_\parallel$, the antiparallel vertical parts of $B_\perp$ are pressed into direct contact, and the condition for reconnection is satisfied. Here we use as usual, an anomalous resistivity that enhances the speed of reconnection. (The essential part of the "classical local model for reconnection" is still left unsolved. We come back to this point in a separate paper.)
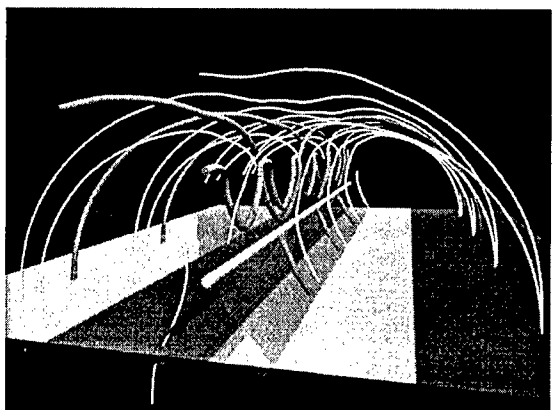
Figure 2. A model magnetic field for quadrupole sources with mass loaded on the field lines near the neutral line, and the footpoints in the photosphere are squeezed nearly homologously toward the central polarity-reversal line (Hirose et al. 1998). (In this particular case, there exists a magnetic island in $B_\perp$ in the neutral sheet region which corresponds to a helix in 3D).

3. MHD Simulation After the Current Injection

Here, we show some results of 2.5D MHD simulations performed for the above-mentioned squeezed quadrupole source model with injection of current as the initial trigger (Hirose et al. 1998) (Figure 3).

It is seen in the first panel (upper left) of Figure 3 that the equilibrium distribution of the dark filament gas held in $B_\parallel$ has a thin partition type shape as seen also in Figure 2, separating the oppositely-directed $B_\perp$ on both sides. In the second panel (upper right), the upper part of the dark filament is squeezed out, while the lower part is pressed down as the current is injected, providing the model counterparts of erupting dark filament, and of the heated S-shaped structure observed low along the polarity-reversal line (down in the tunnel), respectively. As the reconnection of the main $B_\perp$ with the stored stress starts in the part of the neutral sheet from which the dark filament has been squeezed out, the squeezed out dark filament, which "hesitates" to rise, is re-accelerated by the inflating magnetic flux transferred from the squeezed part on both sides into the upper portion through reconnection. The upper part of the dark filament becomes an eruptive dark filament with continued acceleration (lower right). The reconnection produces the main part of the flare, a heated cusped region just like the observed cusps in arcade flares at the limb, *but* with upper connections connecting the top of the heated cusp back to the photosphere on both sides (Uchida 1996). There is also a feature pressed down (S-shaped structure if seen from above), explaining the observed S-shaped feature inexplicable by the classical model.
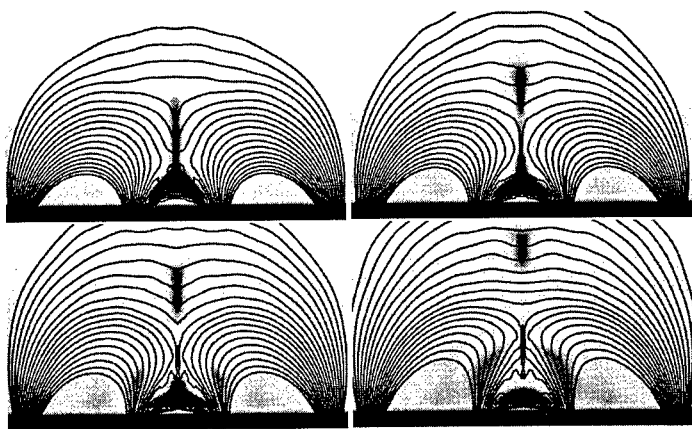
Figure 3. $B_\perp$ and density contour projected on the x–z plane. Time progresses from upper left, upper right, lower left, and lower right. See the text (Hirose et al. 1998).

4.   Advantages of Quadrupole Magnetic Source Model: Conclusion

It was shown in the above that the quadrupole source model can explain several key observational features: the pre-event "overlapped dual arcades" type coronal structure as a "pre-heated separatrix surface", and the high bright loops connecting the flare core to both sides as well as the bright feature on the axis of the dark tunnel. Acceleration, rather than deceleration, of the rising dark filament, is also explained.

The quadrupole source model also has merits for avoiding a few, but essential, difficulties in the classical model: (i) the energy paradox in which the dark filament rise should have greater energy than the flare itself, and (ii) the difficulty of supporting the dark filament gas at the top of the otherwise convex arcade (Uchida 1996).

References

Hirose, S., Cable, S., Uchida, Y. and Uemura, S. 1998, in preparation

Fujisaki, K., Uchida, Y., Morita, S., Hirose, S., and Cable, S. 1998, Publ. Astron. Soc. Japan, submitted

Uchida, Y. 1980, in Solar Flares, (ed.) P.A. Sturrock, University of Colorado Press, Boulder, p. 67 and p. 110

Uchida, Y. 1996, Adv. Space Res., 17, 4/5, 19

Uchida, Y., Fujisaki, K., Morita, S., Torii, M., Hirose, S. and Cable, S. 1998, Publ. Astron. Soc. Japan, submitted

Coronal Plasmoid Dynamics

C. Delannée and S. Koutchmy

Institut d'Astrophysique de Paris, CNRS, 98 bis, bd Arago, 75014 Paris, France

A. Zhukov and I. Veselovsky

Institute of Nuclear Physics, Moscow State University, Moscow 119899, Russia

Abstract. A possible acceleration mechanism by the magnetic force is suggested for a plasmoid, modeled as a spherical body with a magnetic dipole situated in its center of mass. The governing equations of the motion of a dipole in an inhomogeneous magnetic field are solved analytically and numerically. Both methods show the possibility for the plasmoid to be accelerated in the direction of the external field gradient.

1. Introduction

Magnetically isolated clouds of ionized gas, or coronal plasmoids, have been theoretically described by many authors, for example, by Priest (1982), Cargill and Pneuman (1986), Pneuman (1983) and Mullan (1990). A possibility to test these theories experimentally appeared after the observation of the coronal plasmoid by the Canada–France–Hawaii Telescope (CFHT) during the July 11, 1991 total solar eclipse (Vial et al. 1992, Koutchmy et al. 1994). The dynamics of the plasmoid were described in Delannée and Koutchmy (1996), and it was reported in this paper that the plasmoid seen during 230 s at 90,000 km above the solar limb moved at a high velocity (about 75 km s^{-1}). Its dimension was around 1 Mm; it was denser (3×10^9 cm^{-3}) and colder (2×10^4 K) than the surrounding corona (3×10^8 cm^{-3}, 2×10^6 K). To support the external gas pressure the plasmoid had to be more magnetized than the corona; estimates give B$_{plasmoid}$ = 2 G and B$_{corona}$ = 1 G.

In the present paper we discuss a possible acceleration mechanism – the acceleration due to the magnetic force, which is probably dominant in the plasmoid dynamics (Delannée et al. 1998).

2. Outline of the Problem

The plasmoid is assumed to be solid, i.e., incompressible. Inside the magnetic field can be produced by a ring current, which is equivalent to a magnetic dipole if the radius of the ring current is small enough versus the radius of the plasmoid. Outside the magnetic field is produced at the center of the sun or in an active region; both kinds of magnetic field can be modeled by a magnetic dipole
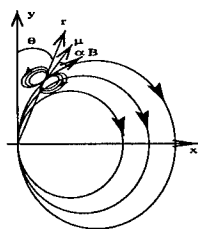
Figure 1.   Diagram of the problem.

but of different sizes and strengths. Additionally, we consider the dipole field frozen inside the plasma contained in the plasmoid. Finally, we fully neglect the influence of the external plasma. So we solve the problem of the motion of a magnetic dipole inside an inhomogeneous magnetic field, see Figure 1. The equation of motion is:

$$m\dot{\vec{v}} = \vec{\nabla}(\vec{\mu} \cdot \vec{B}),\qquad(1)$$

where m is the mass of the plasmoid, v its velocity, μ the magnetic dipole moment inside the plasmoid and $\vec{B}$ the magnetic field outside the plasmoid. The magnetic dipole moment can oscillate around the external magnetic field vector. The equation of conservation of energy is:

$$\frac{mv_0^2}{2} + \frac{1}{2}I_{ik}\theta_{i0}\theta_{k0} - \mu B \cos\alpha_0 = \frac{mv_1^2}{2} + \frac{1}{2}I_{ik}\theta_{i1}\theta_{k1} - \mu B \cos\alpha_1,\qquad(2)$$

where I is the inertia momentum of the dipole, θ the oscillation angle of the dipole in the spherical coordinates of the reference frame of the external magnetic field, α is the angle between the external magnetic field vector and the magnetic dipole moment vector, the subscripts, 0 and 1, correspond to the values of the quantities taken at two different times, t_1 and t_2, and the subscripts, i and k, correspond to the two angular coordinates of the spherical coordinates of the problem.

3.   Equilibrium, Oscillation and Rotation

The equilibrium of the dipole versus its oscillation in the external magnetic field is reached when its potential energy of the oscillations ($E_p = -\vec{\mu} \cdot \vec{B}$) is maximal or minimal. There are two configurations, see Figure 2. The stable configuration is such that the force is directed toward the stronger magnetic field.

When the dipole moves in an inhomogeneous magnetic field, it feels the change in the magnetic field direction and starts to oscillate around the magnetic field direction. We solve the equations of conservation of energy in the reference frame of the center of the dipole. The problem is axisymmetric. The change in direction of the magnetic dipole moment due to the change of the magnetic field
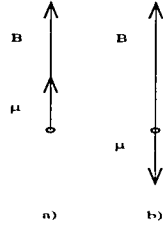
Figure 2. Equilibrium configurations of the magnetic dipole in the external magnetic field. a) is the stable equilibrium and b) is the unstable equilibrium.

direction is considered very small. So, the two components of the oscillation are equal to the angle α. The solution is:

$$t = \pm \frac{2}{\dot{\alpha}_0} F(|\alpha/2|, k) \tag{3}$$

where $k^2 = 4\Omega^2/\dot{\alpha}_0^2$; $\Omega = \sqrt{\mu B/I}$ is the characteristic proper frequency of the plasmoid; $F(|\alpha/2|, k)$ is the incomplete Legendre elliptic integral of the first kind. The two different regimes of the oscillations are described in this solution: if $|k| > 1$, the function $F(|\alpha/2|, k)$ is complex and the motion is a rotation, and if $|k| < 1$, the function $F(|\alpha/2|, k)$ is real and the motion is an oscillation

4. Motion

We develop the gradient of the potential energy. We see in the solution of the problem given in the previous section that $\alpha = \alpha(t)$. This leads to: $\vec{\nabla} \cos \alpha = 0$. Projecting the equation of motion on the axes parallel and perpendicular to the magnetic field gradient direction, we obtain that the velocity perpendicular to the external magnetic field gradient is constant during the motion and only the velocity parallel to it can be accelerated with the equation:

$$m\dot{v} = \mu \cos \alpha \nabla B \tag{4}$$

If $\cos \alpha < 0$ (i.e., $\pi/2 < |\alpha| \leq \pi$), the velocity of the plasmoid increases.

In the case of oscillations, we integrate the equation of motion over a period of oscillation, T. The solution is:

$$v(T) = v_0 + \frac{2\sqrt{2}\mu \nabla B}{m\Omega} \psi(\alpha_{\max}), \tag{5}$$

with

$$\psi(\alpha_{\max}) = \sqrt{2} \left\{ 2E(\sqrt{\frac{1 - \cos \alpha_{\max}}{2}}) - K(\sqrt{\frac{1 - \cos \alpha_{\max}}{2}}) \right\}, \tag{6}$$

where E and K are respectively the complete Legendre elliptic integrals of the second and first kind.

$\alpha_{\max}$ is the maximal angle reached during an oscillation. Using the equation of conservation of the energy, we find $\cos \alpha_{\max} = 1 - \frac{\dot{\alpha}_0^2}{2\Omega^2}$. We define $\alpha_{\max}^*$, the critical value of the maximal angle of the oscillations, such as $\psi(\alpha_{\max}^*) = 0$. In the case of the plasmoid seen in during the 1991 total solar eclipse, $\alpha_{\max}^* \approx 131°$ (or $\alpha_{\max}^* \approx 2.29$). If $\alpha_{\max} > \alpha_{\max}^*$, then $\psi(\alpha_{\max})$ is negative, so the motion is accelerated. If $\alpha_{\max} < \alpha_{\max}^*$, then $\psi(\alpha_{\max})$ is positive, so the motion is decelerated.

In case of fast rotation, the function of the angle versus time can be written as: $\alpha = \dot{\alpha}_0 t$. We average the equation of motion over a period of rotation ($T = 2\pi / |\dot{\alpha}_0|$). The solution is:

$$v(T) = v_0 - \frac{\pi \mu}{|\dot{\alpha}_0| \, m} \left(\frac{\Omega}{\dot{\alpha}_0}\right)^2 \nabla B \tag{7}$$

5. Numerical Simulation

We solved the equations of the motion in the case of an external magnetic field produced by a magnetic dipole situated just under the photosphere, i.e., at 90 Mm. The equations useful to describe the motion are:

$$\begin{cases} m \left(\ddot{r} - r\dot{\theta}^2 - r \sin^2 \theta \dot{\varphi}^2\right) = -\frac{3\mu M \cos \alpha}{r^4} \sqrt{1 + 3 \cos^2 \theta} \\ m \left(2\dot{r}\dot{\theta} + r\ddot{\theta} - r \sin \theta \cos \theta \dot{\varphi}^2\right) = -\frac{3\mu M \cos \alpha}{r^4} \frac{\cos \theta \sin \theta}{\sqrt{1 + 3 \cos^2 \theta}} \\ m \left(2\dot{r} \sin \theta \dot{\varphi} + 2r \cos \theta \dot{\theta}\dot{\varphi} + r \sin \theta \ddot{\varphi}\right) = 0 \\ I\ddot{\alpha} = \frac{\mu M \sin \alpha}{r^3} \sqrt{1 + 3 \cos^2 \theta} \end{cases}$$

where $M = Br_0^3 / \sqrt{1 + 3 \cos^2 \theta_0} \approx 3.1 \times 10^{32}$ G cm^3 is the value of the external magnetic moment. We solve this system using the forth order Runge-Kutta method, including the correction due to the changes of the magnetic field direction during the plasmoid center of mass motion. We computed the equations using physical quantities close to the ones of the observed plasmoid (Delannée et al. 1998).

The results give the two regimes of oscillations and rotation. The dipole can be accelerated, in this case its motion is such that θ increases. In the case of a decelerated motion, θ decreases. In all initial cases, if there is a speed high enough, the oscillation moves to a rotation and the motion is accelerated.

6. Conclusion

This simple model of a dipole inside a plasmoid shows that the plasmoid can be accelerated out of the corona. The main remarks are about the distribution of the current inside the plasmoid. This current is more complicated and some current surface can exist which modifies this internal force. Furthermore, we have to think about the way that the current ring can support the oscillations or the rotations of their axis of symmetry. Finally, we have to detail the differences

between the two theories and compare the two forces computed in these two theories.

References

Cargill P.J. and Pneuman G.W. 1986, ApJ, 307, 820

Delannée C. and Koutchmy S. 1996, C. R. Acad. Sci. Paris, 322, Série II b, 79

Delannée C., Koutchmy S., Veselovsky I.S. and Zhukov A.N., 1998, A&A, 329, 1111

Koutchmy S. et al., 1994, Solar Dynamic Phenomena and Solar Wind Consequences, ESA SP-373, p. 139

Mullan D.J. 1990, A&A, 232, 520

Pneuman G.W. 1983, ApJ, 265, 408

Priest E.R. 1982, Solar Magnetohydrodynamics, Reidel, Dordrecht, Holland

Vial J.-C., Koutchmy S. and CFH Team 1992, in ESA Workshop on Solar Physics and Astrophysics at Interferometric Resolution, Paris, p. 87

Evolution of a Filament/CH/Magnetic Field Complex

B.A. Ioshpa, E.I. Mogilevsky, and V.N. Obridko
IZMIRAN, 142092, Troitsk, Moscow Region, Russia

Abstract. SOHO and YOHKOH images, as well as Hα filtergrams and magnetograms from IZMIRAN have been used to analyze the evolution of the related solar phenomena – filament, active region, and accompanying pair of coronal holes – during six solar rotations, with an emphasis on the events observed during August–September, 1996. The whole complex has been considered against the large–scale magnetic fields calculated under the potential approximation. A peculiar point has been found along the changing filament. It is shown that the phenomena under investigation (filament, active region, and coronal hole) form a single complex connected with the magnetic field structure.

As shown by Mogilevsky et al. (1997), the large–scale magnetic field (LS-MF), the related active regions (AR), and the coronal holes (CH) nearby form a single complex, united by the magnetic field. This result arises from observations, obtained in 1991, when the activity level was still high. In the present paper, the same complex is considered during a deep cycle minimum in the second half of 1996, when it was naturally isolated from the neighbouring active regions. As a rule, the evolution of an active region affects the structure and stability of an Hα filament, that represents the AR magnetic field topology. Most authors usually consider the formation, stability and decay of Hα filaments on relatively short time scales (e.g., Priest 1982, 1989). Since the lifetimes of LSMF+AR+CH complexes are sometimes several solar rotations, it would be interesting to analyze the evolution of the filament over such a long time interval both inside and outside the AR.

The AR complex under investigation (L=266, ϕ=10S) formed in early August, 1996 and existed during 4 solar rotations until it finally decayed in November, 1996. The analysis is based on solar images in different wavelength ranges from the SOHO and YOHKOH space missions, as well as from ground–based observations, obtained through the Internet. We have also used magnetic field and Hα data, obtained with the solar tower telescope at IZMIRAN.

The view of the complex on August 28 when the AR was at the center of the disk is shown in Figure 1. One can see an active region, Hα filaments, and two coronal holes. One of the holes (the Western CH) is well pronounced and extends far towards the North pole. The Eastern CH is less pronounced and extends towards the South pole. According to our concept, the complex in question consists of the above-mentioned AR, the filaments and the two coronal holes, united by the large–scale magnetic field. The Western CH persisted for only 4 solar rotations, whereas the Eastern one was more stable.

Figure 2 illustrates the large–scale radial magnetic field structure, calculated from the Stanford data (3 arc-min spatial resolution) for 6 successive solar
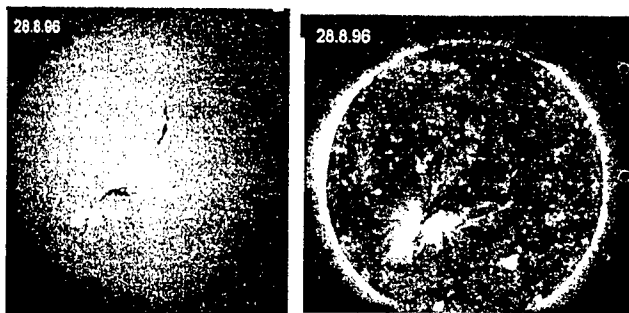
Figure 1.   The August 28, 1966 complex: an Hα filtergram from Big
Bear Observatory (left) and a solar image in FeXII 195Å from the
SOHO EIT (right).

rotations. The maps are centered on the days corresponding to the passage of
the complex near the central meridian. Circles mark the ends of the field lines
calculated under the potential approximation and connecting the source surface
at $2.5R_\odot$ with the inner sphere of unit radius (i.e., the photosphere surface).
The calculation method is described in the literature (e.g., Hoeksema and Scher-
rer 1986 and Mogilevsky et al. 1997). Starting from the source surface, where
the field lines are open by definition and the grid points are evenly spaced, we
have traced every field line down to the photosphere and have found the coor-
dinates of its intersection with the photosphere surface. The ends of the field
lines at this level are not evenly spaced, but are clustered, determining the open
configuration regions.

One can see that the ends of the open field lines in the photosphere are
clustered at the locations of both coronal holes. In July, when the Western
CH is not yet completely shaped, the open field lines end only at the Eastern
CH. The same situation is observed in November, when the Western CH has
already decayed and the Eastern one still exists. In Figure 3, we can see the
configuration of the calculated open field lines for August 30.

Now, let us consider briefly the structure of Hα filaments and note some
peculiarities connected with the evolution of the large–scale magnetic field and
other active phenomena in the Sun.

1. Two filaments were observed inside the complex under investigation: one
   (in the Southern hemisphere) was obviously connected with the AR and
   another (in the Northern hemisphere) lay nearly parallel with the Northern
   part of the Western CH and, as suggested by the analysis of solar images,
   its behaviour was closely connected with that of the respective CH. The
   North filament disappeared at the end of the August rotation. The South
   filament existed during all six solar rotations, but in some periods in Au-
   gust and September it was very unstable, especially inside the AR. This
   instability is probably accounted for by CME activity (on the Eastern limb
   on August 22 and on the solar disk on September 25).
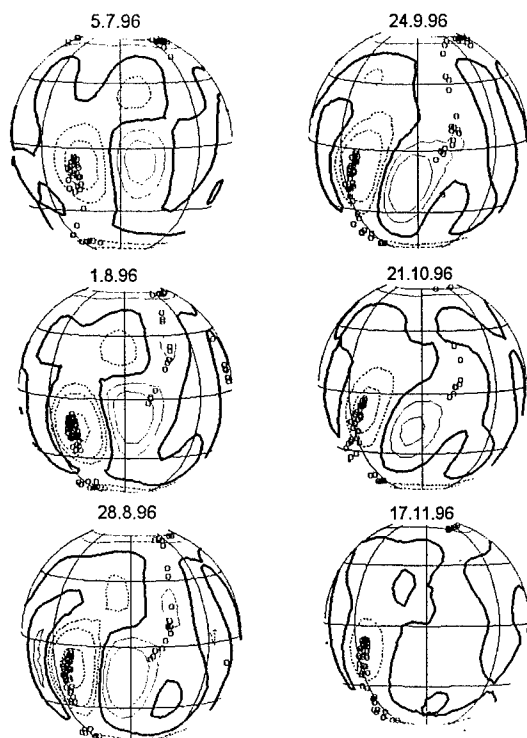
Figure 2.   Large–scale radial magnetic field, calculated from the Stanford data for 6 successive solar rotations. The circles mark the ends of the open field lines.
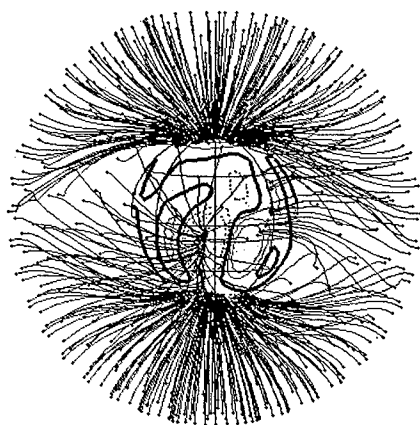
Figure 3.   Open field lines calculated for August 30, 1996.

2. From the beginning of August to the end of October (3 solar rotations), the neutral line of the large–scale magnetic field near AR turned clockwise at an angle of about 45°, and so did the filament aligned with the neutral line. This rotation occurred about a certain part of the filament, rotating with a period of 27 days. We presumed it to be a region of solid–body rotation — the Pivot Point. The existence of such points was established by Mouradian et al. (1987). This hypothesis is corroborated by the Hα filtergrams for August 28–30. One can see a point of enhanced brightness at the filament discontinuity, that exists for 3 days, probably indicating the site of energy supply from subphotospheric layers.

3. The comparison between the Hα filtergrams and SOHO EIT images of the Sun in Fe XII shows that the quiet Northern part of the filament matches the region of reduced EUV radiation, whereas the active part of the Southern filament near the AR coincides with the strip of enhanced EUV radiation.

4. A comparison of the Hα filtergrams and the radio images of the Sun at 17 GHz from the Nobeyama Observatory shows that the stable parts of Hα filaments coincide with radio absorption regions.

References

Hoeksema, J.T. and Scherrer, P.H. 1986, UAG Report 94, WDC-A, Boulder, USA

Mogilevsky, E.I., Obridko, V.N. and Shilova, N.S. 1997, Sol. Phys. 176, 107

Mouradian, Z., Martres, M.J., and Soru–Escout, I. 1987, A&A, 183, 129

Priest, E.R. 1982, Solar Magnetohydrodynamics., D. Reidel Publ. Co., Dordrecht, Holland

Priest, E.R. 1989, Dynamics and Structure of Quiescent Solar Prominences, Kluwer Acad. Publ., Dordrecht, Holland

New Evidence of Chromospheric Evaporation

J. Kašparová[1], P. Kotrč and P. Heinzel

*Astronomical Institute of the Academy of Sciences of Czech Republic,
CZ-251 65 Ondřejov, Czech Republic*

I. F. Nikulin

Sternberg Astronomical Institute, RU-119899 Moscow, Russia

P. Rudawy

*Astronomical Institute of the Wroclaw University, PL-51 622 Wroclaw,
Poland*

Abstract. Hα spectra obtained at Sternberg Astronomical Institute
in Moscow during the gradual phase of the flare on May 16, 1981 are
analysed. The flare-ribbon profiles show a red asymmetry of the emission
peaks, and we interpret this as an absorption in the blue wing of the profile
due to expected upflows. We demonstrate a good correlation between the
observed Hα profiles and those computed with the flare model F1 and
upflows reaching 10 km s^{-1}.

1. Introduction

During the impulsive phase of solar flares, an explosive evaporation scenario
is commonly accepted. Fast upflows in the transition region and simultaneous
downflows in the cooler chromospheric part are usually observed by X-ray spec-
trometers (SMM, Yohkoh) and by optical spectrographs, respectively. In the
case of downflows, a blue asymmetry can be detected, e.g., in the hydrogen
Hα line, which was recently explained by Heinzel et al. (1994). On the other
hand, the plasma flows are much slower during the gradual phase of a typical
two-ribbon flare and, as found by Schmieder et al. (1987), also cool chromo-
spheric plasma exhibits slow upflows, named a 'gentle evaporation', in contrast
to the explosive one. This gentle evaporation as deduced from the Hα line was
evidenced by Schmieder et al. (1987) using the MSDP observations of large
two-ribbon flares. In the flare ribbon, the blue-shifted absorption profile is con-
sistent with upward chromospheric flows of 0.5–10 km s^{-1}. One of the observed
flares was the event of May 16, 1981 for which a series of spectra in Hα and
CaII lines was also recorded at Sternberg Astronomical Institute in Moscow. In
this paper we analyse these Hα spectra and demonstrate that in some places
rather faint emission peaks appear in the ribbons, which is consistent with the

---

[1] Astronomical Observatory Valašské Meziříčí, CZ-757 01 Valašské Meziříčí, Czech Republic

F1 flare model of Machado et el. (1980) but was not observed by MSDP. The observed *red* asymmetry of these emission peaks is then interpreted as a natural consequence of gentle-evaporation upflows in flare ribbons. Note that post-flare loops pertinent to this event have been extensively studied by Schmieder et al. (1987), Heinzel et al. (1992) and, recently, by Gu et al. (1997).
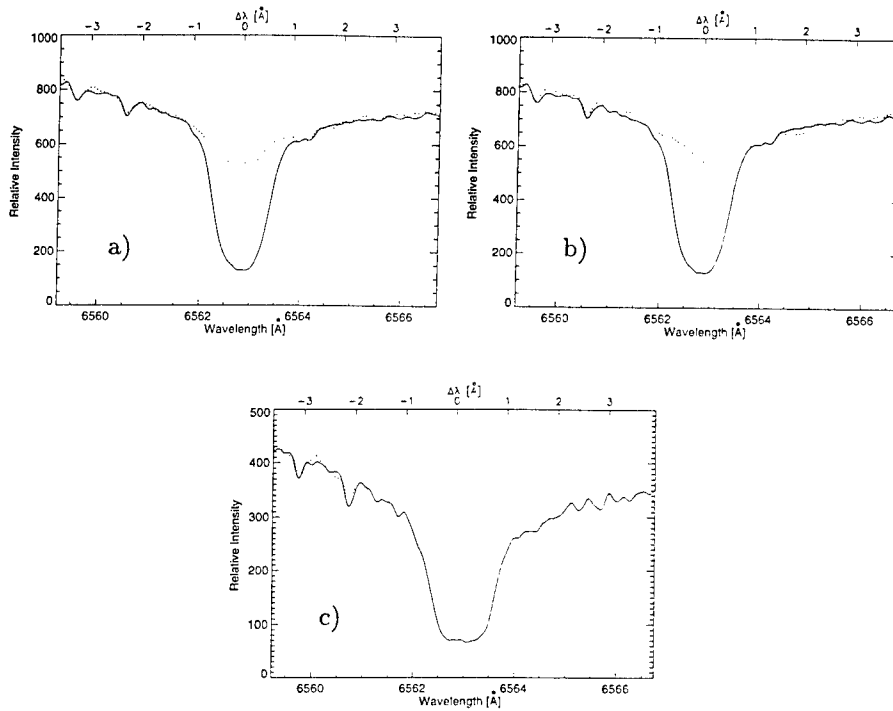
Figure 1.   Profiles of the Hα flare ribbon with the enhanced emission (dashed line); solid line represents the adjacent quiet-chromosphere line profile. **a** – 09:08 UT, **b** – 09:08 UT (closer to the center of the loops), **c** – 09:26 UT.

2. Observations

This 3B/X1 flare (in NOAA active region 3106 on May 16, 1981 at 12N10E) started at 08:14 UT after (07:54 UT) eruption of the filament (Nikulin et al. 1986, Schmieder et al. 1987). The Hα photographic spectra were obtained at the solar tower telescope of the Sternberg Astronomical Institute in Moscow between 09:08 UT and 10:15 UT. As the maximum of the flare was reported at 08:54 UT (Gu et al. 1997), the spectra were taken during the gradual phase of the flare with well developed post-flare loops and flare ribbons. The spectrograph slit was placed on the bright ribbon above which the dark post-flare loops also occurred. Details concerning the telescope and the flare observation were described by Nikulin et al. (1986). The linear dispersion in Hα was 0.7Å mm^{-1}. Spectra were digitized using the Wroclaw Observatory microphotometer.

Hα profiles in the flare ribbon are strongly enhanced as compared to the quiet-Sun profiles – see Figure 1 for three examples. The profile in Figure 1a resembles the MSDP profile displayed in Figure 5 of Schmieder et al. (1987), with a blue-shifted line core and an enhanced emission in the red wing. However, in all our examples we see a small emission peak in the red wing, which is very prominent in Figure 1c. There is also an indication of an emission peak in the blue wing, namely in Figure 1c. Absorption clearly visible in the far red wing (Figures 1b,c) is consistent with large downflows in cool post-flare loops which probably partly overlay the ribbon (see also Figure 5 in Schmieder et al. 1987). The fact that MSDP observations do not indicate small peaks similar to those visible in our Figures 1b,c may be due to the lower spectral resolution, around 0.3 Å or an order of magnitude lower than in our case.

3. Interpretation of the Red Asymmetry

Since the enhanced ribbon emission is roughly similar to that produced by a standard flare model, F1 of Machado et al. (1980), we use this model to simulate numerically the emission peak asymmetry (the temperature structure of the F1 model is shown in Figure 2b). As already mentioned in the Introduc-
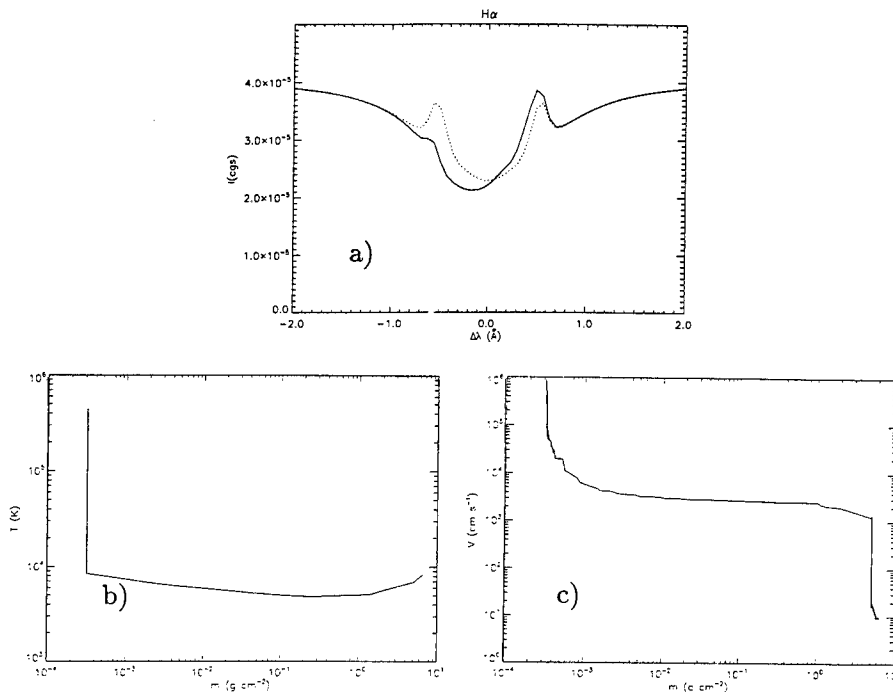
Figure 2.   Results of numerical simulations: **a** – theoretical profiles,
b – temperature structure of F1 model, **c** – velocity field.

tion, Heinzel et al. (1994) have explained a similar, but blue asymmetry by chromospheric downflows imposed on the F1 model. By considering the reverse case of upflows consistent with the gentle evaporation, one would expect the red asymmetry with an enhanced red emission peak, but with the blue-shifted line core (self-absorption profile). This is what we actually observe in our spectra. Numerical simulations of Hα asymmetries in flares were done by Nejezchleba (1998), who also computed an example shown in Figure 2a. The dotted profile with two symmetrical emission peaks corresponds to the static model F1. If we impose an upflow of up to 10 km s^{-1} (Figure 2c) in the upper chromosphere, the red peak becomes more intense and, simultaneously, the line core shifts to blue. The actual effect depends on the velocity gradient, the location of the flow in the chromosphere and the flare model itself (Nejezchleba 1998 and private communication). We see that the blue peak is significantly lowered by an absorption within an upward moving plasma. In this flow, the absorption is lower in the red peak and, thus, we see more emission from deeper ribbon layers. Note that asymmetrical peaks are the result of an interplay between the height variations of the Hα source function and the velocity field.

4.   Conclusions

Comparing line profiles obtained with good spectral resolution with results of numerical simulations, we interpret the red asymmetry of the enhanced Hα emission as a consequence of gentle-evaporation upflows in flare ribbons. This supports the previous conclusions of Schmieder et al. (1987).

References

Gu, X.-M., Ding, Y.-J. and Schmieder, B. 1997 A&A, 324, 289

Heinzel, P., Kotrč, P., Karlický, M. and Švestka, Z. 1994, Solar Phys., 152, 393

Heinzel, P., Schmeieder, B. and Mein, P. 1992, Solar Phys., 139, 82

Machado, M. E., Avrett, E. H., Vernazza, J. E. and Noes, R. W. 1980, ApJ, 242, 336

Nejezchleba, T. 1998, A&A, 127, 607

Nikulin, I. F., Alikaeva, K. V. and Polupan, P. M. 1986, Soln. Dannye, Byull. 1986, No. 1, 89 (*in russian*)

Schmieder, B., Forbes, T. G., Machado, M. E. and Malherbe, J. M. 1987, ApJ, 317, 956

Filament Activity Associated With an Umbral Flare

Wei Li and Jingxiu Wang

Beijing Astronomical Observatory, Chinese Academy of Sciences
Beijing 100080, China

Abstract. An umbral flare in NOAA 6223 was observed at Huairou Solar Observing Station of Beijing Astronomical Observatory. Vigorous filament activity took place in association with this umbral flare. Several filaments formed and/or disappeared, leaving the magnetic neutral lines pointing to or rooted in the P spot in which the umbral flare occurred. We describe the observed configuration and evolution of the vector magnetic fields in the photosphere, and Doppler velocity patterns in the chromosphere during the course of the umbral flare and related filament activity.

1. Introduction

In most case flare patches are in plages. They usually avoid sunspots and, even when they expand, they prefer the spot-free space. Often the flare's expansion stops at the boundary of a large spot. Some large flares do penetrate into the umbra of a spot or spot group. The umbral flare named by Tang (1978) differs from the above-mentioned flares in that the umbra flare patch is confined to the umbra; more importantly, it originates in the umbra. It is not the result of the spreading or expansion of the flare patch. In a survey of many years of H_β movies, only five umbral flares were found (Tang 1978). Since then, two flares which were characterized by umbral flares in the H_β chromospheric line were observed in active region (AR) 6223 at Huairou Solar Observing Station (HSOS) on August 23, 1990. One of the two flares was a 1N/C3.9 flare, and the other a microflare. The dominant P spot with no bridge in the umbra nor gap in the penumbra has north polarity. The F spot is very tiny and has south polarity. In this paper, we shall describe for the first time the observed configuration and evolution of the vector magnetic fields in the photosphere, and Doppler velocity patterns in the chromosphere in the course of the 1N/C3.9 umbral flare and related filament activity.

2. Filament Activity

Figure 1 shows the filtergrams of the active region in H_β chromospheric line. At least six filaments existed within the active region before and during the flares. They pointed to or were rooted in the P spot, and formed and/or disappeared before the flare. We could easily see the filament 2, 5 and dimly see the filament 1 and 4 at 00:54 UT. Later, the filament 2, 4 became darker and thicker and filament 3 appeared, a part of the filament 5 broke, and the position and shape

of the filament 1 changed a little at 03:21 UT. Nevertheless, all of the filaments still were rooted in the umbra of the P spot at 03:21 UT, except the filament 3. It is interesting that a segment of the filament 1 became darker and thicker and another segment of the filament 1 became bright at this time. At 04:41 UT, the filament 2 and 1 were broken, and 3 and 5 disappeared. At 06:53 UT, the filament 1 with a brightening feature appeared again, and filament 2 almost completely disappeared. At 07:30 UT, the filament 2 appeared again and the umbral flare occurred. A segment of the filament 4 became brighter and broken at 07:39 UT. After the flare the filaments 2 and 5 appeared again. Table 1 summarizes the time sequence of filament activities in association with the umbral flares.

Table 1, Temporal Relationship Between Flares and Filaments

Filament	Appearance	Activation	Disappearance
1	00:54	03:21,04:41,06:53	
2	00:54,07:30,08:16	03:21,04:41	06:53,07:33
3	03:21		04:41
4	00:54	03:21,07:30,07:39	
5	00:54	03:21	04:41
Flare	07:30	maximum at 07:39	08:16

3.   Magnetic Field and Velocity Field

Figure 2 shows the vector magnetograms of the active region, and the positions of the flare and the filaments. We can see that both of the flare ribbons 1 and the knotted-like ribbon 2 were far from the neutral line. There was only north polarity longitudinal field and 750–1250 G transverse field in the photosphere underlying a large segment of the filament 1, 2, 4, and 5 which was directly rooted in the umbra of the P spot. However, the other foot of the filament 1, 2 and 4 was located in the polarity inversion zone. In the filament's vicinity, the main sites of new emergent flux and flux cancellations are marked by a square and 'A'. At 00:31 UT, N polarity dominated in the square and, later, S polarity flux emerged and grew quickly in area and in strength. By 07:23 UT, S polarity has already dominated the square in the vicinity of the filament and in the filament channel. We also found that flux cancellation around the mark 'A' in Figure 2 occurred during the period 00:31 to 07:23 UT. We found that the strength of the transverse field in the area of the p spot did not change, but the alignments obviously changed during the period 23:26 to 07:13 UT. Specifically, the alignments of the transverse fields in the north half part of the p spot changed counterclockwise and in the south half part of the p spot changed clockwise.

It seems that the filament 1, 2, 4 and 5 could be divided into two segments along the direction of the filament axis, and the red-shifted feature (downflow) in a large segment of the filament was observed pointing to or rooted in the p spot. The blue-shifted feature in the remaining parts of the filament, especially, in the middle part of the filament, was observed before the flare. At 03:21 UT, a segment of the filament 1 brightened, and at 06:53 UT the full filament 1 brightened again. Therefore, as a result the Doppler velocity pattern showed concentrated red-shift globally, i.e., material was flowing into the P spot along
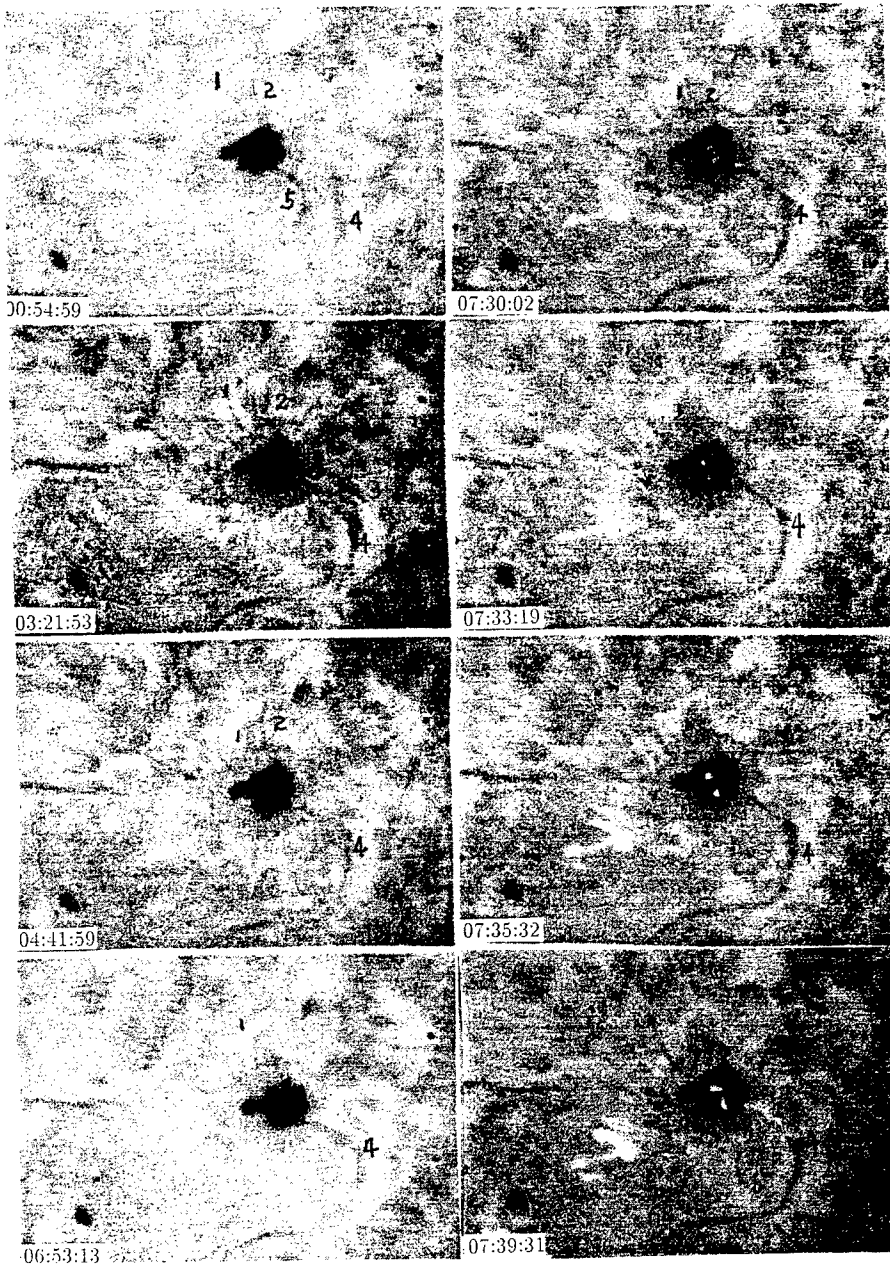
Figure 1.   The filtergrams of the active region AR 6223 in the Hβ chromospheric line.
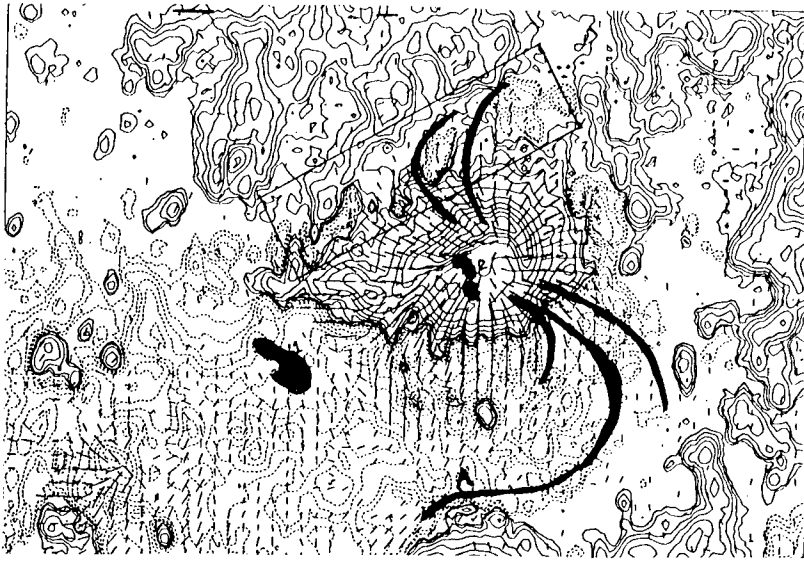
Figure 2. The vector magnetogram of the active region AR 6223.

the filaments. At 07:30 UT, the umbral flare occurred.

4.   Summary

The fact that a flare occurred in the umbra indicates that energy was transported downward along the field lines which were longer than those close to the magnetic neutral line, or that the magnetic field was of a very complicated configuration in the higher atmosphere. Being a rare phenomenon, it is totally unknown what particular configuration of the evolution of the magnetic field causes an umbral flare. However, it has been shown that vigorous filament activity is associated with the umbral flares. Those filaments have one foot rooted in the main P sunspot (McIntosh 1972), while the other outer foot is located in the polarity inversion zones where there is continuous flux emergence and cancellation. We speculate that at the outer feet of the filaments the magnetic lines of force are opened by magnetic reconnection. High energy particles precipitate along the opened field lines into the umbral atmosphere, causing the umbral flares. This scenario might explain the observed field evolution and velocity pattern.

References

McIntosh, P. S. 1972, Rev. Geophys. Space Phys., 10, 837
Tang, F. 1987, Sol. Phys., 60, 119

Global Patterns

Filaments and the Solar Dynamo

N. Seehafer

Institut für Physik, Universität Potsdam, PF 601553, D-14415 Potsdam, Germany

Abstract.
   Filaments are a global phenomenon and their formation, structure and dynamics are determined by magnetic fields. So they are an important signature of the solar magnetism. The central mechanism in traditional mean-field dynamo theory is the alpha effect and it is a major result of this theory that the presence of kinetic or magnetic helicities is at least favourable for the effect. Recent studies of the magnetohydrodynamic equations by means of numerical bifurcation-analysis techniques have confirmed the decisive role of helicity for a dynamo effect. The alpha effect corresponds to the simultaneous generation of magnetic helicities in the mean field and in the fluctuations, the generation rates being equal in magnitude and opposite in sign. In the case of statistically stationary and homogeneous fluctuations, in particular, the alpha effect can increase the energy in the mean magnetic field only under the condition that also magnetic helicity is accumulated there. Generally, the two helicities generated by the alpha effect, that in the mean field and that in the fluctuations, have either to be dissipated in the generation region or to be transported out of this region. The latter may lead to the appearance of helicity in the atmosphere, in particular in filaments, and thus provide valuable information on dynamo processes inaccessible to in situ measurements.

1.   Introduction

The dynamo for the global solar magnetic field is assumed to operate in the convection zone and to consist of the cyclic generation of a toroidal (azimuthal) field from a poloidal one (whose field lines lie in planes containing the rotational axis of the Sun) and the regeneration of a poloidal field from a toroidal one. If there exists a poloidal field, then a toroidal field is generated very effectively by differential rotation. But the regeneration of the poloidal field represents a problem. For this reason the theory of the turbulent dynamo has been developed (Krause and Rädler 1980). The central mechanism in this theory is the generation of a mean, or large-scale, electromotive force $\mathcal{E}$ by turbulently fluctuating, or small-scale, parts of velocity and magnetic field, and it is a major result of the theory that the presence of kinetic and magnetic helicities is favourable for a so-called alpha effect, i.e., a non-vanishing component $\mathcal{E}_{\parallel} = \alpha \langle \mathbf{B} \rangle$ of $\mathcal{E}$ along the mean magnetic field $\langle \mathbf{B} \rangle$. The densities per unit volume of kinetic, magnetic

and current helicity are defined by

$$H_{\mathrm{K}} = \mathbf{v} \cdot (\nabla \times \mathbf{v}),\; H_{\mathrm{M}} = \mathbf{A} \cdot \mathbf{B},\; H_{\mathrm{C}} = \mathbf{B} \cdot (\nabla \times \mathbf{B}), \tag{1}$$

where $\mathbf{v}$, $\mathbf{B}$ and $\mathbf{A}$ denote fluid velocity, magnetic field and a magnetic vector potential. H_{M} and H_{C} are closely related (cf., e.g., Seehafer 1990).

The usually quoted estimate for the alpha-effect parameter α is (Krause and Rädler 1980, Eq. (3.31))

$$\alpha \approx -\frac{\tau}{3} \langle \mathbf{v}' \cdot \nabla \times \mathbf{v}' \rangle, \tag{2}$$

where τ is the correlation time of the velocity fluctuations $\mathbf{v}'$ (angular brackets denote averages and primes the corresponding residuals). This estimate, which relates α to the kinetic helicity of the fluctuations, is derived under the following approximations and assumptions:

1) The first order smoothing approximation (FOSA), which consists of neglecting the unpleasant term $\nabla \times (\mathbf{v}' \times \mathbf{B}' - \langle \mathbf{v}' \times \mathbf{B}' \rangle)$ in the equation for the time evolution of the magnetic fluctuations. This approximation is valid for, e.g., wave turbulence, where a disturbance does not lead to the onset of convection but only to a wave. It is, however, rather doubtful in the case of conventional, convective turbulence, i.e., in the solar convection zone.

2) $\langle \mathbf{v} \rangle = \mathbf{0}$.

3) $\langle \mathbf{B} \rangle = constant$ (in space and time).

4) Statistically stationary and homogeneous fluctuations.

5) η (magnetic diffusivity) $\to 0$.

The alpha effect is more directly related to *current* helicity than to kinetic helicity, namely (see Sec. 3 and Keinigs 1983, Matthaeus et al. 1986, Rädler & Seehafer 1990, Seehafer 1994a, b, Seehafer 1996),

$$\alpha \stackrel{\mathrm{def}}{=} \frac{\mathcal{E} \cdot \langle \mathbf{B} \rangle}{\langle \mathbf{B} \rangle^2} = -\frac{\eta}{\langle \mathbf{B} \rangle^2} \langle \mathbf{B}' \cdot (\nabla \times \mathbf{B}') \rangle. \tag{3}$$

For deriving this relation, of the above five conditions only the fourth one is needed. On the other hand, the traditional estimate, Eq. (2), gives an information on which type of *fluid motion* can produce an alpha effect.

The majority of dynamo studies, in particular those in the frame of mean-field theory, have been kinematic. Kinematic dynamo theory studies the conditions under which a prescribed velocity field can amplify, or at least prevent from decaying, some seed magnetic field, completely disregarding the equations governing the motion of the fluid. A step towards a self-consistent, nonlinear theory is taken by models containing, mainly on the base of physically plausible assumptions, a back reaction of a generated mean magnetic field on the generating turbulent fluid motions. Here, in particular, models with the so-called α-quenching are studied, in which the alpha-effect parameter α is a function of the mean magnetic field (e.g., Rädler et al. 1990).

In principle totally self-consistent are numerical simulations of the complete system of the nonlinear magnetohydrodynamic (MHD) equations (e.g., Meneguzzi et al. 1981, Meneguzzi and Pouquet 1989, Glatzmaier 1984, 1985). In some sense still a step further goes a bifurcation, or qualitative, analysis,

by which one tries to get an overview of the attractor structure of the system, i.e., of the set of the possible time-asymptotic states. In Sec. 2 an example of a numerical bifurcation analysis is presented. The Reynolds numbers reachable here presently are by many orders of magnitude smaller than those at the Sun. Therefore, the statistical mean-field approach remains indispensible. In Sec. 3 it is demonstrated that the alpha effect generates simultaneously and at equal rates fluctuating (turbulent) and mean-field magnetic helicities of opposite signs. Section 4 then gives a final discussion.

2. Bifurcation Analysis of a Magnetofluid with Helical Forcing

Simple examples of strongly helical flows are provided by the so-called ABC flows (see, e.g., Dombre et al. 1986), given by

$$\mathbf{v} = \mathbf{v}_{ABC} = (A \sin z + C \cos y,\ B \sin x + A \cos z,\ C \sin y + B \cos x), \quad (4)$$

where A, B and C denote constant coefficients. The ABC flows are steady solutions of the incompressible Navier–Stokes equation [Eq. (6) below with the magnetic field dropped] if an external body force

$$\mathbf{f} = -\Delta \mathbf{v}_{ABC} = \mathbf{v}_{ABC} \quad (5)$$

– in the following called ABC forcing – just compensating for viscous losses is applied. Here we report results of numerical studies of the complete system of the incompressible MHD equations with this kind of forcing as well as with a generalized ABC forcing with a variable degree of helicity. Comprehensive accounts of the corresponding studies may be found in Seehafer et al. (1996), Feudel et al. (1995, 1996), and Schmidtmann et al. (1998).

We use the incompressible MHD equations in the nondimensional form

$$\frac{\partial \mathbf{v}}{\partial t} + (\mathbf{v} \cdot \nabla)\mathbf{v} = \Delta \mathbf{v} - \nabla p - \frac{1}{2}\nabla \mathbf{B}^2 + (\mathbf{B} \cdot \nabla)\mathbf{B} + \mathbf{f}, \quad (6)$$

$$\frac{\partial \mathbf{B}}{\partial t} + (\mathbf{v} \cdot \nabla)\mathbf{B} = P_m^{-1}\Delta \mathbf{B} + (\mathbf{B} \cdot \nabla)\mathbf{v}, \quad (7)$$

$$\nabla \cdot \mathbf{v} = 0,\ \nabla \cdot \mathbf{B} = 0, \quad (8)$$

where p is the thermal pressure and P_m the magnetic Prandtl number (the ratio between magnetic diffusivity and kinematic viscosity). Periodic boundary conditions are applied and the spatial means of $\mathbf{v}$ and $\mathbf{B}$, and consequently also of $\mathbf{f}$ are assumed to vanish. The ABC forcing, given by Eqs. (4) and (5), is used with with

$$A = B = C = R \quad (9)$$

where R is referred to as Reynolds number. For this forcing the MHD equations are equivariant with respect to a discrete symmetry group which is isomorphic to the octahedral group O (the rotation group of the cube).

Besides the pure ABC forcing also a generalized ABC forcing is applied, given by

$$\mathbf{f} = (1 - \lambda)\mathbf{v}_{ABC} + \lambda \mathbf{v}_{ABC}^-, \quad (10)$$
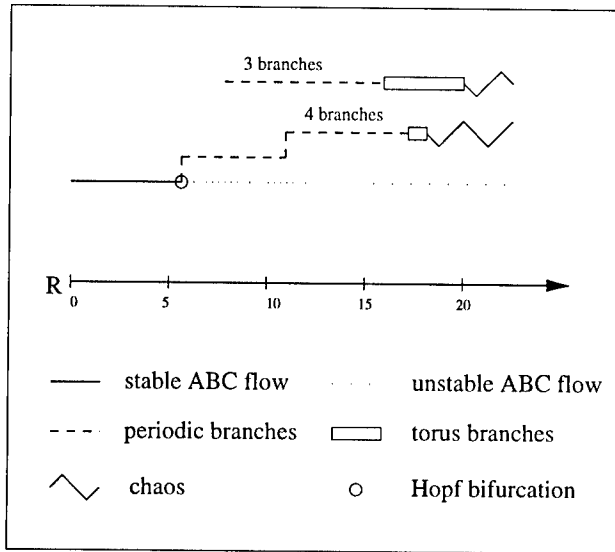
Figure 1.   Schematic bifurcation diagram for pure ABC forcing.

where

$$\mathbf{v}_{ABC}^{-} = (A\cos z + C\sin y,\ B\cos x + A\sin z,\ C\cos y + B\sin x) \qquad (11)$$

and λ is a parameter varying between 0 and 0.5. $\mathbf{v}_{ABC}^{-}$ satisfies $\nabla \times \mathbf{v}_{ABC}^{-} = -\mathbf{v}_{ABC}^{-}$, and for $\lambda = 0.5$ its addition in the forcing term "kills" the helicity on average in the volume, while $\lambda = 0$ corresponds to the original ABC forcing.

We restrict ourselves to the case of $P_m = 1$ and R and λ are our bifurcation parameters.

An overview of the bifurcation structure for pure ABC forcing is depicted in Figure 1. For weak forcing (small R), there exists a stable stationary solution, namely the ABC flow [given by Eq. (4)] with vanishing magnetic field, and all system trajectories are attracted by this solution. If R is raised, the steady state loses stability in a Hopf bifurcation, leading to a periodic solution with a magnetic field as the only time-asymptotic state. The periodic magnetic solution is at first symmetric to the full group O, but for further raised R it bifurcates into four new periodic solutions, which can be be transformed into each other by certain elements of O. Besides that another periodic magnetic branch appears, consisting of three solutions which can be transformed into each other. Both branches undergo secondary Hopf bifurcations leading to quasiperiodic or torus solutions, which in turn eventually decay to chaotic states.

The volume-averaged magnetic helicity [cf. Eq. (1)] is negative, thus opposite in sign to the kinetic helicity, as also found by Galanti et al. (1992).

For the case of the generalized ABC forcing given by Eq. (10), the locations of primary and secondary bifurcations in the parameter plane are shown in Figure 2. For weak forcing (small R), there always exists a stable stationary,
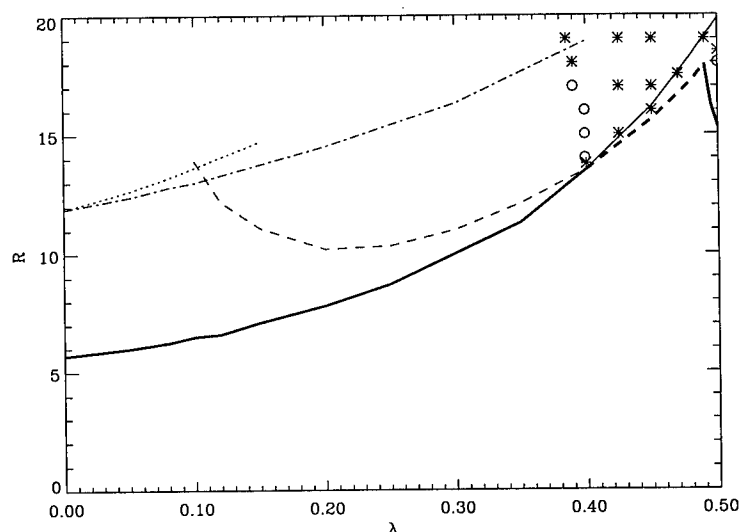
Figure 2. Locations of primary and secondary bifurcations of the original stationary solution in the λ-R plane. Solid line and dashed-dotted line: a single pair of complex conjugate eigenvalues crosses the imaginary axis; dashed line: two real eigenvalues pass through zero; dotted line: two pairs of complex conjugate eigenvalues cross the imaginary axis. Asterisks indicate points at which, by means of simulations, non-magnetic chaotic time-asymptotic states have been found, while circles correspond to magnetic periodic attractors.

nonmagnetic, globally attracting solution (which coincides with the the original ABC flow only in the special case of $\lambda = 0$). Keeping fixed λ and raising R, this steady-solution branch has been traced. Thick solid and dashed lines, respectively, indicate the primary bifurcation of the original steady state. For $\lambda < 0.4$ the steady state loses stability in a Hopf bifurcation, but at $\lambda = 0.4$ the type of the first bifurcation, as well as the character of the time-asymptotic states after this bifurcation, change. While for $\lambda < 0.4$ a magnetic periodic state is the (only) new attractor, for λ between 0.4 and 0.5 new non-magnetic states emerge. Only if the helicity exceeds a certain threshold value, a Hopf bifurcation leads to a magnetic periodic state (i.e., to a dynamo effect). For helicities below the threshold value the transition is more complex, but always the ensuing time-dependent states, including chaotic ones, are non-magnetic (which does not exclude, of course, a dynamo effect for higher Reynolds numbers).

3. Alpha Effect and the Generation of Magnetic Helicity

The mean value of the magnetic helicity can be written as the sum of two contributions resulting from the mean and fluctuating magnetic fields, respectively,

namely

$$\langle H_{\mathrm{M}} \rangle = H_{\mathrm{M}}^{\mathrm{MEAN}} + H_{\mathrm{M}}^{\mathrm{FLUC}}, \tag{12}$$

with

$$H_{\mathrm{M}}^{\mathrm{MEAN}} = \langle \mathbf{A} \rangle \cdot \langle \mathbf{B} \rangle, \quad H_{\mathrm{M}}^{\mathrm{FLUC}} = \langle \mathbf{A}' \cdot \mathbf{B}' \rangle. \tag{13}$$

For the time evolutions of $H_{\mathrm{M}}^{\mathrm{MEAN}}$ and $H_{\mathrm{M}}^{\mathrm{FLUC}}$ one finds (Seehafer 1996)

$$
\frac{\partial H_{\mathrm{M}}^{\mathrm{MEAN}}}{\partial t} = \quad -2\eta \nabla \times \langle \mathbf{B} \rangle \cdot \langle \mathbf{B} \rangle + 2\mathcal{E} \cdot \langle \mathbf{B} \rangle
$$
$$
+ \left(\frac{\partial H_{\mathrm{M}}^{\mathrm{MEAN}}}{\partial t} \right)_{\mathrm{transport}} \tag{14}
$$

and

$$
\frac{\partial H_{\mathrm{M}}^{\mathrm{FLUC}}}{\partial t} = \quad -2\eta \langle \nabla \times \mathbf{B}' \cdot \mathbf{B}' \rangle - 2\mathcal{E} \cdot \langle \mathbf{B} \rangle
$$
$$
+ \left(\frac{\partial H_{\mathrm{M}}^{\mathrm{FLUC}}}{\partial t} \right)_{\mathrm{transport}} \tag{15}
$$

These equations show that the alpha effect (the terms $\mp 2\mathcal{E} \cdot \langle \mathbf{B} \rangle$ on the right-hand sides) corresponds to the simultaneous generation of magnetic helicities in the mean field and in the fluctuations, the generation rates being equal in magnitude and opposite in sign. The mean total magnetic helicity, which is an invariant of ideal magnetohydrodynamics, is not influenced by the alpha effect. This may equally be considered as a transfer of magnetic helicity between the fluctuating (or small-scale) and the mean (or large-scale) fields, mediated by the alpha effect, or as a helicity cascade (cf., Frisch et al. 1975, Pouquet et al. 1976, Stribling and Matthaeus 1990, 1991).

Consider now a situation in which the magnetic fluctuations are statistically stationary. Actually it is assumed throughout traditional turbulent-dynamo theory that the magnetic fluctuations have settled down to a statistically stationary state. If then, furthermore, the fluctuations are spatially homogeneous, Eq. (15) implies that the alpha-effect parameter α is connected to the mean current helicity of the fluctuations by Eq. (3).

Let us, next, examine under which conditions there is a turbulent dynamo effect, i.e., under which conditions the turbulent emf increases the energy in the mean magnetic field. For that purpose we assume $\langle \mathbf{v} \rangle = \mathbf{0}$, since we are not interested in the dynamo action of the mean flow. For the change of the mean-field magnetic energy density one then finds

$$\frac{\partial}{\partial t} \frac{\langle \mathbf{B} \rangle^2}{2} = -\eta (\nabla \times \langle \mathbf{B} \rangle)^2 + \mathcal{E} \cdot (\nabla \times \langle \mathbf{B} \rangle) + \nabla \cdot (\text{Poynting flux}), \tag{16}$$

which shows that the alpha effect contributes to the growth of the mean magnetic field if $\alpha(\nabla \times \langle \mathbf{B} \rangle \cdot \langle \mathbf{B} \rangle) > 0$ or, equivalently (see the definition of α in Eq. (3), $\mathcal{E} \cdot \langle \mathbf{B} \rangle (\nabla \times \langle \mathbf{B} \rangle \cdot \langle \mathbf{B} \rangle) > 0$. For $\mathcal{E} \cdot \langle \mathbf{B} \rangle (\nabla \times \langle \mathbf{B} \rangle \cdot \langle \mathbf{B} \rangle) < 0$ the alpha effect lowers the mean-field energy.

Consider again the case of statistically stationary and homogeneous fluctuations. The condition for a dynamo action of the alpha effect, $\mathcal{E} \cdot \langle \mathbf{B} \rangle (\nabla \times \langle \mathbf{B} \rangle \cdot$

$\langle \mathbf{B} \rangle) > 0$, then becomes $\eta \langle \nabla \times \mathbf{B}' \cdot \mathbf{B}' \rangle (\nabla \times \langle \mathbf{B} \rangle \cdot \langle \mathbf{B} \rangle) < 0$, i.e., as first noted by Keinigs and Gerwin (1986), the current helicities in the fluctuating and the mean magnetic fields must have opposite signs.

Assume now that the alpha effect really overcomes the dissipative term in Eq. (16), i.e., $\mathcal{E} \cdot (\nabla \times \langle \mathbf{B} \rangle) > \eta (\nabla \times \langle \mathbf{B} \rangle)^2$. By using Eq. (3) and the Schwarz inequality $(\nabla \times \langle \mathbf{B} \rangle)^2 \langle \mathbf{B} \rangle^2 \geq (\nabla \times \langle \mathbf{B} \rangle \cdot \langle \mathbf{B} \rangle)^2$ one then finds as a necessary condition for the growth of $\langle \mathbf{B} \rangle^2$

$$-\langle \nabla \times \mathbf{B}' \cdot \mathbf{B}' \rangle (\nabla \times \langle \mathbf{B} \rangle \cdot \langle \mathbf{B} \rangle) > (\nabla \times \langle \mathbf{B} \rangle \cdot \langle \mathbf{B} \rangle)^2. \tag{17}$$

That is, the current helicity of the fluctuations must exceed that of the mean field by modulus.

Condition (17) has an implication for the evolution of the mean-field magnetic helicity: Since $|\eta \langle \nabla \times \mathbf{B}' \cdot \mathbf{B}' \rangle| = |\mathcal{E} \cdot \langle \mathbf{B} \rangle|$ due to the assumed stationarity and homogeneity of the fluctuations, $|\eta \nabla \times \langle \mathbf{B} \rangle \cdot \langle \mathbf{B} \rangle| < |\mathcal{E} \cdot \langle \mathbf{B} \rangle|$. Then, according to Eq. (14) helicity is accumulated in the mean magnetic field, with sign given by the sign of $\mathcal{E} \cdot \langle \mathbf{B} \rangle$, i.e., by the sign of α.

4. Discussion: The Helicity-Sign Puzzle

The two helicities generated by the alpha effect, that in the mean field and that in the fluctuations, have either to be dissipated in the generation region or to be transported out of this region. The latter may lead to the appearance of helicity in the atmosphere, e.g., in filaments (Martin 1998, these proceedings), and through solar eruptions even in interplanetary space. There has been accumulated strong evidence that the atmospheric and interplanetary magnetic helicity is predominantly negative in the northern and positive in the southern hemisphere (Seehafer 1990, Rust 1994, Rust and Kumar 1994, Pevtsov et al. 1995, Abramenko et al. 1996). It is not clear yet, however, whether the fields observed in the atmosphere, e.g., in active regions, can be interpreted as mean fields or fluctuations in the sense of mean-field theory.

Assume that the observed fields are either mainly mean fields or mainly fluctuations. The magnetic helicity accumulated in the mean field has the same sign as the alpha-effect parameter α. So α should be negative in the northern hemisphere if the observed fields are mean fields. Vice versa, α should be positive in the northern hemisphere if the atmospheric fields have to be interpreted as fluctuations. For a proper propagation of the dynamo waves (from the poles to the equator), a negative (positive) α requires a decrease (an increase) of the angular velocity of the solar rotation with depth in the convection zone. Helioseismological measurements (Christensen-Dalsgaard and Schou 1988) indicate near the equator a decrease with depth (the decrease occurs rather low in the convection zone). Consequently, $\alpha < 0$ in the northern hemisphere and the fields observed in active regions are mean fields. It will be interesting to carry out improved helicity measurements in the solar atmosphere as well as in the solar wind and to analyze them with respect to signatures of the two helicities.

References

Abramenko, V. I., Wang, T. and Yurchishin, V. B. 1996, Solar. Phys., 168, 75

Christensen-Dalsgaard, J. and Schou, J. 1988, in Seismology of the Sun and Sun-like Stars, V. Domingo and E. J. Rolfe (eds.), ESA SP-286, p. 385

Dombre, T., Frisch, U., Greene, J. M., Hénon, M., Mehr, A. and Soward, A. M. 1986, J. Fluid Mech., 167, 353

Feudel, F., Seehafer, N. and Schmidtmann O. 1995, Phys. Lett. A, 202, 73

Feudel, F. et al. 1996, Phys. Rev. E, 54, 2589

Frisch, U. et al. 1975, J. Fluid Mech., 68, 769

Galanti, B., Sulem, P. L. and Pouquet, A. 1992, Geophys. Astrophys. Fluid Dyn., 66, 183

Glatzmaier, G. A. 1984, J. Comp. Phys., 55, 461

Glatzmaier, G. A. 1985, Geophys. Astrophys. Fluid Dyn., 31, 137

Keinigs, R. K. 1983, Phys. Fluids, 26, 2558

Keinigs, R. and Gerwin, A. 1986, IEEE Trans. Plasma Sci., PS-14, 858

Krause, F. and Rädler, K.-H. 1980, Mean-Field Magnetohydrodynamics and Dynamo Theory, Akademie-Verlag, Berlin

Matthaeus, W. H., Goldstein, M. L. and Lantz, S. R. 1986, Phys. Fluids, 29, 1504

Meneguzzi, M. and Pouquet, A. 1989, J. Fluid Mech., 205, 297

Meneguzzi, M., Frisch, U. and Pouquet, A. 1981, Phys. Rev. Lett., 47, 1060

Pevtsov, A. A., Canfield, R. C. and Metcalf, T. R. 1995, ApJ, 440, L109

Pouquet, A., Frisch, U. and Léorat, J. 1976, J. Fluid Mech., 77, 321

Rädler, K.-H. and Seehafer, N. 1990, in Topological Fluid Mechanics, H. K. Moffatt and A. Tsinober (eds.), Cambridge Univ. Press, Cambridge, p. 157

Rädler, K.-H. et al. 1990, A&A, 239, 413

Rust, D. M. 1994, Geophys. Res. Lett., 21, 241

Rust, D. M. and Kumar, A. 1994, Solar Phys., 155, 69

Schmidtmann, O., Feudel, F. and Seehafer, N. 1997, Int. J. Bifurcation and Chaos 7(9), in press

Seehafer, N. 1990, Solar Phys., 125, 219

Seehafer, N. 1994a, A&A, 284, 593

Seehafer, N. 1994b, Europhys. Lett., 27, 353

Seehafer, N. 1996, Phys. Rev. E, 53, 1283

Seehafer, N., Feudel, F. and Schmidtmann, O. 1996, A&A, 314, 693

Stribling, T. and Matthaeus, W. H. 1990, Phys. Fluids B, 2, 1979

Stribling, T. and Matthaeus, W. H. 1991, Phys. Fluids B, 3, 1848

Solar and Stellar Dynamo Waves Under Asymptotic Investigation

Kirill M. Kuzanyan[1]

Department of Mathematics, University of Exeter, Laver Building, North Park Road, Exeter EX4 4QE, U.K.

Abstract. The main magnetic activity of the Sun can be visualised by Maunder butterfly diagrams which represent the spatio-temporal distribution of sunspots. Besides sunspots there are other tracers of magnetic activity, like filaments and active regions, which are observable over a wider latitudinal range of the Sun. Both these phenomena allow one to consider a complete picture of solar magnetic activity, which should be explained in the framework of one relatively simple model.

A kinematic $\alpha\omega$-dynamo model of the magnetic field's generation in a thin convection shell with nonuniform helicity for large dynamo numbers is considered in the framework of Parker's migratory dynamo. The obtained asymptotic solution of equations governing the magnetic field has a form of a modulated travelling dynamo wave. This wave propagates over the most latitudes of the solar hemisphere equatorwards, and the amplitude of the magnetic field first increases and then decreases with the propagation. Over the subpolar latitudes the dynamo wave reverses, there the dynamo wave propagates polewards and decays with latitude. Butterfly diagrams are plotted and analyzed.

There is an attractive opportunity to develop a more quantitatively precise model taking into account helioseismological data on differential rotation and fitting the solar observational data on the magnetic field and turbulence, analyzing the helicity and the phase shift between toroidal and poloidal components of the field.

1. Parker's Migratory Dynamo

We are dealing with Parker's migratory dynamo (Parker 1955). This model is a strong simplification of dynamo processes of the solar interior. It is enough to remember that Parker's migratory dynamo gives only a kinematic description of the solar dynamo wave and does not consider nonlinear processes. Nevertheless, it happens that this simple model yields for the value under consideration the results which are comparable with observations.

Mean field magnetohydrodynamics in a thin, differentially rotating convection shell for the axisymmetric case and extremely large dynamo numbers gives

---

[1] Also at: Chair of Mathematics, Faculty of Physics, Moscow State Univ., Moscow 119899, Russia

the following equations governing a dynamo wave (Parker 1955, see also Stix 1989):

$$\frac{\partial A}{\partial t} = \alpha(\theta)B + \frac{\partial^2 A}{\partial \theta^2}, \qquad (1a)$$

$$\frac{\partial B}{\partial t} = -DG(\theta)\cos\theta \frac{\partial A}{\partial \theta} + \frac{\partial^2 B}{\partial \theta^2}. \qquad (1b)$$

Here B is the azimuthal component of the mean magnetic field, A is proportional to the azimuthal component of the magnetic potential, D is the dimensionless dynamo number which characterizes the intensity of the sources of the magnetic field generation. We consider here the case $D < 0$, which gives a basically equatorward dynamo wave. θ is the latitude in the shell that is measured from the solar equator, $\alpha(\theta)$ is the mean helicity, and $G(\theta)$ the radial gradient of the angular rotation, which are normalized with respect to maximum of their values, α_* and G_*, respectively.

An asymptotic solution of equations (1) for $|D| \gg 1$ has been obtained by Kuzanyan and Sokoloff (1995) using the **WKBJ method**. At leading order with respect to small parameter $|D|^{-1/3}$, it has the following form:

$$\begin{pmatrix} A \\ |D|^{-2/3}B \end{pmatrix} = \exp\left(i|D|^{1/3}S + |D|^{2/3}\Gamma_0 t + \ldots\right)(f_0 + \ldots), \qquad (2)$$

where S and vector f_0 are complex functions of latitude θ.

The asymptotic solution under consideration should enable the dynamo wave to decay at locations remote from maximum of the sources of generation, which are in our model represented by function $\hat{\alpha}(\theta) = \alpha(\theta)\cos\theta$. So the solution should vanish remote from the domain where $\hat{\alpha}$ is maximum. In other words, we consider the dynamo wave, decaying at the pole and the equator.

2.   Properties of the Asymptotic Solution

1. The **maximum of the solution** is, however, situated at point $\theta_1 < \theta_0$ at which $Im\, S(\theta)$ is minimum and for which

$$\hat{\alpha}_1 = \frac{\hat{\alpha}(\theta_1)}{\hat{\alpha}_*} = \frac{9\sqrt{3}}{16\sqrt{2}\sqrt{\sqrt{3}-1}} \approx 0.81\,,$$

where $\hat{\alpha}_* = \hat{\alpha}(\theta_0)$ is maximum of function $\hat{\alpha}(\theta)$ (the sources of generation). For $\alpha(\theta) = \sin\theta$ we have $\theta_0 = \pi/4 = 45°$ and $\theta_1 \approx 27°$. So, it is **shifted** from point θ_0 **towards the equator.**

2. The dynamo wave propagates mostly equatorwards. However, at point $\theta_2 > \theta_0$, for which

$$\hat{\alpha}_2 = \frac{\hat{\alpha}(\theta_2)}{\hat{\alpha}_*} = \frac{9\sqrt{6}}{64} \approx 0.35,$$

quantity $Re\,S'(\theta)$ changes its sign, and **the dynamo wave reverses**. For $\alpha(\theta) = \sin\theta$ we have $\theta_2 \approx 80°$, *i. e.*, **near the pole**. This reversal is really observable over the Sun.

Let us note, the location of points θ_1 and θ_2 entirely depends on function $\hat{\alpha}(\theta)$ but not the dynamo number $|D|$. For comparision of these properties with observations see Kuzanyan and Sokoloff (1995, 1997).

3. Comparison with Observations

The following definition for the dynamo number is used in equation (1b):

$$|D| = R_0^4 \frac{\alpha_* G_*}{\beta^2},$$

where $R_0 \approx 7 \cdot 10^{10}\,cm$ is the solar radius, β the turbulent magnetic diffusivity. For a crude estimation we use $G_* \approx \Omega/R_0$, where $\Omega \approx 2.7 \cdot 10^{-6}\,s^{-1}$ is the angular velocity of the Sun. Then the dynamo number is $|D| = R_0^3 \alpha_* \Omega/\beta^2$. Mixing length theory allows us to estimate turbulent diffusivity $\beta \sim 2 \cdot 10^{12}\ cm^2 s^{-1}$ and mean helicity $\alpha_* \sim 10^2\ cm\ s^{-1}$ Taking into account that for large $|D|$ period of the solar cycle $T_o \approx 22\,yr$ according with Parker's migratory dynamo's approach is (in dimensional units)

$$T_o = \frac{2\pi}{Im\Gamma_0} |D|^{-2/3} \frac{R_0^2}{\beta}, \tag{3}$$

we accept below $|D| = 10^3$.

Let us calculate now the location and the half-width of the zone of increased value of the toroidal field (the zone of the dynamo wave's maximum) for different instants of time.

Assuming that the generation of the magnetic field is somehow suppressed by nonlinear or/and diffusion processes, we introduce the following function that is proportional to the magnitude of the toroidal field in the leading order of asymptotic expansion:

$$F(\theta, t) = Re\left\{\exp\left[i|D|^{1/3}S(\theta) + i|D|^{2/3}Im\Gamma_0 t\right]\right\}, \tag{4}$$

where t is the dimensionless time measured in units of diffusion time, R_0^2/β. This function is plotted in Figure 1. The picture is qualitatively the same as the well-known Maunder butterfly diagrams. Further analysis of this function reveals agreement with observations (Kuzanyan and Sokoloff 1997).

4. Conclusion and Perspectives

1. The $\alpha\omega$-dynamo problem, which includes inhomogenity in localization of the sources of the magnetic field's generation without meridional circulation and further complications, reveals a **qualitative** picture of the dynamo wave propagation over the convection zone in one hemisphere which is **consistent with observations**.
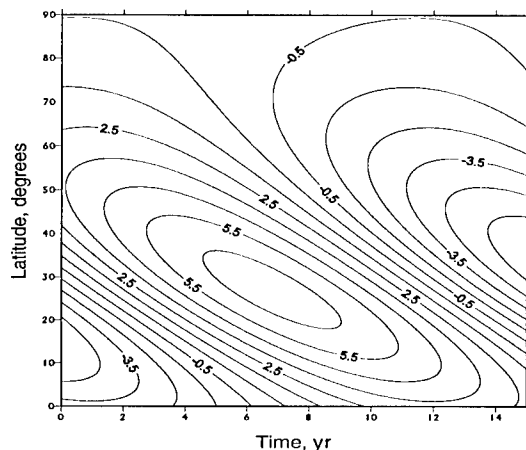
Figure 1.   Values of function $F(\theta, t)$ in formula (4) measured in relative units over the solar cycle. Reproduced from Kuzanyan and Sokoloff (1997), Figure 2, with permission from Kluwer Academic Publishers.

2. It is possible to develop a more quantitatively precise model which includes nonlinearity and some higher order effects to enable one to **reconstruct** the profile αG against θ with **fitting** the solar **observational data** on the magnetic field. Such a model may use:

   (a) helioseismological data of the differential rotation,

   (b) observational data of the turbulence and so, helicity and diffusion,

   (c) information on the phase shift between toroidal and poloidal fields,

   (d) magnetic field observations in sunspots, and active regions.

   We may solve an **inverse problem** of reconstruction of (c) and (d) using of (a) and (b) as an initial guess.

Acknowledgments.   The Author is grateful to the Royal Society for supporting his visiting fellowship to the Mathematics Department of Exeter Unversity (1 October 1996 to 30 September 1997). He also wishes to thank the Royal Society, the Organization committee and sponsors of IAU Colloquium No. 167, and Observatoire de Paris, Meudon, France for partial support of his attending the Colloquium. His thanks go to Dmitry Sokoloff for stimulating discussions.

References

Parker, E. N. 1955, ApJ, 122, 293

Stix, M. 1989, The Sun: An Introduction, Springer-Verlag: Berlin

Kuzanyan, K. M. and Sokoloff, D. D. 1995, Geophys. Astrophys. Fluid Dynam., 81, 113

Kuzanyan, K. M. and Sokoloff, D. D. 1997, Solar Phys., 173, 1

Filament Chirality: A Link Between Fine-Scale and Global Patterns

Sara F. Martin[1]

Helio Research, 5212 Maryland Ave., La Crescenta, CA 91214, USA

Abstract. Solar features that exhibit chirality are: fibril patterns in filament channels, filaments, coronal arcades over filaments, superpenumbral fibrils exterior to sunspots, whole active regions observed with magnetographs, some large-scale X-ray structures, and interplanetary magnetic plasma clouds originating from coronal mass ejections. Their signatures of chirality are briefly reviewed; some details are mentioned to further show relationships which link all of the chirality patterns into a single framework. The helicity of solar magnetic fields is the evident physical phenomena which links each of the seven features to each other and into a broader framework. The chirality system, viewed as a whole magnetic system, reveals: (1) a consistent rotational configuration of the dominant direction of the magnetic field with height of features within and over filament channels from the photosphere to the highest part of the solar corona, and (2) the prominence cavity as a unique space between magnetic fields of opposite helicity.

1. Introduction

Seven patterns of chirality have been found among solar features and are reviewed by Zirker et al. (1997). In the present paper, the seven patterns are revisited to clarify details and to amplify on the relationships between the patterns. The solar features, pictorially summarized in Figures 1 and 2, are: (1) fibrils in filament channels, (2) filaments, (3) systems of coronal loops overlying filaments, (4) super penumbral fibrils exterior to sunspots, (5) active regions as a whole, (6) large-scale X-ray structures, and (7) interplanetary clouds arising from coronal mass ejections which are often accompanied by erupting filaments.

The schematic diagrams in Figures 1 and 2 emphasize the chirality relationships among these solar features. A clear distinction needs to be made between two broad categories of patterns: (1) pairs of one-to-one relationships between each of the seven types of features, and (2) the statistical dominance of one of the two sets of invariant chirality relationships in the northern solar hemisphere and the opposite set in the southern hemisphere. The chirality pairs are represented in rows and the invariant relationships are contained within each column in Figures 1 and 2. The sets of relationships that are dominant in the northern and southern hemispheres are shown respectively in the left and right columns.

---

[1]Also at: California State University, Northridge, CA, USA

S. F. Martin
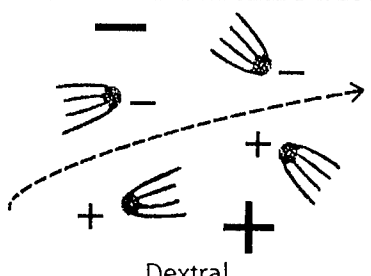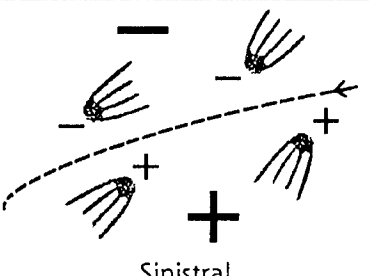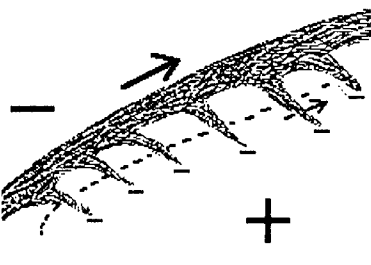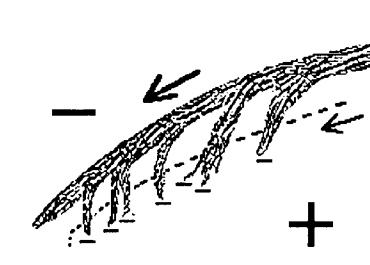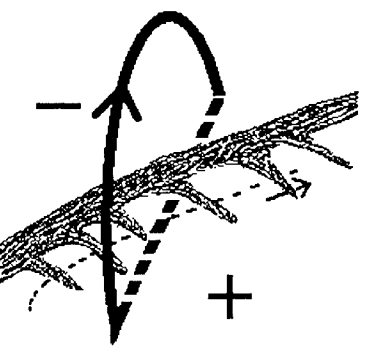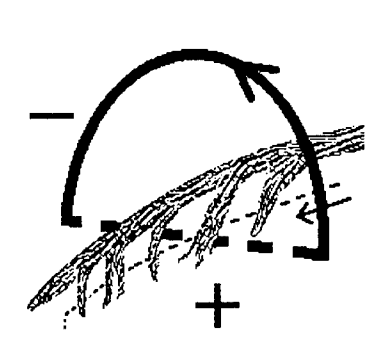
Feature	Chirality $\overset{N}{\llcorner}_W$	
1. Filament Channels Small Scale	Dextral	Sinistral
2. Filaments Medium Scale	Right-Bearing	Left-Bearing
3. Coronal X-Ray Arcades Large Scale	Left-Skewed	Right-Skewed
	Dominant in Northern Hemisphere	Dominant in Southern Hemisphere

Figure 1.   Chirality patterns of solar features involving filaments.
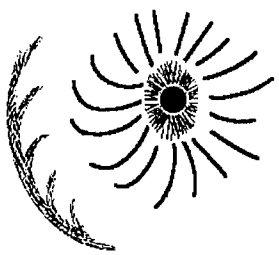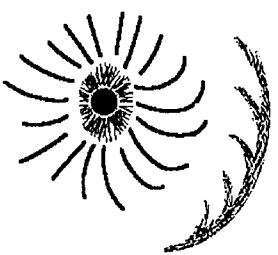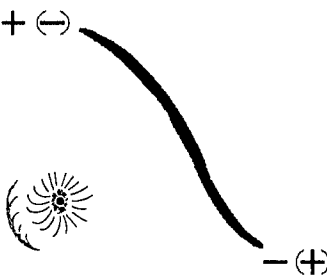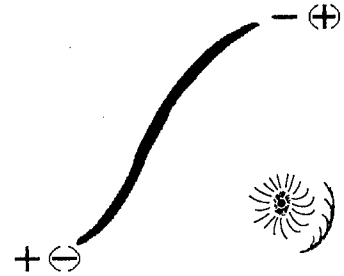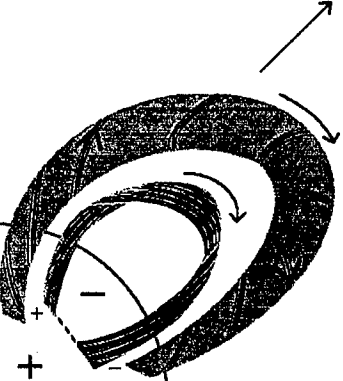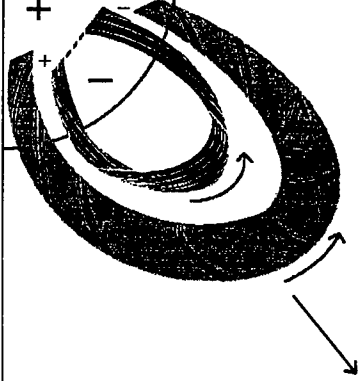
Feature	Chirality	
	Corresponding to Dextral	Corresponding to Sinistral
4. & 5. Fibrils & Photo- spheric Helicity Medium Scale		
6. S-Shaped & Reverse S-Shaped X-Ray Structures Giant Scale		
7. Erupting Filaments & CMEs (Later ... Inter- planetary Clouds) Global Scale		
	Dominant in Northern Hemisphere	Dominant in Southern Hemisphere

Figure 2.   Other chirality patterns of solar features.

Figure 2 is a continuation of Figure 1. Some data sets have revealed as many as one exception to the global hemispheric pattern per 3 chirality pairs while other sets of data have only included a few percent of exceptions to this hemispheric bias (Zirker, Leroy and Gaizauskas, 1998, these proceedings). The exceptions are not illustrated in Figures 1 and 2.

The invariant relationships within each column in Figures 1 and 2 imply physical links between these solar features. The obvious candidate for this linkage is the magnetic fields of these features. Magnetic fields exhibit chirality and are known to be basic to all of these solar features. However, the matching of chirality pairs is fraught with potential for differing interpretations of chirality in terms of magnetic helicity as presented by Rust and Kumar (1994), Low and Hundhausen (1995), and Martin and McAllister (1997). However, all agree that the helicity of solar magnetic fields is an important tool for achieving greater understanding of the physics of all seven features. Together, the chirality of these features offers a new opportunity to gain insight into changes in the solar atmosphere over the solar cycle. Does chirality, interpreted in terms of the helicity of solar magnetic fields, offer new information on the origin of the solar cycle? This possibility has been proposed (Rust and Kumar 1994) and is being questioned (Zirker et al 1997, Foukal 1998, these proceedings). At present, any tentative answer rests on interpretations, which in turn rest on assumptions and other interpretations. These, in turn, relate to the observations of chirality. Below we review the chirality pattern of each solar feature and mention a few salient details which must fit within the grand scheme.

2. Chirality Patterns

2.1. Fibril Patterns

The smallest solar features showing chirality are fibrils; but, fibrils only reveal chirality in relationship to other fibrils rooted in plage or plagettes of opposite magnetic field. The chirality patterns of fibrils are most clearly seen in filament channels (Foukal 1971, Martin et al. 1994). In channels of medium to high photospheric magnetic flux density, the central or key fibrils delineate the channel by their alignment with the polarity inversion. The 'polarity inversion' is the boundary between large-scale fields of opposite vertical component associated with network magnetic fields; 'polarity inversion' is herein used in preference to the older designation of this boundary as the 'neutral line'. In filament channels, the fibrils, associated with the majority polarity plage or network magnetic fields of the majority polarity, have two possible patterns with respect to the polarity inversion and the opposite polarities on the two sides of this inversion. The two patterns, identified as dextral and sinistral, are shown in the first pair of panels in Figure 1. Viewed from the positive network side of the polarity inversion, a channel is dextral if the fibrils emanate to the right from the positive polarity chromospheric plage or plagettes (associated with the photospheric network); from the same view, the channel is sinistral if the fibrils appear to stream from the plage(ttes) to the left.

Dextral and sinistral channels have mirror symmetry relative to each other. In both cases, the polarity boundary, between the oppositely directed fibrils, is not crossed by any single fibrils. This boundary corresponds to a locus of

points where the magnetic field is nearly horizontal at the photosphere and nearly aligned with the polarity inversion. Typical examples are shown in active regions by Hagyard et al. (1984, 1990) and in a decaying active region by Zhang (1990).

The direction of the fibrils with respect to the dominant line-of-sight polarity indicates that the magnetic field of fibrils on both sides of the polarity boundary have a common component parallel to it, as first illustrated by Foukal (1971). Martin et al. (1994) schematically illustrate the inferred magnetic field geometry in a volume cross-section across a filament channel.

As shown by Filipov (1998, these proceedings), the fibrils in many filament channels have a strong tendency to be 'inverse' in the same sense that the magnetic fields in quiescent filaments are 'inverse' (Leroy 1978, 1989; Bommier and Leroy 1998, these proceedings). The inverse component of fibril patterns is not necessarily symmetric with respect to the polarity inversion but the pattern is such that the positive magnetic field has a component away from the polarity inversion and the negative component toward it. This pattern does not include local irregularities due to the development and decay of small bipoles known as ephemeral active regions.

2.2. Filament Patterns

As indicated in the middle pair of schematic diagrams in Figure 1, the chirality of filaments can be revealed by: (1) direct measures of the magnetic field along the axis of a filament relative to the polarity on the two sides of the filament, and (2) the direction of the barbs of filaments relative to filament axis along the polarity inversion, as best seen to date in Hα filtergrams. The chirality of the axial magnetic field is defined when viewing filaments from the positive network magnetic field side as in Figure 1. If its axial magnetic field points to the right, a filament is dextral; if the axial field component is toward the left, the filament is sinistral.

The chirality of the barbs can be defined independently of viewing angle or knowledge of any magnetic field polarity. Viewed from either side of the filament, if the barbs on the near side veer from the filament axis to the right and downward to the chromosphere, the barbs are right-bearing; if on the near side, they veer from the axis to the left and downward to the chromosphere, they are left-bearing. For filaments intermediate to active region filaments and quiescent filaments as illustrated in Figure 1, the barbs tend to be broader near the filament axis and converge to chromospheric points or clusters of chromospheric points. Mass motions can be either up or down along the barbs (Engvold 1998, these proceedings).

Martin and Echols (1994) and Martin (1994) identified the chromospheric ends of filament barbs with pockets of photospheric magnetic fields of the minority polarity along the sides of filaments. This association is consistent with the inverse magnetic fields in filaments as measured by Leroy and colleagues cited above, although these authors could not distnguish at that time between axial fields along the filament spine and barb fields extending away from the spine. In quiescent filaments, the barbs tend to dominate the structure; they are typically the brightest parts of quiescent prominences and much more likely to be measured than the axial component. If the barbs are measured at the limb

instead of the axial component, the magnetic field would have to be 'inverse' to be consistent with their being rooted in small pockets of the minority polarity as schematically represented in Figure 1. The barbs are clearly identified in prominence observations against the solar disk (Martin and Echols, 1995) and, in multi-day observations, large barbs can be traced to the "legs" of prominences when observed above the limbs such as in Figure 6 in Martin, Bilimoria and Tracadas (1994).

2.3. The Skew of Coronal Arcades Overlying Filaments

Martin and McAllister (1995, 1997) studied the skew of coronal arcades seen in X-ray images from the Yohkoh satellite. Skew was defined as the acute angle between the loops and the polarity inversion or filament axis. If the arcade loops cross over the filament or filament channel in the sense of threads of a left-hand screw or right hand screw, they defined the loops as left-skewed or right-skewed, respectively. They investigated the skew of the systems of nearly parallel loops that comprise coronal arcades overlying filaments. As depicted in the third pair of panels in Figure 1, they found a one-to-one relationship between the skew of the arcades and the type of filament. The chirality relationship is in the inverse sense. Left-skewed arcades overlie dextral filaments and filament channels; right-skewed arcades overlie sinistral filaments and filament channels.

The chirality relationship applied to both quiescent arcades and dynamic arcades that evolve after filament eruption/coronal mass ejection events. Many of the dynamic arcades evolved such that the later-forming loops showed apparent rotation relative to the earlier-forming loops. This apparent rotation also has a specific sense. Left-skewed arcades revealed apparent rotation in the counterclockwise sense and right-skewed arcades in the clockwise sense. This is invariably in the direction of decreasing skew and decreasing magnetic shear with time and height of the loops as found previously by other authors. For example, Rust and Bar (1973) discuss post-flare loops, which in their successive formation, collectively showed apparent rotation from a 20° angle to a 90–100° angle with respect to the polarity inversion.

2.4. Chirality of Superpenumbral Fibrils Around Sunspots

Some of the longer, more conspicuous fibrils in active regions are those in an extended area exterior to the penumbra of sunspots. During the early part of the 20th century, these fibrils caught the attention of solar astronomers (Hale 1925, 1927), who recognized the similarity between the fibril patterns and the pattern of iron filings around bar magnets. Richardson (1941) made an extensive study of fibril patterns around large sunspots over parts of 3 solar cycles from Hα spectroheliograms obtained daily at Mt. Wilson Observatory. For 1/3 of these cases, he could identify the fibril pattern as being dominantly clockwise or counterclockwise around a portion of the perimeter of the penumbra. He also found some cases where both senses could be seen around different parts of the perimeter of the same sunspot. Nevertheless, he found, for superpenumbral fibrils with a dominant sense of chirality, that the majority with a counterclockwise pattern were in the northern hemisphere and that a majority with a clockwise pattern were in the southern hemisphere. Counterclockwise and clockwise are defined in following the curvature of the fibrils from the end of the fibril more

distant from the penumbra to the end closest to the penumbra (first pair of panels in Figure 2).

Rust (1994) was the first to point out the consistency of the patterns of chirality in sunspots, filaments, active regions and magnetic clouds. In 1994 D. Rust asked me to check out his prediction of a close association between the chirality of superpenumbral fibril patterns and the chirality of nearby filaments. He anticipated that counterclockwise fibril patterns would be adjacent to dextral filaments and clockwise fibrils would be adjacent to sinistral filaments. I chose the first 10 sunspot pictures with clearly curved fibril patterns that could be found in a local file of photographic prints of high quality images from the Big Bear Solar Observatory. The filaments were either seen in the same prints or in full-disk Hα images taken on the same day. Rust's prediction was correct in all 10 cases (Rust and Martin 1994). This relationship is also illustrated in the first pair of panels in Figure 2. Typically I have observed that the superpenumbral fibrils show the most curvature on the side of the sunspot toward a filament or filament channel.

2.5. The Chirality of Active Regions

Extensive, smoothly curved patterns of fibrils are characteristic of the Hα chromosphere of active regions. Thus, it could be expected that active regions as a whole might exhibit chirality patterns similar to those in filament channels and around sunspots. Seehafer (1990) estimated the electric current helicity in 16 active regions and concluded that the electric current helicity is predominantly negative in the northern hemisphere and positive in the southern hemisphere. Pevtsov, Canfield and Metcalf (1994) also demonstrated the existence of chirality in active regions by analyzing vector magnetograms from the Mees Solar Observatory. Like superpenumbral fibrils, the whole active region does not have to be the same chirality for there to be a dominance of one pattern. Pevtsov, Canfield and Metcalf defined such a pattern using the deviation of vector magnetograph measurements from a potential magnetic field configuration. A dominant sense of chirality was found for most active regions. It is consistent with the chirality of the superpenumbral fibril patterns and Seehafer's estimate of current helicity, as previously pointed out by Rust (1994).

2.6. The Chirality of Large-scale X-ray Structures

Very large scale X-ray structures have been noticed to exhibit a slight S or backwards-S shape as a function of hemisphere (Harvey 1994, Rust and Kumar 1996). Harvey describes the pattern as a systematic twist around magnetic concentrations in both hemispheres which is consistent with differential rotation. The pattern, as viewed from above, is illustrated in the middle pair of panels in Table II. Overall, there is a dominance of reverse S-shaped structures in the northern hemisphere and S-shaped structures in the southern hemisphere.

The reverse-S and S-shaped patterns also apply to many filament channels and sets of X-ray structures closely aligned with filament channels (McAllister et al. 1998, these proceedings). These patterns apply mostly to features in the environment of "diagonal" filaments or filament channels forming within or between the decayed remnants of active regions. The "diagonal" form refers to the mid-section of filaments whose orientation is consistent with differential

rotation acting on initial north-south oriented filament channels. Initial N-S oriented structures aligned or nearly aligned with the polarity inversion of the filament channel evolve to become NE-SW in the northern hemisphere and initial S-N oriented structures become SE-NW in the southern hemisphere. For these polarity inversions, the reverse S-shape in the northern hemisphere and S-shape in the southern hemisphere are as expected if the magnetic ends of these structures are rooted in the polarity of network fields which are consistent with the extreme ends of the dextral and sinistral axial fields of filaments and filament channels.

2.7. The Chirality of Interplanetary Clouds, CMEs and Erupting Filaments

Interplanetary clouds are the ejected parts of coronal mass ejections (CMEs), as first concluded by Marubashi (1986, 1997) and amplified by others. Many such plasma clouds have helical structure detected by magnetometers on board spacecraft (Burlaga 1991, Klein and Burlaga 1982). Gosling (1990) and Gosling and Birn (1995) proposed that helical magnetic fields in interplanetary clouds originate from magnetic reconnection in ascending coronal arcades. Based on the same scenario, Martin and McAllister (1997, 1998) anticipate that left-skewed coronal arcades become left-helical CMEs and later are detectable as left-helical interplanetary clouds; similarly right-skewed coronal arcades should become right-helical CMEs and interplanetary clouds. Consistent with this picture, Rust (1994) found that the majority of interplanetary clouds with left-helical structure come from the northern solar hemisphere and most of those with right-helical structure originate in the southern hemisphere. The outer structure in the lower pair of panels in Figure 2 represent CMEs in each hemisphere which later become interplanetary clouds. The large-scale helical structures of the plasma clouds are consistent with the chirality of CMEs, rather than the chirality of filaments, confirming Marubashi's original association of interplanetary flux ropes with the coronal magnetic fields around filaments.

As represented by the inner twisted structures in the last pair of panels in Figure 2, Martin and McAllister (1997, 1998) have also predicted that dextral filaments develop right-helical twist via magnetic reconnection occurring in the pre-eruptive or early eruptive stage and sinistral filaments develop left-helical twist. Their hypothesis is based on a proposed model of a filament composed of an initially untwisted axial magnetic field aligned with the polarity inversion and barb magnetic fields which extend from the axial field of the filament spine to the chromosphere adjacent to the filament (Martin and Echols, 1994). Except for filaments in areas of low magnetic flux density, mass continuously streams along the spine and barbs, providing evidence of the magnetic fields parallel with the fine structures of the spine and barbs. During the early phase of eruption, the axial magnetic field ascends beneath the rising coronal arcade as observed in many coronal mass ejections. In this model, the magnetic fields of the filament begin to detach from the Sun by magnetic reconnection between barbs with oppositely directed magnetic fields beneath the rising axis of the erupting filament. The expectation of Martin and McAllister is that filament mass, if later identifiable within a plasma cloud, will have helicity opposite in sign to the encasing plasma from the CME. The prediction is more readily tested

as erupting filaments leave the Sun; often helical structure is then quite readily seen (Rompolt 1975, 1990). For the filament only, the Martin and McAllister prediction gives the opposite sign of helicity from the Rust model (1994) and its continuation by Rust and Kumar (1994); the latter authors assume that the filament lies in the lower portion of a larger-scale helical magnetic field which supports the filament mass against gravity. Martin and McAllister make no assumption about the support of the filament mass because the structure of barbs is seen to have large vertical components, mass motions of several km/s, and no evidence of magnetic wells to support mass.

3. Discussion

Figures 1 and 2 present solar features exhibiting chirality from small scales to global scales. The chirality of filament channels, filaments and their overlying coronal arcades are all defined relative to the polarity inversion. The axial fields of quiescent filaments always maintain the chirality of the filament channel where their barbs are rooted. All arcades and features above the arcades exhibit the opposite sense of chirality. Between the filament and the adjacent and overlying coronal arcade is a region, void of emission, called "the cavity". There is no source of empirical information on the cavity magnetic field. Also, there is no requirement to assume that these magnetic fields are necessarily directly connected in the corona. It has already been shown (Figure 1) that the filament and surrounding arcade are rooted in separate magnetic fields of opposite polarity. Hence, it is plausible that the filament magnetic fields and coronal arcade fields are divided by a separatrix surface.

The chirality patterns thus reveal a new significance for the space called "the cavity"; it is the volume between features of opposite chirality. To better understand the significance of the cavity, it can be compared with the characteristics of other volumes of space where features of opposite chirality are juxtaposed. Martin, Bilimoria and Tracadas (1994) found that filaments of opposite chirality do not join. Instead they avoid each other by forming a cusp and this configuration allows the ends of filaments to be juxtaposed but not directly connected. Similarly, Pevtsov and Canfield (1997) have found that, near the equator, active regions of opposite chirality do not have interconnecting coronal loops while those of the same chirality have many interconnecting loops.

Above and below the coronal cavity, we have thus found the third example of solar features of opposite chirality which do not show evidence of being magnetically connected or a tendency to reconnect with each other in their quiescent state; filaments of one chirality are spatially isolated from the coronal loops of opposite chirality above. Even during filament eruptions and CMEs near the Sun, prominence mass remains isolated although encased within the larger CME. Thus, I propose that the existence of a prominence cavity is physically related to its location between features of opposite chirality.

The chirality of solar features can all be interpreted as features with magnetic helicity. Berger (1998, these proceedings) distinguishes between two forms of helicity, linking and twist. These forms of helicity can be increased, decreased or interchanged by magnetic reconnection. Prior to eruption, neither filaments nor coronal arcades exhibit large-scale twist in their fine structure, although the

spatial resolution of many observations is adequate for seeing twist. However, during eruption, filaments often display large-scale twist. Likewise, interplanetary clouds, associated with erupted coronal arcades, exhibit large-scale helical structure. Thus in the pre-eruptive state, the chirality of filaments and coronal arcades can be interpreted either in terms of linking helicity or an absence of twist helicity above the photosphere. In their eruptive and post-eruptive state, their chirality is readily interpreted as twist helicity converted from the prior form of helicity by magnetic reconnection during the eruptive processes.

The nature of the chirality of solar features, and their interpretation in terms of helicity, and of the coronal cavity should become better understood with further study.

References

Burlaga, L.F. 1991, in Physics of the Inner Heliosphere II, (eds.) R. Schwenn and E. Marsch, Springer Verlag, New York, p. 1

Foukal, P. 1971, Solar Phys., 19, 59

Gosling, J.T. 1990, in Physics of Magnetic Flux Ropes, (eds.) C.T. Russell, E.R. Priest, and L.C. Lee, Geophys. Mono. Ser. 58, AGU, p. 343

Gosling, J.T. and Birn, J. 1995, Geophys. Res. Lett., 22, 869

Hagyard, M. J., Smith, J.R., Jr., Teuber, D. and West, E.A. 1984, Solar Phys., 91, 115

Hagyard, M., Venkatakrishnan, P. and Smith, J.B., Jr. 1990, ApJS, 73, 159

Hale, G.E. 1927, Nature 119, 708

Hale, G.E. 1925, Mt. W. Comm. No. 95, Proc. Nat. Acad. Sci. II, p. 691

Harvey, J.W. 1994, BAAS, 26, 1523

Klein, L.W. and Burlaga, L.F. 1982 J. Geophys. Res., 87, 613

Leroy, J.-L. 1978, A&A, 64, 247

Leroy, J.-L. 1989, in Dynamics and Structure of Quiescent Solar Prominences, (ed.) E.R. Priest, Kluwer Acad. Publ., Dordrecht, Holland, p. 77

Low, B.C. and Hundhausen, A. 1995, ApJ, 443, 818

Martin, S.F. 1994, BAAS, 26, 1522

Martin, S.F. and Echols, C.R. 1994, in Solar Surface Magnetism, (eds.) R.J. Rutten and C.J. Schrijver, Kluwer Acad. Publ., Dordrecht, Holland, p. 339

Martin, S.F., Bilimoria, R. and Tracadas, P.W. 1994, in Solar Surface Magnetism, (eds.) R.J. Rutten and C.J. Schrijver, Kluwer Acad. Publ., Dordrecht, Holland, p. 303

Martin, S.F. and McAllister, A.H. 1995a, BAAS, 27, 961

Martin, S.F. and McAllister, A.H. 1995b, in Magnetodynamic Phenomena in the Solar Atmosphere, (eds.) Y. Uchida et al., Kluwer Acad. Publ., Dordrecht, Holland, p. 497

Martin, S.F. and McAllister, A.H. 1997, in Coronal Mass Ejections, (eds.) N. Crooker et al., Geophys. Mono. Ser. 99, AGU, p. 127

Martin, S.F. and McAllister, A.H. 1998, ApJ., submitted

Marubashi, K. 1986, Adv. Space Res., 6, 335

Marubashi, K. 1997, in Coronal Mass Ejections, (eds.) N. Crooker, J.A. Joselyn and J. Feynman, Geophys. Mono. Ser. 99, AGU, p. 147

Pevtsov, A.A., and Canfield, R.C. 1997, ApJL, submitted

Pevtsov, A.A., Canfield, R.C., and Metcalf, T.R. 1994, ApJL, 425, L117

Richardson, R.S. 1941, ApJ, 41, 24

Rompolt, B. 1975, Acta Univ. Wratenslavensis No. 252, 55

Rompolt, B. 1990, Hvar Obs. Bull. 14(1), 37

Rust, D.M. 1994, Geophys. Res. Lett. 21, 241

Rust, D.M. and Bar, V. 1973, Solar Phys., 33, 445

Rust, D.M. and Kumar, A. 1994, Solar Phys., 155, 69

Rust, D.M. and Kumar, A. 1996, ApJ, 464, L199

Rust, D.M. and Martin, S.F. 1994, in Solar Active Region Evolution, (eds.) K.S. Balasubramaniam and G.W. Simon, ASP Conf. Ser., Vol. 68, San Francisco, p. 337

Seehafer, N. 1990, Solar Phys., 125, 219

Zhang, H. 1990, The Solar Cycle, (ed.) K.L. Harvey, ASP Conf. Ser., Vol. 27, San Francisco, p. 124

Zirker, J.B., Martin, S.F., Harvey, K., and Gaizauskas, V. 1997, Solar Phys., 175, 27

The Skew of Polar Crown X-ray Arcades

A. H. McAllister[1]

Helio Research, 5212 Maryland Ave. La Crescenta CA 91214, USA

A. J. Hundhausen

High Altitude Observatory, NCAR, PO Box 3000, Boulder, CO 80307, USA

D. Mackay and E. Priest

University of St. Andrews, St. Andrews, KY16 9SS, U.K.

Abstract.
   The one-to-one relationship between the chirality of filament channels and the skew (relative orientation) of the overlying coronal arcades can be coupled with the predictions for the axial component of polar crown filaments based on past magnetic field observations to predict the skew of polar crown arcades in the recent cycle 22. We have surveyed the actual skew as seen in the Yohkoh SXT images over the declining phase of cycle 22 and found a result opposite to that expected. The SXT arcades have been compared with numerical models to show that while some of this result can be explained by flux distribution around switchbacks, other mechanisms such as differential rotation are also needed.

1. The Basic Structure of Filament Channels

The natural potential field across a photospheric polarity inversion line takes the form of a series of nested arcades. Soft x-ray images from Skylab and the Yohkoh Soft X-ray Telescope (SXT) show that the coronal structures above inversion lines do show this general form. Due to asymmetrical distributions of photospheric flux many arcades are comprised of loops that cross the underlying polarity inversion line at an angle other than 90°. This angle has been called the skew of the arcade by Martin and McAllister (1998) (see Figure 1).

   Strong axially aligned photospheric magnetic fields along an inversion line under a coronal arcade create a filament channel in which a filament may form (e.g., Gaizauskas 1998, these proceedings). These axially aligned fields in filament channels and filaments have been found to come in two varieties, defined as 'dextral' and 'sinistral' (e.g., Martin 1998, these proceedings, and Figure 1). In the quiet sun filaments often have barbs or legs which allow a topological determination of filament chirality (Martin 1998, these proceedings).

---

[1]Current address: High Altitude Observatory, NCAR, PO Box 3000, Boulder, CO 80307, USA

Northern Hemisphere   Southern Hemisphere
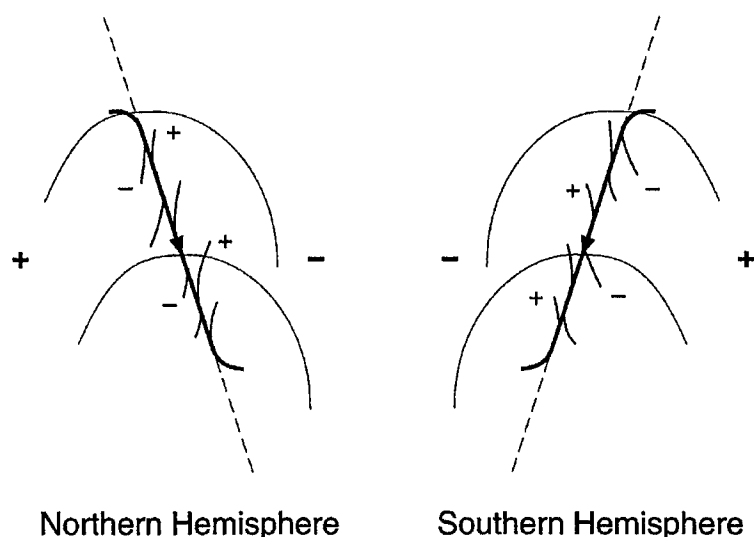
Figure 1.   A cartoon showing the structure of (a) 'dextral' and (b) 'sinistral' filaments and under overlying a) 'left-skewed' and b) 'right-skewed' arcades. The ends of the filament backbone, like the arcade loops, are rooted in the dominant polarities (large '+' and '−'). The barbs are represented by the small side lines rooted in the minority polarity (small '+'s and '−'s). (Martin and McAllister 1998, Figure 5).

Recently it has become apparent that there are certain clear relationships between these structures.

2.   Previous Observations and Correlations

Observations of the axial fields of filaments have been made using both the Zeeman effect (e.g., Rust 1967) and the Hanle effect (e.g., Leroy et al. 1983, Bommier and Leroy 1998, these proceedings). These workers have found that i) the axial field along each polar crown was consistent over each solar cycle (the interval from one polar reversal to the next), ii) these fields were opposite in the northern and southern polar crowns, and iii) they reversed direction with the change of the polar fields near the maximum of each sunspot cycle. Martin, Marquette, and Bilimoria (1992) applied the topological chirality test to filaments through four solar cycles confirming the older findings and extending them into cycle 22.

Martin, Bilimoria, and Tracadas (1994) have shown that the chirality of filaments is always the same as that of the associated filament channel, and Martin and McAllister (1998) found that for mid- and low-latitude filaments the axial component of the magnetic field is the same in the overlying coronal arcades as it is in the filaments. Physically this means that the axial magnetic field is in the same direction from the photosphere up into the corona, but the transverse magnetic field reverses with height.

Based on this work the cycle 22 post-reversal polar crown axial fields are ex-

(a)

(b)
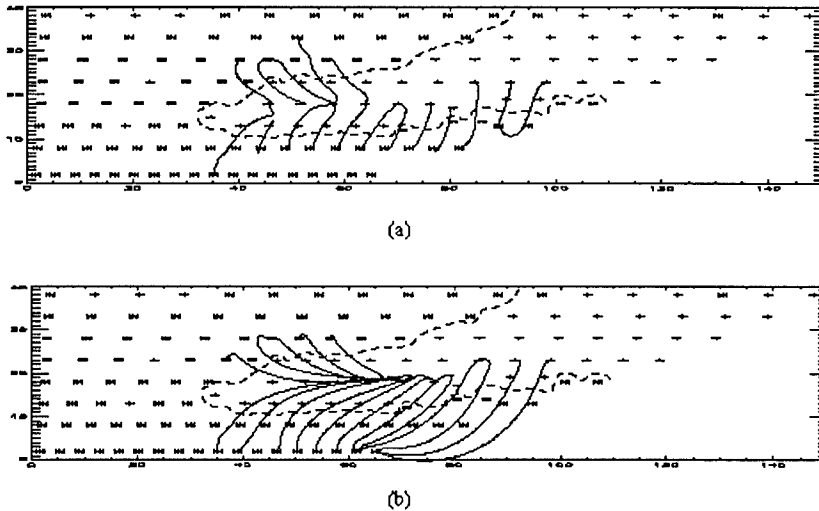
Figure 2.   (a) Field lines plotted at a height of 140,000 km showing a left skew on the horizontal arm and a right skew on the diagonal arm. (b) Oblique view of the field lines at heights of 200,000 km on the horizontal arm and 140,000 km on the diagonal arm.

pected to be eastward in the northern hemisphere and westward in the southern hemisphere, implying that the polar crown arcades will be right-skewed in the southern hemisphere and left-skewed in the northern hemisphere, if the Martin and McAllister relationship holds there as well.

3.   Coronal Observations

To test this prediction we have surveyed the SXT images of the corona over polar crown neutral lines from October 1991 through August 1994 cataloging all indications of skew. Due to observational constraints most of our sample is made up of events in which the corona rises above its normal brightness. These are either large-scale dynamic arcade events following a CME (McAllister et al. 1998), or transient brightenings of loops due to a local event near one end (Solberg and McAllister 1998, these proceedings).

The main result was that the skew indications along the polar crowns are generally not in agreement with the prediction. There were predominantly left-skewed arcades along the southern polar crown and right-skewed arcades along the northern polar crown. This result is based on 47 cases over the three years. In contrast the skew of non-polar crown arcades was dominantly as expected from the previous work. We note that the clarity of the statistics improved from mid 1992 on, as the southern polar reversal was completed.

4. Models

As a first step in understanding our result we have compared the observations with potential models. A model of an idealized switchback (the eastern end of a polar crown neutral line [McAllister et al. 1998]) was created by nesting two pie shaped opposite-polarity regions. At the corner of the switchback this produces a local flux imbalance which is responsible for the skew of the arcades reversing on the polar crown switchback arm (see Figure 2).

On the sun switchbacks are formed, in part, due to the transport of denser lower latitude magnetic fields to high latitude (van Ballegooijen, Cartledge and Priest 1998). Using synoptic magnetograms obtained from the NSO archive we tested our model on a well-formed polar crown switchback that produced two dynamic arcades on February 24–25, 1993 (Figure 2). The comparison shows that in both the SXT data and the potential model the skew reverses on the polar crown.

5. Discussion

While potential models can explain the unexpected skew near the switchbacks, our data suggest that it persists along most of the polar crown. Thus, other mechanisms, such as differential rotation, may also play a role (van Ballegooijen and Martens 1990). The second interesting point is that the possibility of an axial field reversal with height cannot be ruled out along the polar crown.

References

Leroy, J. L., V. Bommier and S. Sahal-Brechot 1983, Solar Phys., 83, 135

Martin, S. F., W. H. Marquette and R. Bilimoria 1992, in The Solar Cycle, (ed.) K. L. Harvey, Astron. Soc. Pacific Conference Series 27, San Francisco, p. 53

Martin, S. F., R. Bilimoria and P. W. Tracadas 1994, in Solar Surface Magnetism, (eds.) R. Rutten and C. J. Schrijver, Kluwer Acad. Publ., Dordrecht, Holland, p. 303

Martin S. F. and A. H. McAllister 1998, The Chirality of X-ray Coronal Arcades Overlying Quiescent Filaments, ApJ, submitted

McAllister, A. H., A. J. Hundhausen, J. T. Burkepile and P. McIntosh 1998, Coronal Evolution and X-ray Arcades, J. Geophys. Res., to be submitted

Rust, D. M. 1967, ApJ, 150, 313

van Ballegooijen, A. A. and P. C. H. Martens 1990, ApJ, 361, 283

van Ballegooijen, A. A., N. P. Cartledge and E. R. Priest 1998, Magnetic Flux Transport and the Formation of Filament Channels on the Sun, ApJ, submitted

Global Pattern of the Magnetic Field Vector Above Neutral Lines from 1974 to 1982: Pic-du-Midi Observations of Prominences

V. Bommier

Laboratoire 'Atomes et Molécules en Astrophysique', CNRS URA 812–DAMAp, Observatoire de Paris, Section de Meudon, F-92195 Meudon, France   E-mail: Veronique.Bommier@obspm.fr

J.L. Leroy[1]

I.A.C.-T.H.É.M.I.S., E-38200 La Laguna, Tenerife, Canary Islands, Spain   E-mail: leroy@themis.iac.es

Abstract. The magnetic field vectors derived from the Hanle effect measured in prominences during the ascending phase and maximum of Cycle 21 have been plotted on the corresponding synoptic maps of Meudon Observatory (e.g., Figure 2). Most of these measurements have been performed in a single line, He I D3. Our previous analysis of 2-line measurements have already proven that prominence magnetic fields have Inverse polarity (Bommier et al. 1994) and remain close to the horizontal plane (Bommier et al. 1986, 1994). We also found earlier that the field component along the filament axis shows a remarkable large scale pattern, especially at high latitudes (Leroy et al. 1983). Given the geometry of horizontal Inverse field, we reinvestigate this large scale organization through our complete set of observations (296 prominences). These new maps fully confirm and extend to medium latitudes the law of reversal of the axial field from one prominence band to the adjacent ones (see Figure 2). This behavior, together with the Inverse polarity pattern, gives a picture consistent with a North-South global field distorted by the differential rotation (see Figure 3).

1. Data Sample

From our full sample of 3297 measurements achieved in 379 quiescent prominences observed at the Pic-du-Midi during the ascending phase of Cycle 21 (1974–1982), we have discarded those prominences for which the identification of the neutral line is doubtful (64 prominences). We have discarded those measurements that are not precise enough (inaccuracy larger than 5×10^{-3} for the linear polarization degree or 10° for the linear polarization direction). The result is a unique determination of the average magnetic field vector of 296 quiescent

---

[1]Permanent Address: Observatoire Midi-Pyrénées, 14 Ave. E. Belin, F-31400 Toulouse, France
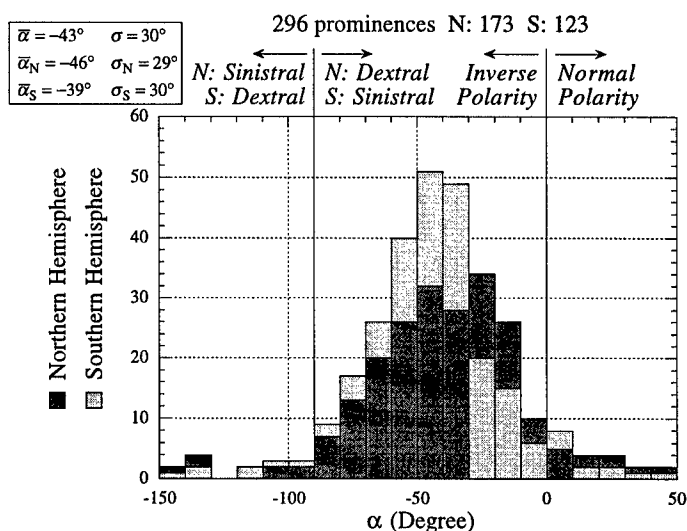
Figure 1.   Histogram of the angle α between the average field vector and the neutral line (following the definition of Leroy et al. 1984, Figure 4).

prominences corresponding to 2390 measurements.

2.   Hanle Effect Interpretation

The full set of linear polarization data obtained with a single line (He I D3) has been reinvestigated by applying the results previously obtained from simultaneous observations of two lines of the same (He I D3 and Hβ, 14 prominences, Bommier et al. 1986) and different (He I D3 and Hα, 18 prominences, Bommier et al. 1994) optical thickness, namely the field vector close to the horizontal plane (dip of field line across the prominence) and inverse polarity with respect to the adjacent photospheric field. In the present analysis, the fundamental 180° ambiguity has been removed in a two-step procedure.

In the first step, the ambiguity has been removed in all cases where the two ambiguous solutions have opposite polarities, by selecting the inverse polarity solution (that we call the 'polarity law'). This is the case for 264 of the full sample of 296 prominences. As the two ambiguous solutions are nearly symmetrical with respect to the line-of-sight, the method fails when the neutral line lies along a meridian because, in this case, the two ambiguous solutions have the same polarity. Most of these 264 prominences are found to obey the chirality law of Martin et al. (1994), already obtained at high latitudes by Leroy et al. (1983, see their Figure 5), i.e., dextral chirality in the northern hemisphere and sinistral chirality in the southern hemisphere.

In the second step the ambiguity has been removed for the 32 remaining prominences, using the above result that their two ambiguous solutions have the
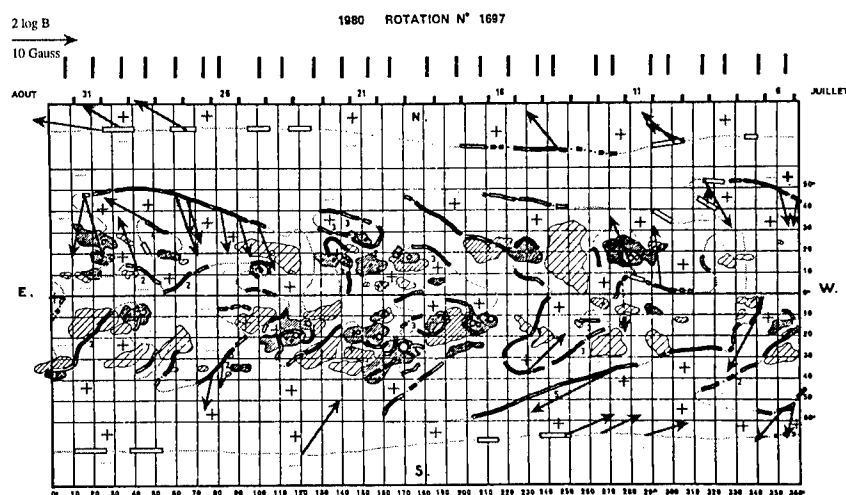
Figure 2.   Rotation 1697. Each arrow has been scaled (in $\log_{10} B$) to the average magnetic field vector of a prominence observed on a given day.

same polarity but opposite chiralities. (Because the two ambiguous solutions are nearly symmetrical with respect to the line-of-sight, this is strictly the case when the neutral line lies along a meridian). The solution selected for these prominences is the one having chirality in agreement with the chirality law.

As the two ambiguous solutions are nearly symmetrical with respect to the line-of-sight, the chirality-law method fails when the neutral line lies along a parallel of latitude, and the polarity-law method fails when the neutral line lies along a meridian. Where one of the two methods fails, the other method will apply. Thus, both methods are complementary and, in those cases where both methods apply, they give results in agreement for nearly all the cases. However, it must be emphasized that the chirality-law method is derived from the result of the polarity-law method. Also, by using this procedure, a few normal-polarity prominences are derived by using the chirality-law method and, accordingly, a few prominences are found to not obey the chirality law, using the polarity-law method to solve the ambiguity. Such 'exceptions' are preferentially found at places where the general direction of a neutral line is changing.

The results of the present analysis fully confirm previous ones (Leroy et al. 1983, 1984) in the limit of the measurement (and other causes of) inaccuracies. As an example, Figure 1 shows the histogram of the angle α between the field vector and the neutral line, oriented as defined by Leroy et al. (1984, see Figure 4). Positive and negative α angles correspond respectively to Normal and Inverse polarity. On the Figure, both hemispheres have been distinguished. In the northern hemisphere, the filament is dextral when α lies inside the interval $[-90°, +90°]$, and sinistral outside (opposite for the southern hemisphere). The average value $\overline{\alpha} = -43°$ and standard deviation $\sigma = 30°$ do not contradict previous results $\overline{\alpha} = -25°$ and $\sigma = 38°$ (Leroy et al. 1984), due to the measurement

296 prominences

——— y = 87 + 0.69x R= 0.75
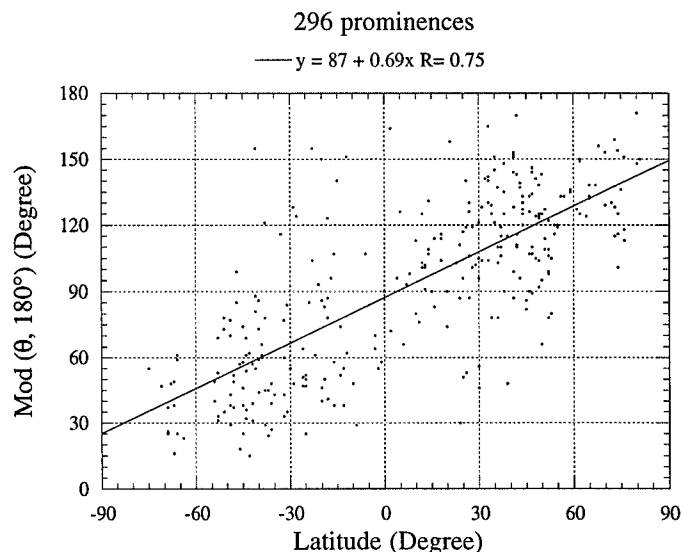
Figure 3.   Angle θ (modulo 180°) between the average field vector of each prominence and the W-oriented solar parallel, as a function of the Latitude. Above, the equation and correlation coefficient of the linear least square fit.

(and other causes of) inaccuracies.

The results have been plotted on the synoptic maps of Meudon Observatory, along with data on the photospheric polarities and neutral lines taken from the McIntosh maps (NOAA/SEC). An example is given in Figure 2. Each arrow corresponds to the average magnetic field (in strength and direction) of a prominence observed on a given day. The full arrows (all except one on Figure 2) correspond to prominences for which the ambiguity has been removed by applying the polarity-law method. The dashed arrows (only one on Figure 2, at latitude 7° and longitude 274°) correspond to prominences for which the ambiguity has been removed by applying the chirality-law method.

These maps show the evidence of a global pattern of the average magnetic field vector of prominences: global direction along a North-South line distorted by the differential rotation (see a linear least square fit in Figure 3), reversal of the field from a neutral line to the adjacent one in both E-W and N-S directions (a result previously obtained at high latitudes by Leroy et al. 1983), antisymmetry of the North and South hemispheres. Inverse polarity is found for both axial and transverse components of the magnetic field vector.

References

Bommier, V., Leroy, J.L., Sahal-Bréchot, S. 1986, A&A, 156, 79
Bommier, V., Landi Degl'Innocenti, E., Leroy, J.L., Sahal-Bréchot, S. 1994,

Solar Phys., 154, 231

Leroy, J.L., Bommier, V., Sahal-Bréchot, S. 1983, Solar Phys., 83, 135

Leroy, J.L., Bommier, V., Sahal-Bréchot, S. 1984, A&A, 131, 33

Martin, S.F, Bilimoria, R., and Tracadas, P.W. 1994, in Solar Surface Magnetism, (eds.) R. Rutten and C. Schrijvers, Kluwer Acad. Publ., Dordrecht, Holland, p. 303

Are All Prominences Either Sinistral or Dextral?

J.B. Zirker
National Solar Observatory, Sunspot, N.M. 88349, USA
E-mail: zirker@noao.edu

J.-L. Leroy
I.A.C. - T.H.È.M.I.S, E-38200 La Laguna, Tenerife, Canary Islands,
Spain   E-mail:leroy@themis.iac.es

V. Gaizauskas
Herzberg Institute of Astrophysics, National Research Council of Canada,
Ottawa K1A OR6, Canada

Abstract. A reanalysis of the prominence magnetic field measurements obtained by Leroy et al. (1983) indicates that only a small fraction of these prominences did not obey the chirality rules they discovered and that Martin et al. (1994) confirmed.

1. Introduction

Martin, Tracadas and Billamoria (1994, hereafter MTB) rediscovered a regularity first uncovered by Leroy, Bommier and Sahal-Brechot (1983). Sinistral (dextral) filaments with axial fields pointing to the left (right) as viewed from the neighboring positive magnetic field region, predominate in the southern (northern) hemisphere. This preference is independent of the solar cycle number.

MTB's hemispheric rule is only statistical; of 72 filaments, 11% were exceptions to the rule. Active region filaments do not show such a regularity. Filaments bordering active regions show only a slight tendency.

MTB also found that the orientation of the "barbs" or "legs" of quiescent filaments is a reliable indicator of the sinistral/dextral characteristic. Dextral filaments were invariably "right-bearing" and sinistrals invariably "left-bearing" whenever both characteristics could be determined with confidence.

MTB inferred the direction of the axial fields from the appearance of the H_α plagettes near the filaments. Although this method yields consistent results, direct measurements of the axial field components would be more objective. Fortunately, we can use the data set of Leroy et al. (1983, 1984, hereafter LBS) to make an independent check on the results of MTB.

LBS measured the depolarization of the HeI D3 line (the Hanle effect) in 256 prominences at the solar limbs, during summer campaigns from 1974 to 1982. Their analysis yields two possible field vectors, symmetric about the line of sight. In many but not all cases, the two vectors have opposite components along the axis of the prominence, a 180° uncertainty in the axial field direction.

In this paper we reanalyzed the data set of LBS, selecting favorable cases in which both possible field vectors have the same direction of the axial component. In such cases an unambiguous classification of a filament as sinistral or dextral is feasible. Full details of our procedure can be found in Zirker et al. (1997).

We also report on an investigation of barb orientation as an indicator of the sinistral/dextral character.

2.   Results for the LBS Data Set

Of 256 prominences in the 1984 catalog, 50 were in active regions and were excluded from this study. Of the remaining 206, 131 permit a definite classification. Of these 131 prominences, 36 do not appear on synoptic H_α maps, so that their orientations to the line of sight (a necessary piece of information) could not be determined.

Of the remaining 95 prominences, only four disobey the hemispheric rule. We examined the four exceptional cases to find a common factor, without success.

3.   A Test of the Barb Regularity

We searched the film archives of the Ottawa River Solar Observatory (ORSO) for the 95 classifiable filaments.

In the years 1978, 1979, 1980 and 1982, 53 filaments were classifiable in the LBS data set. Of these, 32 appeared in the ORSO data set. Of these 32 only 12 were classifiable as sinistral or dextral from the arrangement of their barbs. Many filaments had barbs extending normal to the filament axis, and others had only one or two barbs with definite inclinations. Polar crown filaments usually lacked sufficient fine structure to be classified. Of the 12 classifiable filaments, we found that three disobeyed the hemispheric rule.

4.   Conclusions

This study confirms and strengthens the results of MTB. Quiescent filaments and filaments at the borders of active regions obey the hemispheric rule with only a few exceptions. However, exceptions do exist and, so far, we have no explanation for them.

Our attempts to test barbs as an indicator of sinistral or dextral character were hampered by too small a sample. We recall, however, that MTB found a one-to-one correlation whenever a reliable comparison was possible.

References

Leroy, J-L., Bommier, V. and Sahal-Brechot, S. 1983, Sol. Phys., 83, 135
Leroy, J-L., Bommier, V. and Sahal-Brechot, S. 1984, A&A, 131, 33

Martin, S.F., Billamoria, R. and Tracadas, P.W. 1994, in Solar Surface Magnetism, (ed.) R. Rutten and C.J. Schrijver, Kluwer Acad. Publ., Dordrecht, Holland, p. 339

Zirker, J.B., Martin, S.F., Harvey, K. and Gaizauskas, V. 1997, Sol. Phys., 175, 27

Large-Scale Patterns of Prominences in the Global Solar Cycles During 1880–1995

Dirk K. Callebaut

Physics Dept. UIA, University of Antwerp, B-2610 Antwerp, Belgium

Valentine I. Makarov and Ksenia S. Tavastsherna

Pulkovo Astronomical Observatory, 196140, St. Petersburg, Russia

Abstract. The zonal distribution of prominences, their poleward migration from the sunspot zone to the poles, the polar magnetic field reversals and a correlation of the mean latitude of filament bands at minimum activity with the maximum of Wolf number in the next cycle are briefly discussed for the period 1880–1995. The need for research on the long-term latitude distribution of the prominences is emphasized. New results concerning long-term variations of the torsional oscillations of the Sun and quasi-periodic oscillations of the latitude zonal boundaries from an analysis of H_α charts (1915–1990) are given.

1. Introduction

Prominences are one of the main manifestations of solar activity. Moreover they have the advantage of occurring at all latitudes from the poles to the equator. The latitude-time distribution of prominences is not random. They show the pattern and evolution of the zonal structure of the large-scale magnetic field and demonstrate the process of polar magnetic field reversal. Flares and coronal mass ejections are certainly linked with the instability of prominences. The main observational features concerning the large-scale pattern of the prominences are derived using observational data for 11 cycles of solar activity (Makarov and Sivaraman 1989, Callebaut and Makarov 1992, Makarov 1994).

It has been shown that there is a zonal structure in the distribution of the prominences (Makarov 1984, Makarov and Mikhailutsa 1992). In each hemisphere the predominent distribution of prominences in the polar, middle and equatorial zones may be detected. These zones coincide with the boundaries of the large-scale rotational symmetric component of the magnetic field.

No phase of the cycle shows a regular equatorward migration of the prominence zonal boundaries or of the single filaments. However, they show a poleward migration with a velocity varying from 5 ms^{-1} to 40 ms^{-1} starting after minimum activity up to the polar magnetic field reversal (Makarov 1984, Callebaut and Makarov 1992).

The trajectories of the boundaries of magnetic regions of one polarity were investigated as they migrate to high latitude with the progress of solar activity. The epochs of the reversals of the polar field for the entire period 1870–1991

were determined (Makarov and Sivaraman 1989, Makarov and Makarova 1996).

It was shown that the mean latitude of the filament band at the minimum of the cycle correlates with the maximum Wolf number in the succeeding cycle (Makarov and Mikhailutsa 1992). The dependence between them is given by

$$W(N) = 605 - 10.4 < \Theta_{2,m} >$$

with the correlation coefficient 0.94. The average latitude $< \Theta_{2,m} >$ during 1996 was $39°$, which corresponds to $W(23) \approx 200 \pm 20$.

Hence, the latitude-time distribution of the prominences is a rich source for the investigation of new global properties of solar activity. In the present report we give new results concerning long-term variations of the torsional oscillations of the Sun and quasi-periodic oscillations of the latitude of the zonal boundaries from an analysis of H_α charts during the period 1915 to 1990.

2. Observational Data

Continuous series of the latitude-time distribution of prominences were composed for 1880–1995 on the following bases:

- Meudon (d'Azambuja) charts – C.S.S.S. (1919–1964), Rot. 877–1486;

- Kodaikanal H_α and CaII-K spectroheliograms (Makarov and Sivaraman 1989);

- Italian data (Ricco 1914, Bocchino 1935);

- Wolfer's Catalogue of prominences (Wolfer 1909);

- Kislovodsk Solar Observations (S.D.B. 1960–1995).

The Meudon charts of the filament distribution were completed by the daily observations of prominences. One can see that the prominence samples form global magnetic neutral lines which extend from E to W and form closed contours encircling a region of basically one polarity. Of course they contain some small weaker bipolar fields as well, especially at the photospheric level, but at 10,000 km above the photosphere the latter have lost their importance.

3. Torsional Oscillations of the Sun Derived from the Distribution of Prominences

Long-term variations of the differential rotation of the solar large-scale magnetic fields were investigated. 1024 H_α charts were used for the period 1915–1990. The method of field expansion in terms of Walsh functions was used. From 1915 to 1990, 7 bands of faster-than- and 7 bands of slower-than-average rotation were revealed. These bands drift towards the equator from $\Theta = 45°$ in 2.5 to 8 years. The width of the bands varies from 3 to 7 years and they are in anti-phase with the solar activity. The latitude length of the bands of torsional oscillations varies from $0.4R_\odot$ to $1.3R_\odot$ and they show a long-term variation of about 55 years. The poloidal component of velocity V_Θ varies from 2 ms^{-1} to 6 ms^{-1}.

The maximum velocity of the equatorial drift occurred in the period between 1935 and 1955 and it developed before the maximum activity of the strong 19th solar cycle. During the modern epoch from 1965 to 1985 the value V_Θ did not exceed 3 ms^{-1}, but it shows now a tendency to increase. The bands of slower-than-average rotation correspond to the evolution of magnetic activity towards the equator in the butterfly diagram (Makarov, Tlatov and Callebaut 1997).

4. Oscillations of the Latitude of the Zonal Prominence Boundaries

It was shown that in each hemisphere the zonal structure in the latitude-time distribution of prominences exist. These zones coincide with the boundaries of the large-scale rotation symmetric component of the magnetic field. H$_\alpha$ charts make it possible to calculate the average per rotation of the latitudes of zonal boundaries $\Theta_i(t)$,

$$\Theta_i(t) = \sum_n \Theta_{i,n}(t)/n,$$

where $i = 1, 3, 5...$ denotes the boundary of $+/-$ polarity and $i = 2, 4, 6...$ denotes the boundary of $-/+$ polarity (both starting from N pole). $\Theta_{i,n} =$ the latitude at the nth point of the longitude.

The latitude variations of the zonal boundaries during 1915–1989 consist of the poleward migration and quasi-periodic oscillations. The time-poleward migration depends on whether one-fold or three-fold field reversal occurs. In the case of cycles with one-fold field reversal the time of latitude boundary evolution is about 22 years. For the cycles with a three-fold reversal the zonal evolution time is about 8–12 years. The velocity of poleward migration of the latitude zones $V(N)$ is caused by the sunspot activity, as there is a correlation between $V(N)$ and the total sunspot area for the cycle (N-1), expressed in 10^{-3} area of the hemisphere, $V(N) = 0.18A^2 + 2.5$ ms^{-1}, where $A = \sum Sp(N-1)$.

During 1915–1990 only one-fold polarity reversals were observed in the Southern hemisphere and the life-time of the boundaries was about 300 solar rotations ($\approx$ 22 yr). The latitude oscillations of the boundaries have a period of 16–20 solar rotations (mean $\approx$ 18 sol. rot, $4 \cdot 10^7 s$), their horizontal velocity is about 5 ms^{-1} and the amplitude of the oscillations is about $5 \cdot 10^7$ m. In the same period the sunspot area periods took about 10 solar rotations (Makarov, Petrova and Tavastsherna 1985).

In the Northern hemisphere one-fold and three-fold polarity reversals were observed and the life-time of the boundaries was about 170 solar rotations ($\approx$ 13 yr). The periods of latitude oscillations of boundaries are about 16–18 solar rotations. For fluctuations of sunspot total areas a period of about 6 solar rotations was found.

We conclude that the pattern of the latitude oscillations of the magnetic field with the period of about 18 solar rotations is not directly associated with sunspot activity, as it is observed at minimum activity too. The nature of those oscillations is not yet understood. However, we are now investigating any regularities or periodicities from the observational viewpoint.

5. Conclusions

Of course each individual solar phenomenon has to be investigated fully. However, if one wants to obtain clues for the mechanism(s) of the global solar cycle, it seems important to emphasize the following:

- The need for investigating the long-term behaviour of each solar phenomenon.

- The need for correlating all the solar phenomena: the periods, the phases, the waxing and waning, the long-term variations, intensities, etc. Moreover this has to be done on a restricted scale too, e.g., torsional oscillations may be studied by Doppler-shifts, by H_α charts, by the green coronal line, etc., in fact connecting the appearance of the same phenomenon at various depths.

References

Bocchino G. 1935, Mem. Observ. Arcetri, 67, 7

Callebaut D.K. and Makarov V.I. Solar Phys., 141, 381

C.S.C.S – Cartes Synoptiques de la Chromosphere Solaire: 1919–1964, Meudon

Makarov V.I. 1984, Solar Phys., 93, 393

Makarov V.I., Petrova N.S. and Tavastsherna K.S. 1985, Soln. Dann. Bull., 6, 69

Makarov V.I. and Sivaraman K.R. 1989, Solar Phys., 123, 367

Makarov V.I. and Mikhailutsa V.P. 1992, Solar Phys., 137, 385

Makarov V.I. 1994, Solar Phys., 150, 359

Makarov V.I. and Makarova V.V. 1996, Solar Phys., 163, 267

Makarov V.I., Tlatov A.G. and Callebaut D.K. 1997, Solar. Phys., 170, 373

Ricco A. 1914, Mem. Soc. Spectr. Ital., 33, 17

S.D.B. 1960-1995, Soln. Dann. Bull., Nos. 1-12

Wolfer A. 1909, Publ. Sternwarte Eitg. Polytechn., Zurich, B. 1-4, 1-57

Chirality, Helicity, and Joy's Law

P. Foukal

CRI, Inc., Boston, MA 02134 USA E-mail: pfoukal@world.std.com

Abstract. Connections between the morphology of filaments and the global topology of the sun's magnetic field, are an important topic that seems ready for assembly into a coherent picture. We suggest that the chirality of mid-and high-latitude filaments described by Martin et al. is most easily understood if they form in evolved "Type 1" neutral lines within active region bipoles, rather than in the "Type 2" neutral lines formed at the boundaries between bipoles, where lower-latitude filaments tend to form. This interpretation removes the disagreement between filament chirality and the well-known tilt of bipolar active regions described by Joy's law, which exists if the high-latitude filaments formed at Type 2 neutral lines. Dynamical explanation of these two observed regularities probably implies quantitative understanding of the processes that govern the sign and magnitude of the α and ω-effects in a solar dynamo.

Many interesting topics have been discussed at this meeting, and it would be difficult to do them justice in the space available here. Rather, let me focus on an area where the observations, theory, and modeling seem to be at a stage where we might make progress by knitting together a unified picture from its parts. Our former colleague Spencer Weart told me in 1971, prior to leaving us for a distinguished career in history of science, that solar physicists spend too much time building bricks and not enough time building houses. So let's try to use some of the interesting new bricks presented here to build a house. From what I have heard, the magnetic geometry of filaments and prominences, their dynamics, and the information they provide on the geometry of the global solar magnetic field, seem amenable to such a construction project.

Let me begin with a few brief comments on magnetic neutral lines. The simplest kind of neutral line (I'll call it Type 1) occurs within a bipolar active region (Figure 1a). Since it occurs within a bipole, the field lines connect across it, and often they are visible as elongated dark structures (AFS, fibrils). But filaments of significant size are rarely associated with such a neutral line, at least in its early stages of evolution. A second type of neutral line occurs when two bipolar active regions appear side by side (Figure 1b, c). Here, most of the field does not seem to connect across the neutral line, instead it runs parallel to it. This is the kind of neutral line that produces most filaments in active latitudes.

In principle, the field directions on opposite sides of such a neutral line of Type 2 could be either parallel (Figure 1(b)) or anti-parallel (Figure 1(c)). But, on the sun, only the parallel configuration seems to occur (Foukal, 1971). Some thought suggests why this is so. In the active latitudes, the bipolar axes of active regions are tilted relative to the equator by a significant (10–20°) angle, so that the preceding (p) polarity lies at systematically lower latitude. This tilt, and its

⊕ ⟶ ⊖   (a)   type 1

⊕ ⊖ ⊕ ⊖   (b)   type 2

⊕ ⊖ ⊖ ⊕   (c)   (not observed)
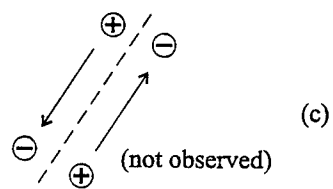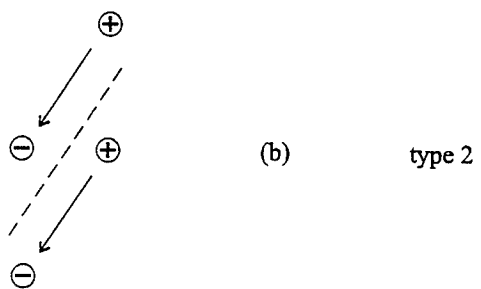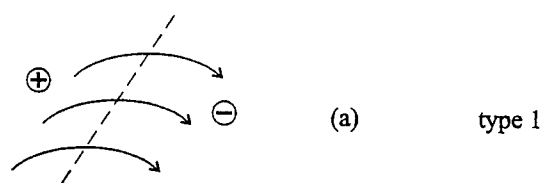
neutral line: – – – – – – – –
field line: ⟶

Figure 1.

latitude dependence, is described by Joy's law, which is one of the key facts we have known about solar magnetism for almost 80 years (Hale et al. 1919).

If we draw the neutral line implied by Joy's law, including both the Type 1 neutral lines within the bipoles, and also the Type 2 lines between them, we obtain a configuration that is idealized in Figure 2. We can see from this Figure that, given the tendency to alignment of the bipolar fields, the parallel (rather than anti-parallel) configuration of the horizontal component of field on either side of the Type 2 neutral line is the only possible arrangement, provided most of the flux in such low-latitude active regions connects internally, rather than externally between active regions. The anti-parallel streaming of fibrils on opposite sides of the Type 2 neutral line indicates that is the case.

From the above, it follows that the directions of horizontal field in most filaments and filament cavities found between active regions will be the same as the field direction across the Type 1 neutral lines within the bipoles themselves. For instance, when (p) polarity is positive, filaments and channels in these latitudes will contain fields with an east-directed horizontal component in the northern hemisphere, and a west-directed component in the southern hemisphere. This polarity of the equatorial component of the prominence fields seems consistent with the Zeeman measurements on prominence magnetic fields carried out by Rust (1967) around activity minimum between cycles 19 and 20. Certainly, it would be hard to understand how the dominant direction of magnetic fields between bipolar active regions could disagree with their direction within the immediately adjacent bipoles.

Let us now investigate the relationship of the two types of neutral lines shown in Figure 2 to the "handedness" or "chirality" of filaments described by S. Martin and her co-workers (Martin et al. 1994). Her key findings are: a) quiescent filaments and filament corridors are predominantly "dextral" in the northern hemisphere and "sinistral" in the south; b) this sense of chirality is invariant from cycle to cycle (although the magnetic field polarity switches every 11 years); and c) this N-S asymmetry of chirality is not seen in active region filaments and corridors, which exhibit both dextral and sinistral behavior in both hemispheres. Let's also note that, since the observed chirality is invariant with respect to polarity switches between cycles, its essence is that the lower-latitude polarity precedes (in the direction of solar rotation) the polarity positioned at higher latitude (see Figure 3).

Now, this observation of predominantly dextral structures in the north and sinistral in the south would not be expected from the configuration at Type 2 neutral lines. As shown in Figure 2, we expect these to be mainly sinistral in the north and dextral in the south. I propose that the observed chirality amongst quiescent filaments and corridors would be easiest to understand if we assume that they form in the later stages of evolution of Type 1 neutral lines. It is well known from studies of the random walk of solar bipolar fields (e.g., Leighton 1964, Sheeley 1992) that, as the bipolar fields mature, the f-polarity migrates toward the poles while the two opposing p-polarities move toward the equator, where they eventually merge. This process occurs over time scales that enable the sun's latitudinal differential rotation to shear the field, and its sense of shearing agrees with the observed shear of neutral lines reported by Martin et al.

N

Sinistral fibrils, filaments

E   Equator   W

Dextral fibrils, filaments

S
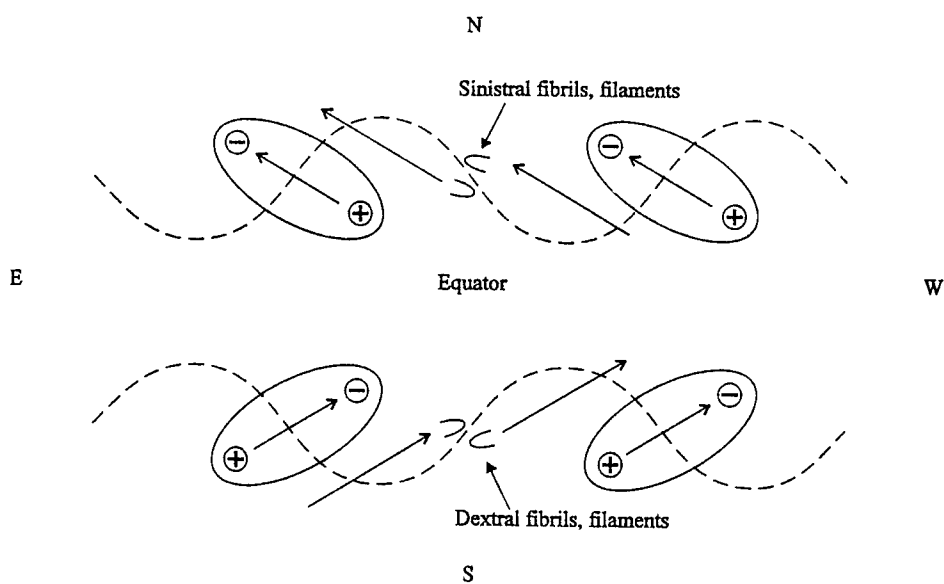
N.B. In this figure, we adopt p, f polarities as +ve, -ve, respectively, in the N. hemisphere.

Figure 2.

N

Dextral

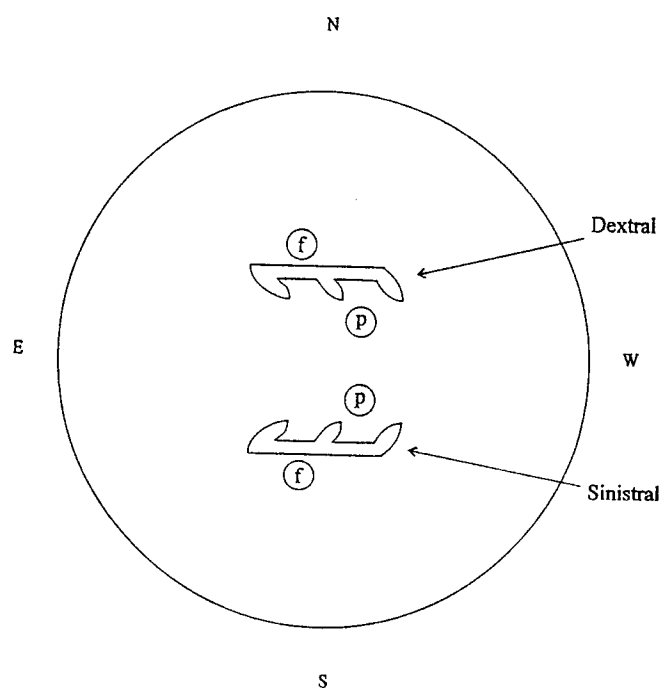E   W

Sinistral

S

Figure 3.

This tendency of differential rotation to produce the observed chirality in Type 1 neutral lines should act on whatever "primordial" chirality may be observed in newly emerged Type 1 neutral lines. In the simple picture illustrated in Figure 2, we would expect no primordial chirality, but emerging AFS probably exhibit non-potential character on emergence. The relative importance of the primordial and evolutionary influences, which would be related respectively to α and ω effect in dynamo language, remains to be established by observations.

In this picture, we would expect that filaments and corridors observed in active latitudes would include a mix of dextral and sinistral structures, produced at both Type 1 and 2 neutral lines. This agrees with Martin et al.'s results. By the time these neutral lines moved to the higher latitudes located at and above the upper limit of the sunspot belt, where most quiescents (and their corridors) are observed, we would expect the progressive shearing of the evolved Type 1 neutral lines to become most noticeable, leading to the observed predominance of dextral structures in the N and sinistral in the S (Figure 3). Another aspect of selection that may contribute to the predominance of one chirality in quiescents, is the progressive tendency of Type 2 neutral lines to contribute fewer filaments, in their later evolutionary stages, for reasons I return to below.

Sheeley and co-workers have developed very useful kinematical simulations of the random walk of photospheric magnetic fields, and shown that they provide sensible explanations to aspects of solar magnetic field evolution that were once considered mysterious. The extension of such models to enable tracking of the connections between magnetic flux elements has been undertaken by van Ballegoijen and his collaborators, and such models will be helpful in deciding which neutral line Type (if either) is preferred. But it is also worth placing some limits both on the new information contained in the findings on chirality (and helicity; e.g, Rust 1997), and also on what we can expect to learn about its underlying dynamics.

On the first subject, we seem to be learning that latitudinal differential rotation may be capable of impressing a systematic shear on long-lived magnetic neutral lines, and on the chromospheric and coronal structures that form along them. This is important to know, but it suggests that study of the chirality and helicity of such structures extends to higher latitudes information that is more likely to be complementary to (rather than qualitatively different from) information available in the sunspot belts from past studies of Joy's law. These studies have used much longer data bases on the motions of photospheric magnetic tracers, than are available for study of Hα structures, and they should be useful in future work on helicity also.

Regarding the second subject, we should consider that if the picture put forward above is correct then the fundamental mechanism underlying the N-S asymmetry of chirality is the same as that underlying the progressive (with time) separation in latitude of p and f polarities. It has been considered since Leighton's pioneering work that this occurs because the p polarity of a bipole tends to erupt at systematically lower latitude than its f polarity (Joy's law). Ideas have been put forward to "explain" Joy's law, (Parker 1955, Babcock 1961, Leighton 1964) based on the winding up (helicity-generation) of flux ropes by both latitudinal and radial gradients of solar rotation. But no good consensus has been reached on a quantitative model. Further study through helioseis-

mology of sub-photospheric velocity fields, together with increasingly sophisti-
cated models of discrete flux-tube interactions with plasma motions (e.g., d'Silva
1992), will eventually show us the way toward an explanation of Joy's law. But
let's be aware that the underlying dynamical question is the same as the classi-
cal problem of defining the sign and magnitude of α-effect in dynamos, and its
relative importance to ω-effect.

A determination of whether quiescent filaments form at evolved neutral
lines of Type 1 rather than of Type 2 would have important implications for
their dynamics, since Type 1 neutral lines favor a Kippenhahn-Schluter support
mechanism, rather than the neutral sheet configuration of the Kuperus-Raadu
scenario. This does not seem consistent with the Hanle observations of Leroy
(1978) and Leroy et al. (1983) which indicate that quiescent prominences ex-
hibit an "inverse" rather than "direct" magnetic geometry. However, careful
interpretation of this Hanle result is necessary, and different analyses are yield-
ing qualitatively different results (Anzer and Heinzel, 1998). An interesting
explanation of how "inverse" polarity might arise at a neutral line that seems of
"direct" polarity has been put forward by Martin et al. (1994). But the expla-
nation seems to apply only to Type 2 neutral lines, not to the Type 1 variety at
issue here. So there is a need to reconcile the Hanle results with the picture of
Type 1 neutral lines producing quiescents.

As a final point, let me return to considering why evolved Type 2 neu-
tral lines may produce progressively fewer filaments than in their early stage of
evolution, a point I suggested earlier. The anti-parallel streaming of fibrils on
either side of Type 2 neutral lines, along with the reversal of the longitudinal
polarity along these neutral lines, indicates a parallel, rather than anti-parallel,
direction of the horizontal field component on either side. But let's not over-
look the equally interesting fact that the large vertical component of the field
is oppositely directed in plagettes located in close proximity across this neutral
line. This abrupt sign switch seems well suited to formation of a neutral sheet.
As the Type 2 neutral line evolves the field gradients and neutral sheets will
decay, making it less likely that a filament will form. This needs to be checked
observationally. Clearly, we need more brick building, but let's keep working on
the house at the same time.

References

Anzer, U. and Heinzel, P. 1998, Solar Phys., 179, 75
Babcock, H. 1961, ApJ, 133, 572
d'Silva, S. 1992, in The Solar Cycle, K. Harvey (ed.), ASP Conf. Ser. 27, San
        Francisco, p. 168
Foukal, P. 1971, Solar Phys., 19, 59

Hale, G., Ellerman, F., Nicholson, S., and Joy, A. 1919 ApJ, 49, 153

Leighton, R. 1964, ApJ, 140, 1547

LeRoy, J. 1978, A&A, 64, 247

LeRoy, J. , Bommier, V., and Sahal-Brechot, S. 1983, Solar Phys., 83, 135

Martin, S., Bilimoria, R., and Tracada, P. 1994, in Solar Surface Magnetism, R. Rutten, and C. Schrijver (eds.), Kluwer Acad. Publ., Dordrecht, Holland, p. 303

Parker, E. 1955, ApJ, 122, 293

Rust, D. 1997, in Coronal Mass Ejections, N. Crooker, J. Joselyn and J. Feynman (eds.), AGU Geophys. Mono., Vol. 99, Washington, DC, p. 119

Rust, D. 1967, ApJ, 150, 313

Sheeley, N. 1992 in The Solar Cycle, K. Harvey (ed.), ASP Conf. Ser. 27, San Francisco, p. 1

A Dynamic Dextral-Sinistral Model for the Structure and Evolution of Prominence Magnetic Fields

E. R. Priest

Mathematical and Computational Sciences Department, St. Andrews University, St. Andrews, KY16 9SS, Scotland, U.K.

Abstract. We propose the following coherent model for prominences.

(i) They are composed of many fine threads whose mass we suggest has two kinds of origin. Some of the mass may be lifted from the upper photosphere in response to cancellation of magnetic flux in small flux tubes. If this rate of mass supply is slow then the mass needs to be supported, but if the mass supply rate is as large as the natural rate of draining then no support is necessary. However, much of the mass may not need to be supplied or supported at all, if it comprises dynamic threads of cool plasma that are in pressure balance with their hot surroundings and are continually forming from the corona and heating up again in response to a localised heating mechanism.

(ii) The overall structure is of a large-scale flux tube along the polarity inversion line with an overlying arcade that links the network on either side of the filament channel. The structure of the channel and of barbs is explained by the distribution of flux sources along the channels, with majority polarity producing plagettes and minority polarity the barbs.

(iii) The chirality of polar-crown prominences is suggested to be caused by a combination of subsurface flows, flux emergence and reconnection. By contrast, two generic types of low-latitude filament, namely those associated with unipolar flux tongues and with the emergence of new active regions near to remnant regions, are a natural consequence of nonuniform flux distribution and converging flux.

1. Introduction

Prominences owe their birth, maintenance and death to the magnetic field, so I plan here to give an overview of the role of the magnetic field in this structure and evolution. At the IAU prominence colloquium in Hvar eight years ago there were several paradigms about prominences, namely:
(A) Formation is by radiative instability when the length is too long;
(B) The structure is a sheared force-free field of Normal or Inverse type;
(C) Prominence material is basically static, supported in a magnetic dip;
(D) The eruption occurs when the twist or shear are too great.
How has our understanding developed since then? In attempting to answer that question I shall consider the local thread structure (Section 2), the large-scale structure (Section 3) and the chirality (Section 4).

2.   To Support or Not to Support – A Dynamical Model

That is a key question about the nature of prominences. The assumption that support is necessary and that a magnetic dip is necessary to provide such support has dominated the theory of prominences for many years. But is support necessary? If a prominence consists of a static slab of uniform plasma, then the answer is clearly yes, since the free-fall speed from a height of, say 30 Mm, is about 100 km s^{-1}, whereas most of the observed plasma is moving much more slowly. Furthermore, hydrostatic equilibrium along an inclined field line would produce an exponential fall-off of pressure with height ($p = p_0 \exp(-z/H)$) with a scale-height (H) of typically 200 km at prominence temperatures, whereas such a rapid fall-off is not observed in prominences. A similar problem would arise in fibril plasma if a cool fibril were in pressure balance with its hot environment and its vertical thickness were more than about 200 km since the pressure would decrease substantially across it.

The most effective way of supporting plasma is in a magnetic dip. Such a dip along the length of a prominence is unlikely since the magnetic field would need to be exceptionally flat: a dip of only 400 km along the 100 Mm length of a prominence would, for instance, make the central pressure ten times the end pressure. The general assumption, therefore, has been that the magnetic field lines cross the prominence at a narrow angle and that they have a very shallow dip, as in a weakly twisted flux tube. Thus, for example, a ratio of vertical to horizontal field in a plane perpendicular to the polarity inversion line of only 0.05 would naturally support a prominence of width 2H/0.05, or about 6 Mm, as observed. Thus the natural explanation of the narrow width of a prominence has been a good feature of a twisted flux tube model.

However, how fast would plasma drain out of a flux tube along a field line inclined at θ to the horizontal? Accelerating from rest under gravity alone a plasma element would fall a vertical distance $h = s \sin \theta$ in a time $t_f = \sqrt{(2h/g \sin^2 \theta)}$. For example, if the vertical distance (h) were 10 Mm, say, and the inclination angle were 5°, the fall time (t_f) would be about an hour, and if the angle were 1° it would be about four hours. Other effects such as pressure gradients and viscous forces could increase these times substantially. If the rate of mass supply is low then the plasma needs to be supported in a prominence. However, the above estimate suggests that in a dynamic model support is not necessary in two distinct variants. The first is if the plasma is continually brought up from the chromosphere and replenished rapidly enough, and the second is if cool plasma threads do not live much longer than a few hours but simply represent coronal plasma that is continually condensing and reheating.

2.1.   Mass Supply in Response to Flux Cancellation

Flux cancellation is a common occurrence under prominences at several locations along a filament channel. We have therefore suggested in our earlier formulation of a chiral dextral-sinistral model (Priest et al. 1996) that such sites represent regions where field lines are reconnecting and carrying mass up into the corona. This represents a natural way of replenishing mass in a prominence. Provided such a rate of mass supply is efficient enough, it can balance the rate of draining and remove the need for support. By means of a simple model we have calculated

the height to which the captured mass is raised and the way the mass spreads out along a field line as it moves upward. These, together with the resulting plasma density, all compare favourably with what is needed in a prominence.

2.2. Dynamic Recycling of Thread Plasma

Instead suppose a prominence consists of threads that are in pressure balance with their surroundings and are continuously forming from coronal plasma by radiative condensation and are then heating up again in a random manner in response to a sporadic heating process. This can either take place in a region of horizontal or dipped field or, if the time for draining exceeds the time between heating bursts, in an inclined field.

Prominence threads are typically 200–300 km wide and 5000 km long and have lifetimes of about 8 min or even as short as 1 min (Engvold 1989). Their temperatures and densities are typically 8000 K and 10^{16} m^{-3} and so could be in pressure balance with an ambient coronal plasma of 10^6K and 10^{14}m^{-3}. The magnetic field is not thought to vary substantially across them (Leroy 1989).

Let us consider an elementary cooling-heating process in a fibril along the magnetic field. Suppose we start with uniform coronal plasma at temperature T_h
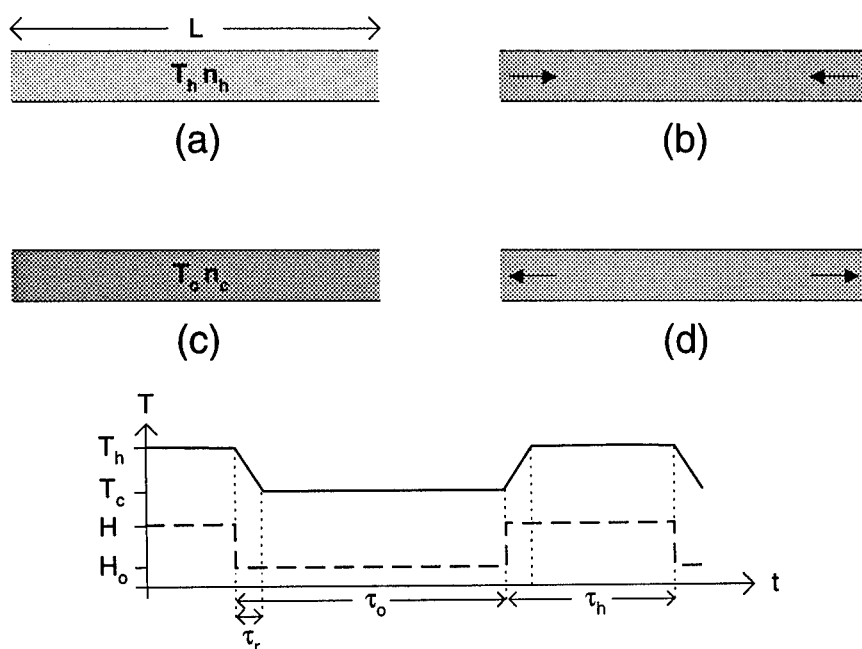
Figure 1.   (a) – (d) An elementary formation-dissolution process for a fibril of temperature T_c that forms from corona of temperature T_h. (e) A schematic of the heating (dashed) and temperature (solid) profiles.

and density n_h (Figure 1a) in equilibrium under a balance between say heating of strength, H, and conduction over a long length-scale, L_e. Suppose next that the heating over a length, L, is switched off and the plasma cools down (Figure 1b)

with plasma flowing into the region of radiative condensation. Eventually after a response time τ_r, say, a new cool fibril equilibrium is set up at temperature, T_c, and density, n_c (Figure 1c), which is maintained for a time, τ_0, after the heating was switched off. Then suppose the heating is switched on again so that for a further time, τ_r, the plasma heats up and expands along the field (Figure 1d) until a new hot equilibrium is established once more for a time τ_h, say.

The whole process will take place at uniform pressure if the time-scales are much longer than the sound-travel time $(\tau_s = L/c_s)$ along the fibril. The responsive time (τ_r) is the minimum of the radiative time (τ_{rad}) and the conduction time (τ_{cond}), provided this is longer than the time (τ_s) it takes to switch off or on the heating process. We suggest that this elementary process is repeated in neighbouring flux tubes due to randomly distributed impulsive heating.

3.   To Twist or Not to Twist – A Global Flux Tube

There are three main elements to the global field around a prominence in our model, namely the polarity inversion line (PIL), a large-scale horizontal flux tube aligned along the PIL (Figure 2) and an overlying magnetic arcade, anchored in the network elements both sides of the PIL.
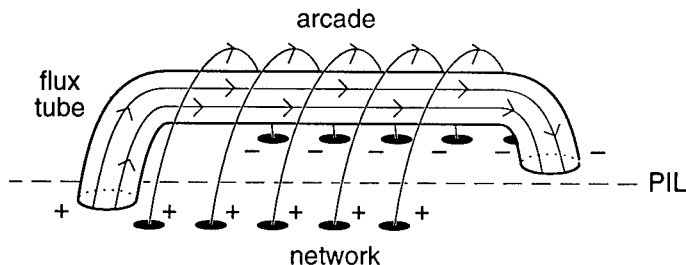

Figure 2.   Global field structure for a dextral prominence with a large flux tube along the polarity inversion line underneath the arcade associated with the network on either side of it.

A key question for the global structure is whether the flux tube is always twisted or not. Often such twist is not observed, but of course absence of evidence is not the same as evidence of absence, since the structures you see in Hα, for instance, do not necessarily always indicate the magnetic structure and a twisted flux tube filled with uniform plasma would show up as uniform untwisted tube. Thus, a weak twist may still be present when it is not observed. Furthermore, such a twist is reasonable on theoretical grounds: it naturally explains the narrow width of a prominence and, if reconnections are taking place, the magnetic helicity will be conserved and will relentlessly build up (unless it cancels with opposite helicity). Furthermore, a helical flux tube is naturally created by reconnection when the opposite-polarity footpoints of two neighbouring loops approach the polarity inversion line and cancel (van Ballegooijen and Martens 1989). Thus some twist is natural, but the question still arises whether twist is essential to the existence of a prominence or not.

Flux tube models naturally stress the component of the field along the prominence. Hood and Priest (1979) suggested that an active-region filament is a flux tube filled by radiative condensation with cool plasma. At the Hvar colloquium we proposed a global flux tube model (Priest et al. 1989) which has since been developed and modified by several authors (e.g., Antiochos and Klimchuk, 1993, Low, 1991, Rust and Kumar, 1995).

3.1. Structure of the Filament Channel

We adopt the basic structure of the prominence environment shown in Figure 2 with a region of strong horizontal flux along the polarity inversion zone between the opposite polarity network. But what creates the detailed structure in filaments and filament channels, such as the kinks and gaps, that are often seen? We suggest they are a natural consequence of the location and strength of individual flux sources along the channel which show up as plagettes in Hα and have the same polarity as the network. We have modelled such a channel by superposing the field of a flux tube and that of plagette sources (Mackay and Priest 1996) and calculate the effect of the plagette flux (f) on the path of the filament and the dimensions of the plagette magnetosphere. As f increases, the kinking of the filament increases in amplitude and the width of the filament, as it passes between two plagettes, decreases. Eventually, when f is too large the width decreases to zero and the filament breaks into two parts.

We next considered the effect of neighbouring network flux on the filament and its channel (Mackay and Priest 1996). The simplest model consists of a pair of line sources (the network sources either side of the polarity inversion line) together with a source (f) and a sink ($-f$) of the filament channel flux. The view from above shows that the filament channel flux linking the source to the sink is bounded by a separatrix (dashed) which separates the filament channel flux from flux that links either the source or the sink to the network. In addition, the side view shows that the separatrix surface possess a lower boundary, which may explain the base of the prominence; below it, flux joins the two networks. Furthermore, the upper boundary may account for the top of the prominence or the coronal cavity; above it again flux links the two networks.

This idea has been used to model a particular filament forming between a remnant active region and a newly emerging region (Figure 3a). The magnetic structure deduced from photospheric magnetograms shows that the filament channel is a very narrow structure enclosed in a separatrix which shields the filament from the surrounding magnetic field (Figure 3b).

3.2. Structure of Barbs

One of the intriguing puzzles about prominences is the presence of barbs or feet, which are transient features with a lifetime of about eight hours, comparable with the lifetime of intra-network magnetic fragments. The key question to begin with, is to ask whether a barb represents a magnetic field line (Figure 4a), along which plasma can flow freely, or whether it represents a region of horizontal field that supports plasma (Figure 4b). The elegant model of Aulanier and Demoulin (1998) is of the second type and is very appealing, although the short lifetime of barbs suggests that support may not be necessary and the observed frequent downflow suggests that our first model may be preferable.
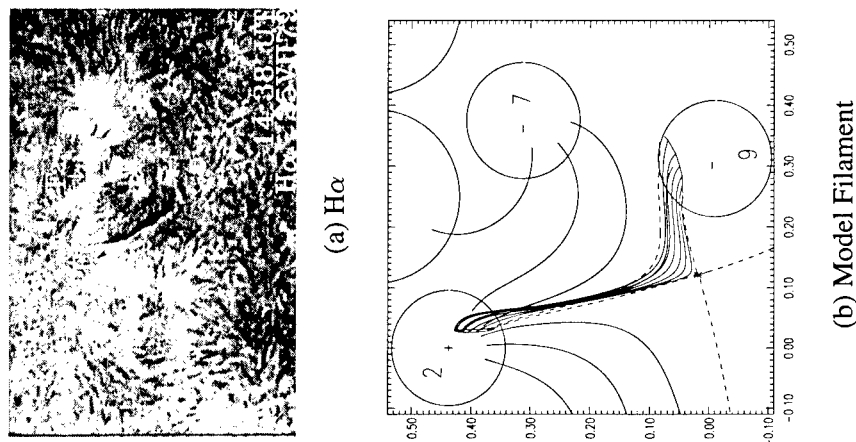
Figure 3.   (a) A newly formed filament (b) a close-up of the magnetic structure near the filament (Mackay et al. 1997).
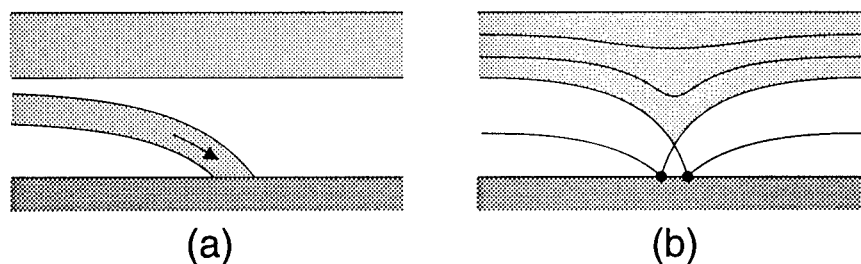

Figure 4.   Two possible configurations for a barb.

The second important question is: why do barbs only appear with the correct sense, i.e., dextral prominences have right-bearing barbs rather than left-bearing ones? We suggest that this is because the new bipoles tend to emerge below or close to the prominence with a preferred orientation due to the direction of the global subsurface flux (Figure 5). Thus when a new bipole emerges with that orientation, it will then reconnect and produce a dextral barb in the northern hemisphere and a sinistral barb in the southern hemisphere.

4.   Chirality

One of the most important discoveries to my mind over the past eight years is that of chiral structure by Martin et al. (1994), the fact that all prominences are either dextral or sinistral and that most quiescent prominences in the northern hemisphere are dextral whereas those in the southern hemisphere are sinistral. So, what is the cause of the chiral structure? I would like to suggest that it is a combination of the convergence of flux towards the polarity inversion line with three distinct effects:
I. Surface flows such as differential rotation, meridional flow and active-region

DEXTRAL BARB CREATION by FLUX EMERGENCE

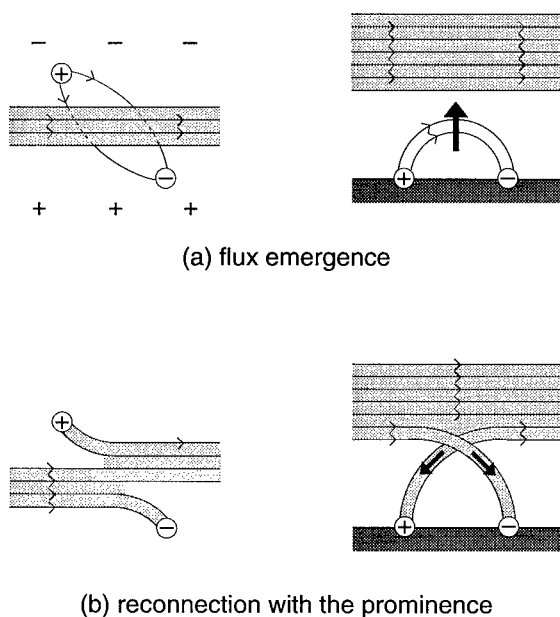(a) flux emergence

(b) reconnection with the prominence

Figure 5.   (a) The emergence of new flux near a filament (b) to give a barb, as viewed from above (left) or the side (right).

evolution, which shear the footpoints of coronal fields;

II. Subsurface evolution and emergence;

III. Generic flux distributions due to the locations of magnetic sources, which produce a potential magnetic field not necessarily normal to the inversion line.

Let us now consider the effect of these three processes to see whether we can explain different types of prominence.

4.1. Polar-Crown Prominences

Differential rotation acting on a north-south polarity inversion line can produce the correct chirality (van Ballegooijen and Martens 1990). However, when it acts on the east-west polarity inversion line that is typical of the polar crown it produces loops that have exactly the wrong chirality for prominences. But differential rotation is certainly present and many Yohkoh loops do have such a skew, so how does the Sun counteract it so powerfully in prominences?

We next consider the possibility of effect III. For the Leroy maps we calculated the potential magnetic field from Kitt-Peak magnetograms (van Ballegooijen et al. 1998) and found that all the polar-crown prominences have potential fields that are essentially normal to the polarity inversion line rather than having the large axial component that is required. (For the low-latitude prominences we found that for one-third of the cases the potential field possesses a strong shear,

most of which have the correct chirality, so for them explanation III works). We then tried hard to avoid a subsurface explanation by taking a realistic source distribution and acting on it with differential rotation, meridional flow and diffusion (van Ballegooijen et al. 1998). The result of this modelling was unsuccessful in that it produced sinistral structures along the northern polar crown.

We were therefore lead naturally to effect II (subsurface evolution) as the only viable mechanism for polar-crown prominences. The simple emergence of a twisted horizontal flux tube from below the photosphere is highly unlikely because the amount of plasma that would be lifted up is too large by a not insignificant factor, namely 10^9! Also it is the plasma that dominates the magnetic field below the photosphere for reasonable field strengths and not the reverse. We agree with Rust and Kumar (1995) that initially it is likely that there is a large-scale flux tube below the photosphere and finally, when the prominence has formed, there is a large-scale tube up in the corona, but the key question is what happens in between. How does the magnetic tube become disconnected from the plasma? A plausible answer is given by Dextral-Sinistral Model (Priest et al. 1996) which builds on the earlier ideas of van Ballegooijen and Martens (1989) as follows.

We suggest that differential rotation (or active-region flow) acts on the field below the surface to produce in a natural way the correct direction for the field component along the polarity inversion (i.e., Figure 6a). The field then floats to the surface and emergence and small-scale cancellation builds up the flux of the filament channel along the inversion line with the correct sense (Figure 6b). Next, large-scale flux cancellations form long field lines parallel to the inversion line which lift cool mass up into the corona (Figure 6c). We suggest that the filament consists of many such threads along the filament channel. The net effect is to create a weakly twisted flux tube, left-handed in the northern hemisphere. The twist arises because of the conservation of magnetic helicity during the reconnections. When the filament and arcade erupt they produce a magnetic cloud in interplanetary space with the correct sense of twist.

4.2. Low-Latitude Prominences

Now consider other kinds of quiescent prominence. There are two generic cases of typical flux distributions that often occur on the Sun and may give the correct chirality by effect III. First of all, the spread and distortion of active-region flux naturally produces dextral fields in the north, as we have confirmed by detailed studies of the evolution of either a simple bipole or of a Kitt Peak map (van Ballegooijen et al. 1998). Once the correct sign for the axial flux has been produced, it may be built up by convergence towards the polarity inversion line.

A second common case is when a new active region emerges at low latitude next to a remnant active region. The resulting flux distribution at the boundary between the new and old regions is found to have the correct chirality either if the relative convergence is included (Galsgaard and Longbottom 1998, these proceedings), or if the force-free field of the new active region with the appropriate helicity for that hemisphere is present (Mackay et al. 1998). For example, emergence of a new active region with positive α in the southern hemisphere produces a sinistral channel when it emerges to the right of the remnant active region and no channel (i.e., normal flux) when it emerges to the left.
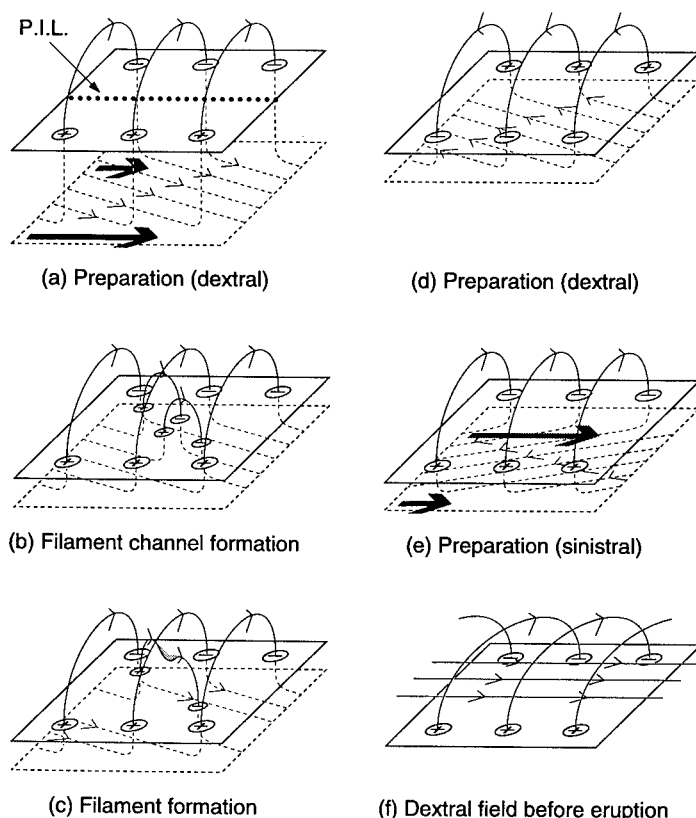
(a) Preparation (dextral)   (d) Preparation (dextral)

(b) Filament channel formation   (e) Preparation (sinistral)

(c) Filament formation   (f) Dextral field before eruption

Figure 6.   The dextral-sinistral model for the formation of a filament channel and a filament.

5.   Conclusion

With helpful suggestions from S. Martin, O. Engvold, T. Forbes, K. Harvey and J. Zirker, the St. Andrews group and A. van Ballegooijen have been trying to set up a coherent model for the prominence phenomena that brings together many diverse observational features and explains them in a natural way. The model has three parts:

(i) an explanation for the global chiral structure of polar-crown prominences in terms of subsurface evolution and of many low-latitude prominences in terms of generic flux distribution;

(ii) the global structure of a prominence and its filament channel, consisting of a flux tube along the channel separated from an overlying arcade by a separatrix surface;

(iii) the local thread-like structure, consisting of plasma that is continually condensing and heating up again and does not need support.

Some of the old paradigms are being replaced in this basic rethinking of the

fundamentals of prominence physics:

(A) Formation may be due to either the lifting of mass magnetically from the lower atmosphere, or it may be the continual forming by radiative condensation and heating in a dynamic way, rather than a single radiative condensation;

(B) The structure is likely to be a flux tube rather than a sheared arcade; in addition, the organisational principle that creates the chirality, forms the flux tube and supplies the mass is a combination of (i) subsurface flows, emergence and reconnection for polar-crown prominences, and (ii) generic flux distributions and converging flux for many low-latitude prominences;

(C) Prominence material is unlikely to be essentially static; instead we suggest that it is either continually replenished by magnetic reconnection at a rate that balances the natural loss; or dynamically recycled between hot and cool components at a rate that means there is no need for support of the material in its cool phase since it does not have time to drain down;

(D) The structure of the filament channel and the barbs may be a natural consequence of the distribution of magnetic flux sources within the channel.

References

Antiochos, S.K. and Klimchuk, J.A. 1993, ApJ, 370, 372

Aulanier, G. and Démoulin, P. 1998, A&A, 329, 1125

Engvold, O. 1989, in Dynamics and Structure of Quiescent Solar Prominences, (ed.) E.R. Priest, Kluwer Acad. Publ., Dordrecht, Holland, p. 47

Hood, A. and Priest, E.R. 1979, A&A, 77, 233

Leroy, J.L. 1989, in Dynamics and Structure of Quiescent Solar Prominences, (ed.) E.R. Priest, Kluwer Acad. Publ., Dordrecht, Holland, p. 77

Low, B.C. 1991, ApJ, 381, 295

Mackay, D. and Priest, E.R. 1996, Solar Phys., 167, 281

Mackay, D., Gaizauskas, V., Rickard, G. and Priest, E.R. 1997, ApJ, 486, 534

Mackay, D. et al. 1998, Solar Phys., in press

Martin, S.F., Bilimoria, R. and Tracadas 1994, Solar Surface Magnetism, R.J. Rutten and C.J. Schrijver (eds.), Springer-Verlag, New York, p. 303

Priest, E.R., Hood, A. and Anzer, U. 1989, ApJ, 344, 1010

Priest, E.R., Van Ballegooijen, A. and Mackay, D. 1996, ApJ, 460, 530

Rust, D.M. and Kumar, A. 1995, Solar Phys., 155, 69

van Ballegooijen, A.A. and Martens, P.C.H. 1989, ApJ, 343, 971

van Ballegooijen, A.A. and Martens, P.C.H. 1990, ApJ, 361, 283

van Ballegooijen, A.A. et al. 1998, ApJ, in press

CMEs and Prominences and Their Evolution Over the Solar Cycle

David F. Webb [1]

Institute for Scientific Research, Boston College, 140 Commonwealth Ave., Chestnut Hill, MA 02467-3862, USA

Abstract. Coronal mass ejections (CMEs) are an important aspect of coronal and interplanetary dynamics. They cause large geomagnetic storms and can drive transient interplanetary shocks, which in turn are a key source of energetic particle events. However, our knowledge of the origins and early development of CMEs at the Sun is limited. CMEs are most frequently associated with erupting prominences and long-enduring soft X-ray arcades, but sometimes with no observed surface activity. I review some of the well determined coronal properties of CMEs and what we know about their source regions, with emphasis on the characteristics of the associated prominences and helmet streamers. One of these characteristics is that many CMEs seem to arise from multipolar magnetic structures with multiple or kinked inversion lines. I also discuss the solar-cycle dependencies of these structures, including the role that erupting prominences and CMEs may play in the ejection of magnetic flux and helicity from the Sun.

1. Introduction

Coronal mass ejections (CMEs) are now considered a key causal link between solar activity and at least the larger interplanetary (IP) particle events and geomagnetic storms. The onsets of CMEs have been associated with both flares and filament eruptions (e.g., Webb 1992), although many CMEs cannot be associated with any observed surface activity. And, even if accompanied by energetic flares, most of the event energy is contained in the ejected mass and shock wave, not the flare. Most flares occur independently of CMEs and even those accompanying CMEs may be a secondary consequence rather than a cause of CMEs (Gosling 1993). Indeed, the basic physics of the two phenomena may be different, though this assertion has been challenged (e.g., Hudson et al. 1995).

In the next two sections I discuss the origins and characteristics of CMEs at and near the Sun in terms of their basic coronal properties and what we know about their source regions. In section 4 I review some important aspects of the manifestation of CMEs in the inner heliosphere. In section 5 I discuss some solar-cycle dependencies of prominences and CMEs, including the role that erupting prominences and CMEs may play in the ejection of magnetic flux and

---

[1] Also at: Air Force Research Lab./VSBS, Hanscom Air Force Base, MA 01731-3010, USA

helicity from the Sun. I conclude with a summary of the main points.

2. Basic Properties of CMEs in the Corona

Most of our understanding of the origins and early development of CMEs has come from analyses of white light observations from spaceborne coronagraphs on the Skylab, P78-1 and SMM satellites viewing within $\sim 10 R_s$, from the ground-based Mauna Loa Observatory (MLO) K-coronameter (1.2–2.9 R_s), and from the Helios photometers viewing the inner heliosphere from 0.3–1 AU. Since early 1996 the SOHO LASCO coronagraphs have been providing unprecedented views of the corona and CMEs from 1.1–30 R_s (Howard et al. 1997).

The measured properties of CMEs include their occurrence rates, locations relative to the solar disk, angular widths and speeds (e.g., Webb 1995). Although important quantities, the masses and energies of CMEs require careful instrument calibrations and have large uncertainties. There is a large range in the basic properties of CMEs. Their speeds, accelerations, masses and energies extend over 2–3 orders of magnitude, and their widths exceed by factors of 3–10 the sizes of flares and active regions.

The basic structure of many CMEs appears to consist of three main components: a bright leading arc followed by a dark, low-density cavity and a bright core of denser material. Bright cores were observed in about 1/4 of the SMM CMEs. One view is that the pre-event structures which erupt to become the CME consist of a prominence, its overlying coronal cavity, and the ambient corona. Figure 1 shows a classic example of a "3-part" CME; as shown here the prominence itself constitutes a small, but dense fraction of the entire CME volume (Gopalswamy et al., these proceedings). The CME "loop" may actually be the skyplane projection of a 3-D, shell-like structure. It must be emphasized that CMEs exhibit a variety of forms, some having complex structure with their interiors filled with bright emitting material. LASCO observations suggest that many CMEs are accompanied by a global response of the corona, especially along the streamer belt.

Sufficient data on CMEs have been obtained to permit study of their frequency of occurrence over about 1.5 solar cycles (Webb and Howard 1994). Data from the earlier coronagraphs and the Helios photometers were corrected for duty cycles and visibility effects to study the annual CME rate. The CME rate tracks the solar cycle in both phase and amplitude, which varies by an order of magnitude over the cycle. The more sensitive LASCO observations indicate that CMEs may be even more frequent, since the CME rate in 1996 was a factor of 2–3 higher than during the previous solar minimum (Howard et al. 1997).

The latitude distribution of the central position angles of SMM CMEs was very broad near cycle maximum but clustered about the equator at minimum. In contrast, the size distribution (i.e., angular widths) of SMM CMEs did not vary much over the cycle, maintaining an average width of about 45° (Hundhausen 1993). However, the SOLWIND CME size distribution did change between cycle maximum and minimum, with the average width decreasing from 45 to 24° (Howard et al. 1985). Thus far, the LASCO CME widths have averaged 45–50°, but more wider, halo-type CMEs have been observed.

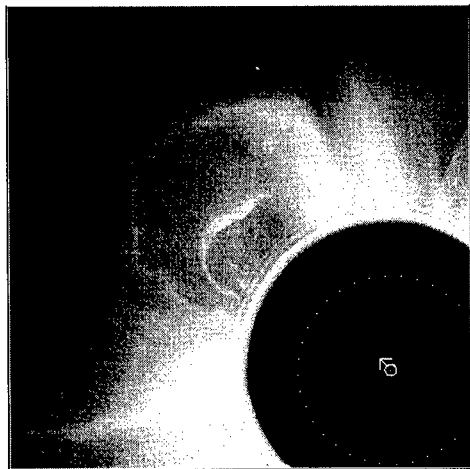Estimates of the speeds of the leading edges of CMEs range from about

Figure 1.   A CME observed from SMM on April 14, 1980. The event shows the "3-part" structure of a CME: an outer, bright loop followed by a darker cavity and bright inner core, here an erupting prominence viewed side on. Courtesy High Altitude Observatory/NCAR.

20 to 2000 km s^{-1}. The annual average speeds of SMM CMEs varied over the solar cycle from 160–460 km s^{-1}, but were not simply related to sunspot number (Hundhausen et al. 1994). The speed of a CME is independent of its heliolatitude. CMEs exhibit a differential speed gradient, having a smooth gradient of speeds from the fast leading edge to the lower, interior material, such as that of the prominence. Higher speed (>400 km s^{-1}) CMEs tend to be associated with coronal and IP shocks, suggesting that the shocks are piston-driven. At least through the lower corona, typical CMEs appear to travel at constant velocity, although some events exhibit significant acceleration. Acceleration has been observed in many LASCO CMEs out to 30 R_s.

The average coronagraph values for CMEs are masses of a few × 10^{15} g and energies of about 3 × 10^{30} erg. However, the average CME masses and kinetic energies derived from Helios photometer data in the interplanetary medium are 2–8 times higher than those determined by coronagraphs (Jackson et al. 1996). With the greater field of view of LASCO, CME mass estimates increase as the CME front moves outward, suggesting continual outward flow (Howard. et al. 1997). This implies that previous coronagraph masses have been underestimated by as much as a factor of ten. The energy spectrum (event rates vs energies) of CMEs does not follow the same simple power law distribution as that of X-ray flares (Figure 2). In addition, SMM CME masses were not distributed like a power law, having a sharp cutoff at 10^{-13} g/deg. Along with other evidence presented here, this suggests that flares and CMEs arise in different physical processes. However, LASCO results reveal many small events travelling through streamers that may refine this distribution. But are these all CMEs?
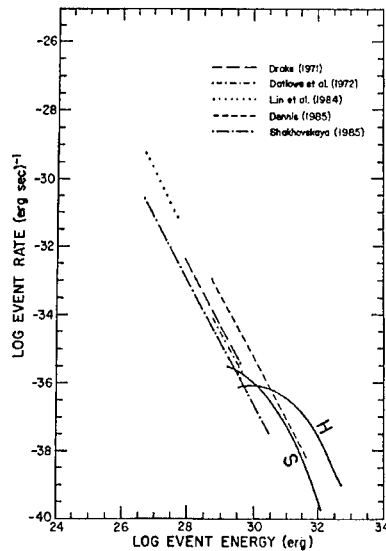
Figure 2. Comparison of solar X-ray flare energy vs. peak flux measurements with CME kinetic energy distributions from Solwind (S) and Helios (H). From Jackson (1996).

3. Source Regions of CMEs

From what kind of structures do CMEs arise? Recent studies suggest that CMEs arise from large-scale, closed structures, most of which are preexisting coronal streamers (Hundhausen 1993). Although the solar origins of CMEs remain obscure, they are often associated with the disruption of large-scale structures such as prominences and loop arcades. Low and Hundhausen (1995) emphasize that the prominence/streamer involves a dual flux system, one part of which is a flux rope which, with its surrounding coronal cavity, may drive the eruption once the streamer is disrupted. CMEs seem to be more closely linked to large-scale weaker magnetic structures than to small-scale stronger-field regions. Many energetic CMEs are actually the disruption ("blowout") of a preexisting streamer, which increases in brightness and size for days before erupting as a CME. Afterwards the streamer and CME are absent, giving the appearance of a "bugle" on white light synoptic maps (Hundhausen 1993). The streamer usually reforms a day or so later and sometimes a bright, narrow ray appears above it, likely tracing the current sheet.

Statistical association studies typically indicate that CMEs are most frequently associated with near-surface activity in the form of erupting filaments and X-ray long duration events, but not optical flares. However, the fastest, most energetic CMEs are usually flare-associated (see Webb 1992 for a review). In these studies a third to a half of all CMEs cannot be associated with any near-surface activity. The bright cores of material within many CMEs also suggest that erupting prominences are more fundamentally involved in the initiation of CMEs than are flares.

We now review results on the source regions of CMEs using soft X-ray and

white light data sets from two different decades; the 1980s and 1990s. During the 1980s there was excellent coverage of white light CMEs from the Solwind and SMM coronagraphs and the HAO MLO K-coronameter. However, X-ray data consisted mostly of whole-Sun GOES X-ray data. Comparing the Solwind CME and GOES X-ray data, Sheeley et al. (1983) found that the probability of associating a CME with a soft X-ray flare increased linearly with the flare duration, reaching 100% for flares of duration ≥ 6 hr.

The SMM CME observations indicated that the departure times of flare-associated CMEs typically preceded the flare onsets. Harrison (1991) suggested a model in which CMEs were initiated during weaker "precursor" soft X-ray bursts that preceded any subsequent main flare by several to tens of min. These precursor bursts consisted of X-ray arches having large scale sizes of 10^5 km. The flares could lie anywhere under the span of the accompanying CME.

The characteristics of SMM CMEs did not seem well correlated with those of any associated X-ray events. For example, Hundhausen (1997) shows examples of two CMEs in 1989, both similar with fast leading loops and cavities and associated with the eruption of prominences extending onto the disk. In each the CME had formed and was moving outward before the onset of any signature in GOES X-rays. However, one CME was associated with a bright M3 long-duration X-ray event, while with the other CME there was no discernable X-ray event above the background. Hundhausen draws three conclusions from his studies: 1) Intense X-ray flares are neither a necessary nor sufficient condition for the occurrence of CMEs; 2) Any significant X-ray emission follows the onset of the CME and peaks much later; and 3) The intensity of any soft X-ray event accompanying a CME is not well related to the characteristics of the CME.

During the present decade of the 1990s, a clearer understanding of CME onset structures has been gained using the temporally and spatially resolved Yohkoh SXT soft X-ray data. However, between late 1989 when SMM ended and early 1996 when SOHO became operational, we had only limited white light CME coverage provided by the MLO K-coronameter. Despite this limited CME data, the Yohkoh data is helping us gain insight into the source regions of CMEs. Klimchuk et al. (1994) identified ~ 30 eruptive X-ray loop events occurring during MLO observing periods in the SXT images at the limb. They concluded that the speeds, widths, and occurrence rates of these loops were consistent with the early phase of CMEs. Hundhausen and colleagues and Hudson and Webb have directly compared MLO CMEs with the SXT images. Hudson and Webb (1997) found that 2/3 of the CMEs had an associated transient X-ray structure, typically a loop with one foot in a flaring active region. Hundhausen (1998) summarized the HAO results and gave examples for CMEs at low heliolatitudes in the active region belt. The CME blows out a typically 40° wide structure at 2 R_s. If an X-ray event is associated, it will be intense but of smaller scale and offset toward one leg of the CME. At higher latitudes the associated X-ray events are of larger scale and longer duration but tend to have weaker emission. Since many characteristics of CMEs appear independent of latitude, we can conclude that CMEs involve the destabilization of large-scale coronal structures which result in magnetic reconnection of the larger-scale, weaker fields at higher latitudes and of the smaller-scale, stronger fields at low latitudes.

Hansen et al. (1974) and Rust and Hildner (1976) noted the depletion of

lower coronal material during eruptive events in the Skylab era. Now in the SXT data areas of subtle dimming, evidence of density depletion, have been observed above the brightening X-ray arcade regions (reviewed by Hudson and Webb 1997; see Gopalswamy et al. and Hiei, these proceedings). Two outstanding examples, on 21 February and 28 August 1992, may provide views along and across the reconnecting arcades (Hudson et al. 1996; Watanabe et al., these proceedings). One interpretation of the dimming signature is that the initially closed field lines are opening during the onset of a CME, in analogy to transient coronal holes observed against the disk. Therefore, such dimming may be one of the first soft X-ray signatures of the mass ejection in the low corona.

Some observations suggest that multiple polarity systems may be involved in many CMEs. The widths of CMEs ($\sim50°$) are large compared with the scale of surface polarity inversion lines (separations of 10-20°). A number of total solar eclipse observations reveal this disparity, showing single streamers overlying twin coronal arcades and parallel filament segments, for instance during the 1966 eclipse. The eruption of such a helmet streamer would then suggest that the source region of the resulting CME consisted of a complex magnetic system of multiple arcades and neutral lines. Webb et al. (1997) find that transient X-ray arcades, used as proxies for CMEs against the disk, can span surface distances of 35 to >100° and cross 2-3 neutral lines or a single, highly convoluted neutral line, implying multipolar magnetic systems. In a separate study we also find that CMEs tended to occur over surface sites where opposite polarity regions were rapidly evolving. Observations and models involving quadrupolar fields supporting prominences and their eruption as CMEs were much in display during this workshop (e.g., papers by Uchida, Demoulin, and Cheng and Choe in these proceedings). The recent LASCO data also support this picture in that the single equatorial streamer belt tends to overlie quadrupolar structures at lower heights (e.g., Howard et al. 1997). This supports the model of Crooker et al. (1993) that the streamer belt, the base of the heliospheric current sheet, can be broad and contain multiple current sheets. Thus, the current sheet acts as a conduit for CMEs and is one reason why transient interplanetary flows in the ecliptic are often associated with stream–stream interaction regions.

4.   Interplanetary Signatures of CMEs

CMEs carry into the heliosphere large amounts of coronal magnetic fields and plasma, which can be detected by remote sensing and in-situ spacecraft observations. CME plasma has been remotely detected by the twin Helios photometers and with limited success by ground-based measurements of IP scintillation. The Helios photometers detected about 200 CMEs over a period of 9 years (Jackson et al. 1994). The morphology, occurrence rates, spans and speeds of these CMEs are consistent with coronagraph measurements made near the Sun (Webb and Howard 1994).

A variety of in-situ signatures have been proposed as proxies for the passage of CME ejecta past spacecraft. These include IP shocks, density changes, decreased temperatures, flows with enhanced helium abundances, and magnetic field structures consistent with looplike topologies (Gosling 1993). Recent efforts have focussed on signatures indicative of the topology of the ejected magnetic

fields, such as magnetic clouds and bidirectional particle flows.

Bothmer and Schwenn (1994), Rust (1994), Bothmer and Rust (1997) and others have associated some magnetic clouds with solar filament disappearances. The close association of CMEs with filament eruptions and shearing fields near the surface has led to the modeling of CMEs as flux ropes. Gosling (1993) suggested that ~1/3 of all bidirectional electron events and magnetic clouds in the heliosphere have the characteristics of flux ropes. Marubashi (1997) and Bothmer and Schwenn found that the IP flux ropes (clouds) they examined had the same orientation and polarity as associated erupting solar filaments. Furthermore, Martin (these proceedings) found that high latitude filaments always have twist in the same sense in a given hemisphere. These results suggest that the sign of the helicity, or twist of the erupting fields can be predicted assuming an association between a given flux rope and a filament eruption. Rust (1994) did so for a list of magnetic clouds at 1 AU and claimed good agreement. Thus, filament eruptions and CMEs may be important ways that the Sun sheds helicity.

Recently, LASCO has observed a number of halo-type CMEs, which had been rarely observed by the earlier less-sensitive coronagraphs. A halo-type CME, especially when associated with solar activity near sun center, suggests the launch of a geoeffective disturbance toward Earth. Indeed, many of the recent halo CMEs have been associated with magnetic clouds and geomagnetic storms at Earth $\leq$4 days later. Several of these events were associated with filament eruptions and X-ray arcades at the Sun (e.g., Gopalswamy et al., Plunkett et al., and van Driel-Gesztelyi et al., these proceedings) followed by in-situ observations from the WIND and SOHO spacecraft at 1 AU providing evidence of cool prominence material at the trailing edge of a magnetic cloud.

Figure 3 shows one such event observed by WIND in January 1997. A halo CME and small, sun-centered disappearing filament on January 6 (Webb et al. 1998) was followed on January 10–11 by a magnetic cloud which drove a geomagnetic storm. An unusually dense "plug" of material at the back of the cloud exhibited an enhanced helium abundance, cool He^+ material, and charge states typical of a large range of temperatures. Such unusual solar wind conditions have always been interpreted as evidence for solar filament material encased in transient CME flows. Burlaga et al. (1998) have modeled the magnetic cloud as a force-free flux rope with its axis nearly parallel to the ecliptic. The cloud contained intervals of bidirectional electron flows indicative of closed, transient fields, and ended at an interface with a corotating high speed stream.

5.   Solar-Cycle Variation of Prominences and CMEs

The temporal and latitudinal distributions of streamers and prominences are similar to those of CMEs, being confined to low latitudes about the current sheet near solar cycle minimum and becoming broadly distributed near maximum (Hundhausen 1993). This evolution is different from that of active regions, flares or sunspots. The impression is that CMEs are more closely linked to large-scale weaker magnetic structures than to small-scale stronger-field regions.

Filaments exhibit their own large-scale "butterfly diagram" on latitude-time plots with two distinct branches "flowing" toward the poles and toward the
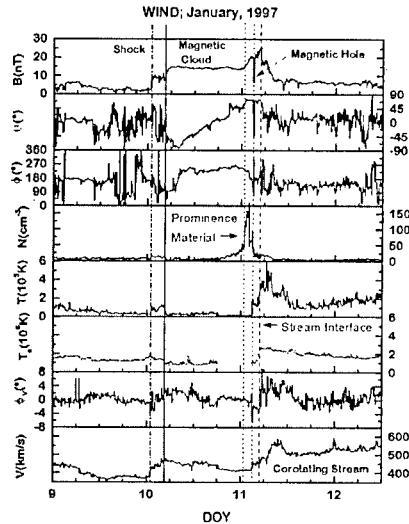
Figure 3.   Solar wind plasma and magnetic field data from the WIND
spacecraft at Earth in January 1997. A shock on Jan. 10, 0100 UT
(dashed line) was followed by a classic magnetic cloud (onset at solid
line), a dense "plug" of material (filament), and a corotating stream.
From Burlaga et al. (1998).

equator (Minarovjech et al., these proceedings). The higher-latitude filaments
display the following characteristic pattern over each solar cycle: a "rush to the
poles" and development of a lower crown during the cycle rise, disappearance of
the polemost, or "true" crown during solar maximum and the polarity reversal,
and subsequent dwelling at ~50° during the fall of the cycle and minimum of the
new polar crown. McIntosh (1992) noted that high-latitude filaments fall into
two groups, those having "correct" polarity for the cycle in that hemisphere,
i.e., the magnetic field lying poleward of the polar filaments will be appropriate
for that cycle, and those having opposite polarity. For cycles 20–22, McIntosh
determined the maximum latitude, north and south of the equator for each
rotation, for both types of filaments. His result is shown in Figure 4.
    Cliver and colleagues have recently published two studies comparing this
pattern of filament evolution with CMEs. Cliver et al. (1994) showed that
the CME rate during cycle 22 exhibited a quasi-discontinuity in October 1988,
when the average daily rate doubled and remained high until the end of SMM
observations in late 1989. This jump was most pronounced in the population of
high-latitude CMEs. They inferred a similar discontinuity in the CME rate at
the same time of the previous cycle in 1978. These discontinuities are marked
on Figure 4 by vertical arrows; they occur at about the time of the start of
the poleward movement of the two filament crowns. Cliver and Webb (these
proceedings) take the next step by statistically comparing high-latitude CMEs
with disappearing solar filaments (DSFs). They find that the fraction of DSFs
arising from the true polar crown decrease until solar maximum when the new,
or emerging polar crown becomes the dominant source of high-latitude DSFs,

Polar Crown Filaments
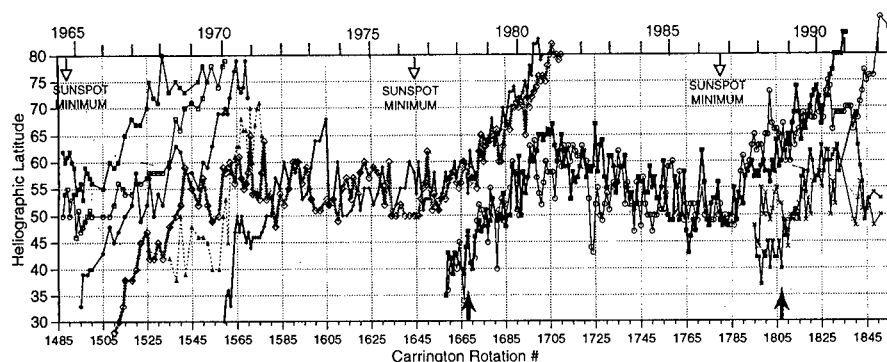## Cycles 20-21-22
MAXIMUM LATITUDE

Figure 4. The maximum latitude of polar crown filaments in the true and emergent polar crowns during cycles 20–22. Filament positions are given separately for the northern and southern hemispheres. Arrows at bottom mark the epochs in cycles 20 and 21 when the CME rate abruptly increased. (Figure courtesy P. S. McIntosh.)

and by inference of high-latitude CMEs. However, at the maxima of the last two solar cycles, there were ~4 times as many high-latitude CMEs as high-latitude DSFs. Possible reasons for this discrepancy are discussed by Cliver and Webb. A related phenomena that has been discovered is that the coronal structures overlying the polar crown regions appear to be hotter than other non-active regions areas in the corona. Guthathakurta et al. (1993), Hick et al. (1996) and others have used Sacramento Peak Observatory Fe-line intensity ratios to calculate large-scale temperatures at several heights in the corona. They find that there are distinct high-latitude ($>50°$) bands of coronal emission which exist over most of the cycle. These bands correspond to high-latitude white light streamers and the current sheet, and are hotter than elsewhere. In a gross sense these high temperature bands overlie the polar crown and follow its poleward movement during the cycle. It is interesting to speculate whether or how these bands are related to the occurrence of high-latitude DSFs and CMEs.

There are important new results concerning the interrelationships among solar filaments and the global helicity balance, and how that helicity builds up during the cycle and is ejected from the Sun. As mentioned earlier, several studies find that magnetic clouds modeled as flux ropes have the same orientation and polarity as associated erupting filaments at the sun. Since higher latitude filaments in a given hemisphere have the same helicity (twist) and the sign of the helicity of DSFs associated with clouds at 1 AU agree, filament eruptions and CMEs seem to be important ways that the Sun can shed the helicity that is built up over a cycle (Seehafer, these proceedings).

Recently, Bothmer and Rust (1997) found a dependence of cloud magnetic

structure on the solar cycle phase. During cycle 20–21 (1974–1981) most magnetic clouds at 1 AU exhibited a southward then northward (SN) field rotation, whereas during cycle 21–22 (1982–1991) clouds with NS rotation dominated. Based on these results, an empirical model from Bothmer and Schwenn (1994), and the helicity rule of Rust and Kumar (1994), Bothmer and Rust show that both the occurrence and rotation of clouds might be predictable. For example, the majority of clouds during the next few years should be SN and, therefore, associated geomagnetic storms may be more intense because SN clouds are more geoeffective. Supporting this, the recent January 1997 storm was caused by a SN cloud (Figure 3). In addition, Rust and Kumar (1994), Martin and McAllister (1997) and others have identified patterns of soft X-ray sigmoid structures and the skew of arcades with filaments and DSFs in each hemisphere. Together, these results suggest that studies relating the solar cycle dependencies of filaments, DSFs, CMEs and magnetic clouds will help us to understand the build up and ejection of magnetic flux and helicity from the Sun.

6. Conclusion

I have reviewed the origins and characteristics of CMEs at the Sun in terms of their basic coronal properties and what we know about their source regions, and some important aspects of their manifestation in the inner heliosphere. The rate of occurrence of CMEs tracks solar activity, but the size scales of CMEs are much larger than and their latitude distributions different than those of near-surface activity like flares or active regions. Most CMEs arise in large-scale closed coronal structures, especially helmet streamers which erupt and reform. Statistically, CMEs are most frequently associated with erupting filaments and X-ray long duration events, not optical flares. However, the Yohkoh data is helping to reshape our ideas on these associations. Large-scale X-ray arcades are frequently observed, and likely result from reconnection of closed field systems opened by CMEs. The size scales and field strengths of these systems are a function of latitude; the arcades are larger-scale but weaker at higher latitudes and smaller-scale and stronger at low latitudes. The magnetic structures involved with the sources of CMEs can be complex and multipolar. The earliest X-ray signatures of the onset of a CME in the low corona appear to include outward-moving loops and the depletion of coronal material above the bright X-ray arcade. These observations and comparison of the energy distributions of X-ray flares and CMEs suggest that the two phenomena may arise in different physical processes.

In terms of solar-terrestrial linkages, CMEs are now identified as a crucial link between solar eruptions and their propagation through the heliosphere to Earth. The IP manifestations of CMEs can result in extensive transient disturbances and can cause major geomagnetic storms at Earth. CMEs are associated with the coronal streamer belt and, therefore, with the heliospheric current sheet. Recent studies show that many magnetic clouds arise as solar filament flux ropes. The magnetic helicity or twist of filaments and DSFs follows specific patterns in time and location, and has been related to the magnetic orientation of clouds. This suggests that DSFs and CMEs may be important ways that the Sun sheds its helicity built up over the cycle. Halo CMEs and associated near Sun-center

DSFs are followed by clouds at Earth, permitting in-situ measurements of the internal CME structure including any filament material.

References

Bothmer, V. and R. Schwenn 1994, in Mass Supply and Flows in the Solar Corona, (eds.) B. Fleck et al., Kluwer, Norwell, MA, p. 225

Bothmer, V. and D. M. Rust 1997, in Coronal Mass Ejections, (eds.) N. Crooker et al., GM 99, AGU, Washington, DC, p. 139

Burlaga, L. et al. 1998, J. Geophys. Res., 103, 277

Cliver, E. W., O. C. St. Cyr, R. A. Howard and P. S. McIntosh 1994, Solar Coronal Structures, (eds.) V. Rusin et al., Veda, Bratislava, p. 83

Crooker, N. U., G. L. Siscoe, S. Shodan, D. F. Webb, J. T. Gosling, and E. J. Smith 1993, J. Geophys. Res., 98, 9371

Gosling, J. T. 1993, J. Geophys. Res. 98, 18,937

Guhathakurta, M., R. R. Fisher and R. C. Altrock 1993, ApJ, 414, L145

Hansen, R. T., C. J. Garcia, S. F. Hansen, and E. Yasukawa 1974, PASP, 86, 500

Harrison, R. A. 1991, Adv. Space Res., 11 (1), 25

Hick, P., B. V. Jackson and R. C. Altrock 1996, in Solar Wind Eight, (eds.) Winterhalter et al., AIP, Woodbury, NY, p. 169

Howard, R. A. and 18 coauthors 1997, in Coronal Mass Ejections, (eds.) N. Crooker et al., GM 99, AGU, Washington, DC, p. 17

Howard, R. A., N. R. Sheeley, M. J. Koomen and D. J. Michels 1985, J. Geophys. Res., 90, 8173

Hudson, H. S. and D. F. Webb 1997, in Coronal Mass Ejections, (eds.) N. Crooker et al., GM 99, AGU, Washington, DC, p. 27

Hudson, H., B. Haisch, and K. T. Strong 1995, J. Geophys. Res. 100, 3473

Hudson, H. S., J. R. Lemen and D. F. Webb 1996, in Magnetic Reconnection in the Solar Atmosphere, (eds.) R. D. Bentley and J. T. Mariska, ASP Conf. Ser. Vol. 111, San Francisco, p. 379

Hundhausen, A. J. 1993, J. Geophys. Res. 98, 13,177

Hundhausen, A. J., 1997, in Cosmic Winds and the Heliosphere, (eds.) J. Jokipi et al., University of Arizona Press, Tucson, AZ

Hundhausen, A. J. 1998, in The Many Faces of the Sun, (eds.) K. Strong et al., Springler-Verlag, New York, in press

Hundhausen A. J., J. T. Burkepile and O. C. St. Cyr 1994, J. Geophys. Res., 99, 6543

Jackson, B. V. 1996, in Magnetic Storms, (eds.) B. Tsurutani et al., GM 98, AGU, Washington, DC, p. 59

474 D. F. WEBB

474   D. F. WEBB

474   D. F. WEBB

Jackson, B. V., R. A. Howard and D. F. Webb 1996, Solar Wind Eight, (eds.) Winterhalter et al., AIP, Woodbury, NY, p. 540

Jackson, B. V., D. F. Webb, P. L. Hick, and J. L. Nelson 1994, Catalog of Helios 90° Photometer Events, PL–TR–94–2040, Phillips Laboratory, Hanscom AFB, MA

Klimchuk, J., L. Acton, K. Harvey, H. Hudson, K. Kluge, D. Sime, K. Strong, and T. Watanabe 1994, in X-ray Solar Physics from Yohkoh, (eds.) Y. Uchida et al., Universal Academy Press, Tokyo, p. 181

Low, B. C. and J. R. Hundhausen 1995, ApJ, 443, 818

Martin, S. F. and A. H. McAllister 1997, in Coronal Mass Ejections, (eds.) N. Crooker et al., GM 99, AGU, Washington, DC, p. 127

Marubashi, K. 1997, in Coronal Mass Ejections, (eds.) N. Crooker et al., GM 99, AGU, Washington, DC, p. 147

McIntosh, P. S. 1992, in The Solar Cycle, (ed.) K. Harvey, ASP Conf. Ser. Vol. 27, San Francisco, p. 14

Rust, D. M. 1994, Geophys. Res. Lett. 21, 241

Rust, D. M. and E. Hildner 1976, Solar Phys., 48, 381

Rust, D. M. and A. Kumar 1994, Solar Phys., 155, 69

Sheeley, N. R., R. A. Howard, M. J. Koomen and D. J. Michels 1983, ApJ, 272, 349

Webb, D. F. 1995, Rev. Geophys. Suppl., 577

Webb, D. F. 1992, in Eruptive Solar Flares, (eds.) Z. Svestka, B. Jackson and M. Machado, Springer-Verlag, New York, p. 234

Webb, D. F. and R. A. Howard 1994, J. Geophys. Res. 99, 4201

Webb, D. F., S. W. Kahler, P. S. McIntosh and J. A. Klimchuk 1997, J. Geophys. Res., 102, 24,161

Webb, D. F., E. W. Cliver, N. Gopalswamy, H. S. Hudson and O. C. St. Cyr 1998, Geophys. Res. Lett., in press

LASCO/EIT Observations of Coronal Mass Ejections from Large-Scale Filament Channels

S.P. Plunkett[1], K.P. Dere, R.A. Howard, D.J. Michels and G.E. Brueckner

E.O. Hulburt Center for Space Research, Naval Research Laboratory, Washington, DC 20375, USA

B.J. Thompson[2]

NASA Goddard Space Flight Center, Greenbelt, MD 20771, USA

J.-P. Delaboudinière

Institut d'Astrophysique Spatiale, Université Paris XI, 91405 Orsay Cedex, France

Abstract. Solar activity in the latter half of 1996 was dominated by the presence of an extended filament channel in the southern hemisphere, forming a switchback configuration where it merged with the polar crown. Several large coronal mass ejections (CMEs) were observed to originate on or near this magnetic neutral line by the LASCO and EIT instruments on SOHO. As this channel gradually disappeared, a new, extended channel formed to the west of the old one, and this new channel also produced a number of large CMEs. We report here on observations of two events (December 23, 1996 and February 7, 1997), and discuss the global nature of these events.

1. Introduction

The dominant feature on the Sun in the latter half of 1996 (corresponding to the transition from cycle 22 to cycle 23) was an extended filament channel in the southern hemisphere, extending from close to the equator down to the polar crown. The channel was formed by the merger of the neutral line through an old, decaying active region at a latitude of about S25° with the polar crown neutral line, forming a 'switchback' configuration. The resulting neutral line can clearly be seen on maps of the photospheric magnetic field recorded at the Wilcox Solar Observatory (http://quake.stanford.edu/~wso/synoptic.html). The emergence of new magnetic flux on Carrington Rotations (CR) 1916 and 1917 destroyed this magnetic configuration. During CR 1917, a new cycle active region emerged some 120° west of the old switchback neutral line. The neutral line through this active region also merged with the polar crown neutral line, to form a new

---

[1] Universities Space Research Association

[2] Space Applications Corporation

extended filament channel, again extending from close to the equator to the southern polar crown. This channel remained visible through the next several rotations.

These two filament channels produced a number of large coronal mass ejections (CMEs) that were observed in late 1996 and early 1997 by instruments on the Solar and Heliospheric Observatory (SOHO). In this paper, we present observations of two of these CMEs by the Large Angle Spectrometric Coronagraph (LASCO, Brueckner et al. 1995) and the Extreme Ultraviolet Imaging Telescope (EIT, Delaboudinière et al. 1995), showing for the first time the onset of and coronal response to a CME at EUV wavelengths.

2.   Observations

2.1.   The December 23, 1996 Event

This CME began with the activation and eruption of a short segment (about 35″ long) of a prominence near an active region at heliographic location S13° W67°, observed at approximately 20:20 UT in the 195 Å channel of EIT. This active region, and its associated filament, lay close to the position of the switchback filament channel described above. The event has been described in detail by Dere et al. (1997), so only a brief description will be given here.
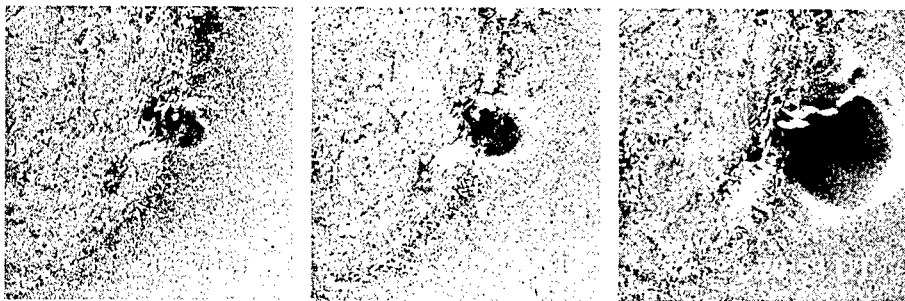

Figure 1.   A sequence of running difference images in the Fe XII 195 Å passband of EIT, showing the onset of the December 23, 1996 CME.

Figure 1 shows a series of 195 Å images recorded by EIT. The images are displayed as running differences, i.e., each image is shown as the difference from the preceding image in the series. This technique allows subtle changes in the coronal structure from one image to the next to be seen easily. A bright rim of emission, almost circular in appearance, surrounding a darker area, can be seen in the image at 20:32 UT, and is more clearly evident in the next two frames as it expands outwards. A complex, twisted structure that can be identified with the erupting prominence is visible within the dark 'cavity'. This three-part structure was also clearly observed by the LASCO C1 coronagraph at about 21:00 UT. The appearance of the CME in the C2 coronagraph is somewhat more complex. The C2 images show a bright loop-like structure moving out along a streamer, with a bright knot of prominence material following behind. The leading edge of the CME in C2 and in C3 had a projected speed of about 335 km s^{-1}.

A number of large scale phenomena accompanying the CME were observed by EIT. Several nearly simultaneous prominence activations were observed to the north and south of the CME launch site. Also, a large-scale wave motion propagated almost symmetrically outwards across the disk from the site of the CME, with a speed of about 100 km s^{-1}. This wave, and other similar events observed by EIT, may be a coronal manifestation of Moreton waves observed in Hα in association with some large flares (Thompson 1998).

2.2. The February 7, 1997 Event
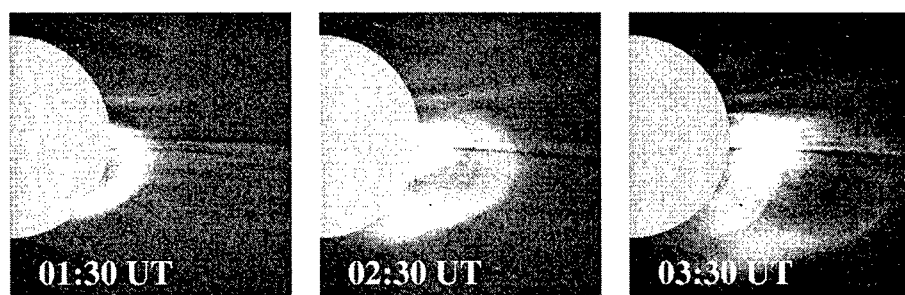
Figure 2. Development of the February 7, 1997 CME as seen by LASCO C2. These are difference images, with a pre-event image subtracted from each image shown.

The partially Earth-directed CME of February 7, 1997 originated from the southwest quadrant of the Sun. The event has been discussed in some detail by Plunkett et al. (1997) and Gopalswamy (1997). LASCO observed the CME from about 01:00–10:00 UT in both C2 and C3 (see Figure 2). The event contained an arcade eruption, extending along the neutral line from close to the equator on the west limb, to the southern polar crown, and occupied the entire southwest quadrant in the LASCO images. Note that the neutral line involved in this event is not the same as that which produced the December 23 event described above; this event occurred some 120° west of the earlier event. Bright prominence structures were clearly visible within the CME, behind the frontal arcade. The leading edge of the CME was observed with an initial (projected) speed of about 170 km s^{-1} in C2 and accelerated to about 650 km s^{-1} by the time it reached 25 R$_\odot$. A faint 'halo' component was also visible, extending to the south and east of the main arcade eruption.

The bright knot of prominence material seen in the LASCO images was clearly seen at the west limb in a He 304 Å EIT image recorded at 02:07 UT (Figure 3). There was also a prominence eruption from the southwest limb over the same neutral line; this can be seen in Figure 3 as a series of faint, elongated structures off the southwest limb. A bright two-ribbon arcade structure was observed on the disk by EIT following the eruption of the CME. The footpoints of this arcade are clearly visible in the 195 Å image shown in Figure 3, parallel to the neutral line from the equator to the polar crown. Images in the hotter Fe XV 284 Å line show a set of sheared loops overlying these footpoints.
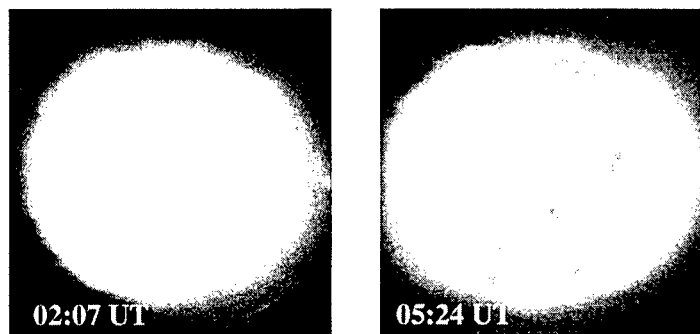
Figure 3.   EIT observations of the February 7, 1997 CME, showing
a prominence eruption to the W and SW in the He II 304 Å line (left
panel) and a post-ejection arcade in the Fe XII 195 Å line (right panel).

3.   Conclusions

We have presented observations of two events that offer some new insights into
the CME phenomenon and confirm some ideas about CMEs. These observations
allow us, for the first time, to study the onset of a CME on the solar disk at EUV
wavelengths, and to study the coronal response to a CME in the same spectral
region.   The observations of the December 23 CME show that the classical
three-part structure (bright front, dark cavity and prominence core) of a CME
is present right from the onset. The global nature of the CME is clear: in both
events, a large fraction of the visible surface of the Sun is involved in the event.
This is especially clear from the observations of prominence eruptions and arcade
formation in the February 7 event. However, the December 23 observations show
that a CME can begin in a very small volume, and that there is a propagation
time delay before activity is observed in other regions of the corona.

References

Brueckner, G.E. et al. 1995, Solar Phys., 162, 357
Delaboudinière, J.-P. et al. 1995, Solar Phys., 162, 291
Dere, K.P. et al. 1997, Solar Phys., 175, 601
Gopalswamy, N. 1997, SHINE Report on the February 7, 1997 CME
Plunkett, S.P. et al. 1997, in The Corona and Solar Wind Near Minimum Ac-
     tivity, ESA SP-404, ESA: Noordwijk, Holland, p. 615
Thompson, B.J. 1998, in preparation

Disappearances of High-Latitude Filaments as Sources of High-Latitude CMEs

E. W. Cliver

Air Force Research Laboratory, Hanscom Air Force Base, Massachusetts 01731-3010, USA

D. F. Webb

Institute for Scientific Research, Boston College, Chestnut Hill, Massachusetts 02467, USA

Abstract. From a statistical comparison of high-latitude coronal mass ejections (CMEs) and disappearing solar filaments (DSFs), we find: (1) Beginning with the "rush to the poles", DSFs arise at an increasing rate from the "emerging" or polar crown relative to the "true" polar crown. At maximum, these "opposite polarity" filaments are the dominant source of high-latitude DSFs. Following polarity reversal, the emergent polar crown becomes the true polar crown and the source of virtually all high-latitude DSFs. (2) At the last two solar maxima, we estimate that there were ~ 4 times as many high-latitude ($\geq$ 60°) CMEs as high-latitude ($\geq$ 45°) DSFs. Possible reasons for this discrepancy include the following: (a) DSFs, particularly small ones, are under-reported, (b) propagation effects, whereby radially propagating CMEs appear at higher latitudes than their underlying source regions, are more important than currently thought, or (c) some combination of these effects.

1. Introduction

The characteristic behavior of high-latitude filaments over the solar cycle, i.e., the "rush to the poles", disappearance near solar maximum, and subsequent residence at ~ 50° during solar minimum, has been known for over a century. McIntosh (1992) has refined this picture by separating high-latitude filaments into two groups, those having "correct" polarity for the cycle and those having opposite polarity. "Correct" polarity implies that the magnetic field lying poleward of east–west oriented filaments will be appropriate for that cycle, e.g., negative or inward-directed in the northern hemisphere for the years 1980–1990. We will refer to the irregular band of high-latitude filaments having correct polarity as the "true" polar crown and high-latitude filaments of opposite polarity as the "emergent" polar crown. For cycles 20–22, McIntosh determined the maximum latitude, north and south of the equator for each rotation, for both types of filaments. His results are shown in Webb (1998, these proceedings) where it can be seen that the emergent polar crown becomes the true polar crown for the next cycle near solar maximum at the time of polarity reversal.

During the past two decades, it has been recognized (e.g., Webb and Hundhausen 1987) that disappearing solar filaments are a common lower atmosphere manifestation of CMEs. In this study, we examine the relative importance of the true and emergent polar crowns as sources of CMEs. In addition, we attempt to determine if each high-latitude CME is associated with a high-latitude DSF.

2. Disappearances of True and Emergent Polar Crown Filaments as Sources of CMEs

We began with Wright's (1991) compilation of DSFs covering the years 1964–1980. For cycle 20 (1965–1976) we used McIntosh's (1979; also Solar-Geophysical Data) synoptic maps to determine whether each listed high-latitude (midpoint $\geq 40°$) DSF originated in the true or emerging polar crown. An example of this determination for Carrington Rotation 1517 is shown in Figure 1 and the results of this analysis are given in Figure 2. In Figure 2, annual rates of $\geq 40°$ latitude DSFs (from Wright 1991) and yearly sunspot numbers are given in panels (a) and (c), respectively. Panel (b) shows that the percentage of DSFs from the true polar crown steadily decreases beginning near the time of the onset of the rush to the poles in 1966 and reaches a minimum of $\sim25\%$ at solar maximum. Following polarity reversal, the emergent crown becomes the true crown and is the dominant source of high-latitude CMEs throughout solar minimum until the next rush to the poles when the process is repeated.
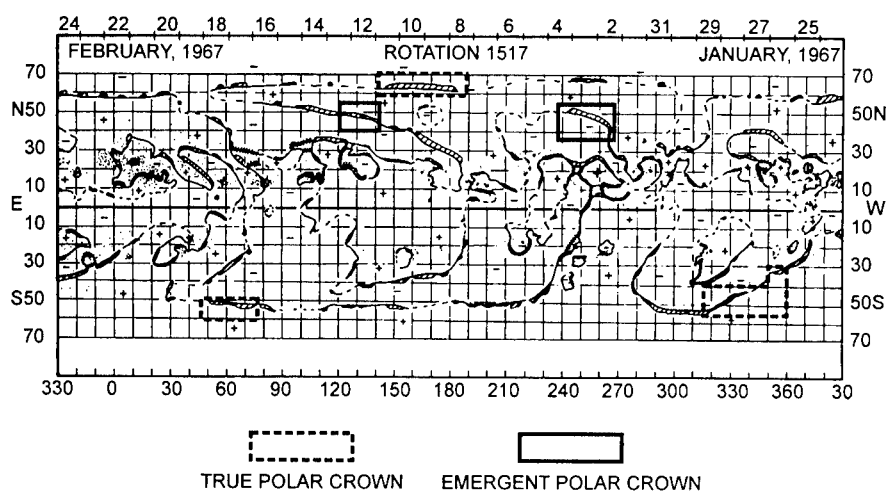

Figure 1.   Classification of disappearing solar filaments as belonging to either the true or the emerging polar crown during Carrington Rotation 1517. The disappearing filaments in the northern hemisphere (solid box) originated in the emergent polar crown; those in the south (dashed boxes) originated in the true polar crown for that hemisphere.
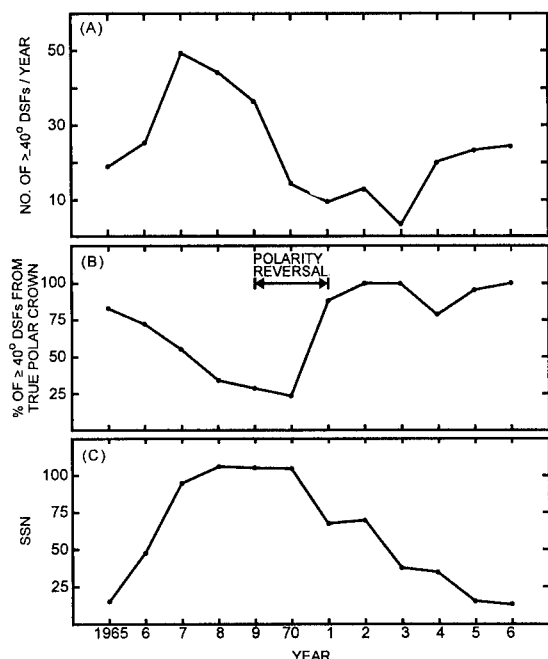
Figure 2.   (a) Annual rates (no corrections applied) of high-latitude
($\geq 40°$) DSFs from Wright's (1991) catalog for cycle 20. (b) Percentage
of high latitude DSFs that originated in the true polar crown over cycle
20. (c) Annual sunspot numbers for cycle 20.

3. Is There a One-to-One Correspondence Between High-Latitude DSFs and CMEs?

We determined the relative frequency of these phenomena for the early rise of
the solar cycle and for solar maximum (Table 1). The CMEs in this table are
those having central position angles (measured from the solar equator) with
absolute values $\geq 40°$ and the DSFs are those having midpoint latitudes $\geq$
$40°$. The coronagraph data are from the Solwind (R.A. Howard, 1997, private
communication) and Solar Maximum Mission (SMM) (Burkepile and St. Cyr
1993), and the DSF data are from Wright's (1991) catalog through 1980 and from
the Meudon Cartes Synoptiques for later years. Previously, we had shown (Cliver
et al. 1994) that the CME rate during cycle 22 exhibited a quasi-discontinuity
in October 1988, when it jumped from an average daily rate of ~0.9 CME/day
to an average rate of ~ 1.8 CME/day where it remained until the end of SMM
observations in late 1989. Thus, we used 1988.7 as a breakpoint between epochs
for the maximum of cycle 21. The other interval endpoints in Table 1 were
determined by the onset of Solwind observations in late March 1979, the end
of the Wright compilation in December 1980, and a 4–month data gap in the
SMM record ending in late March 1987. The following correction factors were
applied to the data: (1) the rate of high-latitude Solwind CMEs was multiplied

by a factor of 1.8 to reflect a ~55% duty cycle (Howard et al. 1985); (2) the
SMM CME rate was multiplied by 1.2 based on a duty cycle of ~85% for the
1987–1989 period (Cliver et al. 1994) for which these data were used; and (3) the
DSF rate was multiplied by a factor of 2.8. This last correction was based on the
assumption that CMEs originating at all longitudes at latitudes $\geq 40°$ are visible
from Earth. Thus we multiplied the DSF rate by a factor of 2 to compensate for
backside DSFs not visible from Earth. In addition, Wright has shown that the
visibility of frontside DSFs decreases near the limbs for an additional correction
factor of 1.4, yielding the final upward correction of 2.8.

Table 1.   Ratio of high-latitude ($\geq 40°$) CMEs to DSFs.

Year	CMEs	DSFs	CMEs/DSFs
1979.3 – 1981.0	493	143	3.4
1987.3 – 1988.7	46	104	0.4
1988.7 – 1989.9	289	115	2.5

The evolution of the high-latitude CME/DSF ratio on the rise of cycle 21
during 1987–1989 (Table 1) is remarkable. We suspect that the low ratio (<0.5)
prior to October 1988 is a reflection of the non-radiality of coronal streamers
that is characteristic of solar minimum.

Here, however, we wish to explore the cause of the high (>2.5) CME/DSF
ratio observed at the maxima of both cycles 21 and 22. The apparent excess
of high-latitude CMEs could result from a projection effect whereby radially
propagating CMEs arising in source regions away from the solar limb appear at
higher latitudes than their source regions. Hundhausen (1993) has argued that
CMEs having apparent central position angles $\geq 60°$ arise from solar sources
lying poleward of about 45°. For the period 1979.3–1981.0, Wright's catalog
contains 25 DSFs at latitudes $\geq 45°$, yielding a corrected count of 70. For
the same interval, Solwind observed 135 CMEs with central position angles
$\geq 60°N$ or $\geq 60°S$ for a duty-cycle corrected count of 243. Thus a factor of
3.5 discrepancy remains after taking the projection effect into account. We
are forced to conclude either that the projection effect is more important than
currently thought or that a significant fraction of high-latitude CMEs originate
in solar eruptions that lack reported DSFs. We repeated the above analysis
for the maximum of cycle 22. During 1988.7–1989.9, 87 high-latitude CMEs
($\geq 60°$) and 27 DSFs ($\geq 45°$) were reported for duty-cycle corrected counts of
104 and 76, respectively. The resultant CME/DSF ratio of 1.4 is significantly
lower than the 3.5 ratio for the maximum of cycle 21. On closer examination,
however, we were only able to associate 8 of the 87 high-latitude CMEs with
high-latitude DSFs (based on timing and position) vs. an expected number of 31
associations (87/2.8). Thus high-latitude CMEs were approximately 4 times as
plentiful (31/8 = 3.9) as high-latitude DSFs at the maximum of cycle 22. Stated
differently, approximately $\frac{3}{4}$ of high-latitude CMEs at the maximum of cycle 22
lacked reported high-latitude DSFs as sources. (Presumably, this CME/DSF
imbalance was even greater for the peak of cycle 21.) Our study also indicates
that a significant fraction of high-latitude DSFs are not followed by CMEs,
but a detailed investigation, taking into account such factors as DSF longitude,

coronagraph patrol windows, thermal Disparition Brusques (Mouradian et al. 1995), and associated CMEs at lower latitudes is needed.

Why do we see so many more high-latitude CMEs than DSFs? One very real possibility is that high-latitude DSFs, and more generally all DSFs, are under-reported. Counts of DSFs by different observers vary widely. For example, during the years 1978–1980 the Wright catalog lists $2\frac{1}{2}$ times as many high-latitude DSFs as the Cartes Synoptiques. For this same interval an unpublished list compiled by Joselyn (see Webb and Howard 1994) contains about $3\frac{1}{2}$ times as many DSFs as are listed in the Wright catalog. For the 1988–1989 epoch Joselyn lists approximately three times as many DSFs as the Cartes Synoptiques. Fortunately, Wright (1991) provided annual size distributions of the cataloged DSFs. From the absence of an experimental roll-over in his lowest bin sizes, we conclude that any non-reported high-latitude DSFs were small, with areas less than about 5 square degrees. Thus many high-latitude CMEs may be associated with relatively small DSFs. That such events exist is underscored by the April 1994 magnetic cloud event that was traced to a high-latitude $\sim 150°$ long soft X-ray arcade but only a minor DSF (McAllister et al. 1996). A second possible cause of the excess of high-latitude CMEs in comparison with DSFs is that some polar ($\geq 60°$) CMEs may arise in low-latitude ($< 45°$) DSFs. To make the numbers of high-latitude CMEs and DSFs (at any latitude) match for the 1979–1980 period, it is necessary to assume that all DSFs in the Wright catalog with midpoint latitudes greater than about 30–35° resulted in a CME with central position angle $\geq 60°$. This seems a strong assumption, implying either that even lower latitude DSFs contribute to the high-latitude CME population or that a significant fraction of high-latitude CMEs originate in eruptions of high-latitude magnetic arcades that lack sufficient mass to be observed as a DSF.

References

Burkepile, J.T. and O.C. St. Cyr 1993, NCAR/TN–369+STR

Cliver, E.W., O.C. St. Cyr, R.A. Howard and P.S. McIntosh 1994, Solar Coronal Structures, (eds.) V. Rusin et al., Veda, Bratislava, p. 83

Howard, R.A., N.R. Sheeley, Jr., M.J. Koomen and D.J. Michels 1985, J. Geophys. Res., 90, 8173

Hundhausen, A.J. 1993, J. Geophys. Res., 98, 13177

McAllister, A.H. et al. 1996, J. Geophys. Res., 101, 27625

McIntosh, P.S. 1992, in The Solar Cycle, (ed.) K. Harvey, ASP Conf. Ser. Vol. 27, San Francisco, p. 14

McIntosh, P.S. 1979, Annotated Atlas of Hα Synoptic Charts, UAG-70, WDC-A

Mouradian, Z., I. Soru-Escaut, and S. Pojoga 1995, Solar Phys., 158, 269

Webb, D.F. and R.A. Howard 1994, J. Geophys. Res., 99, 4201

Webb, D.F. and A.J. Hundhausen 1987, Solar Phys., 108, 383

Wright, C.S. 1991, Catalog of Solar Filament Disappearances, UAG-100, WDC-A

Time-Latitude Prominence and the Green Corona Distribution Over the Solar Activity Cycle

M. Minarovjech, M. Rybanský and V. Rušin

Astronomical Institute of the Slovak Academy of Sciences, 05960 Tatranská Lomnica, Slovakia

Abstract. We present a distribution of prominences over the solar cycle activity. There are found both polar and equatorial branches of prominences that migrate in opposite directions. Prominences of the high-latitude crown migrate, starting in the minimum of the cycle, towards the poles, which they reach at the maximum of the cycle and then decay. The equatorward-migrating branch of prominences appears also in the minimum of the cycle at mid-latitudes and disappears at the end of the cycle. The distribution of the prominences is compared with a time-latitudinal distribution of the green corona. It is assumed that the polar branches in cycle 23 will reach the poles in 2002 (the north pole) and 2003 (the south one), respectively.

1. Introduction

Prominences – cool and dense material in the hot solar corona – feature not only different shapes and physical properties in a wide range but also they occur around the solar limb (Tandberg-Hanssen 1974). On a short time scale they seem to be observed above the solar limb randomly; on a long-term basis, however, we find them to be concentrated into belts, e.g., Secchi (1872), Waldmeier (1973). The structure of these belts with the solar cycle activity is, however, very complicated, especially in mid- and low-latitudes, e.g., Bumba et al. (1990), Makarov and Sivaraman (1989), Minarovjech, Rybanský and Rušin (1997). In the present work, the time-latitudinal distribution of prominences as obtained at Lomnický Štít observatory over the period 1967 – June 1997 is studied, and subsequently compared with the distribution of the green corona (530.3 nm) intensity.

2. Observations

Observations of prominences around the whole solar limb at Lomnický Štít have regularly been made since 1967. A 20-cm lens coronagraph, F=4 m, and an Hα filter (FMHW=1.0 nm) have been used. The following 5 parameters characterizing prominences are derived from these photographic observations: area (A), height (H), projected width (W), relative brightness (RB) and heliographic position. These data have already been published for the period 1965–1986 (Rušin et al. 1988). Since 1987 the data have been available on PC diskettes.
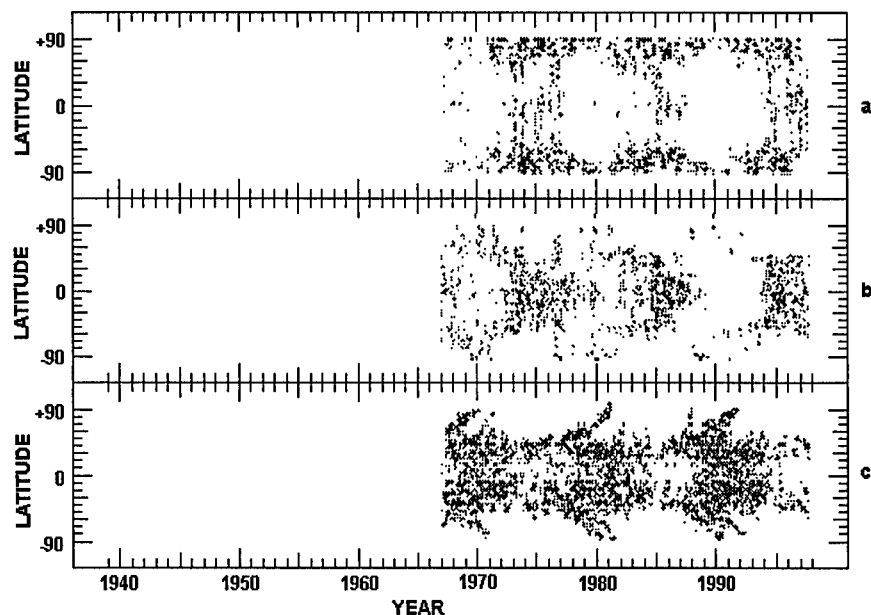
Figure 1. Time-latitudinal distribution of the averaged 'prominence index' local maxima intensities (a) values <7, (b) values 7-17, (c) values > 20.

The source for a time-latitudinal distribution of the green corona local maxima intensities are the data taken from the Homogenous Data Series (HDS) and cover the period from 1939 to 1997 (Altrock et al. 1997 and references therein). In order to find patterns, if any, in the distribution of prominences into individual belts, we divided the prominences into 3 groups according to their dependence on the value – <7, 7-17, and >20 – of a new parameter, PI, the 'prominence index'. This parameter is defined as: RB (scale 1–3) $\times$ A, where $A = W$ (in degrees) $\times$ H (arcsec). Computations were made for 81–day smoothed values and in latitudinal belts of $15°$.

3. Discussion and Conclusion

The corresponding time-latitudinal distribution of prominences is shown in Figure 1a (PI less than 7), 1b (PI = 7–17) and 1c (PI > 20).

One may recognize that prominences of the group $a)$ – small and weak ones – are mainly observed around the poles of the Sun with a maximum of occurrence at latitudes of $60°$ around the minimum of the activity cycle. These prominences disappear in about 1–2 years before the main prominences' zones (MPZ) reach their highest latitudinal distribution. They emerge again when the MPZ vanish. They move from mid-latitudes to the equator prior to the minimum, and later they show a poleward migration where they decay together with those of the type c around the maximum.

Occurrence of prominences of the group b is concentrated mainly in the sunspot zone up to a latitude of 60°. They appear at latitudes of 60° around the maximum of the activity cycle and slowly migrate toward the equator. They disappear when a polar branch of prominences is separated in mid latitudes, or shortly after this period.

Prominences in the group c display a typical distribution of prominences where a formation of polar zones is clearly seen. Moreover, one sees rudiments of prominence branches of a new cycle and small 'chains' as discussed in Minarovjech et al. (1997).

Comparison between the distribution of prominences and local green coronal intensities is shown in Figure 2. Both polar coronal and prominence branches are closely connected. The local maxima of the green corona intensities reach the poles earlier than the prominence maxima. Sometimes these coronal branches are located between two polar prominence branches. Their occurrence is, however, very rare, e.g., Dermendjiev et al. (1994). Behaviour of the equatorial branches for both features of solar activity is very complicated.
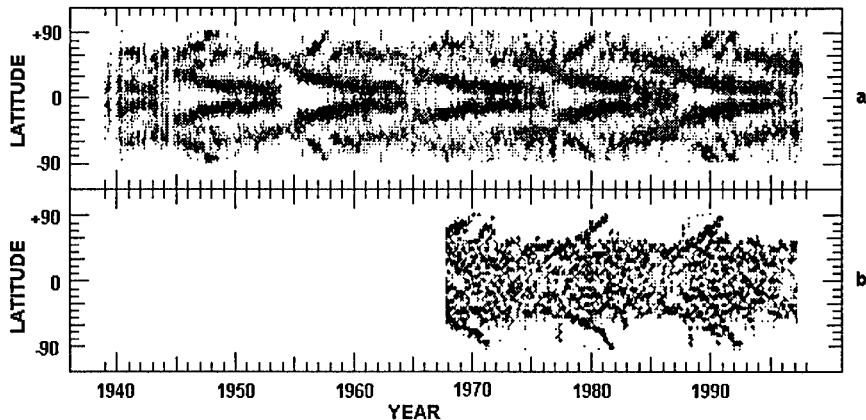
Figure 2.   (a) Time-latitudinal distribution of the green corona local maxima intensities for averages of 27 days as derived from HDS, (b) Time-latitudinal distribution of the values of 'prominence index'.

Prominences, like other pronounced features of solar activity, reflect the existence of magnetic fields (local and global), which originate below the solar photosphere. However, it is well-known that the distribution of magnetic fields on the solar surface is connected with the distribution of the solar wind in the heliosphere. Long-term observations of the prominence distribution and its dynamics could help us predict some properties for the forthcoming solar cycle. Using the above data, it seems to us that a new polar branch has already separated itself from the main equatorial branch, and that this branch could reach the poles in 2002 (north) or 2003 (south).

To forecast the behaviour of both the prominence and coronal development which will occur in the polar regions in cycle 23, we start from Figure 2. When a single polar branch of prominences is observed, then two polar branches are

observed in the green corona. The first branch (principal), which reaches the poles before the prominence branch, is brighter then the second one, occuring after the prominence branch (cycle 21). If two polar prominence branches are observed, the first one is regular, then the distribution of the green corona brightness is dim, and both coronal branches are poorly seen (cycle 20). It seems that such a pattern is observed every 22 years (the Hale cycle). Thus, we suppose that only a single branch of both corona and prominences will occur in the present cycle 23. We note that there is a 1-year timeshift in reaching the poles by the polar prominence branches in favour of the N-hemisphere.

The study of the corona and prominence distributions, especially in high latitudes (which are devoid of sunspots), could also help us solve a question of torsional oscillations as discovered by Howard and LaBonte (1980) and its relation to other solar activity features. As yet, these questions remain open.

References

Altrock, R. C., Rybanský, M., Rušin, V. and Minarovjech, M. 1997, Contrib. Astron. Obs. Skalnaté Pleso, 27, 25

Bumba, V. Rušin, V. and Rybanský, M. 1990, Bull. Astron. Inst. Czechosl. 41, 253

Dermendjiev, V. N., Stavrev, K. Y., Rušin, V. and Rybanský, M. 1994, A&A, 281, 241

Howard, R. and LaBonte, B. J. 1980 ApJ, 239, L33

Makarov, V. and Sivaraman, K. R. 1989, Solar Phys., 123, 367

Minarovjech, M., Rybanský, M. and Rušin, V. 1997, Solar Phys., 177, 357

Rušin, V., Rybanský, Dermendjiev, V. and Stavrev, K. Ya. 1988, Contrib. Astron. Obs. Skalnaté Pleso 17, 63

Secchi, P. A. 1872, Die Sonne, Braunschweig

Tandberg-Hanssen, E. 1974, Solar Prominences, D. Reidel, Dordrecht, Holland

Waldmeier, M. 1973, Solar Phys., 28, 389

Digital "Cartes Synoptiques de la Chromosphere Solaire et Catalogues des Filaments et des Centres d'Activite"

Helen E. Coffey and Christine D. Hanchett[1]

NOAA, National Geophysical Data Center (NGDC), World Data Center A for Solar-Terrestrial Physics, 325 Broadway, Boulder, CO 80303 USA

Abstract. Almost 70 years ago Lucien d'Azambuja published the first "Cartes Synoptiques de la Chromosphere Solaire et Catalogue des Filaments de la Couche Superieure" (d'Azambuja 1928), a compendium of reduced solar observations covering the time period March 1919–January 1920. The compiled database gives both visual and quantitative measures of solar activity beginning with Carrington rotation 876. Since then, data through 1989 have been published in succeeding Cartes Synoptiques issues. The World Data Center A (WDC-A) for Solar-Terrestrial Physics has digitized several long term solar publications, including the numerical text portion of the Cartes Synoptiques. We present an overview of this extraordinary historical solar database. WDC-A is using current technology to meet user requirements for data management, analysis and distribution, has compiled over 100 Megabytes of historical solar data and made it available over the Internet as part of a continuing data rescue effort. The data can be accessed via the World Wide Web at http://www.ngdc.noaa.gov/stp.

1. Cartes Synoptiques

Lucien d'Azambuja investigated solar filament and prominence behavior over many years, and maintained a synoptic program of this phenomena similar to the Zurich sunspot program. He made the connection that the filaments and prominences were the same phenomenon seen from different perspectives on the solar disk (d'Azambuja 1923). He contrasted the behavior of sunspot motions with filaments, noting similarities in rotation rate (equatorial filaments have speeds larger than the higher latitude filaments due to differential rotation of the sun) and lifetimes (d'Azambuja and d'Azambuja 1938). He noted that nearly one half of low latitude filaments suffer disparition brusques and disappear temporarily, reforming in nearly the same shape in 2/3 of all cases (Tandberg-Hanssen 1995). His investigations also included solar-terrestrial effects, connecting the major solar flare of October 13, 1926 with the geomagnetic storm and aurora seen about 31 hours later (d'Azambuja and Grenat 1926), and papers on solar eclipses and comets.

---

[1] Under cooperative agreement with the Cooperative Institute for Research in the Environmental Sciences (CIRES), University of Colorado, Boulder, CO 80309 USA

Figure 1.   Lucien d'Azambuja, photographed in 1961 while working
at McMath-Hulbert Observatory, University of Michigan. Courtesy
of Helen Dodson Prince, reproduced with permission from Sky and
Telescope, September 1970 issue.

D'Azambuja (Figure 1) left a legacy of an extensive historical solar filament
database in the Cartes Synoptiques publications, which began with data for the
year 1919 and continues to the present. In 1960 M. J. Martres assumed respon-
sibility for the publication and maintained the continuing database. Early data
include information about the number of days of observation of the filaments,
their duration, their first and last appearance, the average coordinates, minimum
and maximum length measurements, radial speed maxima, the importance (1 to
10), and general characteristics of the filaments. Several other kinds of statistics
were included over the years. In 1945 d'Azambuja began a detailed listing of
disparition brusques. With the International Geophysical Year (IGY) beginning
in July 1957, a new format for the publication was introduced. The current cat-
alog of filaments contains the filament number in order of decreasing longitude,
coordinates of the center of gravity, importance (1 to 10), height of the promi-
nence at the East and West limb, disparitions brusques observed on the disk,
filaments with lifetimes greater than one rotation, and the number of transits
and number of rotations where the filament has been identified. The current
archive covers 70 years of solar observations, March 1919–December 1989, and
totals 9.12 Megabytes. Figure 2 is a solar butterfly plot of the entire Cartes
Synoptiques filament data archive. In total, there are 41,044 filament regions
recorded. Each data point represents the Central Meridian Passage (CMP) date
of a filament region crossing the solar disk. Note the "rush to the poles" close
to solar maximum when the solar polar magnetic field reversal occurs.

Figure 3 shows the summary of importance values of filament regions for a
given Carrington rotation for the 70 years covered by the the Cartes Synoptiques
archive. Generally, one sees the lower importances at times of sunspot minima.

CARTES SYNOPTIQUES Solar Filament Regions
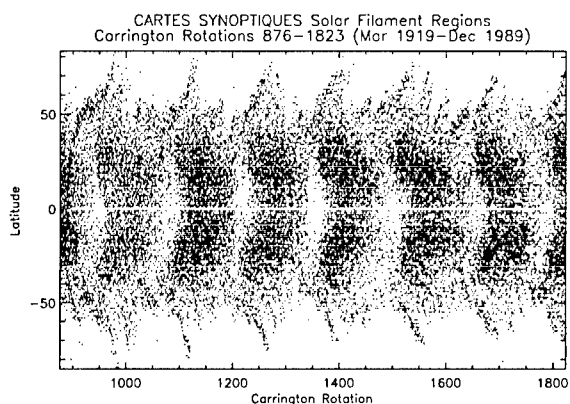Carrington Rotations 876-1823 (Mar 1919-Dec 1989)

Figure 2.   This 70 year solar butterfly plot of the Carte Synoptique
solar filament regions archive by Carrington rotation shows the latitude
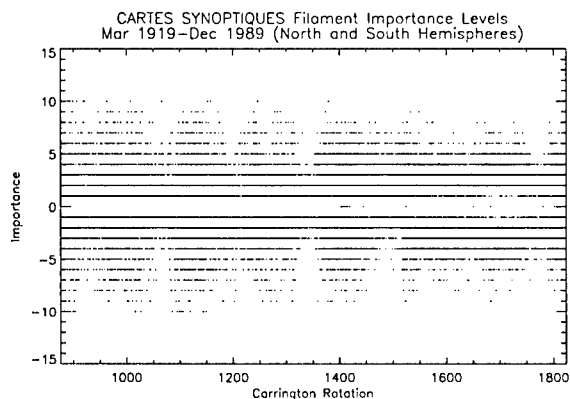distribution of CMP dates of filaments over seven solar cycles.

CARTES SYNOPTIQUES Filament Importance Levels
Mar 1919-Dec 1989 (North and South Hemispheres)

Figure 3.   Importance values of filament regions versus Carrington
rotation for the time period covered by the Cartes Synoptiques archive
(solar cycles 15-22). Northern hemisphere filaments are assigned pos-
itive importance values, while southern hemisphere ones are assigned
negative values.

These importance values are especially low between cycles 18 and 19 (around 1954.3). In addition, there are asymmetries between the two hemispheres. Both hemispheres had low importance values during the 1954.3 minimum. However, the following cycle minimum in 1964.9 shows a predominance of the southern hemisphere contributing to the low values. Anomalously, during the solar cycle 21 maximum (1979.9), a lack of importance 1 values is seen in both hemispheres. Importances cluster around 2 to 5 with a few 6's and 7's seen. Several scientists have noted anomalous behavior during the 1980 time frame (Foukal 1997, private communication). Moreover, there is a general downward trend in large importance values over the 70 years with the most recent large cycles rarely above a value of 6. Early cycles have several importance 10 values and substantial numbers of importance 7 and 8. Perhaps the scaling procedure gradually changed over time.
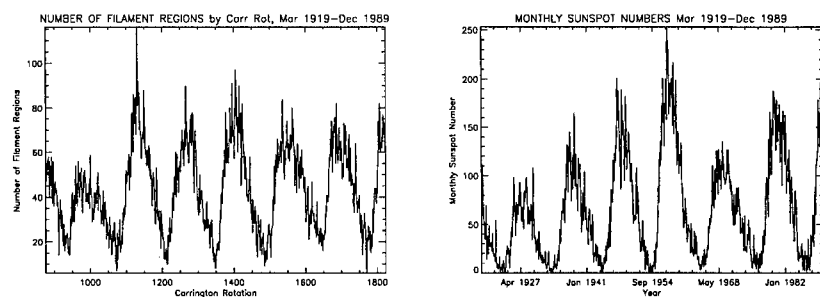
Figure 4.   Left – the number of Cartes Synoptiques filament regions is plotted by Carrington rotation to show the distribution over 70 years. Right – for comparison we plot the Zurich monthly sunspot numbers.

In Figure 4 we show the number of filament regions from the Cartes Synoptiques archive and Zurich sunspot numbers (Sunspot Index Data Center) as a function of time. When these two plots are overlaid, one sees similar behavior, with some delay on the downward curve of the filament data after sunspot maximum, as noted by d'Azambuja and d'Azambuja (1948). However, if you shift the sunspot curve up about 18 units, the curves seem to fit together well. The number of filament regions appears to be more sensitive to solar minima than sunspot number. Perhaps one can use the filament minima behavior to predict the occurrence of sunspot minima and give advance information about the rate of rise of the new solar cycle.

funds. NOAA contributed staff labor for this project.

References

d'Azambuja, L. 1923, Comptes Rendus, 176, 950

d'Azambuja, L. 1928, Annales de l'Observatoire de Paris, Section de Meudon, Tome VI, Fascicule I

d'Azambuja, L., and d'Azambuja, M. 1938, Comptes Rendus, 206, 819

d'Azambuja, L., and d'Azambuja, M. 1948, Annales de l'Observatorie de Paris, Section de Meudon, Tome VII, Fascicule VII

d'Azambuja, L., and Grenat, H. 1926, Comptes Rendus, 183, 701

Tandberg-Hanssen, E. 1995, The Nature of Solar Prominences, Kluwer Acad. Publ., Dordrecht, Holland

Reconstruction of Sun-as-Star Magnetic Field Structure and Evolution Using Filament Observations

Dmitri I. Ponyavin

Institute of Physics, St. Petersburg University, 198904, Russia
E-mail: ponyavin@snoopy.phys.spbu.ru

Abstract. A technique is used to restore the magnetic field of the Sun viewed as star from the filament distribution seen on H_α photographs. For this purpose synoptic charts of the large-scale magnetic field reconstructed by the McIntosh method have been compared with the Sun-as-star solar magnetic field observed at Stanford. We have established a close association between the Sun-as-star magnetic field and the mean magnetic field inferred from synoptic magnetic field maps. A filtering technique was applied to find correlations between the Sun-as-star and large-scale magnetic field distributions during the course of a solar cycle. The correlations found were then used to restore the Sun-as-star magnetic field and its evolution in the late 1950s and 1960s, when such measurements of the field were not being made. A stackplot display of the inferred data reveals large-scale magnetic field organization and evolution. Patterns of the Sun-as-star magnetic field during solar cycle 19 were obtained. The proposed technique can be useful for studying the solar magnetic field structure and evolution during times with no direct observations.

1. Introduction

H_α synoptic charts were first developed by McIntosh to infer magnetic fields from solar images obtained in the $\lambda6553$ line of neutral hydrogen (H_α filtergrams). Each chart is a map of the entire solar globe in cylindrical Carrington coordinates corresponding to the mean solar rotation rate period of 27.2753 days. H_α charts show patterns of neutral lines (lines of magnetic polarity reversals) mapped from filaments and a variety of chromospheric features governed by magnetic fields. Correlations of H_α synoptic charts with direct large-scale magnetic field measurements, like the Stanford data, were well established.

Thus, the inference of lines of polarity inversion could serve as a valuable alternative to data derived by magnetograph observations, especially in the absence of direct measurements. McIntosh (1979) published an Annotated Atlas of H_α synoptic charts for solar cycle 20. Furthermore, Makarov and Sivaraman (1985) inferred photospheric magnetic fields from H_α filtergrams back to the beginning of the century. The purpose of our paper is to show a possibility to infer from H_α synoptic charts another important feature of solar magnetism, the Sun-as-Star magnetic field.

2. Data Analysis and Results

Severny (1969) was first to discover that the Sun was a magnetic variable star. To prove this, he used the mean magnetic field observations seen as a star provided in Crimea since 1968. Later close associations between the Sun-as-Star magnetic field and interplanetary magnetic field sector structure of the solar wind were established by Scherrer et al. (1977). Kotov et al. (1977) showed that the day-to-day Sun-as-Star magnetic field measurements are highly correlated (0.87) with the large-scale magnetic field inferred from H_α observations. The procedure they used was based on averaging the H_α synoptic charts over a range of 50° in latitude. By changing the longitude window, they found the best correlation with 5 days, corresponding approximately to 70° in longitude.

A similar averaging procedure was applied in this paper. H_α synoptic charts were transformed into digital form by scanning latitudes of intersection of neutral lines with the meridian of Carrington longitude passage. The grid used for interpolation contained 36 longitude bins, each 10 heliographic degree wide, and 18 latitude bins, each representing an equal increment of 10°. Magnetic fields were specified to be +1 and −1 to describe the positive and negative polarity. Values in the vicinity of neutral lines were then linearly interpolated.

A moving window of latitudinal and longitudinal extents of 60° by 60° was selected corresponding to the maximum correlation with the magnetograph data. To decrease noise an additional smoothing technique was applied: 5 running synoptic charts were superposed to improve the reconstruction results. The main results of this smoothing procedure are the following:

- Uncertainties in inferring neutral lines using a single H_α synoptic chart could be reduced. It is more important for the much noisier H_α data in the Makarov and Sivaraman reconstruction in the absence of magnetograph observations.

- Long-lived features in the large-scale magnetic field organization (active longitudes and latitudes) are more pronounced.

- Effective synoptic charts of magnetic fields reveal not only the polarity distribution but also effective fluxes of the magnetic field.

- Flux balances in the positive and negative polarity are also supported.

- The contribution of the axisymmetrical dipole component that is poorly manifested in the measured line-of-sight magnetic field has been increased.

Full-disk measurements of the mean magnetic field began at Stanford in 1975 and have continued through the present. A summary of Stanford day-to-day observations of the mean magnetic field seen as star is presented in Figure 1. A running filtering technique was applied to cover gaps and reveal the large-scale magnetic field organization. Figure 1 shows a Bartels display of available data covering solar cycles 21 and 22. Time increases to the right in the panel. In this format horizontal patterns indicate long-lived structures that return with a 27-day synodic rotational period. Sunspot cycle activity during the period 1976–1996 are shown at the top. Similar patterns of the mean magnetic field restored using our technique for solar cycles 19 and 20 have been presented in Figures 2

and 3, respectively. A large-scale organization of magnetic fields can clearly be seen from the Figures. Original magnetic fields reach their maximum values near solar maximum, whereas amplitude variations of the inferred field are less pronounced over the solar cycle. However, comparison of solar cycles 21 and 22 with the previous cycles indicates the general character of the magnetic polarity changing through the whole period of observations. Two systems of magnetic field rotation rate could be observed. The first pattern indicates a rotation rate with a period greater, and the second a little slower than 27 days. These periods are similar to those found earlier by Kotov (1986), 28.2 and 26.9 days, that may reflect the north-south asymmetry of solar activity (Antonucci et al. 1990). In summary, the technique presented here can serve as a meaningful tool to probe the large-scale organization of solar magnetic fields and its evolution in the past.

References

Antonucci, E., Hoeksema, J.T. and Scherrer P.H. 1990, ApJ, 350, 296

Kotov, V.A., Stepanyan, N.N. and Scherbakova, Z.A. 1977, Izv. KrAO, 66, 75

Kotov, V.A. 1986, Izv. KrAO 75, 39

Makarov, V.I. and Sivaraman, K.R. 1986, Atlas of H_α synoptic charts for solar cycle 19 (1955–1964), Kodaikanal Obs. Bull. 7, 2–138

McIntosh P.S. 1979, Annotated atlas of H_α synoptic charts for solar cycle 20 (1964–1974), Report UAG-70, WDC-A, Boulder

Scherrer, P.H. et al. 1977, Solar Phys., 52, 3

Severny, A. 1969, Nature 224, 53
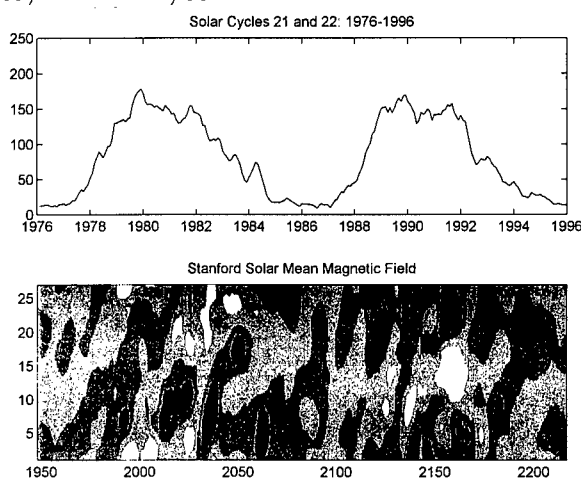
Figure 1.   Bartels display of the mean magnetic field measured at Stanford. Bottom: time increases to the right for Bartels rotations 1948–2217. Negative polarity is darker. Horizontal patterns indicate long-lived structures with 27–day synodic rotation periods. Top: monthly mean sunspot numbers smoothed during 1976–1996.
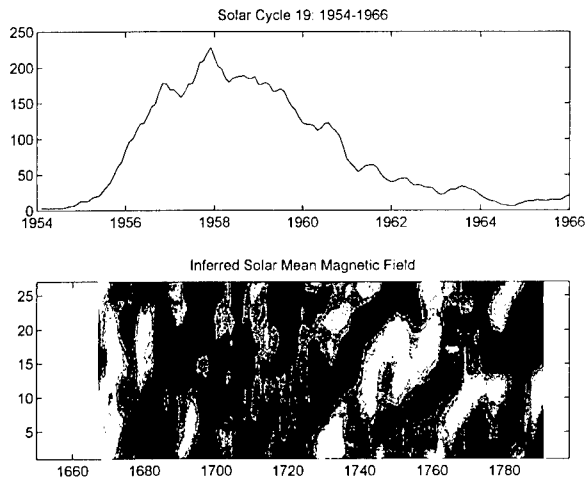
D. I. PONYAVIN

Figure 2. Bartels display of inferred mean magnetic field from H_α synoptic charts. Same as Figure 1 but for Bartels rotations 1650–1798.
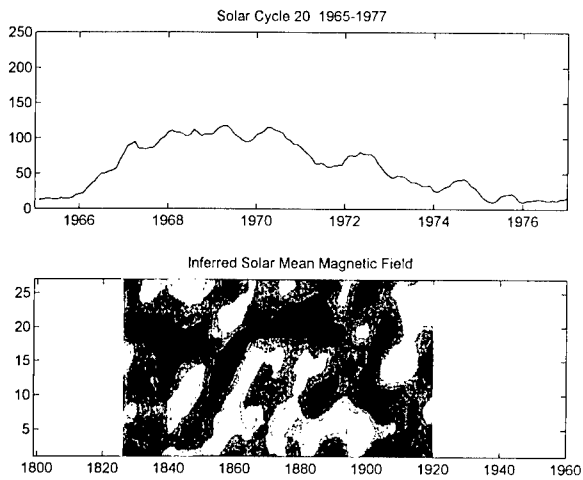

Figure 3. Same as Figure 1 but for Bartels rotations 1820–1920.

Instrumentation

A New Station of Prominence Patrol Observations in Slovakia

I. Dorotovič, B. Lukáč and T. Pintér

Slovak Central Observatory, 94701 Hurbanovo, Slovak Republic. E-mail: suh@netlab.sk

M. Rybanský

Astronomical Institute of the Slovak Academy of Sciences, 05960 Tatranská Lomnica, Slovak Republic. E-mail: rybansky@ta3.sk

Abstract. The data from prominence observations provide an opportunity to study spatio-temporal distribution of prominences over a solar cycle. The Slovak Central Observatory (SCO) at Hurbanovo (South Slovakia) in cooperation with the coronal station at Lomnický Štít (Astronomical Institute of the Slovak Academy of Sciences, Tatranská Lomnica, Slovakia) constructed a Lyot coronagraph with parameters D/f of 90/1250/3750 mm in 1996 for regular prominence patrol at Hurbanovo (112 m above sea level).

The aim of this collaboration is a joint annual publication of a catalogue of the observed prominences for each year. This paper also describes the form of the catalogue. The authors would appreciate if other observational stations would join this activity. The editor of the catalogue will be the SCO at Hurbanovo.

1. Introduction

One of the first results of prominence research was the discovery of the polar zone of prominences (Secchi 1872) and its movement toward the poles. Thanks to a large number of observations of prominences and filaments we have an almost perfect image of their distribution around the solar limb and their evolution during a cycle. The observation of prominences is very important for understanding solar activity. It is generally known that solar activity influences the heliosphere, including our Earth.

The regular photographic observations of prominences at the coronal station at Lomnický Štít (Astronomical Institute of the Slovak Academy of Sciences, Tatranská Lomnica, Slovakia) have been carried out since May 1967. 29,176 prominences were observed through the end of March 1997. Table 1 gives an overview of the number of days with prominence observation every year. The average number of days with prominence observations per year over the period 1968–1996 is 119 days (the year 1967 was not taken into account because observations started in May).

Table 1.   The number of days with prominence observations over the
period 1967–1996.

Year	Number of days	Year	Number of days
1967	78	1982	144
1968	113	1983	126
1969	102	1984	125
1970	100	1985	100
1971	113	1986	147
1972	132	1987	134
1973	91	1988	152
1974	78	1989	142
1975	107	1990	147
1976	87	1991	119
1977	104	1992	136
1978	119	1993	125
1979	129	1994	117
1980	117	1995	112
1981	112	1996	121

2.   Description of the Catalogue of Solar Prominences and Its Use

The Astronomical Institute of the Slovak Academy of Sciences and the Astronomical Institute of the Bulgarian Academy of Sciences published jointly the catalogue of solar prominences (Rušin et al. 1988, 1994). Later the Astronomical Observatory at Valašské Meziříčí in the Czech Republic joined the regular observations of prominences. Table 2 shows the form of the catalogue.

Table 2.   A sample of the catalogue.

1	2	3	4	5	6	7	8	9	10	11
...	...	...	...	...	...	...	...	...	...	...
29100	97	3	9.25	1919	165	+43 E	3	30	1	60
29101	97	3	9.25	1919	165	+36 E	3	40	2	60
29102	97	3	9.25	1919	165	+18 E	2	40	1	50
29103	97	3	9.25	1919	165	+6 E	3	40	1	50
29104	97	3	9.25	1919	165	-44 E	3	30	2	60
29105	97	3	9.25	1919	345	-18 W	5	40	2	120
29106	97	3	9.25	1919	345	+16 W	4	50	1	130
29107	97	3	9.25	1919	345	+45 W	15	30	3	330
...	...	...	...	...	...	...	...	...	...	...

The first column gives the number of the prominence (running from the beginning of observation); the second, third and fourth columns give the time of the observation (year, month, day and decimal fraction thereof); the fifth column gives the number of the Carrington rotation; the sixth column contains the Carrington heliographic longitude of the prominence; the seventh column the heliographic latitude of the prominence centre for the given limb (E or W); the eighth column the width of the prominence in degrees (at the solar limb); the prominence height (in arcsec) above the solar limb is given in the ninth column; the tenth column contains the estimated brightness of the prominence on a three-grade scale (the estimation is made during the observation); and the eleventh column gives the prominence area. The unit of area is 1 degree in the

positional angle times 1 arcsec in height (this value can be easily transformed into standard units, e.g. milionths of the solar surface area, using the factor 0.173).

The data on prominence observations are regularly sent to the international centres and published in Solar Geophysical Data and Solnechnye Dannye.

The data can be used, e.g., for studying the spatio-temporal distribution of prominences over a solar activity cycle according to different criteria. The results of such investigations are presented by Minarovjech et al. (1998, these proceedings).

3.   Observation of Prominences at Hurbanovo

The number of days with prominence observations per year could be increased by increasing the number of observation stations. Therefore, M. Rybanský from the Astronomical Institute of the Slovak Academy of Sciences in Tatranská Lomnica proposed to extend the observational network to other astronomical observatories in Slovakia. Within the framework of this project a Lyot coronagraph of parameters D/f of 90/1250/3750 mm was made in 1996 for the prominence patrol at Hurbanovo. The Astronomical Observatory at Hurbanovo is 112 m above sea level. Due to unfavourable weather conditions only test observations have been made so far. An Hα filter with a bandpass of 0.5 nm was ordered from the Andover Corporation, Salem, NH, USA. Therefore, no preliminary results or examples of photographic observations can be presented here.

4.   Conclusions

The main goal of this project is to obtain as many observations as possible and prepare a joint publication of observed prominences once a year. It is necessary to emphasize that the project is open to all those who want to join this common patrol observations of prominences. A large network of observational stations could lead to an increased number of observational days in one year. On the basis of these observations we could create a better understanding of solar activity from the point of view of the occurrence of prominences. Therefore, the authors would appreciate the participation of other observational stations. SCO will be the editor of the catalogue and will publish it. We intend to collect the data quarterly and make them available on our home page in the future.

References

Rušin, V., Rybanský, M., Dermendyev, V., Stavrev and K. Ya 1988, Contrib. of the Astron. Obs. Skalnaté Pleso, 17, 63

Rušin, V., Rybanský, M., Dermendyev, V., Stavrev and K. Ya 1994, Contrib. of the Astron. Obs. Skalnaté Pleso, 24, 135

Secchi, P. A. 1872, Dier Sonne, Braunschweig, p. 520

The Present and Future of the Prominence Observations at Valašské Meziříčí Astronomical Observatory

L. Lenža and D. Dokoupilová

Astronomical Observatory, Vsetínská 78, 757 01 Valašské Meziříčí, Czech Republic

Abstract. This observatory is not a large institution, though we do carry out long term photographic monitoring of prominences. Our intention is to inform everybody about our observation programmes, the quality of our observations, our archive and the possibilities for its use.

We present examples of our photographic observations, an electronic archive of observation intervals and events, a prominence catalogue, and we discuss possible future co-operation.

1. Introduction

The observatory at Valašské Meziříčí was founded in 1955 and in the year 1964 the building for special observations was opened. One part of our work is the photographic observation of the Sun, showing its activity. We photograph the whole solar disc (overview photos), with details of the photosphere (sunspot groups) and solar prominences. All of the observations are now in our archive.

2. Solar Observations

We have been making photographic observations of the Sun since 1957, when our archive of overview photos started (October 4, 1957) and now there are over 9425 photos. The images are being made by a Zeiss E 120/1920 mm refractor, where the diameter of the solar disc in negative is 66 mm – see Figure 1. We make photographs using planfilm FOMA Repro O5.

Photographs of sunspot groups have been made since 1981 (April 7, 1981) by a Zeiss 200/3000 mm refractor (see Figure 2). We are using negative material ORWO MA8. One millimetre on the negative is 7.5 arc sec. The number of photographic observations is now more than 1750 series of pictures.

3. Prominence Observations

Prominence observations are done with an Hα coronograph with a Zeiss E 150/1950 mm objective with Šolc filter (passband 0.5 nm) and KODAK 2415 Technical Pan film or KODAK SO115 film.

In the period between June 15, 1970 and November 8, 1983 the observations were very irregular, so we have only a few tens of series of observations. Regular
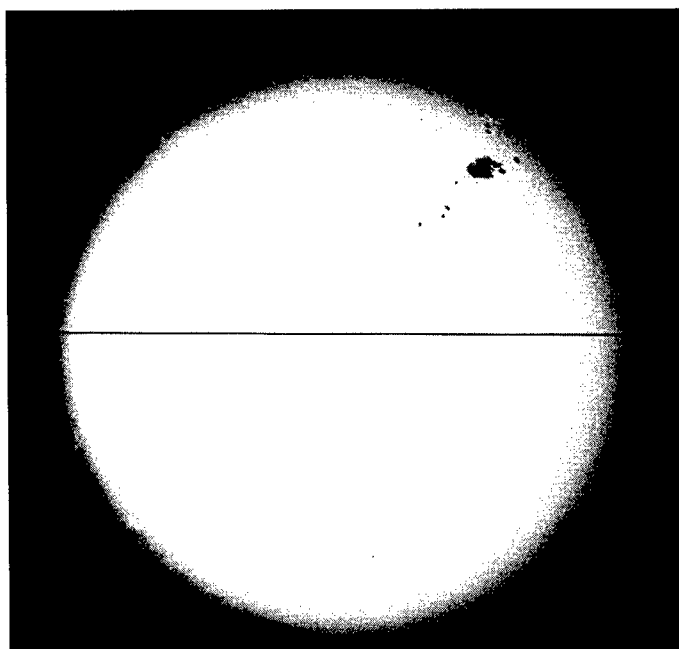
Figure 1. Date: September 27, 1991; Time: 14:28 UT; Device: Zeiss E 130/1930 refractor; Material: ORWO DU3; Observer: Libor Lenža.
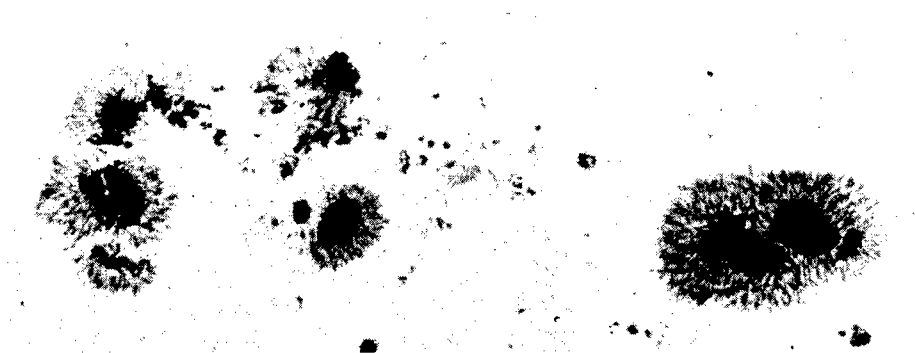

Figure 2. Date: July 4, 1992; Time: 07:52 UT; Device: Zeiss AS 200/3000 refractor; Material: ORWO MA8; Observer: Libor Lenža.

observations began on July 24, 1984 and have continued until today. Since 1991 we have done our observations more intensively. From that period we have over 850 series of pictures. And in 1993 we started to send overview maps to the WDC-A in Boulder.

In May 1991 we started non-periodic photographic observations of active prominences. In 1992 we began with a prominence photographic patrol. Up to the present we have registered about 160 active events.

4. The Quality of Observations

The observation conditions are worst in the winter and best in the summer months. The quality of our images is represented in the pictures shown in Figure 3. The angular resolution reaches about 2 arc sec. Generally we can say that these images are applicable for studying dynamics and the morphology of events.

5. The Archive and its Availability

All the negatives of photographic observations are signed with the necessary data and centrally archived. At present we are putting the archive into electronic files so it could be available to anyone interested in it. Those who are interested in it will then automatically receive updates.

In the first archive is information about observing the photosphere (detail and overview image). This archive provides information on when the observation was done and what its quality was. In case you would like to have any of our images, you can write to us with a particular request based on our electronic archive. At present this archive contains data for the years 1989–1996.

Prominence observations are archived in the same way. Presently it contains data only for the year 1993.

For each observation day a drawn map is available which is used for statistical processing. They can also be used for rating the co-ordinates, altitudes and other statistical parameters of each prominence. Data for the year 1993 are listed in a catalogue, which is identical to the catalogue produced by the Lomnický Štít Observatory in the Slovak Republic.

Information about active events is being archived separately. This includes information about observing intervals. If you are interested in these data, we are able to send standard photographs or digitized images (by TV CCD camera).

6. Conclusion

At present we are putting the basic information from the archive into electronic files for each type of observation. We are also completing the prominence catalogue.

We are now testing our TV CCD system for observing prominences. We would like to co-operate with other observatories. Our observations and data are available to any astronomer.
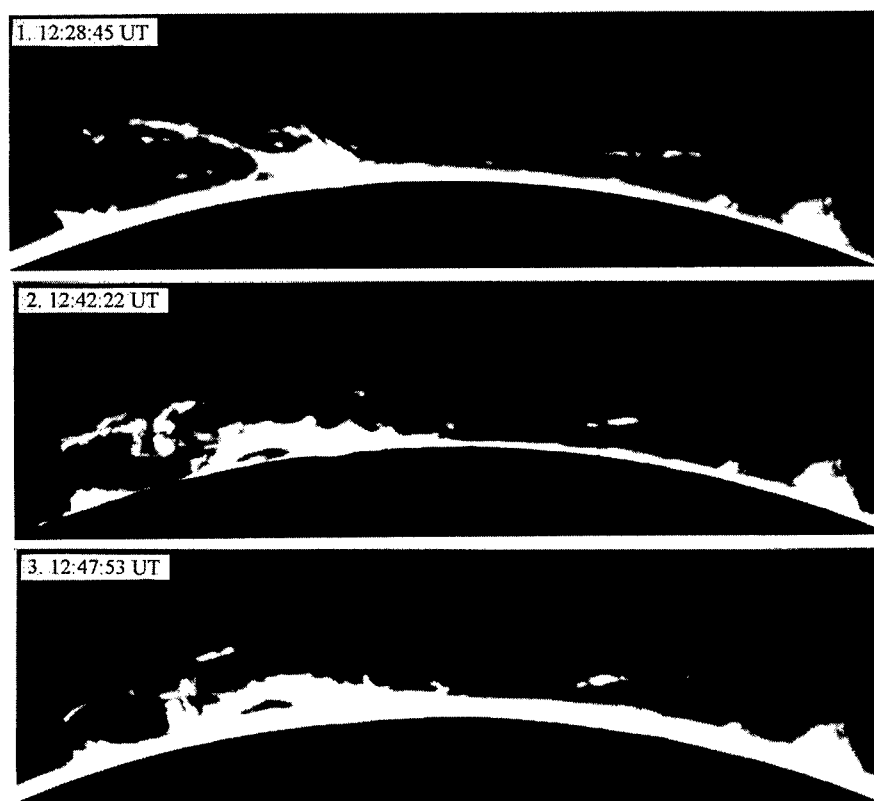
Figure 3.   Date: March 5, 1997; Device: Hα coronograph with Zeiss E 150/1950 mm objective with Šolc filter (passband 0.5 nm); Position: N14E; Material: KODAK SO115; Observer: Ladislav Šmelcer.

Development of an Instrument Based on a Fibre-Bonded CCD Camera for Prominence Observations

V. K. Verma, Wahab Uddin and V. P. Gaur

Uttar Pradesh State Observatory, NainiTal-263129, India

Abstract. We have devloped and tested an instrument based on a fibre-bonded CCD camera for observations of solar prominences. To record faint prominences we have used a solid aluminized glass cone which reflects bright solar disc light outside the telescope tube. The prominence monitor is installed at the back end of a 15-cm f/15 coude refractor telescope after the H-alpha filter. This prominence monitor is capable of recording prominence images at an interval of 5 sec, but during prominence eruptions it can record images at an interval of 2 sec.

1. Introduction

The term prominence is used for a large variety of objects which are characterized by their occurrence in the chromosphere and/or in the corona, by their greater density than the coronal surroundings and by temperatures ranging from about 10^4 K to coronal values at the interface to the corona. They appear as bright (cool and dense) features above the solar limb (Tandberg-Hanssen 1977). High resolution photographs of prominences show that they are made up of fine thread-like structure (Tandberg-Hanssen 1974). The observation of such fine structure in the presence of solar disc light is difficult. Solar prominences are faint coronal features and are best observed through H_α filters of passband 2 to 3Å. The formation and disappearance of solar prominences are not well understood because of the lack of homogeneous data on them. Prominences arouse considerable interest and are generally photographed by means of a prominence attachment or coronagraph. It is possible to construct a prominence attachment or coronagraph for prominence observations as described by Mazereau and Bourse (1985), Volker (1994) and Lille (1995). To reduce bright solar disc light solar observers are using a metallic stop at the prime focus and then reimaging with another lens system. Using the technique described above, coronagraph or prominence attachment systems have been developed by solar scientists at the National Astronomical Observatory, Japan; High Altitude Observatory, Boulder, USA; Mauna Loa Observatory, Hawaii; National Solar Observatory, Sunspot, NM, USA and other places. In the present paper we report on an instrument that has been developed at at the Uttar Pradesh State Observatory (UPSO) in NainiTal, India for the observations of solar prominences.
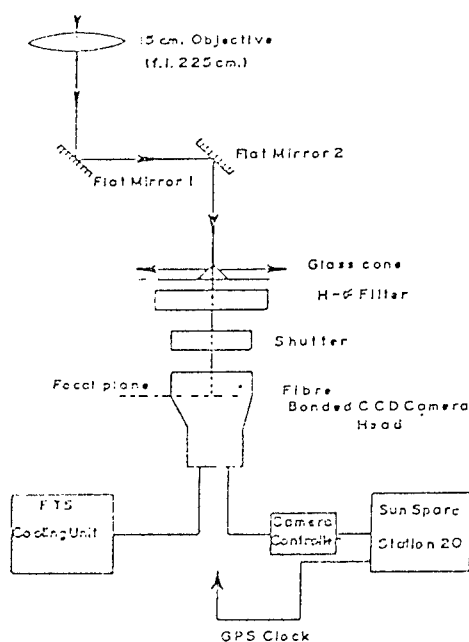
Figure 1.   Schematic diagram of 15-cm Coude refractor telescope and back end instrument.

2.   Design and Specifications of Prominence Monitor

The schematic diagram of the 15-cm f/15 Coude refractor telescope and back end instrument for prominence observations is shown in Figure 1.

The CCD camera system employs a thermoelectrically cooled FTS probe camera head (ambient temperature –42°C) with a TK 1024 CCD class I chip (pixel size 24 × 24 μ). The fibre-bonded CCD instrument is installed at the focus of the 15-cm Coude refractor telescope and yields a pixel size of 58.8 × 58.8 μ and gives a plate scale of 5 arcsec/pixel. The camera controller of the system has a variable readout rate of 0.5–1.0 Mpixels/sec with 12 bit resolution. The software, which controls the working of the camera controller, is installed on a Sun Sparc Station 20, 50 Hz computer having 7.3 GB disk capacity and a 14 GB cartridge tape drive. A GPS (Global Position System) clock is connected to the computer to record time with an accuracy of 1 ms in the header of prominence images. The Sun computer and software help us to record prominence data at high readout rates. The readout rate of the camera controller was set at 990 K pixels/sec because at this readout rate the CCD's dark current was found to be minimum. In Table 1 we show the salient features of the prominence monitor developed at the UPSO.

In the Table, R is the radius of the Sun and the pixels of the CCD chip are square. In Figure 2 we show the prominence monitor which includes the Sun computer, CCD camera head, H_α filter having passband 3Å and aluminized glass cone attached to the back end of the telescope. This telescope forms a 20.6 mm image of the Sun's disk at the chip of the fibre-bonded CCD having an area

Table 1.   Salient Features of the Prominence Monitor

Features	Specifications
Telescope	15-cm f/15
Wavelength	6563Å
Passband	3Å
FOV	5.8 R x 5.8 R
Plate Scale	5.0 arcsec/pixel
Fibre-bonded CCD Chip	1024 x 1024
Pixel size	58.8 micron
Size CCD chip	60 mm
Read out rate	990 kHz
Time accuract	1 ms
Computer	Sun Sparc 20

Figure 2.   Prominence monitor attached to the telescope.

60.2 mm × 60.2 mm. Therefore, each image recorded by the computer gives us a view of a prominence's extension in the corona equal to the diameter of the sun. During initial testing we could see good prominence features, but during the later stage of testing with the CCD camera head, one of the cards was damaged, therefore, we are unable to show actual photograps taken with the prominence monitor. In Figure 3 we show a photograph taken by the Fibre-bonded CCD camera during the total solar eclipse of October 24, 1995. Testing with the repaired camera head is in progress, and we are hopeful that by October 1997 we will be able to begin observations with the prominence monitor.
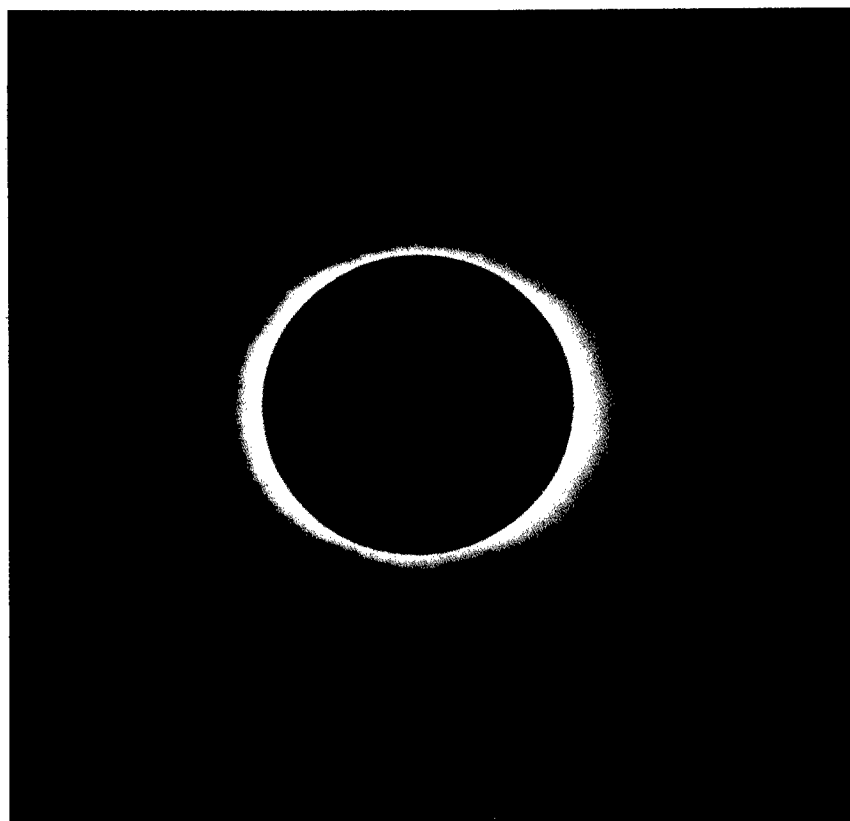
Figure 3.   A photograph taken by the Fibre-bonded CCD camera during the total solar eclipse of October 24, 1995.

References

Lille, W. 1995 in Solar Astronomy Handbook, (eds.) R. Beck, H. Hilbrecht, K.
     Reinsch and P. Volker, Willmann-Bell, Inc, Virginia, p. 49
Mazereau, P. and Bourse, P. 1985, in High Resolution Astrophotography, (ed.)
     Jean Dragesco, Cambridge University Press, Cambridge, p. 75
Tandberg-Hanssen, E. 1974, Solar Prominences, D. Reidel, Dordrecht, Holland,
     p. 10
Tandberg-Hanssen, E. 1977, in Illustrated Glossary for Solar and Solar-Terres-
     trial Physics, (eds.) A. Bruzek and C.J. Durrant, D. Reidel, Dordrecht,
     Holland, p. 97
Volker, P. 1994, in Compendium of Practical Astronomy, G. D. Roth, Springer-
     Verlag, Berlin, p. 31

List of Unpublished Papers

The following papers were presented at the Workshop and appeared in the meeting abstract book, but were not submitted as papers for publication in these Proceedings.

The Origin of Filament Mass (**Review**)
     S. Antiochos

Theory of Prominence Eruption
     J. Chen

Eruption of Prominences and CMEs: Comparison of Theoretical Results and LASCO Observations
     J. Chen, R. Howard, G. Brueckner, O. St. Cyr, P. Lamy, R. Schwenn and G. Simnett

Rapid Variations in Motion and Temperature of a Large Prominence Observed with CDS/SOHO
     P. Brekke, O. Engvold and R. Harrison

Flare-Associated Filament Eruption Observed in Soft X-rays by Yohkoh on 1992 May 7
     J. Khan, Y. Uchida, A. McAllister, Z. Mouradian, I. Soru-Escaut, E. Hiei and T. Watanabe

He I 10830Å Polarimetry of a Filament
     H. Lin, M. Penn and J. Kuhn

The Field Configuration of Filaments, Magnetic Clouds and the Solar Cycle
     D. Rust and V. Bothmer

High Resolution Numerical Simulation of Magnetic Field Emergence Through the Solar Atmosphere and the Formation of Filaments
     D. Spicer, M. Rilee and R. Sudan

Dynamical Characteristics of Disappearing-Filament Associated Interplanetary Disturbances
     T. Watanabe, Y. Nakagawa, Y. Kozuka and M. Kojima

Author Index

Airapetian, V. 37
Alissandrakis, C. 55
Allen, U. 290
Altieri, B. 201
Antonucci, E. 370
Anzer, U. 213
Aulanier, G. 86, 366

Bagenal, F. 290
Ballester, J. 143, 247
Barnes, J. 235
Bashkirtsev, V. 90, 131
Bastian, T. 55
Baudin, F. 139, 314
Beaufort, T. 201, 243
Belenko, I. 66
Benna, C. 370
Berger, M. 102
Bocchialini, K. 55, 314
Bommier, V. 434
Bougaenko, O. 66
Brekke, P. 135
Brueckner, G. 475
Burkepile, J. 366
Byrne, B. 227, 251

Cable, S. 384
Callebaut, D. 111, 442
Cartledge, N. 265
Cheng, C. 115, 278
Chiuderi-Drago, F. 55
Choe, G. 115, 278
Ciaravella, A. 370
Cliver, E. 479
Coffey, H. 488
Collier Cameron, A. 235
Cravatte, S. 201

David, F. 201
de Boer, C. 196
De Forest, C. 366
de Jong, J. 243
Delaboudiniere, J. 55, 135, 475
Delannee, C. 314, 388
Demoulin, P. 78, 86, 350, 366

Dere, K. 475
Dermendjiev, V. 326, 354
Dokoupilova, D. 502
Dorotovic, I. 499
Dumitrache, C. 221
Duvet, L. 201

Eibe, M. 227, 251
Engvold, O. 23, 135

Ferreira, J. 239
Filippov, B. 94, 342
Fineschi, S. 370
Foing, B. 201, 243
Forbes, T. 350
Foukal, P. 119, 446
Fulisaki, K. 384

Gaizauskas, V. 257, 269, 286, 439
Galsgaard, K. 282
Gardner, L. 370
Gaur, V. 506
Giodano, S. 370
Gopalswamy, N. 358
Gorshkov, A. 190, 209
Goudoin, Ph. 243
Gupta, S. 334

Hanchett, C. 488
Hanoka, Y. 358, 366
Harrison, R. 55
Harvey, K. 269
Heinzel, P. 188, 205, 209, 213, 397
Henrich, N. 201
Hiei, E 380
Hirose, S. 384
Howard, R. 475
Hudson, H. 376
Hundhausen, A. 290, 430

Ichimoto, K. 217, 376
Ioshpa, B. 393
Irie, M. 376
Isenberg, P. 350

513